NOTICE

The quality of this microform is heavily dependent upon the quality of the original thesis submitted for microfilming. Every effort has been made to ensure the highest quality of reproduction possible.

If pages are missing, contact the university which granted the degree.

Some pages may have indistinct print especially if the original pages were typed with a poor typewriter ribbon or if the university sent us an inferior photocopy.

Reproduction in full or in part of this microform is governed by the Canadian Copyright Act, R.S.C. 1970, c. C-30, and subsequent amendments.

AVIS

La qualité de cette microforme dépend grandement de la qualité de la thèse soumise au microfilmage. Nous avons tout fait pour assurer une qualité supérieure de reproduction.

S'il manque des pages, veuillez communiquer avec l'université qui a conféré le grade.

La qualité d'impression de certaines pages peut laisser à désirer, surtout si les pages originales ont été dactylographiées à l'aide d'un ruban usé ou si l'université nous a fait parvenir une photocopie de qualité inférieure.

La reproduction, même partielle, de cette microforme est soumise à la Loi canadienne sur le droit d'auteur, SRC 1970, c. C-30, et ses amendements subséquents.

WIND INDUCED NATURAL VENTILATION OF LOW-RISE BUILDINGS FOR LIVESTOCK HOUSING BY THE PRESSURE DIFFERENCE METHOD AND CONCENTRATION DECAY METHOD

by

Yves Choinière, P.Eng.
Engineering Resources Unit
Resource Management Branch
Ontario Ministry of Agriculture and Food
Alfred College of Agriculture and Food Technology
Alfred, Ontario
K0B 1A0

A thesis
presented to the University of Ottawa
in partial fulfillment of the
requirements for the degree of
Master of Applied Science
in
Civil Engineering

Ottawa, Ontario

April, 1991

ISBN 0-315-70518-3

UNIVERSITÉ D'OTTAWA
UNIVERSITY OF OTTAWA

Cet ouvrage est dédié à la douce Hélène

et

à mon petit fiston Jean-Philippe; ses sourires et son insouciance d'enfance

ACKNOWLEDGEMENTS

The author would like to express his deepest appreciation to Dr. H. Tanaka, Head of the Civil Engineering Department, University of Ottawa, for his tremendous support and collaboration in this research project.

The author gratefully acknowledges K. Boyd, P.Eng., Education and Research Fund, Ontario Ministry of Agriculture and Food, Agri-Centre, Guelph, Ontario; C. Weil, P.Eng., Head of the Agricultural Engineering Department and M. Paulhus, P.Ag., Principal, Alfred College of Agriculture and Food Technology, Alfred, Ontario; G. Garland, P.Eng., Head of the Engineering Resources Unit, Resource Management Branch, and V. Spencer, P.Eng., Manager of the Resource Management Branch, Guelph, Ontario for their support and funding.

Special thanks are addressed to Dr. R.L. Wardlaw, Head; M.G. Savage, P.Eng., and Dr. M. Nituch, P.Eng., Research officers; T. Brown and V. Malhoney, Technical officers; all of the Low Speed Aerodynamic Laboratory, National Research Council of Canada for their extensive and helpful contributions during this study.

The author is thankful for technical advice given on scale modeling for low-rise buildings by Dr. B.J. Vickery, of the Boundary Layer Wind Tunnel Laboratory, University of Western Ontario, London, Ontario.

Mr. R. Flaviani, technical officer, and Dr. G.D. Lougheed, research scientist, Fire Research Division, National Research Council of Canada, are acknowledged for their help with the optical device calibration for the laser tests.

Grateful acknowledgements are addressed to Dr. L.P. Lefkovitch, Statistical Services, Research Program Services of

Agriculture Canada, Ottawa, Ontario, for his contribution to the statistical data interpretation of the concentration decay method.

Thanks are also extended to A. Olson, J.-M. Leclerc, engineering technologists; R. Pella, draftsman of the Animal Research Centre, Agriculture Canada, Ottawa, Ontario, for their assistance in association with the wind tunnel tests and drawings' preparation.

The collaboration of Dr. J.A. Munroe of the Animal Research Centre, Agriculture Canada, Ottawa, has been extremely prolific especially for the data analysis and report writing during the entire project.

Mrs. H. Desrochers, P.Ag., Alfred College of Agriculture and Food Technology, is acknowledged for her help during the wind tunnel experiments and continuous support during the writing of the thesis.

Very special thanks are addressed to Mrs. A. S.-Tremblay and Mr. S. Tremblay, Alfred College of Agriculture and Food Technology for their precious help during the wind tunnel tests, their intensive work for the data processing and analysis, as well as their extraordinary productive support for the writing of the thesis.

Finally, the continuous efforts of Mrs. M.-A. Vallée, office manager, Ms D. Lefebvre, agricultural technician and Mrs. D. Gariépy, secretary, for the editing of this thesis have been extremely appreciated.

The financial support provided by the Ontario Ministry of Agriculture and Food, Agriculture Canada, Ontario Hydro Technical Services and Development for Agriculture, the Canadian Electrical Association, and the Ontario Pork Producers' Marketing Board was greatly appreciated.

ABSTRACT

Measurements of the external pressure coefficients around open and sealed 1:20 scale models of a low-rise, naturally ventilated building with a gable roof for livestock housing were made in the NRCC wind tunnel. In addition, the internal pressure coefficients were recorded within the open models. The pressure difference method was used to estimate the local ventilation rates and calculate ventilation rate coefficients for various wind angles of incidence. To complete the study for open models, the concentration decay method was used to measure an "effective" ventilation rate coefficient.

All structural configuration changes of the building had an effect on: the external pressure coefficient distributions, calculated and measured internal pressure coefficients, air inlet and outlet zones, magnitude of the local airflows through individual openings, and on the calculated ventilation rate coefficients. As well, there were considerable differences between results for the sealed and open models especially at the ridge level.

Generally, the comparisons between the ventilation rate coefficients of the open and sealed model suggest that the larger the total sidewall, end wall and ridge opening areas were, the greater the discrepencies were between open and sealed models' predictions.

From the results of the concentration decay method, it appears that the addition of end wall openings had major effects on the "effective" ventilation rate coefficients, while there was little difference reported when the three different ridge types were used.

The calculated ventilation rate coefficients (by the pressure difference method) were generally under-predicting the measured "effective" ventilation rates (by the

concentration decay method) for most building configurations, except for those using the 400 mm ridge with open end walls.

TABLE OF CONTENTS

TABLE OF CONTENTS continued

TABLE OF CONTENTS continued

TABLE OF CONTENTS continued

TABLE OF CONTENTS continued

TABLE OF CONTENTS continued

TABLE OF CONTENTS continued

LIST OF TABLES

LIST OF TABLES continued

LIST OF FIGURES

LIST OF FIGURES continued

LIST OF FIGURES continued

LIST OF FIGURES continued

LIST OF FIGURES continued

LIST OF FIGURES continued

LIST OF FIGURES continued

GLOSSARY

150	full scale size of ridge (mm)
400	full scale size of ridge (mm)
800	full scale size of sidewall (mm)
400	full scale size of sidewall (mm)
A	area (m^2)
A_j	area of the j^{th} opening (m^2)
A_l	leeward sidewall opening area (mm^2)
A_s	reference opening area of the front sidewall (m^2)
A_T	total area of sidewall openings (m^2)
A_w	windward sidewall opening area (mm^2)
Ap	cross sectional area of the aerosol particle (mm^2)
C_d	discharge coefficient, [0]
C_{dj}	discharge coefficient for the j^{th} opening, [0]
C_o	initial tracer gas concentration (ppm)
C_{KQ10}	measured effective ventilation rate coefficient at 10 m reference height, [0]
C_Q	ventilation rate coefficient, [0]
C_{Q10}	calculated ventilation rate coefficient at 10 m reference height, [0]
C_s	tracer gas concentration in the air intake (ppm)
C_T	tracer gas concentration within the airspace (ppm)
Cp	positive pressure coefficient, [0]
-Cp	negative pressure coefficient, [0]
ΔCp	difference between external and internal pressure coefficients, [0]
Cp_{10}	pressure coefficient at 10 m reference height, [0]
Cp_{in}	internal pressure coefficient, positive or negative, [0]
Cp_{ext}	external pressure coefficient, positive or negative, [0]
Cp_j	pressure coefficient the j^{th} opening, [0]
Cp_l	average leeward pressure coefficient, [0]
Cp_{ref}	reference pressure coefficient, [0]
Cp_w	average windward pressure coefficient, [0]
deg	degree (°)
E_e	absorption efficiency, [0]
E_c	extension coefficient of the aerosol, [0]
E_e	extinction efficiency, [0]
E_s	scattering efficiency, [0]
H_{10}	scale height for 10 m (m)
H_{ref}	reference height (m)
K	dimmensionless mixing factor [0]
KQ	effective ventilation rate (m^3/s)
I	turbulence intensity (%)
I_L	light intensity traversing the path length (OD/m)
I_o	initial light intensity at source (OD/m)
L	path length of light beam (m)
L_e	typical building dimension (mm)
N	particle density (number of particles/cm^3)
N_o	original particle density (number of particles/cm^3)

GLOSSARY continued

OD	optical density (bel)
OD_o	original optical density (bel)
OD_s	optical density value of air intake contaminent (bel)
P	external pressure (Pa)
P_s	static pressure (Pa)
ΔP_j	pressure difference across the j^{th} opening (Pa)
Q	volumetric flow rate (m^3/s)
Q_E	ventilation rate by the end wall openings (m^3/s)
Q_j	airflow across the j^{th} opening (m^3/s)
Q_R	ventilation rate by the ridge opening (m^3)
Q_S	ventilation rate by the sidewall openings (m^3/s)
Q_T	total ventilation rate (m^3/s)
r^2	correlation coefficient
Re	dimensionless Reynold's number [0]
T	time (s)
V	volume of the airspace (m^3)
V_{10}	wind speed at 10 m height (m/s)
V_e	typical approach wind speed (m/s)
V_{ref}	reference wind speed, at the 10 m height (m/s)
V_z	average wind speed at height, Z (m/s)
V_z	mean wind speed at height, Z (m/s)
V_{ZG}	maximum freestream wind speed which occurs at height, Z_G (m/s)
Voltage	output from the silicon diode photodetector (mVolt)
w	incident wavelength of light (μm)
Z_G	freestream height (m)
α	topographical roughness coefficient, [0]
ν	kinematic viscosity of air (m^2/s)
θ	wind angle of incidence to the building length (°)
λ	atmospheric length scale (m)
ρ	air density (kg/m^3)
σ	standard deviation (also StD), [0]
σ_{VZ}	standard deviation of the flow wind speed, [0]

Subscripts

j	tap or opening number
o	original

Abbreviations

2-D	two dimensional
3-D	three dimensional
A/D	alternate/direct module
ave.	average
C	closed end wall
calc	calculated Cp_{fn} (also Cal)
CH	chimney (also Ch)
dp	diameter of particle (mm)
He-Ne	helium-neon

GLOSSARY continued

max	maximum
meas	average measured Cp_{in}
min	minimum
NRCC	National Research Council of Canada
O	open end wall
OP	open model
SE	sealed model
SPD	silicon diode photodetector

CHAPTER 1

INTRODUCTION

During hot weather, naturally ventilated buildings depend mainly on wind forces to evacuate gases and excess animal heat from the building. Also, livestock are directly affected by the inside airflow patterns which can be closely associated with the distribution and magnitude of inflows and outflows around the building. The zones of air inlet and outlet change in response to the wind direction and have often been considered unpredictable by many authors.

With the pressure difference method, total ventilation rates, air inlet and outlet zones, as well as the magnitude of pressure differences between the inside and outside can be determined from measurements of the pressure coefficients around a scale model in a wind tunnel.

In addition, measurements of the internal pressure coefficents (Cp_{in}) at various locations inside the model are used to verify the calculated Cp_{in}.

The effects of structural parameters, such as size and type of ridge, end wall and sidewall openings can be analyzed from the pressure coefficient data.

In order to enhance existing knowledge on scale modeling techniques for natural ventilation of low-rise buildings, comparisons are made between sealed models and open models with large wall porosities and different roof openings.

Also, it is extremely important for the designer to know if the ventilation system is "effective" in evacuating toxic gases from the livestock building. Measurements of the "effective" ventilation rates are done by utilizing the concentration decay method for various building configurations. Consequently, the calculated ventilation rate

coefficients obtained by the pressure difference method have to be compared to the measured coefficients using the concentration decay method.

CHAPTER 2

LITERATURE REVIEW

2.1 Pressure distribution around low-rise buildings

Aynsley et al. (1977), Davenport et al. (1977), Vickery et al. (1983), Hoxey (1984), Holmes (1983), Chandra (1987), as well as numerous other authors reported that pressure distributions around low-rise buildings vary according to many geometric parameters such as building length, eave height, width, roof pitch, additional overhang, additional wing walls, and the opening area in sidewalls, end walls and at the ridge. Also typical wind characteristics such as the wind angle of incidence to the building length (θ), the turbulent wind profile, and turbulence levels have some effects on pressure distribution (Davenport et al., 1977, 1978, Aynsley et al., 1977). A summary of the available pressure coefficients around various types of low-rise buildings is found in Appendix A.

Data are restricted to wind tunnel tests or full scale tests done in an open country situation. Aynsley et al. (1977) and Holmes (1983) used exactly the same scale model except that the power law exponent of the wind profile (α) for Aynsley et al. (1977) was for a suburban terrain type ($\alpha = 0.28$) while Holmes (1983) reproduced an open country situation ($\alpha = 0.14$). When Aynsley et al.'s (1977) data are transformed with an $\alpha = 0.28$ to 0.14, the resultant on pressure coefficients are completely different to Holmes' (1983) data for a similar model. This showed the large effect of the incident wind profile on the pressure coefficients over low-rise buildings; these data are presented in Appendix A. Also, the data of Davenport et al. (1977, 1978) and Vickery et al. (1983) on low-rise buildings for the two terrain types

(α = 0.14 and α = 0.28) confirmed that only the pressure coefficients obtained from wind tunnel tests using similar power law exponents can be compared.

Table 2.1 presents previous results on the average pressure coefficients across the ridge (windward and leeward roof faces) measured at mid-length of the building for a wind angle of incidence of 90°. All these coefficients are based on a 10 m elevation for comparison purposes.

The results for sealed buildings, like those numbered FB02 to FB19, and the Dutch Barn, are examples of full scale measurements of pressure coefficients (Cps) on various farm buildings performed in the United Kingdom. The data from Vickery et al. (1983) and Holmes (1983) are based on scale models tested in a wind tunnel.

The building, FB02, had been transformed to study the effect of ridge ventilators, however there were no sidewall openings. The building, FB06, had an open ridge and small sidewall openings at the eave. Both were full scale measurements and more details are presented in Appendix A. Shrestha et al. (1990) used a 1:2 scale farm building in an open field. This building had a continuous ridge opening and two continuous sidewall eave opening areas.

According to the results it would be difficult to infer the effects of building length, width, and eave height on the ridge level Cps.

Table 2.2 presents the pressure coefficients at three locations equally spaced along the ridge length for θ = 0° (wind parallel to the building length). The first data point was placed at the upwind leading edge while the second and the third points were placed at the middle and the last third of the ridge, respectively.

At θ = 0°, data showed similar pressure coefficients along the ridge for most of the length of the model even when using different dimensions.

Table 2.1 Average pressure coefficient across the ridge, $\theta = 90°$, full scale and scale model measurements. For open country situation: $\alpha = 0.14$ to 0.18, reference height = 10 m.

Description	Cp at Ridge Level	Building Length (m)	Building Width (m)	Eave Height (m)	Roof Angle (degrees)	Overhang Present
Sealed buildings						
FB05[a]	-1.42	41	28.0	4.0	15°	
FB03[a]	-1.03	18	11.9	4.0	16°	
FB19[b]	-0.94	36.8	18.4	5.0	15°	
FB16[a]	-0.93	12.0	6.7	4.5	15°	
Dutch barn[c]	-0.84	24.3	11.0	5.5	16.7°	
FB02[d]	-0.60	18.5	7.4	1.77	15°	
Holmes (1983)	-0.42	12.2	6.1	2.6	15°	y
Vickery et al. (1983)	-0.32	38.1	24.4	4.9	18.4°	y
Holmes (1983)	-0.19	12.2	6.1	2.6	20°	y
Open buildings						
FB02	-0.43	18.5	7.4	1.77	15°	
FB06[e]	-0.33	34.2	24.6	2.3	11°	
Shrestha et al. (1990)	-0.28	14.6	10	3.0	18.4°	y

a From Hoxey and Moran (1983)
b From Robertson et al. (1988)
c From Robertson et al. (1985)
d From Moran et al. (1983)
e From Wright and Westgate (1982), Richardson (1989b)

Table 2.2 Average pressure coefficients across the ridge at three locations along the ridge length, $\theta = 0°$, $\alpha = 0.14$ to 0.18, reference height = 10 m.

Description of Sealed Buildings	Average Pressure Coefficient Location 1	Location 2	Location 3	Roof Angle (degrees)
Vickery et al. (1983)	-0.58	-0.16	-0.11	18.4°
Dutch barn	-0.55	-0.11	-0.08	16.7°
Holmes (1983)	-0.51	-0.13	-0.06	15°
	-0.51	-0.14	-0.08	20°
Down et al. (1985)	-0.47	-0.05	-0.07	11°

Note: No data were available for open structures with a continuous ridge opening.

Table 2.3 presents the difference in pressure coefficients (ΔCps) between the windward and leeward walls at mid-height and mid-length of the building for a wind angle of incidence equal to 90°. All pressure coefficients are based on a reference height of 10 m for an open country situation ($\alpha = 0.14$ to 0.18). For the open buildings, the area of opening is given as a percentage of the total sidewall area.

The 1:25 scale model of Bottcher et al. (1986) had no ridge opening while the one of Shrestha et al. (1990) had a continuous ridge opening and the FB06 had a partial ridge opening only at the center of the building.

Table 2.4 contains the pressure coefficient differences across one sidewall at three locations equally spaced along the building. They were taken at mid-height of the sidewall for a wind angle of incidence of 0°. Location 1 is the middle of the upwind end of the building while locations 2 and 3 are at the middle and the last third of the building.

Table 2.3 Pressure coefficient differences across building sidewalls; $\theta = 90°$.

Description	ΔCp	Building Length (m)	Width (m)	Eave Height (m)	Roof Angle (degrees)	Overhang Present
Sealed Building						
Dutch barn	0.89	24.3	11	5.5	16.7°	
Bottcher et al. (1986)	0.78	19.0	10	2.5	18.4°	
Vickery et al. (1983)	0.66	38.1	24.4	4.9	18.4°	y
Holmes (1983)	0.60	12.2	6.1	2.6	20°	y
FB19	0.57	36.8	18.4	5.0	15°	
Holmes (1983)	0.54	12.2	6.1	2.6	15°	y
FB02	0.51	38.5	7.4	1.77	15°	
FB01[a]	0.51	27.8	21.5	4.3	15°	
Open Buildings						
Bottcher et al. (1986)						
Area 10%	0.70	19	10	2.5	18.4°	
20%	0.64					
30%	0.59					
40%	0.54					
Shrestha et al. (1990)						
Area 3.3%	0.51	14.6	9.8	3.0	18.4°	y
10%	0.51					
FB06						
Area 3.8%	0.37	34.25	24.6	2.66	11°	

a From Hoxey and Moran (1983)

Table 2.4 Pressure coefficient differences across the buildings at three locations along the sidewalls, $\theta = 0°$.

Description of Sealed Buildings	Pressure Coefficient Difference			Roof Angle (degrees)
	Location 1	Location 2	Location 3	
Vickery *et al.* (1983)	-0.37	-0.11	-0.10	18.4°
Holmes (1983)	-0.35	-0.13	-0.07	15°
Holmes (1983)	-0.25	-0.11	-0.08	20°
Dutch barn	-0.30	-0.04	-0.05	16.7°
Down *et al.* (1985)	-0.30	-0.03	-0.05	12°

2.1.1 Effect of the wind angle of incidence

All studies showed that changes in the wind angles of incidence from 90° (perpendicular to the building length) to 0° (parallel to the building length) caused completely different distributions of the pressure coefficients. For example, at 90°, the pressure coefficents over a windward wall are always positive, the leeward wall are always negative, and the end walls show high negative pressure coefficients at the leading edge (closest to the windward wall) and gradually decrease across the building's width (Appendix A). The pressure coefficients at the ridge are generally negative (Tables 2.1 and 2.2).

When the building is rotated to 0°, one of the end walls faces the wind. The pressure distributions are reversed and the upwind end wall shows positive pressure while the downwind end wall shows negative. On both sidewalls, the pressure coefficients are highly negative at the leading edge and are gradually reduced along the length of the building (Table 2.4).

Similar behaviors were reported on other building shapes.

2.1.2 Effect of building geometry

Vickery et al. (1983) presented a complete data set of pressure coefficients for low-rise industrial buildings tested with three eave heights and three roof angles (Appendix B). For $\theta = 90°$, an increase in eave height caused the ΔCps across the wall to increase while the ridge's negative Cps (-Cps) did not change significantly. Also at 90°, an increase in the roof angle for the same eave height produced an increase in the ΔCps across the sidewall, but didn't change the ridge's -Cps.

For $\theta = 0°$, the addition of eave height caused the Cps to increase along the sidewalls and the ridge. Also, an increase in the roof angle increased the sidewalls' Cps and ridge's -Cps.

Moran (1980) and Hoxey (1984) described the research program undertaken in the United Kingdom in order to obtain reliable pressure coefficients based on full scale measurements of various farm buildings. They tested buildings of different length, width, eave height and roof angles in order to observe the effect of each of these independent variables on the pressure coefficients. They concluded that geometric factors, such as the ratios of eave height to building width and to roof pitch could not be considered as independent variables; they were considered interrelated.

Hoxey and Moran (1983) discussed their results in establishing a relationship among eave heights, building lengths and widths with similar roof angles for a wind angle of incidence of 90°. Additional results are presented in Table 2.1 and the following conclusions can be drawn:

1 - An increase in the sidewall height caused an increase in -Cps located over the ridge (FB02 versus FB16).

2 - For buildings with eave heights between 4.6 m and 5.5 m, and for building widths ranging from 6.17 m to 18.4 m; very little difference in -Cps over the ridge were noticed (FB03, FB16, FB19 and the Dutch Barn).

3 - For a building width of 28 m (FB05), the ridge's -Cps had drastically increased as compared to the narrower buildings.

From Table 2.3, with a wind angle of 90°, the full scale measurements revealed that:

1 - The buildings' widths and eave heights had little effect on the ΔCps across the sidewalls (FB01, FB02, FB19).

However, the data from the Dutch Barn did not follow this trend. It showed that for a similar eave height (about 5.0 m), a narrower building had greater ΔCps across the sidewalls.

The full scale measurements done in the United Kingdom and the results from Vickery et al. (1983) (Appendix B) were in accordance when they showed an increase in -Cps over the ridge as the eave height increased. However, the full scale measurements did not show a clear effect in the increase of ΔCp across the sidewalls as the eave height increased.

Ashley and Sherman (1984) discussed the effect of building width and length on the ΔCps across the sidewalls. They showed higher ΔCps in longer buildings with roof angles between 15° to 30° without any indication on the eave heights.

In contrast, Davenport et al. (1977) concluded that when the length of the building exceeded the width, there was comparatively little change in the measured pressure coefficients over the length of the building. Instead, they emphasized the large effect of roof angle and eave height.

By analysing Tables 2.1 to 2.4, it would appear that there was no clear trend for the Cps on the ridge and sidewalls related to the building length.

Davenport et al. (1978) studied the effect of an overhang on low-rise buildings. They reported that the addition of an overhang generally reduces the local pressures acting on the roof surface, but in some cases induces additional loads on the wall areas.

The results shown in Tables 2.1 and 2.3 tend to confirm that buildings without overhangs had generally higher -Cps at the ridge while buildings with overhangs had generally higher sidewall ΔCps.

Further full scale measurements with the addition of overhangs would be required to clarify the effect of an overhang on pressure distribution.

At a wind angle of incidence equal to 0°, the results presented on Tables 2.2 and 2.4 did not identify trends on the effect of eave height and building lengths, widths and presence of an overhang.

2.1.3 Effect of an open building

Davenport et al. (1978) collected Cp data over low-rise buildings with sidewall porosities of 0%, 0.5% and 3% of the total building surface. It was observed that certain taps located next to the openings generally showed lower Cp values, especially at 3% porosity. This was tentatively explained by the effect of local flow disturbances close to the holes. In general, they concluded that all data showed minimal variation in the external pressure coefficients with wall opening ratios.

However, many authors have reported that a small roof-level ridge outlet is commonly used on naturally ventilated agricultural buildings. When using small roof-level outlets, Vickery et al. (1983) and Vickery and Karakatsanis (1987) reported a possible 40% over estimation of the ventilation rates from the pressure distribution around a sealed model as compared with the measured internal flows. They discussed the effects of the flow fields around the roof ridge as being modified by the airflow from the ridge vents especially for wind angles from 50° to 90°. Wright and Westgate (1982) observed in full scale low-rise buildings, such as FB06 (Appendix A), that a ridge opening produced a different pressure distribution as compared to a regular closed ridge building.

Also, the FB06 showed lower -Cps values at the ridge opening as compared to other full scale measurements on sealed buildings. Moran et al. (1983) reported a 33% reduction in the -Cps for the open versus the closed ridge vents on FB02 (Table 2.1).

Shrestha's (1990) building, FB02 (Robertson et al., 1985), and FB06 (Wright and Westgate, 1982) were all similar, considering the differences in building geometrics.

Further investigations were undertaken by Robertson and Glass (1988) on the FB19 building with varying continuous ridge openings up to 60 mm wide. No published data on the effect of ridge versus non-ridge pressure coefficients are presently available. Richardson (1989a) studied a plastic structure for livestock housing with a continuous ridge opening of either 250 mm or 150 mm and presented the results of flow visualization and full scale pressure coefficient measurements. He reported that when the continuous ridge was closed, the smoke used for visualization hugged the building surface over almost the entire length. When the ridge vent was opened, there was a marked separation of the flow at the ridge where the influx of air from within the building interrupted and slowed the surface flow over the building. This clearly illustrated the reason for the reduced suction over the vented roof.

Table 2.3 relates the effect of increasing the sidewall opening area on the ΔCps across the building. Bottcher et al. (1986) reported a gradual drop in ΔCps across their scale model with larger sidewall opening areas. Their results seemed to be in accordance with Ashley and Sherman's (1984) who reported that wind tunnel measurements showed that wall openings equivalent to 60% of windward and leeward walls (inlet opening equal to outlet opening) caused an estimated 33% decrease in the pressure difference coefficient at $\theta = 90°$. These differences appeared to decline as wind angles changed from perpendicular to parallel to the building length.

Bottcher et al. (1986) used pitot tubes in front of the windward openings, behind the leeward wall and inside the scale model in order to measure the pressure drop across the building. The wind tunnel speed was very low (1 to 2 m/s), therefore measuring only very low pressures. They reported a ΔCps reduction with larger sidewall openings.

Shrestha et al. (1990) did not report any difference on the ΔCps for sidewall openings areas equivalent to 3% and 10%, and their results were similar to the ones reported for FB01, FB02 and FB19 (although the U.K. farm buildings did not have overhangs). However, FB06 showed lower ΔCps compared to the other farm buildings.

Aynsley (1979) performed scale model studies on different types of model houses for hot climates. One model had three vertical openings from the floor to the eaves and the opening ratios varied from 0% (sealed) to 80%. As reported in Appendix A, Table A.2, larger opening areas caused the ΔCps across the building to increase quite significantly for opening ratios of 0% to 25% and then smoothly decrease to a stable level for an opening area above 45%. Each scale model studied showed a different behavior. Aynsley (1988) reported that a sealed model failed to measure the contribution of the velocity pressure across the opening, which explained the measured increase in ΔCps with open models.

It appears that inconsistency exists among the different authors concerning the effect of opening areas across the sidewall. Further full and reduced scale model studies would be required to evaluate the effect of ridge and sidewall opening areas.

2.2 Internal pressure

The internal pressure in a building, Cp_{in}, is directly related to the opening areas in the walls and ridge as well as the distribution of the external pressure coefficients around the building (Aynsley et al., 1977 and Holmes, 1983).

Vickery (1986) added that the airflow through the openings, the flexibility and mass of the building skin and the volume of the airspace would have an effect on the static and also on the dynamic values of the internal pressure coefficients. Vickery (1986) reported that the speed of transmission of pressure waves within the building (350 m/s) is such that the characteristic travel time is far less than the dynamic response time. Hence spatial variations in internal pressure are insignificant and it is only time variations which are of interest. This would apply to buildings with informal leakages, not with formal large openings.

Davenport et al. (1978) and Stathopoulos et al. (1979) presented data for low-rise buildings with leeward opening porosities of 0%, 0.5% and 3% of the total building surface and frontal surface openings ranging between 0% and 100%. Using a wind angle of 90°, they concluded that there was no or little variation in internal pressure within the building except for regions close to dominant openings.

Aynsley et al. (1977) and Stathopoulos et al. (1979) presented the effects of the wind angles of incidence on the internal pressure coefficients. The highest Cp_{in} was usually recorded at 90° when the wind blew directly on the open sidewall. For other wind angles, the Cp_{in} gradually reduced to become negative at 0°.

No data were presented on the effect of different wind angles of incidence on spatial variations among the measured internal pressure coefficients.

However, Stathopoulos et al. (1979) proposed that the uniformity of internal pressures is likely to be somewhat reduced in buildings with significant openings on more than one wall.

Aynsley (1988) discussed the possible pressure drops and variations of internal pressure through a naturally ventilated building with large sidewall openings due to dynamic and

frictional losses of the circulated air. The dynamic components are associated with flow through an orifice, an abrupt expansion in cross section of the airflow channel, a bend in the airflow channel, or dissipation of jet energy from an outlet. The frictional losses are related to the skin friction of the airways as the viscous air moves past the surfaces.

Chandra (1987) reported internal velocities varying between 0.2 and 0.5 of the external wind speed for a naturally ventilated test house. No data were presented on the variation of internal pressure coefficients. Choinière et al. (1988a, 1988c) reproduced the 2-D and 3-D airflow patterns inside a typical naturally ventilated building for livestock housing. The wind angles of incidence and the various structural components had different effects on the airflow patterns. They reported acceleration, deceleration and some stagnant zones of the airflow according to various corners and internal partitions. They also observed the creation of secondary airflow patterns (recirculation) across the building (Appendix F).

Holmes (1979) showed results on internal pressures for a typical test house with a large central opening. The 1:50 scale model was built to allow the opening of a windward and leeward central window with opening areas varying up to a maximum of 22% of the total wall surface area. Cp_{in}s were measured at 19 locations in the building ceiling and at the floor. Even if assumed uniform by Holmes (1979), the data showed some differences between the total average Cp_{in} and the floor's individual Cp_{in}s. No discussion on these differences and on airflow patterns was presented.

Billsborrow and Fricke (1975) measured external and internal pressure coefficients for a typical cubic scale model representing a three story apartment block. In a wind tunnel, they reproduced two different boundary layer wind profiles, open country and suburban area, with their respective

turbulence intensities. The predictions of the internal pressures were done by the pressure difference method which assumed that the internal pressure adjusted itself in order to keep the inflow of air equal the outflow. They tested three types of facade and sidewall openings varying from 0.5% to 5% of the face area at wind angles of incidence of 0° to 90°.

Their results illustrated the direct effects of different facade opening areas and locations on the values of internal pressures. The internal pressures also varied according to the type of boundary layer wind profile. The internal pressures were much smaller for the suburban velocity profile due to the sheltering effect. For a model with only three openings on oppositing sidewalls, the measured internal pressures were consistently lower than the calculated values for wind angles between 30° to 90°. The larger discrepancy was noted at θ = 0° to 15°. They indicated that a larger proportion of the total pressure difference acting across the model occurred across the windward wall of the model rather than across the leeward wall. In order to obtain an equilibrium between the inflows and outflows, the orifice discharge coefficients required to be readjusted and reevaluated. No comments were made on possible variations among the various Cp_{in} measurement locations.

2.3 Discharge coefficient

Aynsley et al. (1977) and Aynsley (1979) reported that the discharge coefficient (C_d) is used for natural ventilation, instead of the dynamic loss coefficient commonly utilised by duct engineers (ASHRAE, 1981). They related the influence of air inlet type, wind angle and inside circulation pattern on the discharge coefficient. They proposed different discharge coefficients for the windward side (inlet) versus the leeward side (outlet) of the building. Also, the size of the wall opening area was taken into consideration. They recommended to use a discharge coefficient of 0.5 to 0.65 for

windward sidewall porosity less than 10% and 0.6 to 0.7 for 10% to 20% porosity. For the leeward side, the discharge coefficient varied from 0.64 to 0.69 for a wall porosity of 20% to 50%.

From ASHRAE (1981), it can be seen that the discharge coefficient depends on the Reynolds (Re) number and the ratio of the area of opening to the area of the duct before the opening. They recommend having Re greater than 10^5 (based on a square orifice, the width of the orifice being the reference length) to be in the fully turbulent range. The most conservative value for a discharge coefficient is 0.6. This value is recommended for square-edged orifice plates located in smooth pipes.

Vickery et al. (1983) assumed that the inlet-outlet situation encountered in natural ventilation would follow the duct assumption. Their results showed a dependency on Re below 10^4. They attempted to operate the wind tunnel at a high speed to avoid this situation. They proposed two curves for the discharge coefficients, based on area ratios of wall openings to wall surface. For inflows, they used a discharge coefficient of 0.62 for no sidewall opening, and a discharge coefficient of 0.75 for a sidewall opening of 50%. For each of their experiments, the discharge coefficient had to be reajusted according to the sidewall opening ratio.

Subsequently, Vickery and Karakatsanis (1987) expressed their concerns about the influence of the wind direction on the discharge coefficient. They also questioned what was the appropriate value of Re and discharge coefficient when the opening area was in the wake region of the building.

Vickery and Karakatsanis (1987) reported a discharge coefficient of 0.6 for the plate orifice meter with Re above 10^4 and wind direction normal to the orifice. However, they noticed that the flow immediately along the building could be treated as a tangential flow. This flow could be an attached external flow on the windward side or a separated external

flow on the leeward side or on any wake region. They presented correction factors for the discharge coefficient for inflow-outflow according to the determined pressure ratios and velocity ratios for each opening.

For naturally ventilated agricultural buildings, Down et al. (1985) reported a discharge coefficient varying from 0.34 to 0.79. They concluded that a discharge coefficient equal to 0.5 should be used for the ventilation rate calculations, based on thermal effect.

From tests performed in a dairy barn, Zhang et al. (1989) calculated a discharge coefficient equal to 0.605 for sidewall and ridge openings. This value was calculated from the predicted ventilation rates based on an energy balance and their natural ventilation model (wind and thermal forces). Potential errors could be due to the assumption of steady state heat production of dairy animals, and the fact that the weather station used for meteorological data was located 45 km away from the research site.

Assuming that the air inlets and outlets of naturally ventilated buildings could be categorized as sharp-edge openings, Shoda (1950) recommended a discharge coefficient of 0.6 to 0.65, while Bruce (1975) recommended to use 0.6 for all openings.

Bottcher et al. (1986) measured dynamic loss coefficients. When these values were transformed into discharge coefficients, they obtained a value of 0.6 for low wall porosities (10%), but the discharge coefficients tended to increase with large openings. Similarly, Swami and Chandra (1987, 1988) recommended using a discharge coefficient of 0.62 for non-agricultural naturally ventilated buildings.

2.4 Pressure difference method for estimating ventilation rates

Bruce (1974, 1975, 1977) presented the theory of the pressure difference method in order to predict the ventilation rate of a low-rise building. Subsequently, he proposed a computer program that would calculate wind induced ventilation rates for livestock facilities. His results were based on wind tunnel testing of a sealed scale model of a gable roof barn, with full scale measurements of 22 m by 35 m, (12° roof angle). Down et al. (1990), Brockett and Albright (1987), Zhang et al. (1989), Down and McMahon (1990) and Down (1990), used the pressure coefficients obtained by Bruce (1974) to produce models for natural ventilation with wind induced ventilation in addition to thermally induced ventilation.

For a typical single story poultry building, Bottcher et al. (1986) used the pressure difference method and measurements of air inlet velocities to measure ventilation rates in a 1:25 open scale model. They concluded that an increase of the sidewall opening areas from 0% to 75% created a decrease in the pressure differences across the building shell. Curiously they showed a linear increase in the ventilation rates with respect to the sidewall opening area. Their tests were limited to a wind direction perpendicular to the building length and the scale model did not have a ridge opening. Shrestha et al. (1990) measured the pressure difference over a 1:2 open scale model of a low-rise agricultural building. This building was tested outside in open country. They reported an inflow of air through the roof ridge opening for wind parallel to the building length. This contradicts Bruce (1974), who stated that the ridge opening is always an outlet (based on sealed model tests). Also, Shrestha et al. (1990) presented equations to calculate the ventilation rates based on the pressure difference method.

Aynsley et al. (1977) and ASHRAE (1981) described the theory of the pressure difference method for some non-

agricultural applications. Aynsley et al. (1977) reported the advantages of this method to be:

1 - Ability to make use of the growing sources of wind pressure distribution data associated with wind load research.

2 - Estimates of natural ventilation can be made without resorting to wind tunnel studies provided suitable pressure distribution and discharge coefficients are known.

They also reported that when openings through a building are in excess of 20% of the wall area, it becomes increasingly difficult to determine the effective pressure difference responsible for airflow through the openings from the pressure distribution on sealed models. For most of the non-agricultural applications, the opening area represented less than 20% of the sidewall, and sealed scale models were used. Karakatsanis et al. (1986) presented the results of pressure coefficients for buildings employing wind towers with limited sidewall area. Bauman et al. (1988) summarized the theory of natural ventilation by the pressure difference method and presented results on pressure distribution for jack-roof systems over long building rows. This configuration would be similar to the open ridge system used in agriculture except that the design also had the purpose of simultaneously being an air inlet and outlet.

Vickery et al. (1983) and Vickery and Karakatsanis (1987) described the theory for the prediction of natural ventilation by the pressure difference method for low-rise industrial and domestic buildings comparable in shape to ones used in agriculture. Their main objective was to compare the airflows measured with a flow meter inside an open model with the predicted values using the pressure difference method based on pressure coefficients measured over a sealed model. They studied sidewall porosities from 5% to 89% of the wall area. They concluded that small openings (less than 23% of the wall

area) did not significantly affect the accuracy of the flow model based on sealed building pressure data. This was verified for a series of different circular hole sizes and square inlets in the walls. More specifically, for low flows and low porosities (less than 23% of the wall), the predictions and the measurements were in good agreement, but for high flows and wind direction angles not perpendicular to the building, the predictions generally overestimated the airflow rates. This phenomenon was tentatively explained using the flow velocity component parallel to the wall which may influence the discharge coefficient. Their results showed an overprediction of airflows using the sealed model for porosity greater than 25%. A lower static pressure difference through the open model would have explained this phenomenon although it was not measured in their experiments. For high porosity (>25%), they proposed a correction factor for the determined airflow coefficients using the sealed model.

Ashley and Sherman (1984) studied low-rise residential buildings. They used a model for predicting natural ventilation based on wind tunnel measurements of pressure coefficients. For a typical house with an opening area equal to 60% of the windward and leeward wall area, the comparison between the prediction and the full scale airflow rate measurements were in agreement within ±15%.

Billsborrow and Fricke (1975) measured the ventilation rates with the orifice plate method and external-internal pressures for a rectangular scale model. Their results showed that the calculated ventilation rates were higher than the measured ones. They discussed the effect of the wind angle of incidence, internal air circulation and the possible change in orifice efficiencies (discharge coefficient) on the calculations of the flows. A maximum difference of 30% was noticed between the predicted versus measured ventilation rates.

Aynsley (1979, 1988) utilized the pressure difference method to predict natural ventilation for domestic housing. Aynsley (1988) reported that the current common use of pressure difference data from wind tunnel studies of sealed models underestimate the pressure difference by an amount equal to the velocity pressure at inlet. This would be the principal reason why current practices tend to underestimate airflow rates through large openings in building due to wind. Aynsley (1988) reported that an error up to 10% could be attributed to the ignored velocity pressure. He demonstrated that a sealed model could show a underestimation of maximally 10% for the ventilation rates for sidewall openings from 5% to 35%, and an overestimation of the ventilation rates for sidewall openings above 35%. Since the tests reported by Aynsley (1979) involved wind blowing perpendicular to the building length, his results were in contradiction to those of Bottcher et al. (1986) for wall porosities varying from 5% to 35%.

Chandra et al. (1986) and Chandra (1987) compared the pressure coefficient data from Vickery et al. (1983) with their full scale measurements of a domestic house. They concluded that natural ventilation airflows through windows could be predicted accurately by the pressure difference method for wind speeds above 2.5 m/s, but discrepancies were noted for lower wind speeds.

Handa (1979) presented a simple model for wind induced ventilation where the contribution of the fluctuating pressures due to the atmospheric boundary layer turbulence were taken into account. Increased ventilation rates were predicted for high turbulence intensities. He did not present any validation of his model.

Etheridge and Nolan (1979a) compared the measured ventilation rates inside a scale model test house to a prediction model using only the mean pressure difference, and a second model using the mean pressure difference and the

turbulent pressure fluctuations. The scale model had circular holes or cracks around windows representing 0.06% to 0.3% of the frontal area. The effects of Re and minimum tunnel wind speed were well illustrated. The values of pressure coefficients were stable when high wind speed was maintained. Their results showed that ventilation due to turbulence was not negligible at these opening areas. Their results indicated that the prediction would underestimate the ventilation rates if the wind tunnel is used to measure only mean pressure differences for use in a theoretical prediction of ventilation rates. The contribution of the fluctuating pressures was relatively greater for wind angles of incidence parallel to the building length. They also reported that for large opening areas and high Re, insignificant differences were found when neglecting pressure fluctuations, because at that point, the mean pressure coefficient controlled the flow direction and magnitude.

Swami and Chandra (1987, 1988) reported that the ventilation prediction from local pressure coefficients over a wall surface would be very similar to predictions based on an average surface pressure coefficient (error within 5%). They developed an empirical equation to calculate the Cps as a function of the building's shape and the incident wind direction relative to the building length. They presented a complete procedure for calculating natural ventilation airflows in low-rise buildings assuming that:

1 - There was no stack effect.
2 - No pressure drop inside the building due to partitions.
3 - Perfect mixing was achieved.
4 - The airflow was due to mean pressure differences alone and fluctuating pressure effects were ignored.
5 - Average Cps were used over the entire wall surface.
6 - There was no ridge opening.

The first part of the pressure difference method consists of measuring the wind pressure coefficient, Cp, over a solid surface. It is defined as:

$$Cp = \frac{P - P_s}{.5\rho V_{ref}^2} \qquad (2.1)$$

where

P = external pressure measured at each location, Pa
P_s = static pressure in the wind tunnel, Pa
ρ = air density, kg/m^3
V_{ref} = reference wind speed, m/s

According to Vickery and Karakatsanis (1987), theoretical estimates of airflow rates can be calculated using the external pressure distribution around an open or a sealed model assuming that:

1 - The internal flow does not disturb the external pressure fields.
2 - The configuration of external wall openings and internal partitioning is known.
3 - The flow rates through a given opening can be calculated from the following relationship,

$$Q_j = C_{dj} A_j \left(\frac{2\Delta P_j}{\rho}\right)^{1/2} \qquad (2.2)$$

where

Q_j = airflow through the opening, j, m^3/s
C_{dj} = discharge coefficient of the opening, j
A_j = area of the opening, m^2
ΔP_j = pressure difference across the opening, Pa

Aynsley (1979) and Bottcher et al. (1986) reported the variation in the external Cps for open models. As also discussed by Cermak et al. (1984), a fraction of the airflow through a model with relatively large openings may be controlled by the momentum of the external flow. This would

bias the results of the prediction based on static pressure differences across the openings. For the present study, it is assumed that Eq. 2.2 is adequate.

In order to calculate the airflow in the building, an internal pressure coefficient, Cp_{in}, was needed. Then Eq. 2.2 becomes:

$$Q_j = C_{dj} A_j V_{ref} \frac{Cp_j - Cp_{in}}{|Cp_j - Cp_{in}|^{1/2}} \qquad (2.3)$$

The sign associated with (Cp_j - Cp_{in}) determines the direction of the airflow at the j^{th} opening; positive implies inward and negative implies outward. As explained by Aynsley (1977), Vickery et al. (1983) and Swami and Chandra (1987), the internal pressure coefficient is assumed to be uniform inside the ventilated air space.

Since the tests were performed for isothermal conditions, the inflow was equal to the outflow to satisfy continuity, then:

$$\sum_{j=1}^{n} Q_j = 0 \qquad (2.4)$$

From this procedure, the internal Cp_{in} was determined by iteration using a computer.

2.5 Ventilation rate coefficient

ASHRAE (1981), Hellickson et al. (1983), Krishnakumar et al. (1985), Vickery and Karakatsanis (1987) and Vickery et al. (1983) presented a simpler model for wind induced natural ventilation, which is

$$Q = C_Q V A_T \qquad (2.5)$$

where

C_Q = flow coefficient
A_T = total area of sidewall openings, m^2

In fact, C_q contains the combination of the discharge coefficient and pressure coefficient differences. ASHRAE (1981) and Hellickson et al. (1983) proposed that C_q values range from 0.2 to 0.3 for a wind angle of 0° and 0.5 to 0.6 for a wind angle of 90°. This method is then very easy to use by designers but it is very unprecise.

Vickery et al. (1983), Vickery and Karakatsanis (1987) and Krishnakumar et al. (1985) demonstrated that any change in the opening areas of the sidewall and the ridge would produce a different C_q curve.

The results of Etheridge and Nolan (1979a) with those of Vickery et al. (1983) and Vickery and Karakatsanis (1987) suggested that a minimum wind speed should be maintained in the wind tunnel in order to have a constant value for C_q. Their results showed dependency of C_q on the Re.

2.6 Prediction of inlet-outlet zones

Bruce (1974) and Hellickson et al. (1983) discussed the influence of pressure distribution around naturally ventilated buildings in order to identify the air inlet and outlet zones on the sidewall and ridge openings. Mitchell and Ross (1977), Ström (1987) and Choinière et al. (1988a) all described the interior airflow patterns and the air inlet and outlet zones for a two dimensional scale model of a gable roof barn with large sidewall openings and a continuous ridge opening. Similar airflow patterns were shown by Bottcher et al. (1986) for a naturally ventilated building without a ridge opening. Kelly et al. (1986) presented results from flow visualization of a three dimensional model of a naturally ventilated calf barn using a water flume.

A 1:20 scale model of a naturally ventilated swine finishing barn with a gable roof and sloped ceiling was built and tested in a wind tunnel by Choinière et al. (1988c). Smoke was injected into the model to observe the airflow patterns under isothermal conditions (wind induced ventilation

only). Tests to determine the effect of different sidewall, ridge and end wall openings were completed for four wind directions (0°, 30°, 60° and 90°). The zones of air inlet and outlet were identified, but airflows were only compared qualitatively.

In order to obtain more precision on the air inlet and outlet zones around a naturally ventilated agricultural building, Bruce (1974, 1975) recommended using the pressure coefficient method.

Shrestha et al. (1990) presented a fairly complete description of the inlet-outlet zones around a low-rise agricultural building by using the mean of a set of graduated contour lines around the building.

2.7 Concentration decay method for evaluating ventilation rates

The concentration decay method has been used extensively for studies in air infiltration, as well as for natural and mechanical ventilation rate measurements inside full scale buildings (Shaw, 1984). Hitchin and Wilson (1967), Hunt (1980), ASHRAE (1981), Barber and Ogilvie (1984a, 1984b), Charlesworth (1988) and many other authors explained the theory of the concentration decay method. Basically, a tracer gas is introduced into an airspace until an equilibrium concentration is obtained. Then the injecting of the tracer is stopped and the rate of decay of the tracer concentration within the airspace is monitored. The rate of change in concentration of the gas is given by the difference in the amount of gas leaving the airspace from the amount of gas entering the airspace. Hunt (1980) and Charlesworth (1988) presented the basic equation for the concentration decay method, which is:

$$\frac{C_T}{C_o} = e^{-\frac{QT}{V}} \qquad (2.6)$$

where

C_T = tracer gas concentration within the airspace, ppm
C_o = initial tracer concentration, ppm
Q = volumetric flow rate, m^3/s
V = volume of the airspace, m^3
T = time, s

To accept the equation, the following assumptions are made.

1 - Perfect mixing.
2 - Constant flow rate.
3 - No contamination of the incoming air.
4 - Constant specific volume.
5 - Isothermal conditions.

Hitchin and Wilson (1967) reported that the efficiency of the measure of the air exchange rate depends on the constant volume of air and on the perfect mixing assumption. "Perfect mixing" means that at any given moment, at any location inside the airspace, the tracer gas has an instantaneous and homogenous concentration. Where there is "no mixing", the incoming fresh air by-passes the contaminated inside air and there is a short circuit or ventilation.

West (1977), Barber and Ogilvie (1982, 1984a, 1984b), and Ogilvie and Boyd (1985) introduced the concept of "mixing factor" and elaborated on the basic equation in function of the possible tracer gas concentration at the air intake. They proposed the following equation:

$$\frac{C_T - Cs}{C_o - Cs} = e^{-\frac{KQT}{V}} \qquad (2.7)$$

where

Cs = tracer concentration in the supply air, ppm
K = mixing factor
if K > 1, stagnant zone
K < 1, short circuit, air inlet to the outlet
(Barber and Ogilvie, 1984b)

West (1977) studied the perfect mixing assumption and tried to characterize the dispersion and dilution of air contaminants in an enclosed airspace to verify the departure from perfect mixing. The ventilation rates, the source locations of the injected tracer gas and the sampling points were the three variables investigated in function of the tracer concentrations and mixing. West (1977) identified four basic zones in any ventilated airspace:

1 - Entrainment region.
2 - Turbulent mixing region.
3 - Still air region.
4 - Exhaust air.

He reported that the source locations had no effect on the concentration of the tracer and on the mixing. The data show more noise when the source was located in the turbulent mixing region. He recommended that the source of the tracer gas should be located in the entrainment region because when the gas was released in a region of high air velocity, the gas was dispersed rapidly with fair uniformity.

The sampling points had an effect on the readings of the tracer concentrations but not on mixing. Using a large number of sampling points may alleviate this problem. The ventilation rates had a direct effect on the tracer concentrations and mixing, since increasing the ventilation rates would change the tracer concentration. However, the effect of increasing the ventilation rates created a decrease

in the mixing. Barber and Ogilvie (1984a) and Boyd (1985) reported similar results. As reported by Timmins (1984) and Choinière (1988a) a threshold Reynold's number for flow stability (airflow patterns) should be maintained. The low ventilation rates used by West (1977) may have introduced differences in the mixing quality due to the change of airflow patterns if the fully turbulent regime was not obtained.

According to Barber and Ogilvie (1984a, 1984b) the reasons for incomplete mixing in a ventilated airspace were the short-circuiting and the presence of stagnant zones in a fully turbulent regime. The existence of secondary flow zones would be a cause of incomplete mixing. They introduced the "n,m" model to take in account the well mixed region and the fraction of air which was short-circuited to the outlet. Ishizu et al. (1983) proposed to take into consideration the effect of the source location of tracer gas with a mixing factor and a position fraction, called a "n,p" model.

West's study (1977) on the effects of parameter combinations such as, ventilation rates with source locations, ventilation rates with sampling points, and source locations with sampling points revealed that the use of multi-sampling and multi-source locations may prevent errors on ventilation rate measurements because of the reduction of effects of tracer concentration variations inside the building and local mixing problems (Barber and Ogilvie, 1984b).

In order to predict the interior ventilation rates with the concentration decay method, the assumption that ventilation rates have no effect on the mixing factor had to be made. In fact, Ogilvie and Boyd (1985) discussed that measurements from the concentration decay method would be more representative of an "effective ventilation rate" or "KQ".

West (1977) and Boyd (1985) reported excellent data replications by tracer gas measurements. They recommended that only limited replications were necessary to obtain accurate values for the tracer's rate of decay.

Hunt (1980) presented typical result curves expected when both perfect mixing and tracer refeeding from the air intake occurred. Hitchin and Wilson (1967), Costello et al. (1982) and many others reported that the introduction of "Cs" in Eq. 2.7 solved the problem of tracer gas concentration in the supply air.

2.7.1 Types of tracer

Shaw (1984) reviewed the effect of different tracer gases on the accuracy of the air change rate measurements for full-scale tests. He concluded that many different gases could be used independently of their molecular weight as long as the airspace tracer concentration was well mixed.

Shoda (1950) studied wind and stack effects for various scale models of naturally ventilated buildings. He measured the ventilation rates with the concentration decay method using CO_2 as the tracer gas. From his tests on scale models with relatively small opening areas and low wind tunnel speeds, he showed that stratification of CO_2 occurred in the scale models. Then, he created some additional mixing with a small stirring fan and obtained data very close to the desired theoretical concentration decay model.

Etheridge and Nolan (1979a, 1979b) tested the effect of fluctuating components of the wind pressure on the ventilation rates of a typical low-rise residential building. They used the concentration decay method to measure the ventilation rates which provided data for the combined effects of the average and fluctuating pressures. They reported that an error could be introduced because of the extraction of a certain amount of air for sampling purposes, especially at low wind speed and when only cracks were simulated (long decay period).

Ogilvie and Boyd (1985) tested a 1:20 scale model of a naturally ventilated building for swine housing with an opening area up to 50% of the frontal area. CO_2 was the

tracer gas used. They discussed the mixing problem due to the occurrence of short-circuiting through the model when high wind speeds were associated to large opening areas. They reported the following problems:

1 - A stable initial concentration of tracer gas was difficult to obtain because of the large amount injected.
2 - Due to the high ventilation rates, the rate of decay measurements had to be taken within seconds, which was reading the limits of the monitoring equipment.
3 - The presence of many sampling tubes and their supports may have affected the mixing inside the model.

2.7.2 Decay rate measurements with an optical device

Etheridge and Nolan (1979b) utilized an optical technique for measuring ventilation rates in scale models. They used a light emitting diode and an appropriate detector to sense the rate of decay of smoke from tobacco or ventilation smoke tubes. To release smoke into the model the test tube was broken or the tobacco was burned inside. When combustion was completed, a mixing fan was started and the decay rate was measured during 3 to 5 minutes according to the wind tunnel speed and the opening areas of the cracks around the scale model. They presented comparable results of the rate of decay between the optical density measurements versus the conventional helium decay technique. In order to minimize the noise problem, they recommended use of a monochromatic light source to prevent interferences and build the models with opaque materials.

The key to the system was to use optical density measurements instead of tracer gas concentration, then,

$$\frac{C_T}{C_o} = e^{-\frac{KQT}{V}} = fn\left(\frac{OD}{OD_o}\right) \qquad (2.8)$$

where

OD = optical density at time, T
OD_o = initial optical density

2.7.3 Advantages

Zollars (1980), Melik and Fogler (1983), Gulari et al. (1987) and Gülder (1989) used similar optical techniques to evaluate particle size distributions and their concentrations with time of various aerosols.

Melik and Fogler (1983) listed some advantages to using optical density measurements for studying the dispersion of particle sizes of aerosols.

1 - The measurements are rapid and simple.
2 - Sampling problems are minimized for in situ study.
3 - Measurement causes no disturbances of the system which is simply illuminated with a beam of light.

Some extra advantages listed by Etheridge and Nolan (1979b) are:

1 - No extraction of air inside the model.
2 - Instantaneous response.

2.7.4 Theory

The presence of an aerosol alters the visibility across an airspace. Visibility is measured in terms of optical density or by its inverse, transmissivity (Hinds, 1982).

As shown on Fig. 2.1, optical density is the measure of the attenuation of a light beam traversing a scattering medium. Hinds (1982) reported that the attenuation is given by Bouger's Law (also known as the Lambert-Beer's Law),

$$\frac{I_L}{I_o} = e^{-E_c L} \qquad (2.9)$$

where E_c is the extinction coefficient of the aerosol and L is the path length of the light beam through the aerosol. I_L/I_o is the ratio of the light intensity traversing the aerosol, I_L (OD/m), to the initial light intensity at the source, I_o (OD/m). As stated by Clark (1985), the Lambert-Beer's Law is strictly valid for a monochromatic light source. Many authors defined the optical density as being

$$OD = -\log_{10}\left(\frac{I_L}{I_o}\right) = -0.4343 \ln\left(\frac{I_L}{I_o}\right) \qquad (2.10)$$

Rasbash and Phillips (1978) reported that the appropriate unit for optical density (OD) is the bel. Clark (1985) explained that an optical density of about 0.5 per metre (OD/m) reduces visibility to about 2 m; to obtain 10 m visibility, a density ≤ 0.1 OD/m is required.

According to Hawksley et al. (1977), the optical density of smoke depends on the concentration, size distribution, and optical properties of the particles.

$$E_c = N\,Ap\,Ee \qquad (2.11)$$

where

N = number of particles per cm^3
Ap = cross sectional area of the aerosol particle, cm^2
Ee = extinction efficiency

According to Friedlander (1977), light could be scattered and/or absorbed by the aerosol particle, then the extinction efficiency corresponds to

$$Ee = \frac{\text{radiant power scattered and absorbed by a particle}}{\text{radiant power geometrically incident on the particle}}$$

Scattering is defined as a reradiation of the incident light in all directions, but usually with different intensities. Where adsorption corresponds to radiant energy transformed into other forms of energy such as heat, chemical reactions, or radiation of a different wavelength. For example, the loss of visibility through water droplets is mainly due to scattering. Also, black smoke would attenuate visibility by absorption and scattering, but white smoke would cause little absorption.

Then the extinction efficiency of a particle is the sum of its scattering efficiency and its absorption efficiency.

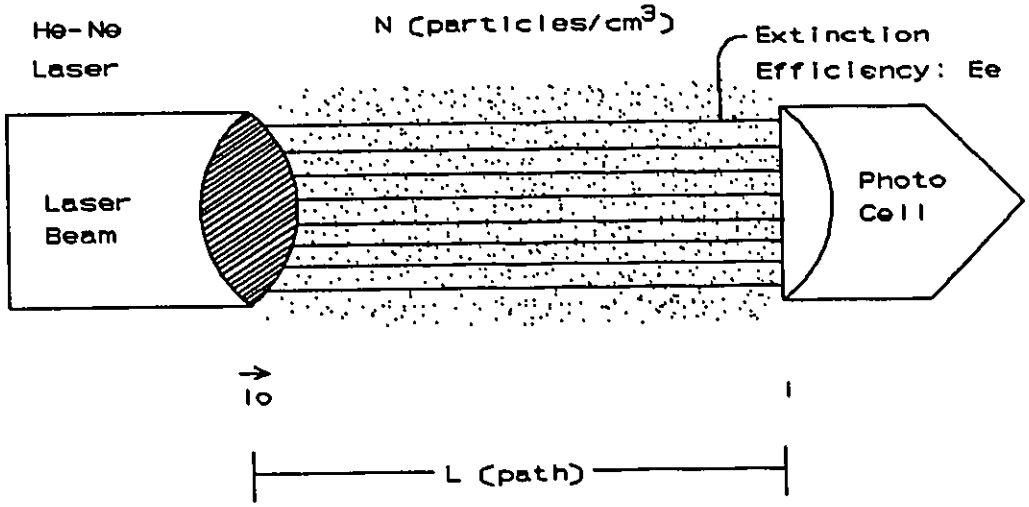

Figure 2.1 Representation of the light attenuation process (Lambert-Beer's Law).

$$Ee = Es + Ea \qquad (2.12)$$

No single equation gives the extinction efficiency for all particle sizes. Ee depends on the particle refractive index and shape and its size relative to the wavelength of light. According to Hinds (1982) and many authors, three regions could be identified in function of the particle size.

They are:

1 - Rayleigh region; dp/w ⟨⟨ 1

2 - Mie region; .1 dp/w ⟨⟨ 1

3 - Extinction Paradox region; dp/w ⟩⟩ 1

where

dp = particle diameter, mm
w = incident wavelength, mm

The Rayleigh region applies for small particles with a diameter smaller than 0.05 μm. It is possible to assume that a geometric optic attenuation applies. The cross-section of the light scattered corresponds to the cross-section area of the particle. For this particular region, it is possible to calculate Ee with a specific refractive index value.

In contrast, for particles larger than 2 mm, (Hinds, 1982) the scattering efficiency approaches 2. This means that, a large particle removes from the beam twice the amount of light intercepted by its geometric cross-sectional area. This is the extinction paradox.

But for most of the visible light (3.5 μm ⟨ w ⟨ 8 μm), the light scattering and absorption process is not simple. This is within the Mie region. In this region, there is a specific, Ee for each particle size of a particular aerosol. Friedlander (1977), Hinds (1982) and Gulari et al. (1987) presented curves for the variation in extinction efficiency in function of different refractive indices, particle sizes and light wavelengths.

2.7.5 Concentration of particles by optical density measurements

Rea et al., (1985) tested the visibility of exit signs through smoke. In order to compare the results, they used an apparatus to measure the changes in optical density through smoke over time. Clark (1985) described how a simple helium-neon laser could be used to measure the optical density

through various types of smoke. He calibrated this instrument according to the ASTM Standard F814-845 (1988).

They used a helium-neon laser (w = 0.632 μm) with vaporized oil produced by a MDG smoke generator. According to Hinds (1982), the particle size distribution is from 0.01 μm to 10 μm for a mist of liquid. No data exist on the particle size distribution of the vaporized oil, which depends on the temperature and pressure used to perform the vaporization. Also, its white appearance would indicate that it covers the entire range of the visible light.

Equation 2.10 could be transformed by the following,

$$OD = -0.4343 \ln \left(\frac{I_L}{I_o}\right) \tag{2.13}$$

where

$$OD = -0.4343 \ln(e^{-E_c L}) \tag{2.14}$$

$$OD = 0.4343 E_c L \tag{2.15}$$

$$OD = 0.4343 N Ap Ee \tag{2.16}$$

into the rate of decay equation,

$$\frac{OD}{OD_o} = \frac{0.4343 N Ap Ee}{0.4343 N_o Ap Ee} \tag{2.17}$$

then

$$\frac{OD}{OD_o} = \frac{N}{N_o} \tag{2.18}$$

which would be a measure of the change in smoke concentration.

This equation was used by Etheridge and Nolan (1979b). The assumption of the stability of the particle size distribution function and their particular refractive index would have to be made.

2.7.6 Change in the particle size

Friedlander (1977) and Hinds (1982) also discussed the fact that most of the aerosols are polydisperse, which means that they do not have a specific diameter but mainly a large particle size distribution. This distribution changes with time due to the initial particle concentration by the coagulation and/or colloidation of particles. Clark (1985) expressed concern about the change in the particle size distribution due to the possible coagulation of the vapour particles, even if this fact did not disturb the full scale experiment of Rea et al. (1985).

Etheridge and Nolan (1979b) reported the rapid condensation of the vaporized oil on the interior surface of the scale model. They recommended to not use oil for experiments with long term residential times above 1 minute.

CHAPTER 3

OBJECTIVES

The objectives of this study were to use a 1:20 scale model of a low-rise, naturally ventilated building in the NRCC wind tunnel to measure external and internal pressure coefficients as well as the rate of decay of injected smoke in order to:

1 - Visualize the effect of various structural configurations on the distribution of the external pressure coefficents, Cps, around the building and on the variations of the internal pressure coefficients, $Cp_{in}s$.

2 - Observe the airflow inlet and outlet zones and the relative magnitude of ΔCps and Q_j over each opening area.

3 - Calculate the ventilation rate coefficients, C_{q10}.

4 - Compare the Cps' distributions, calculated Cp_{in} , ΔCps and Q_j distributions and magnitudes and the C_{q10} values of the open versus sealed scale model.

5 - Compare the calculated ventilation rate coefficients, C_{q10}, obtained with the pressure difference method to the measured "effective" ventilation rate coefficients, C_{kq10}, obtained with the concentration decay method.

CHAPTER 4

METHODS AND PROCEDURES

4.1 Scale model

Different scale models have been used for the purpose of flow visualisation and airflow measurements in natural ventilation studies. Choinière et al. (1988a, 1988c) used a geometric 1:20 scale model, while, Ogilvie and Boyd (1985) used a 1:10 and a 1:25 scale model, Bottcher et al. (1986) a 1:25 scale model, and Cermak et al. (1984) a 1:25 scale model. They discussed the effect of scaling on the interior velocity and natural ventilation measurements. Tieleman et al. (1978) and Allen (1984) reported that scalings of 1:50 to 1:100 are necessary for low-rise buildings in order to model relatively small surface features which are important for flow separation. In addition, at such a size, the effect of the Re distortion does not influence the flow phenomenon's modelling.

The present 1:20 scale model represents a typical dairy or swine, gable roof barn, 12.2 m wide by 24.4 m long, with 2.7 m high sidewalls and a roof with a 4/12 slope and a 300 mm eave overhang. There are no interior partitions and the ceiling has the same slope as the roof. This model is based on Canada Plan Service's plan M-3434.

4.2 Wind tunnel facilities

The 2 x 3 m low speed wind tunnel of the National Research Council of Canada (NRCC), located in Ottawa, Ontario, was the testing site for this study. Brown (1986) and Hansen (1986) have provided complete information on the facilities and monitoring equipment.

4.3 Boundary layer simulation

Cermak (1975), Cermak et al. (1984), Aynsley et al. (1977), Tieleman et al. (1978), Holmes (1983) and Allen (1984) described the necessary conditions for the simulation of an isothermal boundary layer flow representative of the wind for the lower neutral atmospheric surface in order to study the wind loading over low-rise buildings. They are:

1 - Undistorted scaling of the model geometry.
2 - Vertical profile of wind speed.
3 - Turbulence intensity.
4 - Turbulence integral scale.
5 - Small blockage of the wind tunnel.

Davenport (1960) used the power law (Eq. 4.1) to describe a vertical wind speed profile over an open country field.

$$\frac{V_z}{V_{z_G}} = \left(\frac{Z}{Z_G}\right)^{\alpha} \qquad (4.1)$$

where

V_z = the mean wind speed (m/s) at any given height, Z
V_{ZG} = the maximum free wind speed (m/s) which occurs at height, Z_G
α = the topographical roughness coefficient

Aynsley et al. (1977) reported that a typical Z_G of 300 mm to 600 m and $\alpha = 0.15$ is used for an open country with low scrub and scattered trees. Ogilvie and Boyd (1985) and Choinière et al. (1988c) used an $\alpha = 0.17$, while Davenport et al. (1977) used an $\alpha = 0.14$ for smooth terrain in their studies on low-rise buildings. Allen (1984) explained that the use of a large, 1:50 scale model required a profound simulation of the atmospheric boundary layer. However, Cook (1978) demonstrated that only the lower portion of the wind profile, which envelopes the model and the vicinity, has to be simulated in the wind tunnel. This allows the use of large

scale models if the wind tunnel is not large enough. Irwin (1979) described the design method for the construction of spires for natural wind simulation. The spires were prepared in order to produce a 350 mm thick boundary layer with an $\alpha = 0.1735$, as shown in Figs. 4.1a and 4.2.

For this study, only the horizontal wind speed component of the airflow along the wind tunnel was measured using a hot wire anemometer system (TSI, model 1054). The anemometer was installed on a 2-axis traverse apparatus described by Brown (1986) and the measurements were made 10 cm in front of the 1800 mm diameter turntable (Hansen, 1986). Measurements were made over a three minute period at each indicated elevation. Wind speeds at the 350 mm and 500 mm height were not used for the calculation of α, since these speeds were above the ridge line. Since the model had to rotate, the flow properties were measured at 1 m in front of the model's center. Wind speed measurements were made after the installation of the scale model, when the wind was perpendicular to the building length. An assumption was made that the upwind flow would remain similar when the model rotated. The boundary layer velocities produced by the spires in the wind tunnel were measured with a freestream wind speed of 10 m/s. However, the tests for pressure coefficients were performed at freestream wind speeds approximating 20 m/s. Since Irwin (1979) had demonstrated the independence of the x-axis wind speed component as long as the turbulent range was achieved, it would be expected that a similar shear flow was obtained. To compute the pressure coefficient for each test, the reference wind speed, V_{ref}, was measured at an elevation of 110 mm above the floor, 1100 mm in front of the model center, at the center of the tunnel width, and at mid-height of the scale model sidewall openings. The measurements were made with a pitot tube as described by Brown (1986). The freestream wind speed was also continuously monitored by a pitot tube located at the top section of the wind tunnel. All pressure coefficients were transformed to a

reference height of 0.5 m (10 m, full scale) with Eq. 4.2 because of the following advantages: it is readily available to be used with standard meteorological data and it is independent of the building form (Allen, 1984).

$$Cp_{10}-Cp_{ref}\left(\frac{H_{10}}{H_{ref}}\right)^{2\alpha} \qquad (4.2)$$

where

Cp_{10} = pressure coefficient at 10 m reference height
H_{10} = scaled height for 10 m

4.4 Turbulence intensity

According to Aynsley et al. (1977) the turbulence intensity, I, is defined as:

$$I-\frac{\sigma_{V_z}}{V_z} \qquad (4.3)$$

which is the ratio of the standard deviation of the flow wind speed over the average wind speed, at a particular height, Z. In this study, turbulence intensity was restricted to along the wind direction. Values of the turbulence intensity were automatically computed with the TSI hot wire anemometer system. Data are reproduced on Fig. 4.1b.

These intensity curves are similar to values shown by Davenport et al. (1977) and Handa (1979) for smooth terrain. They are also similar to values presented by Irwin (1979) for an α = 0.16 or higher. However, they are higher than the turbulence intensities used by Vickery et al. (1983). Holmes (1983) reported that the simulations at eave height and the lower portions of the building are important for exact mean pressure coefficients and especially for peak pressure coefficients. The present turbulence intensity profile was therefore considered as satisfactory.

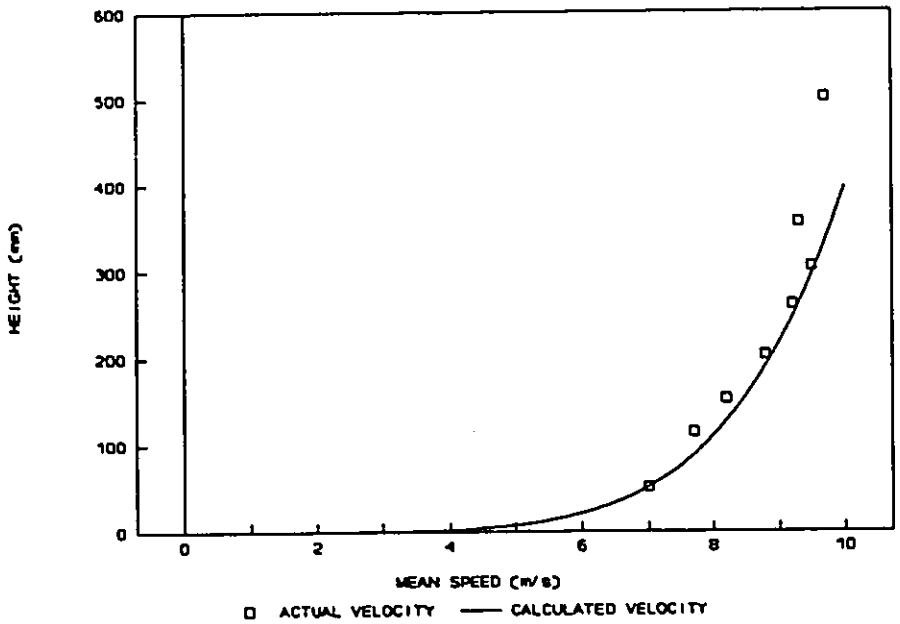

Figure 4.1a Vertical wind speed profile (α = 0.1735).

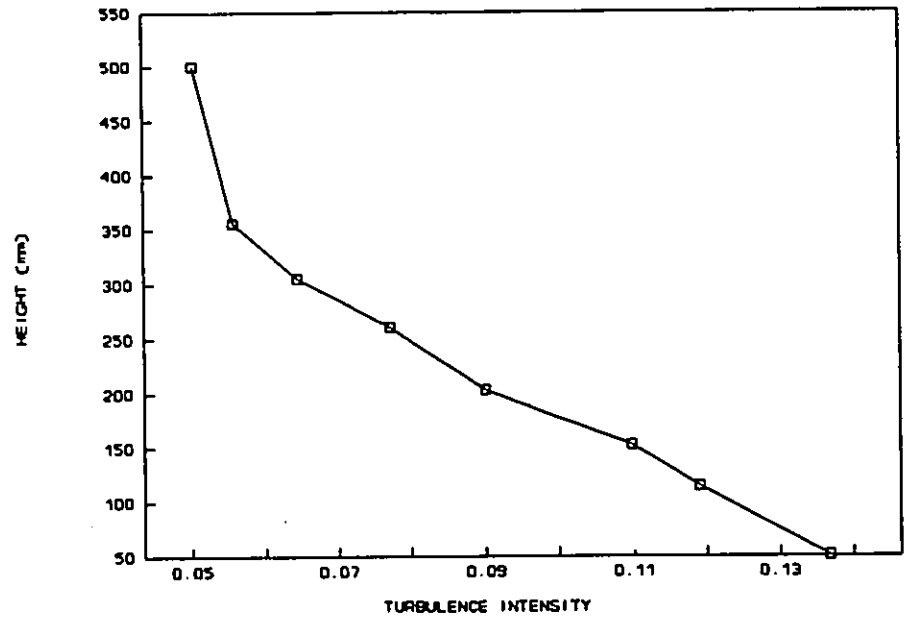

Figure 4.1b Vertical turbulence intensity profile.

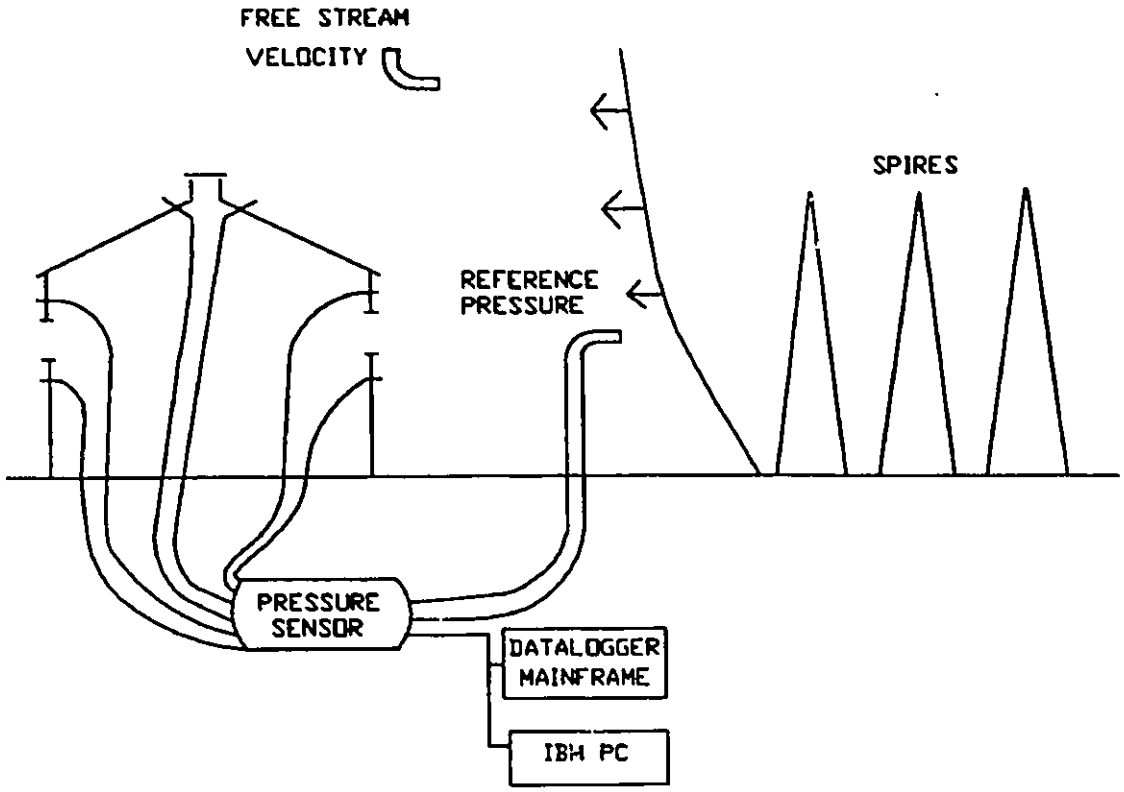

Figure 4.2 Scale model installation in wind tunnel.

4.5 Turbulence integral scale

As explained by Cermak (1975), the integral length scale is a basis for comparing turbulence spectra for similarities. He reported on the work of Kolmogorov who reported that a high wave number range exists in the turbulent spectrum, which is governed by kinematic viscosity and energy dissipation. He showed results where similar energy spectra, as compared to neutral atmosphere flow, were obtained in a long wind tunnel. He proposed that a scale of 1:100 be the minimum to respect the length scale condition. Tieleman et al. (1978) obtained a length scale of 0.23 m at their reference velocity (10 m height) for a study on a 1:50 scaled low-rise building. They operated the wind tunnel at 12 m/s and used a spire disposition similar to the present study, except that some

additional roughness blocks were added to induce a higher turbulent intensity (19.5% at reference height). Since the average atmospheric length scale for a crowded suburban area (α = 0.29) is about 50 m, they were working to obtain a length scale of about 0.7 m as compared to 0.23 m. Full scale measurements of the tested structure revealed good agreement with the mean pressure coefficient obtained in the wind tunnel, even if the turbulence integral scale was about one-third the value required for a 1:50 scale flow simulation.

Aynsley et al. (1977) and Handa (1979) reported values of length from 50 m to 200 m for an open country situation. To correctly reproduce the energy spectra, the length scale in the wind tunnel should be about 5 m to 10 m. Holmes (1983) and Allen (1984) reported the difficulty to match the length scale at 1:50 to 1:300 scale, but some relaxation could be made as long as the turbulence scale, related to eddy sizes, was larger than the building dimensions. Irwin (1979) reported that with the spire design method used at the NRCC 2 x 3 wind tunnel, the resultant length scales measured were in agreement with the atmospheric length scale for various scales from 1:100 to 1:2000 and for α = 0.10 to 0.42. It was assumed that the length would be reproduced in an appropriate manner although not measured.

In order to relax the length scale simulation and obtain precise mean pressure coefficients, Wardlaw (1989) recommended testing over three recording periods: 1 second, 3 seconds and 5 seconds. The freestream wind speed of the wind tunnel was increased to 20 m/s in order to generate enough wavelengths over the building. A sampling frequency of 200 Hz was selected as being the standard. Results are in Appendix C.

There have been very few differences among the testing periods. From the analysis of the differences between the 1 s, 3 s and 5 s recording period, there was an absolute average Cp difference of 0.024 (σ = 0.019) between 1 s and 3 s, an absolute average Cp difference of 0.025 (σ = 0.019)

between 1 s and 5 s, and finally an absolute average Cp difference of 0.017 (σ = 0.013) between 3 s and 5 s. Also, the test (5 s - 3 s) showed the lowest maximum difference between two measurements of a particular tap to be 0.065. Due to the very small difference between 5 s and 3 s, a recording period of 3 s was used for all the other wind tunnel tests. Also, it was assumed that a $\pm\Delta$Cp equal to 0.02 would be attributed to experimental error.

The effects of 1 s, 3 s and 5 s recording time were also analyzed for the global error introduced when many points are used to calculate the ventilation rates. The strict average of the Cp differences for the test (5 s - 3 s) showed an average difference of -0.002, σ = 0.021. This value indicated that the use of many points for the calculation of the ventilation rates for each opening area may help to minimize the experimental error.

Subsequent tests were carried out using a 3 s interval which would theoretically allow about 12 wavelengths [(20 m/s x 3 s)/(5 m/λ)].

4.6 Effect of Reynolds number

From previous research work, Choinière et al. (1988c) reported that a threshold Re has to be respected in order to obtain stable airflow patterns inside the ventilated airspace.

Etheridge and Nolan (1979a) reported on the effect of the Re on the ventilation rate coefficient, C_q. They noticed a stable C_q for wind speeds above 5 m/s even when the scale model had small openings.

Choinière et al. (1988c) used a three dimensional 1:20 scale model for flow visualisation. They reported the stability of the airflow patterns for reference velocities of 0.5 m above the floor varying between 0.9 and 2.0 m/s. Cermak et al. (1984) reported that for bluff bodies with sharp edges such as low-rise buildings tested in isothermal flows, the

pressure distribution would be independant of the Re above a value of 2×10^4.

$$Re = \frac{L_e V_e}{\nu} \geq 2x10^4 \qquad (4.4)$$

where

L_e = typical building dimension, m
V_e = typical approach wind speed, m/s
ν = kinematic viscosity, m^3/s

For the present study, the reference wind speed was about 16 m/s (freestream wind speed was 20 m/s) which would maintain a Re of 6.5×10^4, based on L_e = width of the building. The selection of a scale of 1:20 and a freestream wind speed of 20 m/s was appropiate with respect to the recommendations of Cermak et al. (1984).

4.7 Blockage effect

As recommended by Cermak (1975), Aynsley et al. (1977) and others, the blockage of the wind tunnel should not exceed 5%. For this particular study, the scale model had a maximum blockage of 5%. Also, a minimum space of 450 mm was left between the end of the building and the bottom light system on the sidewalls of the wind tunnel (Hansen, 1986) to avoid a side effect.

4.8 Measurement of external pressure coefficients

4.8.1 Scale model description

Figures 4.3 and 4.4 present the dimensions of the scale model and the pressure tap locations used for the sealed model and the open model. The model was constructed of plexiglass and attached to a wooden base.

Both figures show 10 windows on both sidewalls and 2 windows on both end walls. In the open model, two sets of

sidewall windows were used, each having a dimension of 110 mm x 40 mm which simulated a continuous opening of 800 mm, or a dimension of 110 mm x 55 mm which simulated a continuous opening of 1100 mm. The former set of sidewall windows was equal to 27% of the sidewall surface and the later set equal to 37%. A vertical support was left between each window, which represented the building's posts, 2.4 m apart. Two end wall windows of 60 mm x 100 mm were employed. The building had a 4/12 roof slope with a 15 mm eave overhang above the sidewall.

Three roof opening configurations were tested. As shown in Figs. 4.3 and 4.4, four chimneys of 26 mm x 26 mm (interior dimensions) (600 mm x 600 mm, full scale) were built in order to respect the recommendations for a minimum ridge opening by Choinière et al. (1988b, 1989). Also, continuous ridge openings of 7.5 mm and 20 mm (150 mm and 400 mm, full scale) were built because they are commonly used in agricultural buildings.

The pressure tap locations for the sealed model are shown on Fig. 4.3. A pressure tap was installed in the center of each window simulating a continuous opening of 800 mm. The same tap locations were used for the prediction of ventilation rates of the window openings of 1100 mm, assuming minor changes for the Cp measurements (Vickery et al., 1983, Swami and Chandra, 1987). The airflow through the end wall openings was predicted using an average Cp from the four surrounding pressure taps.

For a sealed model, Vickery (1989) recommended using pressure taps inside each chimney and along the continuous ridge (Fig. 4.5) in order to measure the inside pressures generated by the presence of such openings. Consequently, Fig. 4.3 shows one pressure tap in each chimney and 10 taps along the open ridge. Taps were concentrated at the end of the ridge in order to measure the end effects discussed by Davenport et al. (1977), Hellickson et al. (1983) and many others. Also,

expected high negative pressures at the ends of the building explain the higher concentration of taps near the ends on the sidewalls.

Figure 4.4 presents the pressure locations used with the open model. The calculation of airflow rates for each sidewall or end walls openings were calculated using the average Cp measurements of the three or four closest taps. Etheridge and Noland (1979a) stated that the average Cp measurements would be representative of the center orifice measurement. A total of 26 pressure taps were utilised on each sidewall.

Figure 4.6 shows how the pressure taps were installed for the chimneys and the open ridges. For each chimney, the Cp measurements of the four nearest taps were averaged in order to obtain a single value. For example, for the first chimney, the average of measurements at pressure taps 17, 18, 27 and 28 was used. These taps were installed as close as physically possible to the ridge line (8 mm from the side) in order to sense the pressure in the immediate vicinity of the opening where large negative pressure peaks have been reported by Aynsley *et al.* (1977) and Holmes (1983). The continuous ridges were separated in 10 sections with a specific area in which the average of two pressure taps were used to calculate the airflow rate for that area. For example, pressure taps 11 and 12 were used for the first section. For both chimney and continuous ridge openings, a total of 20 taps were installed, 10 on each side of the ridge.

All pressures were measured by low range pressure transducers, Setra Systems, Inc., Model 237. Their range was ± 750 Pa, with 0.1% precision. Since five pressure transducers were available, they were used with scanivalves, as described by Brown (1986).

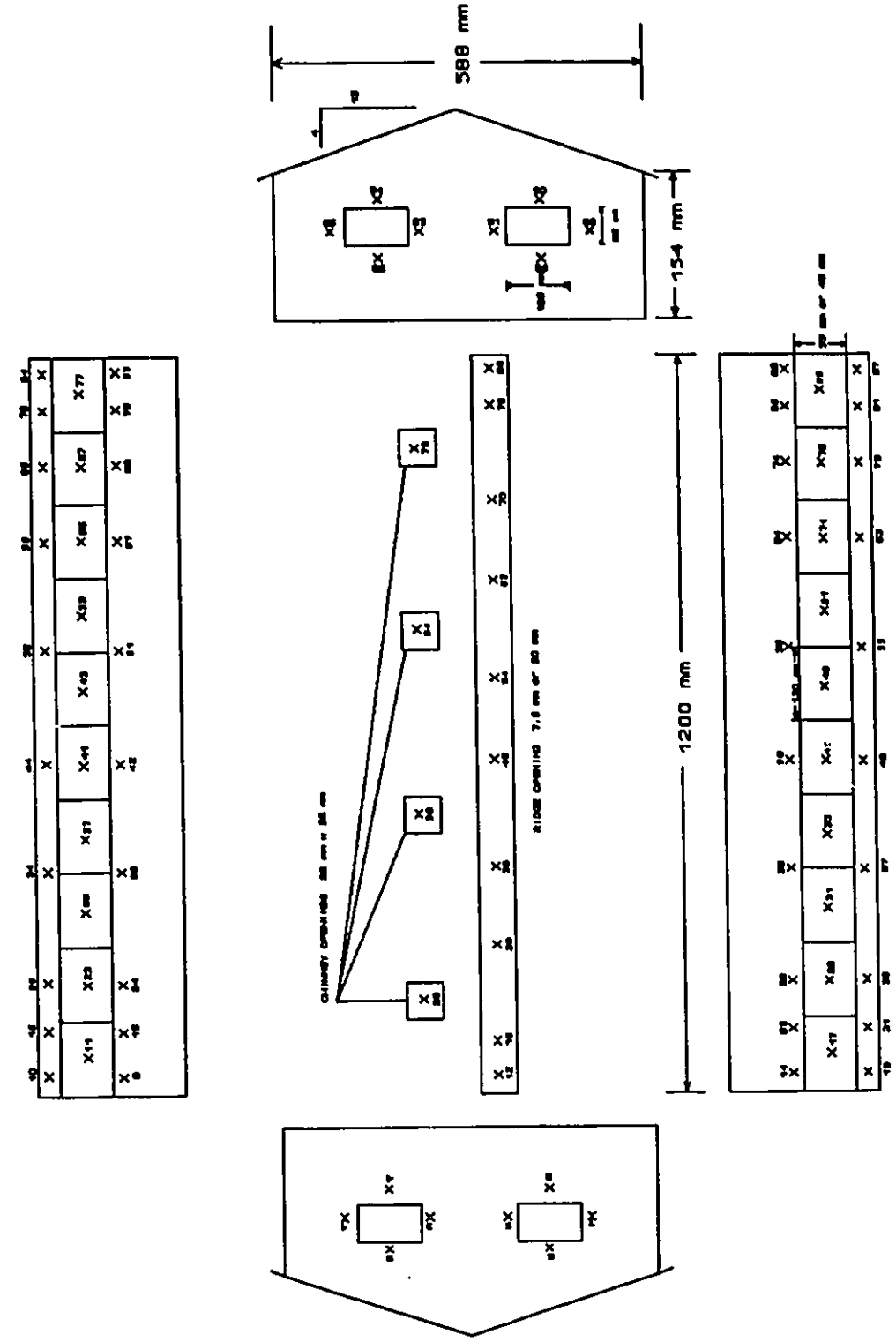

Figure 4.3 Scale model dimensions and tap locations for the sealed model.

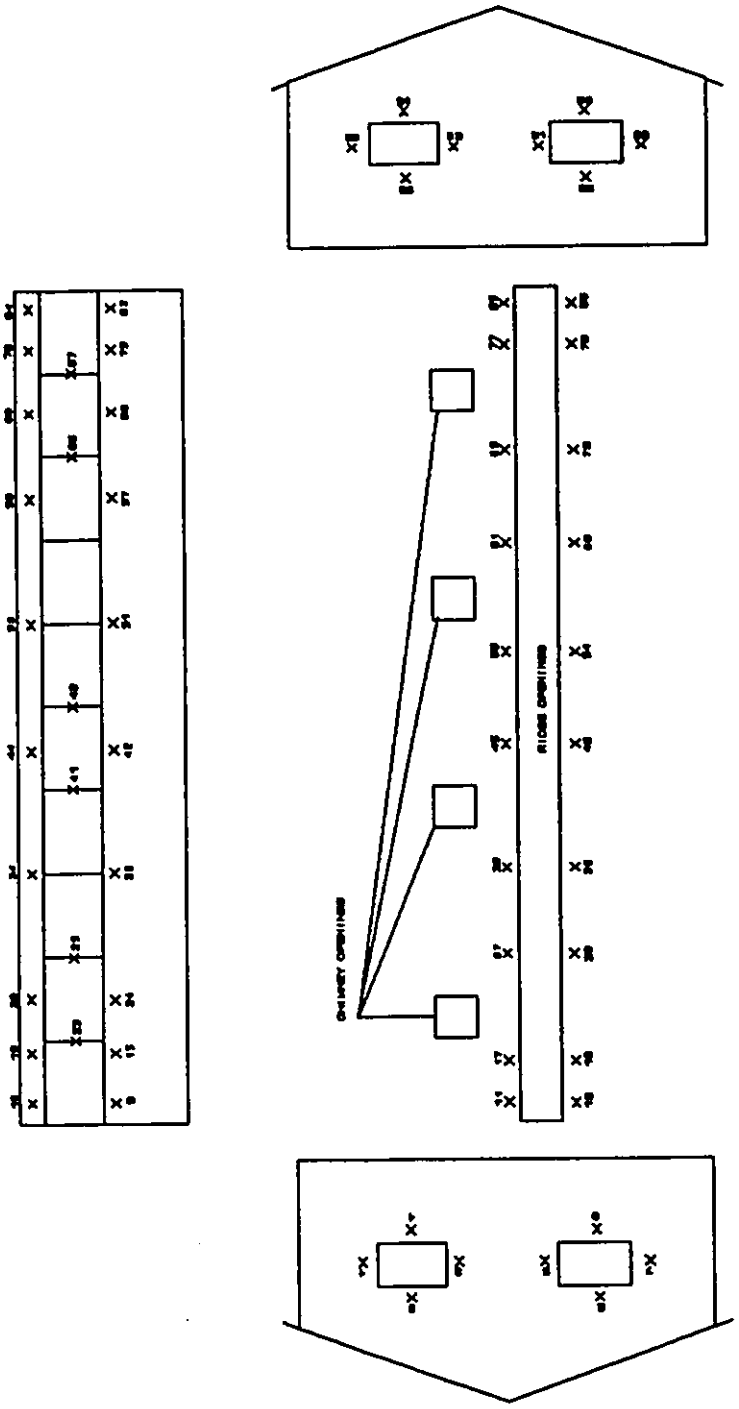

Figure 4.4 Tap locations for the open model.

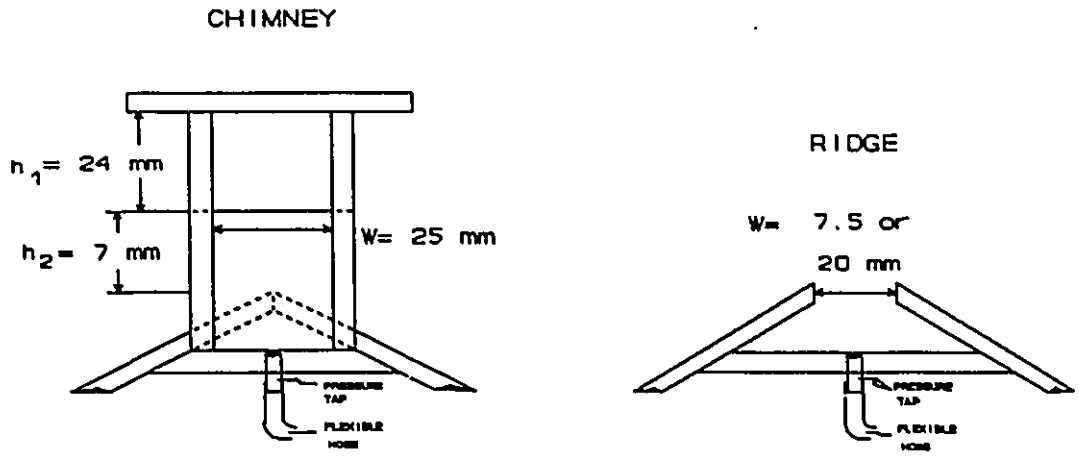

Figure 4.5 Sealed model - location of pressure taps for chimney and ridge opening widths simulating 150 mm or 400 mm.

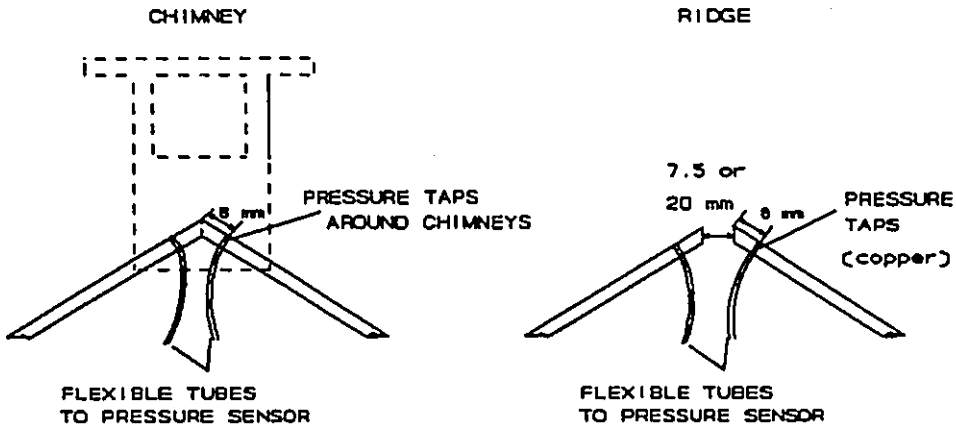

Figure 4.6 Open model - location of the pressure taps for chimney and ridge opening widths simulating 150 mm or 400 mm.

4.8.2 Description of variables

Table 4.1 indicates the tests performed on the open model in relation to the three structural variables:

1 - Three types of roof openings (chimney or continuous ridge of 150 mm or 400 mm width, full scale).

2 - Two sidewall opening areas.

3 - The use of two openings in the barn end walls.

With the sealed model, three types of roof openings were used, but the sidewall and end wall openings remained closed. Each of these variables were studied for seven wind angles of incidence relative to the building length: 0°, 10°, 20°, 30°, 45°, 60° and 90°. A wind parallel to the building length would be referred to as a wind at 0°. More measurements were made at angles between 0° and 45° due to expected changes in the results, as demonstrated by Vickery et al. (1983). A total of 84 and 21 tests were performed for the open and sealed model, respectively.

4.8.3 Measurement of internal pressures

According to Davenport et al. (1978), Stathopoulos et al. (1979) and Vickery et al. (1983), the internal pressure coefficient, Cp_{in}, should remain uniform across the ventilated airspace. Based on these studies, only 10 taps were allocated to measure the internal pressure in the open scale model. However, during the wind tunnel tests, large Cp_{in} differences among these tap locations were recorded at various wind angles of incidence. Figures. 4.7 to 4.11 relate all the tap location changes which occurred during testing.

Table 4.2 summarizes tests done with the arrangements for internal pressure. Figure 4.7 shows the first arrangement of internal pressure taps. The taps were simply mounted on the sidewall with little plexiglass blocks. In Fig. 4.8, a piece of cardboard was added to protect the pressure tap from any direct air currents inside.

Table 4.1 Combination of parameters tested in the NRCC's wind tunnel for seven wind angles of incidence.

Test Catagories	Parameters			
	Simulated Roof*	Simulated Sidewall Opening* (mm)	End Wall	Configuration Number
Open model	Ch	800	O	1
	Ch	800	C	2
	Ch	1100	O	3
	Ch	1100	C	4
	150 mm	800	O	5
	150 mm	800	C	6
	150 mm	1100	O	7
	150 mm	1100	C	8
	400 mm	800	O	9
	400 mm	800	C	10
	400 mm	1100	O	11
	400 mm	1100	C	12
			7 angles x 12 = 84 tests	
Sealed model	Ch	--	--	1
	150 mm	--	--	2
	400 mm	--	--	3
			7 angles x 3 = 21 tests	
			Total = 105 tests	

Note: Ch = Chimney C = Closed O = Open
* The measurements are full scale values.

Consequently, six taps were moved to the ceiling to check if the same Cp_{in} differences would be recorded (Fig. 4.9). Since large fluctuations were still noticed, the ceiling taps were moved to their final positions, shown in Fig. 4.10. Finally, four pressure taps on the walls were installed extending perpendicularly to the walls (Fig. 4.11). This was to avoid

the possibility that the blocks themselves may have disturbed the flows.

Table 4.2 Configurations for internal pressure measurements with the open model.

Configuration Number	Simulated Roof	Simulated Sidewall Opening (mm)	End Wall
1	Ch	1100	C
2	Ch	800	C
	Ch	800	O
3	150 mm	800	C
	150 mm	800	O
4	400 mm	800	C
5	400 mm	800	O
	400 mm	1100	O
	150 mm	1100	C
	150 mm	1100	O
	Ch	1100	O
	400 mm	1100	C

4.8.4 Calculated internal pressures

The standard pressure difference method was used to obtained a calculated internal pressure based on Eqs. 2.2, 2.3 and 2.4. The iteration process was stopped when a difference of 0.001 between the predicted inflows and outflows was obtained.

All basic assumptions of uniformity for the interior pressure coefficient and an equal pressure drop across the windward and leeward walls were respected.

4.8.5 Data collection and processing

Average pressure coefficients, Cp, Cp RMS, freestream wind speed, reference wind speeds and dynamic pressures of the wind tunnel were transferred from the wind tunnel's computer centre to an IBM-PC for storage. The calculations of the airflow rates, Q, and internal pressure coefficients were done on site to compare them with measurements during the tests.

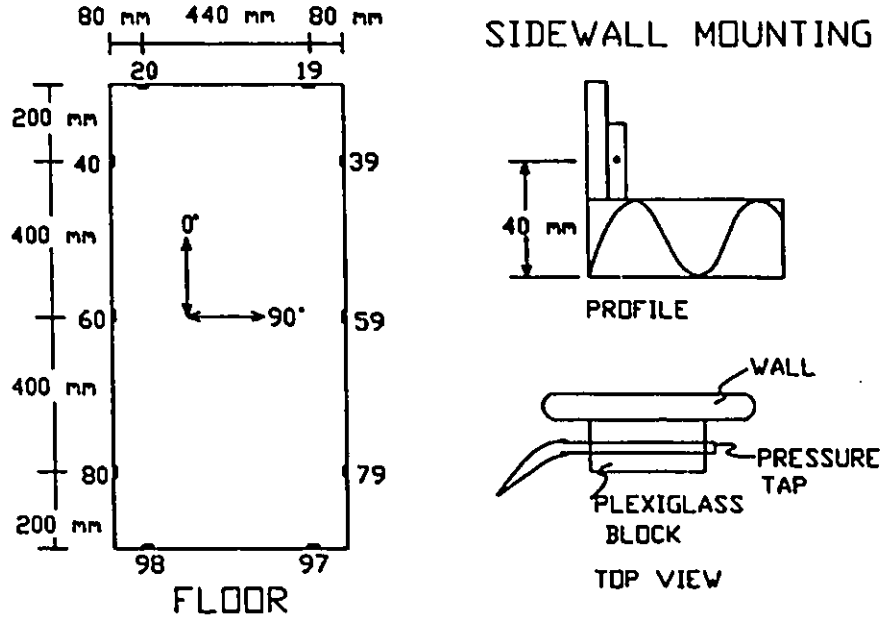

Figure 4.7 Configuration no. 1, internal pressure measurements.

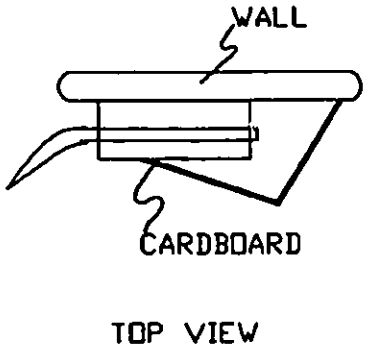

Figure 4.8 Configuration no. 2, addition of protective cardboard.

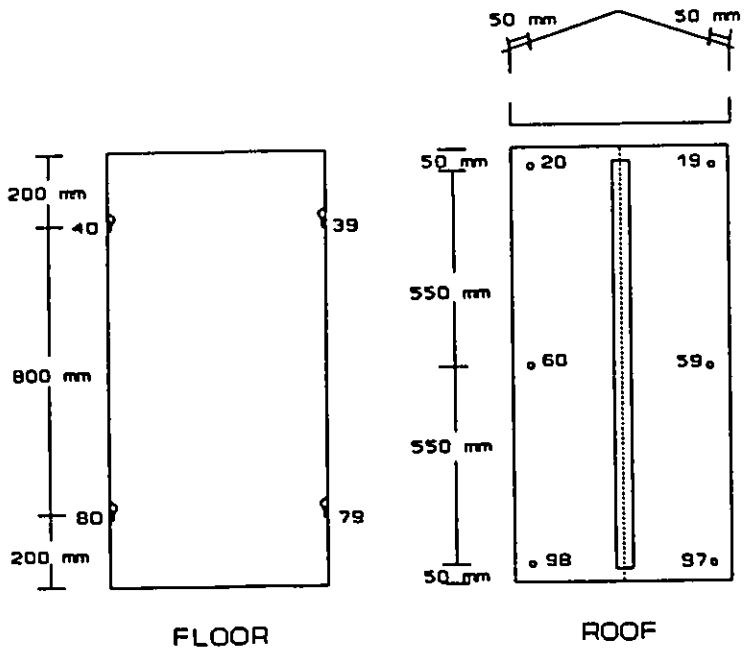

Figure 4.9 Configuration no. 3, six taps installed on the ceiling.

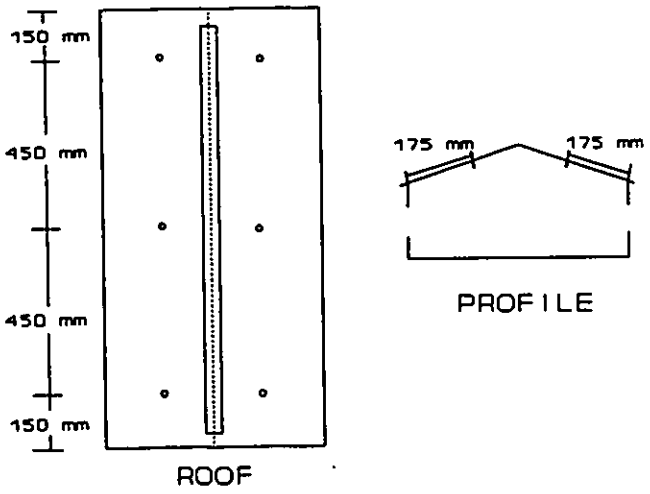

Figure 4.10 Configuration no. 4, taps placed at the middle width of the ceiling slopes.

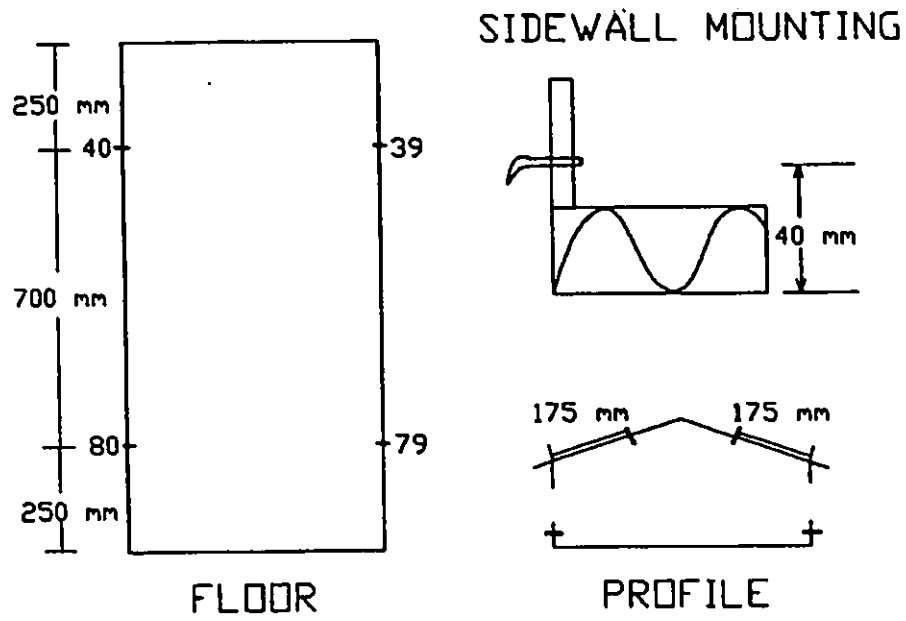

Figure 4.11 Configuration no. 5, final wall and ceiling tap locations for CP_{in} measurements.

4.8.6 External pressure coefficients

Contour lines were used to plot the external pressure coefficients over the building surfaces. The mapping program, Macdrain, (Tremblay, 1987) was adapted to produce contour lines similar to those in Davenport et al. (1978) and Holmes (1983). The program interpolates between tap values and extrapolates over the control surface. For the sealed model, 30 tap locations were used on each sidewall and 8 taps on each end wall. With the open model, 26 tap locations were used on each sidewall and the same eight taps on each end wall. For both model conditions, the Cp distributions for the chimney and continuous 150 mm and 400 mm ridge were numerically represented for the 10 sealed and 20 open tap locations.

4.8.7 Internal pressure coefficients

A program written in Quick Basic 4.5, was prepared to produce the measured internal pressure data in graphic form. The calculated Cp_{in}s were plotted against the wind angles of incidence using Lotus 1-2-3.

4.8.8 External-internal pressure differences

Another program, also written in Quick BASIC 4.5, calculated and plotted the ΔCp values ($Cp_j - Cp_{in}$), using the calculated internal pressure coefficient. The directions of the arrows in Figs. 5.26 to 5.35 indicate the inflows or outflows of air. For all drawings, the length of the arrows are proportional to the magnitude of the pressure coefficient differences. It occasionally occurred that no arrows were plotted along the walls or the ridge, leaving a blank space; this indicated a zone where $\Delta Cp = 0$.

For the sealed model simulating the 400 mm ridge opening width, presented on Fig. 4.3 the third pressure tap on the left side of the ridge opening had been obstructed during the test (pressure tap 70, Fig. 4.3). There were no arrows plotted at this location, however the airflow was approximated

by averaging the two neighboring pressure coefficients (pressure taps 62 and 78).

Also, errors of -Cps measurements over the ridge occurred for the OP-400-800-C tests for θ = 0° to 45°, for taps 77, 48, 54 and 36. The data were processed but the predictions have been impaired by these erratic measurements.

4.8.9 Plots of the local ventilation rates

In addition to the plots of the inside-outside pressure coefficient differences, plots of the local ventilation rates, Q_j, for each opening added extra information on the relative magnitude of the airflow rates, which are linearly affected by the area of each respective opening. For this study, the airflow rate of each opening was calculated by Eq. 2.3,

$$Q_j = C_d A_j V_{ref} \frac{Cp_j - Cp_{in}}{|Cp_j - Cp_{in}|^{1/2}} \qquad (2.3)$$

where

C_d = 0.6 for all openings
Cp_{in} = calculated internal pressure

The total ventilation rate, Q_T, is equal to the total inflow and the total outflow. The values for the C_d presented in the literature varied from 0.35 to 0.85. The conservative value of 0.60 was used according to recommendations from ASHRAE (1981) and Vickery et al (1987).

The continuous line method of Shrestha et al. (1990) was used to illustrate the airflow rates through each opening. Lines outside the model indicate outflows and the reverse inflows. A Quick BASIC 4.5 program was written to plot these continuous lines. The magnitudes of the lines were adjusted in order to obtain clear drawings and visualize the effects of the different ridge opening types and sidewall openings on the local ventilation rates.

4.8.10 Ventilation rate coefficients

The procedure of Etheridge and Nolan (1979a), Vickery and Karakatsanis (1987) and Vickery et al. (1983) was followed and Eq. 2.5 was transformed in order to calculate the ventilation rate coefficients for each tests. The following formula was used:

$$C_{Q10} = \frac{Q}{V_{10} A_s} \qquad (4.5)$$

The use of a non-dimensional ventilation rate coefficient or ventilation efficiency factor "E" (ASHRAE, 1981, Hellickson et al., 1983) is a simple and rapid method for designers to calculate the ventilation rates of any structures. There will be a different C_{Q10} value for each building orientation, reference velocity height and each type of opening areas.

The reference area of opening, A_s, differs according to the various authors. Etheridge and Nolan (1979a), Vickery and Karakatsanis (1987) and Vickery et al. (1983) used the total opening area on both sidewalls of their scale models while it is common in agriculture to use only the frontal sidewall opening area (Hellickson et al., 1983). For this study, the advantages for using only the frontal sidewall area as a reference opening are:

1 - Visualisation of the ridge's effects.
2 - Visualisation of the end wall openings' effects.
3 - Visualisation of the respective sidewall opening areas' effects.

All visualisations are in reference to the flow coefficients, C_{Q10}, at each wind angle of incidence. The values of C_{Q10} for the sealed and open models were tabulated and then plotted using Lotus 1-2-3.

4.9 Concentration decay method

4.9.1 Optical density measurements by laser

The optical density equipment described by Clark (1985) was used. A 0.5 mW, random polarization, He-Ne laser was the light source. The signal receiver was a silicon diode photodetector (S.D.P.) with 1 cm^2 active area (Silicon Detector Corporation, Model SD-444-12-12-171). A He-Ne laser line filter (band width, 10 nm at mid-peak) was installed just over the photodetector to eliminate any other light frequencies from other light sources. The laser and the mirror were installed in a sealed enclosure to prevent smoke infiltration between the laser and the light entrance in the model. Smoke infiltration also alters the laser output when condensing on the emitting laser tube. During tests, the laser and the mirror had to be cleaned when the S.D.P. was indicating abnormally low output voltages. Since the plexiglass deformed the light beam, two holes were drilled in the plexiglass model to install two pieces of clear glass. This allowed the laser beam to go through the end walls unaltered. These two glass slides required regular cleaning to prevent the deposition of oil droplets.

4.9.2 Model installation in the wind tunnel

Figure 4.12 is a schematic diagram of the experimental scale model with the optical density measuring devices.

The laser had to be mounted below the floor surface in order to prevent interference with the pressure measurements. The laser output had to be calibrated on site with optical filters after its installation in the wind tunnel, as described by Clark (1985). The calibration curve was:

$$OD = 14.195 \times Voltage + 5.6196 \qquad (4.6)$$

where

r^2 = 0.9998
OD = optical density
Voltage = output of the silicon diode photodetector, mV

The silicon diode photodetector sent an output voltage to a high speed A/D module (Sciemetric Instrument, Model 233), which was relayed to an IBM PC. Graphical representations of the output are found in Appendix D.

As shown in Fig. 4.12, the laser beam travelled across the entire length of the building, mid-width of the building and at an elevation of 75 mm (1.5 m full scale) above the floor surface. This location was selected because farm operators spend most of their time in this control corridor.

The optical density technique presented many advantages for this study, such as:

1 - An average measurement of the rate of decay along the entire building length.
2 - No extraction of gases.
3 - Near instantaneous response.
4 - Very sensitive tool.

4.9.3 Smoke generation

A smoke generator similar to the one described by Rea et al. (1985) was used. The MDG Smoke Generator, Model 3020, (Les Entreprises MDG, Inc., Montréal) was used in this experiment. At high temperatures, this smoke generator vaporises an odourless oil mixed with carbon dioxide pressurized at 900 kPa. According to the manufacturer, high CO_2 pressure produces smaller vaporized oil particles, ranging from 0.5 μm to 4.5 μm.

The vaporised oil was sent through a pressurized distribution manifold to enter into the scale model by eight

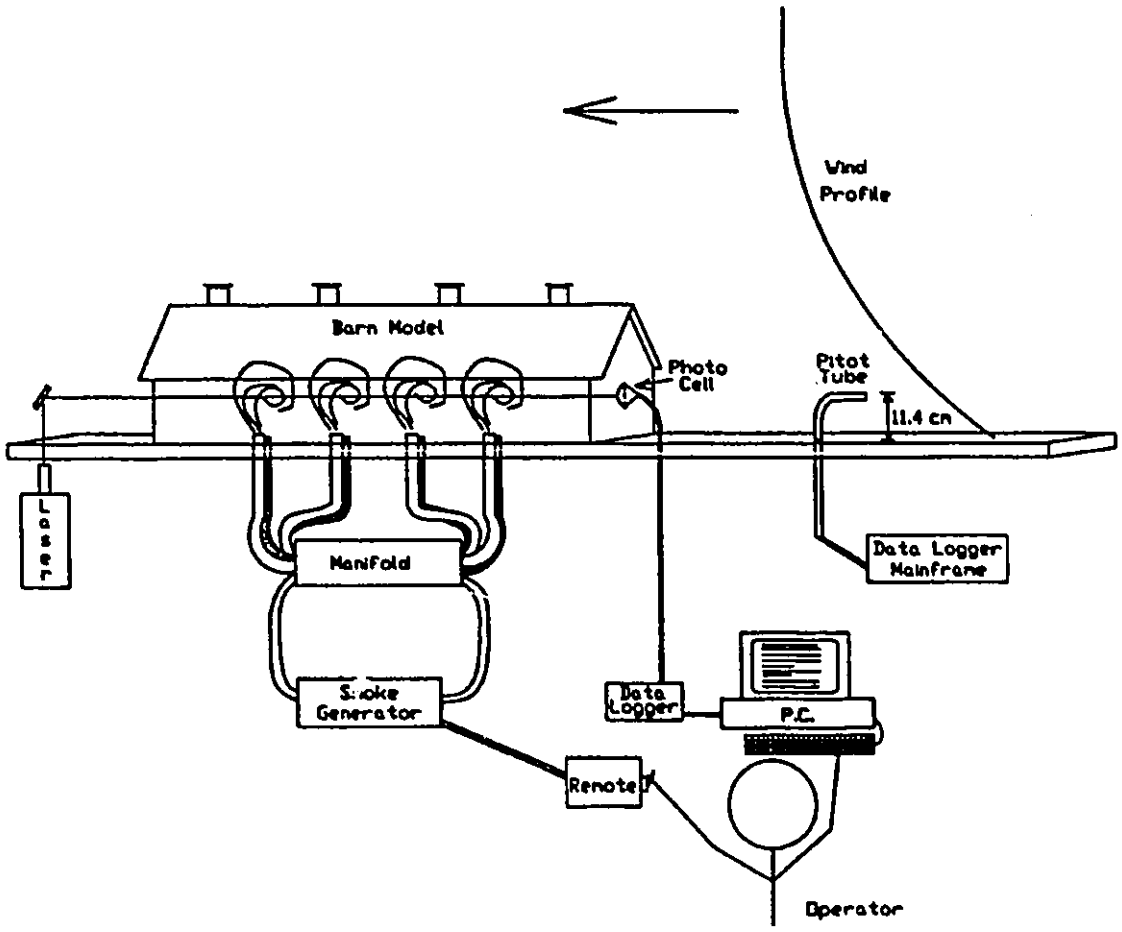

Figure 4.12 Experimental installation for optical density measurements.

equally distributed plastic tubes. The smoke was injected into a zone of high air speed. Due to the large opening area and the high wind speed in the tunnel, the distribution of the smoke inside the building was very rapid and the airflow patterns corresponded to observations made by Choinière et al. (1988c). A remote control was available to stop the smoke generation in order to prevent subsequent oil entrance. Flexible plastic valves were installed over each entrance hole. Their weight was enough to shut the entrance from vaporized oil for most cases even if the pressure was negative inside the scale model and residual positive pressure remained in the manifold.

4.9.4 Sampling and data recording

Optical density measurements were done at a sampling frequency of 200 Hz or 250 Hz during a 6 s to 10 s interval, depending on the scale model's orientation and opening areas. These were the operator's tasks:

1 - Injection of large quantities of vaporized oil within a period of 5 s to 10 s, until the smoke was evenly distributed along and across the scale model.
2 - Data recording commenced within 5 s after halting the injection.
3 - Read the instantaneous velocity from the wind tunnel velocity meter.
4 - The whole operation was repeated five times.

The rate of decay of the smoke was monitored by measuring the optical density as it decreased over time. Data gathering was done from the completely opaque stage to the totally cleared scale model. Most of the useful measurements occurred within a period of 0.5 s to 2 s.

The assumption of no change in the refractive properties and particle sizes of the vaporised oil was supported by the data presented by Hinds (1982). He reported that vaporised hot oil used in a stagnant airspace starts to coagulate and

condense after a period varying from minutes to hours depending on the airspace surface temperature and the inside air temperature. Therefore, the short duration of the experiments may eliminate this potential problem.

A total of 420 tests were recorded during the testing periods (84 configurations x 5 replicates).

4.9.5 Minimum wind speed for decay rate measurements

Choinière et al. (1988c) observed the internal airflow patterns of the same scale model with vaporized oil at a velocity of 2 m/s within a low wind speed tunnel. A minimum wind speed of 0.64 m/s was necessary to obtain stable airflow patterns inside the 1:20 scale model. The rate of decay tests were performed at a freestream velocity of 10 m/s because it was close to the minimum stable wind speed available with the low wind speed tunnel at NRCC, Ottawa (Brown, 1986).

4.9.6 Data processing

The rate of decay of smoke could be calculated by using Eqs. 2.6 and 2.18,

$$\frac{C_T}{C_o} = e^{-\frac{QT}{V}} \qquad (2.6)$$

and

$$\frac{OD}{OD_o} = \frac{N}{N_o} \qquad (2.18)$$

Since the ratio C_T/C_o is directly proportional to the number of particles in the airspace N/N_o, it could be assumed that

$$\frac{OD}{OD_o} = e^{-\frac{KQT}{V}} \qquad (4.7)$$

then

$$\ln\left(\frac{OD}{OD_o}\right) = -KQ\frac{T}{V} \qquad (4.8)$$

where

-KQ = effective ventilation rate

In fact, the data from the optical density measurements were an indication of KQ.

With these tests, it was neither possible nor was it the intent of this work to calculate the mixing factor, K. The laser beam was used to potentially obtain an average "effective" ventilation rate through the over ventilated and under ventilated zones in the building.

Appendix D contains the complete methodology for the calculation of the effective ventilation rate, KQ. Basically, the voltage outputs were transformed by Eq. 4.6 to obtain OD values. Etheridge and Nolan (1979b) used the voltage output directly. This procedure could be used, but the simple transformation to OD provided information on the potential refeeding of smoke into the model, or smoke contaminating the laser.

After the first 10 to 20 tests, the closed circuit wind tunnel was already contaminated with smoke. The OD measurements at the end of later tests did not decrease to 0. From this fact, the calculation procedures were changed to take account of the C_s, air contaminants in the intake, and obtain the following formula:

$$\ln\left(\frac{OD-OD_s}{OD_o-OD_s}\right) = -KQ\frac{T}{V} \qquad (4.9)$$

where

OD_s = optical density value of air intake contaminant

The value of OD_s for each test was obtained from the difference between the measured OD at the end of the test and 0.0 (clear model). The effect of air intake concentration of smoke was then eliminated.

According to the procedure of Etheridge and Nolan (1979b), Hunt (1980) and Shaw (1984), the KQ value was calculated from the slope of the logarithmic curve (Appendix D). They also discussed choosing the initial and final values to be used for these calculations. This creates some differences in the KQ values. Generally, the curve is fairly flat at the initial stage. When the laser beam passed through the smoke, the measurements of the rate of decay were started. From the average initial points, initial starting points for the calculations were selected when the variation between the opaque stage and the decay stage was above 0.6 OD. At the end of the process, the selection of a difference in OD from the last values ranged between 0.44 to 0.35. These differences were selected due to spikes or bumps, occurring in the final stage of the curve.

The bumps were mainly caused by infiltration of dense smoke through the injection tubes and the manifold because the simple gravity valves used were not perfectly sealed. As soon as extra smoke entered and passed in front of the laser beam, a bump in the curve would appear. The OD measurements nearer to the smoke-free stage were very sensitive.

All KQ values were calculated using a program written in Quick BASIC 4.5. They were transformed to obtain a dimensionless effective flow coefficient of:

$$C_{KQ10} = \frac{KQ}{V_{10} A_a} \qquad (4.10)$$

where

C_{KQ10} = effective airflow coefficient at 10 m.

The data were tabulated and plotted using Lotus 1-2-3.

CHAPTER 5

RESULTS AND DISCUSSION

5.1 External pressure coefficients

5.1.1 Open model

The results of the open model are used as the standard for comparisons and all pressure coefficients are based on the 10 m reference height. Appendix E contains a complete set of pressure coefficient contour lines.

5.1.1.1 General observations

Figures 5.1a through 5.1g present the results for the chimney, simulated 800 mm sidewall openings and closed end wall tests, (OP-CH-800-C). The results at $\theta = 90°$ (Fig. 5.1a) show a uniform Cp distribution along the windward sidewall. The contour lines indicate a slight increase in the Cps from the base to the top of this wall (near the overhang). This phenomenon was also indicated by Holmes (1983). Cps decrease rapidly at both ends, near the corners. Aynsley et al. (1977), ASHRAE (1981) and many other authors have previously discussed the acceleration of the flow at corners which causes this decrease. The pressure distribution on the leeward sidewall is fairly uniform along its length. On the vertical axis, there is an average Cp difference of 0.15 from the base of the wall to the overhang height. Hoxey (1984) showed similar behaviour for full scale buildings. Both end walls are subjected to a large Cp gradient from the upwind to the downwind edge and similar contour lines have been shown by Aynsley et al. (1977), Davenport et al. (1977) and Holmes (1983).

The Cps are generally negative at the ridge level. Higher negative Cps were recorded on the leeward side of the ridge as compared to the windward side. This result was reported by Aynsley et al. (1977), Vickery et al. (1983) and many other authors. As compared to most of the previous tests with continuous ridge opening or regular closed ridge, these Cps do not show uniform values along the ridge line. For example, the second set of pressure taps from the top part of Fig. 5.1a are very close to the upstand of the first chimney and both Cps are lower than their closest taps. The same phenomenon is noticed with the two last pressure taps at the bottom part of Fig. 5.1a.

At $\theta = 60°$ and 45°, the Cps are higher at the upwind end of the windward sidewall for about a quarter of the building length and they rapidly drop and stabilize on the remainder of this wall. The negative Cps are fairly uniform over the leeward sidewall at 60°, but a high negative corner on the upwind end is visible at $\theta = 45°$.

Bauman et al. (1988) reported that upstands and jack roof covers over the ridge drastically changed the pressure distribution over the ridge line. Local flow disturbances may be created by the chimney. Since there are no data on the Cps around a building, this may potentially change the local -Cps. Instrumentations of many pressure taps around and inside a chimney may provide more information on the effects of the chimney design. For the present study, it was assumed that the average of the four closest pressure taps around each chimney could be used to calculate the ventilation rates.

At $\theta = 30°$, the windward sidewall shows some -Cps over the upwind end (about 15% of the length) indicating a complete change in the airflow distribution over the windward sidewall. The upwind end of the leeward sidewall shows high -Cps. The upwind end wall is entirely positive and the Cp gradient at the downwind endwall is less. The effects of air circulation tend to disappear around the chimneys. For example, at $\theta=20°$,

only the first windward chimney is surrounded by high -Cps. The upwind end wall shows a vertical gradient of pressure which may be due to the upwind airflow over the building and the air stream divided to flow around and above the building (ASHRAE, 1981). The downwind end wall shows stable -Cps. The chimneys still create local flow disturbances as shown by the two -Cps values recorded for the second set of taps on the top part of Fig. 5.1e.

At $\theta = 10°$, about 50% of the upwind windward sidewall shows high -Cps; the behaviour is echoed on the leeward sidewall. At $\theta = 0°$, the Cp distribution along both sidewalls is nearly symmetrical. Negative Cps decline for 50% of the upwind length and stabilize for the remaining part of the sidewall. The upwind end wall behaves in the same way as the windward sidewall did at $\theta = 90°$ except that the vertical Cp gradient is influenced by the shape of the roof. At the ridge, high -Cps are noticed on the upwind part only and are stabilized shortly after. These pressure distributions are fairly similar to the data of Aynsley et al. (1977), Davenport et al. (1977, 1978) and Holmes (1983).

5.1.1.2 Effect of sidewall openings with closed end walls

Figures 5.1a-g (OP-CH-800-C) and Figs. 5.2a-d (OP-CH-1100-C) reveal that at $\theta = 90°$, the windward sidewall has higher Cps with the 1100 mm opening versus the 800 mm opening. However, the leeward sidewall -Cps have been consistently increased by -0.05 for the 1100 mm opening. The same increase in -Cps on the leeward sidewall have been noticed in Figs. 5.3a versus 5.4a and for the other tests with 150 mm and 400 mm ridge (Appendix E). The end wall and the chimney Cp distributions were not affected by the increase of the sidewall area.

At $\theta = 60°$ and 45°, Figs. 5.1b, 5.1c, 5.2b, 5.2c and Fig. E.2c (Appendix E) show different Cp distributions over the windward sidewall surface. Higher Cps are recorded with the

800 mm opening as compared to the 1100 mm opening at the upwind corner of the sidewall. The larger sidewall opening area (1100 mm) may allow air to go through the opening area, reducing the blockage or the turbulent upwind effect at the corner. On the other hand, the increase in outflow through the leeward sidewall seems to create slightly more negative -Cps. The upwind and downwind end walls and the chimney show fairly similar Cps.

At $\theta = 30°$, $20°$, and $10°$, the 1100 mm sidewall opening shows higher -Cps at the upwind corner of the windward wall while both end walls, leeward sidewall and chimneys are identical. At $\theta = 0°$, there is no effect by the opening area on the Cps. The comparison among the data with continuous ridge openings of 150 mm and 400 mm (Appendix E) shows similar effects of the sidewall opening areas on the Cp distribution. The increase in the ridge opening accentuates the difference in -Cps for the leeward sidewall at $\theta = 90°$, $60°$, and $45°$, and shows very similar results for the upwind windward corner at $\theta = 30°$, $20°$, $10°$ and $0°$.

From all tests, increasing the sidewall area from 800 mm to 1100 mm, with the closed end walls, produce the following:

1 - Higher Cps over the upwind windward corner for the 800 mm at $\theta = 90°$, $60°$ and $45°$.
2 - Higher -Cps over the upwind windward corner for the 1100 mm at $\theta = 30°$, $20°$ and $10°$.
3 - Higher -Cps over the leeward wall for the 1100 mm for $\theta = 90°$ and $60°$.
4 - Negligible effect at $\theta = 0°$.

The same behaviours are noted with either ridge opening width of 150 mm or 400 mm.

5.1.1.3 Effect of end wall openings

By comparing Figs. 5.1a-g (OP-CH-800-C) and 5.3a-d (OP-CH-800-O), similar Cp distributions over the windward wall at $\theta = 90°$ as observed. The leeward wall shows a small

increase in -Cps when the 1100 mm sidewall opening is used. Major changes in Cp distributions occur at both end walls. The Cp distribution is completely changed when the end wall windows are open. Rather than a gradual decrease in Cps over the end walls, the distribution show a lower -Cp zone at the center of both end walls. Negligible changes in the Cp distribution occur at the chimney level.

At $\theta = 60°$, $45°$ and $30°$, the Cp distribution over the windward and leeward sidewalls are not affected by the opening of the end wall windows. However, the Cp distributions over the upwind and downwind end walls are different, depending on whether the end walls are open or closed. It appears that the -Cps over the ridge are not affected by opening the end walls.

For angles of $\theta = 20°$ and $10°$, the model with the open end walls show a reduction in the -Cps at the upwind corner of the windward wall and on the upwind corner of the leeward sidewall. Both end walls differ from the closed end wall model.

At $\theta = 0°$, both the sidewall and chimney pressure distributions show no difference with either closed or open end walls. However, the Cp distribution over the upwind end wall surface shows a large increase of about 0.05 to 0.1. The -Cps were slightly higher at the downwind end wall also.

The comparison between Fig. 5.2a-d (OP-CH-1100-C) versus Fig. 5.4a-d (OP-CH-1100-O) with the larger sidewall area of 1100 mm showed similar effects on the Cp distribution compared to the effect presented by Fig. 5.1a-g (OP-CH-800-C) and Fig. 5.3a-d (OP-CH-800-O).

When the data of Figs. 5.5a-d (OP-150-800-C) and 5.6a-d (OP-400-800-C) are compared to the results contained in Appendix E for open end walls, it appears that the same effects on both end walls are noticed. Very small effects were noticed on the sidewalls.

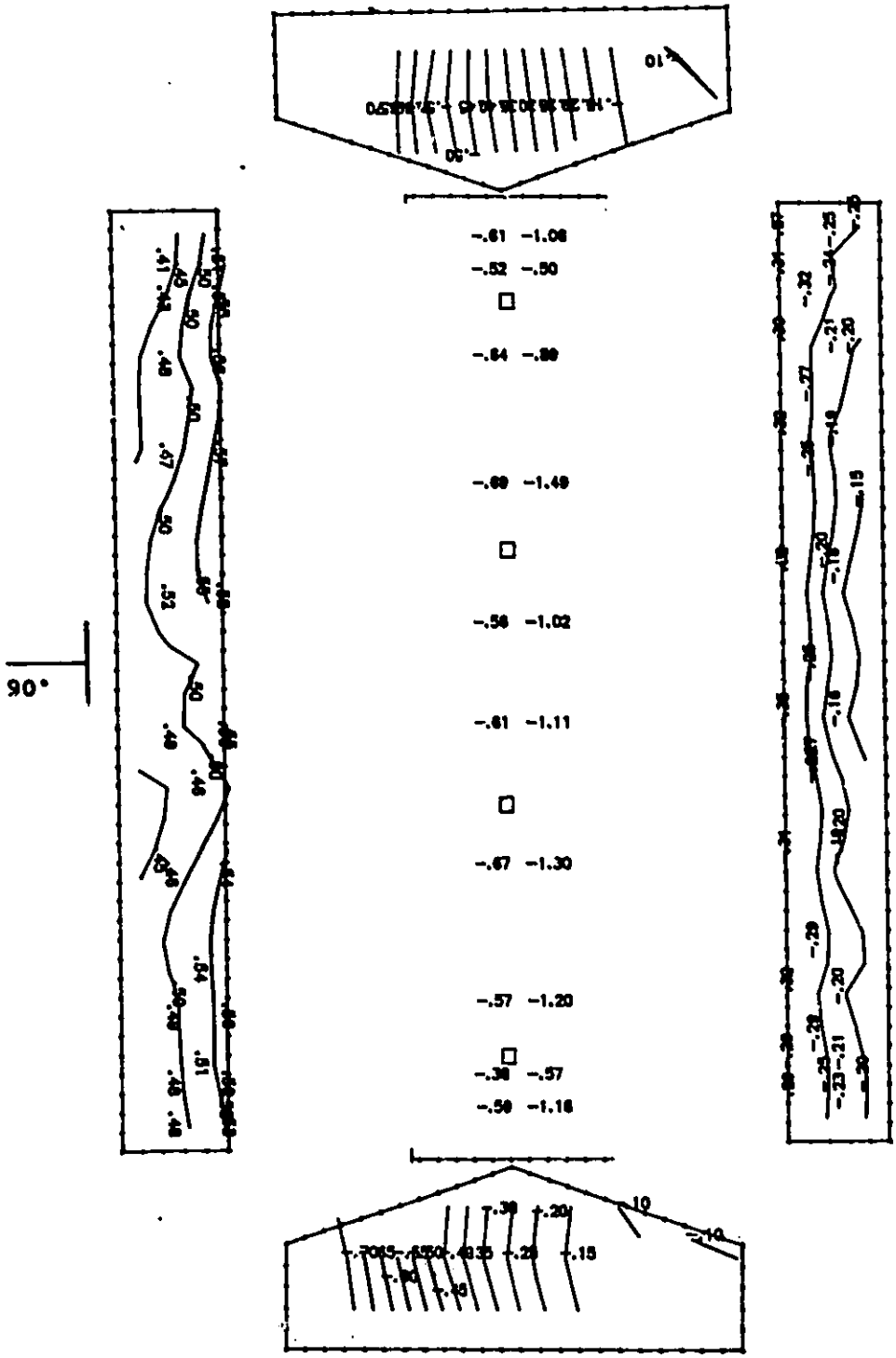

Figure 5.1a Cps contour lines: open model, chimney, simulated 800 mm sidewall openings, closed end walls, wind angle of 90°.

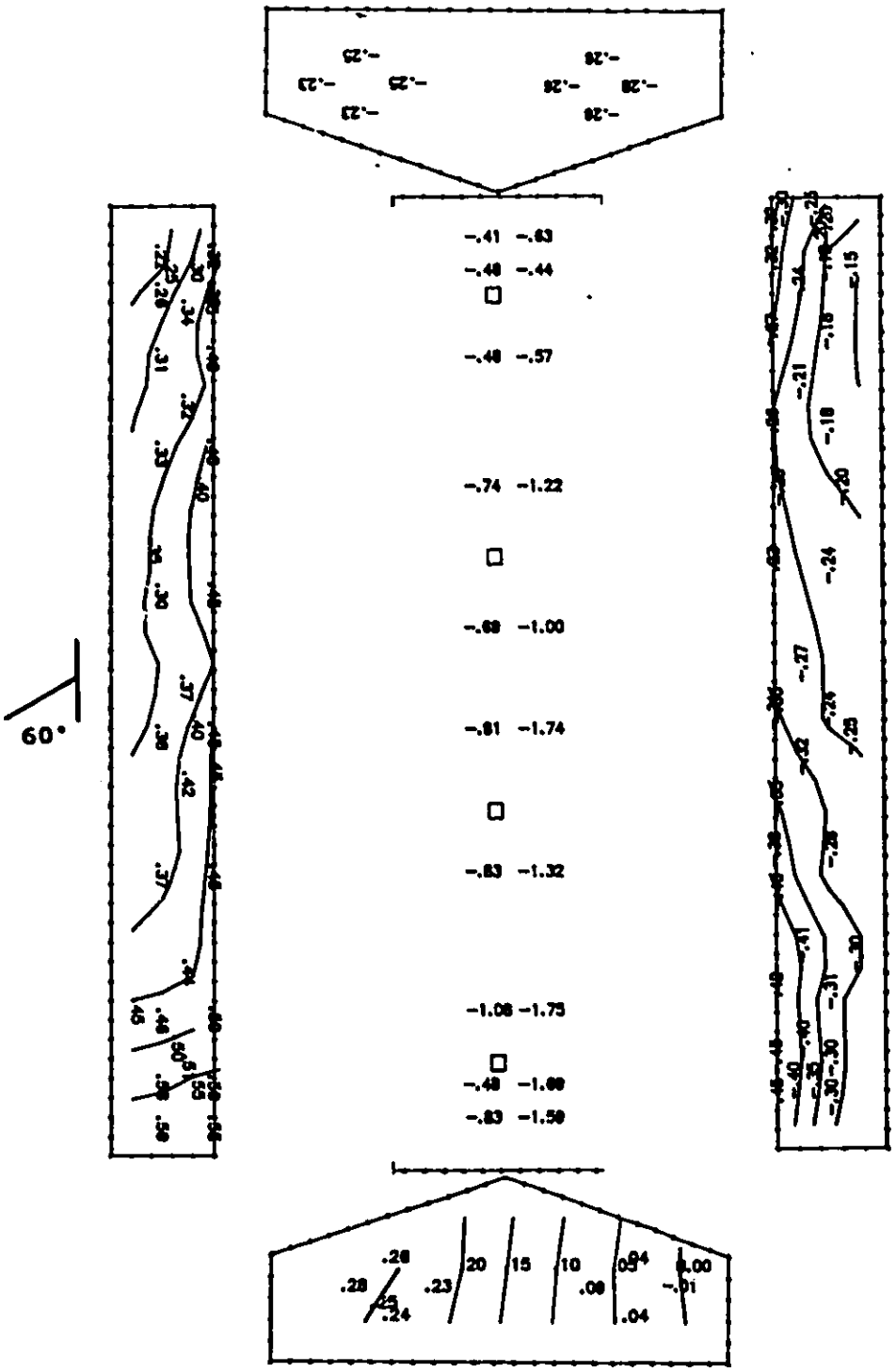

Figure 5.1b Cps contour lines: open model, chimney, simulated 800 mm sidewall openings, closed end walls, wind angle of 60°.

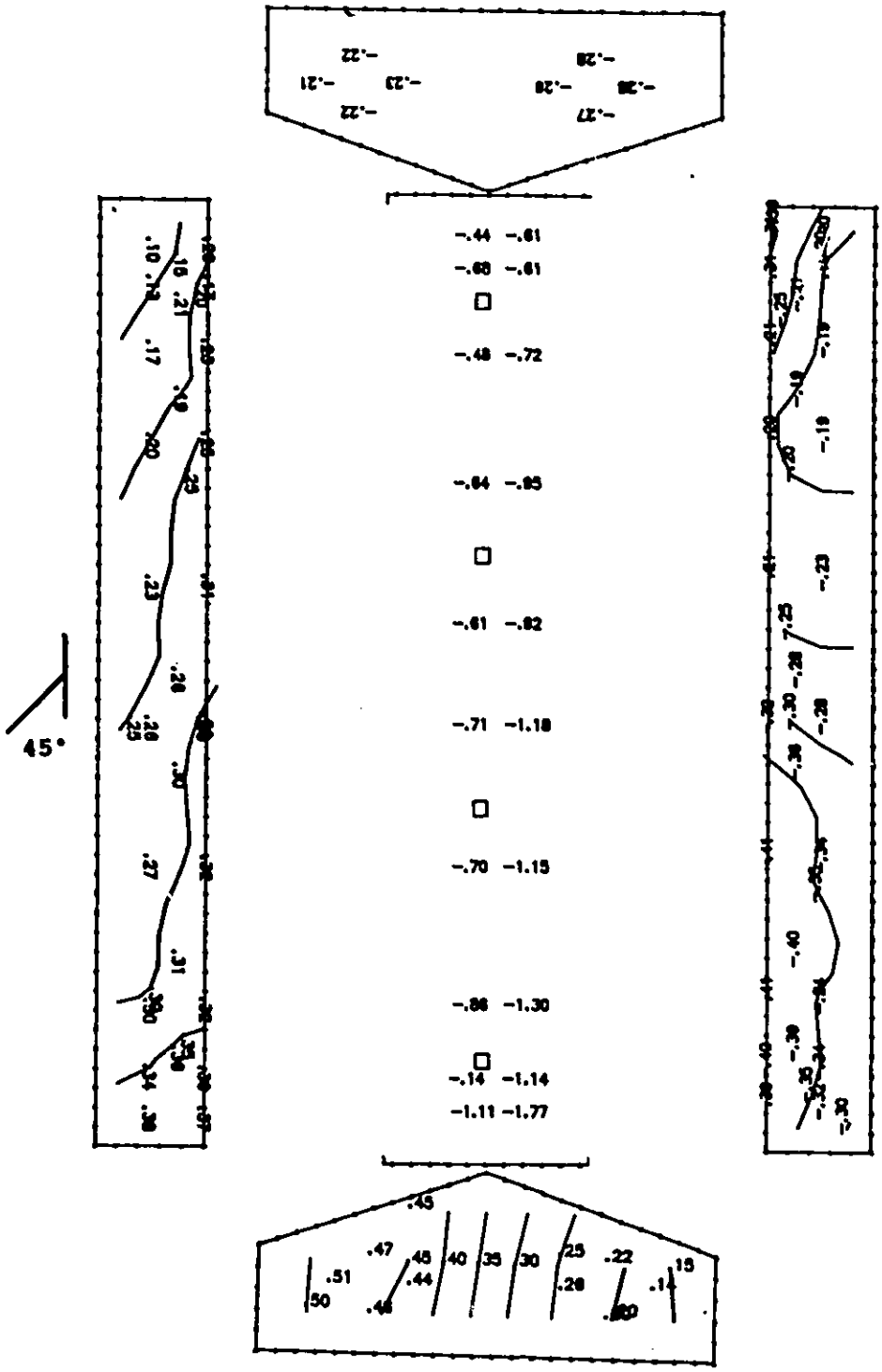

Figure 5.1c Cps contour lines: open model, chimney, simulated 800 mm sidewall openings, closed end walls, wind angle of 45°.

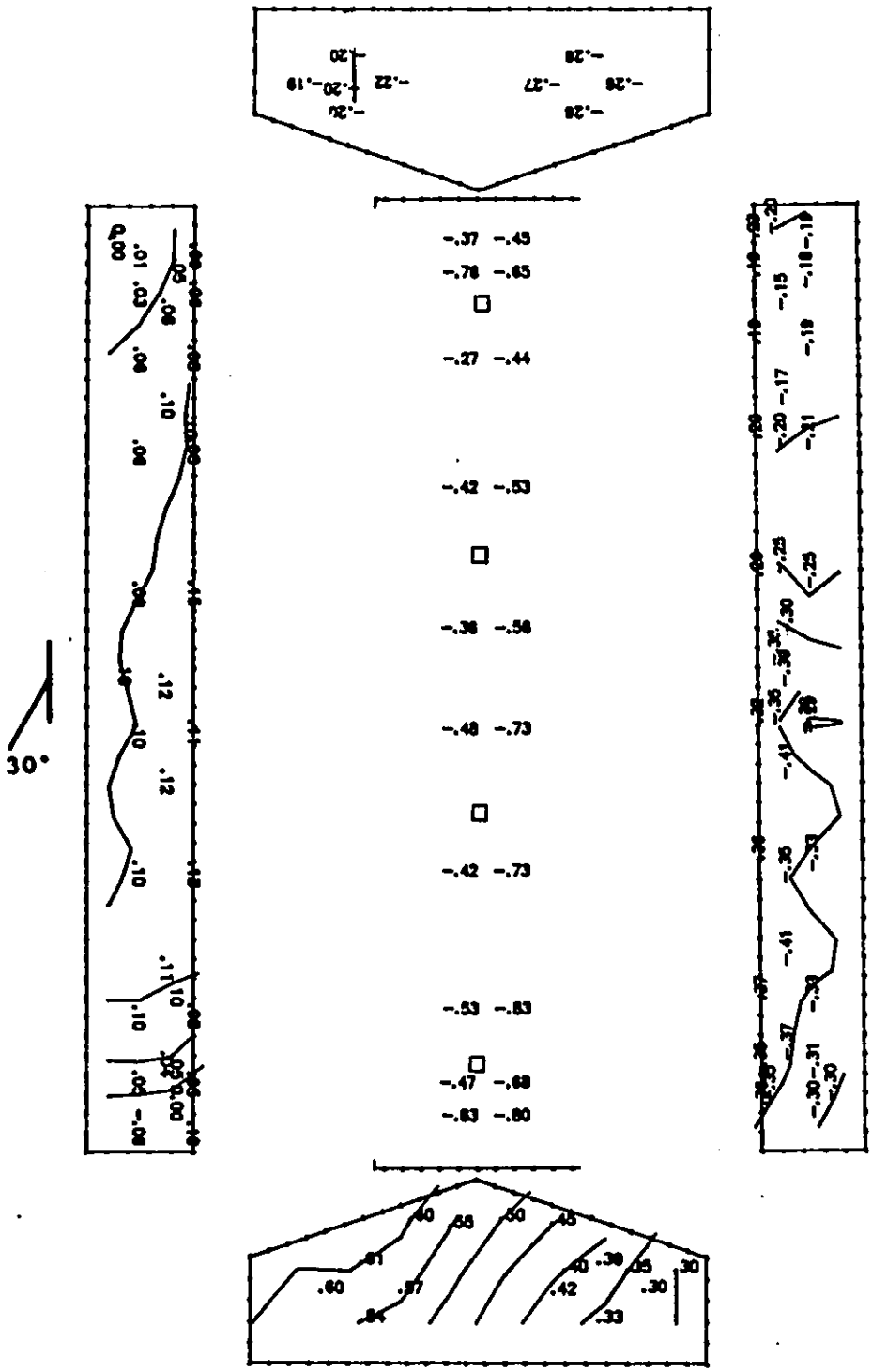

Figure 5.1d Cps contour lines: open model, chimney, simulated 800 mm sidewall openings, closed end walls, wind angle of 30°.

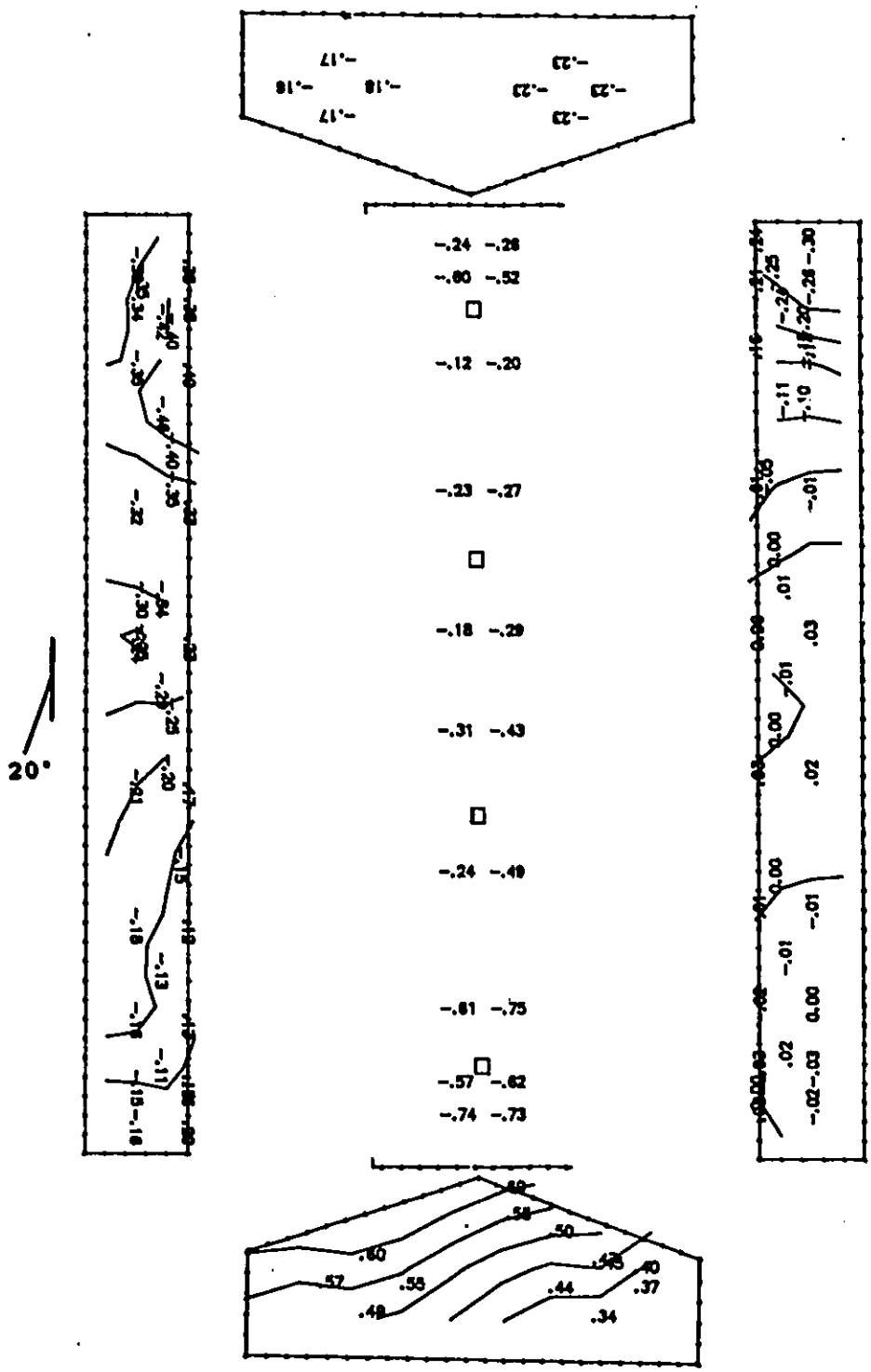

Figure 5.1e Cps contour lines: open model, chimney, simulated 800 mm sidewall openings, closed end walls, wind angle of 20°.

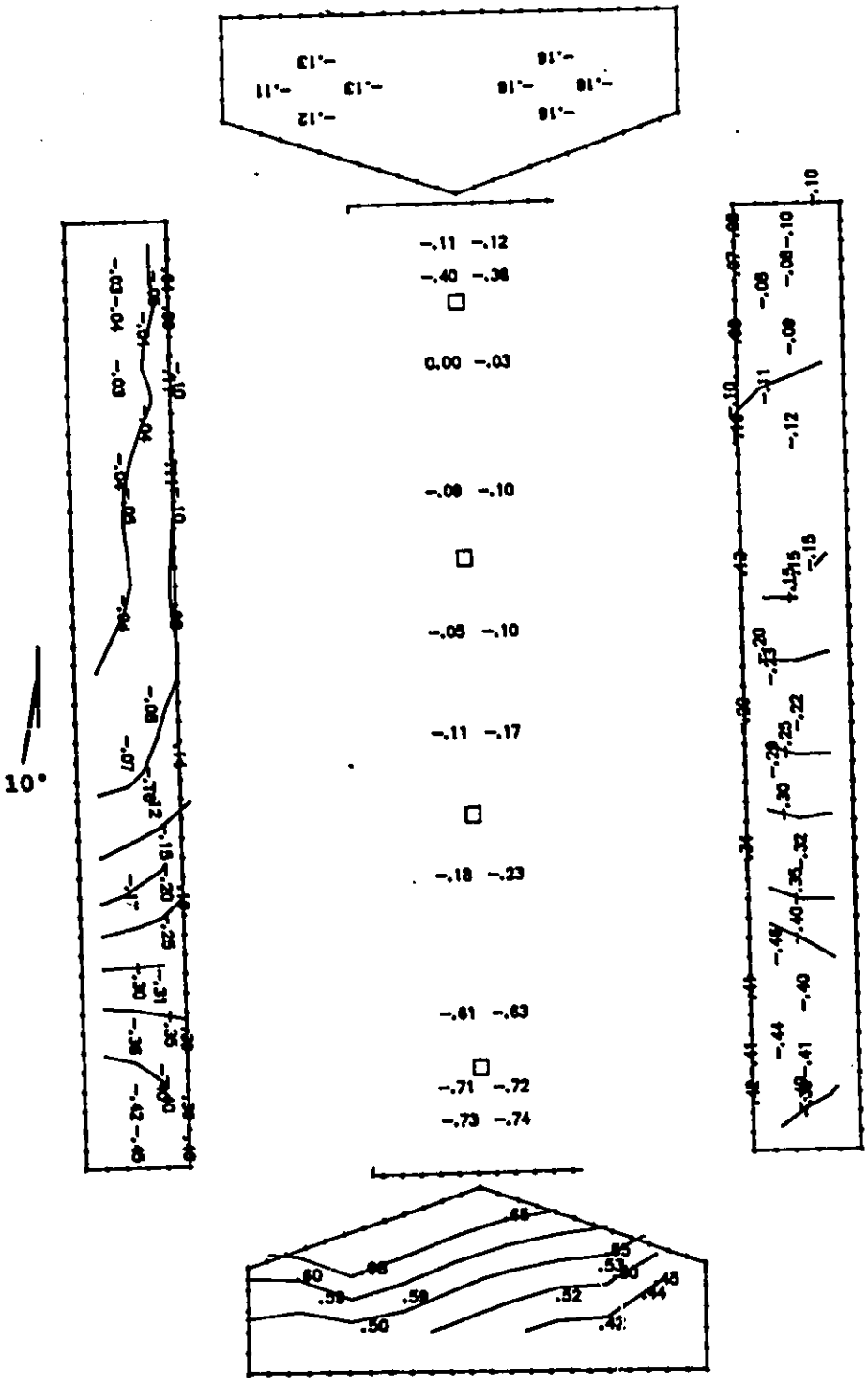

Figure 5.1f Cps contour lines: open model, chimney, simulated 800 mm sidewall openings, closed end walls, wind angle of 10°.

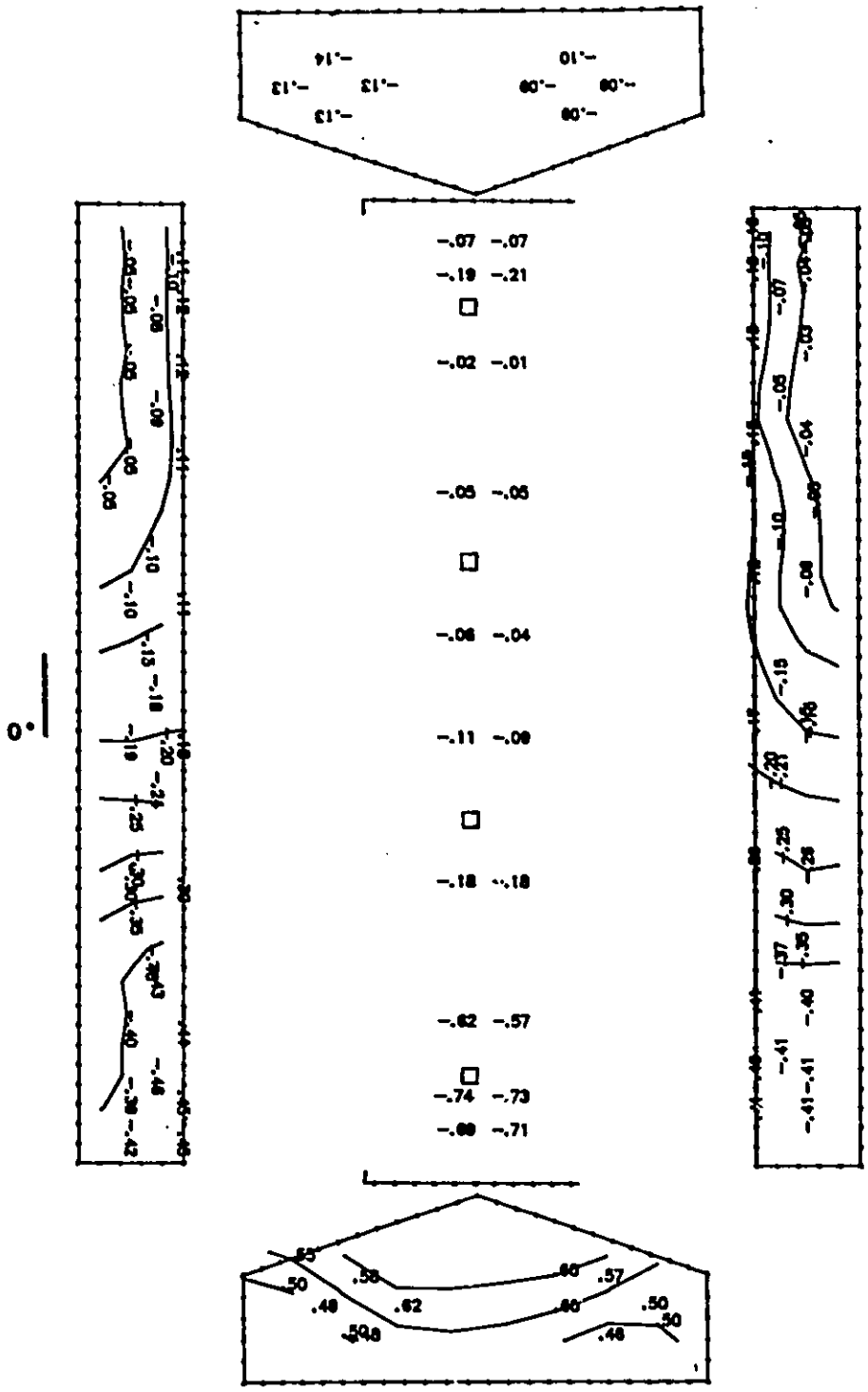

Figure 5.1g Cps contour lines: open model, chimney, simulated 800 mm sidewall openings, closed end walls, wind angle of 0°.

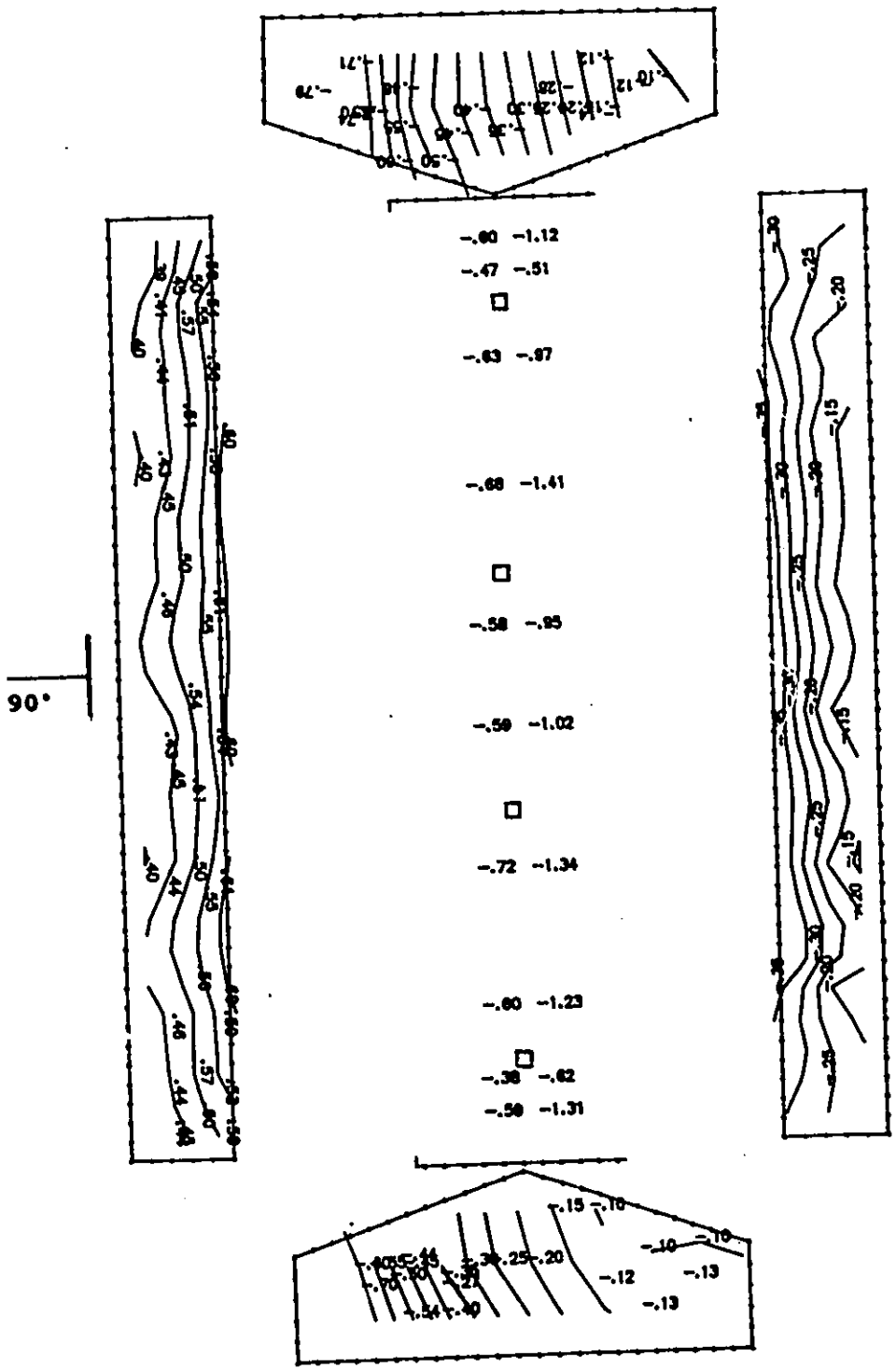

Figure 5.2a Cps contour lines: open model, chimney, simulated 1100 mm sidewall openings, closed end walls, wind angle of 90°.

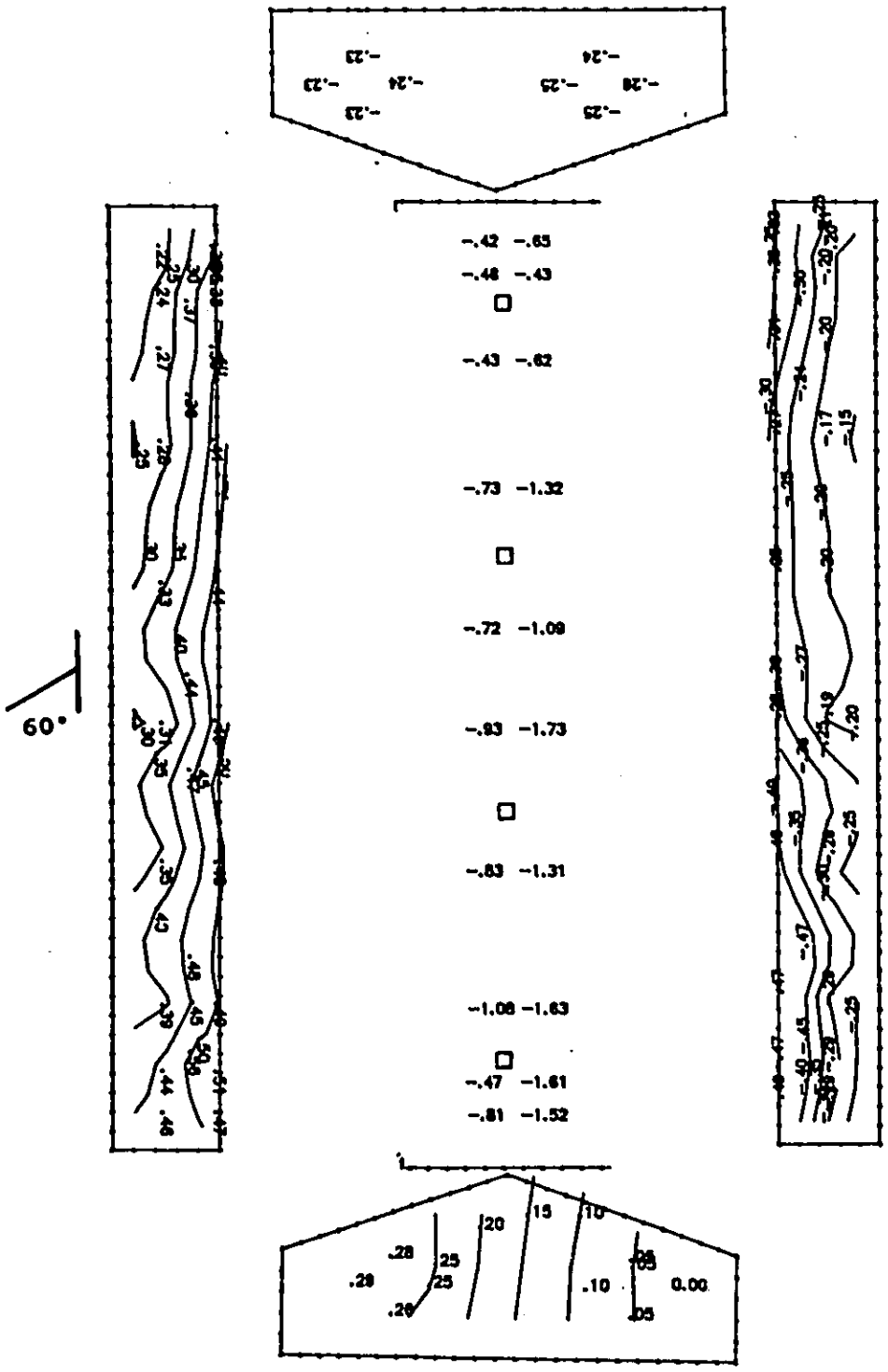

Figure 5.2b Cps contour lines: open model, chimney, simulated 1100 mm sidewall openings, closed end walls, wind angle of 60°.

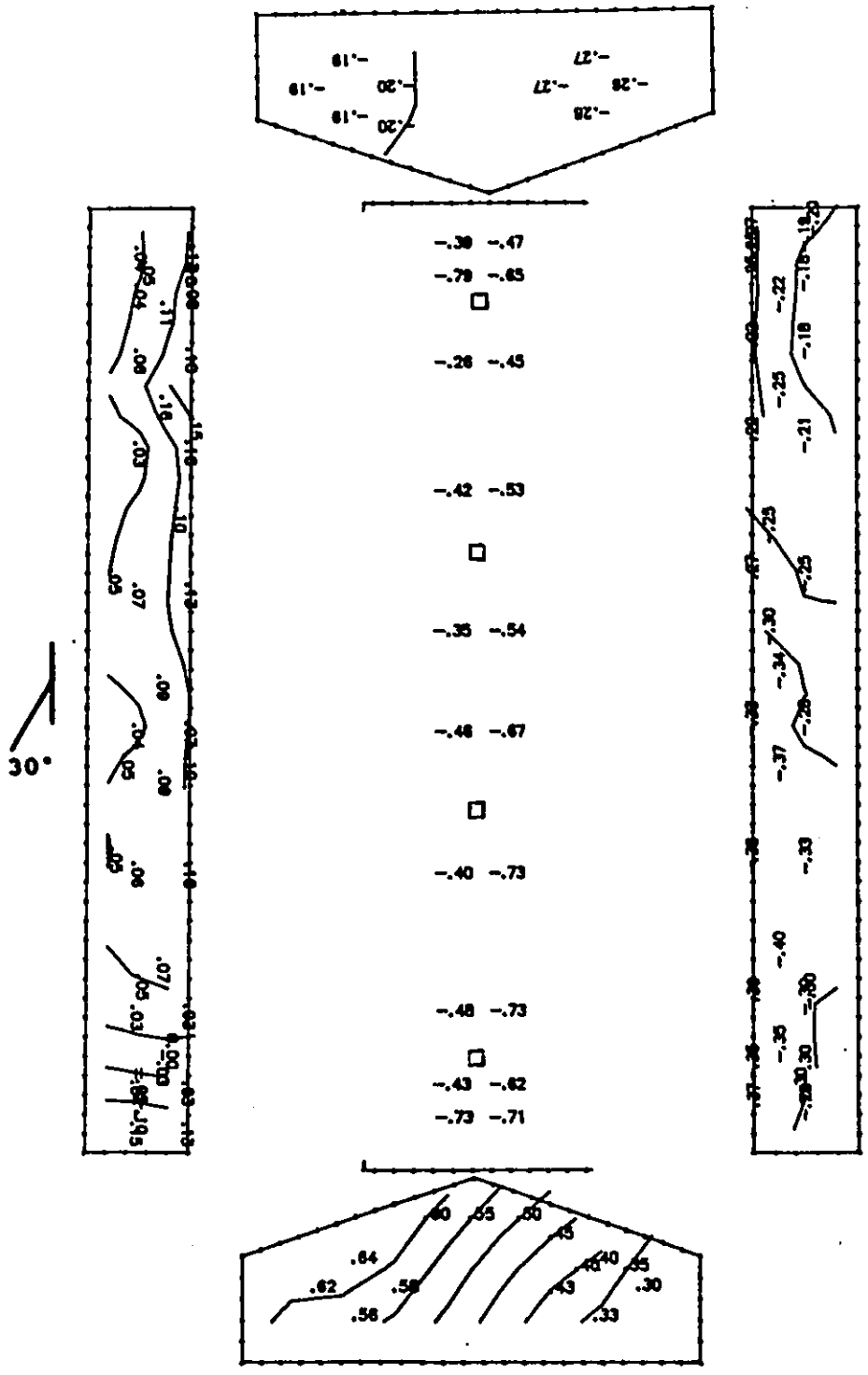

Figure 5.2c Cps contour lines: open model, chimney, simulated 1100 mm sidewall openings, closed end walls, wind angle of 30°.

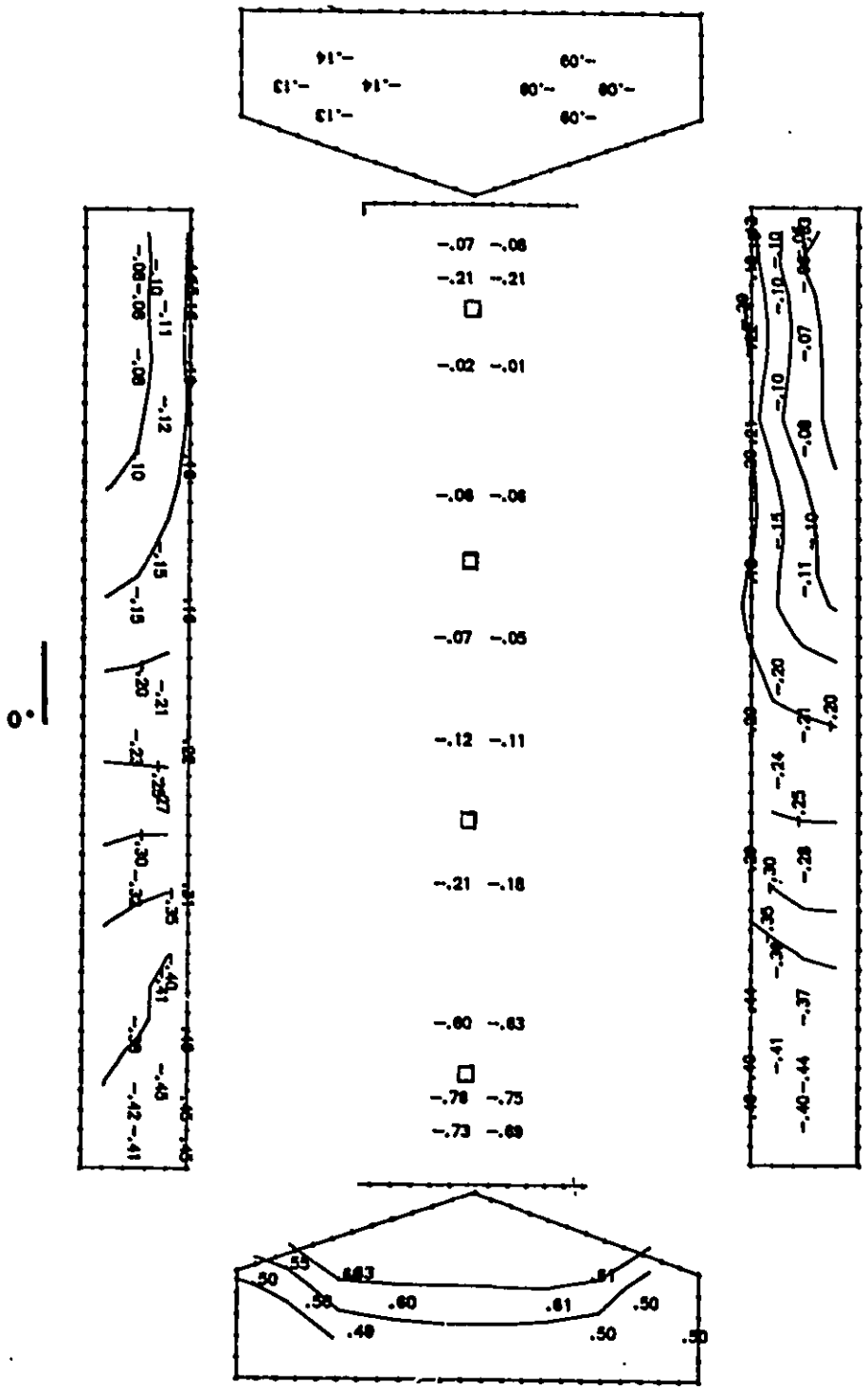

Figure 5.2d Cps contour lines: open model, chimney, simulated 1100 mm sidewall openings, closed end walls, wind angle of 0°.

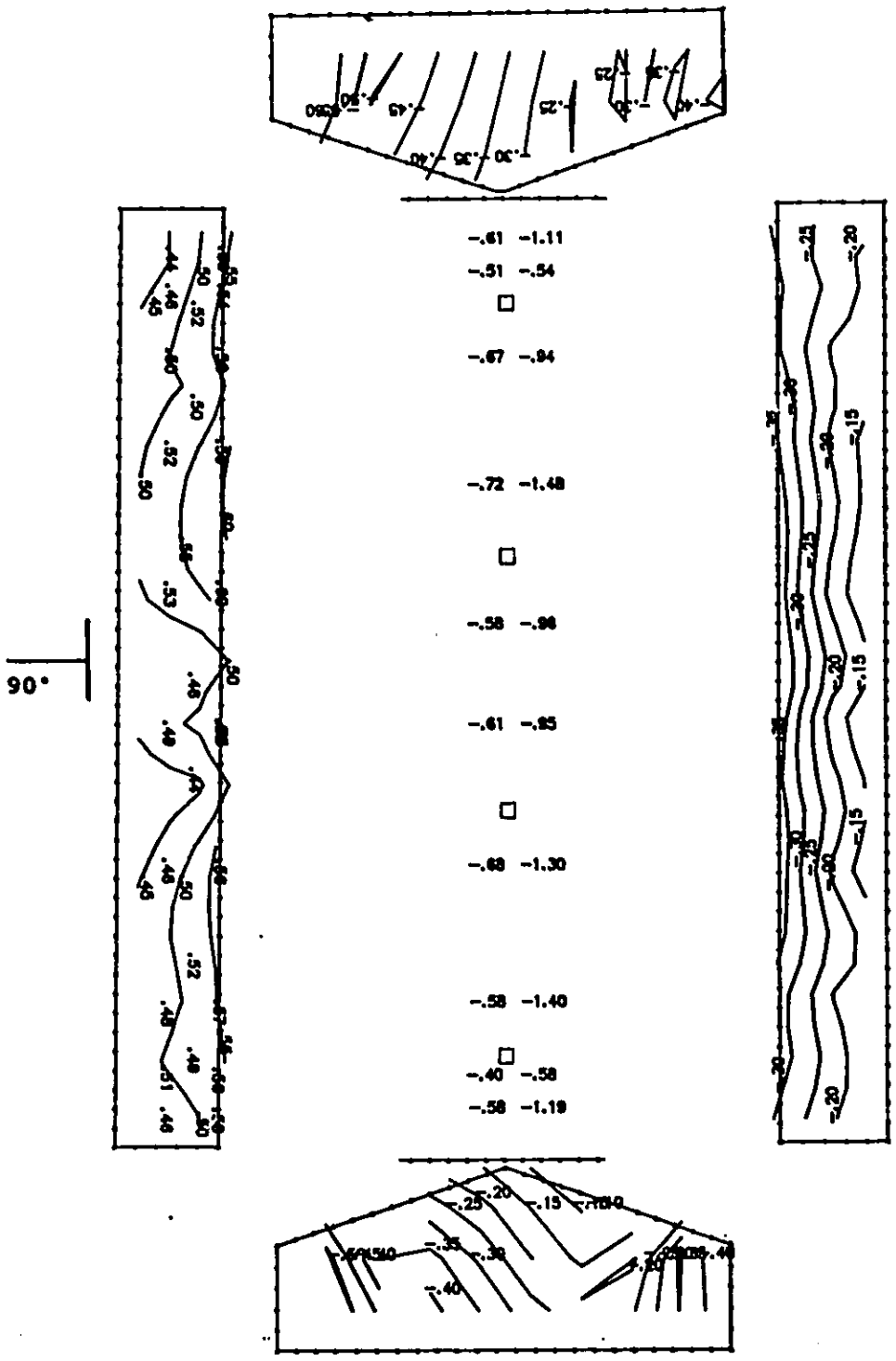

Figure 5.3a Cps contour lines: open model, chimney, simulated 800 mm sidewall openings, open end walls, wind angle of 90°.

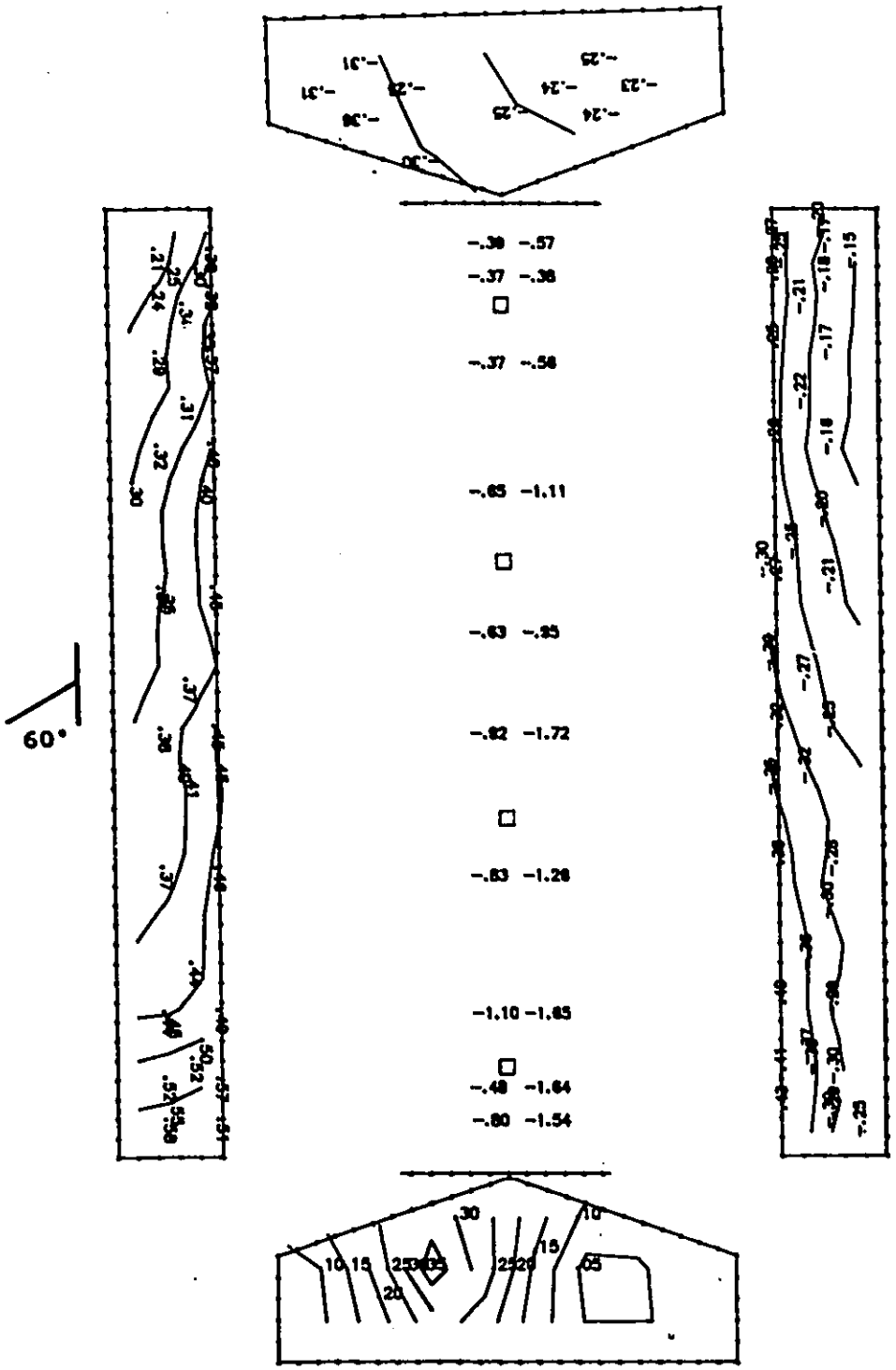

Figure 5.3b Cps contour lines: open model, chimney, simulated 800 mm sidewall openings, open end walls, wind angle of 60°.

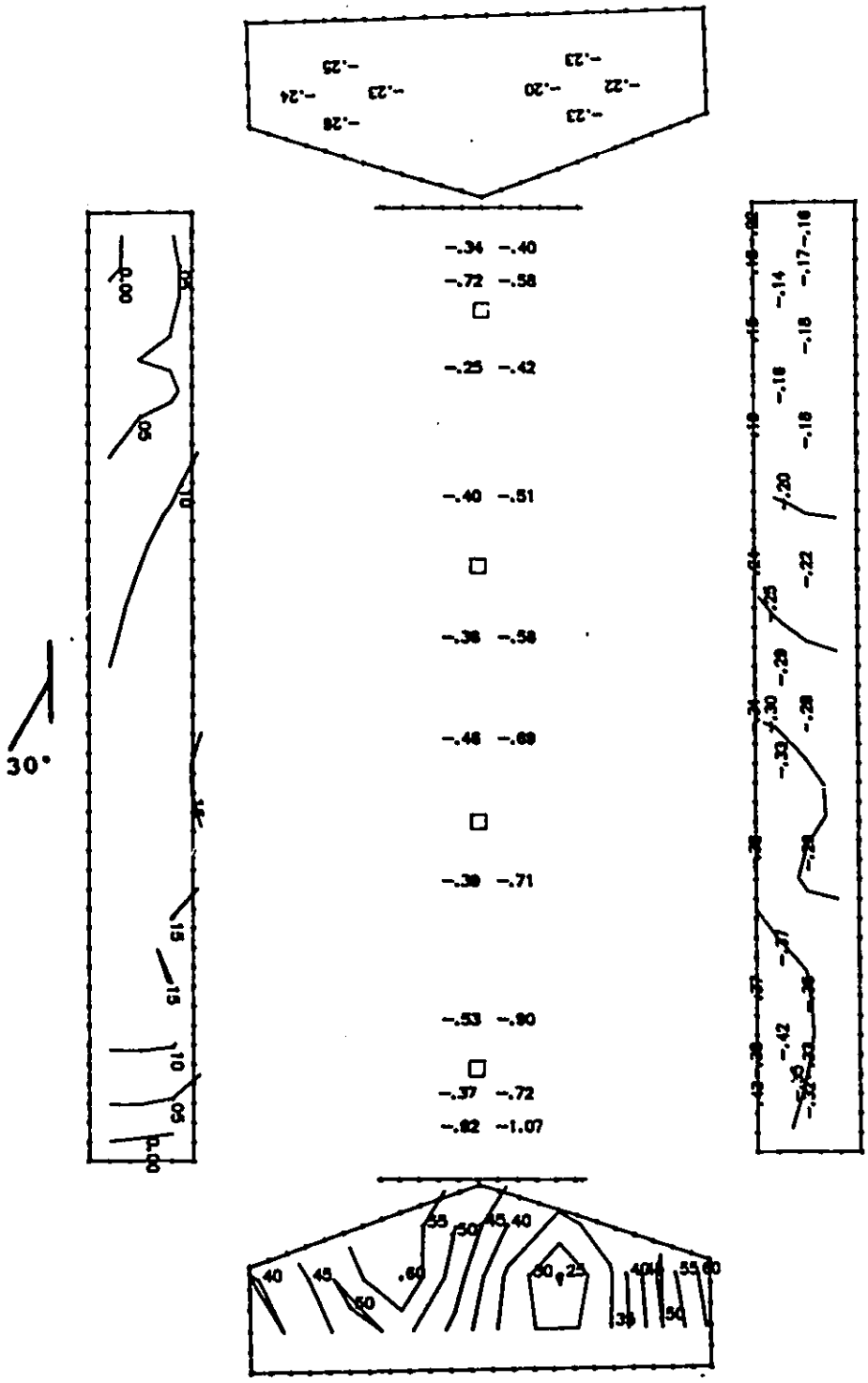

Figure 5.3c Cps contour lines: open model, chimney, simulated 800 mm sidewall openings, open end walls, wind angle of 30°.

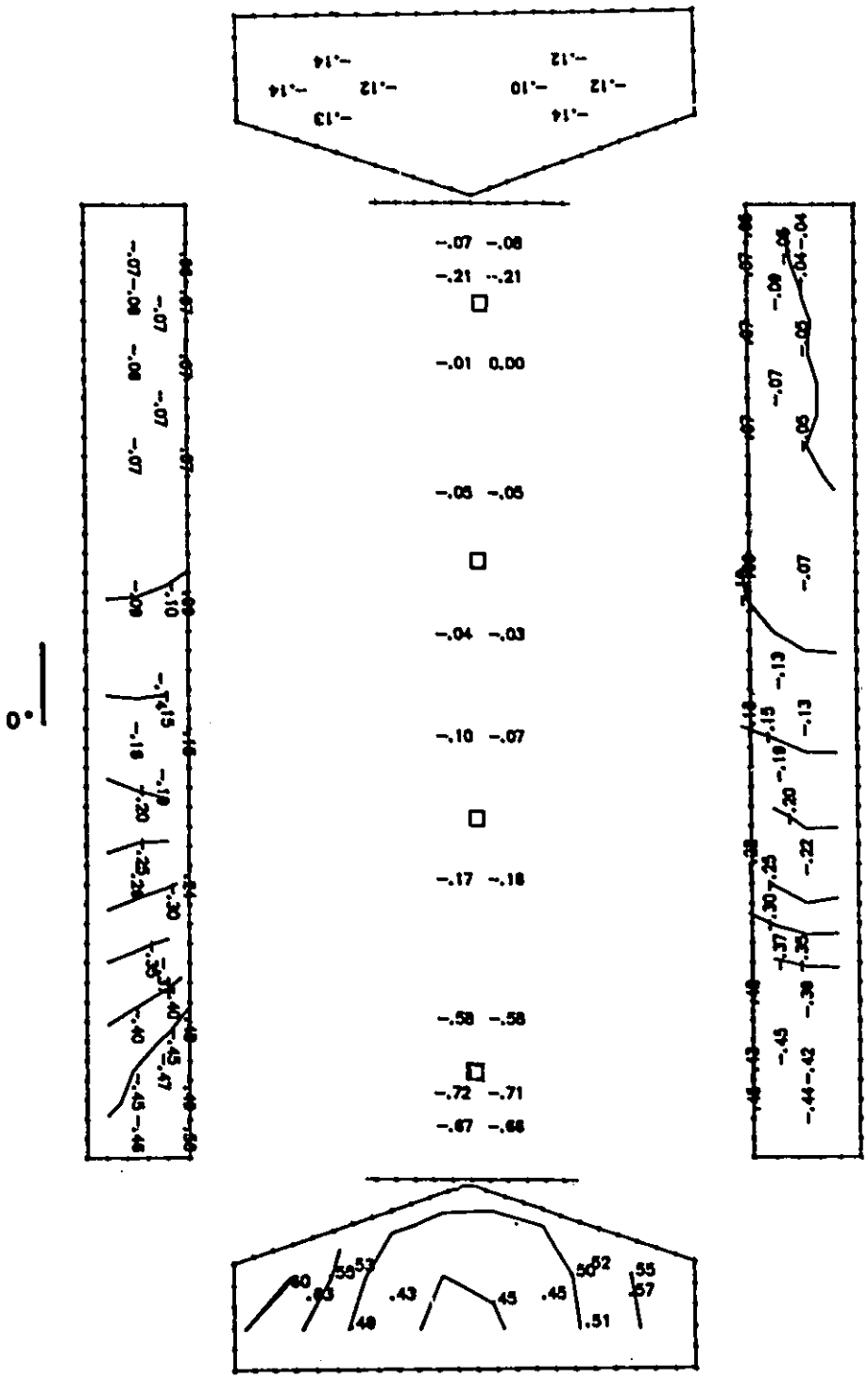

Figure 5.3d Cps contour lines: open model, chimney, simulated 800 mm sidewall openings, open end walls, wind angle of 0°.

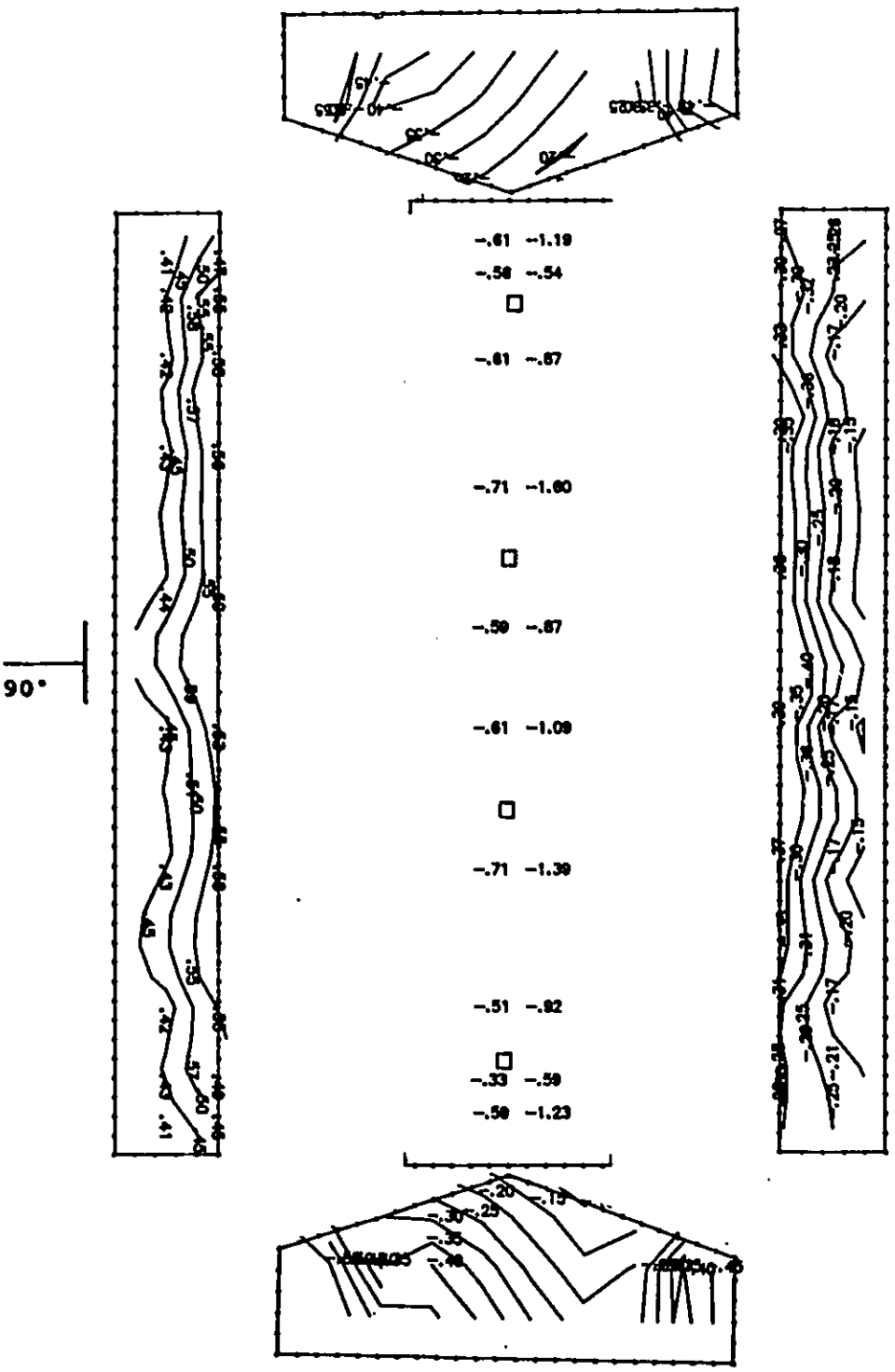

Figure 5.4a Cps contour lines: open model, chimney, simulated 1100 mm sidewall openings, open end walls, wind angle of 90°.

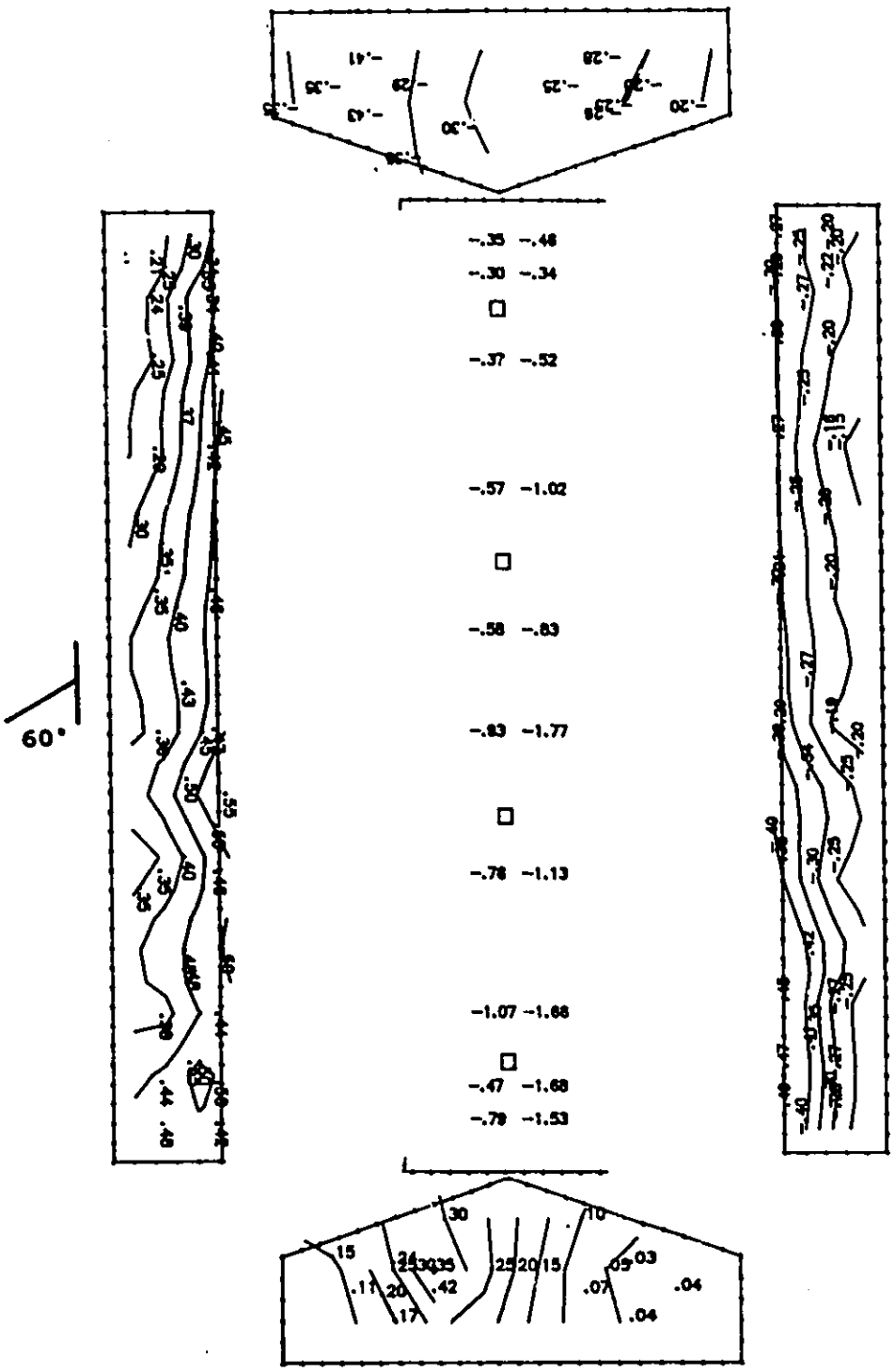

Figure 5.4b Cps contour lines: open model, chimney, simulated 1100 mm sidewall openings, open end walls, wind angle of 60°.

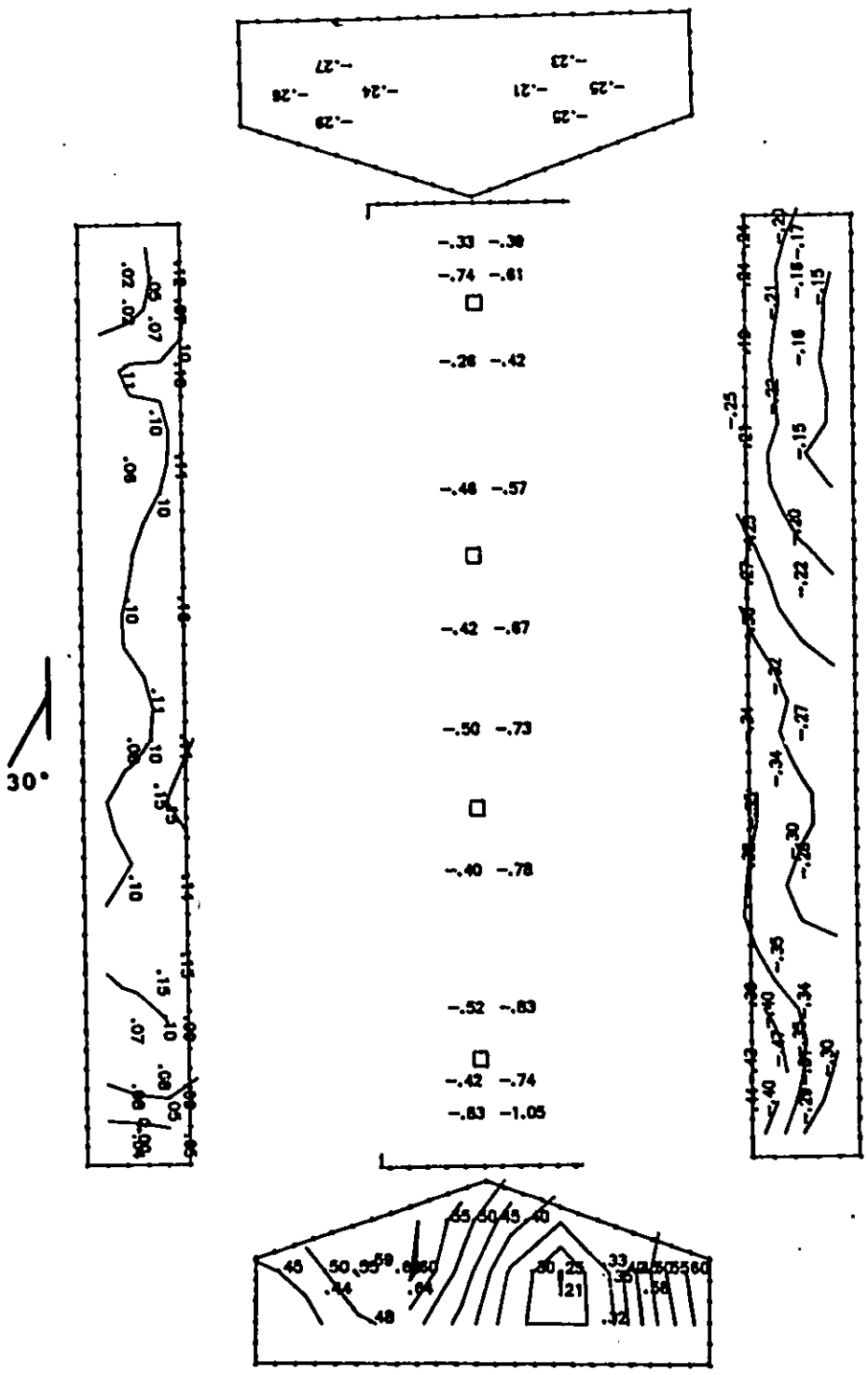

Figure 5.4c Cps contour lines: open model, chimney, simulated 1100 mm sidewall openings, open end walls, wind angle of 30°.

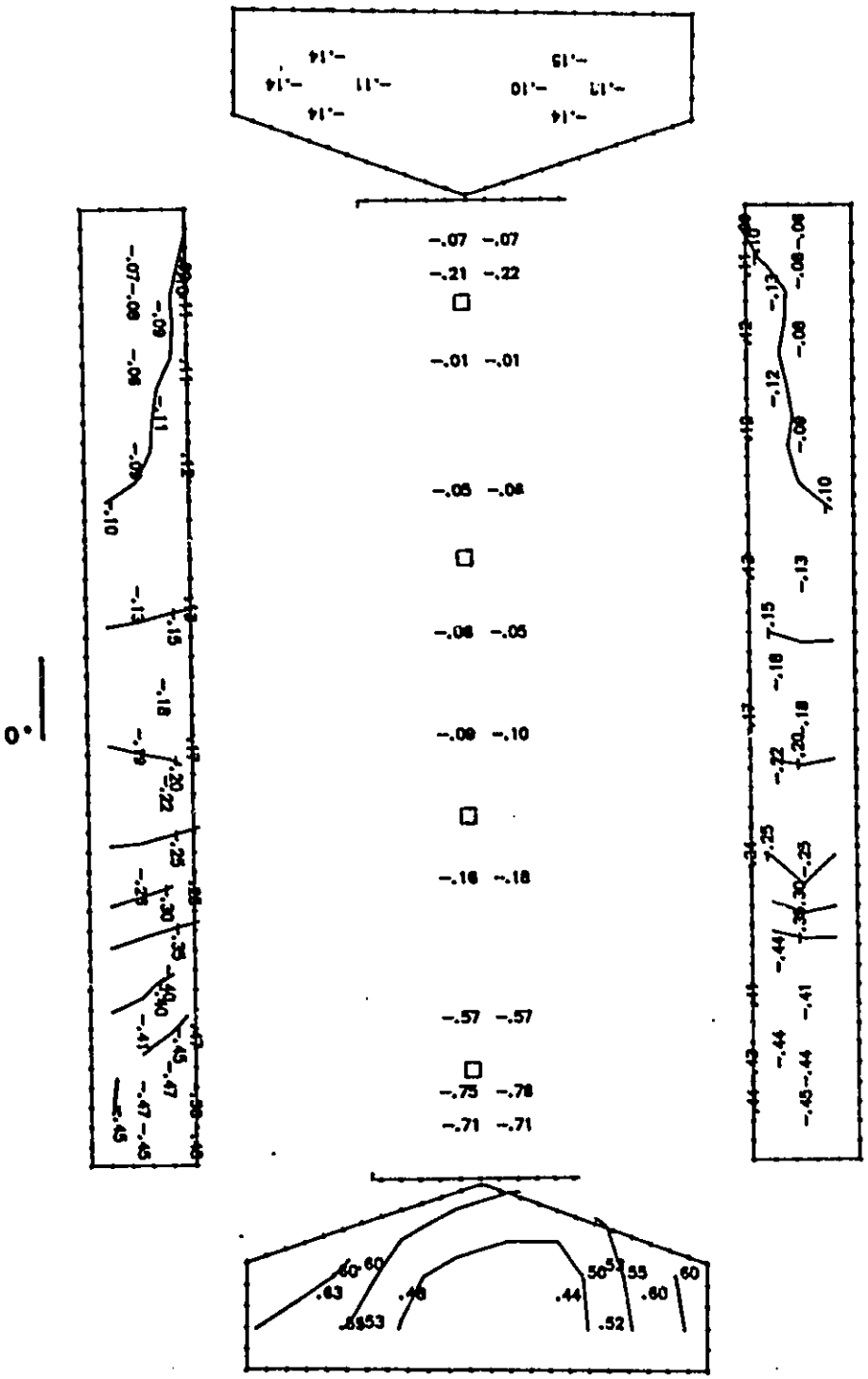

Figure 5.4d Cps contour lines: open model, chimney, simulated 1100 mm sidewall openings, open end walls, wind angle of 0°.

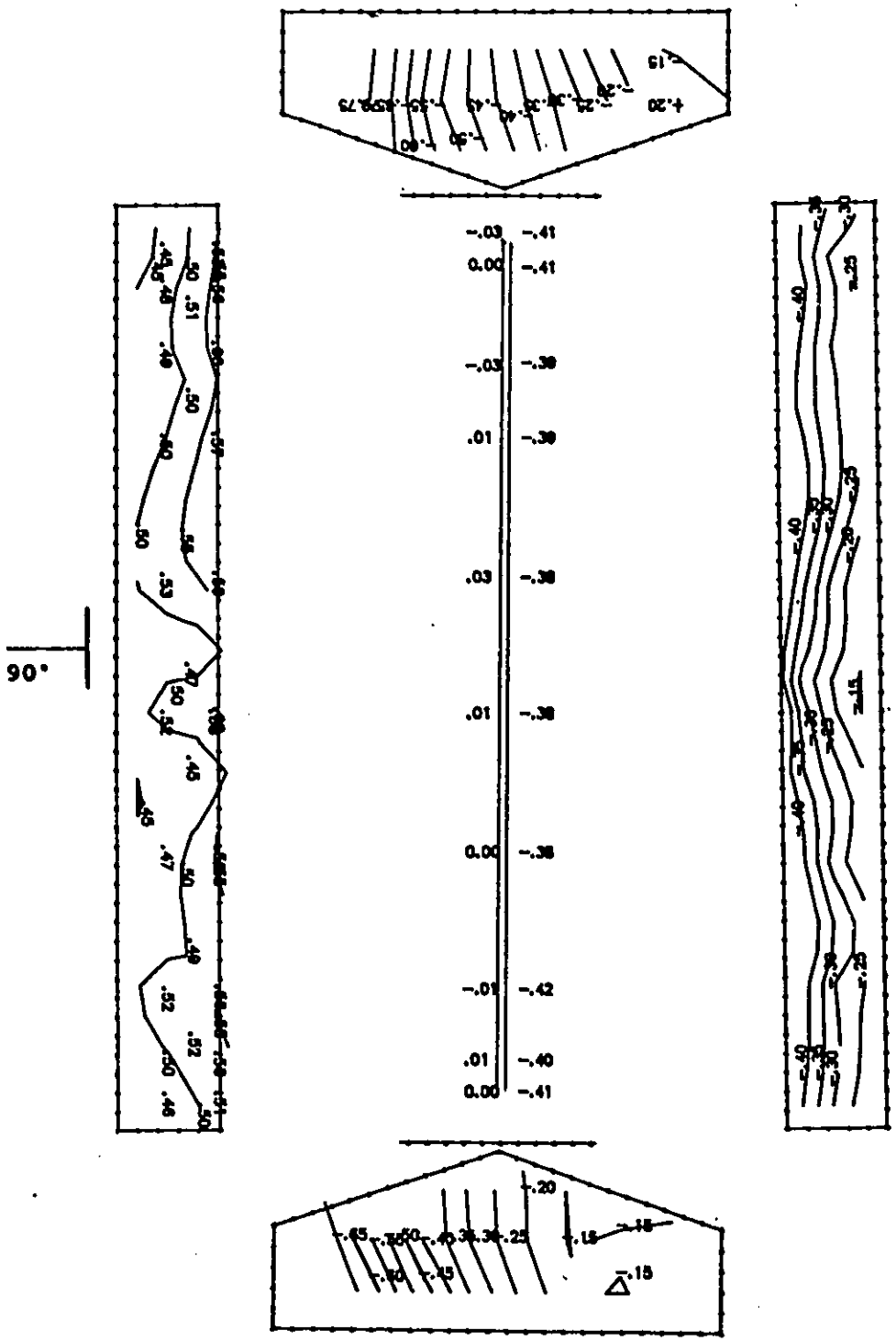

Figure 5.5a Cps contour lines: open model, simulated 150 mm ridge and 800 mm sidewall openings, closed end walls, wind angle of 90°.

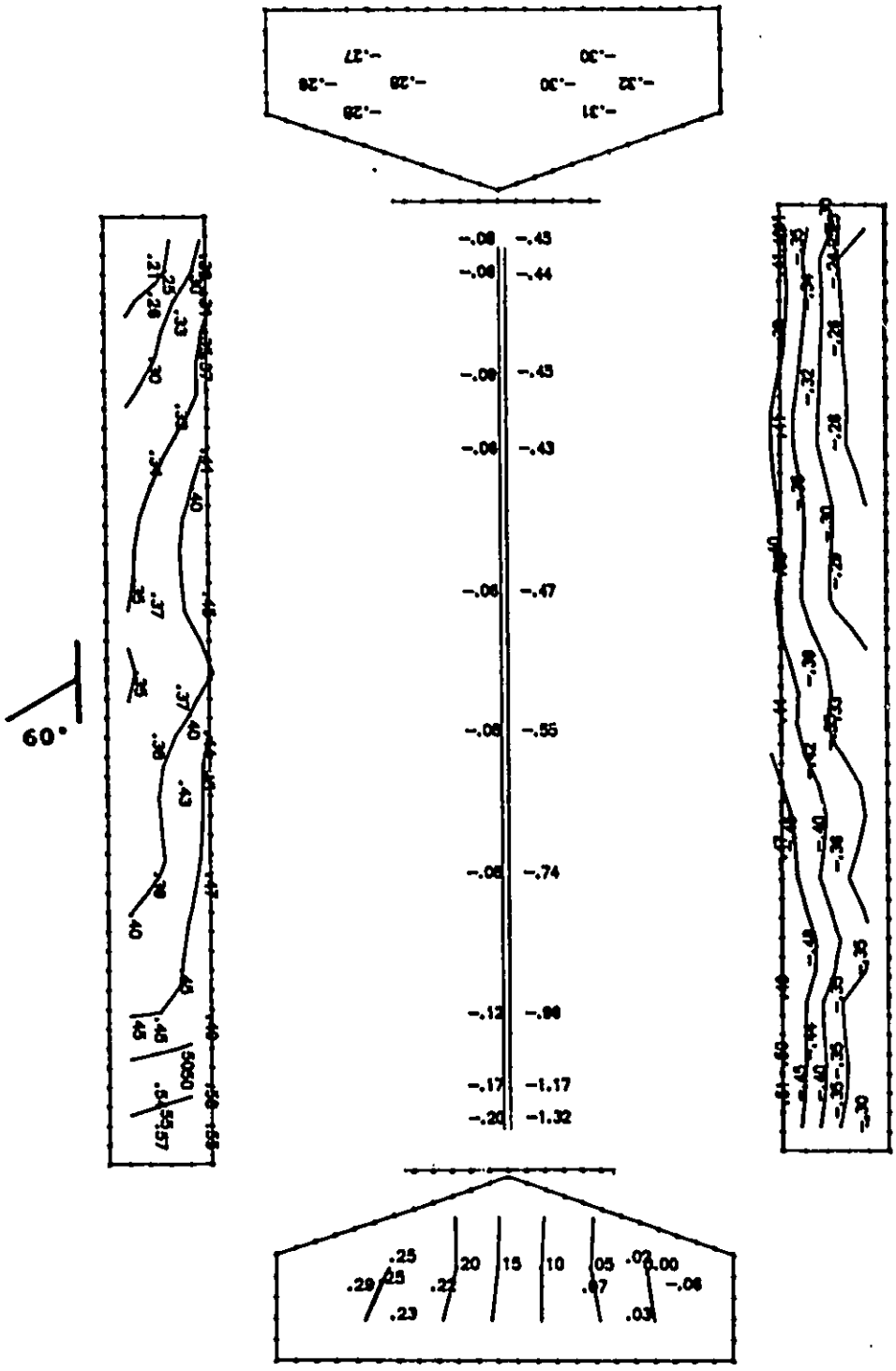

Figure 5.5b Cps contour lines: open model, simulated 150 mm ridge and 800 mm sidewall openings, closed end walls, wind angle of 60°.

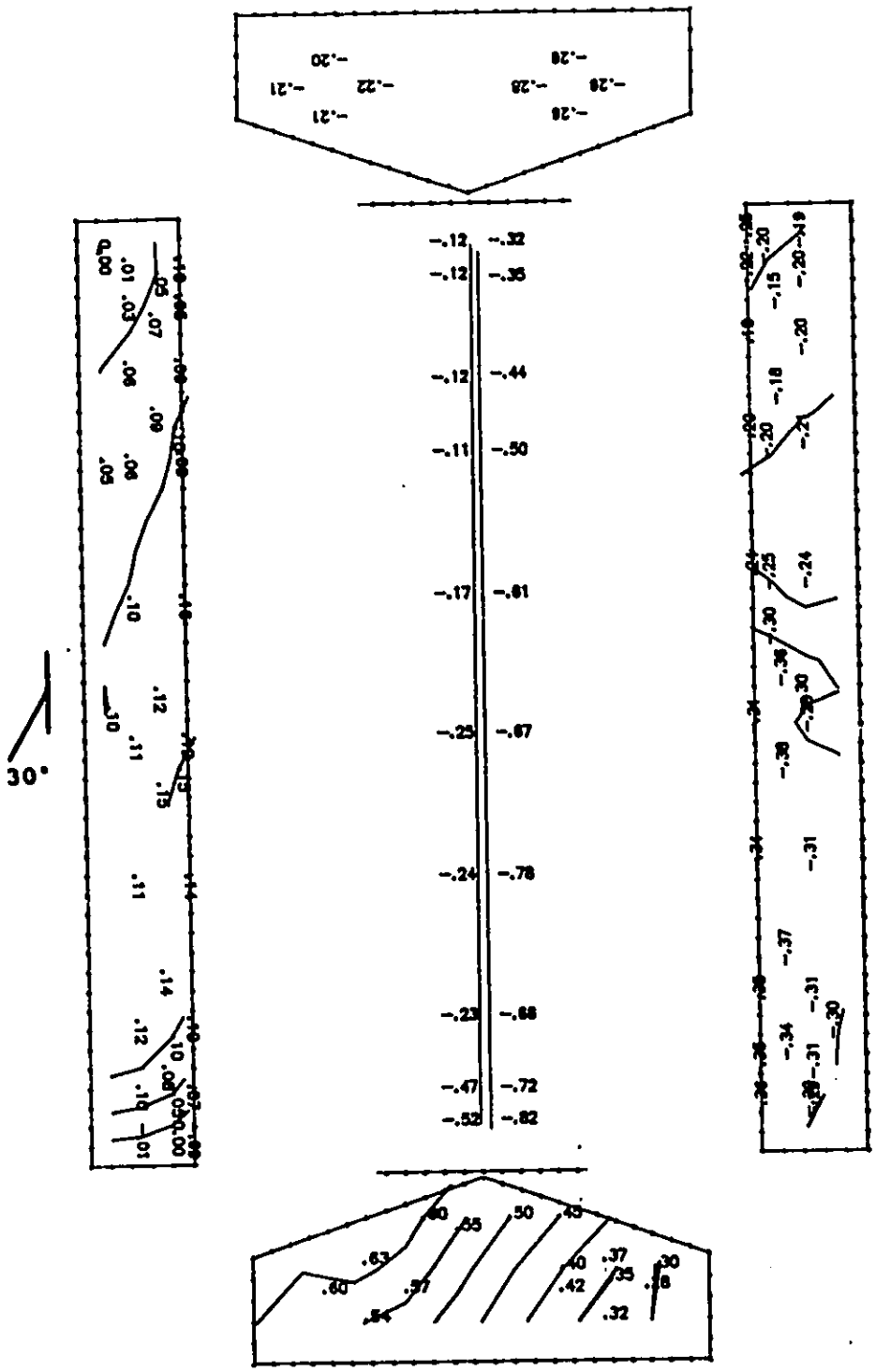

Figure 5.5c Cps contour lines: open model, simulated 150 mm ridge and 800 mm sidewall openings, closed end walls, wind angle of 30°.

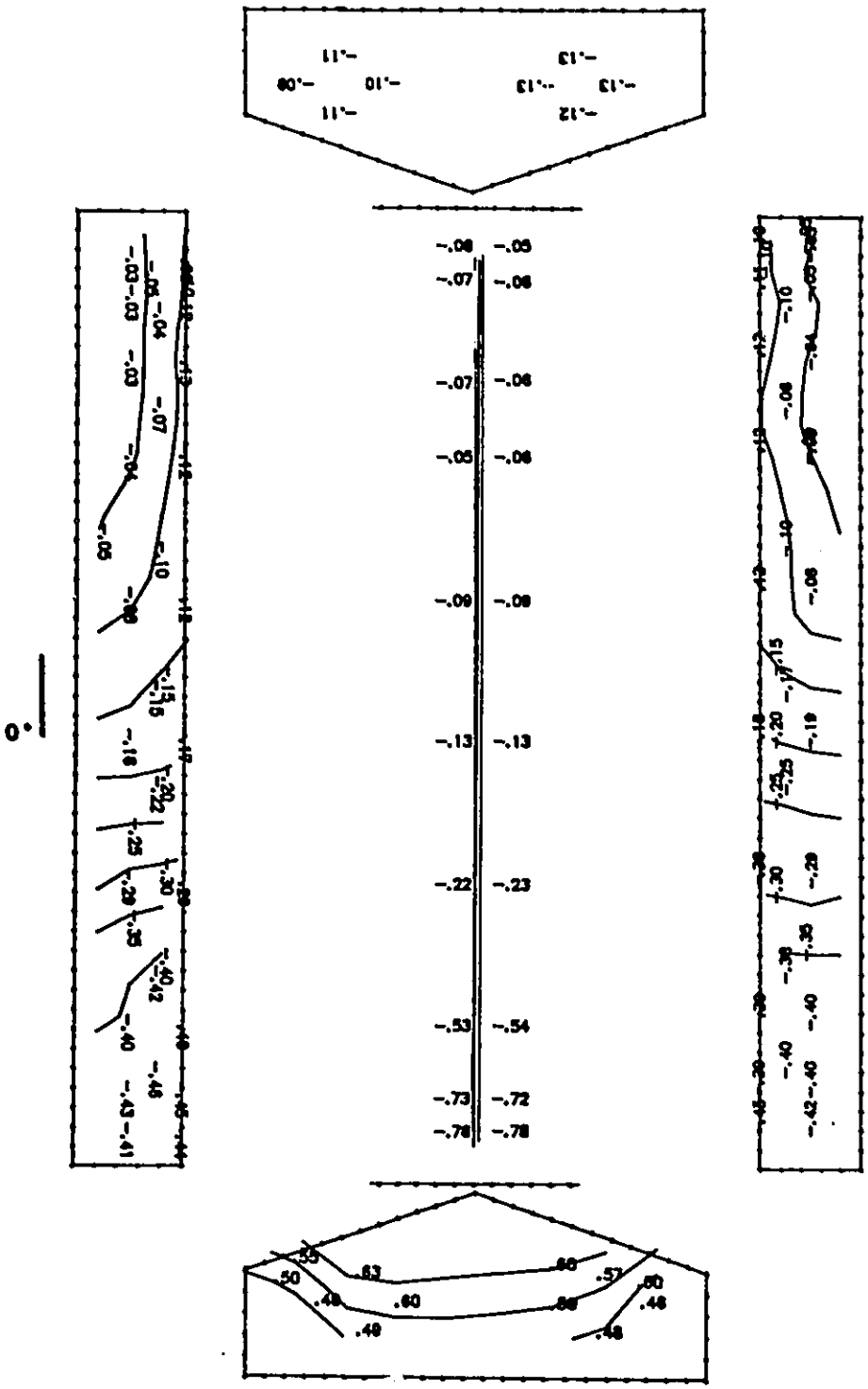

Figure 5.5d Cps contour lines: open model, simulated 150 mm ridge and 800 mm sidewall openings, closed end walls, wind angle of 0°.

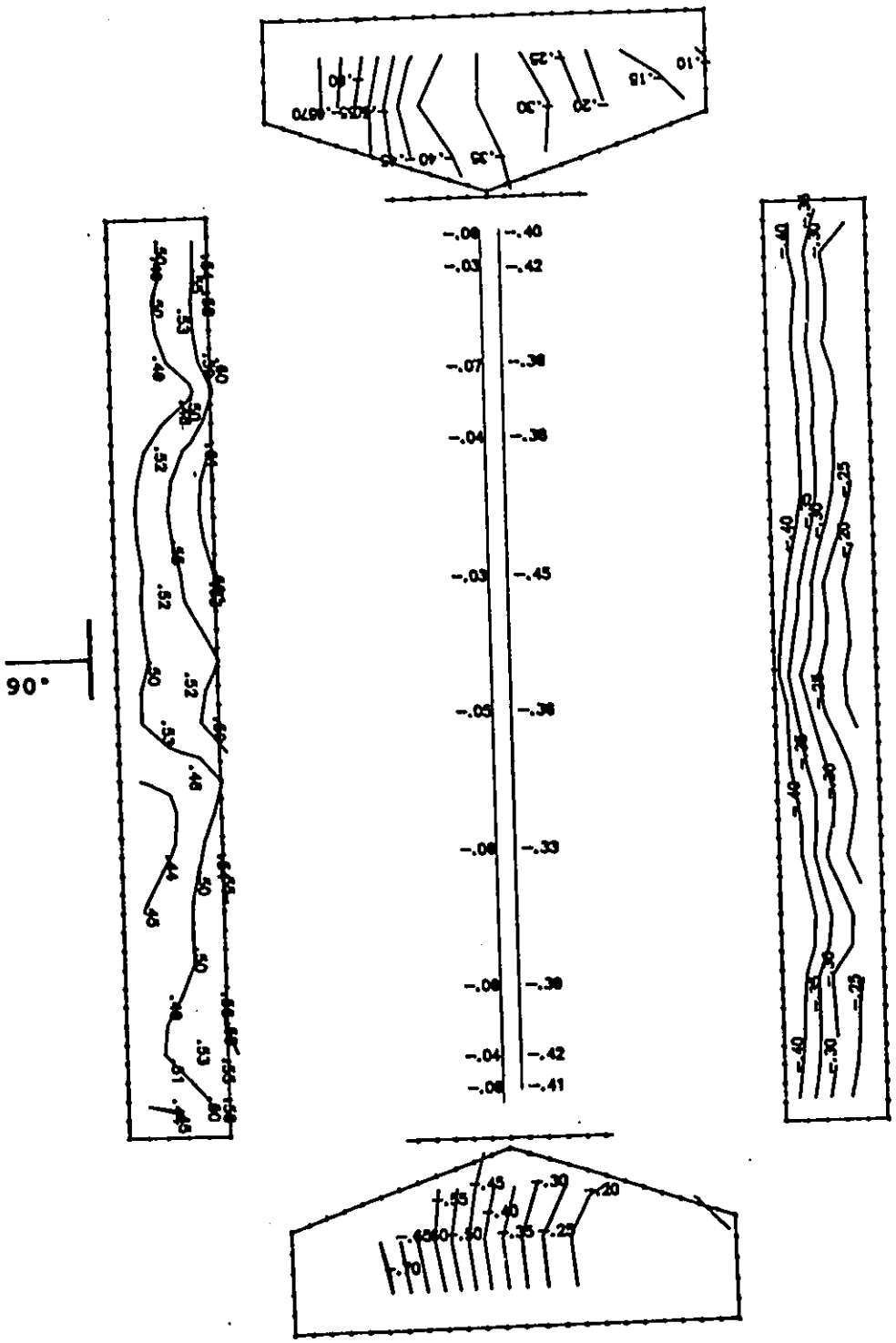

Figure 5.6a Cps contour lines: open model, simulated 400 mm ridge and 800 mm sidewall openings, closed end walls, wind angle of 90°.

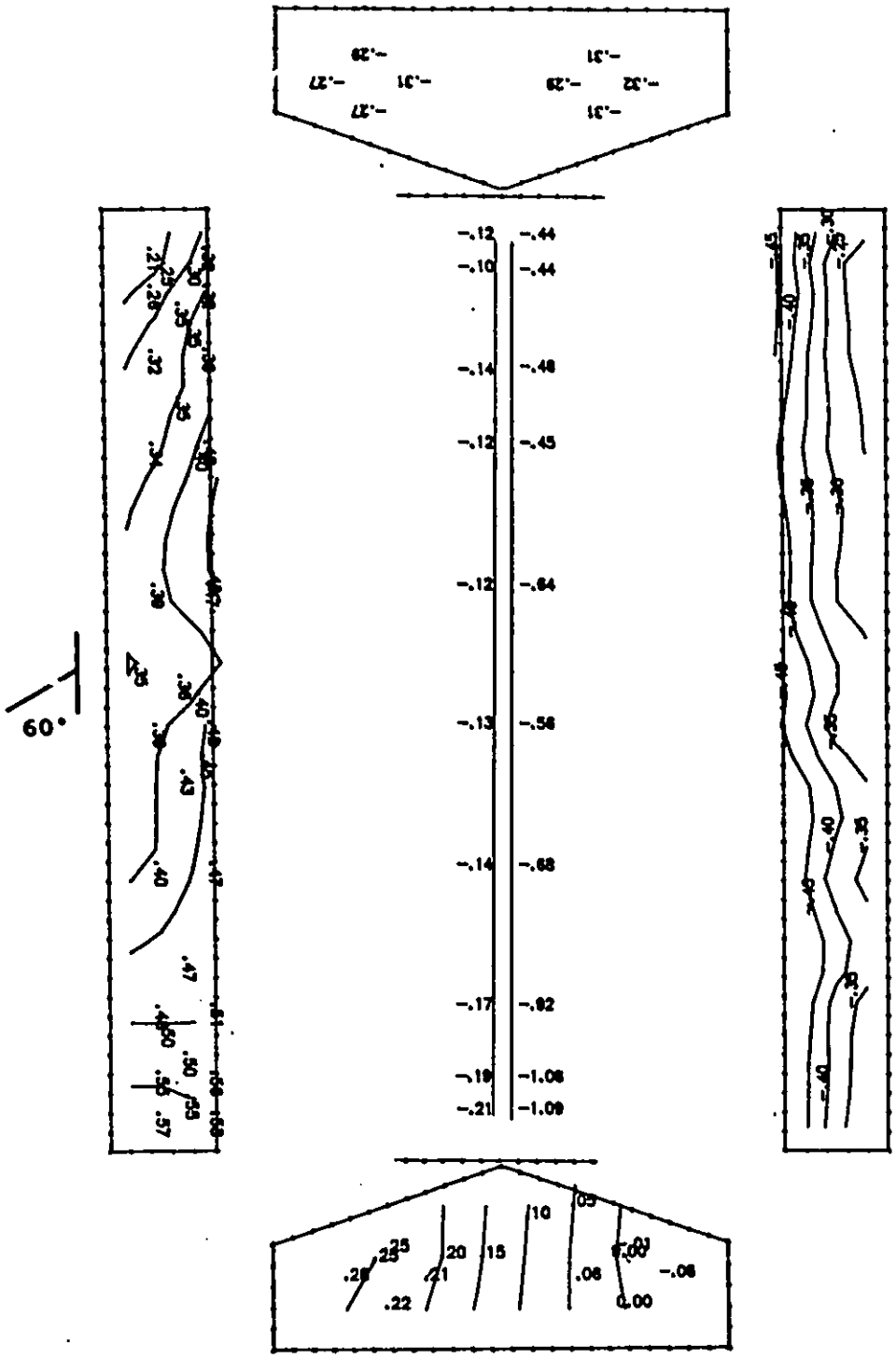

Figure 5.6b Cps contour lines: open model, simulated 400 mm ridge and 800 mm sidewall openings, closed end walls, wind angle of 60°.

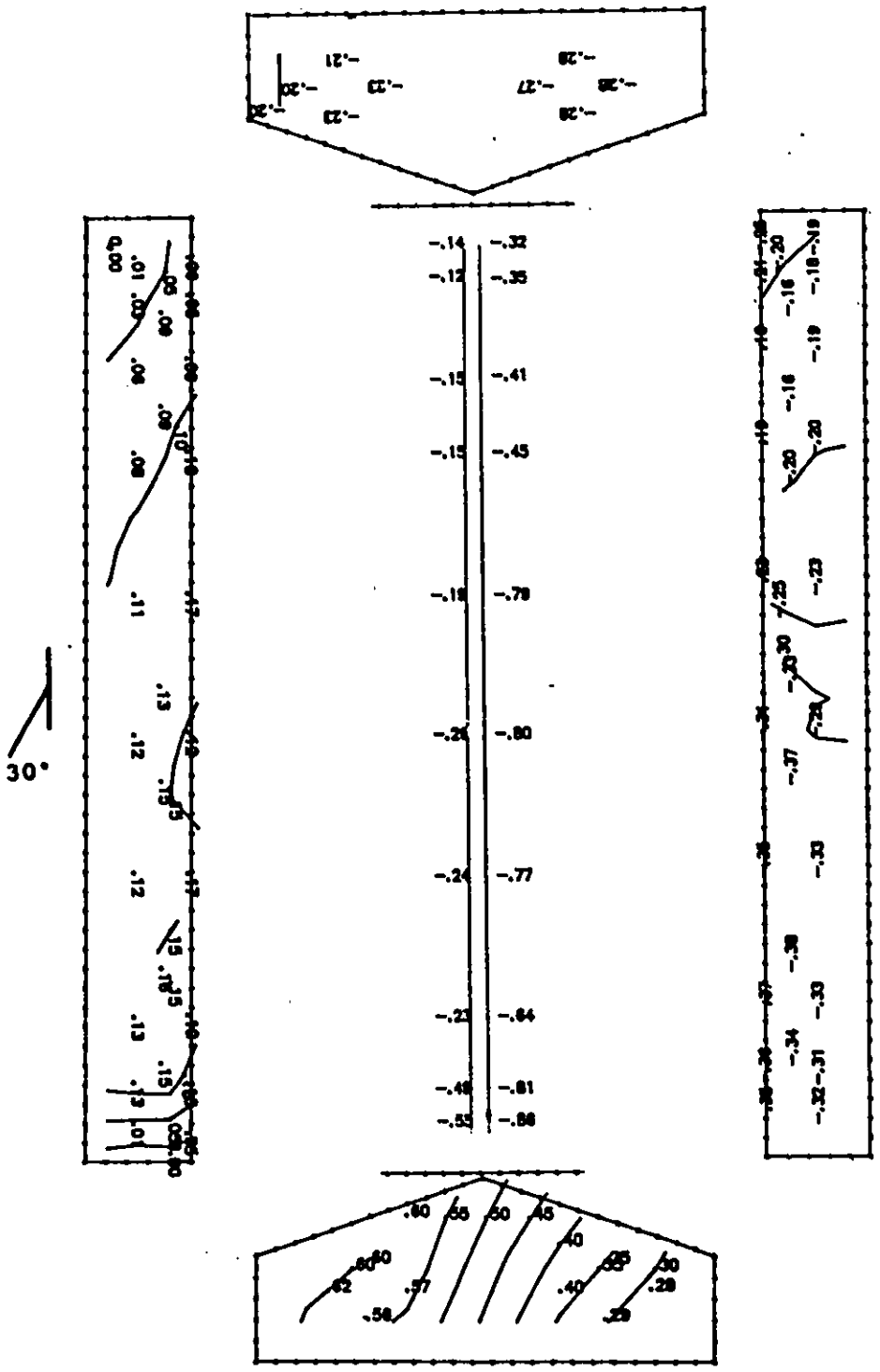

Figure 5.6c Cps contour lines: open model, simulated 400 mm ridge and 800 mm sidewall openings, closed end walls, wind angle of 30°.

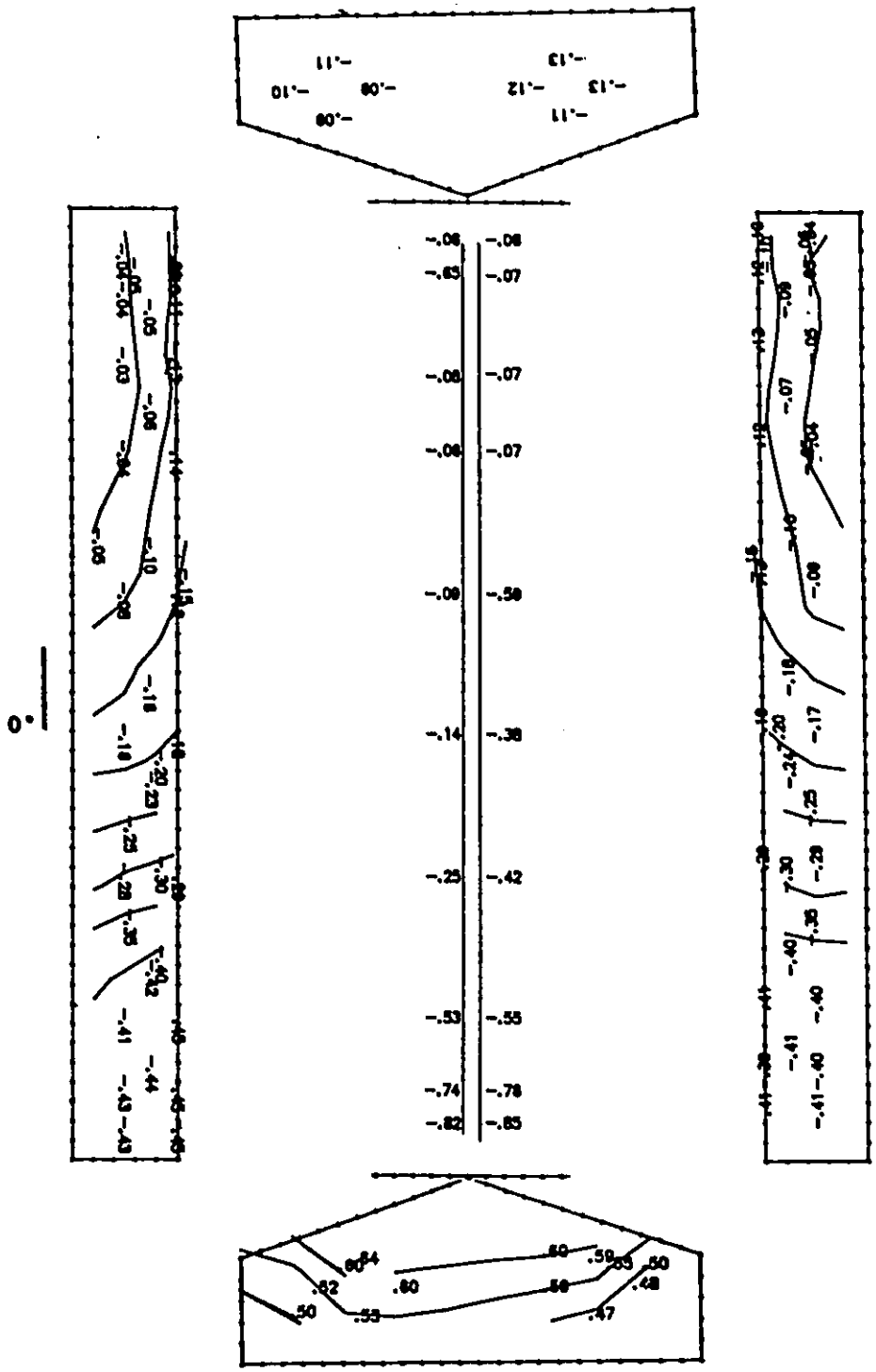

Figure 5.6d Cps contour lines: open model, simulated 400 mm ridge and 800 mm sidewall openings, closed end walls, wind angle of 0°.

With both 150 mm and 400 mm ridges, there is a general tendency to have slightly lower -Cps at the ridge level when open end walls are used with wind angles between 60° and 0°.

From the observations of the Cp distribution around the models it appears that:

1 - End wall openings have a very small effect on the Cp distribution at both sidewalls and a negligible effect on the chimney area.
2 - Major changes in the Cp distribution over both end walls are noticed for all wind angles.
3 - At both 150 mm and 400 mm ridge openings, for θ = 60° to 0°, slightly lower -Cps are recorded when open end walls are used.

5.1.1.4 Effect of ridge openings

Figure 5.1a-g (OP-CH-800-C), Fig. 5.5a-d (OP-150-800-C) and Fig. 5.6a-d (OP-400-800-C) are used to compare the effect of the ridge opening on the Cp distribution. At θ = 90°, the windward sidewall Cps are not affected by the use of any ridge type, but on the leeward sidewall, the 150 mm and 400 mm ridge both had an increase in -Cps from about -0.1 to -0.2 as compared to the chimney. Also, the -Cps at the ridge with the chimneys versus the 150 mm and 400 mm ridge opening are about 4 times higher. The higher -Cps with the chimney accompanied with lower leeward sidewall -Cps may be explained by a different flow circulation over the building with the chimney. During full scale observations, Richardson (1989b) reported that outflow through the continuous ridge opening had a large effect. The outflow disturbed the typical flow separation pattern at the ridge line. Also, from Figs. 5.5a-d (OP-150-800-C) and 5.6a-d (OP-400-800-C), it appears that the larger outflow exhausted by the 400 mm ridge generates slightly higher -Cps at the ridge and over the leeward sidewall.

At $\theta = 60°$, Figs. 5.1b (OP-CH-800-C), 5.5b (OP-150-800-C) and 5.6b (OP-400-800-C) show identical contour lines among the three ridge types over the windward sidewall. The -Cps on the leeward sidewall are always lower in magnitude with the chimney compared to the 150 mm and 400 mm ridge, while the 400 mm ridge presents higher -Cps over the leeward sidewall as compare to the 150 mm ridge. The Cps over the upwind end wall are identical, but the downwind end wall present lower -Cps with larger ridge. The chimney -Cps are consistently higher (about twice more negative) than the 150 mm and 400 mm ridges, and the -Cps for the 400 mm ridge are slightly higher than the 150 mm ridge. At $\theta = 30°$, all ridges and walls show fairly similar Cp distributions.

At $\theta = 20°$ and 10°, all respective walls are similar. The 400 mm ridge data show slightly higher -Cps as compare to the 150 mm ridge. Some recording problems occurred during the OP-400-800-C test; certain tap readings at the ridge level were fairly high (-Cps), especially at $\theta = 0°$ to 20°. The results for the sidewalls and end walls are reliable, but not for the ridge.

Finally, at $\theta = 0°$, the chimney -Cps do not show a gradual reduction from the upwind to the downwind end, instead variations in -Cps that are probably due to local flow disturbances induced by the chimney upstands and roofs. At $\theta = 0°$, in general, the -Cps are fairly similar for all three types of ridge opening.

The ridge opening types have the following general effects:

1 - The chimney -Cps are higher than 150 mm and 400 mm for $\theta = 90°$, 60° and 45°.

2 - At $\theta = 90°$, the 400 mm ridge shows slightly higher -Cps at the ridge versus the 150 mm, but they have similar -Cps for all other angles.

3 - The larger ridge has higher -Cps over the leeward sidewall for $\theta = 90°$, 60° and 45°.

4 - Using 1100 mm versus 800 mm sidewall openings causes only small differences in the magnitude of the ridge -Cps with similar Cp distributions around the building.

5.1.2 Sealed model

The contour lines of Cps distributions around the sealed scale models are presented in Figs. 5.7a-d (SE-CH), 5.8a-d (SE-150) and 5.9a-b (SE-400). Figs. 5.7a (θ = 90°), b (θ = 60°) and d (θ = 0°) show countour lines which are very close to the results of Holmes (1983) for a residential low-rise building with an overhang. Similar Cp distributions are also presented by Aynsley et al. (1977) and Davenport et al. (1977).

The ridge opening types have an effect on the Cp distributions. At θ = 90°, the positive Cps over the windward sidewall slightly increase as the ridge type changes from 400 mm to 150 mm, and finally they are the highest with the chimney. For the leeward sidewall, the 400 mm shows the lowest -Cps with a gradual increase with the 150 mm and the highest -Cps are noticed with the chimney. The reverse situation occurs with the ridge opening types. The lowest -Cps are noticed with the chimney and the -Cps rapidly increase through 150 mm to reach their peaks with the 400 mm ridge.

At θ = 60° and 30°, the contour lines of Figs. 5.7b and c are very similar to the results of Davenport et al. (1977) and Holmes (1983). There is a gradual change from the uniform Cp distributions over the windward and leeward sidewalls to high positive Cps at the upwind windwall sidewall and high -Cps at the upwind leeward sidewall. Generally, the leeward sidewall's -Cps are higher with the 150 mm and 400 mm ridge types as compared to the chimney. The chimney shows higher -Cps values at the upwind end wall.

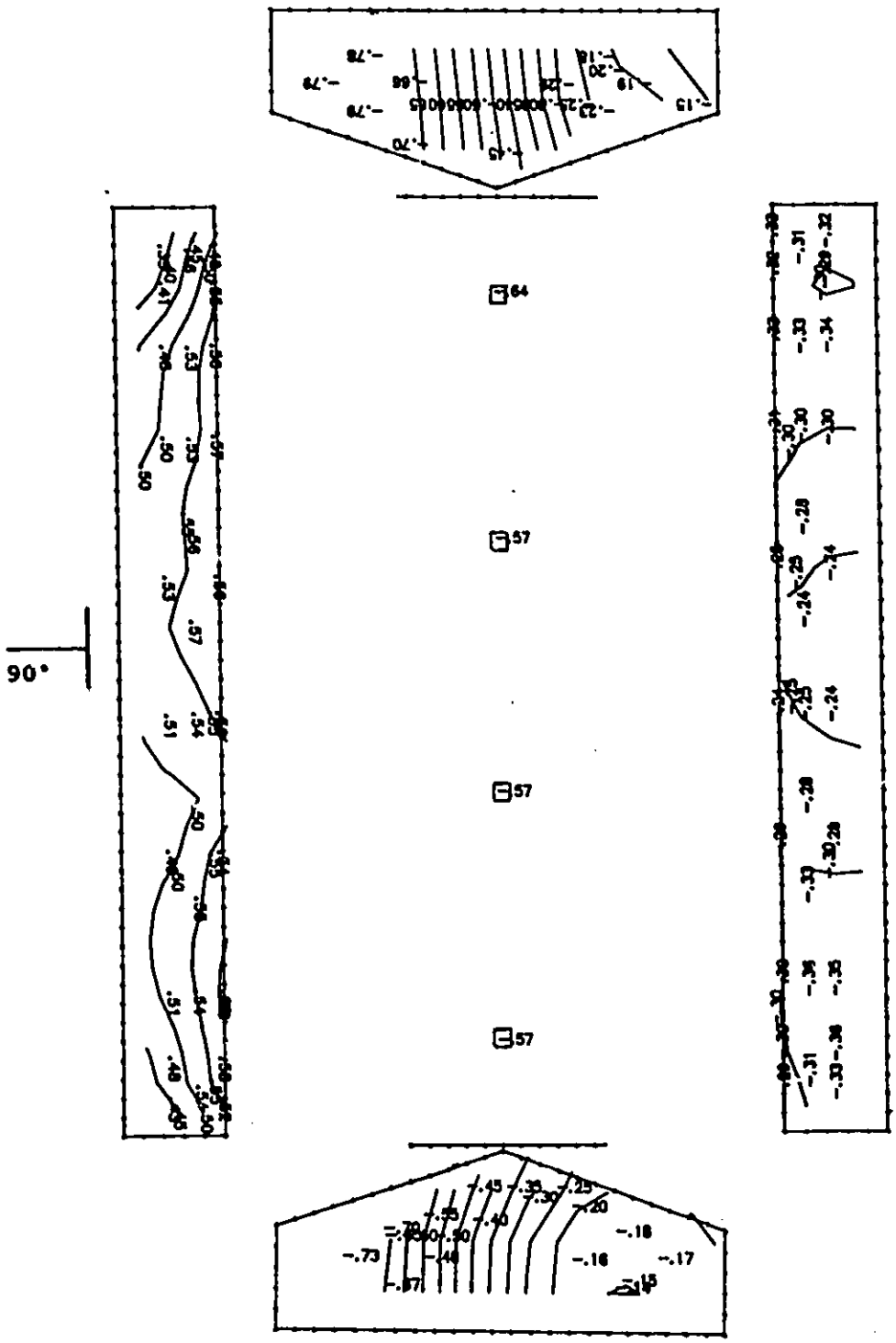

Figure 5.7a Cps contour lines: sealed model with chimney, wind angle of 90°.

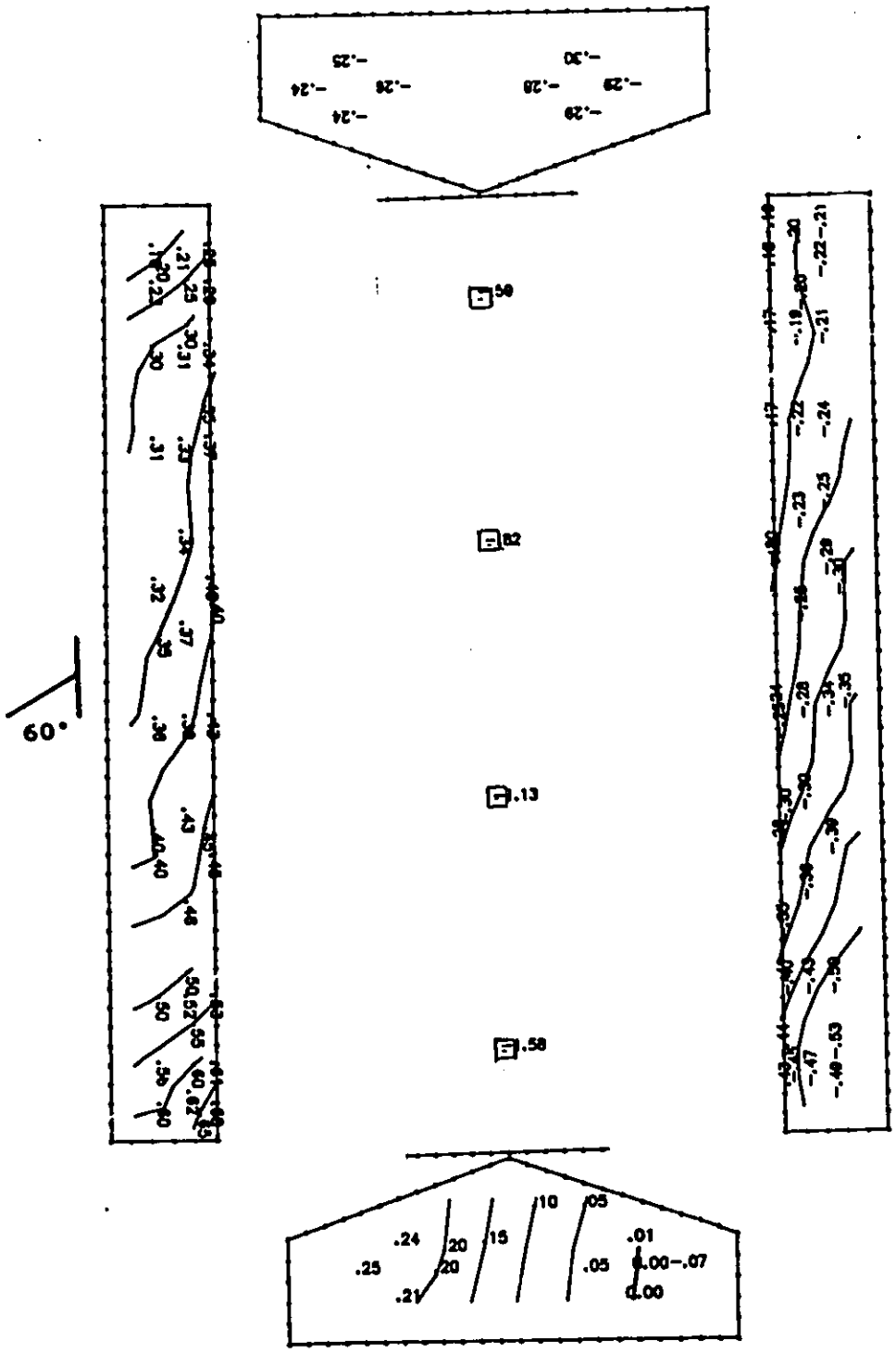

Figure 5.7b Cps contour lines: sealed model with chimney, wind angle of 60°.

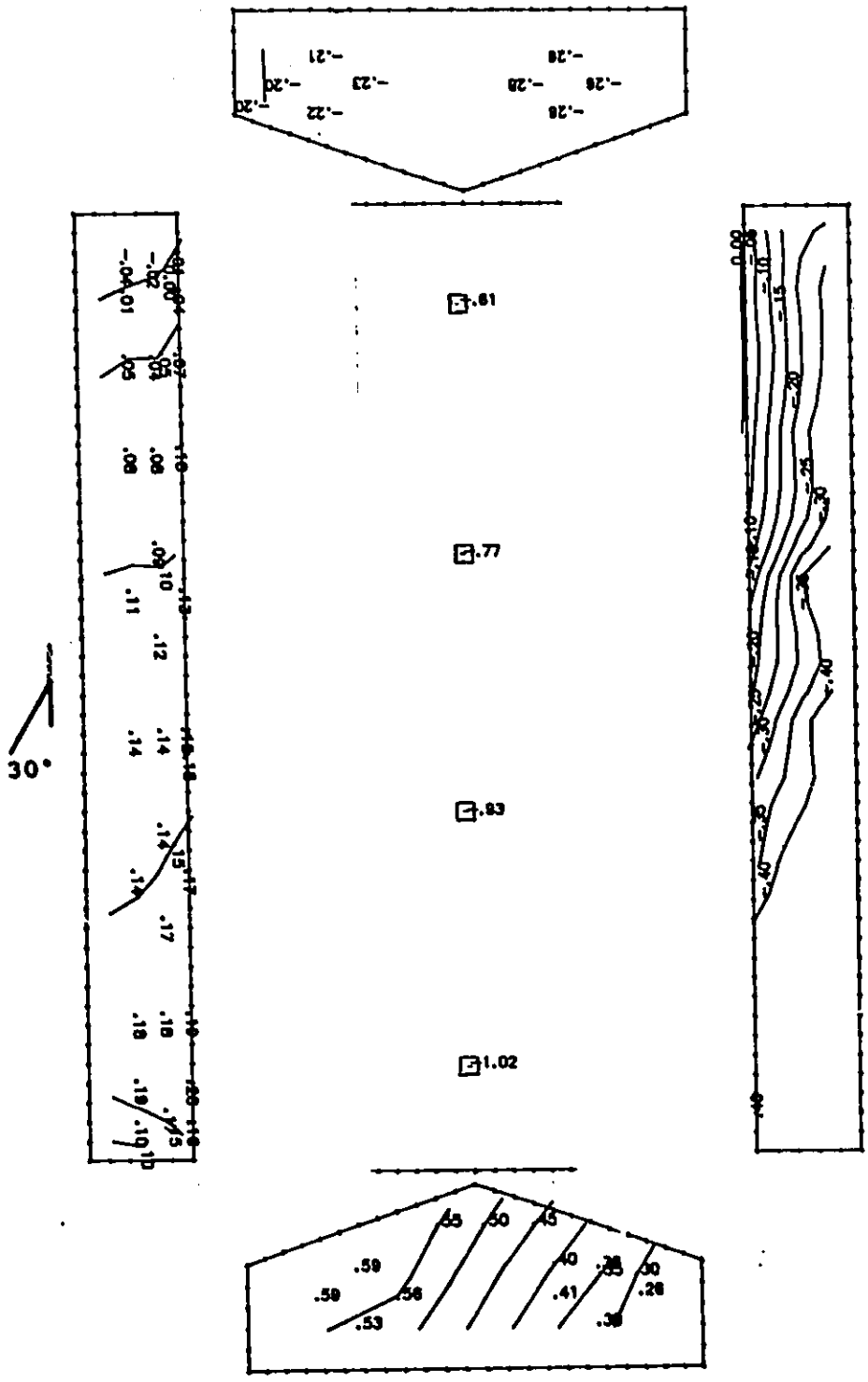

Figure 5.7c Cps contour lines: sealed model with chimney, wind angle of 30°.

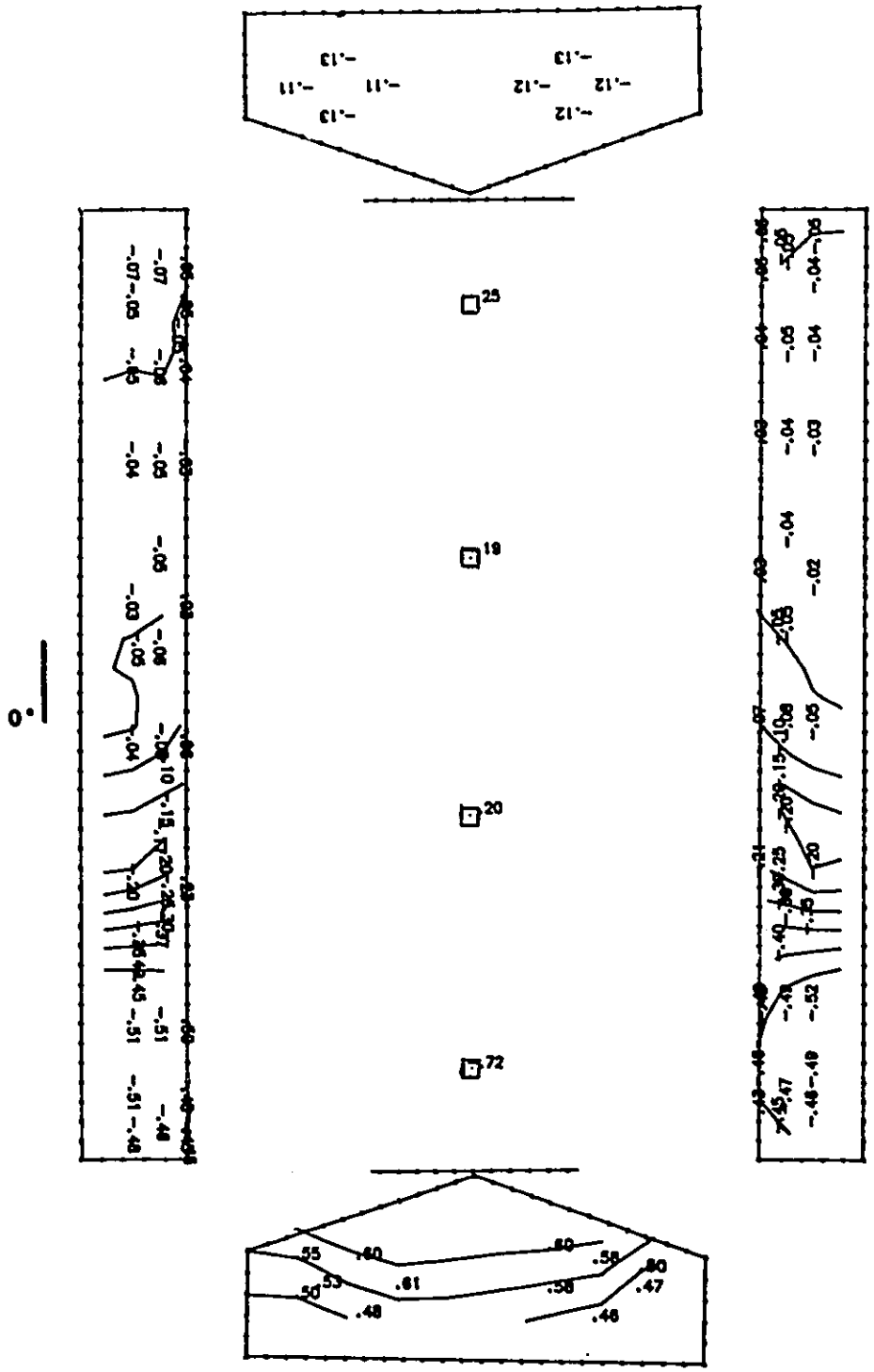

Figure 5.7d Cps contour lines: sealed model with chimney, wind angle of 0°.

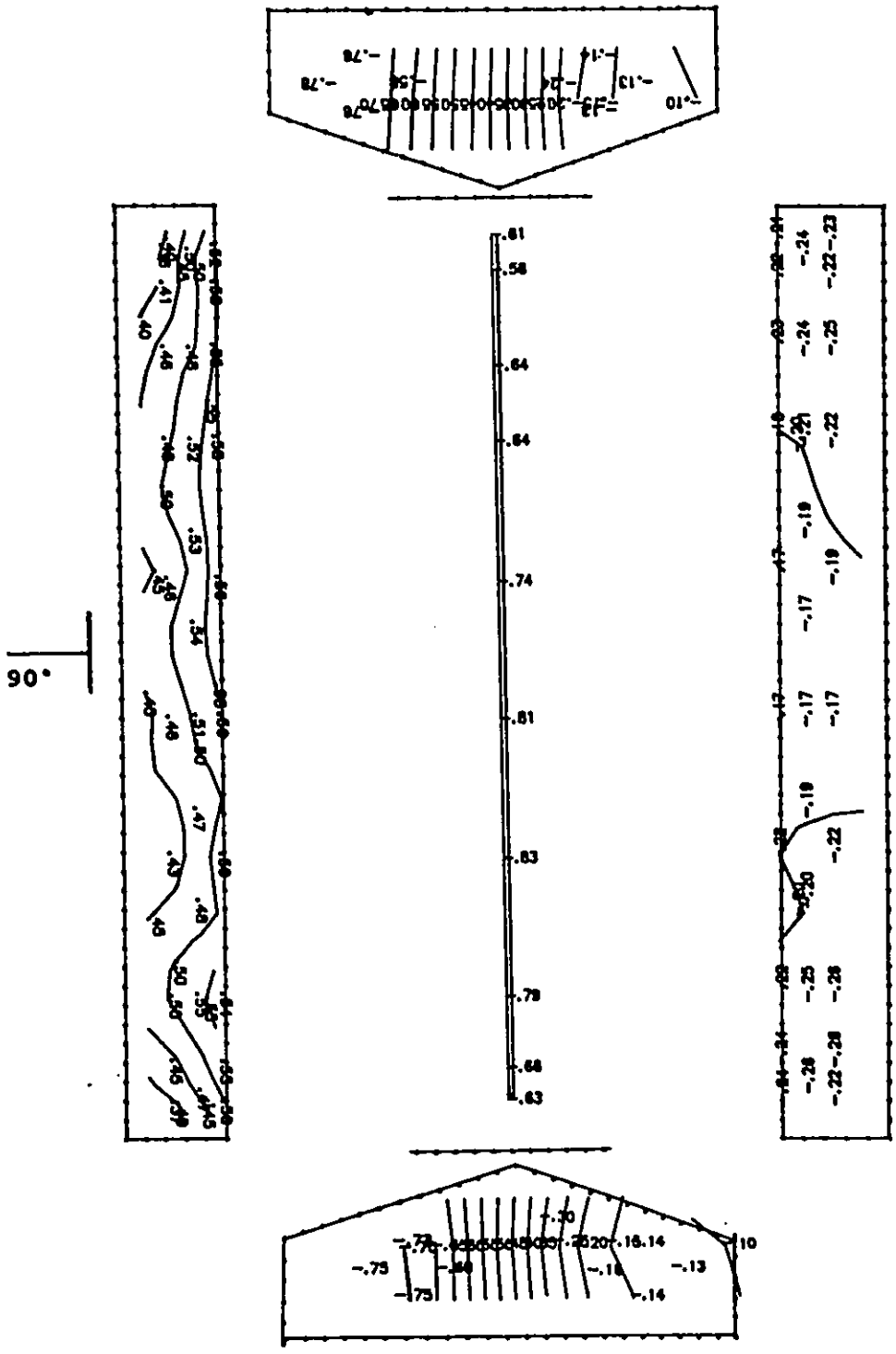

Figure 5.8a Cps contour lines: sealed model with simulated 150 mm ridge, wind angle of 90°.

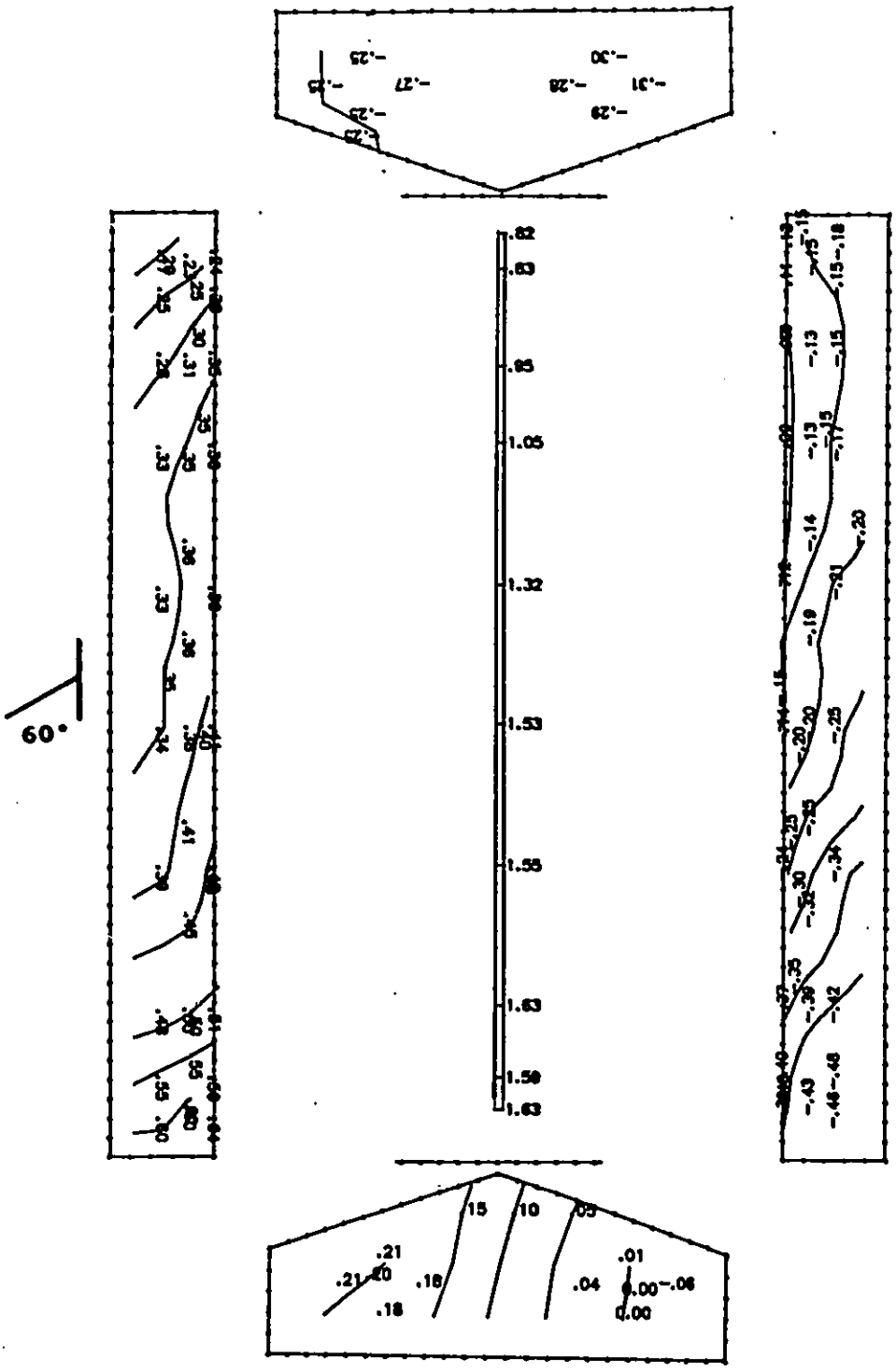

Figure 5.8b Cps contour lines: sealed model with simulated 150 mm ridge, wind angle of 60°.

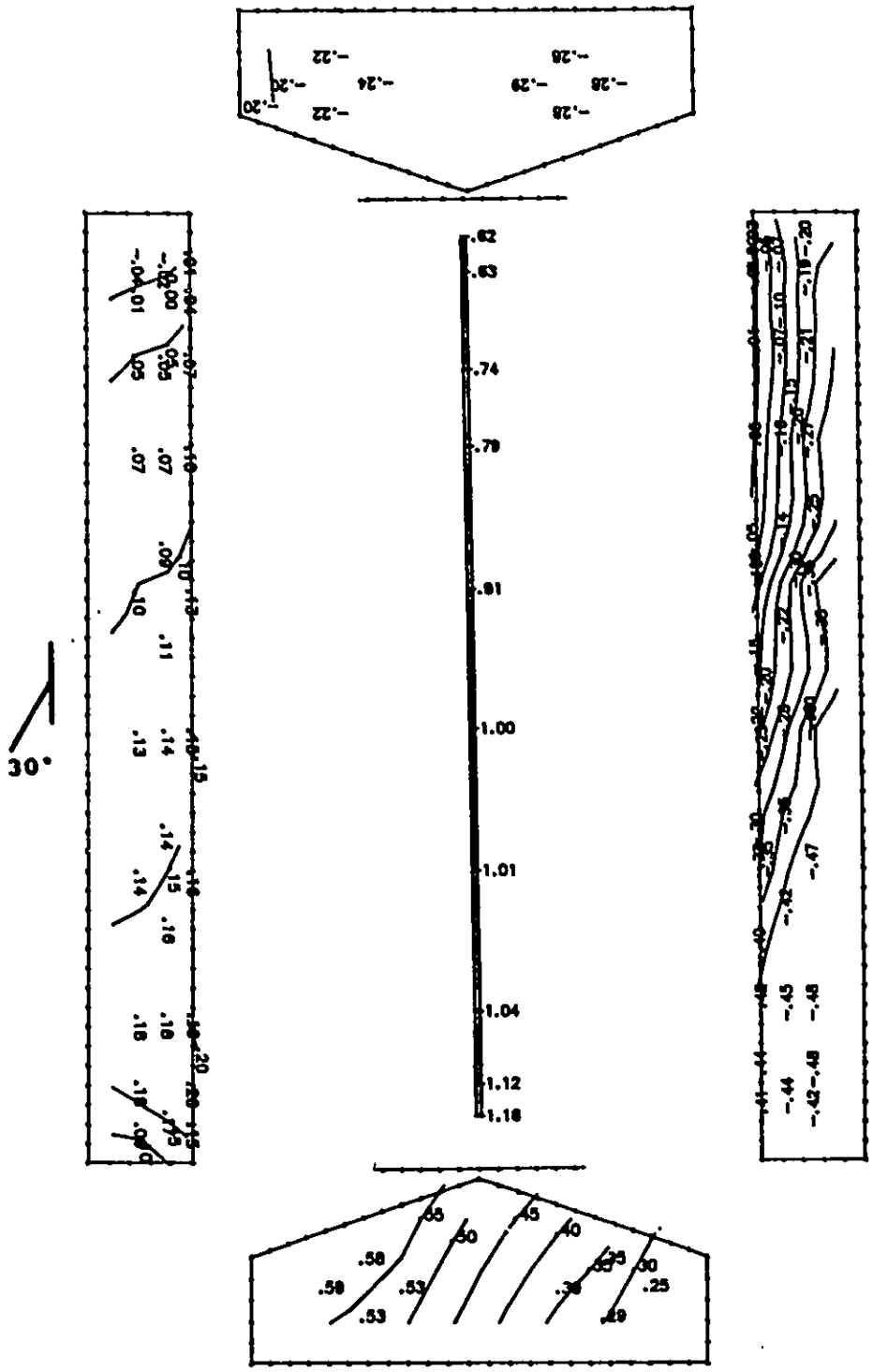

Figure 5.8c Cps contour lines: sealed model with simulated 150 mm ridge, wind angle of 30°.

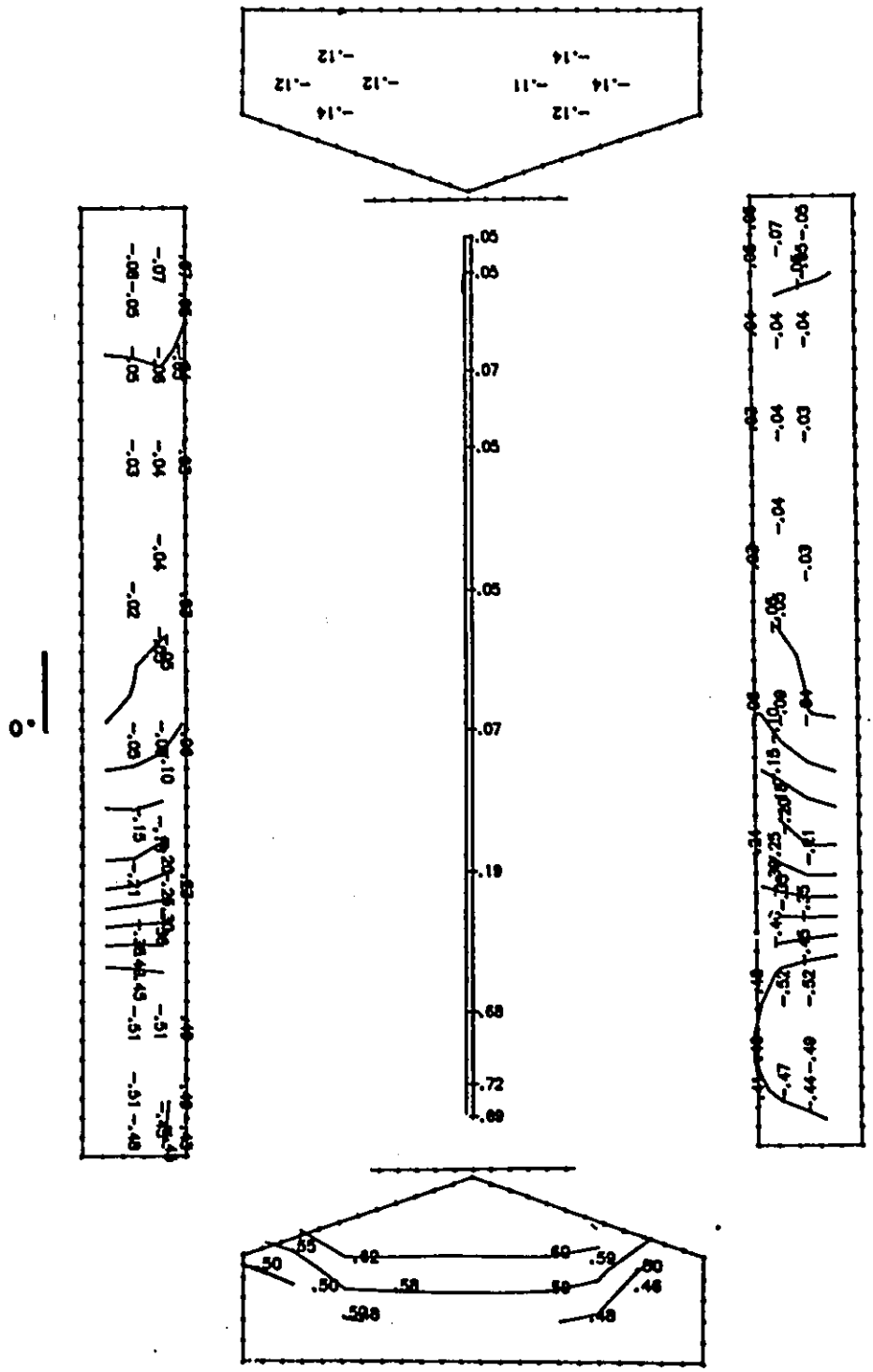

Figure 5.8d Cps contour lines: sealed model with simulated 150 mm ridge, wind angle of 0°.

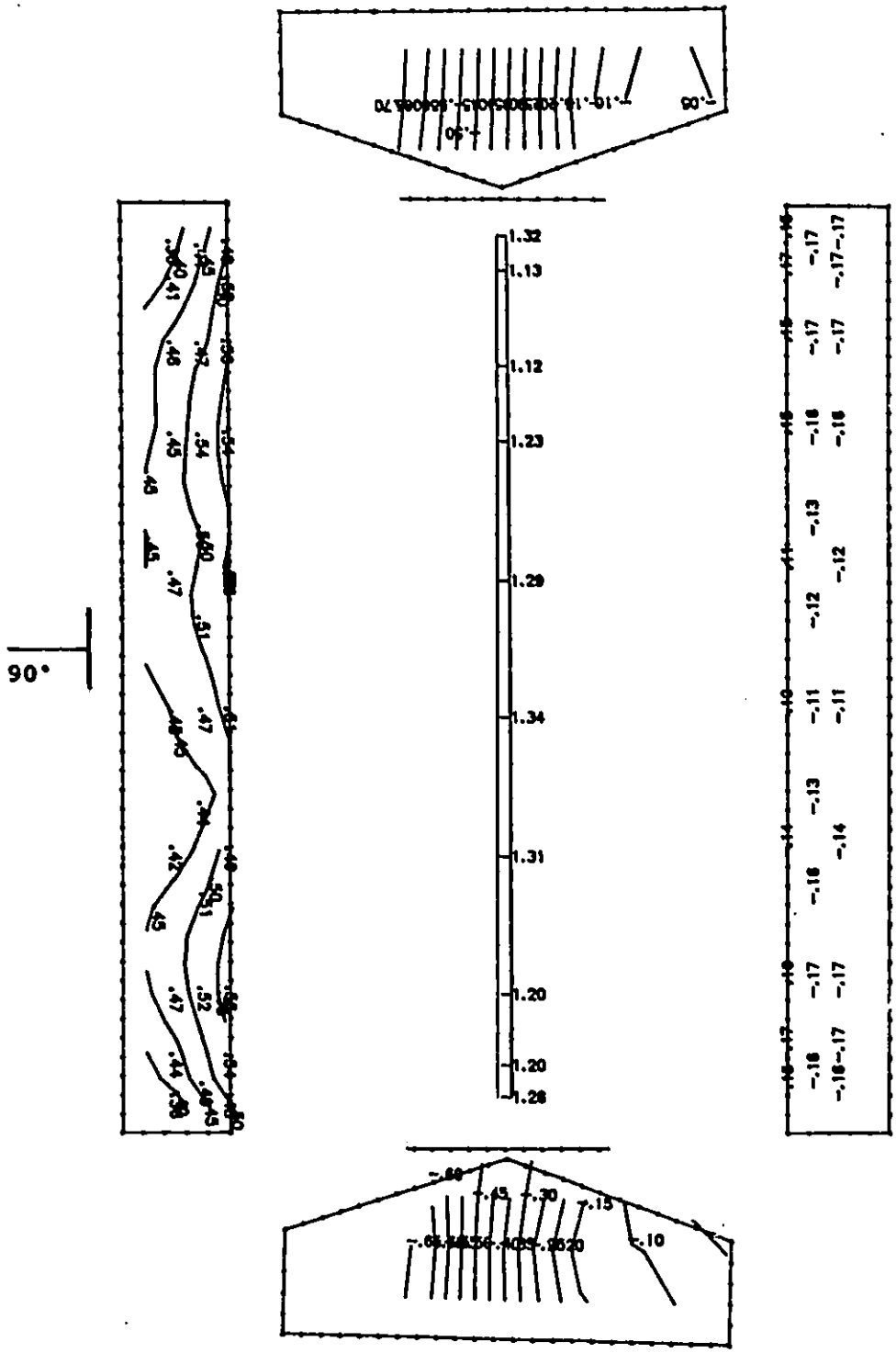

Figure 5.9a Cps contour lines: sealed model with simulated 400 mm ridge, wind angle of 90°.

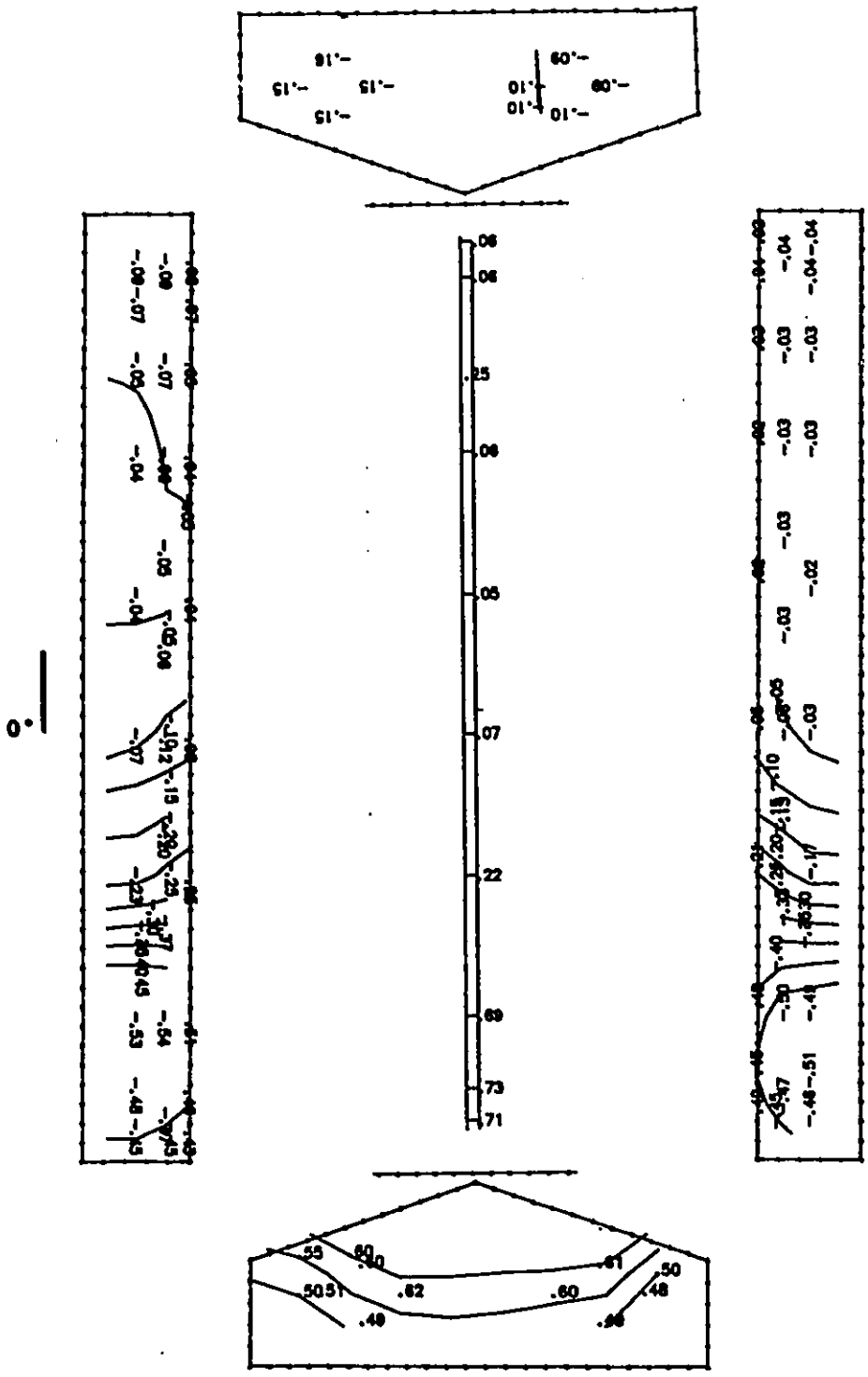

Figure 5.9b Cps contour lines: sealed model with simulated 400 mm ridge, wind angle of 0°.

At $\theta = 0°$, there is really no difference among the Cp distributions over the sidewalls and end walls for the chimney, 150 mm and 400 mm ridges. Only at the ridge level, the two downwind chimneys show higher -Cps compared to the 150 mm and 400 mm. This might be due to the effects of the upstands of the chimney.

From the results of the sealed models, the following points could be obtained:

1 - At $\theta = 90°$, $60°$ and $30°$, all three ridge opening types have different effects on the Cp magnitudes over the windward and leeward sidewalls.

2 - At $\theta = 90°$, $60°$ and $30°$, the larger ridge types show the higher -Cps at the ridge opening.

3 - At $\theta = 0°$, no difference in Cps is noticed over the sidewalls and end walls. Only the two downwind chimneys show higher -Cps.

5.1.3 Sealed versus open models

5.1.3.1 Tests with chimney

The comparisons between Figs. 5.1a-g (OP-CH-800-C) and 5.7a-d (SE-CH) reveal large differences in Cp distributions and magnitudes. At $\theta = 90°$, the Cp distributions over the open model's windward and leeward sidewalls are fairly uniform along the building length while with the sealed model, there are higher Cps at the center of the windward sidewall and a reduction in the -Cps at the center of the leeward sidewall. Similar data for sealed models are presented by Aynsley *et al.* (1977), Vickery *et al.* (1983) and Holmes (1983). The effect of porosity in the open model, in allowing air to go through, may help to obtain a more uniform distribution of the Cps over the wall surfaces. The -Cps at the ridge are considerably higher for the sealed model than for the open model.

At $\theta = 60°$, both the windward sidewall and both end walls' Cp distributions are similar for the sealed and open models. The Cp distributions are more uniform over the leeward sidewall with the open model as compared to the sealed model. The chimney -Cps are higher with the sealed model. At $\theta = 45°$, higher Cps are recorded over the upwind windward sidewall corner and upwind end wall corner with the open model.

At $\theta = 30°$, $20°$, $10°$ and $0°$ the windward and leeward sidewalls have different Cp distributions. A larger gradient of Cps occur with the sealed model from the upwind to the downwind end of the buildings. Both end walls behave similarly and the chimney -Cps are consistently higher with the sealed model.

For larger sidewall openings, Figs. 5.2a-d (OP-CH-1100-C) and 5.7a-d (SE-CH) show similar comparisons that were obtained with the OP-CH-800-C versus the SE-CH. The enlargement of the sidewall opening changes the Cp distributions slightly, but has a large effect on the difference in magnitudes between the sealed and open models.

The effects of opening the end walls are shown by comparing Fig. 5.3a-d (OP-CH-800-O) to Fig. 5.7a-d (SE-CH). The largest differences are noticed at both end walls where the Cp distributions and magnitudes are completely different.

Generally the comparisons between the sealed versus the open models with the chimney show that:

1 - For all wind angles, the -Cps are higher at the sealed model's chimneys.
2 - For all wind angles except $60°$, the windward and leeward sidewalls show considerably different Cp distributions.
3 - For larger sidewall openings of 1100 mm, the differences in Cp magnitudes between the sealed versus the open models are accentuated.

4 - The opening of the end walls in the open model completely changes the pressure distributions and magnitudes over the end walls.

5.1.3.2 Tests with 150 mm and 400 mm ridges

The comparisons between Figs. 5.5a-d (OP-150-800-C) and 5.8a-d (SE-150), as well as between Figs. 5.6a-d (OP-400-800-C) and 5.9a-b (SE-400) tend to show that the larger the opening areas are, the larger the differences in Cp distributions and magnitudes are between the open and sealed models. For all wind angles, very high -Cps at the ridge level are recorded with the sealed model while -Cps over the leeward sidewall are lower. Larger differences on the uniformity of the Cp distributions over the windward sidewall at $\theta = 90°$ and $0°$ are accentuated.

For open versus sealed models, the results in Appendix E show that the Cp distributions over both end walls are completely reversed, with the open versus sealed models for most wind angles. The air flowing around and through the building may create this inversion in pressure distribution.

From the results of the sealed versus open models, with 150 mm and 400 mm ridge, the following points can be made:

1 - The -Cps at the ridge are considerably higher with the sealed model.

2 - The -Cps over the leeward walls are higher with the open models.

3 - With the end walls open, the Cp distributions over both end walls are totally reversed for the sealed models versus the open models.

4 - When the sidewall opening areas in the open model are increased, larger differences in Cp distributions and magnitudes occur.

5.1.4 Comparison to previous work

Appendix A contains a complete review of pressure coefficients for comparable full scale and scale model experiments. They were selected based on similarity of the wind profile (open country) and basic shapes. Tables 5.1 and 5.2 provide a summary of the average Cps recorded over the ridge opening for sealed and open models at $\theta = 90°$ and $0°$ while Tables 5.3 and 5.4 present the results of the pressure differences across the building sidewalls at $\theta = 90°$ and $0°$. The dimensions of each building are added in order to compare results among buildings with similar shapes. All reported data for the open model have closed end walls. The reference height is 10 m.

For $\theta = 90°$, the pressure coefficients at the ridge line reported on Table 5.1 show large differences among the various past experiments for sealed buildings. The full scale measurements from the U.K. show generally higher -Cps than the scale models. With the exception of the SE-400 test, there is no evident trend for the effects of the building lengths, widths, eave heights or the presence of an overhang on the pressure coefficients at the ridge line.

For the open buildings, the results are also widely spread for all the reported tests. The chimney tests show considerably higher -Cps than the others. The limited opening area and the local flow disturbances around the chimney may cause higher -Cps by the chimney compared to the continuous 150 mm and 400 mm ridge openings.

The results from Shrestha et al. (1990) can be compared to the OP-400 and OP-150 tests. The two building widths and heights are very close, but the opening area ratio was smaller for Shrestha et al.'s (1990) tests. The 1100 mm sidewall opening areas produced very little effects on the -Cps for the 150 mm and 400 mm ridge. With the chimney tests, there were higher -Cps with the 800 mm sidewall compared to the 1100 mm opening. The experiments with the FB02 and FB06 were

Table 5.1 Average pressure coefficient across the ridge, $\theta = 90°$, full scale buildings and scale models for open country situations; $\alpha = 0.14$ to 0.18.

Description	Cp	Building Length (m)	Width (m)	Eave Height (m)	Roof Angle (degrees)	Overhang Present
Sealed buildings						
FB05	-1.42	41.0	28	4.0	15.0	
SE-400	-1.32	24.4	12.1	2.7	18.4	y
FB03	-1.03	18.5	11.9	4.6	16.0	
FB19	-0.94	36.8	18.4	5.0	15.0	
FB16	-0.93	120	6.7	4.5	15.0	
Dutch barn	-0.84	24.3	11.0	5.5	16.7	
SE-150	-0.78	24.4	12.1	2.7	18.4	y
FB02	-0.60	18.5	7.4	1.77	15.0	
SE-CH	-0.57	24.4	12.1	2.7	18.4	y
Holmes (1983)	-0.42	12.2	6.1	2.6	15.0	y
Vickery et al. (1983)	-0.32	38.1	24.4	4.9	18.4	y
Holmes (1983)	-0.19	12.2	6.1	2.6	20.0	y
Open buildings						
OP-CH-800-C	-0.83	24.4	12.1	2.7	18.4	y
OP-CH-1100-C	-0.79	24.4	12.1	2.7	18.4	y
FB02	-0.43	18.5	7.4	1.77	15.0	
FB06	-0.33	34.4	24.6	2.66	11.0	
Shrestha et al. (1990)	-0.28	14.6	10	3.0	18.4	y
OP-400-800-C	-0.22	24.4	12.1	2.7	18.4	y
OP-400-1100-C	-0.21	24.4	12.1	2.7	18.4	y
OP-150-800-C	-0.20	24.4	12.1	2.7	18.4	y
OP-150-1100-C	-0.20	24.4	12.1	2.7	18.4	y

Table 5.2 Average pressure coefficients across the ridge at three locations along the ridge length, $\theta = 0°$, full scale buildings and scale models.

Description	Cp Locations 1	2	3	Roof Angle (degrees)
Sealed buildings				
SE-CH	-0.72	-0.19	-0.25	18.4°
Vickery et al. (1983)	-0.58	-0.16	-0.11	18.4°
SE-400	-0.58	-0.06	-0.06	18.4°
SE-150	-0.57	-0.06	-0.06	18.4°
Dutch barn	-0.55	-0.11	-0.08	16.7°
Holmes (1983)	-0.51	-0.14	-0.08	20.0°
Holmes (1983)	-0.51	-0.13	-0.06	15.0°
Down et al. (1985)	-0.47	-0.05	-0.07	12.0°
Open buildings				
OP-400-800-C*	-0.62	-0.18	-0.07	18.4°
OP-150-1100-C	-0.59	-0.11	-0.07	18.4°
OP-CH-1100-C	-0.57	-0.09	-0.09	18.4°
OP-150-800-C**	-0.56	-0.11	-0.06	18.4°
OP-400-1100-C	-0.56	-0.11	-0.06	18.4°
OP-CH-800-C	-0.55	-0.08	-0.08	18.4°

* The -Cps measurements at the ridge level were impaired by recording problems during the wind tunnel test. The -Cps at Location 2 is too high as compared to the others at this location.

** In Fig. 5.1g versus Figs. 5.2d and 5.3d, the alignment of OP-150-800-C was not exactly 0°.

Table 5.3 Pressure coefficient differences across the sidewalls of full scale buildings and scale models, $\theta = 90°$.

Description	ΔC_p	Building Length (m)	Width (m)	Eave Height (m)	Roof Angle (degrees)	Overhang Present
Sealed buildings						
Dutch barn	0.89	24.3	11.0	5.5	16.7°	
Bottcher et al. (1986)	0.78	19.0	10.0	2.5	18.4°	
SE-CH	0.78	24.4	12.2	2.7	18.4°	y
SE-150	0.68	24.4	12.2	2.7	18.4°	y
Vickery et al. (1983)	0.66	38.1	24.4	4.9	18.4°	y
Holmes (1983)	0.60	12.2	6.1	2.6	20°	y
SE-400	0.59	24.4	12.2	2.7	18.4°	y
FB19	0.57	36.8	18.4	5.0	15°	
Holmes (1983)	0.54	12.2	6.1	2.6	15°	y
FB02	0.51	38.5	7.4	1.77	15°	
FB01	0.51	27.8	21.5	4.3	15°	
Open buildings						
OP-400-1100-C	0.94	24.4	12.1	2.7	18.4°	y
OP-150-1100-C	0.90	24.4	12.1	2.7	18.4°	y
OP-400-800-C	0.82	24.4	12.1	2.7	18.4°	y
OP-150-800-C	0.80	24.4	12.1	2.7	18.4°	y
OP-CH-1100-C	0.75	24.4	12.1	2.7	18.4°	y
OP-CH-800-C	0.72	24.4	12.1	2.7	18.4°	y
Bottcher et al. (1986)						
Opening = 10%	0.70	19	10	2.7	18.4°	
area = 20%	0.64	19	10	2.7	18.4°	
= 30%	0.59	19	10	2.7	18.4°	
= 40%	0.54	19	10	2.7	18.4°	
Shrestha et al. (1990)						y
Opening = 3%	0.51	14.6	9.8	3.0	18.4°	y
area = 10%	0.51	14.6	9.8	3.0	18.4°	
FB06	0.37	34.25	24.6	2.66	11°	

Table 5.4 Pressure coefficient for full scale buildings and scale models at three locations along the sidewalls, $\theta = 0°$.

Description	Cp 1	Cp 2	Cp 3	Length (m)	Width (m)	Eave Height (m)	Roof Angle (degrees)
Scaled buildings							
Vickery et al. (1983)	-0.37	-0.11	-0.10	38.1	29.4	4.9	18.4°
Holmes (1983)	-0.35	-0.13	-0.07	12.2	6.1	2.6	15.0°
Holmes (1983)	-0.25	-0.11	-0.08	12.2	6.1	2.6	20.0°
SE-400	-0.36	-0.12	-0.06	24.4	12.2	2.7	18.4°
SE-150	-0.35	-0.12	-0.06	24.4	12.2	2.7	18.4°
SE-CH	-0.35	-0.13	-0.06	24.4	12.2	2.7	18.4°
Dutch barn	-0.30	-0.04	-0.05	24.3	11	5.5	16.7°
Down et al. (1985)	-0.30	-0.03	-0.05	35	22	2.2	12°
Open buildings							
OP-400-1100-C	-0.37	-0.20	-0.10	24.4	12.1	2.7	18.4°
OP-150-1100-C	-0.36	-0.20	-0.10	24.4	12.1	2.7	18.4°
OP-CH-1100-C	-0.35	-0.19	-0.09	24.4	12.1	2.7	18.4°
OP-400-800-C	-0.34	-0.16	-0.08	24.4	12.1	2.7	18.4°
OP-150-800-C	-0.34	-0.15	-0.08	24.4	12.1	2.7	18.4°
OP-CH-800-C	-0.32	-0.15	-0.07	24.4	12.1	2.7	18.4°

performed with and without a limited sidewall opening area (Appendix A), and this may have presented different airflow patterns at the open ridge level.

For $\theta = 0°$, all the experimental results for the sealed and the open structures are similar (Table 5.2). Only the SE-CH test shows higher -Cps at the upwind end. For the open building, there was no difference among the 150 mm and 400 mm ridge openings except for the case of OP-400-800-C. At $\theta = 0°$, the differences in -Cps may be attributed to the reported monitoring errors during the wind tunnel tests (Fig. 5.6d). There was no sidewall opening area effect on Cps.

The pressure coefficient difference across the building was equal to the average windward Cp (Cp_w) minus the average leeward Cp (Cp_l) at mid-length of the sidewall. For $\theta = 90°$, the presented Cps were an average of the central Cps shown on the contour lines of Figs. 5.1 to 5.9 and Appendix E. Table 5.3 reviews the $Cp_w - Cp_l$ differences across full scale buildings and sealed scale models at $\theta = 90°$. Again, there were large differences among the previous research work combined with the present data. No specific trend for the effect of building length, width, eave height and overhang could be determined. The ridge design effects of chimney, 150 mm and 400 mm openings were evident with a ΔCp reduction of about 0.1 between each test.

For the open structures, Table 5.3 presents a controversy between the present results and the data of Bottcher et al. (1986). The scale models with continuous ridges of 150 mm and 400 mm showed that, the larger sidewall opening area of 1100 mm present higher ΔCps across the building. For both continuous ridge openings, the effect of the sidewall opening area was dominant over the ridge width effect on these particular cases. The chimney tests with 1100 mm and 800 mm showed the same effect of the sidewall opening area. Bottcher et al. (1986) presented results which are completely in contradiction to the results of this experiment. However, it should be noticed that the measuring techniques of the windward and leeward pressure coefficients were different. Bottcher et al. (1986) installed pitot tubes across the opening windows as compared to pressure taps installed flat over the surface of the scale model. The ΔCp results of Shrestha et al. (1990) are lower than the present results for the sidewall openings of 800 mm and 1100 mm. When they were compared with the sealed models, SE-150 or SE-400, the differences were limited to only a ΔCp of 0.17 and 0.08, respectively. The FB06 shows a considerably lower ΔCp. The two building shapes differ in length, width, roof angle and

also, the FB06 had very small sidewall openings compared to the present study.

Comparisons between sealed versus open buildings help to study the relative effect of the ridge openings on the ΔCps across the building. The 150 mm ridge results for SE-150 ($\Delta Cps = 0.68$) versus OP-150-800-C ($\Delta Cps = 0.80$) and OP-150-1100-C ($\Delta Cps = 0.90$), show that creating an opening in the model increases the ΔCp across the building. This would be in contradiction with Bottcher et al. (1986) and Ashley and Sherman (1984), since they studied buildings without any ridge opening.

For the cases of the continuous open ridge, 150 mm and 400 mm, the pressure distributions at the ridge are completely disturbed and this may have caused the increase in ΔCps with the larger opening areas. Aynsley (1979) reported that ΔCps across the sidewall should be greater than the ΔCps of a sealed model for scale models with sidewall openings between 5% to 35%. These results are in accordance with Table 5.3, where the ΔCps are higher with 37% (1100) versus 27% (800) of open sidewall areas for both 150 and 400 mm ridge.

For $\theta = 0°$, the results of Table 5.4 show very little difference among all the open and the sealed building tests. For the open model, there was a trend for the larger sidewall opening area of 1100 mm to generate higher ΔCps along the sidewalls.

Generally, observations done from the results in Tables 5.1, 5.2, 5.3 and 5.4 reveal that:

1 - At $\theta = 90°$, the results on -Cps at the ridge opening and ΔCps across the building vary widely among all experiments.

2 - At $\theta = 0°$, the results on -Cps at the ridge opening and ΔCps across the building are very similar among all experiments.

No specific trends could be established on the effects of building length, width, eave height and the addition of an overhang for wind angles of 90°.

5.1.5 Discussion on the methodology for Cp measurements over ridge openings

As shown on Figs. 5.1a-g and 5.7a-d, the Cp distributions for the chimney models present little differences between the open and the sealed models. The measurements were made on the edge of the ridge line (Figs. 4.5 and 4.6). It appears that they are not affected by the flow through the chimney, but only by the interferring effects of the upstands.

The comparisons of open and sealed models, such as Figs. 5.5a-d versus 5.8a-d and Figs. 5.6a-d versus 5.9a-b, display large differences in the magnitudes of the Cps. Figures 5.8a-d and 5.9a-b show high negative areas over the ridge which is consistent with the data presented by Aynsley *et al.* (1977), Davenport *et al.* (1977), Vickery *et al.* (1983) and many others.

However, with continuous ridge openings the -Cps are completely different for the open model as compared to the sealed model. This fact would confirm the presumption of Vickery *et al.* (1983) concerning the effect of the outflow through the ridge altering the negative pressure distribution and in agreement with the full scale Cp observations for low-rise buildings performed by Wright and Westgate (1982), Moran *et al.* (1983), Richardson (1989a) and Shrestha *et al.* (1990).

The method used for estimating the -Cps for the chimney in the open model requires further investigation. With the present method it is assumed that the effective -Cps applied to the chimney are the average of the four nearest pressure tap readings. This assumption means that the -Cps generated by the ridge line apply directly to the chimney without any extra air outflow effects. The presence of the upstand over

the ridge line may create even a higher negative pressure, as demonstrated by Froehlich et al. (1974).

5.2 Internal pressure coefficients

The calculated Cp_{in}s for the sealed and open models and the plots of the measured Cp_{in} for the open models are all contained in Appendix F. Choinière et al. (1988c) studied the wind direction effects on the airflow patterns in naturally ventilated scale models for livestock housing. Some drawings of the airflow patterns which apply in this case are added in Appendix F.

5.2.1 Open model, calculated Cp_{in}

Figures 5.10, 5.11 and 5.12 show the calculated internal pressure coefficients with respect to the wind angles of incidence for the three ridge openings: chimney, continuous 150 mm and 400 mm ridges. The Cp_{in}s are also presented in function of the sidewall opening areas of 800 mm and 1100 mm in Figs. 5.13 and 5.14.

The results of Figs. 5.10 (chimney) and 5.11 (150 mm ridge) with the closed end walls show a gradual decrease in the Cp_{in} from $\theta = 90°$ to 0°. Similar types of curves are presented by Bilsborrow and Fricke (1975), Aynsley et al. (1977), Holmes (1979) and Stathopoulos et al. (1979) for different models without a ridge opening.

With open end walls, the Cp_{in} results of Bilsborrow and Fricke (1975), for their scale model with open sidewalls and no ridge opening, show very similar curve shapes and compared to the results presented on Figs. 5.10 and 5.11. The Cp_{in} at 90° increases as the wind angle becomes equal to 45° or 60°. The angle when the Cp_{in} peak occurs is directly related to the model type and the relative end walls and sidewall opening areas.

5.2.1.1 Effect of sidewall openings

The results of the sidewall openings of 800 mm and 1100 mm (open or closed) for the chimney case are presented in Fig. 5.10. The Cp_{in}s for the 800 mm and 1100 mm with closed end walls are similar for θ = 90°, 60° and 45°, but for θ = 0° to 30°, the 1100 mm sidewall Cp_{in}s are lower. For the open end walls, the Cp_{in}s for the 1100 mm sidewall are lower for θ = 0° to 20° and are similar for both 800 mm and 1100 mm openings for θ = 30° to 90°. The general effects of the 800 mm versus the 1100 mm for the open and closed end walls are fairly similar with the 150 mm ridge opening (Fig. 5.11).

For the 400 mm ridge with the closed end walls, the 800 mm sidewall shows the lowest Cp_{in} for all angles except 90°. When the end walls are open, the 1100 mm shows lower Cp_{in} at θ = 90° to 45° and higher Cp_{in} with θ = 0° and 10°. The results of the OP-400-800-C should be treated with care, especially at θ = 0° to 45° because some Cp monitoring problems occurred during the wind tunnel tests.

Then, both sidewall openings with open or closed end walls have an effect on the calculated internal pressures according to the type of ridge opening used. According to Holmes (1979, 1983), the internal pressures should not be affected by the sidewall opening areas for buildings without ridge openings if their area ratios are equal (A_w/A_l) and if the Cp_w and Cp_l are equal. For the 800 mm and 1100 mm sidewall opening, the area ratio was always equal to 1 ($A_w = A_l$). Then the difference in the predicted Cp_{in} may be attributed to the difference in ($Cp_w - Cp_l$) for 800 mm and 1100 mm openings noticed on the pressure contour lines and reported in Table 2.3 for each combination of sidewall and ridge opening types.

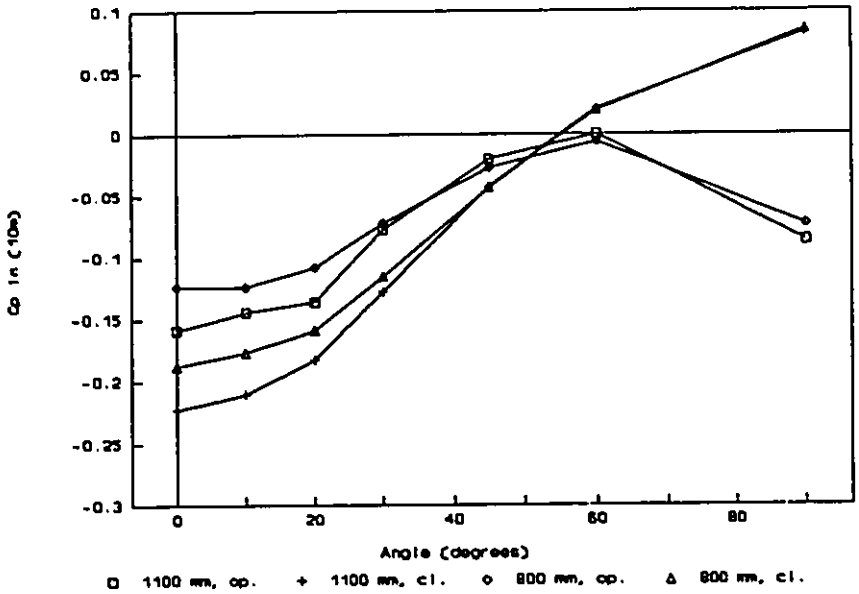

Figure 5.10 Open model, chimney, internal pressure coefficients, open and closed end walls.

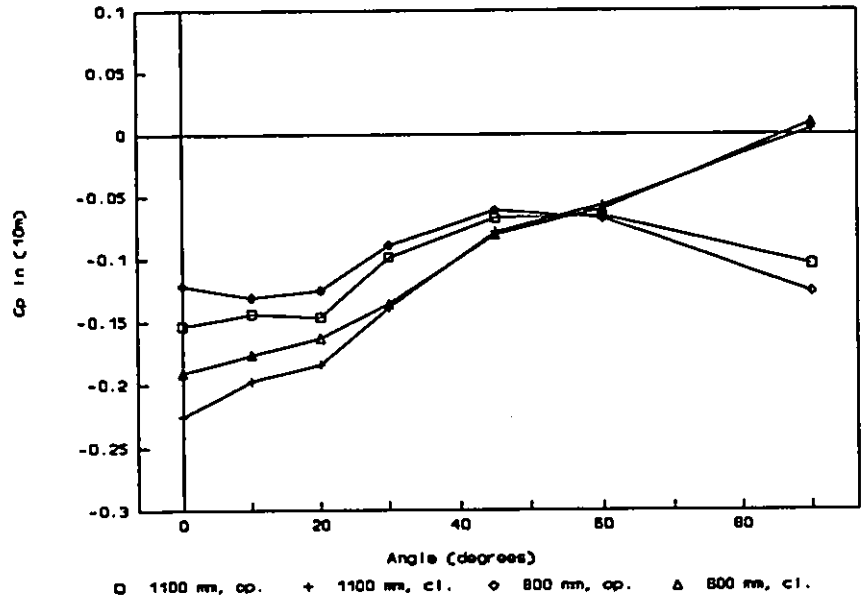

Figure 5.11 Open model, simulated 150 mm ridge, internal pressure coefficients, open and closed end walls.

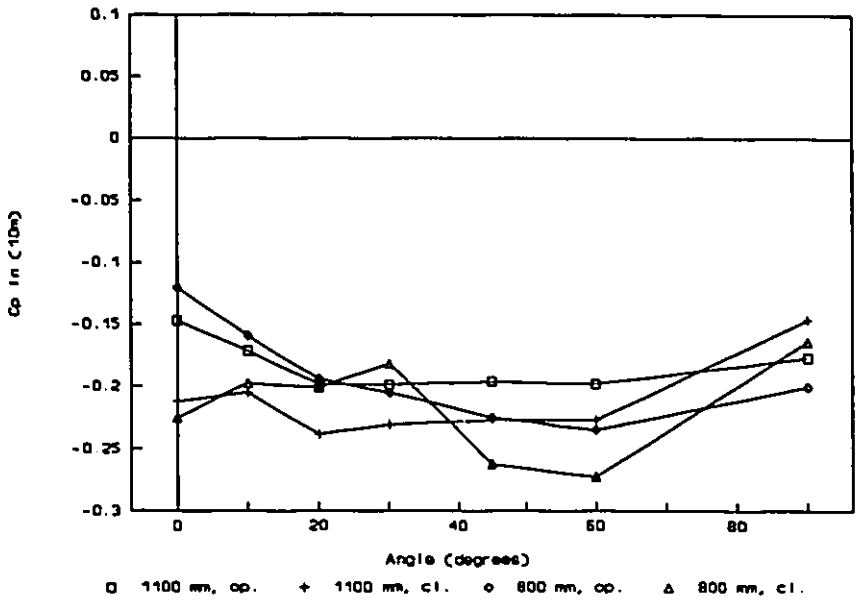

Figure 5.12 Open model, simulated 400 mm ridge, internal pressure coefficients, open and closed end walls.

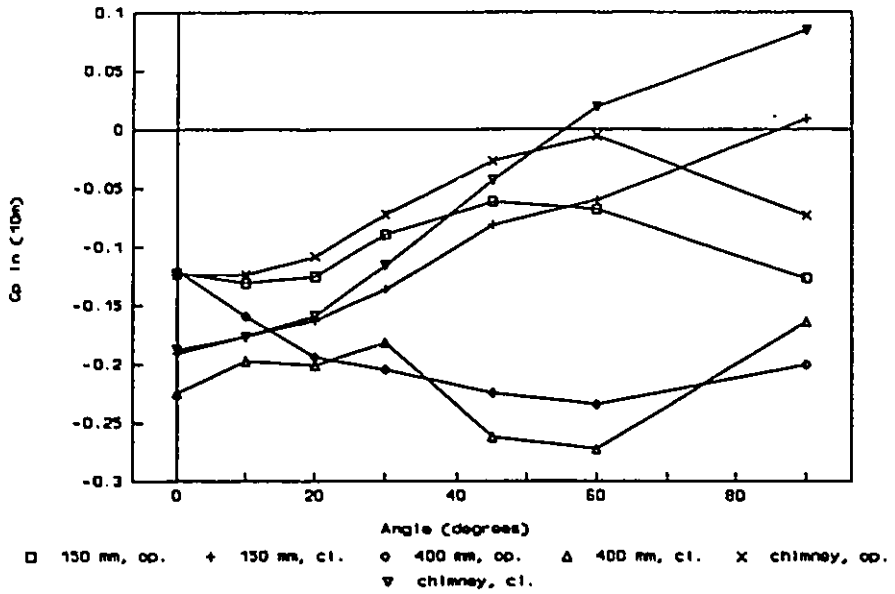

Figure 5.13 Open model, simulated 800 mm sidewall, internal pressure coefficients, open and closed end walls.

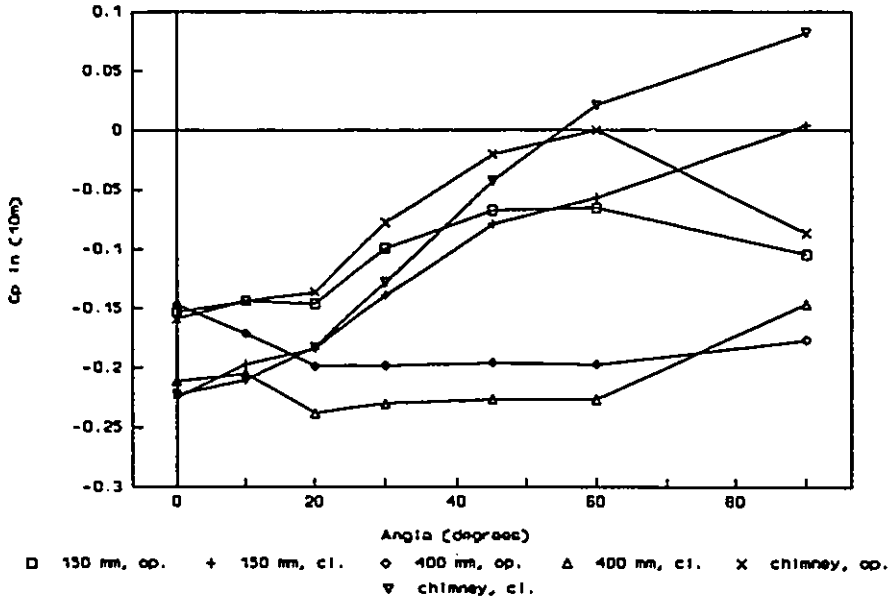

Figure 5.14 Open model, simulated 1100 mm sidewall, internal pressure coefficients, open and closed end walls.

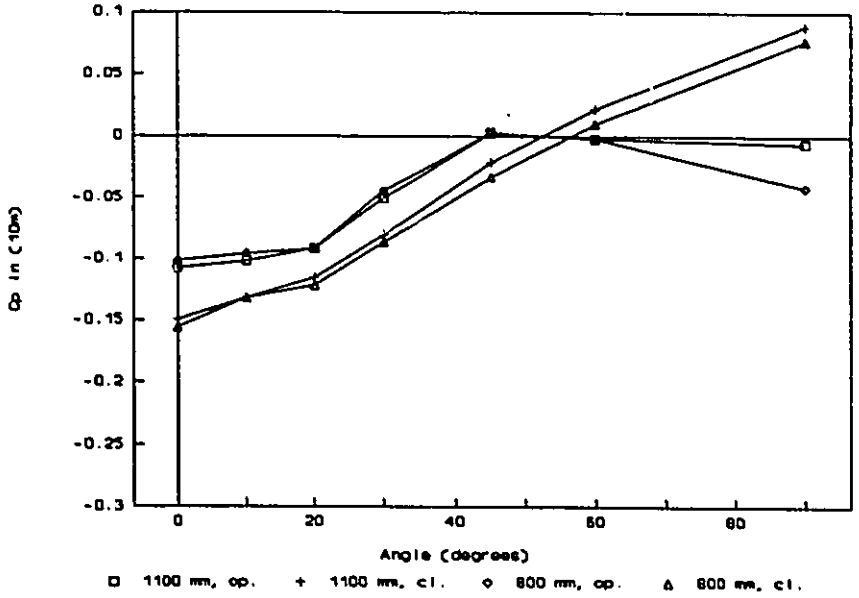

Figure 5.15 Sealed model, chimney, internal pressure coefficients.

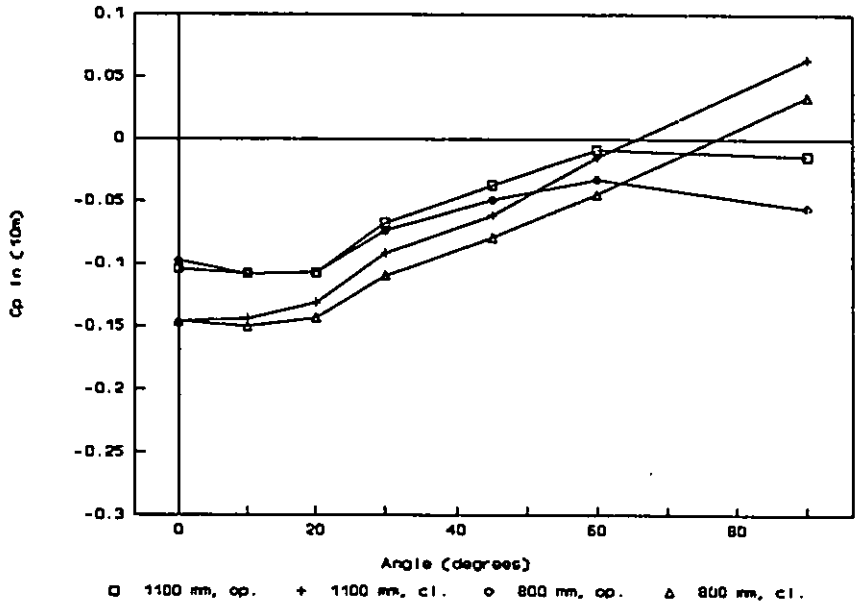

Figure 5.16 Sealed model, simulated 150 mm ridge, internal pressure coefficients.

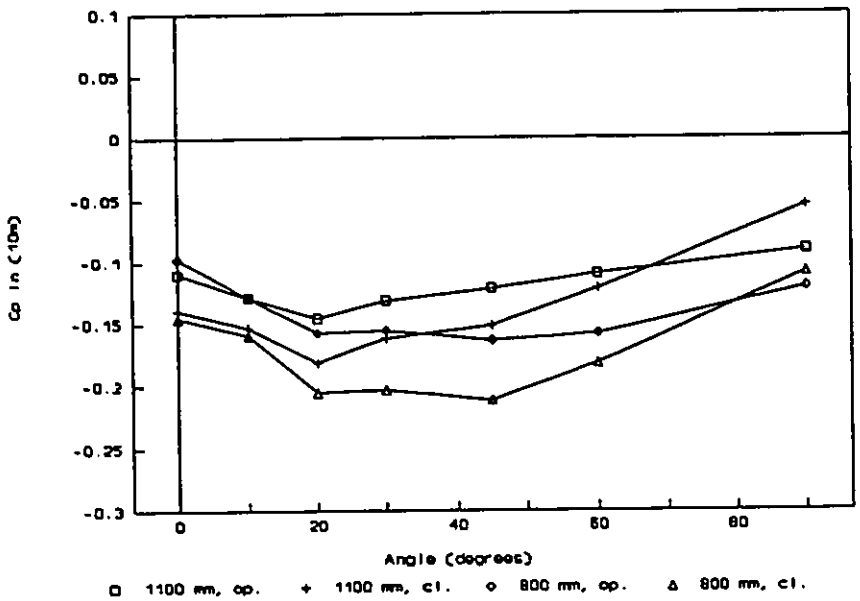

Figure 5.17 Sealed model, simulated 400 mm ridge, internal pressure coefficients.

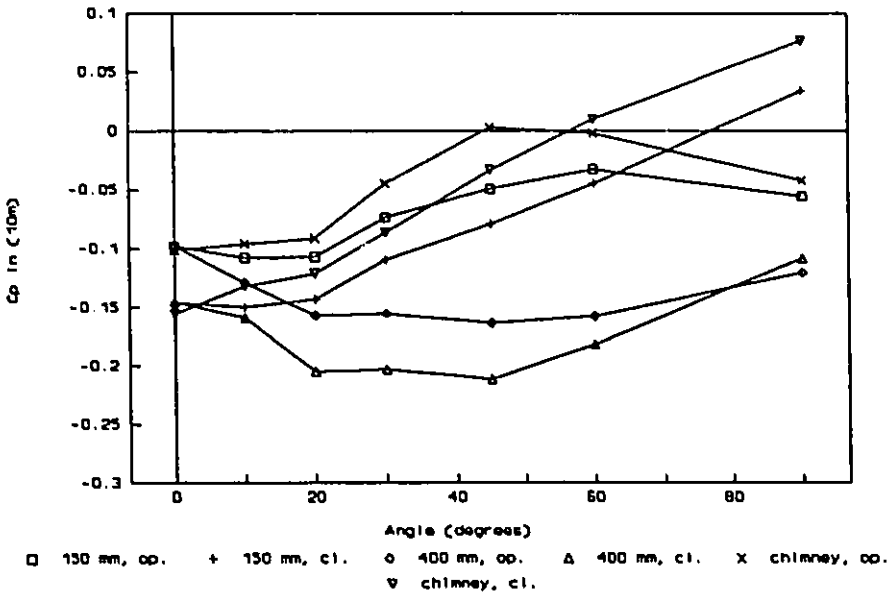

Figure 5.18 Sealed model, simulated 800 mm sidewall, internal pressure coefficients.

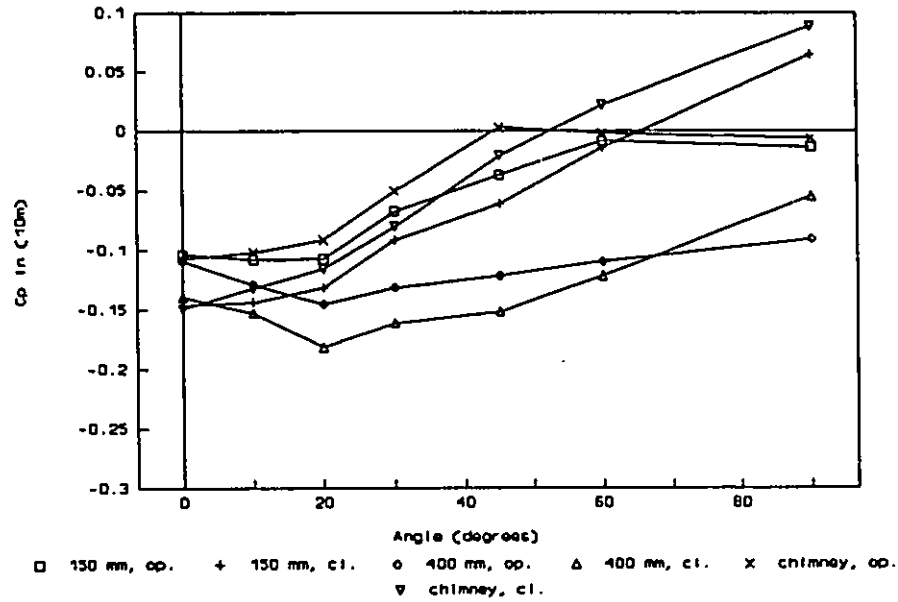

Figure 5.19 Sealed model, simulated 1100 mm sidewall, internal pressure coefficients.

5.2.1.2 Effect of end wall openings

As reported by Bilsborrow and Fricke (1975), the Cp_{in} curves for open and closed end walls are different. Figs. 5.10 and 5.11 show lower Cp_{in}s for 800 mm and 1100 mm walls with open end walls at $\theta = 60°$ and 90°, and higher Cp_{in} at $\theta = 0°$, 10°, 20° and 30°. For the ridge opening of 400 mm (Fig. 5.12), the lowest Cp_{in}s are recorded with open end walls for both sidewall openings.

Generally, the curves of Cp_{in} with open end walls tend to be more uniform or equal for all wind angles while the curves with closed end walls show large differences between $\theta = 0°$ versus $\theta = 90°$.

5.2.1.3 Effect of ridge openings

Figures 5.13 and 5.14 illustrate the effects of the three ridge opening types for the 800 mm and 1100 mm sidewall openings with closed or open end walls. The highest Cp_{in}s are noticed with the chimney followed closely by the 150 mm ridge. The Cp_{in}s recorded with the 400 mm ridge are the lowest.

At $\theta = 90°$, the combined effects of the ridge opening Cps and the pressure difference across the sidewalls (ΔCps) presented in Tables 5.1 and 5.3 would explain the large effect of the ridge opening on the Cp_{in}. Also, the areas of the respective ridge and sidewall openings are directly proportional to the airflow balance Eqs. 2.3 and 2.4, which are used for the calculation of the internal pressure coefficient. Then, at $\theta = 90°$, the lower $-Cp_{in}$ recorded with the 400 mm ridge opening would be attributed to the larger ΔCp across the sidewalls, the higher -Cps over the ridge and the large ridge opening area with the 400 mm width.

At $\theta = 0°$, the ΔCps across the sidewalls and the -Cps at the ridge (Tables 5.2 and 5.4) are similar for all ridge types. Consequently, the calculated internal pressures are fairly similar to closed end walls or open end walls (Figs. 5.13 and 5.14).

Generally, the open model results for the Cp_{in} reveals the following:

1 - Both 800 mm and 1100 mm sidewall openings with closed or open end walls have an effect on the calculated Cp_{in}s.

2 - The curves for Cp_{in} with open end walls tend to be more uniform for all wind angles as compared to the closed end walls.

3 - The Cp_{in}s are largely influenced by the ridge opening types due to the combined effects of the changing ΔCps ($Cp_w - Cp_l$) across the sidewalls by some differences in -Cps at the ridge level and the respective opening areas of each ridge types.

5.2.2 Sealed model, calculated Cp_{in}

Figures 5.15, 5.16 and 5.17 show the calculated Cp_{in} with respect to the wind angles of incidence for the three ridge openings; chimney and continuous ridges of 150 mm and 400 mm. The Cp_{in}s are also presented in function of the sidewall opening areas of 800 mm and 1100 mm in Figs. 5.18 and 5.19.

The curves of the calculated Cp_{in} for the sealed model are comparable to the results presented by Bilsborrow and Fricke (1975) and Aynsley et al. (1977).

5.2.2.1 Combined effect of sidewall and end wall openings with ridge types

There is little effect with both 800 mm and 1100 mm sidewalls and open or closed end walls on the Cp_{in} curves for the chimney (Fig. 5.15). Some differences appear for the 150 mm ridge and are evident with the 400 mm ridge (Figs. 5.16 and 5.17, respectively). Also the Cp_{in} with the open end walls are more uniform for all θ with each ridge types. Figures 5.18 and 5.19 demonstrate the large effect of the ridge opening types on the Cp_{in} for the sidewalls openings of 800 mm and 1100 mm.

The same general conclusions for the effect of various openings on Cp_{in} could be drawn with the sealed model Cp_{in} as compared to the open Cp_{in}.

5.2.3 Open versus sealed models, calculated Cp_{in}

The comparisons among Figs. 5.10 (OP-CH) and 5.15 (SE-CH), Figs. 5.11 (OP-150) and 5.16 (SE-150) and Figs. 5.12 (OP-400) and 5.17 (SE-400) show that the differences in Cp_{in} between the 800 mm and 1100 mm sidewall opening areas increase in open models as compared to sealed models. This is attributed to the differences in ΔCp (Cp_w-Cp_l) at the sidewalls and different -Cps at the ridge for open models, in contrast, the ΔCps and -Cps were identical for both sidewall openings for the sealed model.

When Figs. 5.13 (OP-800) and 5.14 (OP-1100) are compared to Figs. 5.18 (SE-800) and 5.19 (SE-1100), the Cp_{in}s are generally more negative with the open model for all ridge types and all angles. Also, for the 800 mm and 1100 mm sidewalls, the differences in Cp_{in} for the chimney and 400 mm ridge are always greater with the open model. For example with the open model, at $\theta = 90°$, the Cp_{in} for OP-CH-1100-C is 0.08 and the Cp_{in} for the OP-400-1100-C is -0.15, a difference of 0.23. While with the sealed model, the Cp_{in} for SE-CH-1100-C is 0.09 and the Cp_{in} for the SE-400-1100-C is -0.06, a difference of 0.15. It appears that when the larger sidewalls and ridge opening areas are used, the discrepancies between the sealed model Cp_{in}s and the open model Cp_{in}s have increased.

The following points are obtained when the calculated Cp_{in}s for the sealed versus open models are compared:

1 - The general shape of the Cp_{in} curves for both sidewalls with open or closed end walls are fairly similar for each ridge type.

2 - The discrepancies between the calculated Cp_{in} with the sealed versus the open models increase when larger sidewall ridge and end wall openings are used.

5.2.4 Open model, measured internal pressure coefficients

Initially, the interior pressure taps were installed inside the scale model with the assumption that equal Cp_{in} measurements would be obtained. This was based on the statements of Aynsley et al. (1977), Davenport et al. (1978), Holmes (1979), Stathopoulos et al. (1979) and Vickery (1986). Table 4.2 shows that the pressure tap locations for measuring the Cp_{in} were changed five times during the experiment. Also, since it was not originally one of the objectives to study the internal pressures, only a limited number of pressure taps were used and there was no repetition of any test with each Cp_{in} arrangement.

5.2.4.1 Discussion on the methodology for measuring Cp_{in}

The three first tests were done with the pressure taps along the sidewalls, 15 mm above the interior floor surface. The results of the first test with configuration no. 1 showed large variations in Cp_{in} across and along the building. It was thought that the high air speed inside the model created this problem. The little blocks were then covered with a bent piece of cardboard to protect the taps from direct air speed thereby obtaining a static pressure reading.

Figure 5.20 (OP-CH-800-C) shows the results obtained with the second configuration. Large variations along and across the building are recorded, meaning that the difference in Cp_{in} was not be attributed to the air speed hitting the little blocks where the taps were installed.

Six pressure taps were moved to the roof, as in configuration no. 3 (Fig. 5.21). Again, large Cp_{in} fluctuations are noticed along and across the building and also, there are differences between the roof and the floor

Cp_{in}. Based on the statement of Davenport et al. (1978) that a possible error in Cp_{in} could be attributed to the proximity of the tap location to depressions or zones of high air circulation near the inlets, the roof taps were moved to the center of the roof, with the configuration no. 4. However, the same fluctuations across the building are recorded. Finally, to solve the problem of air circulation with the little sidewall blocks, the sidewall taps were installed flush with the interior wall surface to obtain the last configuration no. 5 (Figs. 5.22 to 5.25). From that point, all the tests were performed with configuration no. 5. The previous test were not redone because of the time constraint in the NRCC wind tunnel.

5.2.4.2 Cp_{in} associated with airflow patterns

Aynsley et al. (1977) reported that internal air speeds vary between 0.1 to 0.6 of the reference wind speed for naturally ventilated buildings with large openings. For a naturally ventilated test house, Chandra et al. (1986) measured internal air speeds between 20% of the reference wind speed for winds parallel to the building and 50% for perdendicular winds. These high air speeds inside the scale model with perpendicular winds and low air speeds with parallel winds were reported by Choinière et al. (1988c).

At $\theta = 90°$, the results of Fig. 5.20 indicate that the air direction should be from the positive Cp at the bottom part of the rectangular toward the upper surface. This air direction would be in the opposite direction to the incoming wind. The results from Choinière et al. (1988c) on airflow patterns for a similar model are in Appendix F. The direction of the observed airflow patterns with the Cp_{in} at $\theta = 90°$, 60°, 30° and 0° are very closely related. At $\theta = 0°$, the floor airflow patterns show a recirculation movement from the downwind to upwind end. Cp_{in}s indicate a lower -Cps at the upwind end and attract the air according to airflow patterns.

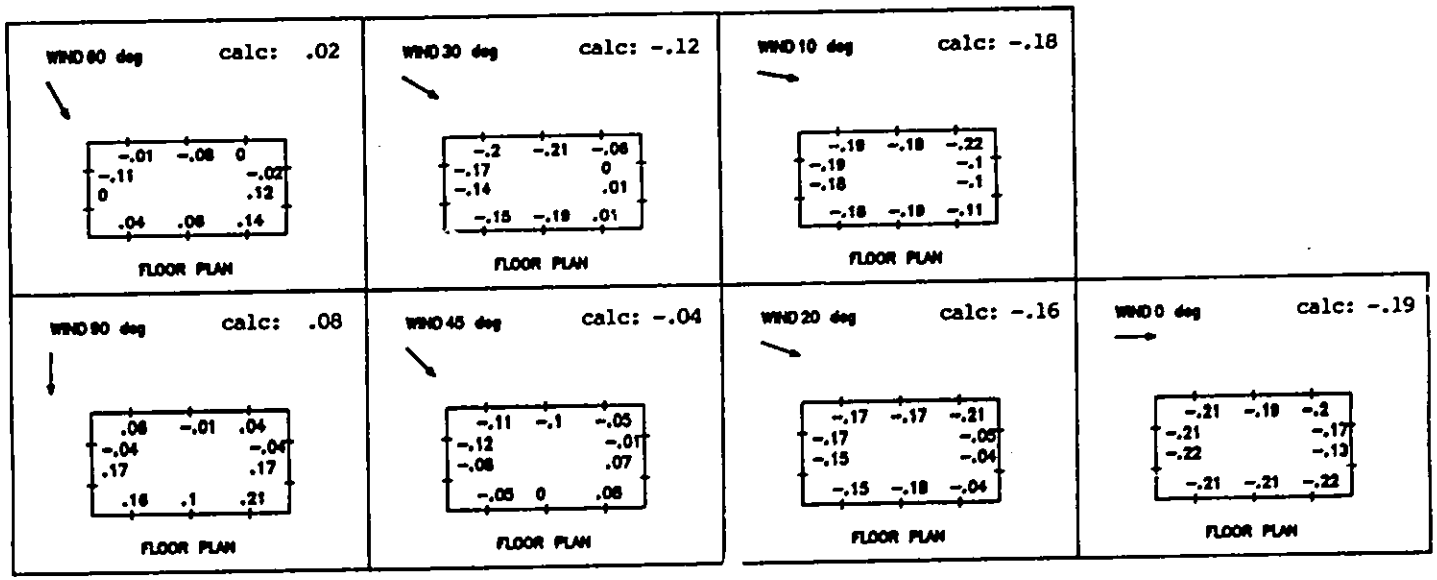

Figure 5.20 Measured Cp_{in}, open model, chimney, simulated 800 mm sidewall openings, closed end walls, wind angles = 90°, 60°, 45°, 30°, 20°, 10° and 0°.

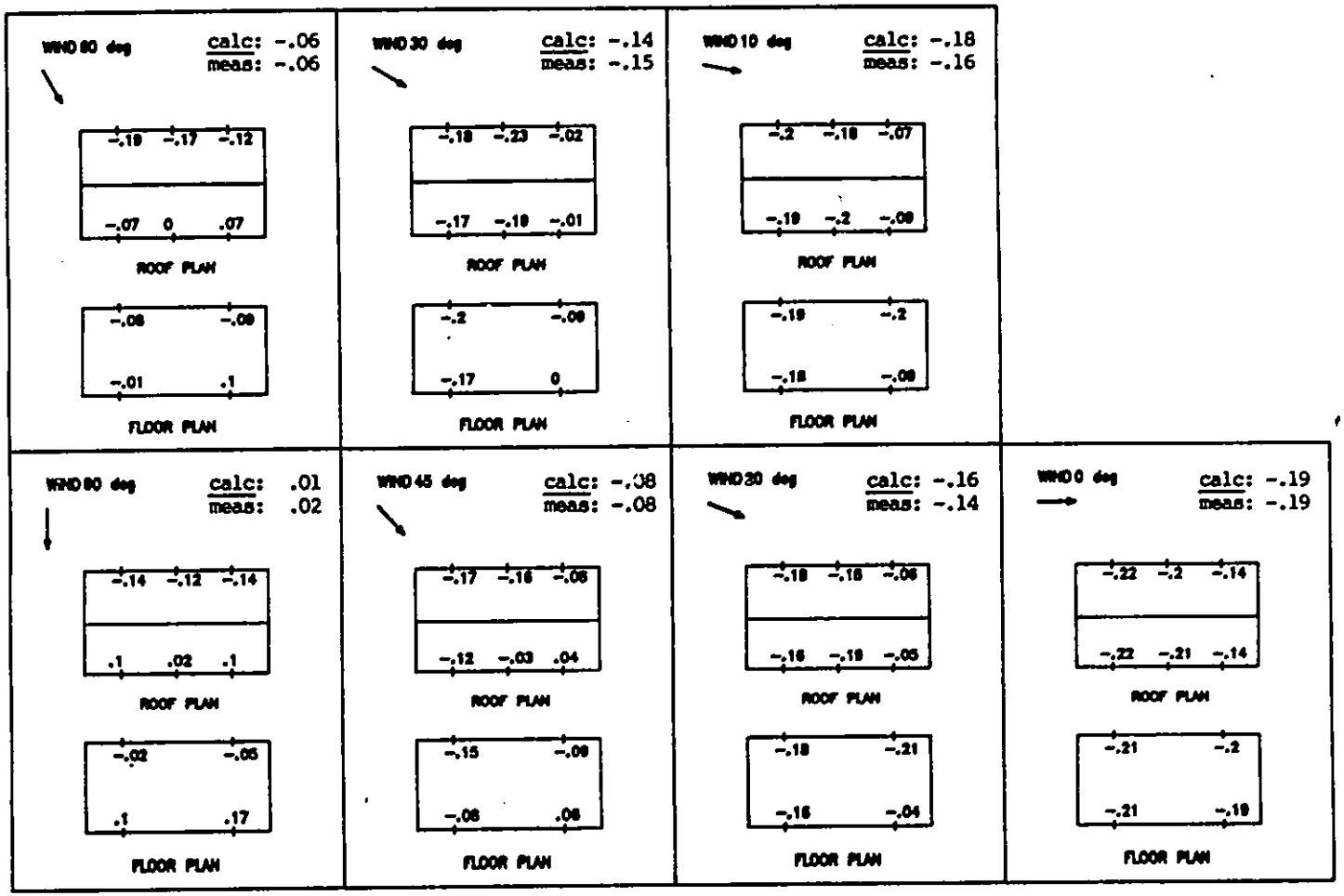

Figure 5.21 Measured Cp_{in}, open model, simulated 150 mm ridge and 800 mm sidewall openings, closed end walls, wind angles = 90°, 60°, 45°, 30°, 20°, 10° and 0°.

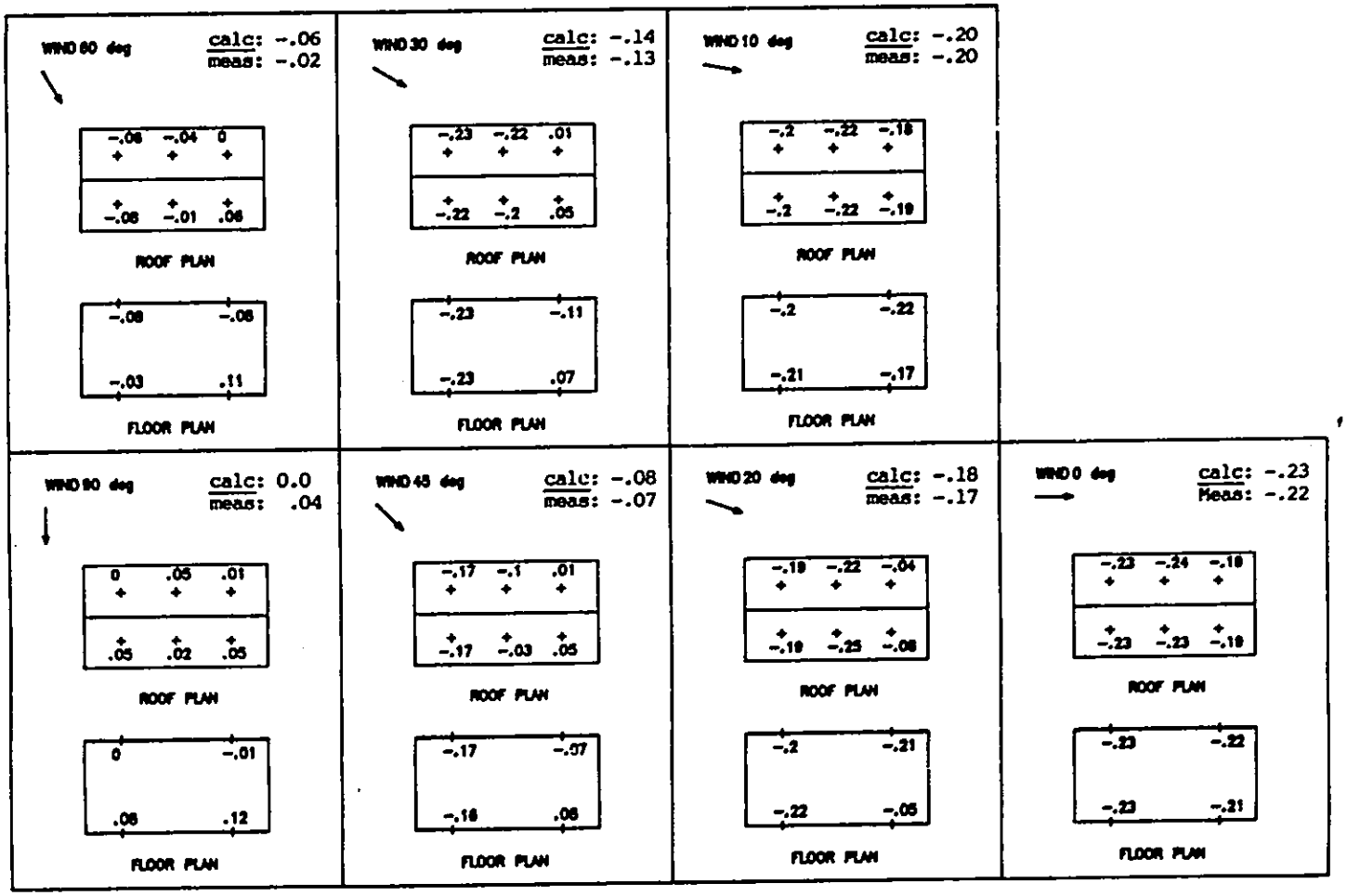

Figure 5.22 Measured Cp_{in}, open model, simulated 150 mm ridge and 1100 mm sidewall openings, closed end walls, wind angles = 90°, 60°, 45°, 30°, 20°, 10° and 0°.

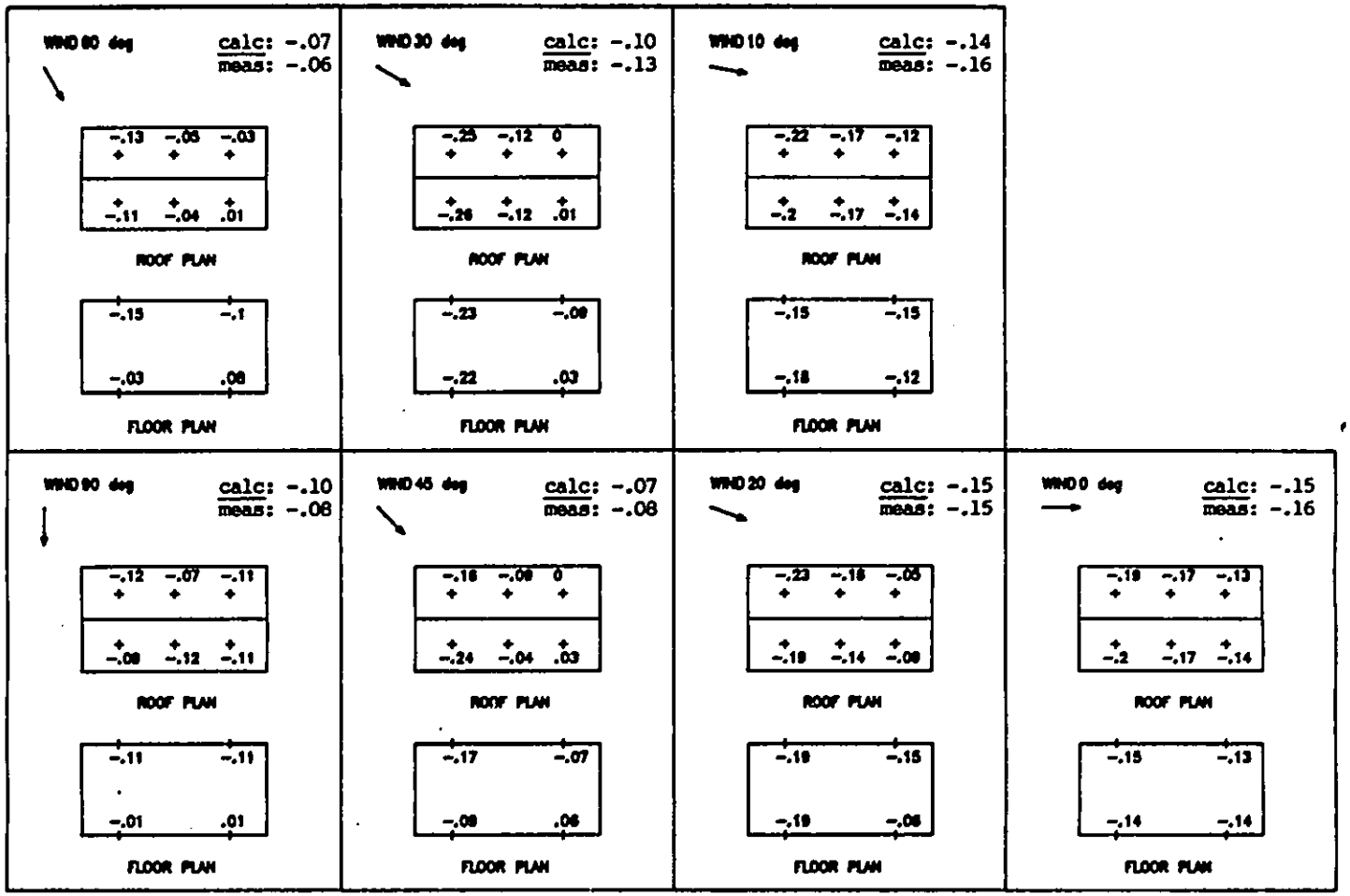

Figure 5.23 Measured Cp_{in}, open model, simulated 150 mm ridge and 1100 mm sidewall openings, open end walls, wind angles = 90°, 60°, 45°, 30°, 20°, 10° and 0°.

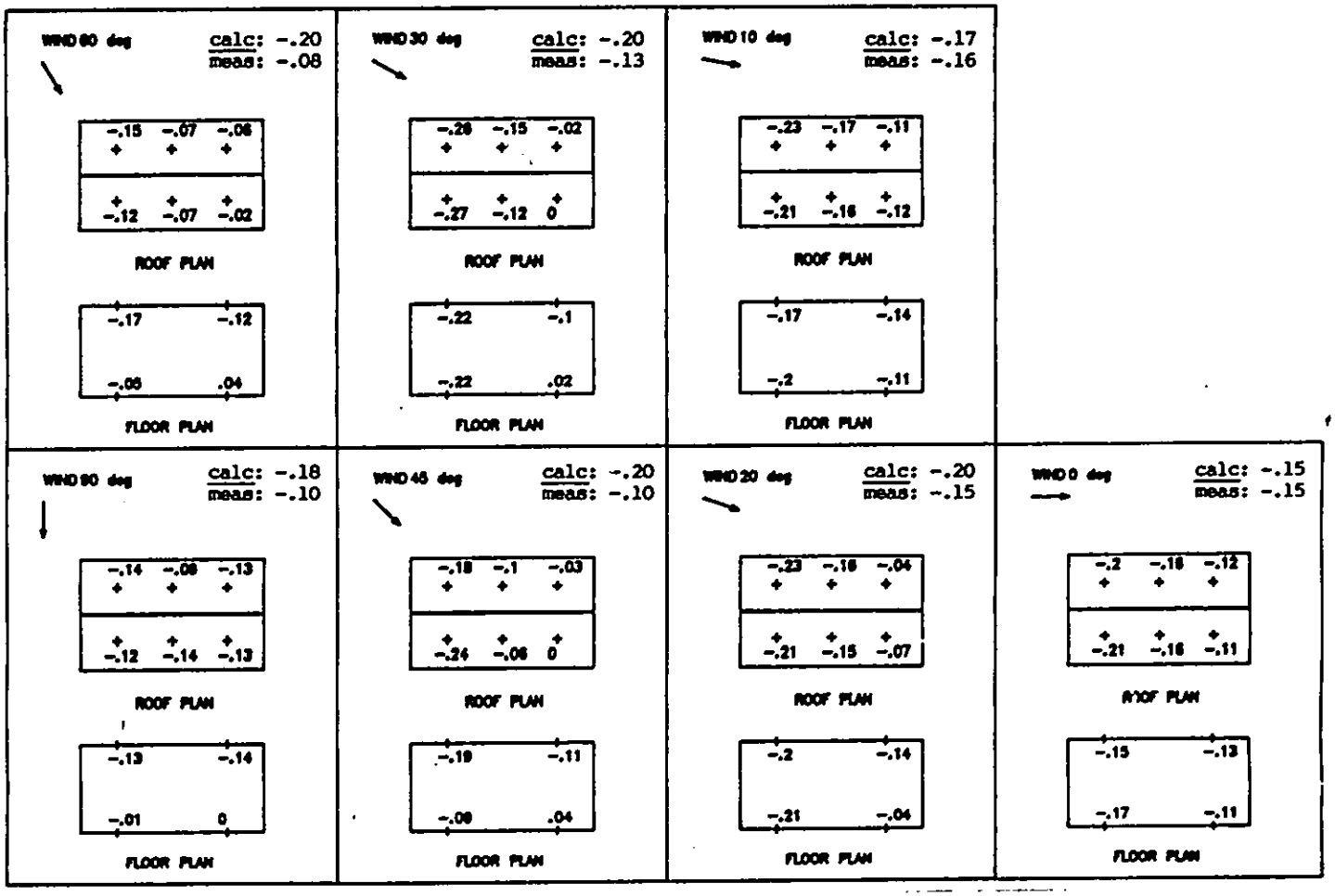

Figure 5.24 Measured Cp_{in}, open model, simulated 400 mm ridge and 1100 mm sidewall openings, open end walls, wind angles = 90°, 60°, 45°, 30°, 20°, 10° and 0°.

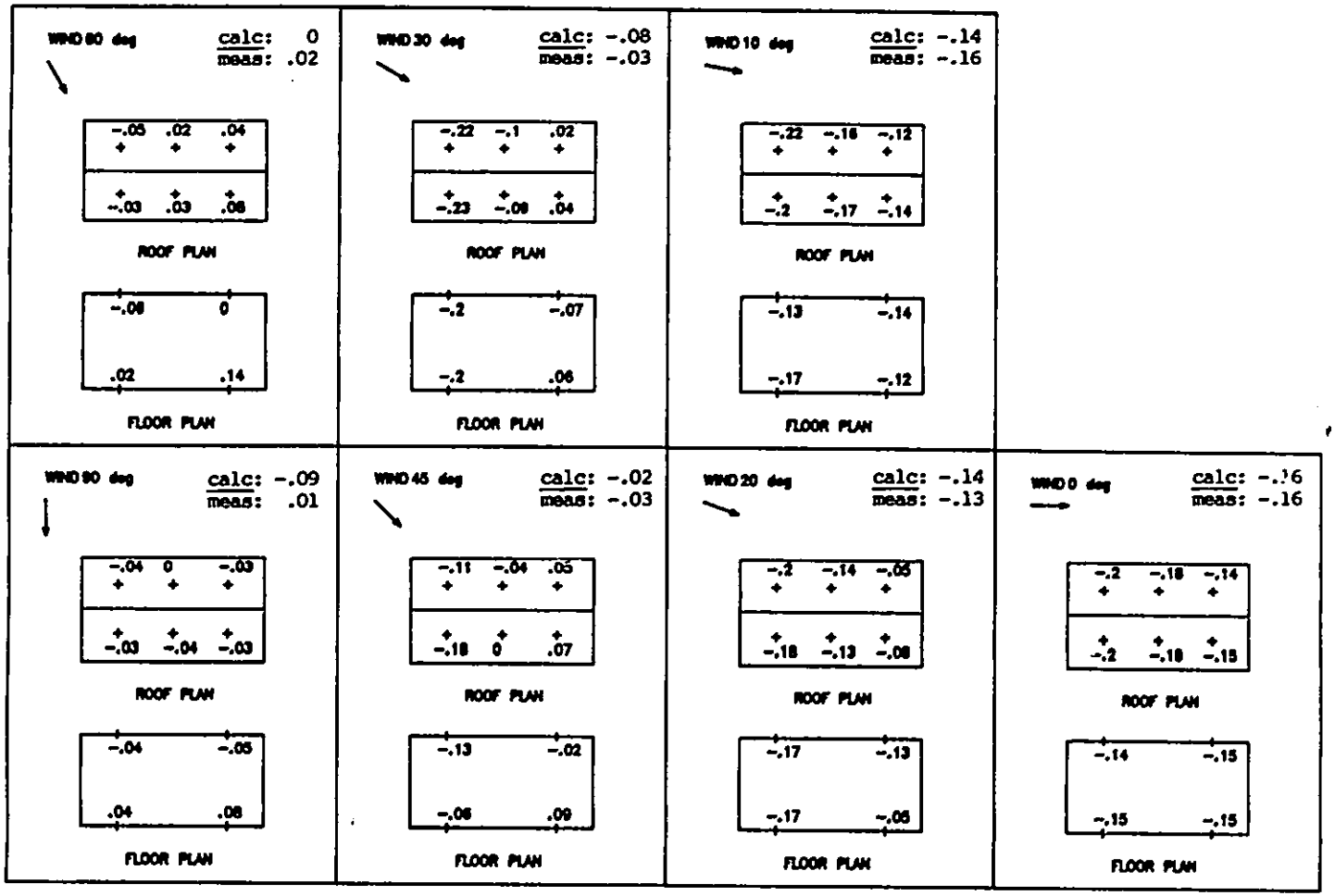

Figure 5.25 Measured Cp_{in}, open model, chimney, simulated 1100 mm sidewall openings, open end walls, wind angles = 90°, 60°, 45°, 30°, 20°, 10° and 0°.

The close relationship between the inside floor airflow patterns and the Cp_{in} variations are remarkable.

When a third dimension is added with the roof taps (Figs. 5.21 to 5.25), the association between the inside airflow patterns and the Cp_{in} becomes more complicated. At $\theta = 90°$, the air enters by the windward opening and follows the ceiling towards the leeward sidewall. However, when the air reaches the leeward wall, it is forced to bend, then a certain part of the air exhausts through the leeward opening while the other fraction recirculates to the windward sidewall at the floor level. On Fig. 5.21, the taps were close to the opening on the windward sidewall and on the leeward sidewall. These high -Cps noted on the windward sidewall may be due to the turbulence caused by the entering air. Also, the leeward Cp_{in}s are positive, which indicates a drastic reduction of the air speed when the leeward sidewall is reached (increase in static pressure).

When the taps are moved further away from the sidewalls toward the center (Figs. 5.22 to 5.25), the large differences among the windward-leeward taps diminish. This would be mainly due to the minimal reduction of the air speed due to the slight change in wind direction at the roof peak and also the limited amount of air exhausting by the ridge.

The direct relationship between the airflow patterns and the Cp_{in}s are evident when the roof airflow patterns at $\theta = 90°$, $60°$, $30°$ and $0°$ are over-imposed with the Cp_{in}s reported in Figs. 5.21 to 5.25.

The effect of the end wall openings from Figs. 5.23 to 5.25 are also well illustrated by the observation of the airflow patterns in Appendix F. Some differences could be noticed because the sidewall opening areas and the simulated building lengths are different.

From the comparisons of the results, it was concluded that the configurations no. 3, 4 and 5 provide a fairly good overview of the variations of Cp_{in} along and across the

building at the floor and roof level as well as providing information on the difference between the roof and the floor levels.

Detailed studies are required to evaluate the optimum number of interior pressure taps and their locations in order to obtain an accurate picture of the Cp_{in} variations inside naturally ventilated buildings with large continuous sidewall ridge or chimney and end wall openings.

From the results on the methodology of recording the internal pressures, the following points could be obtained:

1 - Large 3-dimensional Cp_{in} variation should be anticipated inside these types of naturally ventilated buildings.
2 - The observed and reported airflow patterns seems to coincide with the gradients of Cp_{in}.
3 - The ten taps installed according to configuration no. 5 would be a minimum basis for the analysis of internal pressure.

5.2.4.3 Effect of sidewall and end wall openings on the measured Cp_{in}

Tables 5.5 to 5.7 present the average, minimum and maximum values of the measured Cp_{in}s for each wind angle of incidence. Also, the differences between the calculated values of the internal pressure by standard pressure difference method (Eqs. 2.3 and 2.4) and the average measured Cp_{in}s are included.

The effects of the sidewall opening areas, 800 mm versus 1100 mm, are illustrated in Fig. 5.21 (OP-150-800-C) and Fig. 5.22 (OP-150-1100-C). The results presented on Table 5.5 demonstrate that the Cp_{in}s are slightly higher with the 1100 mm sidewall opening, for θ = 90° to 45°, and they are more negative for θ = 0° to 20°. With the 400 mm ridge (Table 5.6), the measured Cp_{in}s are not influenced by the change in sidewall opening for the closed end walls. With the open end

Table 5.5 150 mm ridge opening, average minimum and maximum measured Cp_{in}s and difference between the calculated and the average measured Cp_{in}s, configurations 3, 4 and 5.

Angle (degrees)	Description							
	OP-150-800-C				OP-150-800-O			
	Ave.	min	max	ΔCal-meas	Ave.	min	max	ΔCal-meas
90	-0.02	-0.14	0.17	-0.01	-0.12	-0.29	0.07	-0.01
60	-0.06	-0.19	0.10	-	-0.10	-0.33	0.04	0.03
45	-0.08	-0.17	0.06	-	-0.09	-0.27	0.03	0.03
30	-0.13	-0.23	0.0	-0.01	-0.12	-0.23	0.04	0.03
20	-0.14	-0.19	-0.04	-0.02	-0.12	-0.22	0.05	-0.01
10	-0.16	-0.20	-0.09	-0.02	-0.13	-0.22	0.01	0.0
0	-0.19	-0.22	-0.14	-	-0.13	-0.23	0.07	0.03
	OP-150-1100-C				OP-150-1100-O			
	Ave.	min	max	ΔCal-meas	Ave.	min	max	ΔCal-meas
90	0.04	-0.01	0.12	-0.04	-0.08	-0.12	0.01	-0.02
60	-0.02	-0.08	0.11	-0.04	-0.06	-0.15	0.08	-0.01
45	-0.07	-0.17	0.08	-0.01	-0.08	-0.24	0.06	0.01
30	-0.13	-0.23	0.07	-0.01	-0.13	-0.26	0.03	0.03
20	-0.17	-0.25	-0.05	-0.01	-0.15	-0.23	-0.06	0.0
10	-0.20	-0.22	-0.17	0.0	-0.16	-0.22	-0.12	0.02
0	-0.22	-0.23	-0.19	-0.01	-0.16	-0.19	-0.13	0.01

Table 5.6 400 mm ridge opening, average, minimum and maximum measured Cp_{in}s and difference between the calculated and the average measured Cp_{in}s, configurations 3, 4 and 5.

Angle (degrees)	Description							
	OP-400-800-C				OP-400-800-O			
	Ave.	min	max	ΔCal-meas	Ave.	min	max	ΔCal-meas
90	-0.03	-0.09	-0.12	-0.13	-0.15	-0.19	-0.06	-0.05
60	-0.09	-0.16	-0.06	-0.18	-0.12	-0.19	-0.03	-0.11
45	-0.12	-0.19	0.03	-0.14	-0.11	-0.22	-0.02	-0.12
30	-0.16	-0.22	-0.03	-*	-0.14	-0.26	-0.05	-0.06
20	-0.17	-0.23	-0.03	-*	-0.14	-0.22	-0.07	-0.05
10	-0.19	-0.21	-0.10	-*	-0.15	-0.22	-0.10	-0.01
0	-0.21	-0.21	-0.18	-*	-0.13	-0.19	-0.09	-0.01
	OP-400-1100-C				OP-400-1100-O			
	Ave.	min	max	ΔCal-meas	Ave.	min	max	ΔCal-meas
90	-0.02	-0.07	0.07	-0.13	-0.10	-0.14	0.0	-0.08
60	-0.08	-0.14	0.06	-0.15	-0.08	-0.17	0.04	-0.12
45	-0.12	-0.22	0.03	-0.11	-0.10	-0.24	0.04	-0.10
30	-0.16	-0.27	0.04	-0.07	-0.13	-0.27	0.02	-0.07
20	-0.18	-0.26	-0.04	-0.06	-0.15	-0.23	-0.04	-0.05
10	-0.21	-0.23	-0.17	0.0	-0.16	-0.23	-0.11	-0.01
0	-0.21	-0.24	-0.16	0.0	-0.15	-0.21	-0.11	0.0

* Recording problems during wind tunnel test.

Table 5.7 Chimney, average, minimum and maximum measured Cp_{in}s and difference between the calculated and the average measured Cp_{in}s, configuration 5.

Angle (degrees)	Description			
	OP-CH-1100-O			
	Ave.	min	max	ΔCal-meas
90	0.01	-0.05	0.08	-0.08
60	0.02	-0.06	0.14	-0.02
45	-0.03	-0.18	0.09	0.01
30	-0.10	-0.23	0.06	0.02
20	-0.13	-0.20	-0.05	-0.01
10	-0.16	-0.22	-0.12	-0.02
0	-0.16	-0.20	-0.14	0.0

Note: Tests OP-CH-800-C, OP-CH-800-O and OP-CH-1100-C are not available for comparison (configurations 1 and 2).

walls, the 1100 mm sidewall shows generally lower $-Cp_{in}$s as compared to the 800 mm openings. No data are available to study the effects of 800 mm sidewall with the chimneys.

5.2.4.4 Effect of end wall openings

The Cp_{in} values are equal for open end walls for both 800 mm and 1100 mm sidewalls and all types of ridge opening.

5.2.4.5 Effect of ridge openings

For the open end walls, the results of Tables 5.5 to 5.7 demonstrate that the 150 mm and 400 mm ridge openings have fairly similar Cp_{in}s. The chimney presents higher Cp_{in}s for all angles especially when compared to the 400 mm ridge. Then, with the open end walls, the ridge opening widths of

150 mm and 400 mm have little effect on the average Cp_{in}s but the chimneys present higher Cp_{in}s.

With the end walls closed, some differences are noticed between the 150 mm and 400 mm ridge at θ = 90°, 60°, 45° and 30°. Generally, the small differences in Cp_{in}s are measured among two continuous ridges. No data are available to compare with the chimney.

5.2.5 Calculated versus measured Cp_{in}

For the 150 mm ridge opening, the differences between the average measured Cp_{in} and the calculated Cp_{in} values are very small (Table 5.5). The only available data for the chimney (Table 5.7) show a small differences, except for θ = 90°. With the 400 mm ridge, (Table 5.6) large differences are reported and the calculated Cp_{in}s are always lower than the average Cp_{in} measurements, especially at θ = 90° to 30°.

Also, Table 5.5 shows the maximum and minimum measured Cp_{in}s inside the building. For example, at θ = 90°, with the OP-400-800-C test, there would be a maximum-minimum difference of ΔCp_{in} = 0.21 inside the building. The maximum difference occurred with the OP-150-800-O tests at θ = 60°, where the maximum = 0.09 and the minimum = 0.33, for a total difference of ΔCp_{in} = 0.37.

The 150 mm ridge presents the larger ΔCp_{in}s (max-min) as compared to the chimney (only OP-CH-1100-O) and to the 400 mm ridge. Also, the largest ΔCp_{in} (max-min) occurred at wind angles from 45°to 90°, where the highest internal air speeds were observed during the wind tunnel test.

Differences between predicted and measured internal pressures have been reported by Billsborrow and Fricke (1975). They measured generally lower Cp_{in}s on average, which indicated higher pressure drops through the windward openings, but a lower drop through the leeward wall. The only method to alleviate this unbalance in pressure drop is to adjust the discharge coefficient between the air inlet and outlet zones.

The difference in Cp_{in}s inside the building may produce local effects on the air inlet and outlet zones as well as on the ventilation rates. Sufficient data are not available to be able to study the effects of the variations of Cp_{in} on the local and total ventilation rates.

The observations of the effects of the two sidewall areas, the open or closed end walls and the three ridge openings tend to show:

1 - For the 800 mm versus the 1100 mm sidewalls with open or closed end walls, some differences in Cp_{in} are recorded at θ = 90° and 60°, only for the 150 mm and 400 mm ridges.

2 - The distributions of the Cp_{in} are more uniform through the building when the end walls are open.

3 - There are only small differences for the 150 mm and 400 mm ridge openings on the measured Cp_{in}s for both 800 mm and 1100 mm with open or closed end walls.

4 - The differences between the calculated and the average of the measured Cp_{in} were small with the chimney and 150 mm ridge, but larger with the 400 mm ridge.

5 - Although not studied, the observed differences in Cp_{in} across the building may have an effect on the local and total ventilation rates.

5.3 Air inlet and outlet zones based on pressure difference

The measurements and observations of the Cps allowed visualisation of the effects of wind angle and various structural configurations on the pressures exerted on the building surfaces and, calculation of a value of Cp_{in} per test.

The differences between the exterior Cps over the building surfaces and the calculated Cp_{in} provide the basic information on the directions of air inflows and outflows. This difference is annotated as ΔCp. Figures 5.26 to 5.35 help to visualise the effect of various structural configurations on the airflow inlet and oulet zones, and the

relative magnitude of ΔCps over each opening area. Also, the ΔCp distributions and magnitudes are compared with respect to the open models versus the sealed models. Appendix G contains a complete set of drawings for the ΔCps.

5.3.1 Open model

5.3.1.1 Effect of wind angles of incidence

The results on the open model are used as the standard for comparisons. Figure 5.26 presents the results for the chimney tests with chimney, simulated 800 mm sidewall openings, and closed end wall, (OP-CH-800-C). The results at $\theta = 90°$ show uniform positive ΔCps over the windward surface and uniform negative ΔCps on the leeward surface. These results are comparable to Down *et al.* (1985). The chimney acts as an outlet. With $\theta = 45°$ and 60°, the ΔCps uniformity disappears. This pressure distribution change was also noted by Aynsley *et al.* (1977) and Davenport *et al.* (1977). At $\theta = 20°$ and 30°, the wind pressure distributions at the leading edge of the building change. Flow reversal is observed at the top left corner of the windward sidewall. Inflows are visible at the bottom right corner of the leeward sidewall. At $\theta = 0°$ and 10°, air enters by both sidewalls to exit at the upwind edge. Such high negative pressures were also noted by Bruce (1974). The leftmost chimney acts as an outlet while the other three act as inlets. This phenomenon has been observed by Shrestha *et al.* (1990).

The qualitative observations of the zones of inlet-outlet made by Choinière *et al.* (1988c) on a similar model appear to be in agreement with the present measurements. Similar zones of air inlets and outlets were observed in a full scale swine barn by Choinière *et al.* (1987). The zones of air inlet and outlet associated with colder and warmer temperature zones, created a temperature gradient along the naturally ventilated warm building for swine housing.

5.3.1.2 Effect of sidewall openings

Sidewall openings of 800 mm (OP-CH-800-C) versus 1100 mm (OP-CH-1100-C) present similar ΔCp distributions for all angles (Figs. 5.26 and 5.27). Only a slight reduction in the ΔCps is observed on the sidewall and the ridge with the larger sidewall openings. The only exception is the ΔCp for the chimney at $\theta = 90°$, which is higher with the 1100 mm sidewall opening than with the 800 mm sidewall opening.

5.3.1.3 Effect of end wall openings

Comparison of Figs. 5.26 (OP-CH-800-C) versus 5.28 (OP-CH-800-O) and Figs. 5.27 (OP-CH-1100-C) versus 5.29 (OP-CH-1100-O) show a slight reduction of ΔCps over both sidewalls with openings in the end walls, for $\theta = 45°$, 60° and 90°. At $\theta = 0°$, 10°, 20° and 30°, the addition of the end wall openings does not change the inlet and outlet zones along the walls, however, the extra air entering the building contributes to reducing the ΔCp magnitudes for both inlets and outlets, except for the zones shown at the bottom left corners (highly negative zones), where ΔCps have increased.

Similar changes in the ΔCp distributions are observed with larger ridge openings simulating 150 mm and 400 mm. The increase of the sidewall openings area from 800 mm to 1100 mm with open end walls does not cause significant changes in ΔCp distributions around the building and the same general decrease in ΔCps for the inlet zones.

The addition of the end wall openings for both sidewall openings (800 mm and 1100 mm) as well as with the three ridge configuration creates the following:

1 - A reduction in ΔCps for the windward and leeward walls for $\theta = 45°$, 60° and 90°.
2 - A reduction in ΔCps on sidewalls for $\theta = 0°$, 10°, 20° and 30°, except for the exhaust corner where ΔCps were increased.

3 - A reduction in ΔCps over the ridge opening for $\theta = 60°$ and 90°.

4 - An increase in ΔCps over the ridge for $\theta = 0°$, 10°, 20°, 30° and 45°.

5.3.1.4 Effect of ridge openings

A comparison of Figs. 5.26 (OP-CH-800-C) and 5.30 (OP-150-800-C) reveal similar pressure distributions on the windward and leeward sidewalls. Also, the effect of increasing the sidewall openings to 1100 mm and/or adding end wall openings show effects similar to those noted with the chimney test. The major differences occur at the ridge where the ΔCps noted with the simulated 150 mm ridge opening are drastically reduced as compared to those noted with the chimneys. This phenomenon is consistent for angles from 30° to 90°. Similar ΔCps are observed for $\theta = 0°$, 10° and 20°, mainly because of the complete change in the pressure distribution patterns.

The results of Figs. 5.30 (OP-150-800-C) and 5.31 (OP-400-800-C) indicate that an increase in the continuous ridge opening width causes a reduction in the ΔCp over the ridge area, an increase in ΔCps for the inlet zones and a slight reduction in the ΔCps for the outlet zones. It should be noticed that some -Cp measurements problems occurred at the ridge level with the 400 mm ridge for $\theta = 45°$ to 0°.

The observations of the Cp distributions around the buildings for 400 mm versus 150 mm would indicate slightly higher -Cps at the ridge, similar or lower +Cps on the windward sidewall and higher -Cps on the leeward sidewalls which would be exactly the opposite picture of the results from ΔCps. The reverse effects for ΔCps are directly related to the lower Cp_{in} calculated for the 400 mm ridge versus the 150 mm.

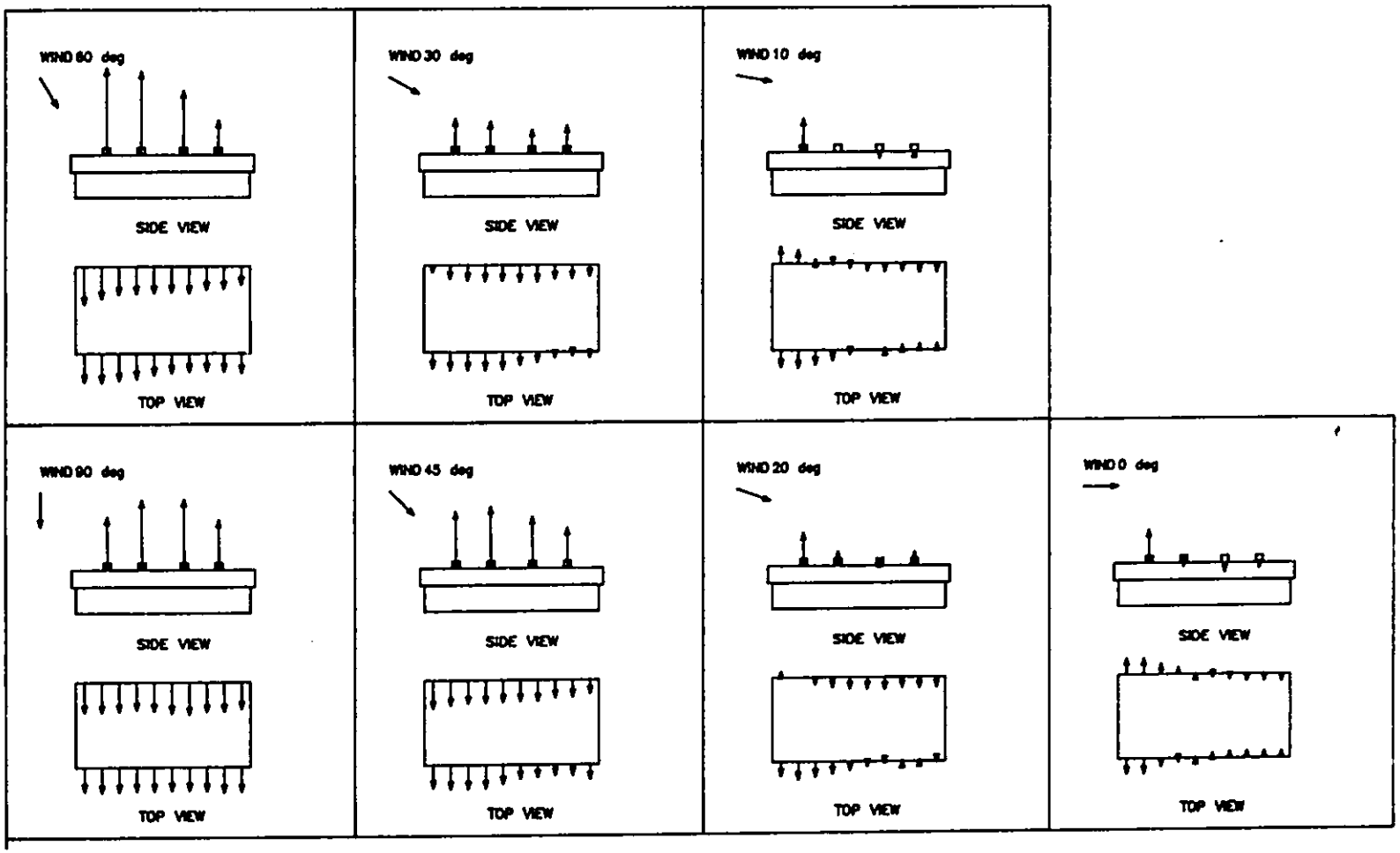

Figure 5.26 ΔCps (in-out), open model, chimney, simulated 800 mm sidewall openings, closed end walls, wind angles = 90°, 60°, 45°, 30°, 20°, 10° and 0°.

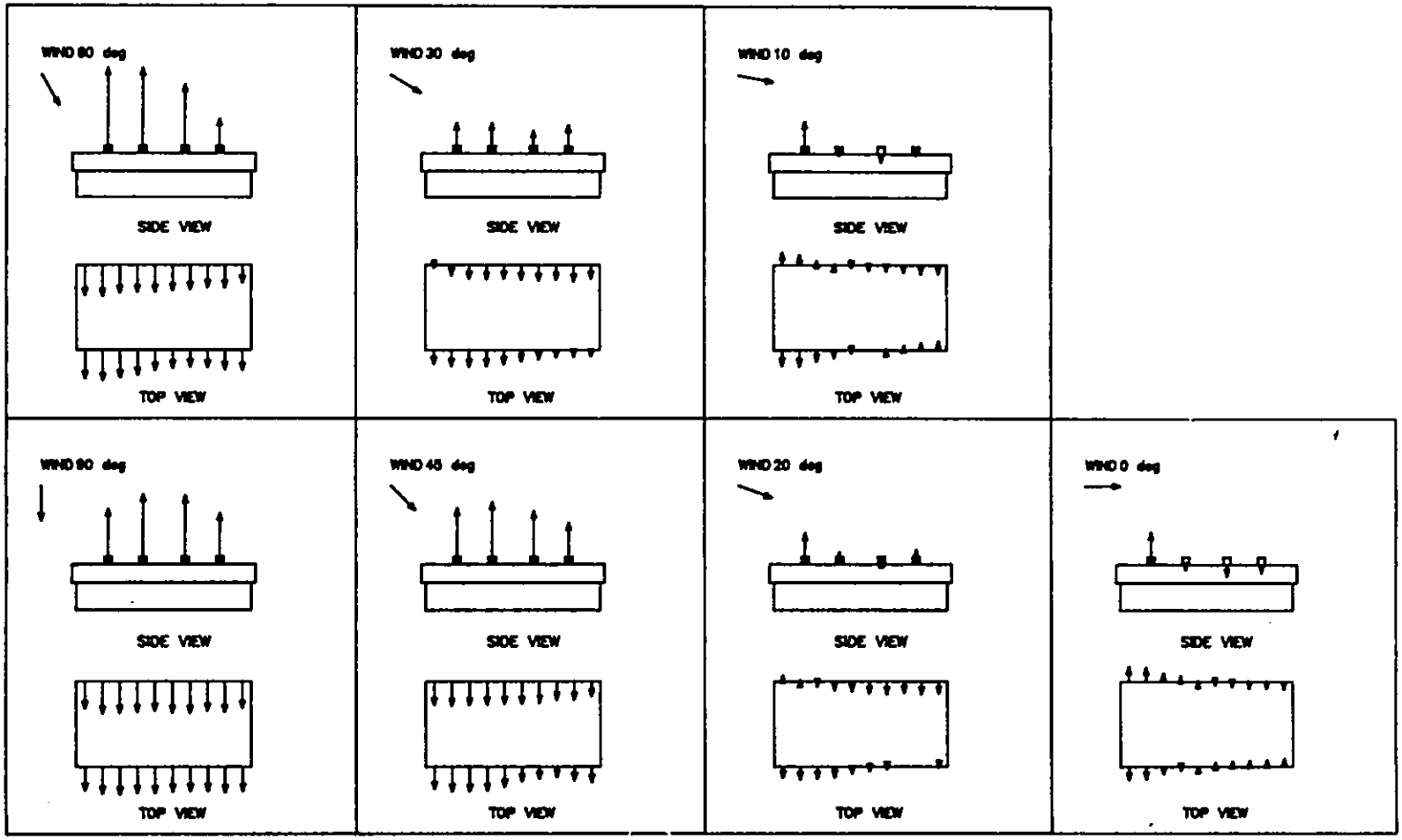

Figure 5.27 ΔCps (in-out), open model, chimney, simulated 1100 mm sidewall openings, closed end walls, wind angles = 90°, 60°, 45°, 30°, 20°, 10° and 0°.

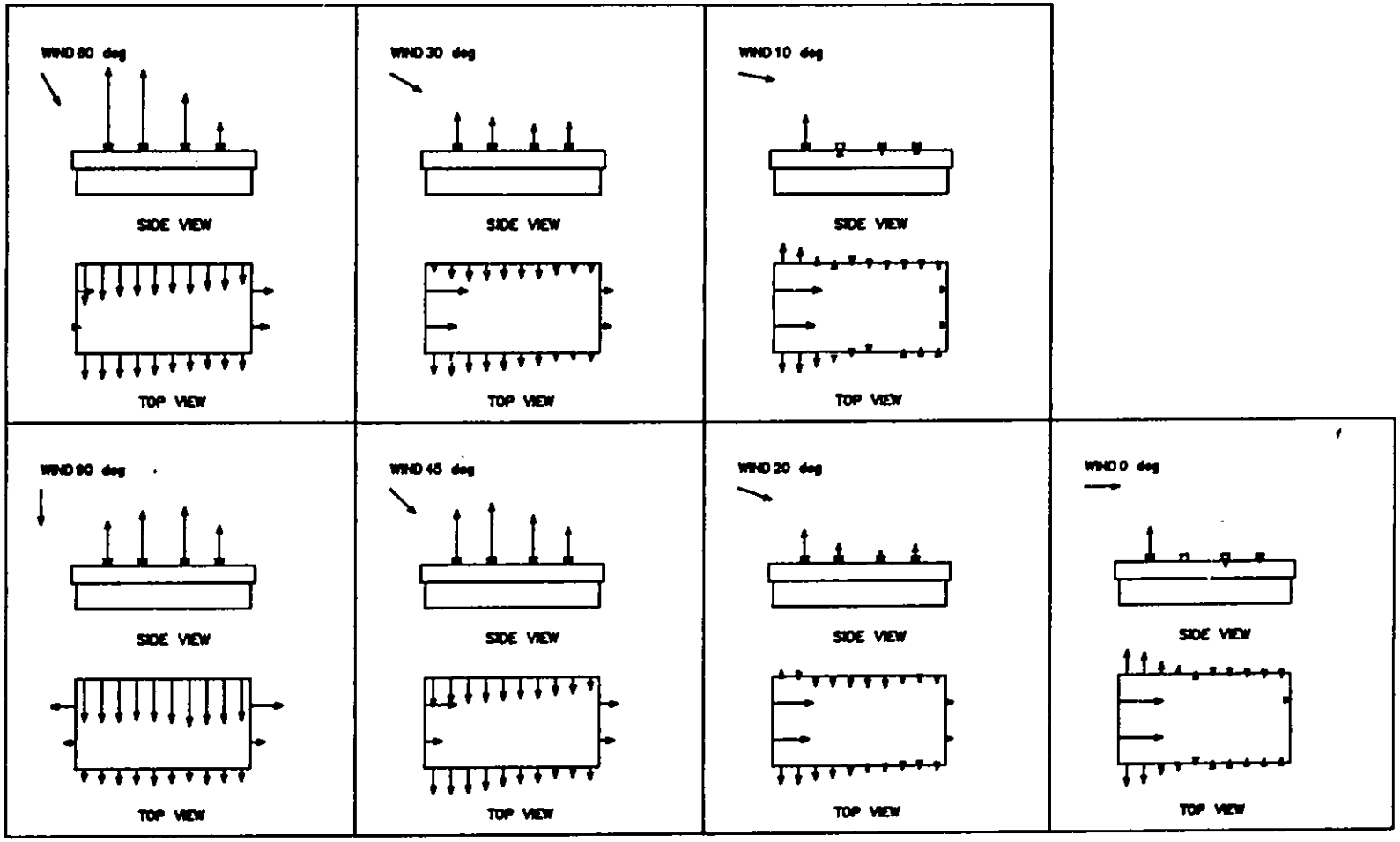

Figure 5.28 ΔCps (in-out), open model, chimney, simulated 800 mm sidewall openings, open end walls, wind angles = 90°, 60°, 45°, 30°, 20°, 10° and 0°.

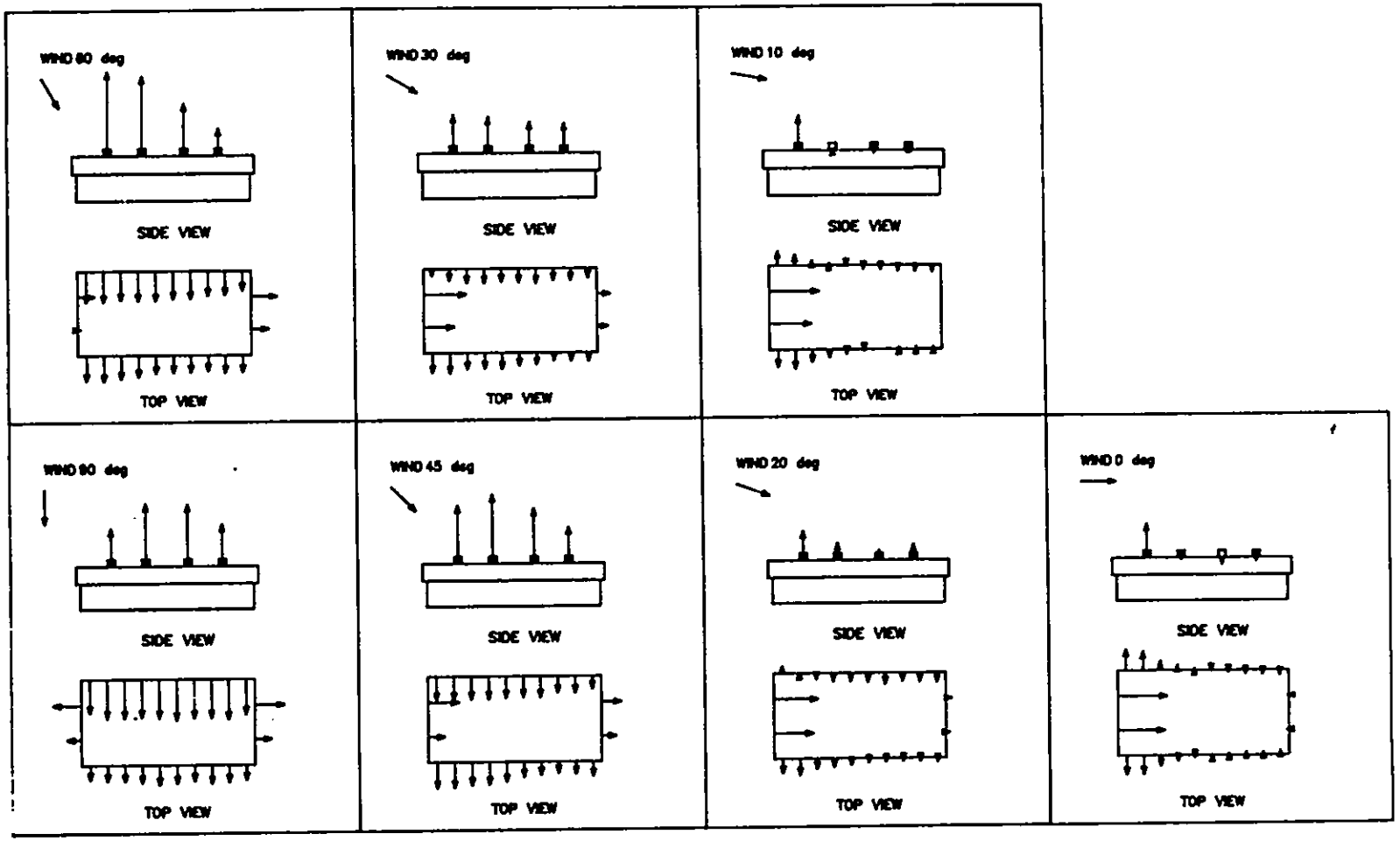

Figure 5.29 ΔCps (in-out), open model, chimney, simulated 1100 mm sidewall openings, open end walls, wind angles = 90°, 60°, 45°, 30°, 20°, 10° and 0°.

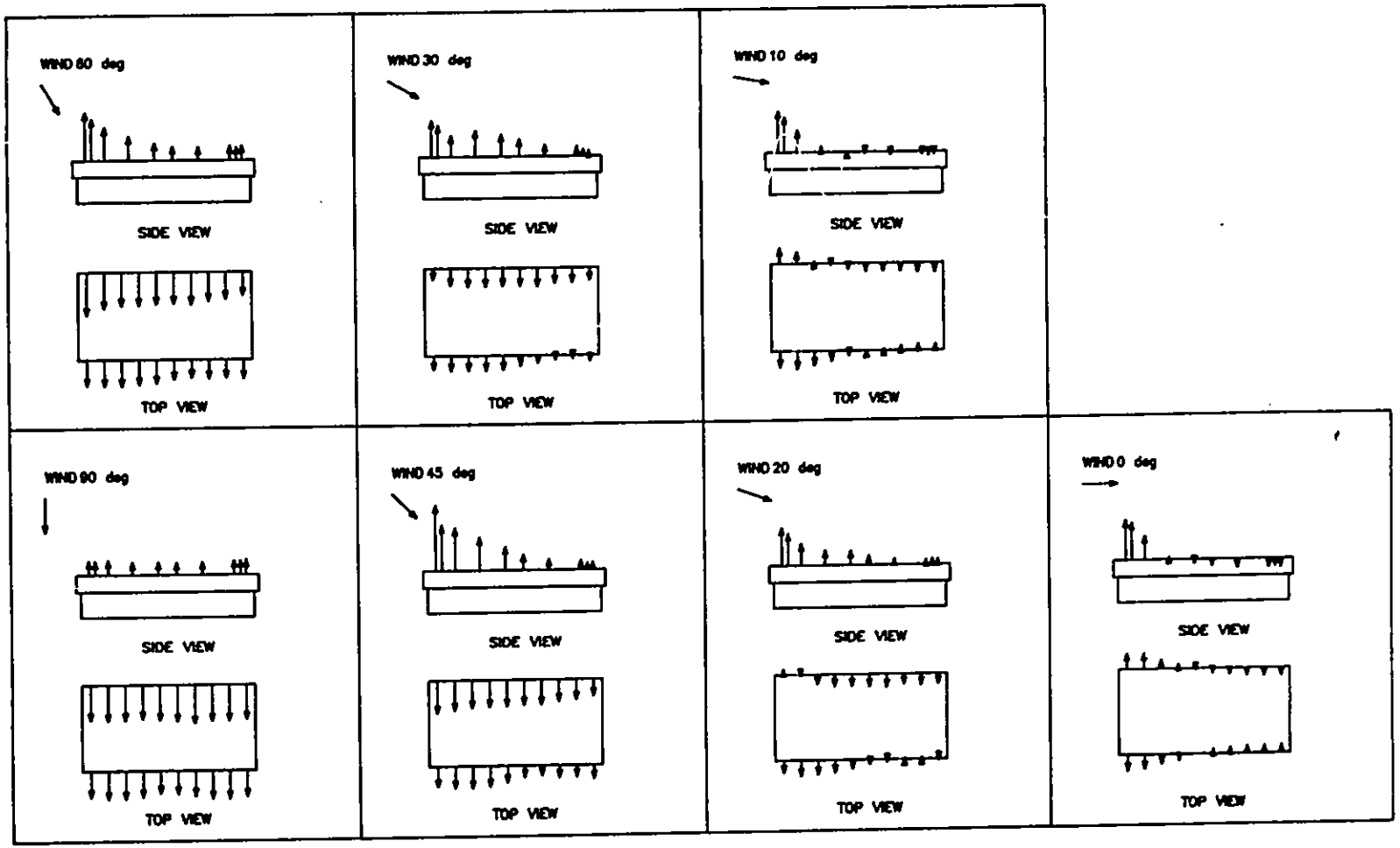

Figure 5.30 ΔCps (in-out), open model, simulated 150 mm ridge and 800 mm sidewall openings, closed end walls, wind angles = 90°, 60°, 45°, 30°, 20°, 10° and 0°.

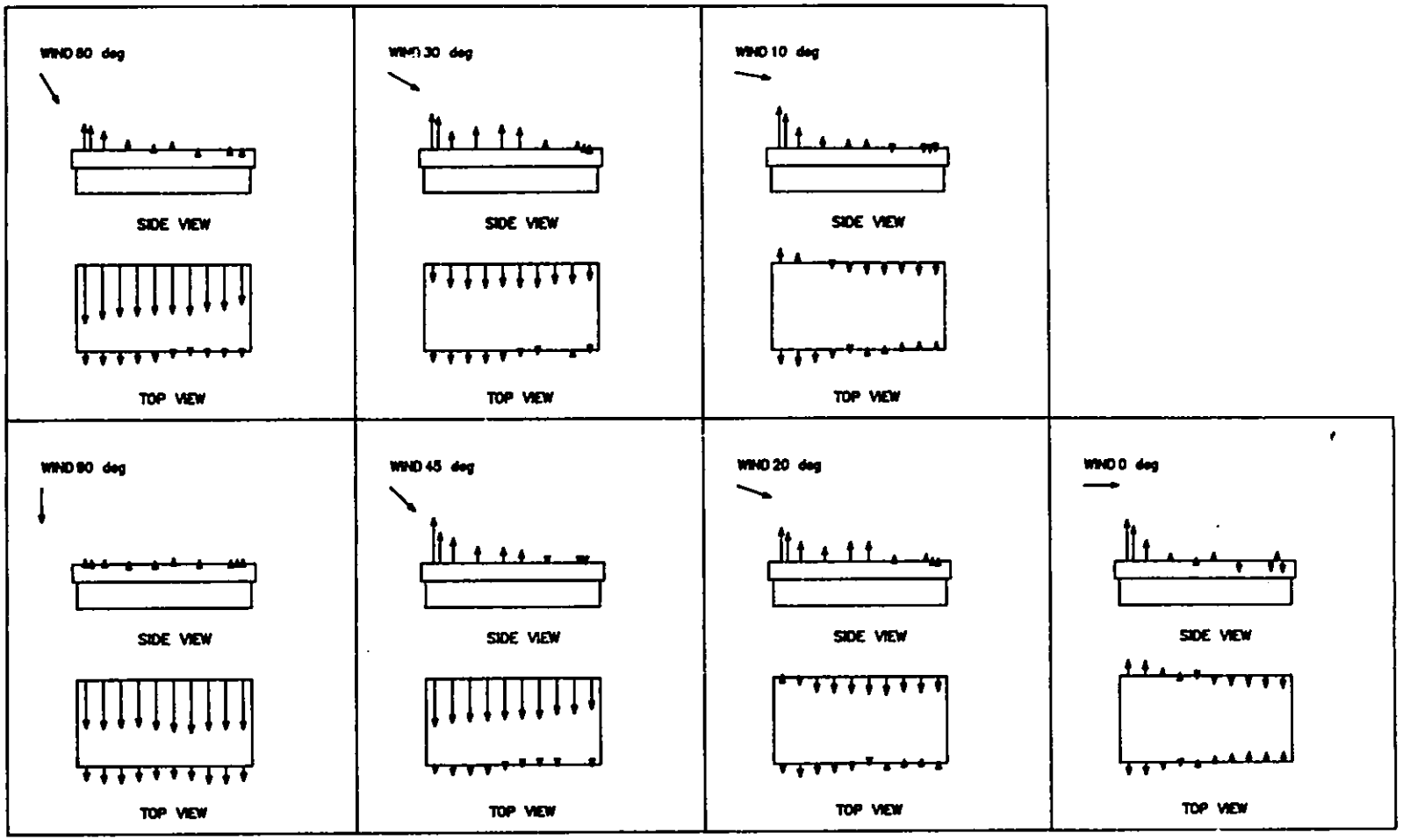

Figure 5.31 ΔCps (in-out), open model, simulated 400 mm ridge and 800 mm sidewall openings, closed end walls, wind angles = 90°, 60°, 45°, 30°, 20°, 10° and 0°.

From the study with the three ridge configurations, it can be concluded that a larger ridge opening does not change the ΔCp distribution zones around the building except for:

1 - A slight increase of ΔCps over the inlet zones.
2 - A decrease of ΔCps over the outlet zones.
3 - A decrease of ΔCps over the ridge opening.

Similar behavior was observed for 1100 mm sidewall, with open end walls.

5.3.2 Sealed model

Figures 5.32 (SE-CH-800-C) and 5.33 (SE-CH-800-O) show similar zones of ΔCp distributions with closed or open end walls. Also, the magnitudes of the ΔCps are fairly constant for all angles.

Figures 5.34 (SE-150-800-C) and 5.35 (SE-400-800-C) show that an increase in the ridge width causes an increase in the ΔCps over the ridge. With the simulated 400 mm ridge, the sidewall ΔCps decrease for $\theta = 45°$, 60° and 90°. Different inlet and outlet zones were observed for $\theta = 0°$, 10°, 20,° and 30°.

The results presented are similar to the results obtained with the larger 1100 mm simulated sidewall openings.

5.3.3 Open versus sealed models

Comparison could be done with Figs. 5.26 (OP-CH-800-C) and 5.32 (SE-CH-800-C) for the open versus sealed models with chimney, simulated 800 mm sidewall openings and closed end walls. The ΔCp distributions shows similar inlet-outlet zones around the building walls. The open model data show higher ΔCps for the inlets and outlets, but the sealed model data show severe increases of ΔCps over the ridge area (the only exception being at $\theta = 90°$). The observations of Vickery et al. (1983) showed that sealed model pressure coefficient would over-predict the flow through the ridge vents for angles of 50° to 90° by 40%.

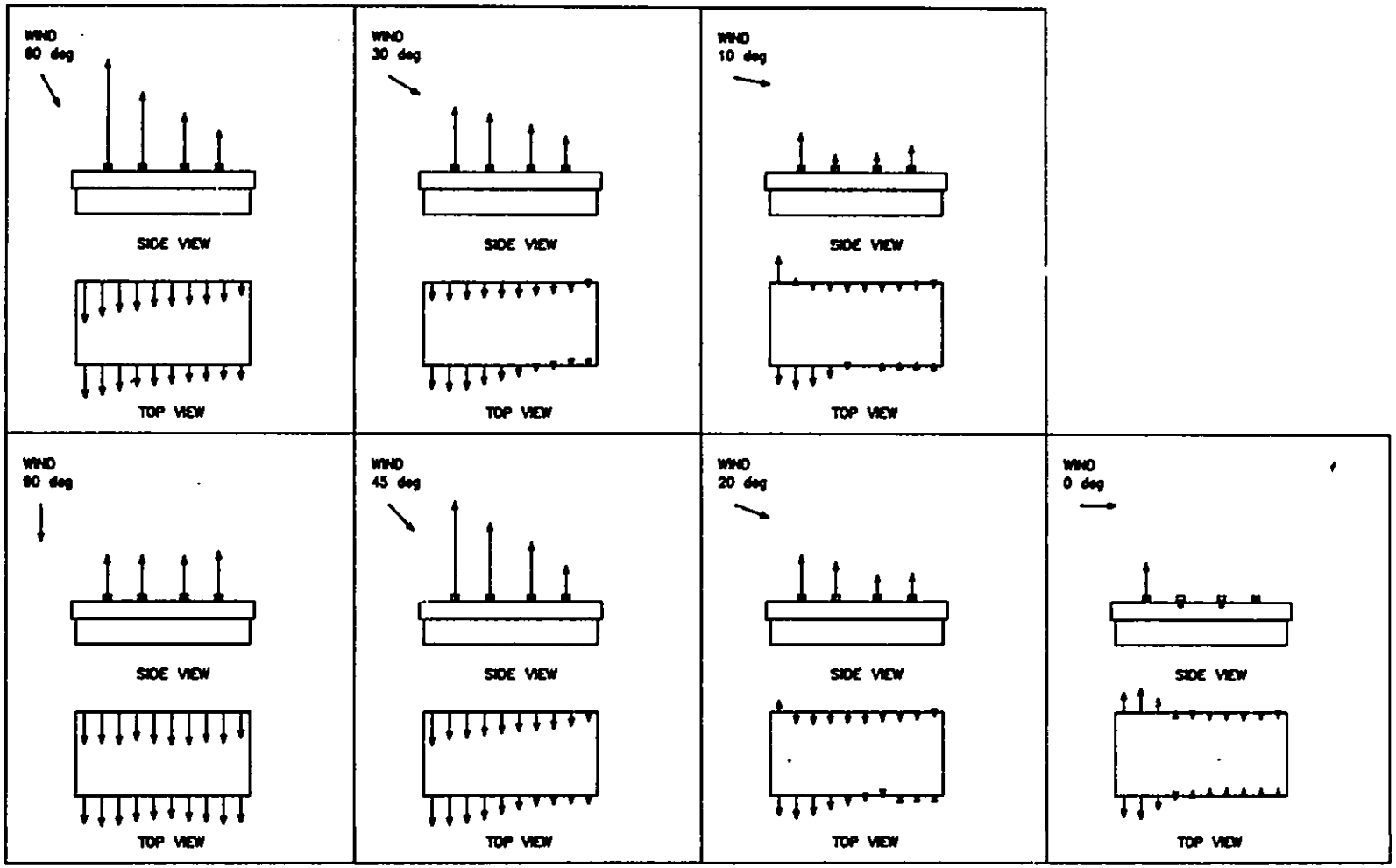

Figure 5.32 ΔCps (in-out), sealed model, chimney, simulated 800 mm sidewall openings, closed end walls, wind angles = 90°, 60°, 45°, 30°, 20°, 10° and 0°.

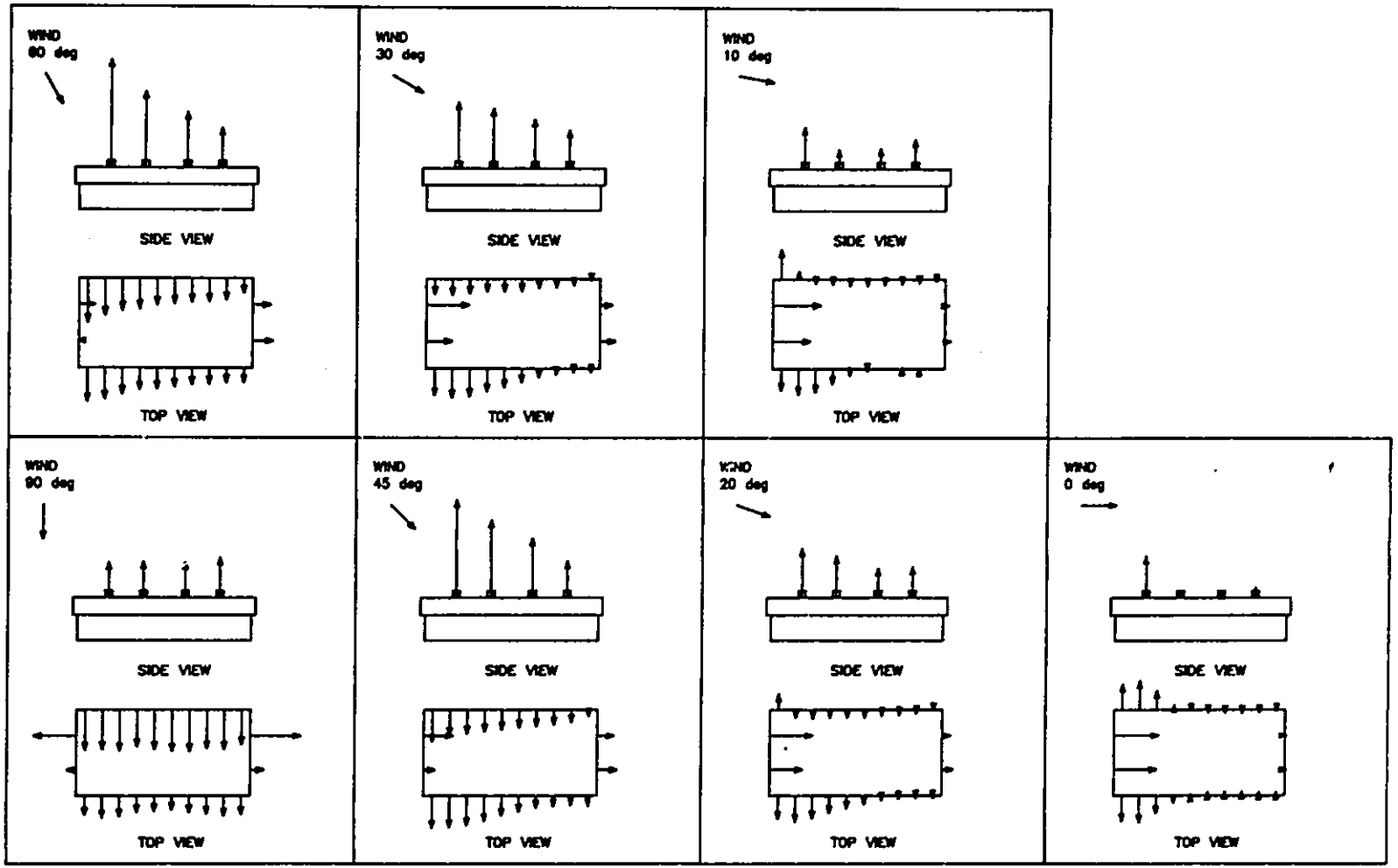

Figure 5.33 ΔCps (in-out), sealed model, chimney, simulated 800 mm sidewall openings, open end walls, wind angles = 90°, 60°, 45°, 30°, 20°, 10° and 0°.

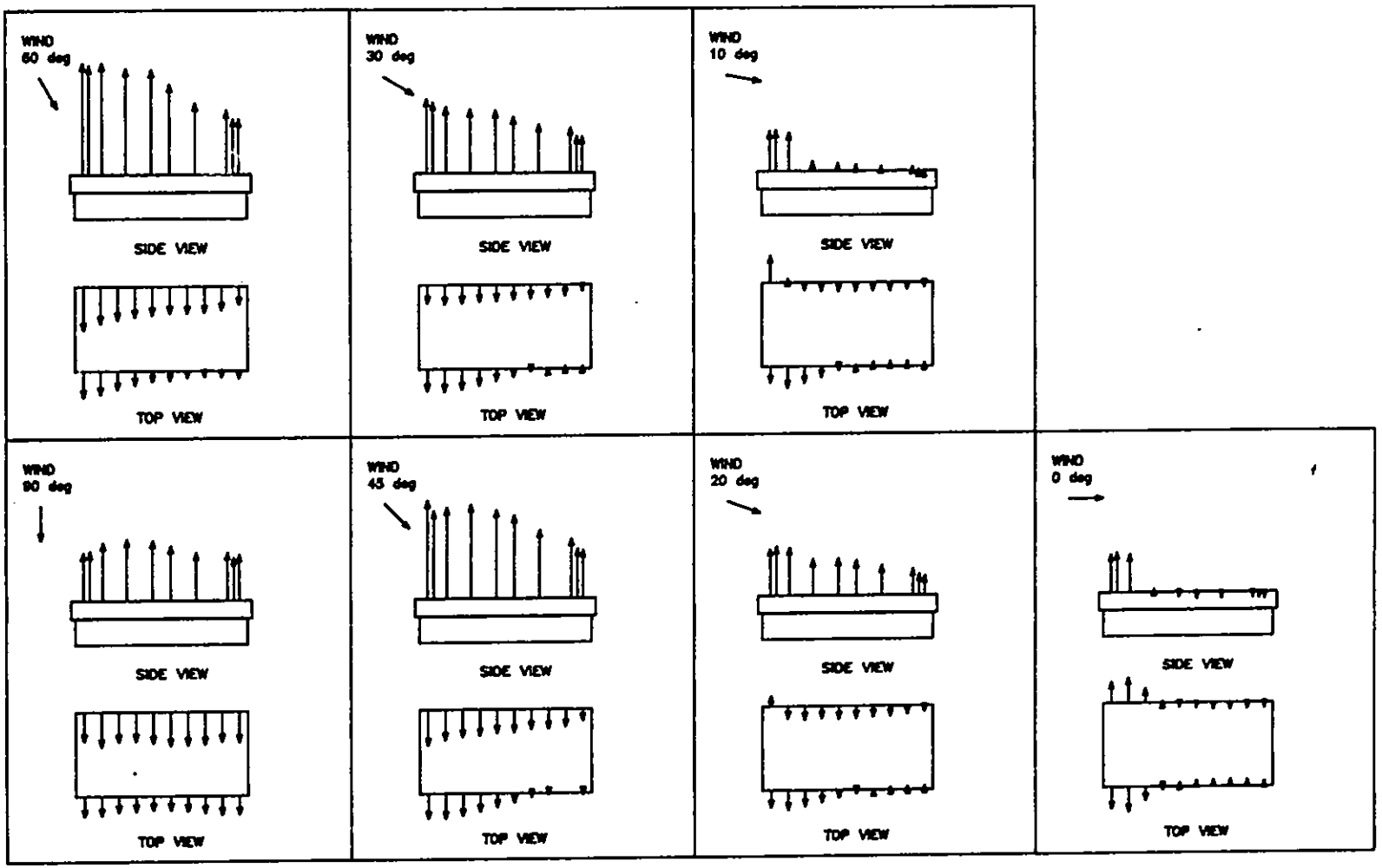

Figure 5.34 ΔCps (in-out), sealed model, simulated 150 mm ridge and 800 mm sidewall openings, closed end walls, wind angles = 90°, 60°, 45°, 30°, 20°, 10° and 0°.

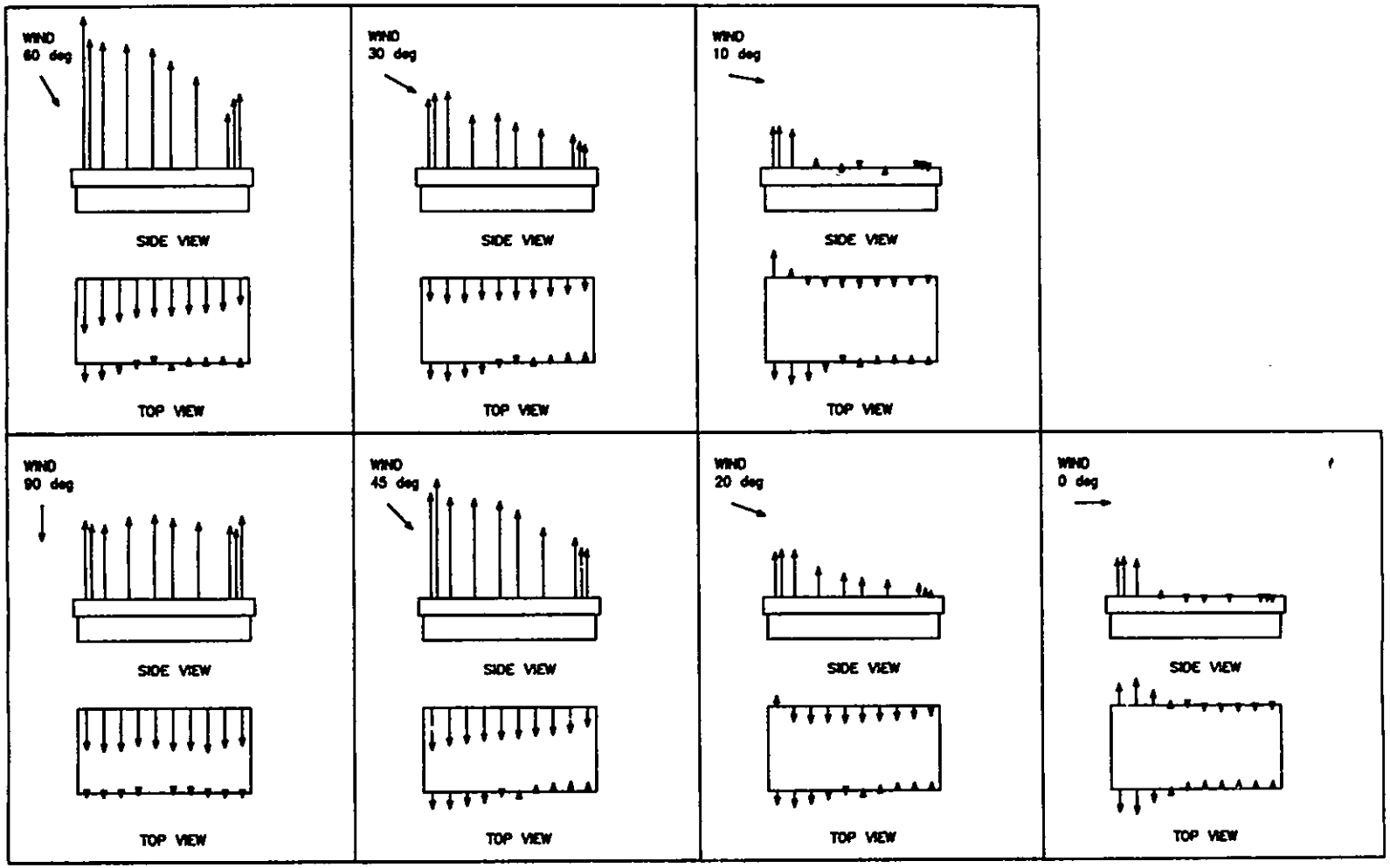

Figure 5.35 ΔCps (in-out), sealed model, simulated 400 mm ridge and 800 mm sidewall openings, closed end walls, wind angles = 90°, 60°, 45°, 30°, 20°, 10° and 0°.

When the end walls are open, the ΔCps over the ridge area are higher with the sealed model according to Figs. 5.28 (OP-CH-800-O) and 5.33 (SE-CH-800-O). From the results presented in Appendix G, for the simulated 1100 mm sidewall opening, the ΔCp distributions around the building are similar, although there is a noticeable increase in the magnitudes of the ΔCps over the walls.

Figures 5.30 (OP-150-800-C) and 5.34 (SE-150-800-C) present the results with a simulated 150 mm ridge opening width. For wind angles of 30° to 90°, the ΔCps are reduced over the sidewalls with the sealed model. There also is a noticeable difference in the inlet-outlet zones for θ = 0° to 20°. The ΔCps for the ridge are completely different for θ = 20° to 90°, but similar for θ = 0° and 10°.

With open end walls, the sealed model shows higher ΔCps at the end walls for θ = 90° (Fig. 5.33, SE-CH-800-O) versus the open model (Fig. 5.28, OP-CH-800-O).

The results for the open versus sealed model with the simulated 150 mm ridge opening and 1100 mm sidewall openings are included in Appendix G. It was noted that some changes in the inlet-outlet zones are accentuated at θ = 0°, 10°, and 20° for the larger ridge.

Figures 5.31 (OP-400-800-C) and 5.35 (SE-400-800-C) demonstrate that the ΔCps over the sidewalls are lower with the sealed model versus the open model for θ = 60° and 90°. Apparently this tendency is reversed for θ = 0°, 10°, 20°, 30° and 45°, when the wall ΔCps are higher with the sealed model. For all angles, the ΔCps over the ridge opening are much greater with the sealed model.

For the 400 mm ridge, results of Appendix G show that by opening the end walls, similar ΔCps are observed for θ = 45°, 60° and 90°. The end walls ΔCps are considerably higher with the sealed model. For θ = 0°, 10°, 20° and 30°, the ΔCps are increased over the inlet zones but decreased over the outlet zones, with the sealed model.

With a 400 mm ridge opening, when sidewall openings simulating 1100 mm are used, drastic changes in the inlet-outlet zones are noticed at $\theta = 30°$, 45° and 60°. The sealed model predicts inflows at $\theta = 60°$ over the leeward wall, while the open model predicts inflows at $\theta = 30°$. The ΔCps over the ridge are also much higher with the sealed model for $\theta = 10°$ to 90°, but similar for $\theta = 0°$. For the sealed model with open end walls and sidewall openings simulating 1100 mm, a reduction in the ΔCps over the outlet zones at the leeward walls is observed. The previous flow reversal between the open and sealed model is accentuated. The open model predicts inflows on the leeward wall at $\theta = 10°$ while the sealed model shows an inflow on the leeward wall at $\theta = 60°$.

Generally, the comparisons of the results for the open model versus the sealed model indicate:

1 - Some differences in the ΔCps distributions around the building.
2 - A difference in ΔCps magnitudes for inlet and outlet zones over the walls.
3 - A different ΔCps with open end walls at $\theta = 90°$, and also flow reversal at $\theta = 0°$ and 10°.
4 - For all ridge opening configurations, the sealed model would over-predict the airflow through the ridge openings as compared to the open model.

These observations are consistently accentuated for the larger sidewall openings of 1100 mm versus the 800 mm openings, which would lead one to believe that the larger the total opening area is, the larger the discrepencies in ΔCps distribution zones and magnitudes are between the open and sealed model.

5.4 Visualization of the local airflows

The ΔCp distributions with various opening areas are helpful to visualise the inlet and outlet zones as well as the magnitude of the pressure differences over the building

envelope. However, the quantity of air entering or exhausting a building is also directly proportional to the discharge coefficient, C_d, and each opening area for the ridge, sidewalls and end walls. The airflow (Q_j) for various types of openings has been plotted in Figs. 5.36 to 5.45 for the open and sealed models. Inflows are indicated when the continuous line is inside the enclosure, and outflows when the contour line is outside. For the chimney cases, the airflow lines are only representative over the chimney itself; they were joined to help in visualisation. For the 150 mm and 400 mm ridge openings, the entire surface under the airflow line is proportional to the inflow or outflow. The magnitude of the airflow lines are adjusted equally for all tests in order to fit the drawing space available and for proportional comparison purposes.

5.4.1 Open model

The results for the open model are used as a standard for comparisons. Fig. 5.36 (OP-CH-800-C) presents the results for the chimney, simulated 800 mm sidewall openings, and closed end walls. The distribution of the airflow lines on both sidewalls are fairly identical to the ΔCp distributions. However, at the chimney level, the outflows or inflows are small due to the effect of the restricted opening area as compared to the flows across the sidewalls. Complete data sets are in Appendix H.

5.4.1.1 Effect of sidewall openings

Sidewall openings of 800 mm (OP-CH-800-C) versus 1100 mm (OP-CH-1100-C) present similar zones of air inlet and outlet. For all θ, the results for the 800 mm or 1100 mm sidewall show negligible differences in the airflow through the chimney. Even if a reduction in ΔCps has been noticed with the 1100 mm as compared to the 800 mm sidewall, the airflow through the 1100 mm sidewalls are increased due to the larger opening areas.

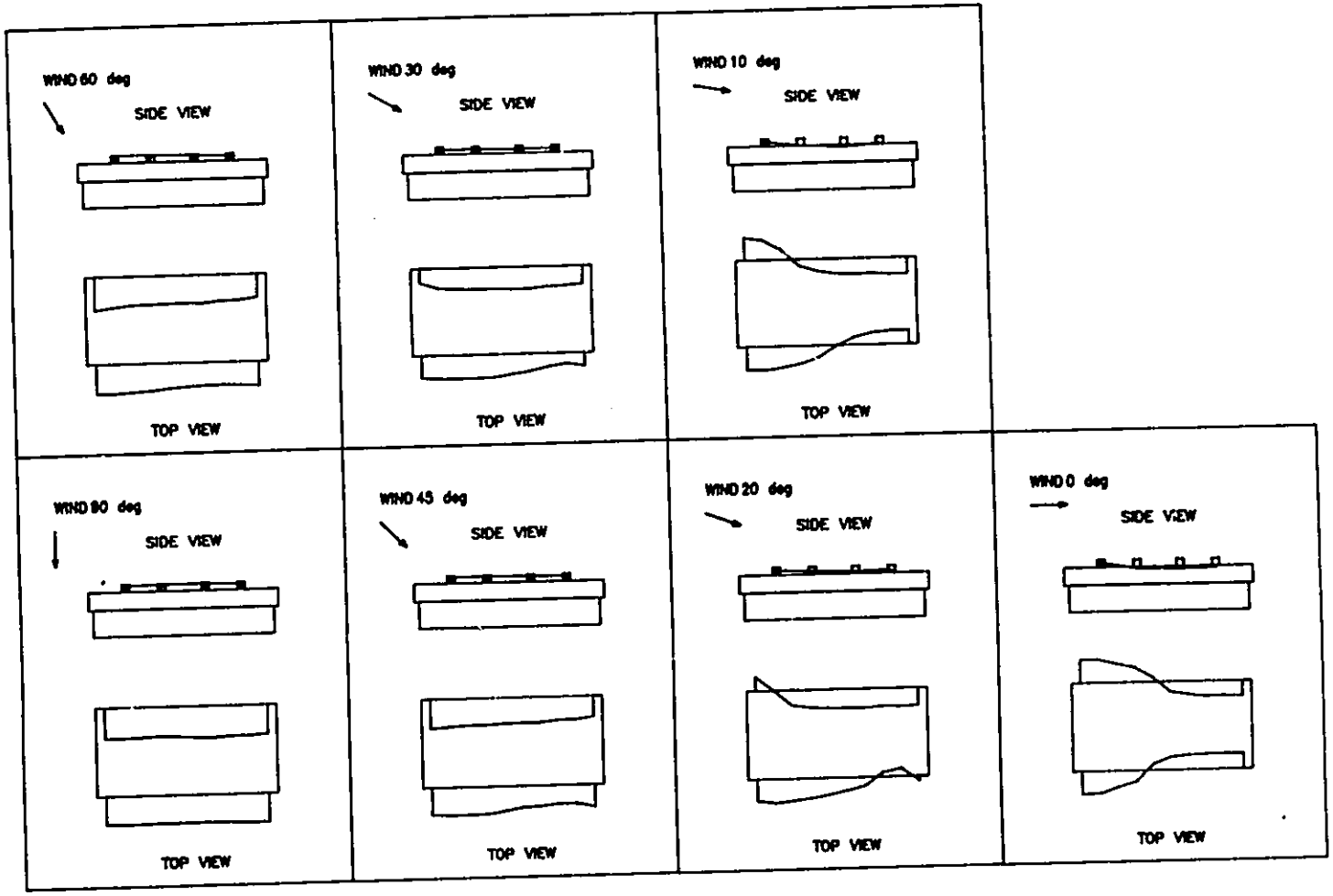

Figure 5.36 Airflow diagrams, open model, chimney, simulated 800 mm sidewall openings, closed end walls, wind angles = 90°, 60°, 45°, 30°, 20°, 10° and 0°.

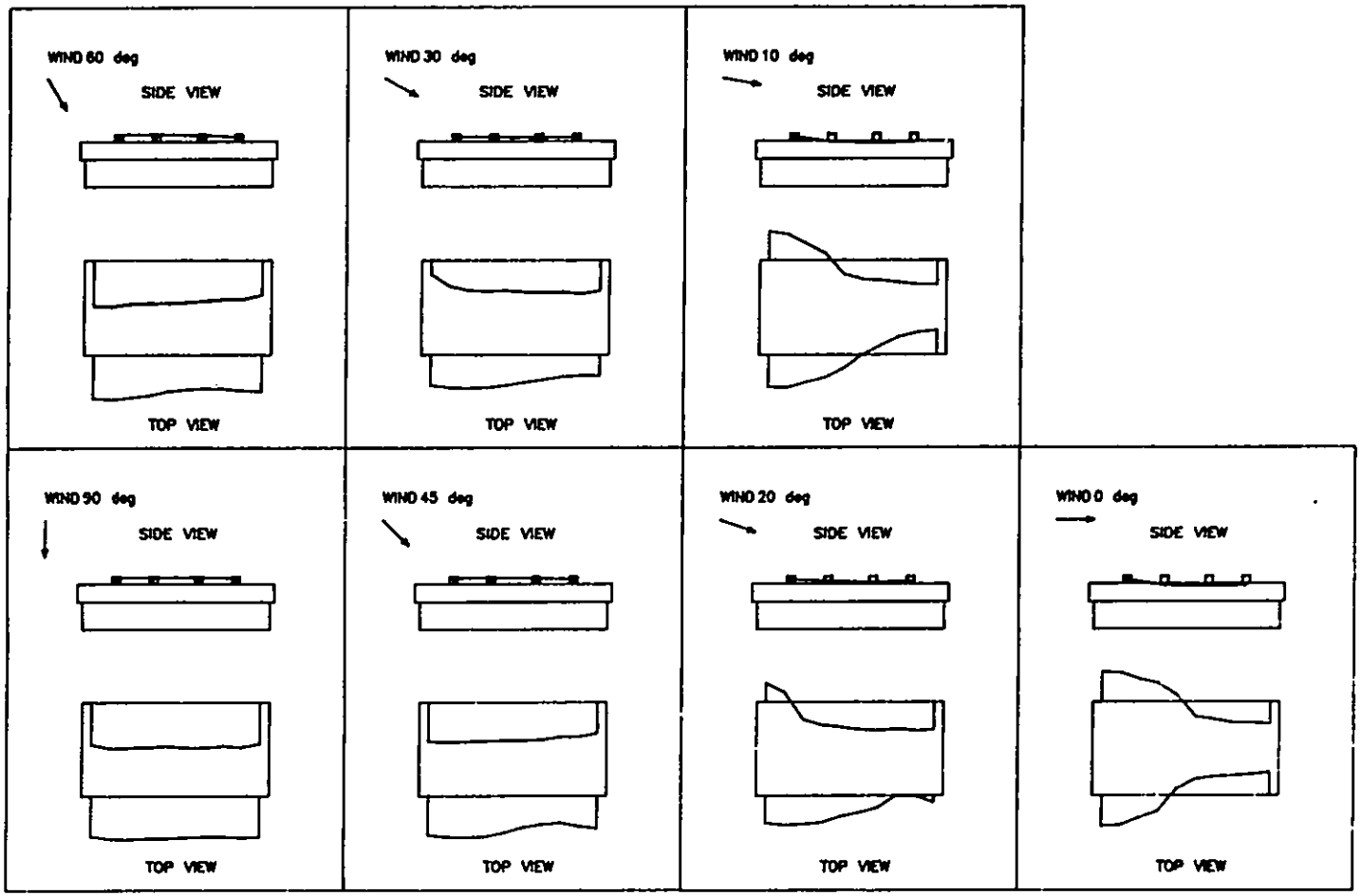

Figure 5.37 Airflow diagrams, open model, chimney, simulated 1100 mm sidewall openings, closed end walls, wind angles = 90°, 60°, 45°, 30°, 20°, 10° and 0°.

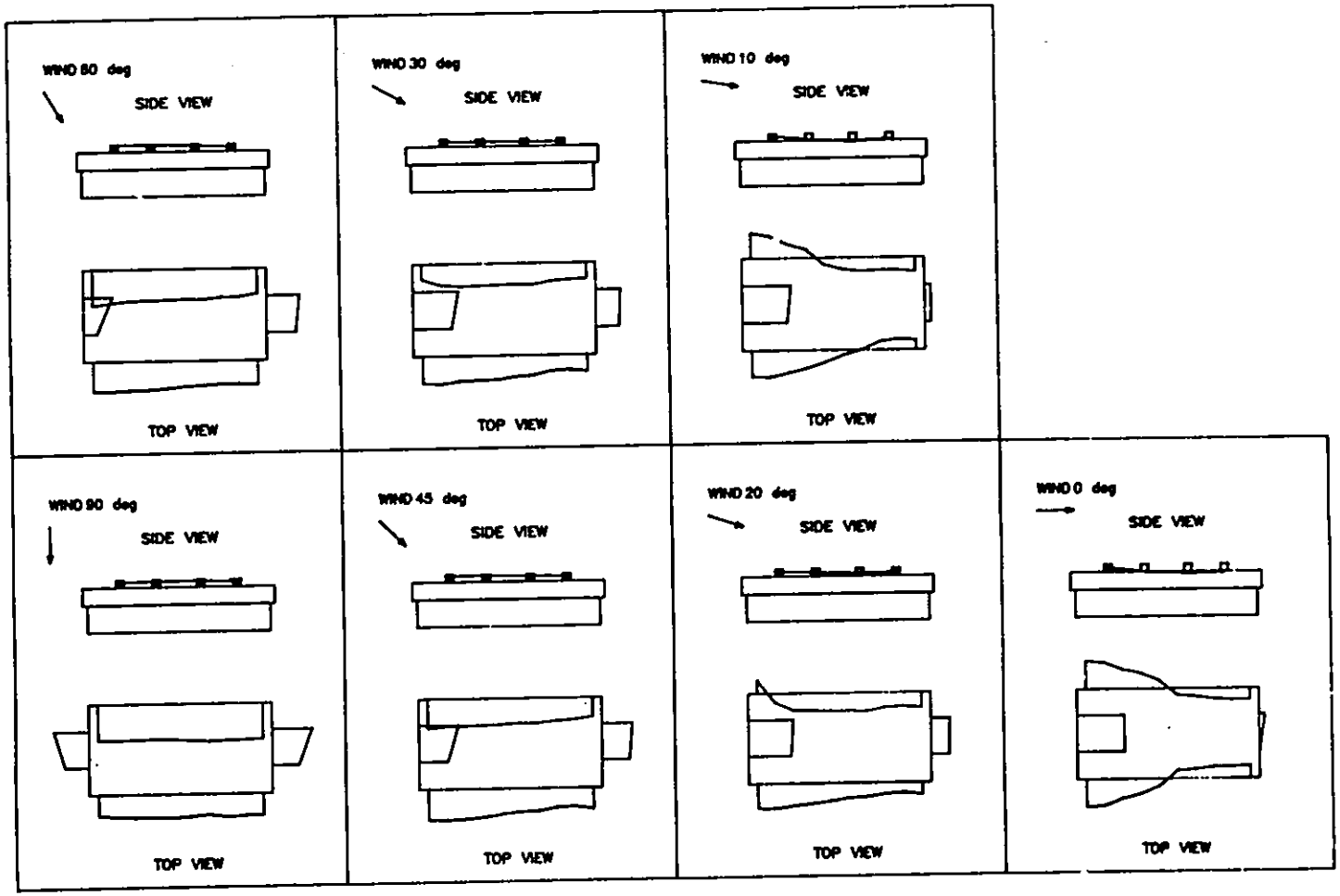

Figure 5.38 Airflow diagrams, open model, chimney, simulated 800 mm sidewall openings, open end walls, wind angles = 90°, 60°, 45°, 30°, 20°, 10° and 0°.

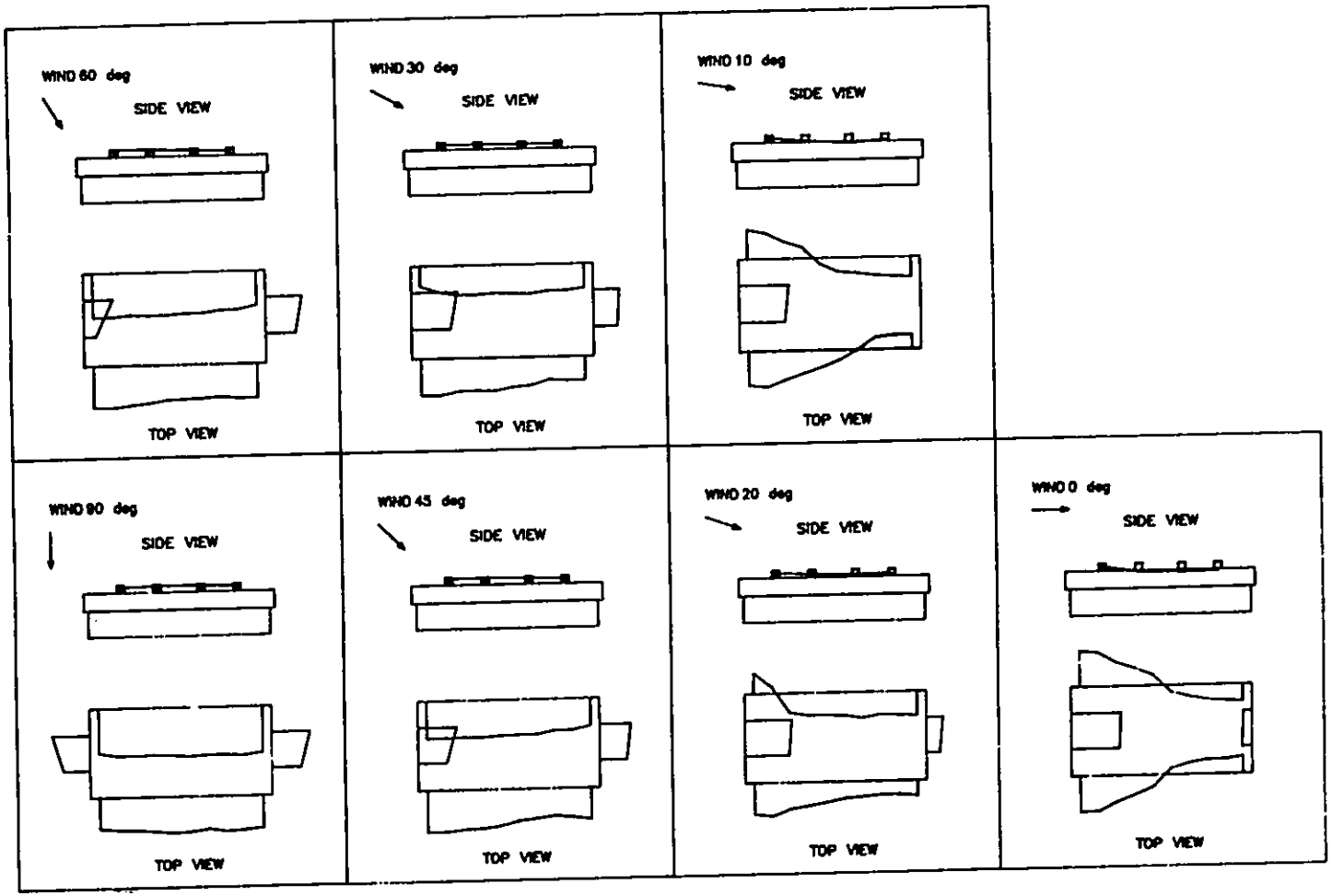

Figure 5.39 Airflow diagrams, open model, chimney, simulated 1100 mm sidewall openings, open end walls, wind angles = 90°, 60°, 45°, 30°, 20°, 10° and 0°.

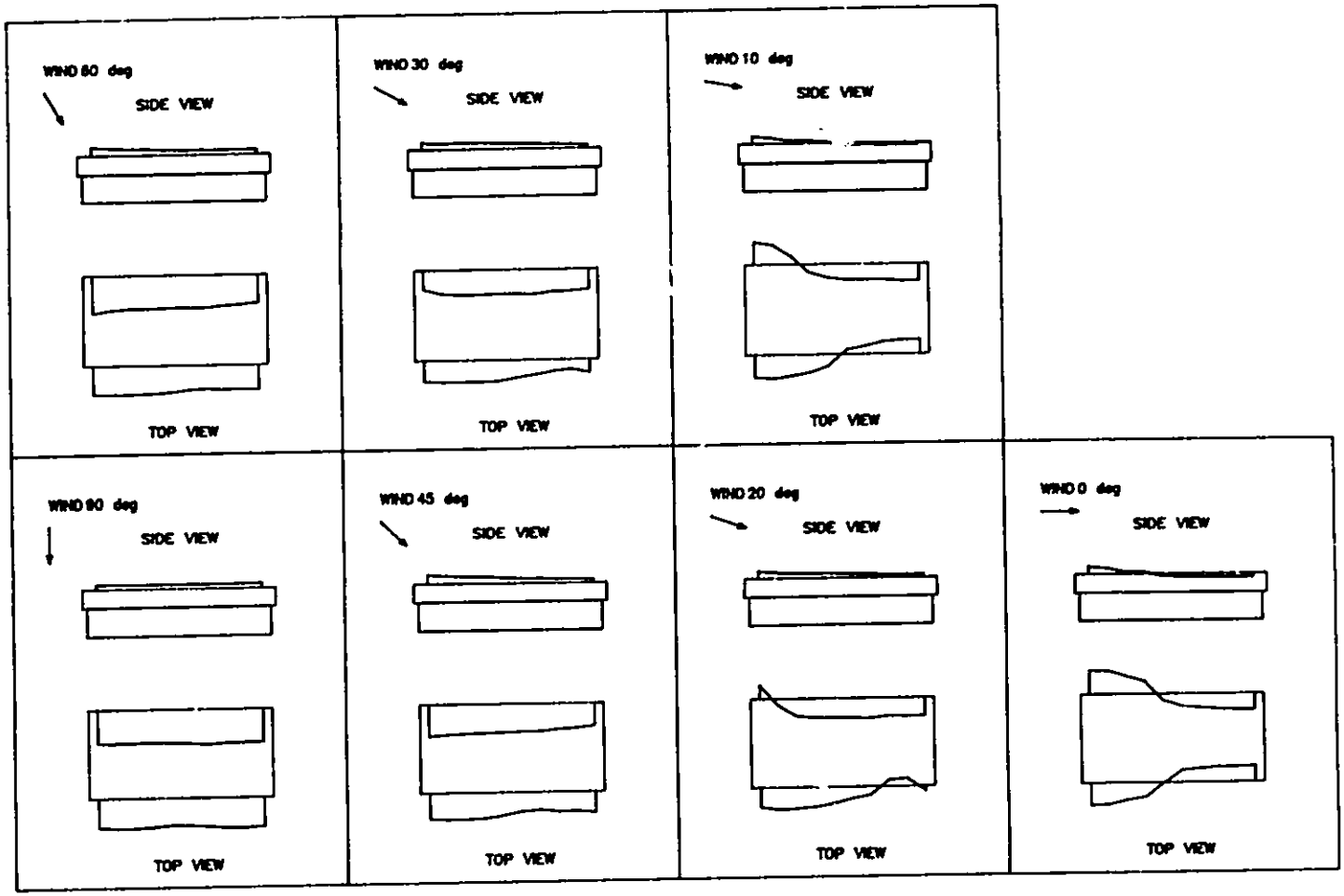

Figure 5.40 Airflow diagrams, open model, simulated 150 mm ridge and 800 mm sidewall openings, closed end walls, wind angles = 90°, 60°, 45°, 30°, 20°, 10° and 0°.

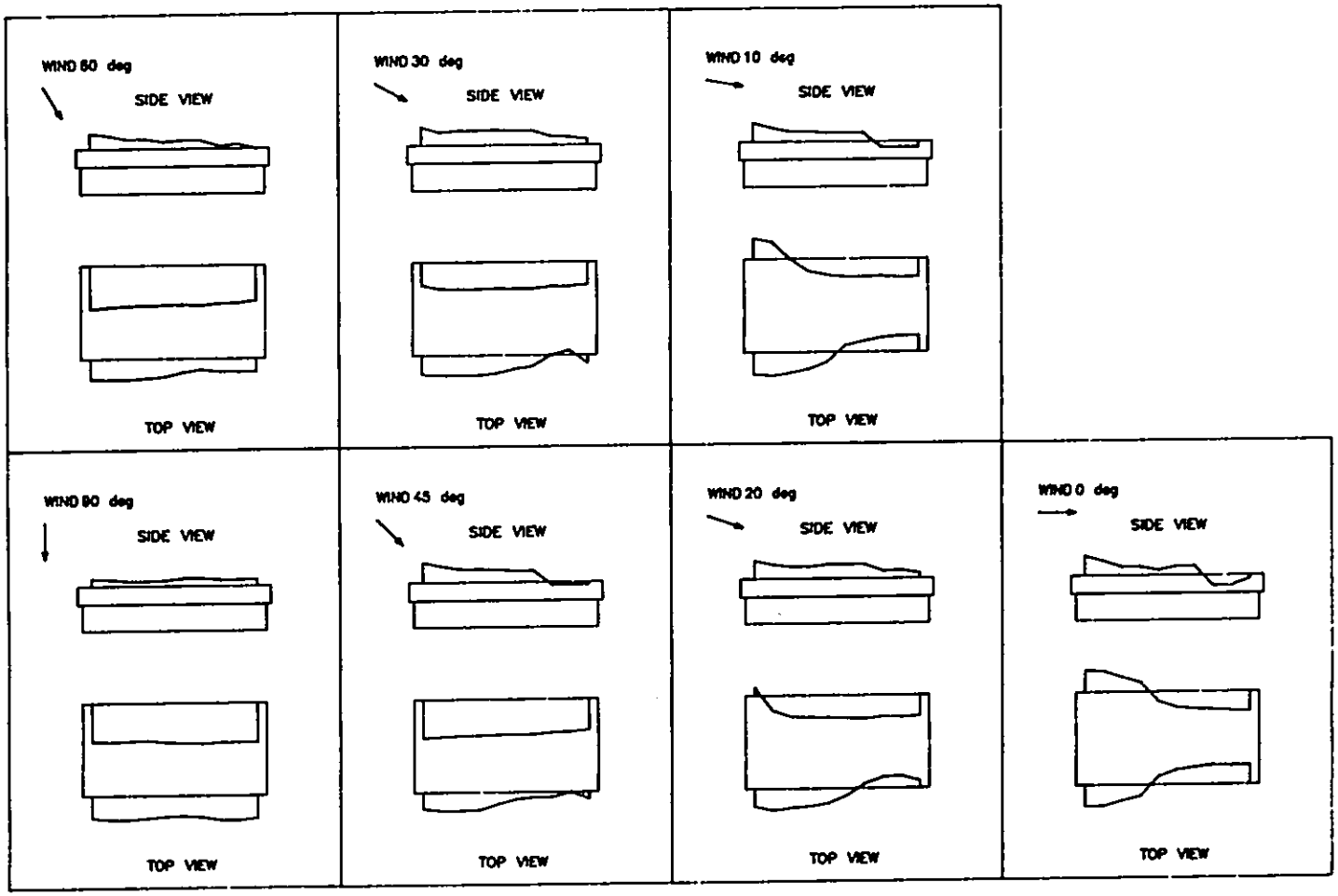

Figure 5.41 Airflow diagrams, open model, simulated 400 mm ridge and 800 mm sidewall openings, closed end walls, wind angles = 90°, 60°, 45°, 30°, 20°, 10° and 0°.

5.4.1.2 Effect of end wall openings

For θ = 45°, 60° and 90°, the results presented in Figs. 5.36 (OP-CH-800-C) versus 5.38 (OP-CH-800-O) and Figs. 5.37 (OP-CH-1100-C) versus 5.39 (OP-CH-1100-O) show small increases in the inflow on the windward sidewalls and a slight reduction of the outflow on the leeward wall, with open end walls. For all tests (Appendix H), at θ = 0°, 10° and 20°, the models with open end walls show a reduction in the inflow by the downwind leeward sidewall and an increase of outflow by the upwind windward sidewall. For all wind angles, there is little effect on the chimney flows. The effects of end wall openings are even smaller when the 1100 mm sidewall openings are used.

5.4.1.3 Effect of ridge openings

For θ = 30°, 45°, 60° and 90°, comparisons of Figs. 5.36 (OP-CH-800-C) versus 5.40 (OP-150-800-C) reveal an increase in the inflow through the windward wall, similar leeward wall outflow and an increase in ridge exhaust flow with the 150 mm ridge versus the chimney. At θ = 0°, 10° and 20°, both sidewalls show very similar inflows and outflows; however it appears that there is more inflow and outflow by the 150 mm ridge than the chimney.

The results of Figs. 5.30 (OP-150-800-C) versus 5.31 (OP-400-800-C) also indicate an increase in windward inflow, a decrease in leeward outflow and an increase in the ridge outflow for θ = 20°, 30°, 45° 60° and 90°. Similar to the chimney results, at θ = 0° and 10°, the OP-400-800-C results show more inflow by both sidewalls at the downwind end and a reduction of the outflow at the upwind end of the building. Also, there are more inflow and outflow through the 400 mm ridge than the 150 mm ridge.

Generally, larger ridge openings have the following effects:

1 - An increase of the windward inflows, a decrease of the leeward outflows and an increase of the outflows through the ridge at θ = 30°, 45°, 60° and 90°.

2 - At θ = 0° and 10°, there are similar sidewall flows for the chimneys and 150 mm ridge and also more inflows and outflows through the 150 mm ridge itself. The 400 mm ridge show more inflows but less outflows through both sidewalls, while there would be more inflows and outflows at the ridge level.

5.4.2 Sealed model

The complete set of airflow diagrams for the sealed models are added in the Appendix H. Similarly to the open model results, the wind angles of incidence dictate the magnitude and direction of the airflow rates through each opening. At θ = 90°, Fig. 5.42 (SE-CH-800-C) shows uniform airflows through the sidewall openings and the chimney while other wind directions have different distribution patterns for the airflow rates.

5.4.2.1 Effect of sidewall openings

From the comparisons among Figs. 5.42 (SE-CH-800-C), 5.44 (SE-150-800-C), 5.45 (SE-400-800-C), and with the data in Appendix H, it is observed that a larger sidewall opening (1100 mm) produces larger inflows and outflows for all model configurations.

By enlarging the sidewall opening from 800 mm to 1100 mm, the chimney tests show that there is no difference on the zones of inflows and outflows, only an increase in magnitude of the airflows. With the 150 mm ridge opening, both the inflow-outflow zones and the airflow magnitudes are affected for θ = 30° to 0°. More effects on zones and magnitudes are noticed with the 400 mm ridge opening, especially for θ = 60° to 0°.

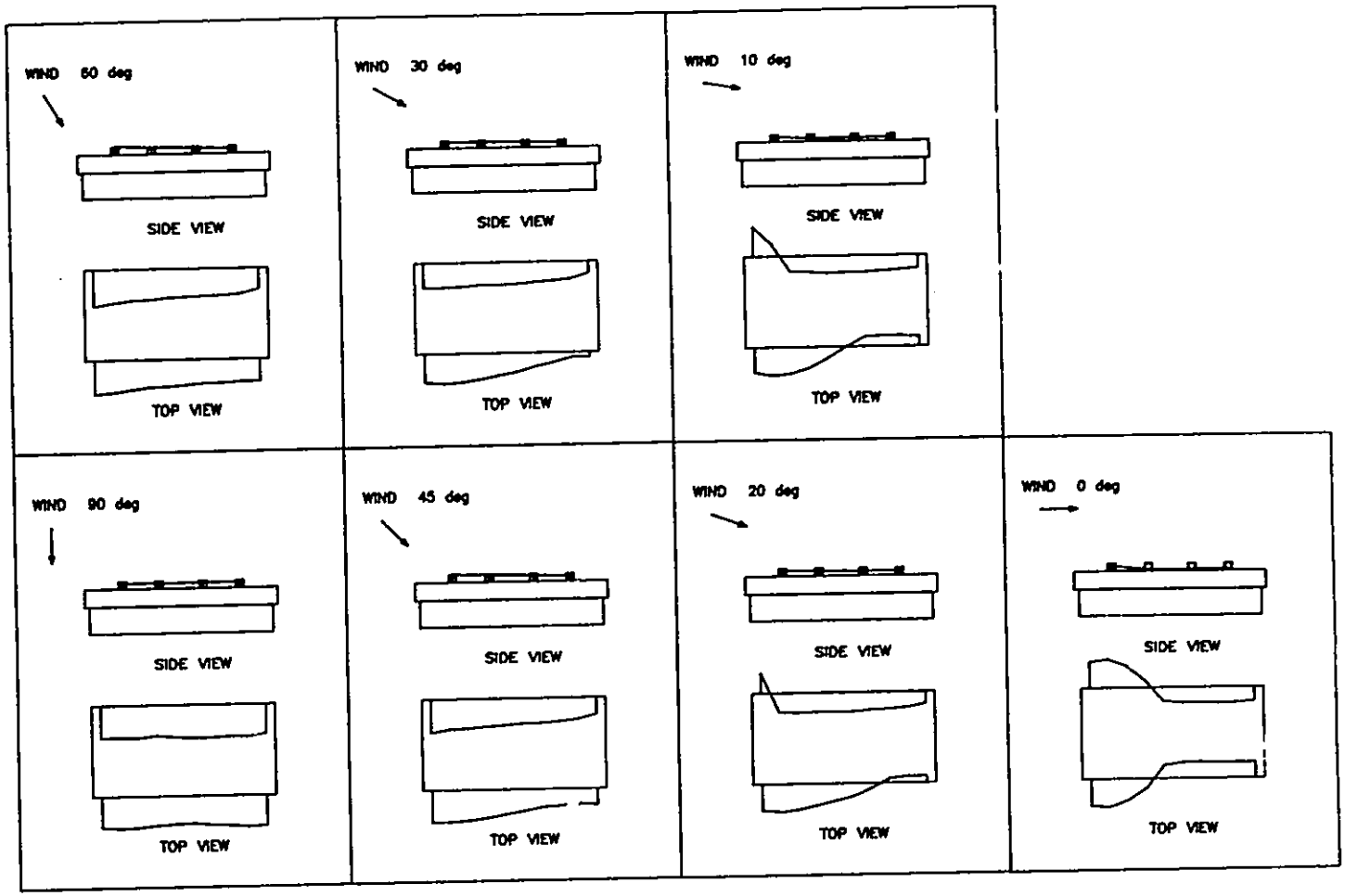

Figure 5.42 Airflow diagrams, sealed model, chimney, simulated 800 mm sidewall openings, closed end walls, wind angles = 90°, 60°, 45°, 30°, 20°, 10° and 0°.

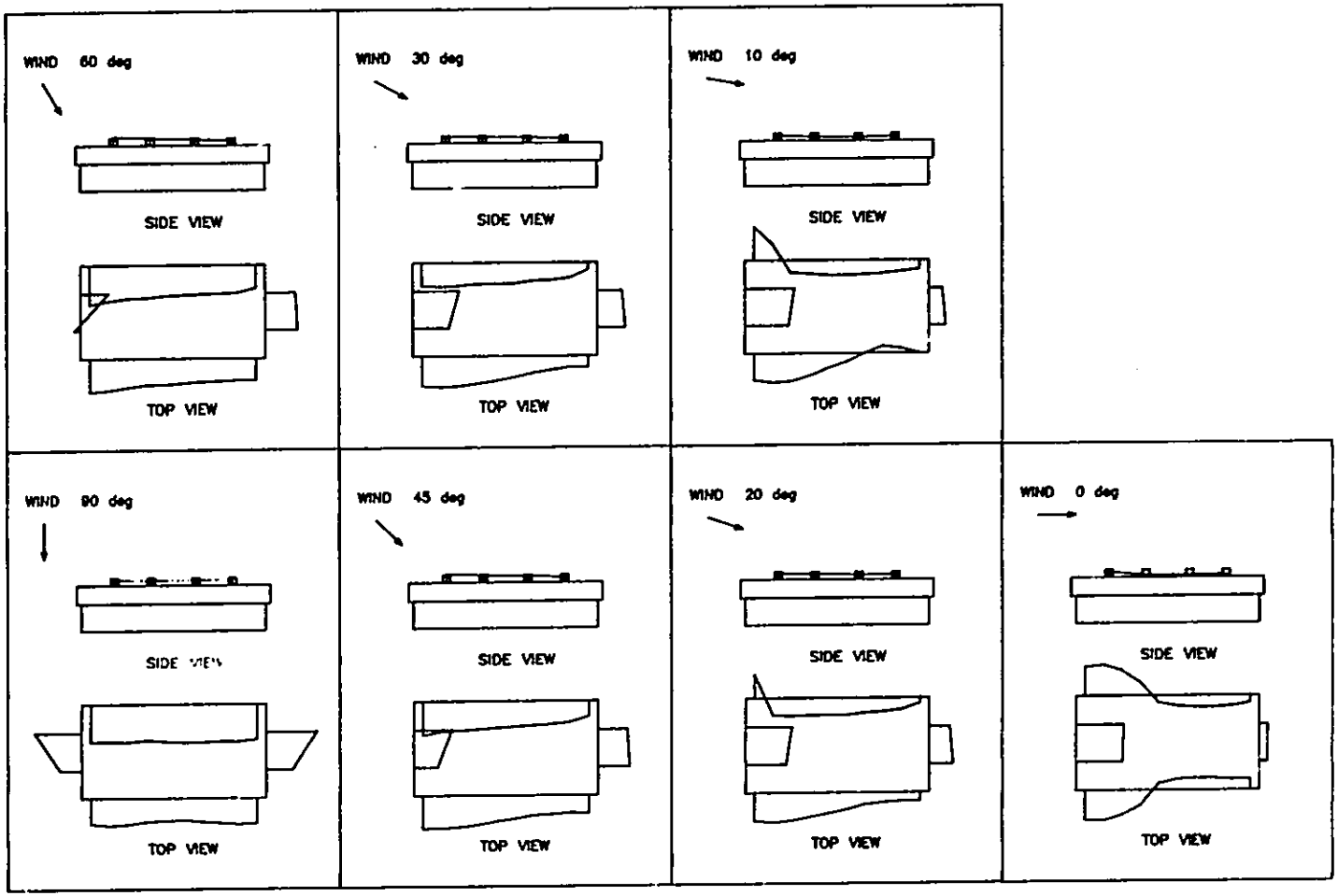

Figure 5.43 Airflow diagrams, sealed model, chimney, simulated 800 mm sidewall openings, open end walls, wind angles = 90°, 60°, 45°, 30°, 20°, 10°, and 0°.

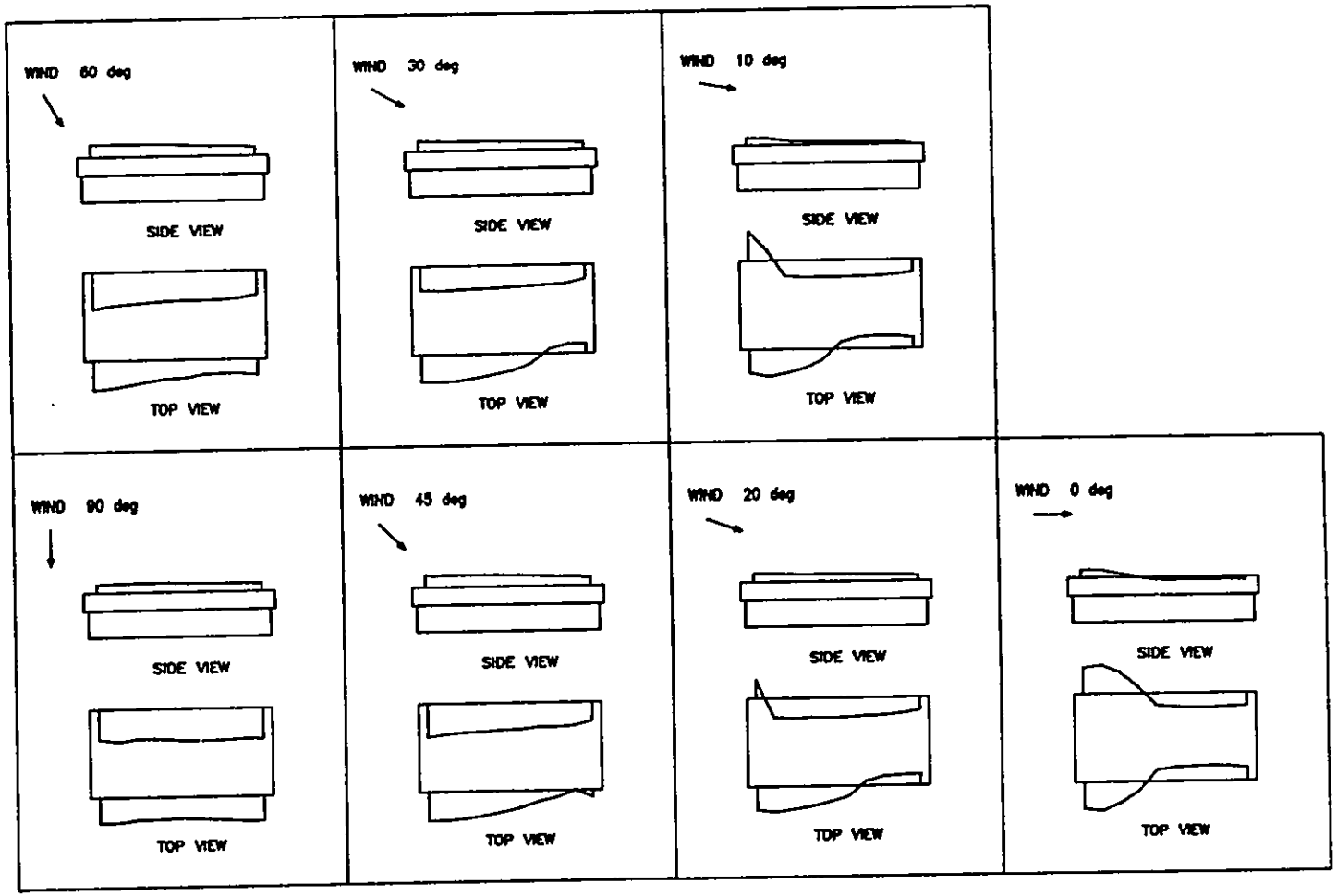

Figure 5.44 Airflow diagrams, sealed model, simulated 150 mm ridge and 800 mm sidewall openings, closed end walls, wind angles = 90°, 60°, 45°, 30°, 20°, 10° and 0°.

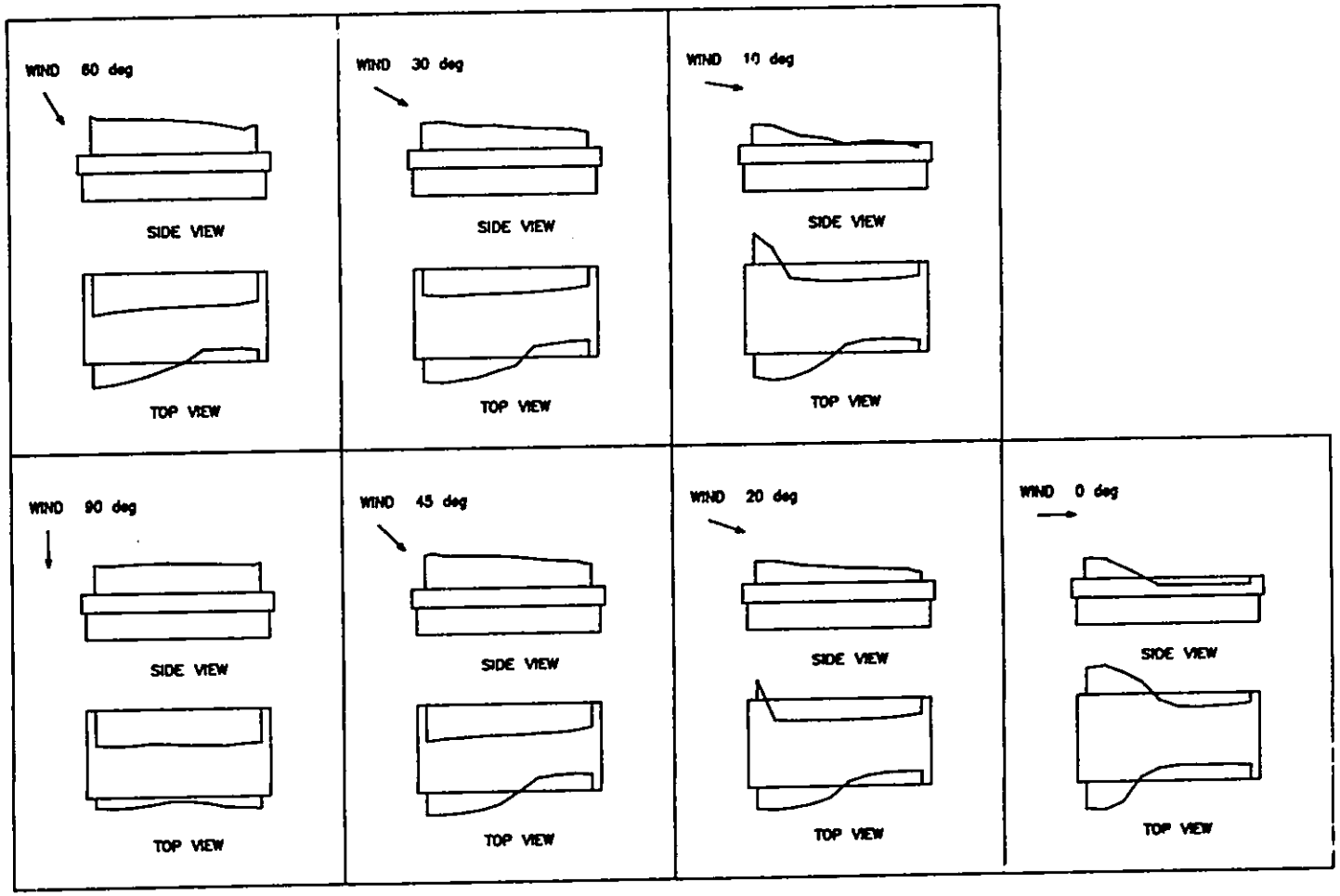

Figure 5.45 Airflow diagrams, sealed model, simulated 400 mm ridge and 800 mm sidewall openings, closed end walls, wind angles = 90°, 60°, 45°, 30°, 20°, 10° and 0°.

5.4.2.2 Effect of end wall openings

The comparison of Figures 5.42 (SE-CH-800-C) versus 5.43 (SE-CH-800-O) as well as the comparison of Figs. 5.44 (SE-150-800-C) and 5.45 (SE-400-800-C), with results of Appendix H indicate that opening the end walls has little effect on the inflow-outflow zones at the ridge level and on the windward walls for all wind angles. For $\theta = 90°$, a reduction of outflows through the leeward wall is noticeable, while, in contrast, general increases of outflows through both sidewalls are visible for $\theta = 60°$ to $0°$.

5.4.2.3 Effect of ridge openings

The comparison among Figs. 5.42 (SE-CH-800-C), 5.44 (SE-150-800-C) and 5.45 (SE-400-800-C) confirms that larger outflows through the ridge would generally occur with the increase of the ridge opening width. Also, for the 150 mm and 400 mm ridges, some inflows would occur at the ridge level at $\theta = 0°$ and $10°$. This is in contradiction with Bruce (1974) and Down et al. (1985), but in accordance with the results of Shrestha et al. (1990).

By enlarging the ridge opening, some changes in airflow directions and magnitudes on both sidewalls are noticeable for most wind angles.

Generally, observations of the airflow diagrams for the sealed model indicate that:

1 - An increase of the sidewall opening area causes more inflows and outflows through the model for all wind angles.
2 - Any changes of sidewall opening areas, end walls opening or ridge types would have an effect on the inflows-outflows zones and their relative magnitudes.
3 - Large outflows are predicted by the continuous 150 mm and 400 mm ridge openings.

5.4.3 Open versus sealed models

The observations of the airflow diagrams provide important extra information over the ΔCps alone because they take into account the opening area factor, which has a linear effect on the magnitude of the inflows and outflows for each opening area. The ventilation rate through each opening differs when the pressure coefficient data used changes from the sealed to the open model.

The results of Figs. 5.36 (OP-CH-800-C) and 5.42 (SE-CH-800-C) reveal no difference in the airflows at the chimney level. However, for θ = 30° to 0°, there are different inflow and outflow zones and relative magnitudes at the sidewall with the 1100 mm sidewall (Appendix H). There are inflows at the chimney levels with the open model for θ = 10° and 0°. This is attributed to the lower Cp_{in} observed in Fig. 5.10, with large sidewall openings in the open model.

With open end walls, Figs. 5.38 (OP-CH-800-O) and 5.43 (SE-CH-800-O) shows more inflow through the chimney for θ = 20° to 0° with the open model versus the sealed one. At θ = 90°, the sealed model predicts more outflow by both end walls. For θ = 60° to 0°, there is always more outflow through the downwind end wall openings with the sealed model. The effects of the completely different exterior Cp distributions observed in Figs. 5.3 (OP-CH-800-O) and 5.4 (OP-CH-1100-O) versus Fig. 5.7 (SE-CH) are reflected by the airflow diagrams.

With the continuous 150 mm ridge opening, Figs. 5.40 (OP-150-800-C) versus 5.44 (SE-150-800-C) show inflows at the downwind part of the ridge for θ = 10° and 0° with the open model, while some inflows are visible only at θ = 0° with the sealed model. Also, the relative magnitude of the chimney outflow is higher with the sealed model for all wind angles. On the leeward wall, inflows are present at θ = 45° with the sealed model, as compared to θ = 20° with the open model. The combinations of higher -Cps over the roof and lower ΔCps

across the sidewalls observed with the sealed model on Fig. 5.8 (SE-150) and Table 5.3 result in the over-prediction of the ridge outflow and under-prediction of the leeward wall outflow when compared to the open model tests.

With the 150 mm ridge, enlarging the sidewall opening to 1100 mm creates larger differences in the ridge and leeward wall inflows and outflows when comparing open and sealed models (Appendix H).

For the 400 mm ridge opening, the comparisons between Figures 5.41 (OP-400-800-C) and 5.45 (SE-400-800-C) indicate that the sealed model shows larger ridge outflows for all angles, lower outflows by the leeward sidewall and more inflows by the leeward sidewall. By using the 1100 mm sidewall opening, these effects are accentuated.

Generally, from the observations of the inflow and outflow distribution and magnitude for the open versus the sealed models, for all wind angles and the various model configurations; it can be inferred that:

1 - The sealed model results always predict inflows through the leeward wall at a higher wind angle of incidence.
2 - For all θ with the sealed model, the ridge and the downwind end wall outflows are considerably over predicted and the leeward wall outflows are under predicted as compared to the open model.
3 - More inflows at the ridge level are predicted with the open model ($\theta = 20^\circ$ to 0°).
4 - Maximum discrepancies between the sealed versus the open model are always noticed with the larger ridge, larger sidewall openings and open end walls.

5.5 Ventilation rate coefficients

5.5.1 Open model

5.5.1.1 General observations

Vickery et al., (1983), ASHRAE (1989) and many others transformed their data on ventilation rates in order to obtain dimensionless ventilation rate coefficients described by Eq. 4.5

$$C_{Q10} = \frac{Q}{V_{10} A_S} \qquad (4.5)$$

With this formula it is very easy to predict the building's ventilation rates, as well as to use it in conjunction with meteorological data (Choinière, 1989). Being a dimensionless coefficient, it is very convenient to study the effect of any changes to sidewall, end wall and ridge opening areas on the ventilation rate coefficient, C_{Q10}.

Figures 5.46, 5.47 and 5.48 present the results of the ventilation rate coefficient as a function of the wind angle of incidence for the chimney, and 150 mm and 400 mm ridge openings, respectively. The complete data sets are in Appendix I. For example, at $\theta = 90°$, the OP-CH-800-C has a C_{Q10} of 0.39 while at $\theta = 0°$, C_{Q10} equals 0.20. The results predict a 50% reduction in the ventilation rate when the wind is parallel to the building length versus when it blows perpendicularly to the building.

These values may seem low when compared to a conventional discharge coefficient of 0.6, which applies to a sharp edge square orifice. However, the ventilation rate coefficient, C_{Q10}, can be defined as in Eq. 5.1. It depends on the discharge coefficient and difference between external and internal pressure coefficient, which are all less than 1.0 with the present data.

$$C_{Q10} = C_d \sum \left(\frac{Cp_j - Cp_{in}}{|Cp_j - Cp_{in}|^{\frac{1}{2}}} \right) \qquad (5.1)$$

Then C_{Q10} values from 0.20 to 0.40 mean that only 20% to 40% of the theoretical potential ventilation rates are obtained through these specific arrangement sidewall openings and chimney, according to a reference wind speed at a 10 m height.

The data in Figure 5.46 show that the lowest C_{Q10} occurs at $\theta = 10°$. This interesting phenomenon has been observed by Choinière (1989) for similar ventilation rate coefficient measurements in a full scale swine building. Also, the C_{Q10} values for $\theta = 90°$ and 60° are fairly close and they are rapidly decreasing between $\theta = 45°$ to 20°. This coincides with the major changes in the Cp distribution around the building observed in Figs. 5.1a-g to 5.4a-d.

Similar curve shapes are observed on Figs. 5.47 and 5.48 with the simulated 150 mm and 400 mm ridges. Exceptionally, the C_{Q10} curves of the 400 mm ridge with open end walls show higher C_{Q10} values at $\theta = 60°$, 45° and 30° as compared to $\theta = 90°$. For all tests with both ridges, the lowest C_{Q10} values always occur at $\theta = 10°$.

5.5.1.2 Effect of sidewall openings

In Figs. 5.46 (chimney) versus 5.47 (150 mm ridge) the C_{Q10} values are similar with both 800 mm and 1100 mm sidewall openings at $\theta = 90°$ to 30° with closed end walls. At $\theta = 20°$ to 0°, the 1100 mm sidewall presents slightly lower C_{Q10} values. With open end walls, the C_{Q10} values with the 1100 mm sidewall openings are always lower than the 800 mm sidewall.

The C_{Q10} values are influenced by the ΔCps over the sidewall and end wall openings and by the ridge types. When the sidewall area is increased from 800 mm to 1100 mm, the ΔCps across the building are greatly increased at $\theta = 90°$

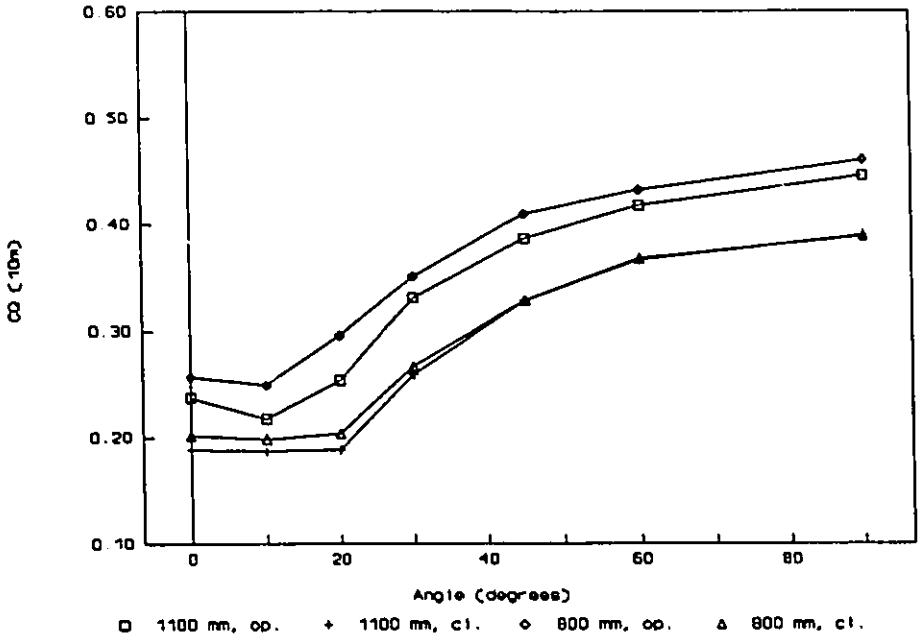

Figure 5.46 Open model ventilation rate coefficients, C_{Q10}, chimney.

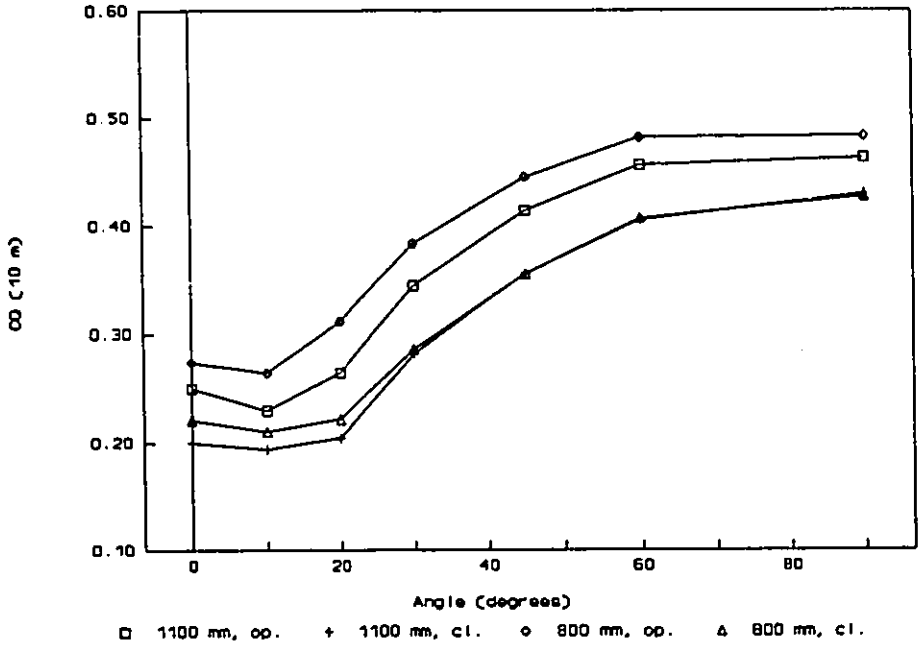

Figure 5.47 Open model ventilation rate coefficients, C_{Q10}, simulated 150 mm ridge .

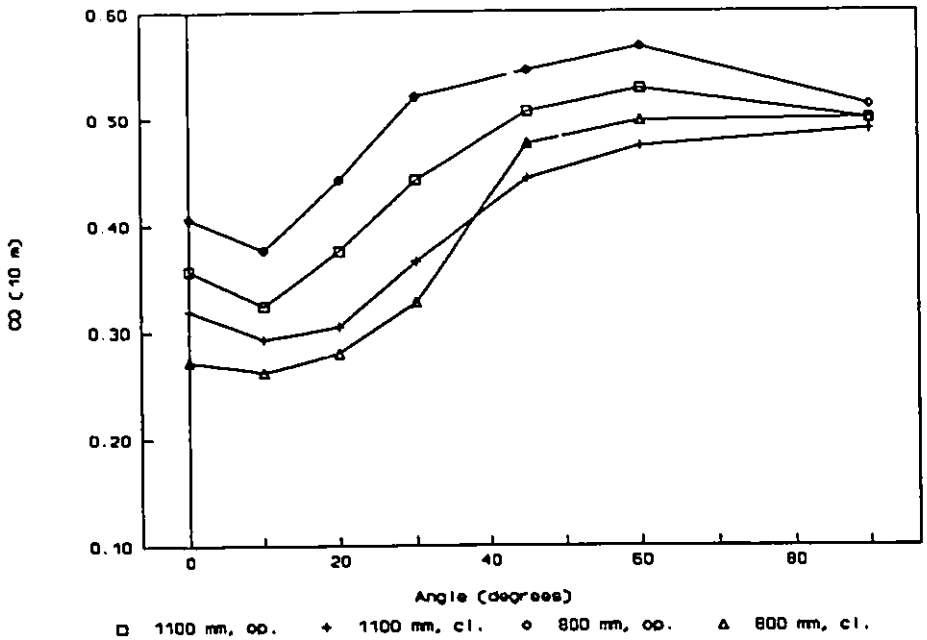

Figure 5.48 Open model ventilation rate coefficients, C_{Q10}, simulated 400 mm ridge.

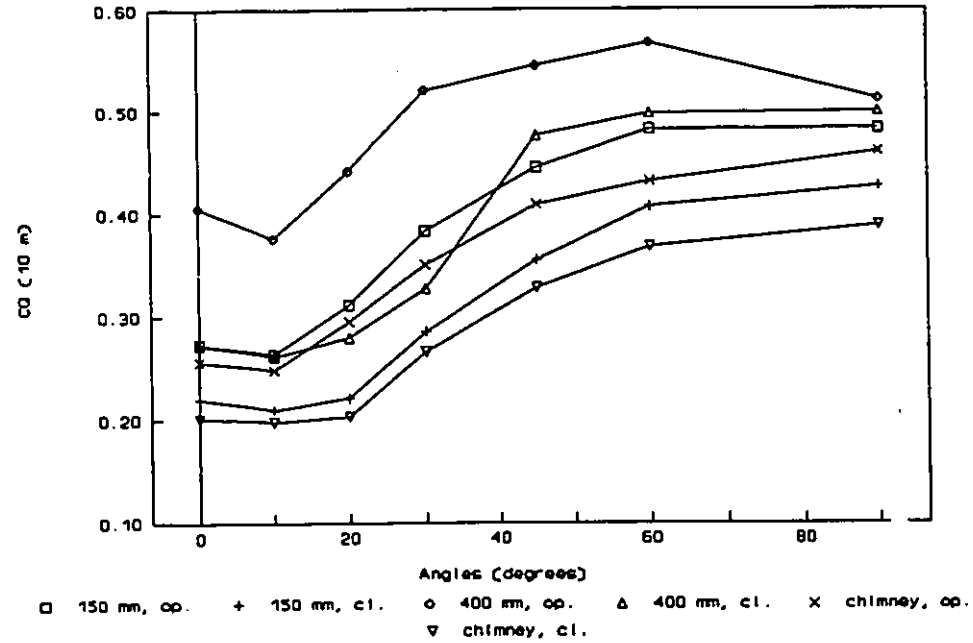

Figure 5.49 Open model, comparison among chimney, simulated 150 mm and 400 mm ridges with simulated 800 mm sidewall.

(Table 5.3) which should normally lead to an increase in the C_{q10} value. For the total flow calculation, the extra airflows through the ridge and both end wall openings break this simple estimation. Figures 5.10 to 5.14 show the large effects of the ridge types, as well as end wall and sidewall openings on the internal pressure coefficients, Cp_{in}, which completely change the total ventilation rate, Q_T through each opening. Even with an increase of ΔCps across the sidewall with the 1100 mm sidewall, the extra ventilation rates produced by enlarging the sidewall area from 800 mm to 1100 mm are just sufficient to have similar C_{q10} values for θ = 90° to 30°, but not enough for θ = 20° to 0°, with closed end walls. With open end walls, the extra ventilation rates through the end walls added to the ridge ones are the main cause of the lower C_{q10} values with the 1100 mm sidewall openings.

With the 400 mm ridge, the results in Fig. 5.48 show higher C_{q10} values with the 800 mm sidewall for closed and open end walls, for all angles.

The results in Figs. 5.46 (chimney) and 5.47 (150 mm ridge) with closed end walls suggest that the sidewall opening area has a linear effect on the Q_T since the C_{q10} values are nearly identical. Then, if the sidewall opening area are doubled, the Q_T would also be doubled. With open end walls, this direct relationship does not apply anymore. By doubling the sidewall area, the ventilation rates would be increased by a slightly lower factor.

With the 400 mm ridge, C_{q10} values of Fig. 5.48 suggest that the linear relationship between the 800 mm and 1100 mm sidewall openings and the Q_T would never apply since the C_{q10} values with the 1100 mm sidewall are always different for both closed or open end walls.

5.5.1.3 Effect of end wall openings

The results in Figs. 5.46 (chimney), 5.47 (150 mm ridge) and 5.48 (400 mm ridge) indicate that the addition of end wall

openings greatly increases the C_{q10} values for all wind angles. Figures 5.26 (OP-CH-800-C) to 5.29 (OP-CH-1100-O) show that open end walls create various changes in ΔCps around the sidewalls and ridge openings as well as cause large effects on the internal pressure coefficients (Figs. 5.13 and 5.14). However, the major contribution to the increase of the ventilation rates are due to the extra ventilation by the end wall openings themselves.

For example, the chimney tests with 800 mm sidewall, at $\theta = 0°$, $C_{q10} = 0.26$ with open end walls and $C_{q10} = 0.20$ with closed end walls. This would mean a 30% increase in the ventilation rates (0.26-0.20)/0.20 x 100% = 30%). When they are open, the end wall openings produce 24 000 mm^2 of opening area (4 x 60 mm x 100 mm) while the total sidewall area is 88 000 mm^2 (20 x 40 mm x 110 mm) with the 800 mm sidewall and 121 000 mm^2 (20 x 55 mm x 110 mm) with the 1100 mm sidewall. Then, the addition of the end wall openings cause a 27% increase in the total sidewall openings (24 000 mm^2/88 000 mm^2) x 100% = 27% with the 800 mm sidewall and a 20% increase with the 1100 mm sidewall. This quick estimation would lead one to say that an increase in the total sidewall area with open end walls would lead to a higher percent increase in the ventilation rates at $\theta = 0°$ with chimney. Table 5.8 presents a compilation of the percentages in ventilation rate increases, from the C_{q10} values for closed versus open end walls at $\theta = 0°$ and 90°.

The results show that open end walls have a different effect for each building configuration. The percent increases are higher for all ridge types and their respective sidewall opening at $\theta = 0°$ versus $\theta = 90°$. This is mainly due to the fact that the reference initial C_{q10} values are always higher with $\theta = 90°$. Generally, the C_{q10} values with open end walls are about 0.05 to 0.06 higher with the chimney and 150 mm ridge and 0.04 higher with the 400 mm ridge at $\theta = 0°$.

Table 5.8 Percent increases of the ventilation rate coefficients with open end walls at = 0° and 90°.

Description	θ = 0° C_{Q10}	θ = 0° % Increase	θ = 90° C_{Q10}	θ = 90° % Increase	% Increase in Total Sidewall Area
CH-800-C	0.20		0.39		
CH-800-O	0.26	30%	0.46	18%	27%
CH-1100-C	0.19		0.39		
CH-1100-O	0.24	26%	0.45	15%	20%
150-800-C	0.22		0.43		
150-800-O	0.27	23%	0.48	12%	27%
150-1100-C	0.20		0.43		
150-1100-O	0.25	25%	0.46	7%	20%
400-800-C*	0.27		0.50		
400-800-O	0.41	52%	0.51	2%	27%
400-1100-C	0.33		0.49		
400-1100-O	0.36	9%	0.50	2%	20%

* At θ = 0°, some -Cps measurement errors at the ridge level occurred during the wind tunnel tests.

The addition of end wall openings is more efficient when the chimney and the 150 mm ridge are used because the relative percentage increase on the total ventilation rate is higher with smaller ridge openings. Generally, at θ = 0°, the addition of 20% or 27% of total sidewall area with open end walls causes an increase in the C_{Q10} value from 23% (OP-150-800-O) to 30% (OP-CH-800-O). Therefore, end wall openings are very effective for increasing ventilation rates.

5.5.1.4 Effect of ridge openings

The C_{q10} values for the chimney, simulated 150 mm and 400 mm ridge openings with 800 mm sidewall are presented in Fig. 5.49. The highest C_{q10} values are obtained with the 400 mm ridge opening for all θ, with the exception of OP-400-800-C at θ = 0° to 30° due to experimental error. The OP-CH-800-C test presents the lowest C_{q10} values for all angles. It appears that the addition of two end wall openings produces higher C_{q10} values than replacing the chimneys by the 150 mm ridge opening. The graph with the 1100 mm sidewall opening data (Appendix I) shows similar curve shapes.

Comparisons on the ventilation rate efficiencies among the ridge types are presented in Table 5.9. The increase in the C_{q10} values are based on the reference C_{q10} value. For example, at θ = 0°, with OP-CH-800-C, C_{q10} = 0.20 and with OP-150-800-C, C_{q10} = 0.22; then the percent increase is: (0.22-0.20)/0.20 x 100% = 10%. The first value in the grouping indicates the reference C_{q10} value. Compared to open end walls, it is not possible to establish a percent increase of the sidewall opening area with the ridge openings. The relative percent increase of ventilation rate coefficient is compared with the relative percent of the ridge opening area over the sidewall area. For example, the chimneys have 2 704 mm^2 of opening area over 88 000 mm^2 for the 800 mm sidewall, representing a 3% of the sidewall area.

At θ = 0°, the use of the 150 mm ridge versus the chimney (800 mm - closed end walls) provides an increase of 10% for the C_{q10} with a ridge opening area increase from 2 704 mm^2 (chimney) to 9 000 mm^2 (150 mm ridge). Generally, using a 150 mm ridge versus a chimney produces a small increase of between 4% to 10%, in the C_{q10}. This would represent a ridge opening area increase from 3% to 10% of the total sidewall area. When the chimney is replaced by a 400 mm ridge, the C_{q10}

Table 5.9 Percent increases of the ventilation rate coefficients with the chimney, simulated 150 mm and 400 mm ridge openings for θ = 0° and 90°.

	θ = 0°			θ = 90°			% Ridge/ Sidewall Area
Description	C_{q10}	% Increase		C_{q10}	% Increase		
CH-800-C	0.20			0.39			3%
150-800-C	0.22	10%		0.43	10%		10%
400-800-C*	0.37	23%	35%	0.50	16%	28%	27%
CH-800-O	0.26			0.46			3%
150-800-O	0.27	4%		0.49	7%		7%
400-800-O	0.41	52%	58%	0.51	4%	11%	22%
CH-1100-C	0.19			0.39			3%
150-1100-C	0.20	5%		0.43	10%		10%
400-1100-C	0.32	60%	65%	0.49	14%	26%	27%
CH-1100-O	0.24			0.45			3%
150-1100-O	0.25	4%		0.46	2%		7%
400-1100-O	0.36	36%	50%	0.50	9%	11%	22%

Percent of ridge/sidewall area		
Ridge area	Sidewall area 88 000mm^2	121 000mm^2
chimneys, 4 x 26mm x 26mm = 2 704mm^2	3%	2%
150 mm, 1 200mm x 7.5mm = 9 000mm^2	10%	7%
400 mm, 1 200mm x 20mm = 2 400mm^2	27%	22%

* Potentially a too high C_{q10} value at θ = 0° for OP-400-800-C, due to -Cps experimental measurement errors.

value for the 800 mm sidewall, closed end walls, would be increased by 35% if this value had not been affected by some recording problems in the wind tunnel. Now, the ridge opening area represents 27% of the total sidewall area instead of only 3%.

The increase in C_{q10} values among the chimney, 150 mm and 400 mm ridges reflects the noticed changes in Cp distributions around the building, and Cp_{in} due to the ridge types and the effective opening areas which linearly influence Q_T. The comparisons between the OP-150-800-C versus the OP-400-800-C, show that there would be a C_{q10} value increase of 23% with only 17% increase in area based on the total sidewall.

Generally, the percentages of increase for C_{q10} values are the highest for the model with the smallest opening areas for the ridge, sidewall and closed end walls.

At $\theta = 90°$, there is generally an increase of the C_{q10} values when larger ridge opening areas are used, but at a lower percent when compared to $\theta = 0°$. With the present data, the most remarkable benefits of using a 400 mm ridge would come with the 1100 mm sidewall and closed end walls.

5.5.1.5 Effect of added openings on predicted ventilation rates

Most designers desire to know what would be the most efficient and economical type of opening to enlarge in order to increase the ventilation rates if needed. The direct comparisons among the present C_{q10} curves provide the relative effect of end walls and ridge, but if the sidewall area is the reference opening area, it would appear as though sidewall area is added without an increase in the ventilation rate. Table 5.10 presents calculations on the predicted ventilation rates where the sidewall, end walls and ridge opening have been enlarged by 24 000 mm^2 as compared to the basic OP-CH-800-C test.

For this particular building shape, the most efficient way to increase the ventilation rate, if a 24 000 mm^2 area had to be added, is to considerably enlarge the ridge opening area to 400 mm. The second most profitable option would be to place 24 000 mm^2 of end wall openings or, finally, to enlarge

Table 5.10 Percent increases of the total ventilation rates by adding 24 000 mm^2 of sidewall, end wall or ridge opening areas.

Description	C_{Q10}		Velocity (m/s)		Sidewall Area (mm^2)		Q_T	Ventilation Rate Increases by
CH-800-C	0.20	X	1	X	88 000	=	17 000	
150-800-C[1]	0.22	X	1	X	88 000	=	19 360	10%
CH-1100-C[2]	0.19	X	1	X	112 000	=	22 280	27%
CH-800-O[3]	0.26	X	1	X	88 000	=	22 800	30%
400-800-C[4]	0.27	X	1	X	88 000	=	23 760	40%

1 - Adding 6 296 mm^2 of ridge area.
2 - Adding 24 000 mm^2 of sidewall area.
3 - Adding 24 000 mm^2 of end wall area.
4 - Adding 21 296 mm^2 of ridge area (24 000 mm^2 - 2 704 mm^2), the strict addition of 24 000 mm^2 would probably produce a slightly higher C_{Q10} value. Note that the C_{Q10} value at $\theta = 0°$ may have been impaired by -Cp experimental errors in the wind tunnel with OP-400-800-C.

the total sidewall area by 24 000 mm^2. An interesting phenomenon is that opening the sidewalls or end walls would produce 27% and 30% greater ventilation rate as compared to only 10% if the chimneys are replaced by a 150 mm ridge opening. This fact shows the non-linear relationship between the increase of the ridge opening area and the total ventilation rates.

It should be remembered that these percentages apply only when the OP-CH-800-C model is used as the starting basis. As reported on Table 5.9, each change in the basic building configuration would have different effects on the increase of the total ventilation rate.

Careful designers should assess the costs/ratios of using one or another type of building openings in order to provide the desired ventilation rate at the lowest cost.

5.5.1.6 Discussion on the methodology used

The use of the sidewall opening area, A_s, as a reference opening area may have been very appropriate to Vickery et al. (1983), ASHRAE (1989) and many other authors where no ridge or end wall openings were used. For these building prototypes, it would be recommendable to use only a C_{q10} coefficient which would also contain the total opening areas around the building, as Eq. 5.2.

$$C_{q10} = C_d \sum \frac{Cp_j - Cp_{in}}{|Cp_j - Cp_{in}|^{\frac{1}{2}}} \times A_T \qquad (5.2)$$

where:

A_T = total opening areas

With this procedure, the effects of the ridge versus end wall versus sidewall openings would be reflected directly by the dimensionless C_{q10} value.

Generally, the comparisons of the ventilation rate coefficients, C_{q10} , and the predicted ventilation rates among the chimney, simulated 150 mm or 400 mm ridges used in combination with the simulated 800 mm or 1100 mm sidewall opening with closed or open end walls reveal that

1 - Generally, C_{q10} curves plotted against θ, have similar shapes, with the maximum C_{q10} value at $\theta = 90°$, the minimum C_{q10} value at $\theta = 10°$, and most curves show the largest drop in C_{q10} between $\theta = 45°$ to $20°$.

2 - Using the chimney and 150 mm ridge, the C_{q10} values are not influenced by the 800 mm sidewall openings versus the 1100 mm sidewall opening when the end walls are closed. The C_{q10} values are generally lower with the 1100 mm sidewall as compared to the 800 mm sidewall opening.

3 - According to the present building configurations with chimney or 150 mm ridge, the total ventilation rates, Q_T would be increased by a linear factor or less by

enlarging the sidewall opening areas. Then, if the sidewall area is doubled, the Q_T would be doubled or slightly less than doubled.

4 - The use of end wall openings generally increase the C_{q10} values and consequently the total ventilation rate for both 800 mm and 1100 mm sidewall opening used with each type of ridge opening.

5 - The greatest effects of end wall openings are noticed at $\theta = 0°$ with the building configuration presenting the smallest openings, such as the chimney with 800 mm sidewall openings. The end wall opening efficiency reduce gradually when larger sidewall and ridge opening areas are used.

6 - At $\theta = 0°$, the use of the 150 mm ridge opening versus the chimney would increase the C_{q10} values between 4% to 10% for all tested sidewall and end wall opening areas while enlarging the ridge to 400 mm would increase C_{q10} values from 23% to about 65%.

7 - From the present data, it appears that the relationship between the ridge opening areas and the ventilation rate coefficients would not be linear at $\theta = 0°$ based on using the OP-CH-800-C as the basic model and the sidewall opening area as the standard value for the C_{q10} calculations.

For studying naturally ventilated buildings with sidewall, end wall and ridge openings, it is recommended that the total opening area of the building should be used as the reference area for the calculation of the C_{q10}.

5.5.2 Sealed model

The results of the C_{q10} values for the chimney, simulated 150 mm and 400 mm ridges are presented in Figs. 5.50 to 5.52. The complete data set is in Appendix I. With the chimney and the 150 mm ridge, the maximum C_{q10} value occurs at $\theta = 90°$ while the lowest one are at $\theta = 0°$. With the 400 mm ridge

(Fig. 5.52), the maximum C_{q10} value is noticed at $\theta = 60°$ and the minimum at $\theta = 10°$ with the closed end walls, and $\theta = 0°$ with the open end walls.

With the closed end walls, the C_{q10} values are reduced by 40% to 45% (for SE-400-800-C and SE-CH-1100-C, respectively) from $\theta = 90°$ to 0°. The C_{q10} values appear to be less affected with open end walls. When the wind angles change from 90° to 0°, a C_{q10} reduction of 35% to 40% (for SE-400-800-O and SE-CH-1100-O tests, respectively) is calculated.

5.5.2.1 Effect of sidewall openings

Since the sidewall opening areas are used as the basic reference area for the calculation of the C_{q10} values, it is expected that the C_{q10} values should remain unchanged if the sidewall opening area is enlarged by a given percent and the total ventilation rate is also increased by the same percent. However, the total ventilation rate is equal to the sum of the airflow rates through the sidewall, end walls and ridge openings.

The results in Figs. 5.50 (chimney), 5.51 (150 mm ridge) and 5.52 (400 mm ridge) demonstrate that the C_{q10} values with the 800 mm sidewall openings are always higher for all wind angles. This phenomenon is explained by the fact that, by enlarging the sidewall area from 800 mm to 1100 mm, the ventilation rate through the sidewall increases linearly, but the airflows through the ridge and the end wall openings remain unchanged. When the C_{q10} value is calculated from the new total ventilation rate and divided by the new reference opening area (1100 mm sidewall), the increase in the total ventilation rate is not sufficient to compensate for the enlargement of the new sidewall opening area. The difference between the C_{q10} values with 800 mm and 1100 mm sidewalls is increased when larger ridge openings and open end walls are used.

In Fig. 5.52 (400 mm ridge), C_{q10} values with the 800 mm sidewall are always higher for all angles, but the SE-400-800-C curve crosses the SE-400-1100-O at θ = 45°. Since the ΔCps across the sidewall are never changed with the simulated 800 or 1100 mm sidewall, and the extremely high negative ΔCps recorded over the ridge opening, and the higher Cp_{in} with open end walls all suggest that the sealed model results predict greater ventilation rate coefficients occurring at θ = 90° to 30° with the 800 mm sidewall with closed end walls versus the 1100 mm sidewall with open end walls.

5.5.2.2 Effect of end wall openings

Generally, the addition of end wall openings strictly add inflows and outflows to the total ventilation rate. Then, for each ridge type and simulated 800 or 1100 mm sidewalls, all the C_{q10} values increase when end walls are opened.

5.5.2.3 Effect of ridge openings

The ridge effects could be visualised in Fig. 5.53 where the C_{q10} curves for the chimney, simulated 150 mm and 400 mm ridges are plotted using the same 800 mm sidewall, with closed or open end walls. With closed end walls, as well as with open end walls, the lowest to the highest C_{q10} values are observed with the chimney followed by the 150 mm ridge and finally by the 400 mm ridge. Large differences among the three ridge types are noticeable, especially at θ = 60° to 20° when the ΔCps over the 400 mm ridge (Fig. 5.28) are considerably higher than the chimney and 150 mm ΔCps (Figs. 5.26 and 5.27). For θ = 20° to 0°, the ΔCps are similar over the three ridges, but the larger effective ridge opening areas directly increase the total ventilation rates.

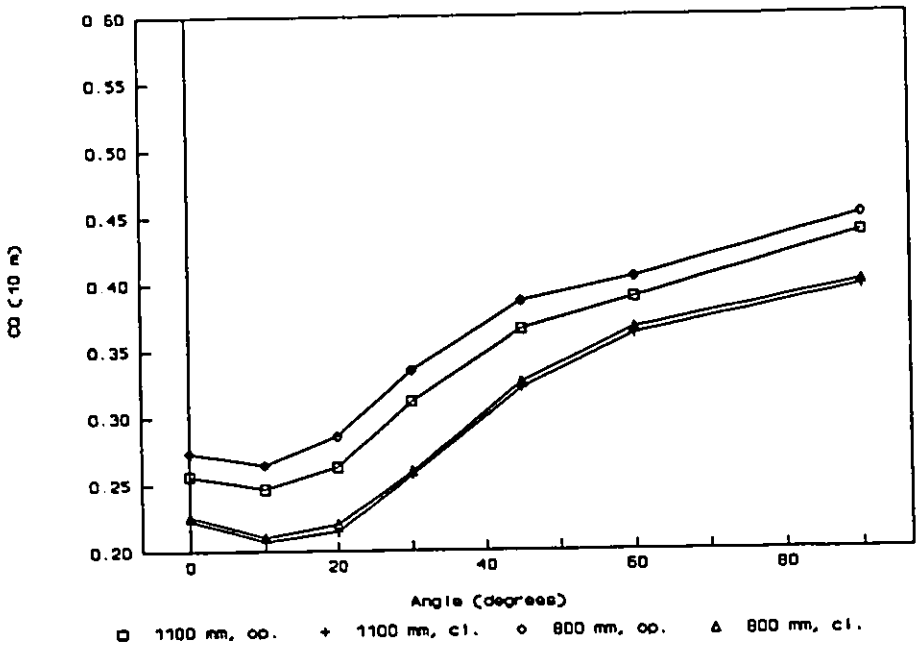

Figure 5.50 Sealed model ventilation rate coefficients, C_{Q10}, chimney.

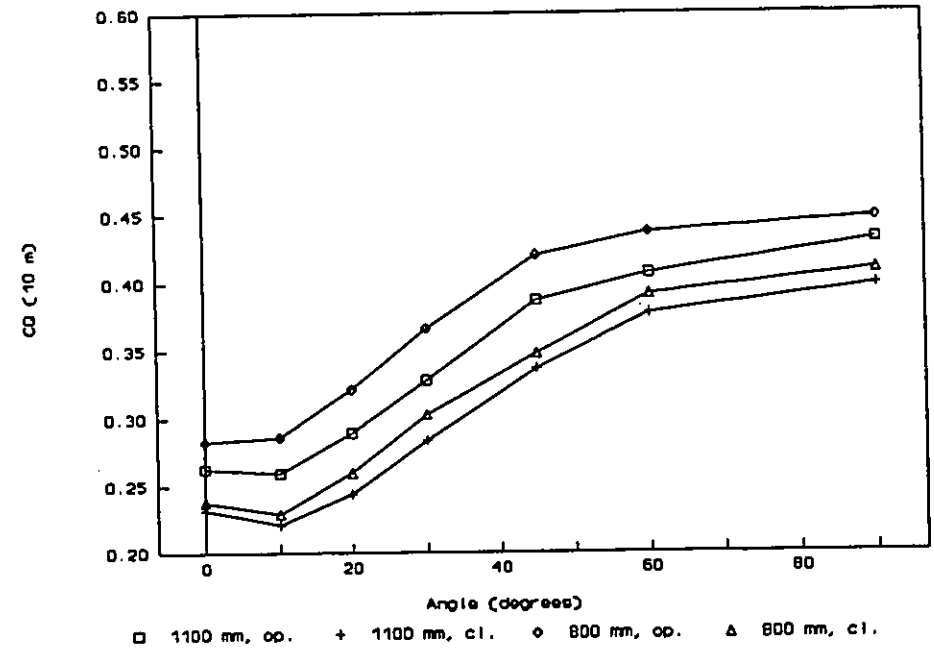

Figure 5.51 Sealed model ventilation rate coefficients, C_{Q10}, simulated 150 mm ridge .

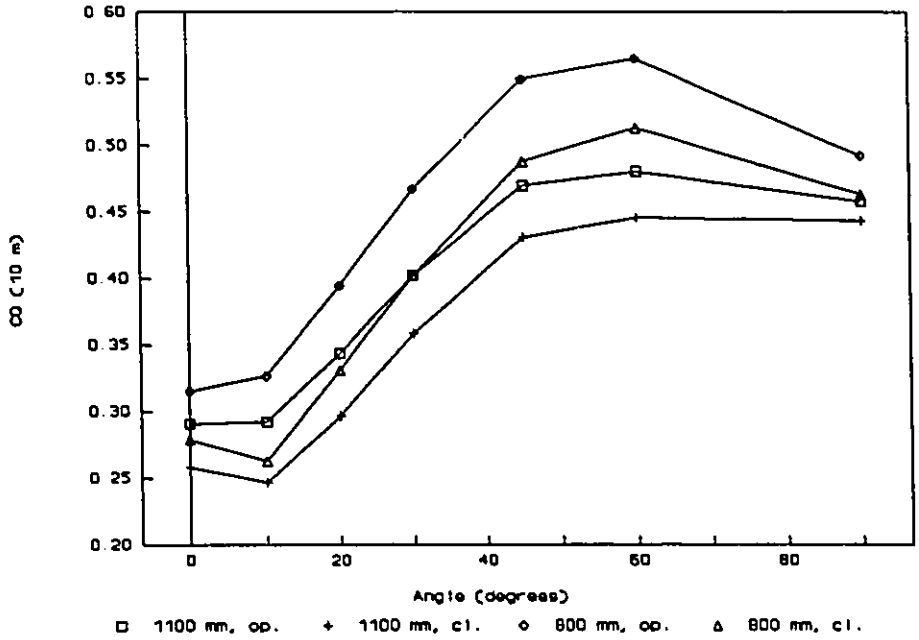

Figure 5.52 Sealed model ventilation rate coefficients, C_{Q10}, simulated 400 mm ridge.

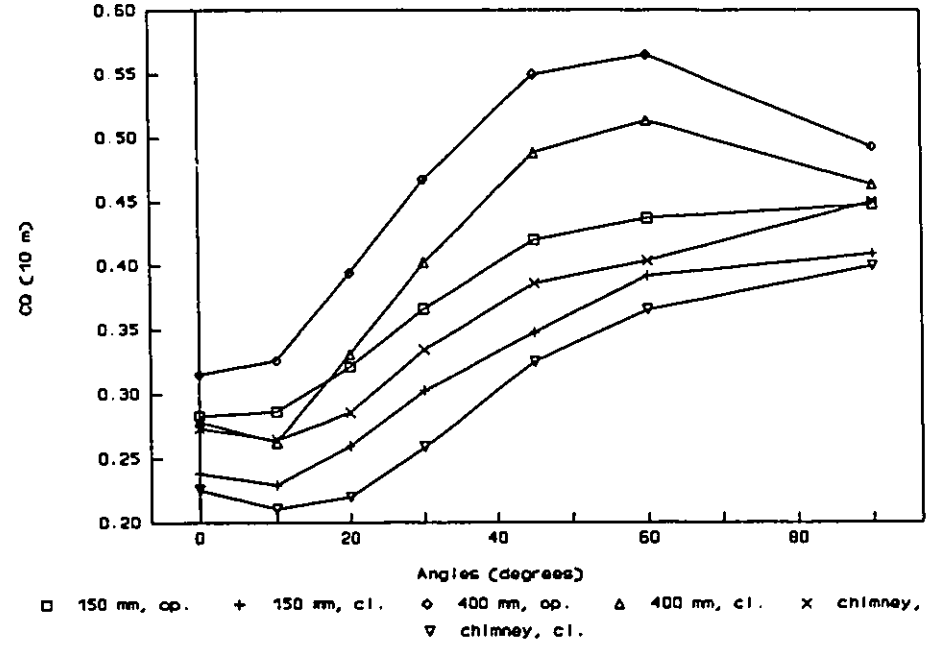

Figure 5.53 Sealed model, comparison among chimney, simulated 150 mm and 400 mm ridges with simulated 800 mm sidewall.

Generally, the results for the ventilation rate coefficients, C_{q10}, with the sealed model reveal that:

1 - With the chimney and 150 mm ridge, the maximum C_{q10} values are calculated for $\theta = 90°$, the minimum C_{q10} are at $\theta = 10°$. With the 400 mm ridge, the maximum and minimum C_{q10} values are calculated for $\theta = 60°$ and $\theta = 10°$ to $0°$, respectively.

2 - C_{q10} values with the 800 mm sidewall are always higher than the 1100 mm sidewall for all angles and ridge types.

3 - Opening end walls substantially increases the C_{q10} values for each ridge type, and both sidewall openings for all wind angles.

4 - For all angles, 800 mm or 1100 mm sidewall with closed or open end walls, the larger ridge opening area always causes the C_{q10} values to increase.

5.5.3 Open versus sealed models

Figures 5.54 (chimney), 5.55 (150 mm ridge) and 5.56 (400 mm ridge) present the C_{q10} value differences between the open and the sealed model. The tabulated results are added in Appendix I.

With the chimney, the C_{q10} values of Fig. 5.54 are generally higher for $\theta = 90°$ to $30°$ and then lower for $\theta = 20°$ to $0°$. Then the results of the open model versus the sealed model suggest higher ventilation rates for wind perpendicular to the building length down to $\theta = 30°$ with the open model while the results constantly show lower ventilation rates for the critical wind angles of $\theta = 20°$ to $0°$. Similar results are shown in Fig. 5.55 with the 150 mm ridge. In Fig. 5.56, the C_{q10} values are generally higher with the open model for all angles except with the 400-800-C tests.

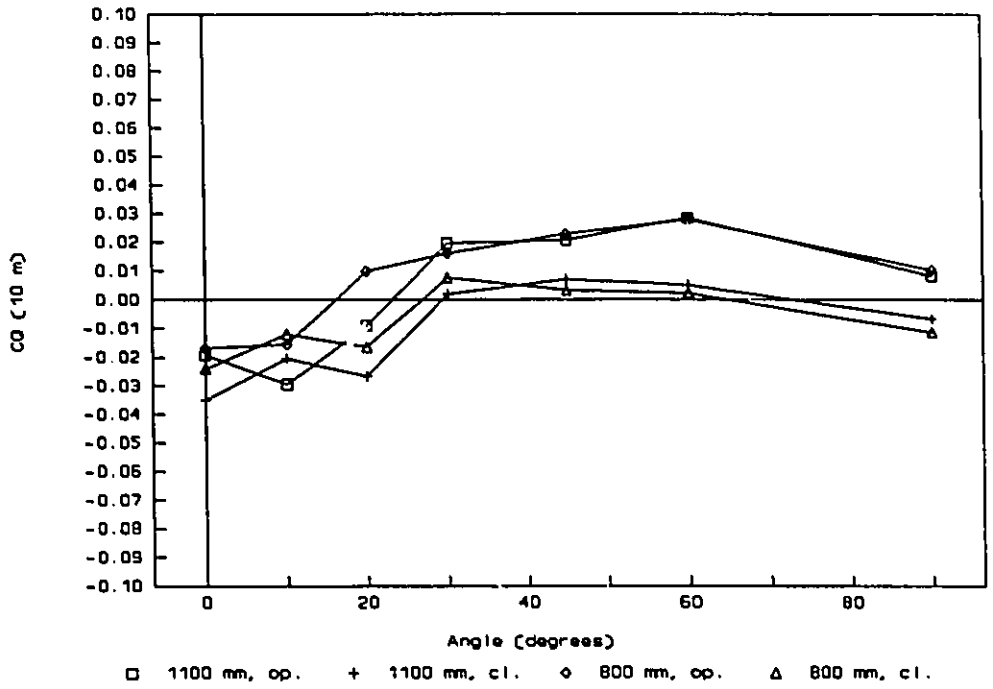

Figure 5.54 C_{q10} differences (open - sealed), chimney.

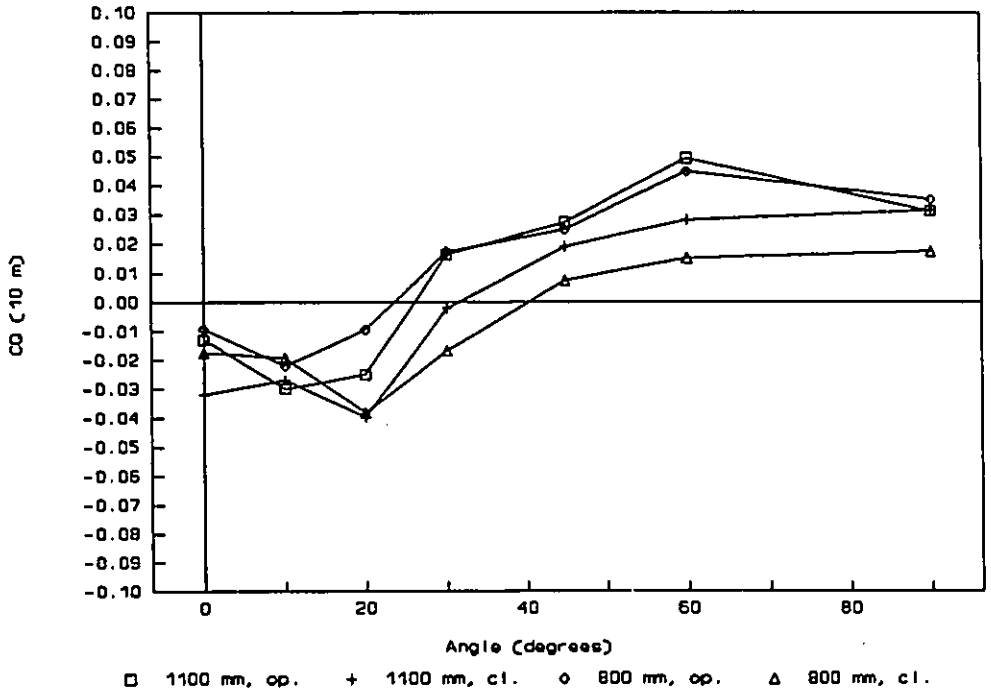

Figure 5.55 C_{q10} differences (open - sealed), simulated 150 mm ridge .

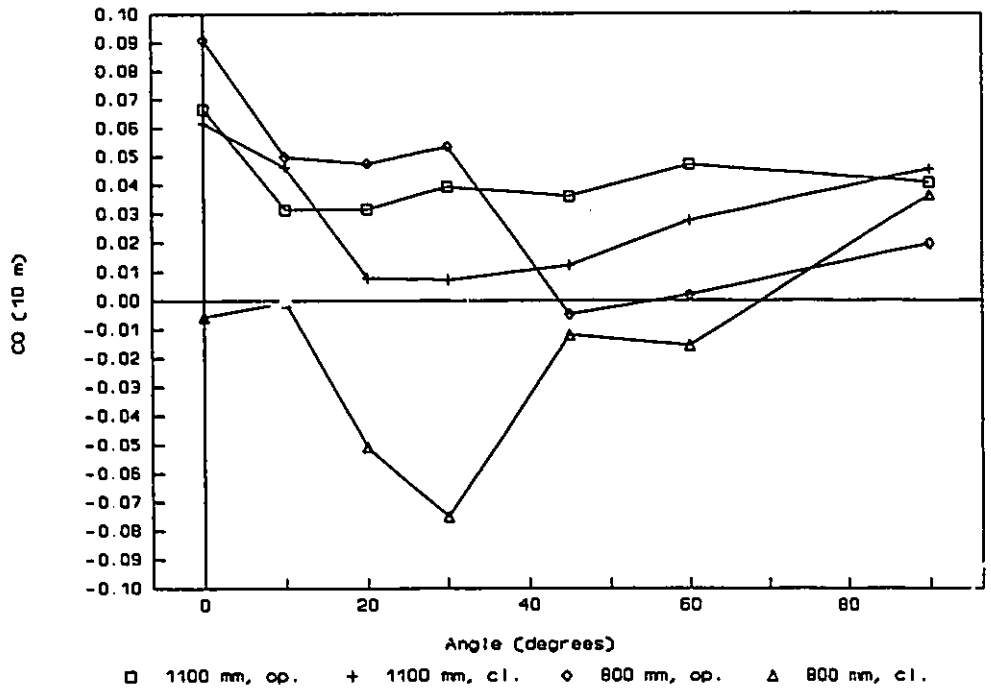

Figure 5.56 C_{q10} differences (open - sealed), simulated 400 mm ridge.

5.5.3.1 Effect of sidewall openings

From Fig. 5.54 (chimney) there are few effects by the 800 mm or 1100 mm sidewall opening on the differences between the C_{q10} values of the open and the sealed model. With the 150 mm ridge and the 400 mm ridge, the 1100 mm sidewall show higher departures of the sealed model's C_{q10} values with closed or open end walls.

5.5.3.2 Effect of end wall openings

The results in Figs. 5.54 (chimney) and 5.55 (150 mm ridge) indicate that the C_{q10} value differences are higher for $\theta = 90°$ to 30° with both 800 mm and 1100 mm sidewall when with open end walls than with any others. The results in Fig. 5.56 (400 mm ridge) follow that trend with the exception of the 400-800-C test. The contrast, between wind angles of 0° to 20°, the higher C_{q10} differences between the sealed and open model occur with the closed end walls.

5.5.3.3 Effect of ridge openings

Comparisons between Figs. 5.54 (chimney) and 5.55 (150 mm ridge) show consistently higher differences of C_{q10} values between the open and sealed model with the 150 mm ridge versus the chimney for $\theta = 90°$ to 20°. The C_{q10} differences are similar for both ridge types at $\theta = 0°$ and 10°. With the 400 mm ridge (Fig. 5.56), the curves are more dispersed. This indicates that the C_{q10} values with the sealed model are consistently under-predicting the ventilation rate coefficients. The absolute values for the differences are generally higher with the 400 mm ridge as compared to the chimney or 150 mm ridge.

From the observations of the differences of C_{q10} values between the open and sealed models, the results show that:

1 - The C_{q10} values with the chimney and 150 mm ridge for the open models are higher than the sealed models at $\theta = 90°$ to 30° and lower at $\theta = 20°$ to 0°. The C_{q10} values are

usually higher with the open model for all angles with the 400 mm ridge.

2 - The C_{q10} differences (open-sealed) are consistently higher with the 1100 mm versus the 800 mm sidewall for all ridge types and both open or closed end walls.

3 - The C_{q10} differences (open-sealed) with open end walls are considerably higher for θ = 90° to 30°, but in contrast, the C_{q10} differences with closed end walls are higher for θ = 0° to 20°.

4 - The differences between the C_{q10} values of the open and the sealed model are generally higher when the ridge opening area is increased from the chimney to the 400 mm ridge.

Generally, the results on the differences of C_{q10} values (open-sealed) would lead one to believe that the larger the total opening areas are on the sidewalls and end wall openings and at the ridge level, the larger the discrepancies in C_{q10} values are between the open and sealed model.

5.6 Effective ventilation rate coefficients measured by the concentration decay method

An attempt was made to obtain the effective ventilation rate coefficients, C_{KQ10}, based on the concentration decay method. An optical density device (laser and silicone diode detector) was used to measure the rate of decay of injected smoke in the scale model. The optical density readings were then transformed according to the rate of decay model in order to obtain a measurement of C_{KQ10} (Appendix D).

These measured ventilation rate coefficients were "effective" because they represent an average C_{KQ10} for the entire building length at the center width and 1.5 m above the floor (full scale). The effective ventilation rate, KQ, measurements include the controversial mixing factor.

As reported in Appendix J, most of the curve correlation factors were very high (between 0.980 and 0.999) which shows

a relatively good application of the rate of decay model from Eq. 4.9, even with the smoke contamination in the wind tunnel.

Five repetitions were done for each wind angle and building configurations. The complete results are in Appendix J.

Table J.1 presents the results of the average C_{KQ10} values and their standard deviations based on the five replicates. Figures J.1 to J.3 show the standard deviation (StD) for the C_{KQ10} for each wind angle of incidence. Generally, higher values of StD are obtained for θ = 30° to 60°, but overall, the standard deviations are fairly low.

There is no apparent relationship on the 800 mm or 1100 mm sidewall, open or closed end walls, or types of ridge opening on the different StD values.

It should be noticed that the higher standard deviations occur mainly for θ = 30° to 60° which coincide with higher ventilation rate coefficients C_{KQ10} (Figs. 5.57 to 5.59). With the concentration decay method, higher ventilation rates mean lower a number of data points and consequently a shorter decay period. This may lead to a potentially larger error margin. The selection of the lowest possible wind speed in the wind tunnel would be one way to alleviate this problem. One other way would be to use multiple optical density devices and then, reduce the path length, L. One added advantage of multiple point sampling would be the possibility to study the mixing phenomenon at different building locations.

The values for the standard deviations should be regarded with care simply because of the limited number of replications. The observation of the five C_{KQ10} values reveals very low variations among them (Appendix J). There are some exceptions, such as the test OP-CH-800-0 at θ = 30° where the StD = 0.10. By coincidence, the average curve fitting correlation factor is about 0.90. During this experiment, some problems with the smoke injection system occurred and the rate of decay curve showed bumps and irregularities. The same

phenomenon occurred for the OP-150-1100-C test at θ = 30° where StD = 0.17 and the average curve fit correlation factor is equal to 0.96. It appears that leakages through the gravity valves of the smoke injection system was one of the major sources of error. Sealed shut-off valves should be used for subsequent experiments.

For the OP-400-1100-C at θ = 60°, the average correlation curve fit is about 0.98, but the C_{KQ10} values differ widely and the standard deviation is equal to 0.11. This shows that the optical density techniques require some refinements. One major avenue of work would be on the mathematical treatment of the data. Presently, the initial and final cut-off points have to be decided by the interpreter. Even if consistency was attempted, there are always some variations among the tests concerning which part of the curve is representative of the rate of decay or not. Also, the use of a simple correlation factor for each curve and standard deviation for the five replicates should be changed in order to evaluate a more realistic average C_{KQ10} standard deviation and standard error for all the data points of the five replicates. This is beyond the scope of these preliminary trials.

Consequently, the major part of the average C_{KQ10} values may be considered to be fairly accurate, but the ones with low curve fit correlation factors (below 0.98) and high standard deviations should be regarded with scepticism.

5.6.1 General observations

Figures 5.57 (chimney), 5.58 (150 mm ridge) and 5.59 (400 mm ridge) show the C_{KQ10} curves for the simulated 800 mm and 1100 mm sidewall, with closed and open end walls. At θ = 90°, the C_{KQ10} values vary from 0.40 (OP-400-1100-C) to 0.48 (OP-150-800-C) and at θ = 0°, from 0.21 (OP-CH-1100-O) to 0.35 (OP-400-800-C). The range of 0.2 to 0.3 for θ = 0° recommended by ASHRAE (1989) would be appropriate, but the values of θ = 0.5 to 0.6 at θ = 90° would be too high.

Surprisingly, this range of the maximum C_{KQ10} values is obtained for θ = 45° and 60° according to the various building configurations.

All curves show an increase in C_{KQ10} values from θ = 90° to 45° and 60°. This means that the effective ventilation rates would be higher when the wind angles of incidence are not perfectly perpendicular to the building length. The C_{KQ10} values at θ = 90° are fairly close together for all tests of Figs. 5.57 to 5.59. The data points are more spread for θ = 45° to 60°. The major drops of C_{KQ10} values occur between θ = 45° to 20°.

Generally, the highest and lowest values of C_{KQ10} are obtained with the closed end walls situation.

In all Figs. at θ = 30°, there is a crossing of the high C_{KQ10} values with closed end walls to become the lowest values at θ = 20° or 10°. This switch is evident in Figs. 5.58 (150 mm ridge) and 5.59 (400 mm ridge). Also, the C_{KQ10} drops occur at a smaller wind angle of incidence when the 400 mm ridge is used as compare to the chimney.

Choinière et al. (1988c) reported the major changes of airflow patterns and observed recirculation and stagnant zones at wind angles of incidence from 0° to 30°. Finally, the lowest C_{KQ10} values occur for angles between 0° to 20°.

Table 5.11 reports the maximum-minimum C_{KQ10} values and their respective wind angles of incidence.

The highest peak obtained for the OP-CH-1100-C test (Fig. 5.57) may be disregarded because of the poor curve fit correlation factor and its high standard deviation (Table 5.11). Most of the high StD are observed with the high C_{KQ10} values and especially with the closed end walls. Most of the measurements of low ventilation rates showed very little standard deviation.

Table 5.11 Maximum-minimum C_{Q10} values with their wind angle of incidence.

Description	C_{Q10} Maximum	C_{Q10} Minimum	Wind angles (degrees) Maximum	Wind angles (degrees) Minimum
CH-800-C	0.57	0.21	60°	20°
CH-800-O	0.52*	0.25	45°	10°
CH-1100-C	0.76***	0.20	60°	10°
CH-1100-O	0.47	0.21	60°	10°
150-800-C	0.54	0.25	60°	10°
150-800-O	0.48	0.26	90°	0°
150-1100-C	0.62	0.27	45°	10°
150-1100-O	0.52	0.22	45°	0°
400-800-C	0.64*	0.26	45°	20°
400-800-O	0.48	0.25	45°	10°
400-1100-C	0.64**	0.24	60°	10°
400-1100-O	0.48*	0.23	45°	0°

* standard deviation, $0.5 \leq StD < 0.1$
** standard deviation, $0.1 \leq StD < 0.15$
*** standard deviation, $0.15 \leq StD$

5.6.2 Effect of sidewall openings

The results in Table 5.12 suggest that the sidewall opening effect is related to the wind angle of incidence, but is independent of the end walls' status. It should be noted that all the differences between the C_{Q10} values with the 800 mm and 1100 mm sidewall are fairly small.

Table 5.12 Effects of the simulated 800 mm and 1100 mm sidewall openings on the C_{Q10} values for each type of ridge and end wall opening.

Ridge Type	Wind Angles (degrees)	Sidewall Effects on C_{Q10} Values	End Wall Openings
Chimneys	$0° \leq \theta \leq 45°$	800 > 1100	open and closed
150 mm	$10° \leq \theta \leq 30°$	800 > 1100	open and closed
	$45° \leq \theta \leq 60°$	1100 > 800	open and closed
400 mm	$0° \leq \theta \leq 20°$	800 > 1100	open and closed
	$30° \leq \theta \leq 60°$	1100 > 800	open and closed

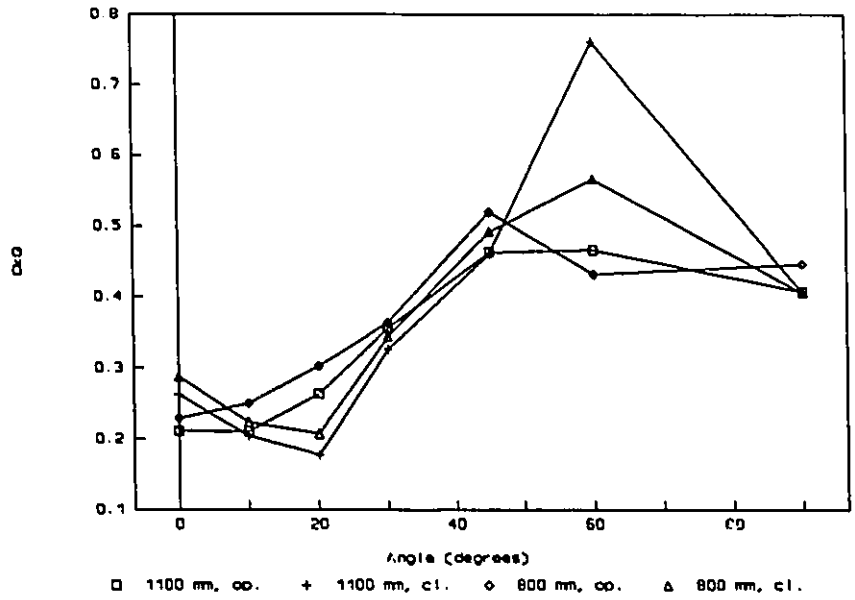

Figure 5.57 Open model, effective ventilation rate coefficients, C_{KQ10}, chimney.

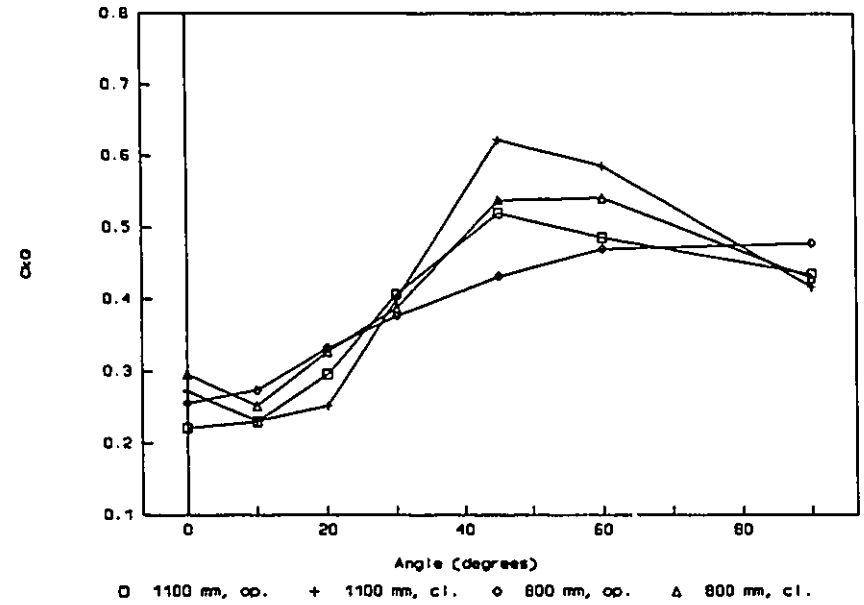

Figure 5.58 Open model, effective ventilation rate coefficients, C_{KQ10}, simulated 150 mm ridge opening.

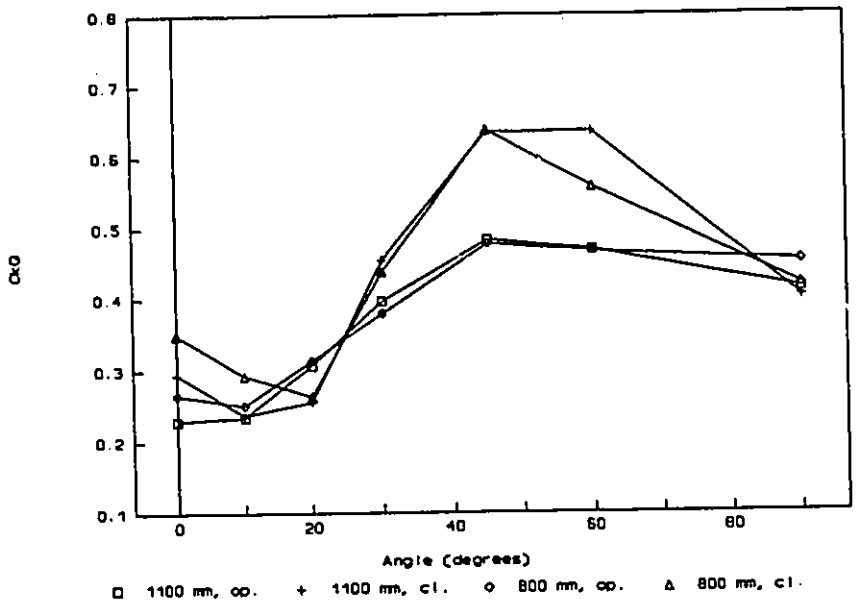

Figure 5.59 Open model, effective ventilation coefficients, C_{KQ10}, simulated 400 mm ridge opening.

It appears that for low wind angles of incidence, the C_{KQ10} values with the 800 mm sidewall are higher than with the 1100 mm sidewall and the reverse is observed for higher wind angles.

Equation 5.3 indicates that the total ventilation rate is equal to the addition of the sidewalls, ridge and end walls inflows and outflows, knowing that continuity must be respected.

$$Q_T = Q_S + Q_R + Q_E \qquad (5.3)$$

where

Q_T = total ventilation rate, m^3/s
Q_S = ventilation rate by the sidewall, m^3/s
Q_R = ventilation rate by the ridge, m^3/s
Q_E = ventilation rate by the end walls, m^3/s

The concentration decay method only provides an estimate of Q_T.

Since the C_{KQ10} values are calculated with Eq. 5.1 with the sidewall area as the basic denominator, there would be no sidewall opening effect if the C_{KQ10} values were identical. On the basis of Q_T, this means that if the sidewall area is increased by 37.5% (800 mm to 1100 mm), then Q_T will be increased by 37.5% for both situations with closed or open end walls. Table 5.13 reports two examples extracted from Fig. 5.58 using the data of Appendix J, Table J.1.

At $\theta = 45°$, Q_T increases by 58.4%. Since the end walls are closed, there are only three possibilities: Q_S or Q_R increases; Q_S increases and Q_R stays the same; or, Q_S is stable and Q_R increases. The Cp distributions in Figs. E.5c (OP-150-800-C, $\theta = 45°$) and E.6c (OP-150-1100-C, $\theta = 45°$) of Appendix E reveal that the -Cps over the ridge are identical, that the Cps on the upwind corner of the windward side are reduced, but the -Cps on the leeward side are generally increased with the 1100 mm sidewalls. The results of the Cp_{in} in Figs. 5.21 (OP-150-800-C) and 5.22 (OP-150-1100-C) show only minor local Cp_{in} differences inside

Table 5.13 Effect of sidewall areas on the increase of total ventilation rates, Q_T, measured with the concentration decay method.

Description	Wind Angles (degrees)	C_{KQ10}	Q_T[a]	Increase in Sidewall Area (%)	$\%Q_T$
OP-150-800-C	45°	0.54	23.8		
OP-150-1100-C	45°	0.62	37.7	37.5%[b]	58.4%[c]
OP-150-800-C	10°	0.25	11.0		
OP-150-1100-C	10°	0.23	13.9	37.5%	26.4%

a: $Q_T = C_{KQ10} \times Area \times 1\ m/s$ *b*: $37.5\% = \left(\frac{1100-800}{800} \times 100\%\right)$

c: $58.4\% = \left(\frac{37.7-23.8}{23.8} \times 100\%\right)$

the model, but the same Cp_{in} average. From the pressure difference method, this would mean that Q_R would be hardly affected by the larger sidewall and the major part of Q_T's increase could be directly attributed to the sidewall's Q_S.

With the present data obtained from the concentration decay method, there is no possibility to evaluate Q_S and Q_R separately. However, there are three hypotheses which could explain this 58% increase in Q_T. Firstly, the pressure difference method is under-predicting the sidewall effect (too low a C_d value or an erratic Cp_{in} evaluation). Secondly, the mixing effectiveness is increased by the larger sidewall openings, producing a higher Q_T. Thirdly, the laser beam passed through a short circuit zone which would show a higher effective ventilation rate on that specific line of reference.

Ogilvie and Boyd (1985) reported a reduction in the mixing factor with larger sidewall openings for a scale model of a monoslope naturally ventilated swine building. Although not measured, Choinière et al. (1988a) observed a potential short circuit effect during flow visualization in a wind

tunnel test of a similar gable roof building. A large clear zone along the ceiling occurred when the larger sidewall openings were used. During these present wind tunnel tests, the laser beam was too low above the floor to be in this short circuit zone, but it still may have been affected by the phenomenon.

On the other hand, at $\theta = 10°$, the effective ventilation rate has been increased by 26.4% with the 1100 mm sidewall. During the wind tunnel tests, stagnant zones have been observed at the upwind end of the scale model as reported by Choinière et al. (1988c) (Appendix F). The question again is to know if the laser beam is effectively measuring the average ventilation rate or if it was only measuring the rate of decay of this stagnant zone.

Generally, the sidewall opening areas showed the following effects for all ridge types, with closed or open end walls:

1 - For $\theta = 45°$ and 60°, the 1100 mm sidewall opening shows higher C_{KQ10} values than the 800 mm sidewall which would indicate a higher percent of increase for the effective ventilation rates as compare to the percent increase of the sidewall area.

2 - For low wind angles, $\theta = 0°$ to 20°, the C_{KQ10} values with the 800 mm sidewall are generally higher than with the 1100 mm sidewalls.

5.6.3 Effect of end wall openings

Figures 5.57 (chimney), 5.58 (150 mm ridge) and especially Fig. 5.59 (400 mm ridge) show the clear effects of end wall openings on the C_{KQ10} values. Using the results in Table 5.11, for all types of ridges with 800 mm or 1100 mm sidewalls it is noticed that:

1 - The maximum C_{KQ10} values with the closed end walls are always higher than with open end walls.

2 There are few differences in the minimum C_{KQ10} values with the 150 mm and 400 mm ridges except with the chimney, where the C_{KQ10} values with open end walls are definitively higher.

3 - Generally, the C_{KQ10} values with closed end walls are higher than with open end walls at $\theta = 0°$.

Figure 5.60 presents observations of the effects of open end walls on the airflow patterns. The flow visualisations show that there would be a strong possibility of short circuit of the incoming air when the end wall openings are used because of the short distance to travel between the air inlet and outlet zones. While the end walls are closed, the incoming air often has to cross the entire building width or a part of its length before reaching the outlet zones. As stated by Choinière et al. (1988c), the main advantages of open end walls are to eliminate the stagnant zone which occurs at the upwind end of the building with closed end walls and to show a more uniform rate of decay of the smoke throughout the building length. This is reflected by the results in Figs. 5.61 (800-C) versus 5.62 (800-O) and Figs. 5.63 (1100-C) versus 5.64 (1100-O), which demonstrate that the C_{KQ10} curves with open end walls are less subject to high and low peaks as compare to the closed end walls situation.

During the present wind tunnel tests at $\theta = 0°$ to 20°, the observations of the airflow patterns with open end walls reveal that the smoke at the upwind and downwind ends disappears faster than the smoke at the center of the building, which coincides with the trajectory of the laser beam.

There are definitely zones of under- and over-ventilation within this naturally ventilated airspace and the present concentration decay measurements indicate only the average effective ventilation rates through the building length at the

center width. From the results of the end wall opening effects on C_{KQ10}, the following points could be obtained:

1 - The maximum C_{KQ10} values are always measured with closed end walls.
2 - There is little effect by the end wall openings on the minimum C_{KQ10} values, except with the chimney when the closed end walls produce the lowest C_{KQ10} values.
3 - At $\theta = 0°$, the C_{KQ10} values with the closed end wall are always higher as compared to the open end walls.
4 - Generally, the open end wall situations show more uniform C_{KQ10} curves.

5.6.4 Effect of ridge openings

Figures 5.61 to 5.64 present the C_{KQ10} curves for the chimney, 150 mm and 400 mm ridges with each combination of sidewall and end wall openings.

With the closed end walls, Fig. 5.61 (800-C) shows similar C_{KQ10} values for all ridge types at $\theta = 90°$ and 60°. For $\theta = 45°$ to 0°, the chimney C_{KQ10} values are the lowest while the 400 mm C_{KQ10} are the highest. The same general observations can be done in Fig. 5.63 (1100-C). It should be noticed that the C_{KQ10} of 150 mm and 400 mm ridges are very close for all wind angles. Only the chimney C_{KQ10} values are visibly lower for $\theta = 0°$ to 45°.

With open end walls, Fig. 5.62 (800-O) shows little C_{KQ10} differences among the three ridge types. In Fig. 5.64 (1100-O) the C_{KQ10} values with the 150 mm ridge are the highest for $\theta = 90°$ to 45° and they coincide with the 400 mm ridge for $\theta = 30°$ to 0°. The C_{KQ10} values for the chimney are slightly lower than for the 150 mm and 400 mm ridge for $\theta = 45°$ to 0°. Again, there are only slight differences among the three types of ridges.

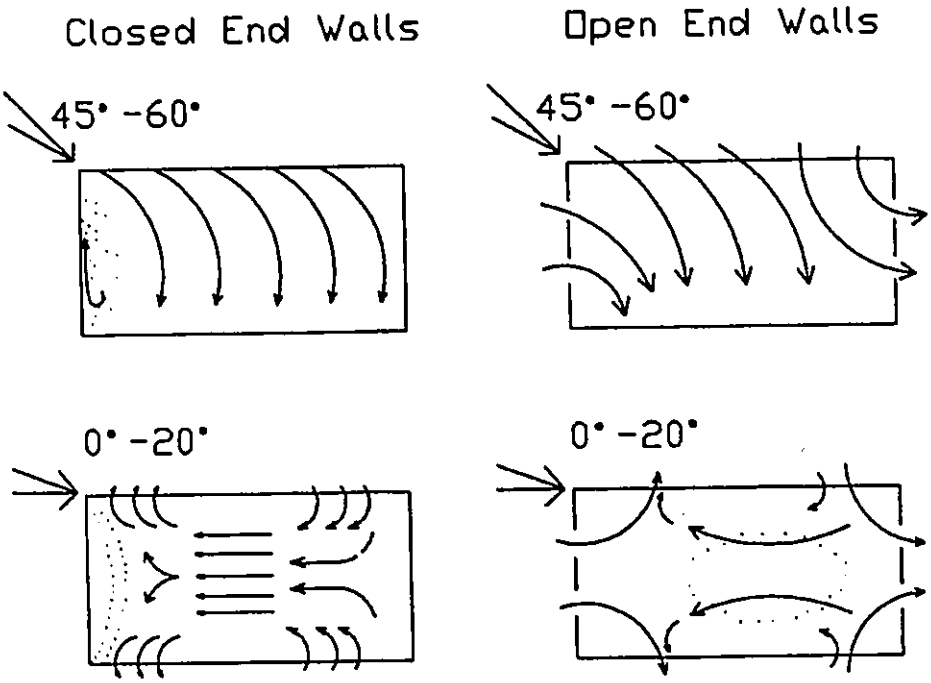

Figure 5.60 Effects of end wall openings on the airflow patterns.

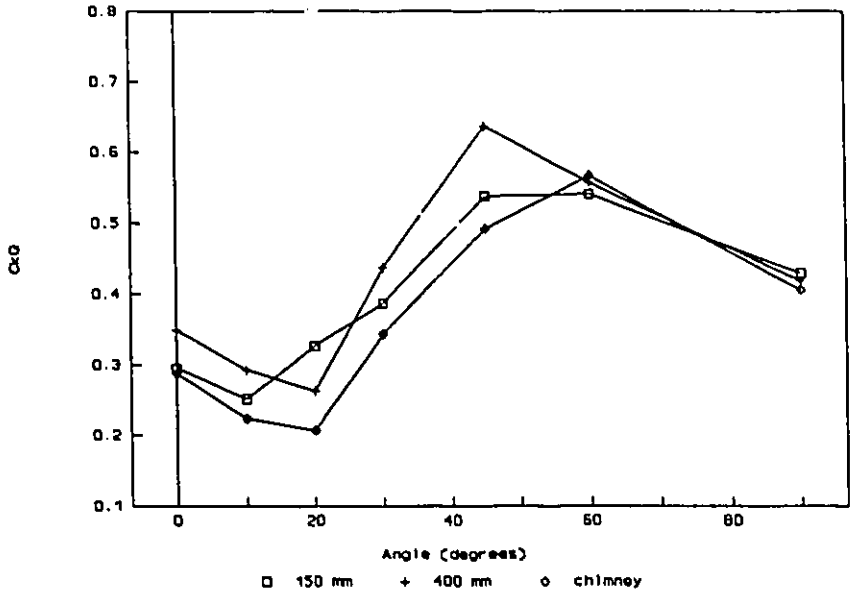

Figure 5.61 Ridge effects on the C_{KQ10} with the simulated 800 mm sidewall with closed end walls.

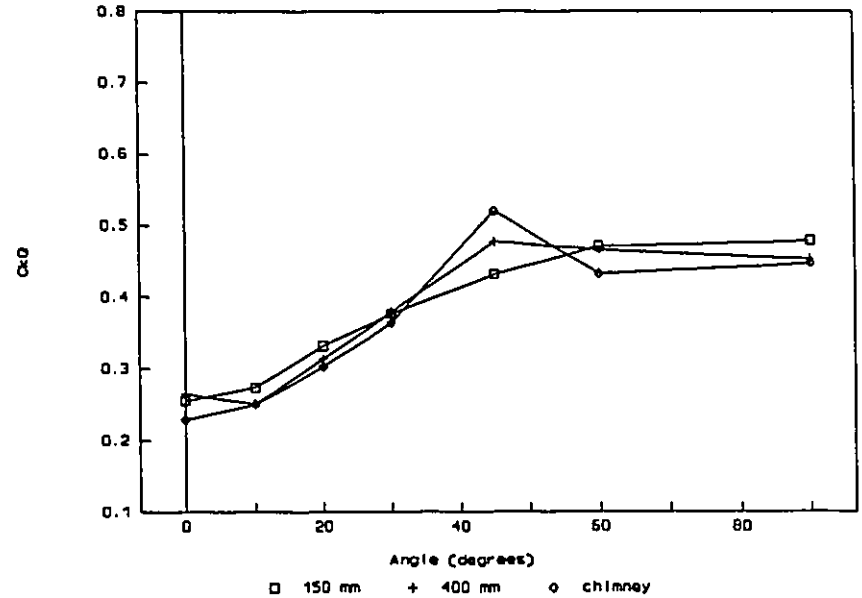

Figure 5.62 Ridge effects on the C_{KQ10} with the simulated 800 mm sidewall with open end walls.

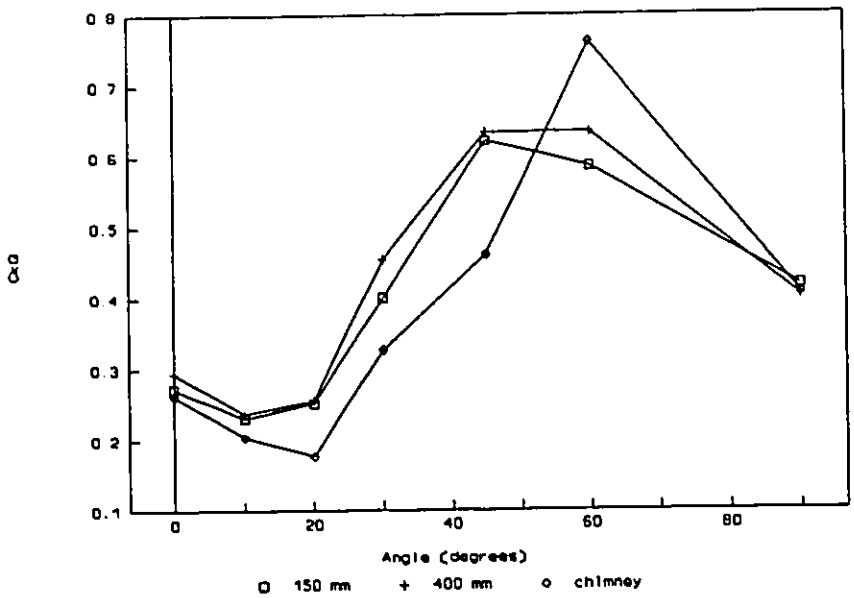

Figure 5.63 Ridge effects on the C_{Kq10} with the simulated 1100 mm sidewall with closed end walls.

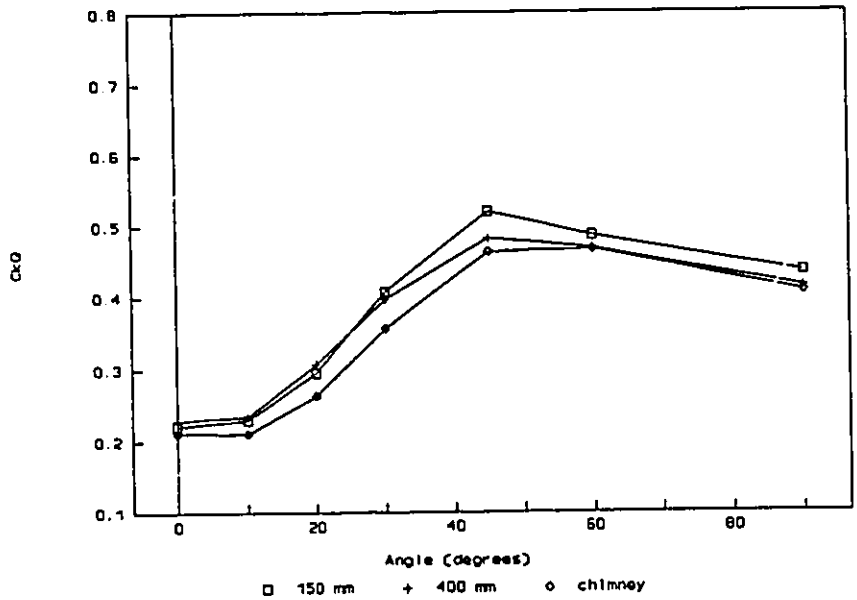

Figure 5.64 Ridge effects on the C_{Kq10} with the simulated 1100 mm sidewall with open end walls.

Choinière et al. (1988c) studied the effects of three continuous ridge opening widths of 150 mm, 300 mm and 600 mm (full scale) with closed and open end walls on the airflow patterns inside a scale model. Although not measured, they reported that the closed end wall models with larger ridge openings showed a slightly faster rate of decay of injected smoke for θ = 0°to 30°. However, the overall rates of decay of the smoke did not seem to change much among the three ridge widths when open end walls were used.

The results of the airflow diagrams provide indications on the calculated inflows or outflows for each openings. For low wind angles (θ = 0° to 20°), when Figs. 5.36 (OP-CH-800-C) and 5.40 (OP-150-800-C) are compared, it appears that the inflows or outflows of the sidewall openings are not influenced by either ridge type. In contrast, there are more inflows and outflows by the 150 mm ridge. When the 400 mm ridge is used, the inflows by the sidewalls increase while the outflows are reduced. Again, there appear to be more inflows and outflows with the larger ridge. With closed end walls, there is a gradual increase in the effective ventilation rate from the chimney to the 400 mm ridge which is basically shown in Fig. 5.61.

When the 1100 mm sidewall openings are used, for θ = 0° to 30°, there are fewer differences in the sidewalls inflows and outflows for the 150 mm versus the 400 mm ridge (Appendix H, Figs. H.7 and H.11). Only the ridge inflows and outflows appear to increase with the 400 mm ridge. With the 1100 mm sidewall, Fig. 5.63 shows that the differences in the effective ventilation rates between the 150 mm versus the 400 mm ridge are minimal. There might be a possibility that the predicted extra airflows through the 400 mm ridge may also be a short-circuit from the downwind end of the ridge to the upwind end.

When Fig. 5.37 (OP-CH-1100-C) is compared to Fig. H.7 (OP-150-1100-C, Appendix H), the sidewall inflows and outflows are similar. Consequently, the increase of the ridge opening from the chimney to the 150 mm width would have some benefit. Figure 5.64 shows that the extra inflows and outflows of the ridge level or movement from the incoming sidewall air to the 150 mm ridge exhaust has a positive effect on the effective ventilation rate coefficients.

For θ = 60° and 90°, it appears that there are very few differences among the chimney, 150 mm and 400 mm ridges in Figs. 5.61 (800-C) and 5.63 (1100-C) for all sidewall and end wall openings. As stated by Choinière et al. (1988a, 1988c), the airflow patterns show that incoming air from the windward sidewall closely follows the inside windward ceiling and reaches the chimney or open ridge. At this moment, definite clear zones are visible at the ceiling level. This presents a potential for a direct short circuit of ventilation from the sidewall inlets to the exhaust ridge, which would then reduce the quality of mixing. Accordingly, the average effective ventilation rates are reduced by the occurrence of a short circuit of ventilation.

Choinière et al. (1989) studied a full scale naturally ventilated building for swine housing which had similar dimensions to the present scale model. It also had continuous sidewall openings and closed end walls. The building had a continuous ridge opening which was tested at three positions: closed, 30 mm wide (equivalent to chimney opening area) and 120 mm wide. The ventilation rates were measured using the equilibrium concentration method with carbon dioxide as the tracer gas. Carbon dioxide is produced by finishing hogs' metabolism and the differences of interior-exterior concentrations were recorded continuously as well as the exterior wind speed and direction. Knowing the sidewall opening areas, C_{Q10} curves were produced for the three ridge openings. They reported a limited increase of the ventilation

rate coefficient between the 30 mm and 120 mm ridge which would be very similar to the results in Figs. 5.57 and 5.58 for the 800-C situations.

From the results of the effective ventilation rate coefficients with the closed end walls, it appears that:

1 - With the 800-C situation, larger ridge openings show higher C_{KQ10} values for θ = 0° to 45° while similar C_{KQ10} are obtained at θ = 60° and 90° for all ridge types.

2 - With the 1100-C sidewall, the chimney shows lower C_{KQ10} values at θ = 0° to 45°, but there are only few differences between C_{KQ10} values of the 150 mm and 400 mm ridges for all angles.

5.6.5 Ridge effect with end wall openings

With the use of end wall openings, Fig. 5.63 (800-O) hardly shows any differences between the chimney, 150 mm or 400 mm ridges for all angles. In Fig. 5.64 (1100-O), the chimney C_{KQ10} is slightly lower than the 150 mm and 400 mm ridges for θ = 0° to 45° while the 150 mm ridge shows the highest C_{KQ10} values for θ = 45° to 90°. Again, there are only small differences between the three types of ridge opening.

The observations of the airflow diagrams in Fig. 5.38 (OP-CH-800-O) versus Fig. H.6 (OP-150-800-O, Appendix H) reveal similar sidewall and end wall inflows and outflows with extra exhaust with the 150 mm ridge. For all angles, the contribution of the 150 mm ridge to the total ventilation rate is not large as compared to the ventilation produced by the end walls and sidewall openings. On the other hand, the use of the 400 mm ridge (Figs. H.6, OP-150-800-O) over the 150 mm ridge (H.10, OP-400-800-O) causes more inflows by the windward sidewall, less outflows by the leeward sidewall and more exhaust by the 400 mm ridge for θ = 45° to 90°. Again, there is a potential for short-circuiting between the windward sidewall and the open ridge.

For θ = 0° to 30°, the ridge inflows and outflows are increased with the 400 mm ridge, but the airflow diagrams for both sidewall and end wall openings appear to be fairly similar among the three ridge types. Again, as presented in Fig. 5.60, there is a possibility that the end wall and sidewall effects with their respective potential short-circuits may overcome the ridge effects.

With the 1100 mm sidewall opening, the same general effects on the airflow patterns and airflow diagrams are produced. This explains the minimal differences in C_{KQ10} between the three ridge types for θ = 0° to 90° in Fig. 5.64.

Generally, the following points can be noticed from the observations in Figs. 5.61 to 5.64 on the ridge effects for both 800 mm and 1100 mm sidewall with closed or open end walls:

1 - With the closed end walls, for θ = 0° to 45°, the chimney C_{KQ10} values are slightly lower for both 800 mm and 1100 mm sidewall while the 150 mm and 400 mm ridges show similar C_{KQ10} values for all angles especially with the 1100 mm sidewall.

2 - By using open end walls, it appears that the type of ridge has minimal effects on the C_{KQ10} values for all angles with both 800 mm and 1100 mm sidewall openings.

5.6.6 Concluding remarks

The analysis of the effects of the 800 mm versus the 1100 mm sidewall, with closed or open end walls combined with the chimney, 150 mm or 400 mm ridge openings on the effective ventilation rate coefficients C_{KQ10} reveal that:

1 - The sidewall effects vary with each type of ridge and are also dependent on the wind angle of incidence.

2 - The addition of end wall openings appears to have major effects on the uniformity of the C_{KQ10} curves by attenuating the large minimum-maximum differences noticed for all ridge types with closed end walls.

3 - The use of the chimney, 150 mm or 400 mm ridges has some effects on the C_{KQ10} values with closed end walls, but there are minimal C_{KQ10} differences between the three types of ridge openings when end walls are open.

The use of an optical device (laser and silicone diode detector) seems to be a promising technique to accurately measure the "effective" ventilation rate based on the concentration decay method. Further work on airflow mixing could also be done if multiple-sampling locations are used.

5.7 Comparison between the measured C_{KQ10} and the calculated C_{Q10}

In order to compare the results between the "effective" ventilation rate coefficient, C_{KQ10}, and the calculated ventilation rate coefficient, C_{Q10}, it should be remembered that the differences between these results may be attributed to the main assumptions previously made. With the pressure difference method, (Eq. 2.3), there are two potential sources of error which are: the use of a uniform discharge coefficient equal to 0.6 for each type of opening and for all wind angles, and the use of the calculated value for the internal pressure coefficient for the ventilation rate computation. The use of the measured Cp_{in} may create local differences on the ventilation rates, but this is beyond the scope of this project.

For the concentration decay method, no attempt was made to evaluate the mixing coefficient, K. Also since stagnant or short-circuit zones have been reported by Choinière et al. (1988a, 1988c) Ogilvie and Boyd (1985) and many others, the measured effective ventilation rate coefficients, C_{KQ10}, apply only to the specific line along the building through which the laser beam passed.

5.7.1 General observations

When the curve shapes of the calculated C_{Q10} (Figs. 5.46 to 5.48) are compared with the measured C_{KQ10} (Figs. 5.57 to 5.59), four major differences are noticed. First, C_{Q10} curves show definite effects of both 800 mm and 1100 mm sidewall areas on the C_{Q10} values with closed or open end walls for all wind angles of incidence, while the C_{KQ10} curves for both sidewalls and end walls tend to cross themselves at different wind angles of incidence, therefore showing wind angle effects. Second, the maximum C_{KQ10} values are generally reported for θ = 45°to 60° (Table 5.11) rather than at θ = 90° (or 60° for the 400 mm ridge with open end walls).

Third, the use of open end walls causes the C_{Q10} curves to shift upward proportionally to the added amount of inflows or outflows. In contrast, the use of open end walls produces lower effective ventilation rate coefficents for θ = 45° to 60°. Surprisingly, at θ = 0°, the C_{KQ10} values with the open end walls are always lower than with closed end walls.

Finally, the concentration decay measurements show limited C_{KQ10} differences for the three types of ridge openings, which is remarkable especially with open end walls. While the results from the pressure difference method show some C_{Q10} differences between the chimney and the 150 mm ridge, there is a large C_{Q10} increase with the 400 mm ridge.

5.7.2 Measured C_{KQ10} less calculated C_{Q10}

Table J.2 (Appendix J) presents the differences between the measured C_{KQ10} and the calculated C_{Q10} obtained with the open and sealed models. Figures 5.65 to 5.69 present the differences between the C_{KQ10} versus the C_{Q10} of the open model classified by ridge type or end wall opening status. The curves above the 0.0 line indicate an under-prediction of the pressure difference method while an over-prediction is indicated for C_{KQ10}-C_{Q10} differences below the 0.0 line.

In Figs. 5.65 (chimney) and 5.66 (150 mm ridge), the 1100 mm sidewall generally shows higher $C_{KQ10} - C_{Q10}$ differences with closed and open end walls, but the $C_{KQ10}-C_{Q10}$ difference are negligible at $\theta = 90°$ for both 800 mm and 1100 mm sidewall with closed or open end walls. This indicates that the use of the external Cps with the calculated Cp_{in} and a $C_d = 0.6$ is fairly adequate in all cases, in order to coincide with the effective ventilation rate coefficients.

At $\theta = 30°$ to $60°$, the $C_{KQ10}-C_{Q10}$ with the closed end walls indicate a large under-prediction with the pressure difference method while the $C_{KQ10}-C_{Q10}$ with open end walls are relatively small. Specifically, the $C_{KQ10}-C_{Q10}$ for the OP-150-800-0 are equal to 0.0.

Using the pressure difference method, there are two unknowns, the exact C_d for the ridge, sidewall and end wall openings as functions of the wind angles (Aynsley et al. (1977), Vickery and Karakatsanis (1987)), and the exact Cp_{in} to use knowing that spatial variations within the model have been measured. With the concentration decay method, the unknown factor is the measured average effective ventilation rate coefficient.

Assuming that the C_{KQ10} measurements are the reliable basis for design, the results with the closed end walls indicate that the sidewall C_d might be increased by specific factors for $\theta = 0°$ to $60°$ in order to obtain similar predictions between C_{Q10} and C_{KQ10}. Then, if the sidewall C_d is increased, the curves with the open end walls would be shifted downward, indicating an over-prediction with the pressure difference method. To alleviate this problem, the C_d of the end walls and/or the ridge may have to be reduced in order to compensate for the excessive ventilation rate prediction. Then the iteration process would have to be redone with closed and open end walls with all ridge types in order to estimate different C_ds applicable to each type of opening. This is beyond the scope of the present study.

The other factors to consider are the large end wall effect and the visible zones of over- and under-ventilation observed during the wind tunnel tests. It may be possible that the predictions of the ventilation rate with the pressure difference method are exact, but the measured C_{KQ10}-C_{Q10} differences are fully attributable to the mixing phenomenon.

For the 400 mm ridge opening with closed end walls, C_{KQ10}-C_{Q10} are positive for θ = 30° to 60° and negative for θ = 0° to 20° and 90°. In contrast, the pressure difference method generally over-predicts the effective ventilation rate when open end walls are used. For C_{Q10} predictions, major differences between the calculated and the measured Cp_{in}s are reported in Table 5.6. This factor may have effects on the predictions with the pressure difference method. Also, the C_{KQ10}-C_{Q10} values with closed end walls differ more widely than with open end walls.

Information on end wall and ridge effects are provided in Figs. 5.68 and 5.69. With end walls closed, it appears that there is a general over-prediction for all angles, but greater differences in C_{KQ10}-C_{Q10} are noticed at θ = 45° and 60°. Under-predictions are only noticed with the 400 mm ridge at θ = 0° to 20° and 90°. With end walls opened, the data (Fig. 5.69) show only minor C_{KQ10}-C_{Q10} differences with the chimney and the 150 mm ridge. Only the 400 mm ridge seems to be over-predicted with the pressure difference method.

5.7.3 The use of the pressure difference method for design purposes

With the present comparisons between the C_{KQ10}-C_{Q10} data for buildings with closed end walls, designers using the predictions obtained with the pressure difference method have a built-in safety factor. This factor comes from the under-prediction at angles of 45° and 60°, an accurate prediction at 10° to 30°, and 90°, and the over-prediction at 0° (400 mm ridge, only).

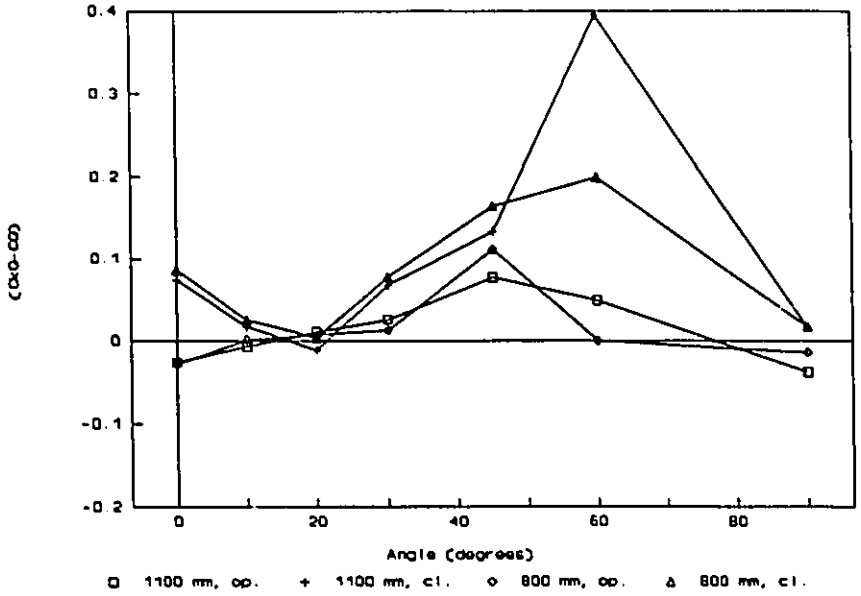

Figure 5.65 Chimney, differences between measured C_{KQ10} and calculated C_{Q10}.

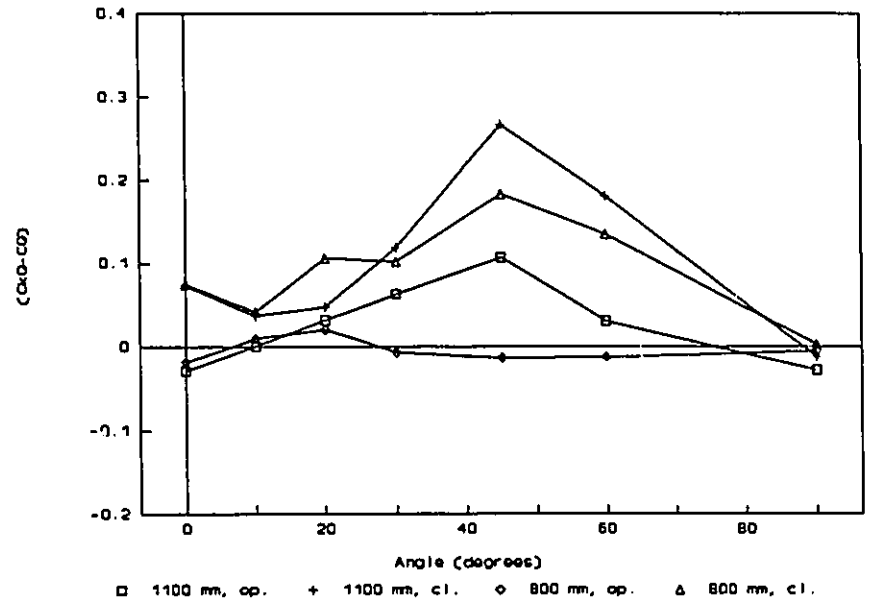

Figure 5.66 150 mm ridge, differences between measured C_{KQ10} and calculated C_{Q10}.

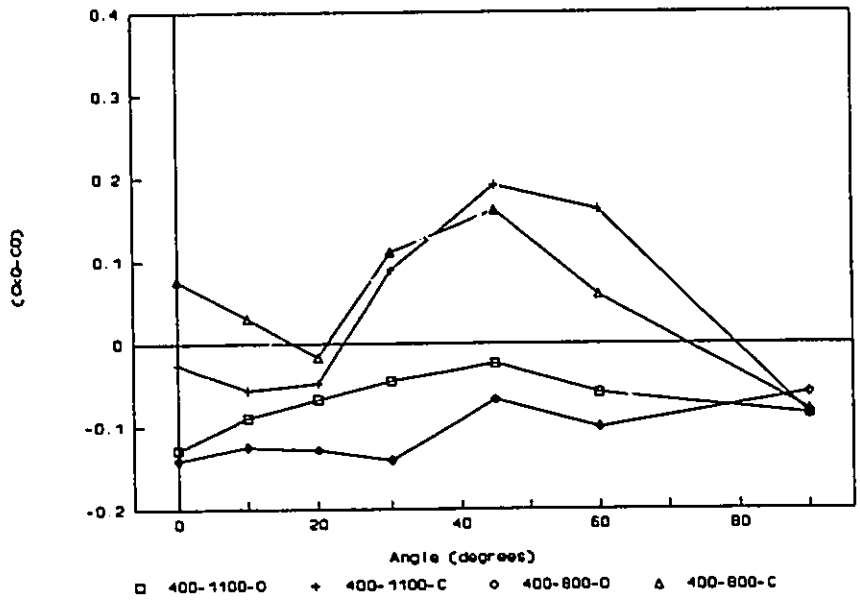

Figure 5.67 400 mm ridge, differences between measured C_{KQ10} and calculated C_{Q10}.

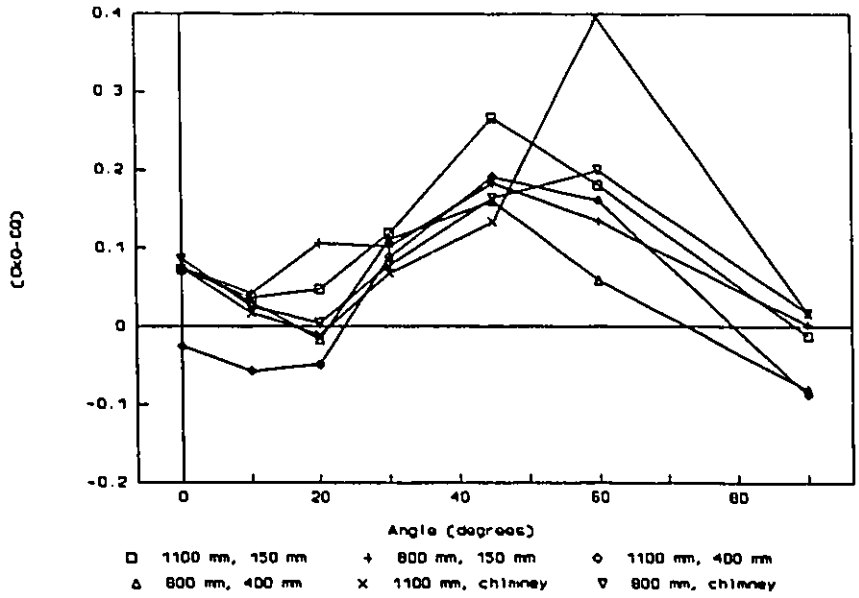

Figure 5.68 Closed end walls, differences between measured C_{Kq10} and calculated C_{q10} for 800 mm and 1100 mm sidewalls used with chimney, 150 mm and 400 mm ridges.

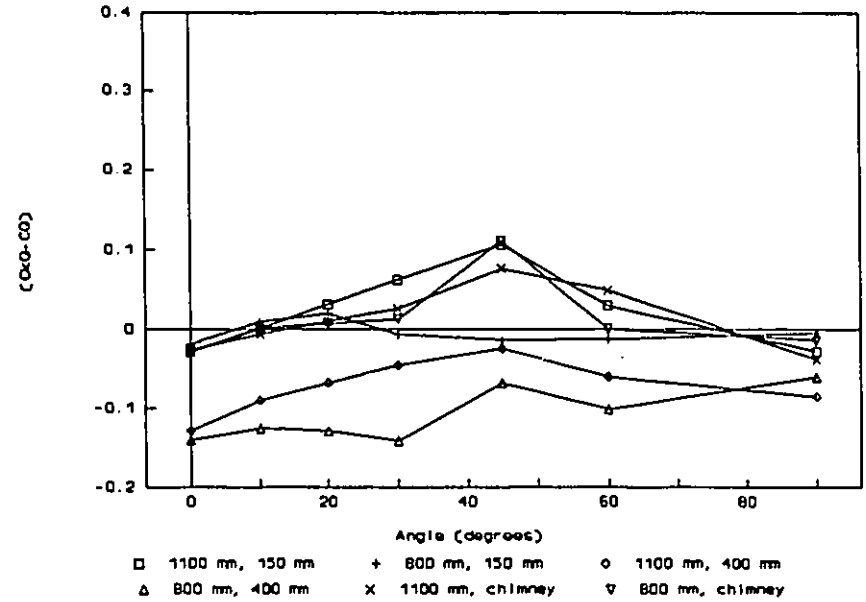

Figure 5.69 Open end walls, differences between measured C_{Kq10} and calculated C_{q10} for 800 mm and 1100 mm sidewall used with chimney, 150 mm and 400 mm ridges.

With open end walls, the prediction by pressure difference method with the chimney and 150 mm ridge appears to be very accurate. The designer should expect a general over-prediction with the 400 mm ridge for all angles.

5.7.4 Concluding remarks

At the present stage of knowledge, the pressure difference method may be used to design naturally ventilated buildings with large sidewall openings, closed and open end walls, and chimney or 150 mm ridge using the calculated Cp_{in} and a $C_d = 0.6$ for each type of opening and for all angles. Care should be taken with the 400 mm ridge, especially with the open end walls because of the possible over-prediction with the pressure difference method.

CHAPTER 6

SUMMARY AND CONCLUSION

Measurements of the external pressure coefficients around the 1:20 open and sealed models of a low-rise, naturally ventilated livestock building with gable roof were made in the NRCC wind tunnel. In addition, the internal pressure coefficients were recorded in the open models. The pressure difference method was used to estimate the local ventilation rates and calculate the ventilation rate coefficients C_{q10}, for various wind angles of incidence.

Comparisons between the open and sealed models were based on graphical representations of the external pressure coefficients, Cps, internal pressure coefficients, Cp_{in} , local external-internal pressure differences, ΔCps, airflow diagrams showing the predicted ventilation rate for each opening, Q_j, and the ventilation rate coefficients, C_{q10}, for all building configurations.

An attempt was made to measure the effective ventilation rate, KQ, for open models by the concentration decay method. During a test, smoke was injected inside the scale model and the rate of decay was measured by an optical device (laser and silicone diode detector). The calculated ventilation rate coefficients, C_{KQ10}, were said to be "effective" because they were measuring an effective average ventilation rate along the entire building length including all the potential zones of under- or over-ventilation and possible short circuits of ventilation.

For the open models, the predicted ventilation rate coefficients, C_{q10}, using the pressure difference method were compared with the measured effective ventilation rate coefficients, C_{KQ10}.

A total of 105 tests were done with open and sealed models. The model was transformed in order to study the following structural parameters:

1 - Three ridge opening configurations consisting of intermittent chimneys, simulated 150 mm or 400 mm wide continuous ridge openings.
2 - Two sidewall opening areas, simulating 800 mm or 1100 mm high continuous sidewall openings.
3 - The use of two end wall openings in the open or closed position.

Each building configuration was investigated for seven wind angles of incidence.

6.1 Pressure difference method

The general observations of the Cps distributions around the scale model reveal the following observations:

With the open model:

1 - The highest -Cps at the ridge were recorded with the chimney, not the 150 mm or 400 mm ridges.
2 - The 800 mm and 1100 mm sidewalls do not produce large changes in the Cp distributions, except at $\theta = 60°$ and 90°, where the 1100 mm sidewall generates higher pressure differences across the building.
3 - The use of closed or open end walls completely changes the Cp distributions at both end walls of the open model.

With the sealed model:

1 - The -Cps at the ridge are increased considerably when using the 400 mm ridge versus the chimney.
2 - The ridge types affect the leeward pressure coefficients.

Open versus sealed model:

1 - The -Cps at the ridge level are considerably higher with the sealed model.
2 - The -Cps over the leeward sidewalls are slightly higher with the open model.

3 - With the open end walls, the Cp distributions over both end walls are totally reversed with respect to the sealed versus open models.

4 - When the opening areas of the open model are increased, larger differences in Cp distributions and magnitudes occur.

The internal pressure coefficients, Cp_{in}, were calculated for the open and sealed models using the pressure difference method and, in addition, 10 measurements of Cp_{in} were made inside the open model. The results show that:

Open model, calculated Cp_{in}:

1 - All modifications of the building sidewall, end walls and types of ridge openings in function of the wind angles of incidence have an effect on the Cp_{in}.

Open model, measured Cp_{in}:

1 - Large 3-dimensional Cp_{in} variations should be anticipated inside these types of naturally ventilated buildings.

2 - The observed and reported airflow patterns seem to coincide with the gradient of the measured Cp_{in}.

3 - The differences between the calculated and the average of the measured Cp_{in}s are small with the chimney and 150 mm ridge, but rather large with the 400 mm ridge.

Open versus sealed, calculated Cp_{in}:

1 - The general shape of the Cp_{in} curves for sidewalls with closed or open end walls are fairly similar.

2 - The discrepancies between the calculated Cp_{in} of the sealed versus open models are increased when larger sidewall, open end walls and ridge opening areas are used.

The difference between the exterior Cps over the building surfaces and the calculated Cp_{in} provide the basic information on the directions and magnitudes of the air inflows and outflows for each opening area.

Open model:

1 - The use of the simulated 800 mm or 1100 mm sidewall openings show minor effects for all angles, except for $\theta = 90°$ where the 1100 mm sidewall show higher ΔCps on the leeward sidewall.

2 - The use of open end walls have various effects on the sidewall and ridge ΔCps for most angles.

3 - From the study of the three ridge configurations, it appears that the 400 mm ridge opening is the only one of the three that has changes, a slight increase in ΔCps over the inlet zones, decreases in ΔCps over the outlet zones and a decrease in ΔCps over the ridge opening.

Open versus sealed model:

1 - Some differences in ΔCp distributions and magnitudes over the sidewall (especially the leeward wall) and end walls openings are visible for most angles.

2 - For all types of ridge openings, the sealed model show considerably higher ΔCps through the ridge as compare to the open model.

The use of the airflow diagrams for the sealed and open models helped to visualise the effects of the discharge coefficient, to estimate the effect of the area for each opening on the local inflows and outflows, and to evaluate the magnitude of Q_j. From the results, the following could be inferred,

Open model:

1 - When the sidewall openings are enlarged from the simulated 800 mm to the 1100 mm opening width, the percent increase of the total flow varies according to the types of ridge and end wall openings used as well as the wind angle of incidence.

2 - With open end walls, the inflows and outflows over the sidewall and the ridge are slightly different for all angles.

3 - The larger ridge openings show an increase in the windward inflows, decrease in the leeward outflows and an increase in the outflows through the ridge at θ = 30° to 90°.

4 - At θ = 0° and 10°, there are similar sidewall flows for the chimney and 150 mm ridge and also more inflows and outflows through the 150 mm ridge itself. The 400 mm ridge shows more inflows over both sidewalls, and also reduced outflows through both sidewalls while there were more inflows and outflows at the ridge level.

Open versus sealed model:

1 - For all angles with the sealed model, the ridge and the downwind end wall outflows are considerably over-predicted and the leeward wall outflows are under-predicted as compare to the open model.

2 - More inflows at the ridge level are predicted with the open model (θ = 0° to 20°).

The dimensionless ventilation rate coefficient, C_{Q10}, is very convenient in order to study the effect of any structural changes of the sidewall, end walls and ridge openings. Also it utilises all the basic building information to predict the total ventilation rate, Q_T, when used in conjunction with meteorological data of wind speed and direction. The C_{Q10} values are plotted against various wind angles of incidence. From the study of the C_{Q10} curves for the open and sealed models, the following conclusions were drawn.

Open model:

1 - When the larger 1100 mm sidewall openings are used instead of the 800 mm opening, similar or slightly lower C_{Q10} values are obtained. This indicates that the total ventilation rates, Q_T, are enhanced proportionally to the percent increase in sidewall area.

2 - The addition of two end walls openings generally increases the C_{Q10} values for all angles with each building configuration. This is an extremely efficient

way to provide higher C_{q10} values especially at $\theta = 0°$ to $20°$.

3 - Small increases of the C_{q10} values are produced when the chimney is replaced by the 150 mm ridge, but the 400 mm ridge shows considerably larger C_{q10} increases compared to the chimney and the 150 mm ridge.

Open versus sealed model:

1 - With the chimney and the 150 mm ridge, the C_{q10} values with the open model predict higher total ventilation rates, Q_T, compared to the sealed model at $\theta = 90°$ to $30°$ and lower Q_Ts at $\theta = 20°$ to $0°$.

2 - With the 400 mm ridge, the C_{q10} values of the open model generally predict higher total ventilation rates for all angles.

Generally, the comparisons between the C_{q10} values of the open and the sealed models would lead one to believe that the larger the total opening areas are on the sidewall, end walls and ridge openings, the larger the discrepancies in C_{q10} values.

For future research work of naturally ventilated buildings with large sidewall, end walls and ridge opening areas, it appears that the use of open models should be recommended basically because of the reported large 3-dimensional Cp_{in} variations within the open model and the different external pressure coefficients measured with various structural building configurations.

6.2 Effective ventilation rate coefficients measured by the concentration decay method

An attempt was made to obtain the effective ventilaton rate coefficients, C_{kq10}, based on the concentration decay method. An optical density device (laser and silicone diode detector) was used to measure the rate of decay of injected smoke into the scale model.

These measured ventilation rate coefficients are said to be "effective" because they represent an average C_{KQ10} for the entire building length at the center width and 1.5 m above the floor (full scale). The C_{KQ10} measurements include the controversial mixing factor.

The analysis of the effects of the 800 mm versus 1100 mm sidewall with closed or open end walls combined with the chimney, 150 mm or 400 mm ridge openings on the effective ventilation rate coefficients C_{KQ10} revealed the following:

1 - The sidewall effects vary with each type of ridge and are also dependent upon the wind angle of incidence.

2 - The addition of end walls openings appears to have major effects on the uniformity of the C_{KQ10} curves by attenuating the large minimum-maximum differences noticed for all ridge types with the closed end walls.

3 - The use of chimney, 150 mm or 400 mm ridges has some effects on the C_{KQ10} values with closed end walls but it appears that there were minimal C_{KQ10} differences among the three types of ridge openings when open end walls were used.

The use of an optical device (laser and silicone diode detector) seems to be a promising technique to accurately measure the "effective" ventilation rate based on the concentration decay method. Further work on airflow mixing could also be done if multi-sampling locations are used.

6.3 Measured C_{KQ10} versus calculated C_{Q10}

The effective ventilation rate coefficients, C_{KQ10}, measured by the concentration decay method were compared to the calculated ventilation rate coefficients, C_{Q10}, with the pressure difference method. Four major points of difference were noticed.

Firstly, for all wind angles, the general C_{Q10} curves show definite effects of both 800 mm and 1100 mm sidewall areas with closed or open end walls while the C_{KQ10} curves tend to

cross themselves at different wind angles of incidence. Secondly, the maximum C_{KQ10} values were recorded at θ = 45° to 60° as compared to θ = 90° for the C_{Q10} values.

Also, the addition of two end wall openings caused the calculated C_{Q10} values to increase proportionally to the added amount of inflows and outflows. In contrast, when open end walls are used, the effective ventilation rate coefficients, are generally lower than the C_{Q10} for θ = 45° and 60°. Surprisingly, at θ = 0°, the C_{KQ10} values with the open end walls are always lower than with closed end walls.

Finally, the results from the pressure difference method generally show C_{Q10} differences between the chimney and the 150 mm ridge but very large C_{Q10} increases when the 400 mm ridge was used. At the opposite end, the results of the concentration decay method show only limited C_{KQ10} differences for the three types of ridge openings with closed end walls. With open end walls, there are about no C_{KQ10} differences among the three ridge types.

During the wind tunnel tests, zones of over and under-ventilation were visualised from the smoke's rate of decay. Also, there are potential short circuits of ventilation with the incoming air which may go directly through the exhaust openings, especially because of the proximity of the inlet and outlet zones. Short circuits from the windward sidewall to the ridge opening at θ = 60° and 90° as well as from the open end walls to the sidewalls or the ridge openings at θ = 0° to 30° are possible. The effective ventilation rates would be impaired due to these short circuits.

With the pressure coefficient method, possible prediction errors of the C_{Q10} values are likely to occur because the values are calculated with C_d = 0.6 for all types of sidewall, end wall and ridge openings at all wind angles. Also, the reported 3-dimensional variations of Cp_{in} may change the calculation of the total ventilation rates.

6.4 Use of the pressure difference method for design purposes

At the present stage of knowledge, the calculation of C_{q10} with the pressure difference method may be used to design naturally ventilated buildings with large sidewall openings, with closed or open end walls for all wind angles. The designer must remember that with the chimney versus the 150 mm ridge, the use of a uniform $C_d = 0.6$ for all openings and the calculated Cp_{in} will cause a slight under-prediction of the C_{q10} values for $\theta = 0°$, $10°$, $45°$ and $60°$ compared to the measured C_{kq10} values. From the designer's point of view, under-prediction of the ventilation rate coefficents provides a safety factor. Care should be taken with using the 400 mm ridge especially with open end walls where over-prediction with the pressure difference method are reported for all wind angles.

CHAPTER 7

RECOMMENDATIONS FOR FUTURE WORK

The comparison between the open and sealed models revealed major differences at the ridge level, at the end wall openings and some differences on both sidewall openings. It should be considered that future work on natural ventilation for buildings with large sidewall, end wall or ridge openings must be done with open models.

The prediction of the inflows and outflows at each opening is based on the local differences between Cp_{ext} and Cp_{in}. Large differences in Cp_{in} values have been generally recorded along and across the building. Even if the averages of the measured Cp_{in}s are close to the calculated Cp_{in} values with the chimney and the 150 mm ridge, localised variations in Cp_{in} may have some effect on the total ventilation rates, as well as on local zones of inflow and outflow and their respective magnitudes. Definitively, the predictions would have been impaired with the 400 mm ridge where the measured-calculated Cp_{in}s are completely different. The spatial variations in Cp_{in} with their potential effects on the ventilation rates should be investigated. Then, it would be recommended to substantially increase the number of CP_{in} measurements taken for subsequent research work.

The measurements of the "effective" ventilation rate coefficients using the concentration decay method with injected smoke and an optical device appears to be very promising. The rate of decay method is adequate as indicated by the very good curve fitting correlations obtained with the majority of the tests. The optical devices (laser and silicone diode detector) provide accurate measurements as indicated by the fairly low standard deviations obtained from

the average $C_{k\theta 10}$ values for the five replicates. Further work would be required on the mathematical treatments of the data, especially to reduce the problem of the initial and final cut-off points used for the calculation of the rate of decay and obtain a more accurate estimation of the standard deviation and standard error.

With the present study, it was possible to obtain an average value of the "effective" ventilation rate coefficients, but zones of under- and over-ventilation were still visible within the scale model. For further studies, it is recommended to use multiple recording locations along and across the model. This would obtain relatively accurate values for the average $C_{k\theta 10}$ and data to study the "mixing" phenomenon.

Finally, if precise measurements of Cp_{ext} and Cp_{in} are done with the addition of measurements of the ventilation rates by the concentration decay method, it would then be possible to calculate the C_d for each type of sidewall, end wall and ridge opening in function of the wind angles of incidence.

Also, there would be a possibility to validate more complicated models, including the effects of wind turbulence (Handa, 1979; Gustén, 1989) which would not change the average Cps and C_d, but may change the "effective" ventilation rates.

REFERENCES

Allen, C. (1984), "Wind Pressure Data Requirements for Air Infiltration Calculations", Tech. Note AIVC 13, Air Infiltration and Ventilation Centre, University of Warwick Science Park, Barclays Venture Centre, Coventry CV4 7EZ Great Britain, 124 pp.

Ashley, S. and Sherman, M. (1984), "The Calculation of Natural Ventilation and Comfort", ASHRAE Trans., Vol. 90(1B), pp. 253-271.

ASHRAE. (1981), "ASHRAE Handbook. 1981 Fundamentals", Am. Soc. of Heating, Refrigerating and Air Conditioning Eng. Atlantic, GA 30329, 4th Edition.

ASHRAE. (1989), "ASHRAE Handbook, 1989 Fundamentals", Am. Soc. of Heating, Refrigerating and Air Conditioning Eng., Atlantic, GA., 30329, 6th Edition.

ASTM. (1988), "Standard Test Method for Specific Optical Density of Smoke Generated by Solid Materials for Aerospace Applications, Designation F-814-84b", Annual Book of ASTM Standards, Sec. 15, Vol. 15.03, ASTM, 1916 Race St., Philadelphia, PA 19103, USA. pp. 589-612.

Aynsley, R.M., (1979), "Wind-Generated Natural Ventilation of Housing for Thermal Comfort in Hot Humid Climates", Proc. of the Fifth Intrn'l Conf. on Wind Engng., Permagon Press, Vol. 1, pp. 243-254.

Aynsley, R.M. (1988), "A Resistance Approach to Estimating Airflow Through Buildings with Large Openings Due to Wind", ASHRAE Transaction, Vol. 94(2), Pt 2, pp. 1661-1669.

Aynsley, R.M., Melbourne, W. and Vickery, B.J. (1977), "Architectural Aerodynamics", Applied Science Publishers Ltd., London, 254 pp.

Barber, E.M. and Ogilvie, J.R. (1982), "Incomplete Mixing in Ventilated Airspaces, Part I, Theoritical Considerations", Can. Agric. Engng., Vol. 24(1), pp. 25-31.

Barber, E.M. and Ogilvie, J.R. (1984a), "Incomplete Mixing in Ventilated Airspaces, Part II, Scale Model Study", Can. Agric. Engng., Vol. 26(2), pp. 189-196.

Barber, E.M. and Ogilvie, J.R. (1984b), "Interpretation of Tracer Gas Experiments in Ventilation Research", J. Agric. Engng. Res., Vol. 30, pp. 57-63.

Bauman, F.S., Ernest, D.R. and Arens, E.A. (1988), "Asean Natural Ventilation Study: Wind Pressure Distributions on Long Building Rows in Urban Surroundings", Center for Environmental Design Research, University of California, Berkeley, CA 94720, 65 pp.

Billsborrow, R.E. and Fricke, F.R. (1975), "Model Verification of Analogue Infiltration Predictions", Building Science, Vol. 10, pp. 217-130.

Bottcher, R.W., Willits, D.H. and Baughman, G.R. (1986), "Experimental Analysis of Wind Ventilation of Poultry Buildings", Trans. of ASAE, Vol. 29(2), pp. 571-578.

Boyd, K.G. (1985), "Experimental Analysis of Ventilation Due to Wind in Models of a Modified Open Front (MOF) Swine Finishing Barn", M.Sc. Thesis, Un. of Guelph, Ontario, 117 pp.

Brockett, B.L. and Albright, L.D. (1987), "Natural Ventilation in Single Airspace Buildings", J. Agric. Engng. Res., Vol. 37, pp. 141-154.

Brown, T.R. (1986), "Description of the 6 Ft X 9 Ft Low Speed Wind Tunnel", Report No. LTR-LA-285, Nat. Aero. Esta. Nat. Res. Council of Canada, Montreal Road, Ottawa, Canada, 10 pp.

Bruce, J.M. (1974), "Wind Tunnel Study: Suckler Cow Building". Farm Building Progress, October, pp. 15-17.

Bruce, J.M. (1975), "A Computer Program for the Calculation of Natural Ventilation Due to Wind", Farm Building, R&D Studies, Nov., pp. 12-19.

Bruce, J.M. (1977), "Natural Ventilation, Its Role and Applications in the Bio-Climatic System", Farm Building, R&D studies, Feb., pp. 1-8.

Cermak, J.E. (1975), "Application of Fluid Mechanics to Wind Engineering, a Freeman Scolar Lecture", J. of Fluid Eng. ASME, Vol. 97(1), 30 pp.

Cermak, J.E., Doreb, M., Peterka, J.A. and Ayad, S.S. (1984), "Wind Tunnel Investigations of Natural Ventilation", J. of Transp. Eng., Vol. 110(1), pp. 67-79.

Chandra, S. (1987), "Passive Cooling for Residences in Hot Humid Climates, a Review of Recent Research", Progress in Solar Engineering, Hemisphere Publ., pp. 183-207.

Chandra, S., Fairey, P.W., Koresteclogiu, A.A. and Kamel, A.A. (1986), "Wind Tunnel and Full-Scale Data on Airflow from Natural Ventilation and Ceiling Fans", ASHRAE Trans., Vol. 92, (2B), pp. 804-812.

Charlesworth, P.S. (1988), "Air Exchange Rate and Air Tightness Measurements Techniques, An Application Guide", Air Infiltration and Ventilation Centre, Un. of Warwick Science Park, Barclays Venture Centre, Coventry, CV4 7EZ, Great Britain, 214 pp.

Choinière, Y. (1989), "Natural Ventilation of Low-Rise Buildings by the Wind; Development of a Model to Predict Average Ventilation Rates and the Frequencies of Consecutive Hours Below Minimum Limits of Ventilation Rate with Summer Meteorological Data", Research Report, presented to Dr. H. Tanaka, Ottawa University, Alfred College of Agricultural and Food Technology, Alfred, Ontario, April, 48 pp.

Choinière, Y., Blais, F. and Munroe, J.A. (1988a), "Wind Tunnel Study of Airflow Patterns in a Naturally Ventilated Building", Can. Agric. Eng., Vol. 30(2), pp. 293-297.

Choinière, Y., Ménard, O., Blais, F. and Munroe, J.A. (1987), "Thermostat Location for a Naturally Ventilated Swine Barn", Am. Soc. of Agric. Eng., Paper No. 87-4554, St-Joseph, MI 49085 USA.

Choinière, Y., Munroe, J.A., Desmarais, G., Renson, Y. and Ménard, O. (1988b), "Minimum Ridge Opening Widths of an Automatically Controlled Naturally Ventilated Swine Barn for a Moderate to Cold Climate", Can. Soc. of Agric. Eng., Paper No. 88-115, 151 Slater St., Ottawa, Ont.

Choinière, Y., Munroe, J.A., Dubois, H., Desmarais, G., Larose D. and Blais, F. (1988c), "A Model Study of Wind Direction Effects on Airflow Patterns in Naturally Ventilated Swine Buildings Under Isothermal Conditions", Can. Soc. of Agric. Eng., Paper No. 88-113, 151 Slater St., Ottawa, Ont.

Choinière, Y., Munroe, J.A., Desmarais, G., Dubois, H. and Renson, Y. (1989), "Effect of Different Ridge Opening Widths on the Thermal Performance and Ventilation Rate of a Naturally Ventilated Swine Building During Warm Summer Conditions", Am. Soc. of Agric. Eng., CSAE-ASAE Paper No. 89-4065, St-Joseph, MI 49085 USA.

Clark, F.R.S. (1985), "Assessment of Smoke Density With a Helium-Neon Laser", Fire and Materials, Vol. 9(1), pp. 30-35.Cook, N.J. (1978), "Determination of the Model Scale Factor in Wind Tunnel Simulation of Adiabatic Atmospheric Boundary Layer", J. of Industrial Aerodynamics, Vol. 2(4), pp. 321-331.

Costello, T.A., Meador, N.F. and Shanklin, M.D. (1982), "CO_2 Compared to SF_6 as an Air Infiltration Tracer", Am. Soc. of Agric. Eng., Paper No. 82-4014, St-Joseph, MI, 49085, USA.

Davenport, A.G. (1960), "Rationale for Determining Design Wind Velocities", J. of the Structural Division, Proceedings of the Am. Soc. of Civil. Engng., Vol. 86 (St5), pp. 39-68.

Davenport, A.G., Surry, D. and Stathopoulos, T. (1977), "Wind Loads on Low-Rise Buildings: Final Report of Phases I and II, Text and Figures", BLWT-SS8-1977, Boundary Layer Wind Tunnel, Un. of Western Ontario, London, Ont. N6A 5B9, 74 pp.

Davenport, A.G., Surry, D., Stathopoulos, T. (1978), "Wind Loads on Low-Rise Buildings: Final Report of Phase III, Part I, Text and Figures", BLWT-SS4-1978, Boundary Layer Wind Tunnel Laboratories, Un. of Western Ontario, London, Ont. N6A 5B9, 124 pp.

Down, M.J. (1990), "A Computer Program to Predict the Climate in Intensive Piggery Buildings, II: Description", Conference on Agricultural Engineering, Burndaberg, Australia, 6 pp., in print.

Down, M.J., Foster, M.P., McMahon, T.A. and Redding, G.J. (1985), "The Design of Livestock Buildings for Natural Ventilation; The Theoretical Basis and a Rationale Design Method", Agric. Eng., Rep. No. 73/85, The University of Melbourne, Victoria, Australia 3052, 112 pp.

Down, M.J. and McMahon, T.A. (1990), "A Computer Program to Predict the Climate in Intensive Piggery Buildings, I: Background and Validation", Conference on Agricultural Engineering, Burndaberg, Australia, 5 pp., in print.

Etheridge, D.W. and Nolan J.A. (1979a), "Ventilation Measurements at Model Scale in a Turbulent Flow", Building and Environment, Vol. 14, pp. 53-64.

Etheridge, D.W. and Nolan, J.A. (1979b), "An Optical Technique for Measurements of Ventilation Rates in Models", Building and Environment, Vol. 14, pp. 65-68.

Friedlander, S.K. (1977), "Smoke, Dust and Haze, Fundamentals of Aerosol Behavior", John Wiley and Sons, Inc., 317 pp.

Froehlich, D.P., Hellickson, M.A. and Young, H.G. (1974), "Ridge Ventilation Effects on Model Ventilation Characteristics". Am. Soc. of Agric. Engng., Paper No. 74-4055, St-Joseph, MI 49085, USA.

Gulari, E., Bazzi, G., Gulari, E. and Annapragada, A. (1987), "Latex Particle Size Distributions from Multiwavelength Turbidity Spectra", Part. Charact., Vol.4, pp. 96-100.

Gülder, Ó.L. (1989), "Influence of Hydrocarbon Fuel Structural Constitution and Flame Temperature on Soot Formation in Laminar Diffusion Flames", Combustion and Flame, 0:000-000. Published by Elservier Science Publishing Co., Inc., 655 Ave. of the Americas, N.Y., N.Y. 10010, 16 pp.

Gustén, J. (1989), "Wind Pressures on Low-Rise Buildings, An Air Infiltration Analysis Based on Full-Scale Measurements". Pub 1989:2, Division of Structural Design, Chalmers University of Technology, Gothenburg, Sweden, 218 pp.

Handa, K. (1979), "Wind Induced Natural Ventilation", Swedish Council for Building Research, Document D10, 86 pp.

Hansen, K. (1986), "Installation of Models in the 6 ft X 9 ft Low Speed Wind Tunnel", Report LTR-LA-286, Nat. Aero. Esta. Nat. Res. Council of Canada, Montreal Road, Ottawa, Canada, 2 pp.

Hawksley, P.G.W., Badzioch, S., Blackett, J.H. (1977), "Measurements of Solids in Flue Gases", 2nd Edition, Edited by the Institute of Fuel, London, pp. 231-235.

Hellickson, M.A., Hinckle, C.N. and Jedele, D.G. (1983), "Natural ventilation", Chapter 5 of Ventilation of Agriculture Structures, ASAE Monograph, Am. Soc. of Agric. Eng., St-Joseph, MI 49085, USA, pp. 81-102.

Hinds, W.C. (1982), "Aerosol Technology, Properties Behavior and Measurements of Airborne Particles", John Wiley and Sons, 424 pp.

Hitchin, E.R. and Wilson, C.B. (1967), "A Review of Experimental Techniques for the Investigation of Natural Ventilation in Buildings". Building Science, Vol. 2, pp. 59-82.

Holmes, J.D. (1979), "Mean and Fluctuating Internal Pressures Induced by Wind", Proc. of the Fifth Intnl Conf. on Wind Engng., Permagon Press, Vol. 1, p. 435-450.

Holmes, J.D. (1983), "Wind Loads on Low-Rise Buildings, A Review", Commonwealth Scientific and Industrial Research Organization, Division of Building Research, Australia, 91 pp.

Hoxey, R.P. (1984), "Design Wind Loads for Closed Farm Buildings", J. Agric. Engng. Res., Vol. 29, p. 305-311.

Hoxey, R.P. and Moran, P. (1983), "A Full Scale Study of the Geometric Parameters That Influence Wind Loads on Low-Rise Buildings", J. of Wind Engineering and Industrial Aerodynamics, Vol. 13, p. 277-288.

Hunt, C.M. (1980), "Air Infiltration, A Review of Some Existing Measurement Techniques and Data, in Building Air Change Rate and Infiltration Measurements", ASTM STP 719, Am. Soc. for Testing and Mat., Vol. 1, pp. 3-23.

Irwin, H.P.A.H. (1979), "Design and Use of Spires for Natural Wind Simulation, Report LTR-LA-233, Nat. Aero. Esta., Nat. Res. Council of Canada, Montreal Road, Ottawa, Canada, 37 pp.

Ishizu, Y., Kaneki, K. and Tomita, H. (1983), "Validity of the Application of Mixing Factor and Position Factor to the Expression for Indoor Air Pollution", Proceedings of the Fourth Intnl Symp. on the Use of Computers for Envi. Engng. Related to Buildings, Tokyo, Japan, p. 96-99.

Karakatsanis, C., Bahadori, M.N. and Vickery, B.J. (1986), "Evaluation of Pressure Coefficients and Estimation of Airflow Rates in Buildings Employing Wind Towers", Solar Energy, Vol. 37(5), pp. 363-374.

Kelly, T.G., Dood, V.A. and Ruane, D.J. (1986), "Ventilation and Airflow Patterns in Climatic Calf Houses", J. Agric. Engng. Res., Vol. 33, pp. 187-203.

Krishnakumar, C.K., Herringer, R.h., Schafer, C.K., Fields, S.F. and Bettge, D.A. (1985), "A Correlation for Estimating Wind Ventilation", ASHRAE Trans. Vol. 91(2), pp. 511-520.

Melik, D.H. and Fogler, H.A. (1983), "Turbimetric Determination of Particle Size Distributions of Colloidal Systems", J. Coll. Inter. Sc., Vol. 92(1), pp. 161-180.

Mitchell, C.D. and Ross, P.A. (1977), "Model Study of Airflow in Two Calf Houses", Farm Building Progress, Jan., pp. 19-22.

Moran, P. (1980), "Full-Scale Experiments to Acquire Wind Loading Data for Use in the Design of Agricultural Buildings", J. Agric. Engng. Res., Vol. 25, p. 287-297.

Moran, P., Wright, D.I. and Westgate, G.R. (1983), "Wind Loads on Farm Buildings: (10) Further Full-Scale Measurements on an 18.5 m Long Single 7.4 Span Building", Div. Note DN 1148, AFRC Inst. Engng. Res., Silsoe, Jan., (unpubl.), 12 pp.

Ogilvie, J.R. and Boyd, K.G. (1985), "Tracer Gas Analysis of Ventilation Due to Wind in Models of a Modified Open-Front (MOE) Swine Finishing Barn", Can. Soc. Agric. Eng., Paper No. 85-413, 151 Slater St. Ottawa, Ont.

Rasbash, D.J. and Phillips, R.P. (1978), "Quantification of Smoke Produced at Fires. Test Methods for Smoke and Methods of Expressing Smoke Evolution", Fire and Materials, Vol. 2(3), pp. 102-109.

Rea, M.S., Clark, F.R.S. and Ouellette, M.J. (1985), "Photometric and Psychophysical Measurements of Exit Signs Through Smoke", Nat. Res. Council of Canada, 24627, Division of Building Research, Paper No. 1291, pp. 42.

Richardson, G.M. (1989a), "Low Cost Housing for Livestock; A Plastic Solution", AFRC Inst. Engng. Res., Silsoe, U.K., Personal communication, 2 pp.

Richardson, G.M. (1989b), "Private Communications, Additional Comments of FB06 from the Report # DN 1124", AFRC Inst. Engng. Res., Silsoe, UK, June, 14 pp. (unpublished).

Robertson, A.P. and Glass, A.G. (1988), "The Silsoe Structures Building - Its Design, Instrumentation and Research Facilities", Div. Note DN 1482, AFRC Inst. Engng. Res., Silsoe, UK, October, 59 pp.

Robertson, A.P., Hoxey, R.P. and Moran, P. (1985). "A Full-Scale Study of Wind Loads on Agricultural Ridged Canapy Roof Structures and Proposals for Design", J. of Wind Engineering and Industrial Aerodynamics, Vol. 21, p. 167-205.

Robertson, A.P., Hoxey, R.P. and Moran, P. (1988), "Full-Scale Measurements of Wind Pressures on General-Purpose Farm Building FB19 at Pondersbridge", Div. Note DN 1464, AFRC Inst. Engng. Res., Silsoe, UK, May, 18 pp.

Shaw, C.Y. (1984), "The Effect of Tracer Gas on the Accuracy of Air Change Measurements in Buildings", ASHRAE Trans., Vol. 90(1a), pp. 212-225.

Shoda, T. (1950), "Experimental Studies on Natural Ventilation", Report on Institute of Industrial Science, University of Tokyo, Vol. 1(2), 55 pp.

Shrestha, G., Cramer, C., Holmes, B.J. (1990), "Wind Induced Natural Ventilation of an Enclosed Building", Am. Soc. of Agric. Engng., Paper No. 90-4001, St-Joseph, MI 49085, USA.

Stathopoulos, T., Surry, D. and Davenport, A.G. (1979), "Internal Pressure Characteristics of Low-Rise Buildings Due to Wind Action", Proc. of the Fifth Intnl. Conf. on Wind Engng., Permagon Press, Vol. 1, p. 451-463.

Ström, J.S. (1987), "Natural Ventilation and Its Control", Pig Magazine, May-June, pp. 16-17.

Swami, M.V. and Chandra, S. (1987), "Procedure for Calculating Natural Ventilation Airflow Rates in Buildings", Florida Solar Energy Center, Report No. FSEC-CR-163-86, Cape Carnaveral, Flo. 32920, 27 pp.

Swami, M.V. and Chandra, S. (1988). "Correlations for Pressure Distribution on Buildings and Calculation of Natural Ventilation Airflow", ASHRAE Trans., Vol. 94(1), Preprint No. 3127.

Tieleman, H.W., Reinhold, T.A. and Marshall, R.D. (1978), "On the Wind Tunnel Simulation of the Atmospheric Surface Layer for the Study of Wind Loads on Low-Rise Buildings", J. of Ind. Aerodynamics, Vol. 3, pp. 21-38.

Tremblay, S. (1987), "A Microcomputer Software Package to Design Agricultural Drainage Plans", M.Sc. Thesis, Dept. of Agric. Engng., McGill Un., Macdonald College, Ste-Anne-de-Bellevue, Qc., 296 pp.

Vickery, B.J. (1986) "Gust-Factors for Internal Pressures in Low-Rise Buildings", J. of Wind Engineering and Industrial Aerodynamics, Vol. 23, pp. 259-271.

Vickery, B.J. (1989), Personal Communications, Boundary Layer Wind Tunnel, Un. of Western Ontario, London, Ontario, N6A 5B9.

Vickery, B.J., Baddour, R.E. and Karakatsanis, C. (1983), "A Study of External Wind Pressure Distributions and Induced Internal Ventilation Flow in Low-Rise Industrial and Domestic Structure". Boundary Layer Wind Tunnel Laboratory, The University of Western Ontario, London, Canada, Report No. BLWT-SS2-1983, 90 pp.

Vickery, B.J. and Karakatsanis, C. (1987), "External Wind Pressure and Induced Internal Ventilation Flow in Low-Rise Industrial and Domestic Structures", ASHRAE Trans., Vol. 93(2), pp. 2198-2213.

Wardlaw, R.L. (1989), "Personal Communication", Aerodynamic Low Wind Speed Laboratory, Nat. Res. Council of Canada, Montreal Rd, Ottawa, Canada.

West, D.L. (1977), "Contaminant Dispersion and Dilution in a Ventilated Space", ASHRAE Trans., Vol. 83(1), pp. 125-140.

Wright, D.I. and Westgate, G.R. (1982), "Wind Loads on Farm Buildings: (8) Full-Scale Measurements on a 34.2 m Long Single 24.6 m Span Ridged Roof Building of 2.3 m Eaves Height and 11° Roof Pitch", Div. Note DN 1124, AFRC Inst. Engng. Res., Silsoe, UK, June (unpubl.), 14 pp.

Zhang, J., Janni, K.A. and Jacobson, L.D. (1989), "Modeling Natural Ventilation Induced by Combined Thermal Buoyancy and Wind", Trans. of ASAE, Vol. 32(6), pp. 2165-2174.

Zollars, R.L. (1980), "Turbidimetric Method for On-Line Determination of Latex Particle Number and Particle Size Distribution", J. Coll. Inter. Sc., Vol. 74(1), pp. 163-172.

WIND INDUCED NATURAL VENTILATION OF LOW-RISE BUILDINGS FOR LIVESTOCK HOUSING BY THE PRESSURE DIFFERENCE METHOD AND CONCENTRATION DECAY METHOD

APPENDICES

by

Yves Choinière, P.Eng.
Engineering Resources Unit
Resource Management Branch
Ontario Ministry of Agriculture and Food
Alfred College of Agriculture and Food Technology
Alfred, Ontario
K0B 1A0

A thesis
presented to the University of Ottawa
in partial fulfillment of the
requirements for the degree of
Master of Applied Science
in
Civil Engineering

Ottawa, Ontario

April, 1991

APPENDIX A

Reference pressure coefficients

Pressure coefficients were gathered and summarized in order to compare the results among previous researchers and the present work. Only the pressure coefficients obtained for an open country situation (α = 0.14 to 0.18) were kept, with the exception of Aynsley et al. (1977) which were used to compare the effect of the power law exponent on the Cps. All data were also transformed to a reference height of 10 m in order to use it with meteorological data.

List of previous tests on pressure coefficients around buildings.
NB: transformed to 10 m; α = 0.14 to 0.18, open country situation.

Holmes (1983)
Model house (sealed)
Length = 12.2 m, width = 6.1 m, eave height = 2.6 m
overhang = 1.1 m, roof angle = 10°, 15°, 20°, θ = 0°, 45°, 90°, rural terrain, α = 0.17

Aynsley et al. (1977)
Model house (sealed)
length = 12.2 m, width = 6.1 m, eave height = 2.6 m
overhang = 1.1 m, roof angle = 10°, θ = 45°, 90°
city area, α = 0.28

Vickery et al. (1983) from Davenport et al. (1977, 1978)
Model industrial building (sealed)
length = 38.1 m, width = 24.4 m, height = 4.9 m
overhang = 1.5 m, roof angles = 4.7° and 18.4°, θ = 0°, 45°, 90°, open country, α = 0.14

Aynsley (1979)
Model house (open)
length = 12.2 m, width = 6.1 m, eave height = 2.6 m,
overhang = 1.1 m, roof angle = 10°, θ = 90°,
city area, α = 0.28
sidewall opening area = 0%, 10%, 20%, 30%, 40%

Ashley and Sherman (1984)
Model house (sealed)
length/width ratio = 1, 2, 3, and 4, height = unknown,
no overhang, roof angle = between 15° and 30°, θ = 90°,
country with scattered windbreaks, α = 0.20

Agricultural buildings

Down et al. (1985), data from Bruce (1974)
Sealed model
length = 35 m, width = 22 m, eave height = 2.2 m,
roof angle = 12°, θ = 0°, 30°, 60°, 90°,
open country, α = 0.15 to 0.17

Brockett and Albright (1987)
Sealed model
full scale length = 60 m, width = 12 m, eave height = 2.5 m,
no overhang, θ = 0°, 45°, 90°, roof angle = 14.0°
open country

Bottcher et al. (1986)
Open model (1:25 scale)
length = 762 mm, width = 400 mm, eave height = 100 mm
roof angle = 18.4°, no overhang
open country

Shrestha et al. (1990)
Open model (1:2 scale), with ridge opening
length = 7.3 m, width = 4.9 m, eave height = 1.5 m
overhang = 0.30 m, roof angle = 18.4°, θ = 90°
ridge opening width = 89 mm; = 1.8% of floor area
open country

Full scale measurements

Wright and Westgate (1982), Richardson (1989b)
Full scale, open versus closed ridge, (FB06)
length = 34.25 m, width = 24.6 m, eave height = 2.66 m,
ridge height = 4.79 m, roof angle = 11°,
partial ridge opening width = 200 mm,
sidewall opening (top part) = 100 mm, no overhang
open country, $\alpha = 0.17$, $\theta = 90°$

Moran et al. (1983)
Full scale, with or without intermittent ventilators, (FB02)
length = 18.5 m, width = 7.4 m, eave height = 1.77 m,
roof angle = 15°. intermittent ventilators with covers, no
sidewall opening, no overhang, $\theta = 90°$
open country, $\alpha = 0.17$

Hoxey and Moran (1983)
1) Full scale sealed building (FB01)
length = 27.8 m, width = 21.5 m, eave height = 4.3 m,
roof angle = 15°, no overhang
open country, $\alpha = 0.17$
* Low confidence level because of close leeward interferences
(Robertson et al., 1988)

2) FB16
length = 120.0 m, width = 6.7 m, eave height = 4.5 m,
roof angle = 15°, no overhang,
open country

3) FB03
length = 18.5 m, width = 11.9 m, eave height = 4.6 m,
roof angle = 16°, no overhang,
open country

4) FB05
length = 41.0 m, width = 28.0 m, eave height = 4.0 m,
roof angle = 15°, no overhang,
open country

Robertson et al. (1985)
Full scale, Dutch barn, with all solid walls
length = 24.3 m, width = 11.0 m, eave height = 5.5 m,
roof angle = 16.7°, no overhang, θ = 0°, 90°,
open country

Robertson et al. (1988)
FB19, Full scale
length = 36.84 m, width = 18.4 m, eave height = 5.0 m,
roof angle = 15°, no overhang, but rain gutter 0.15 m wide,
open country

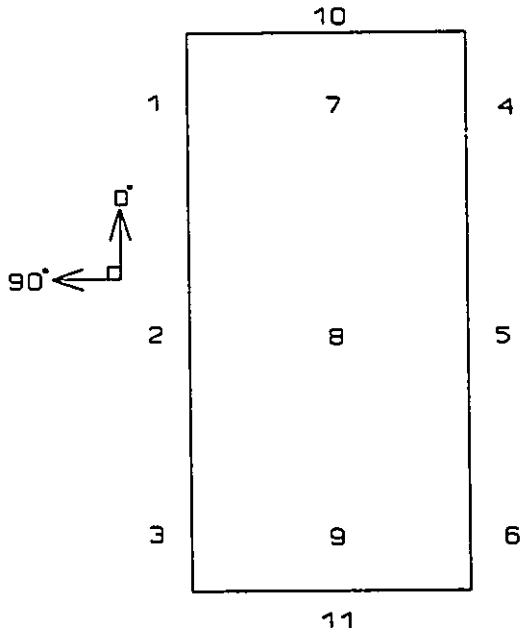

Figure A.1 Reference locations for pressure coefficients around the building.

Table A.1 Pressure coefficient locations around the buildings.

Description	Windward Sidewall			Leeward Sidewall			Ridge			End Walls		Internal
	1	2	3	4	5	6	7	8	9	10	11	
Aynsley (1979) roof angle = 10°												
θ = 90°	0.63	0.80	0.625	-0.19	-0.16	-0.19				-0.63	-0.63	
θ = 45°	0.47	0.16	-0.16	-0.47	-0.39	-0.25				-0.20	-0.15	
Holmes (1984) roof angle = 10°												
θ = 90°	0.32	0.38	0.32	-0.08	-0.08	-0.08	-0.44	-0.48	-0.44	-0.25	-0.25	
θ = 45°	0.35	0.22	0.13	-0.35	-0.25	-0.19	-0.57	-0.32	-0.28	0.22	-0.19	
θ = 30°	0.16	0.13	0.06	-0.35	-0.27	-0.19	-0.60	-0.22	-0.19	0.38	-0.16	
θ = 0°	-0.25	-0.13	-0.06	-0.25	-0.13	-0.06	-0.44	-0.06	-0.05	0.44	-0.08	
roof angle = 15°												
θ = 90°	0.35	0.38	0.35	-0.16	-0.16	-0.16	-0.45	-0.42	-0.45	-0.32	-0.32	
θ = 0°	-0.35	-0.13	-0.07	-0.35	-0.13	-0.07	-0.51	-0.13	-0.06	0.50	-0.11	
roof angle = 20°												
θ = 90°	0.38	0.41	0.38	-0.19	-0.19	-0.19	-0.22	-0.19	-0.22	-0.32	-0.32	
θ = 0°	-0.25	-0.11	-0.08	-0.25	-0.11	-0.08	-0.51	-0.14	-0.08	0.52	-0.09	

Table A.1 Cont'd.

Description	Windward Sidewall			Leeward Sidewall			Ridge			End Walls		Internal
	1	2	3	4	5	6	7	8	9	10	11	
Vickery et al. (1983)												
roof angle = 4.7°												
θ = 90°	0.34	0.36	0.34	-0.12	-0.09	-0.12	-0.67	-0.67	-0.67	-0.16	-0.16	
θ = 45°	0.27	0.17	0.10	-0.34	-0.26	-0.20	-0.37	-0.42	-0.35	0.16	-0.20	
θ = 0°	-0.26	-0.08	-0.06	-0.26	-0.08	-0.06	-0.41	-0.08	-0.08	0.40	-0.10	
roof angle = 18.4°												
θ = 90°	0.32	0.37	0.30	-0.35	-0.29	-0.36	-0.34	-0.32	-0.34	-0.25	-0.25	
θ = 45°	0.22	0.14	0.07	-0.37	-0.30	-0.21	-1.1	-0.66	-0.50	0.16	-0.25	
θ = 0°	-0.37	-0.11	-0.10	-0.30	-0.11	-0.08	-0.58	-0.16	-0.11	0.41	-0.14	
Down et al. (1985)												
θ = 90°	0.44	0.42	0.44	-0.06	-0.03	-0.06	-1.2	-1.4	-1.2			
θ = 60°	0.44	0.30	0.28	-0.23	-0.03	-0.04	-1.32	-1.17	-0.94			
θ = 30°	0.11	0.08	0.07	-0.32	-0.09	-0.05	-0.92	-0.51	-0.46			
θ = 0°	-0.30	-0.03	-0.05	-0.30	-0.03	-0.05	-0.47	-0.05	-0.07			

Table A.1 Cont'd.

Description	Windward Sidewall			Leeward Sidewall			Ridge			End Walls		Internal
	1	2	3	4	5	6	7	8	9	10	11	
Brockett and Albright (1987)												
$\theta = 90°$	0.40	0.50	0.40	-0.30	-0.20	-0.30	-0.80	-0.70	-0.80	-0.10	-0.10	
$\theta = 45°$	0.50	0.40	0.30	-0.20	-0.20	-0.30	-0.30	-0.20	-0.20	0.10	-0.10	
$\theta = 0°$	-0.30	-0.30	-0.20	-0.30	-0.30	-0.20	-0.60	-0.60	-0.60	0.70	-0.40	
Shrestha et al. (1990)												
$\theta = 90°$	0.39	0.44	0.38	-0.07	-0.07	-0.07	-0.32	-0.28	-0.28			
Full Scale												
Wright and Westgate (1982)												
open ridge FB06 $\theta = 90°$		0.25			-0.12			-0.33				-0.14
closed ridge FB06 $\theta = \pm 70°$		0.16			-0.11			-0.59				-0.12
Moran et al. (1983) $\theta = 90°$												
closed ridge FB02		0.25			-0.26			-0.60				-0.19
open ridge		0.25			-0.26			-0.60				-0.19
Hoxey and Moran (1983) FB01*												
$\theta = 90°$		0.40			-0.11			-0.67				

* close obstruction discussed by Robertson, (1988) FB01 vs FB19

Table A.1 Cont'd.

Description	Windward Sidewall			Leeward Sidewall				Ridge		End Walls		Internal
	1	2	3	4	5	6	7	8	9	10	11	
FB16								-0.93				
FB03								-1.03				
FB05								-1.42				
Robertson et al. (1985) $\theta = 90°$	0.40	0.45	0.40	-0.34	-0.34	-0.34	-0.68	-0.84	-0.69	-0.57	-0.50	-0.18
$\theta = 0°$	-0.30	-0.04	-0.05	-0.30	-0.14	-0.10	-0.55	-0.11	-0.08	0.61	-0.12	-0.11
Robertson et al. (1988) FB19 $\theta = 90°$		0.37			-0.20			-0.94				
Choinière SE-CH $\theta = 90°$	0.52	0.53	0.50	-0.33	-0.25	-0.32	-0.57	-0.57	-0.64	-0.40	-0.40	
$\theta = 45°$	0.38	0.28	0.12	-0.48	-0.32	-0.18	-1.44	-1.01	-0.55	0.30	-0.26	
$\theta = 0°$	-0.35	-0.13	-0.06	-0.34	-0.12	-0.05	-0.72	-0.19	-0.25	0.58	-0.12	
SE-150 $\theta = 90°$	0.48	0.50	0.48	-0.24	-0.18	-0.23	-0.73	-0.78	-0.62	-0.40	-0.40	
$\theta = 45°$	0.38	0.26	0.12	-0.45	-0.28	-0.13	-1.47	-1.25	-0.85	0.30	-0.28	
$\theta = 0°$	-0.35	-0.12	-0.06	-0.35	-0.12	-0.06	-0.57	-0.06	-0.06	0.55	-0.12	

Table A.1 Cont'd.

Description	Windward Sidewall			Leeward Sidewall			Ridge			End Walls		Internal
	1	2	3	4	5	6	7	8	9	10	11	
SE-400												
θ = 90°	0.50	0.47	0.47	-0.16	-0.12	-0.16	-1.25	-1.32	-1.21	-0.35	-0.35	
θ = 45°	0.38	0.26	0.14	-0.45	-0.32	-0.15	-1.81	-1.55	-1.10	-0.35	-0.28	
θ = 0°	-0.36	-0.12	-0.07	-0.34	-0.11	-0.03	-0.58	-0.06	-0.06	0.58	-0.12	
OP-CH-800-C												
θ = 90°	0.50	0.48	0.50	-0.25	-0.24	-0.25	-1.0	-0.83	-0.80	-0.35	-0.30	
θ = 45°	0.33	0.25	0.17	-0.35	-0.27	-0.20	-1.0	-0.85	-0.64	0.35	-0.25	
θ = 0°	-0.33	-0.19	-0.05	-0.33	-0.19	-0.05	-0.55	-0.08	-0.08	0.55	-0.11	
OP-CH-1100-C												
θ = 90°	0.50	0.50	0.50	-0.25	-0.25	-0.25	-0.85	-0.79	-0.80	-0.30	-0.25	
θ = 45°	0.30	0.26	0.20	-0.36	-0.25	-0.20	-1.0	-0.87	-0.70	0.35	-0.25	
θ = 0°	-0.35	-0.20	-0.10	-0.35	-0.20	-0.10	-0.57	-0.09	-0.09	0.55	-0.11	
OP-150-800-C												
θ = 90°	0.50	0.50	0.50	0.35	-0.30	-0.35	-0.20	-0.20	-0.21	-0.30	-0.40	
θ = 45°	0.34	0.25	0.18	-0.38	-0.30	-0.25	-0.77	-0.38	-0.22	0.35	-0.26	
θ = 0°	-0.35	-0.17	-0.05	-0.35	-0.15	-0.05	-0.56	-0.11	-0.06	0.50	-0.11	
OP-150-1100-C												
θ = 90°	0.48	0.50	0.48	-0.40	-0.40	-0.40	-0.21	-0.20	-0.20	-0.30	-0.35	
θ = 45°	0.31	0.28	0.20	-0.38	-0.30	-0.25	-0.78	-0.39	-0.21	0.35	-0.27	
θ = 0°	-0.37	-0.21	-0.10	-0.37	-0.22	-0.10	-0.59	-0.11	-0.07	0.60	-0.11	

Table A.1 Cont'd.

Description	Windward Sidewall			Leeward Sidewall			Ridge			End Walls		Internal
	1	2	3	4	5	6	7	8	9	10	11	
OP-400-800-C												
$\theta = 90°$	0.53	0.52	0.50	-0.35	-0.30	-0.35	-0.22	-0.22	-0.22	-0.35	-0.40	
$\theta = 45°$	0.35	0.28	0.18	-0.38	-0.30	-0.25	-0.70	-0.47	-0.25	0.30	-0.28	
$\theta = 0°$	-0.35	-0.16	-0.05	-0.35	-0.15	-0.05	-0.62	-0.18	-0.07	0.58	-0.11	
OP-400-1100-C												
$\theta = 90°$	0.50	0.54	0.50	-0.40	-0.40	-0.40	-0.22	-0.21	-0.22	-0.30	-0.35	
$\theta = 45°$	0.30	0.28	0.20	-0.35	-0.30	-0.25	-0.66	-0.32	-0.19	0.35	-0.27	
$\theta = 0°$	-0.35	-0.15	-0.05	-0.35	-0.15	-0.05	-0.56	-0.11	-0.06	0.60	-0.12	

Table A.2 Pressure coefficient difference accross low rise building at $\theta = 90°$ ($Cp_{windward} - Cp_{leeward}$): 10 m height reference.

Author		Average ΔCp	
Industrial Buildings			
Holmes (1983)			
roof = 10°		0.34	L = 12.2, W = 1.1, H = 2.6 Overhang
roof = 15°		0.54	
roof = 20°		0.60	
Vickery et al. (1983)			
roof = 4.7°		0.44	L = 38.1, W = 24.4, H = 4.9 Overhang
roof = 18.4°		0.66	
Aynsley (1979)			
sidewall opening area =	0%	0.36	
	10%	0.56	
	20%	0.57	
	30%	0.54	
	40%	0.50	
Ashley and Sherman (1984)			
length/width ratio =	1	0.52	
	2	0.58	
	3	0.77	
	4	0.80	
Agricultural Buildings			
Down et al. (1985)		0.48	L = 35, W = 22, H = 2.2 $\theta = 10°$
Brockett and Albright (1984)		0.70	
Bottcher et al. (1986)			
Sidewall openings are =	0%	0.78	L = 19, W = 10 m, H = 2.5 $\theta = 18.4°$
	10%	0.70	
	20%	0.64	
	30%	0.59	
	40%	0.55	

Table A.2 Cont'd.

Author		Average ΔC_p	
Shrestha et al. (1990) (open ridge)			
Sidewall opening area	3.3%	0.51	L = 14.6, W = 9.8, H = 3.0 Overhang θ = 18.4°
	10%	0.51	
Full Scale Study			
Robertson et al. (1985) Dutch barn		0.89	L = 24.3, W = 11, H = 5.5, θ = 16.7
Wright and Westgate (1982)			
FB06, open ridge		0.37	L = 34.25, W = 24.6, H = 2.60, θ = 11°
FB06, closed ridge		0.27	
Moran et al. (1983)			
FB02, open ridge		0.51	L = 88.5, W = 7.4, H = 1.79, θ = 15°
FB02, closed ridge		0.51	
Hoxey and Moran (1983)			
FB01*		0.51	L = 27.8, W = 21.5, H = 4.3, θ = 15°
Robertson et al. (1988)			
FB19		0.57	L = 37, W = 18.4, H = 5.0, θ = 15°
Choinière (present study)			
SE-150		0.67	
SE-400		0.61	
SE-CH		0.74	
OP-150-800-C		0.80	
OP-400-800-C		0.80	
OP-CH-800-C		0.75	
OP-150-1100-C		0.90	
OP-400-1100-C		0.85	
OP-CH-1100-C		0.75	

* Data has been reevaluated by Robertson et al. (1988) with FB19.

APPENDIX B

Results from Vickery et al. (1983)

Tables B.1 and B.2 contain the results of the pressure coefficient differences across a scale model of a low-rise industrial building. The effect of three eave heights and three roof angles can be analysed. All the data from Vickery et al. (1983) were transformed to a reference height of 10 m. For these tests, the wind tunnel was calibrated to reproduce an open country situation ($\alpha = 0.14$). Only the results for wind angles of incidence parallel to the building length ($\theta = 0°$) and perpendicular ($\theta = 90°$) are presented. The average pressure coefficient differences were taken at mid-length and mid-height of both the windward and leeward sidewalls. The pressure coefficients at the ridge are based on the average of -Cps across the ridge line at mid-length of the building.

Table B.1 Effect of eave heights on the average pressure coefficient difference across the sidewalls and average pressure coefficients across the ridge, $\theta = 90°$, roof angle = 18.4°.

Eaves Heights (m)	ΔCp Sidewalls	-Cp Ridge
4.9	0.66	-0.32
7.3	0.74	-0.33
9.7	0.77	-0.32

Table B.2 Effect of roof angles on the average Cp difference across the sidewalls and the average pressure coefficient across the ridge, θ = 90°, eave height = 4.9 m.

Roof Angles (degrees)	ΔCp Sidewalls	-Cp Ridge
4.7°	0.66	-0.32
18.4°	0.74	-0.33
45°	0.77	-0.32

Tables B.3 and B.4 present the pressure coefficients at three locations equal distant along the mid-height of the building for a wind angle of incidence parallel to the building length (θ = 0°). The Cps distributions were similar on both sidewalls. The -Cps at the ridge are the average -Cps on each side of the ridge line for three equal lengths along the building.

Table B.3 Effect of eave heights on the average Cps at three locations along the sidewalls and the ridge, θ = 0°, roof angle = 18.4°.

Eaves Heights (m)	Cp Sidewall Locations			Cp Ridge Locations		
	1	2	3	1	2	3
4.9	-0.37	-0.11	-0.10	-0.58	-0.16	-0.11
7.3	-0.45	-0.15	-0.10	-0.65	-0.16	-0.12
9.7	-0.51	-0.19	-0.17	-0.75	-0.30	-0.13

Table B.4 Effect of roof angles on the average Cps at three locations along the sidewalls and the ridge, $\theta = 0°$, eave height = 4.9 m.

Roof Angles (degrees)	Cp Sidewall Locations			Cp Ridge Locations		
	1	2	3	1	2	3
4.7°	-0.26	-0.08	-0.06	-0.41	-0.08	-0.08
18.4°	-0.37	-0.11	-0.10	-0.58	-0.16	-0.11
45°	-0.54	-0.15	-0.10	-0.78	-0.23	-0.14

Table B.5 Summary of the effect of eave heights and roof angles.

Sidewalls			
$\theta = 90°$ if Eave Height ↑,	ΔCp ↑,	Cp Ridge similar	
$\theta = 0°$ if Eave Height ↑,	Cp ↑,	Cp Ridge ↑	
Roof Angles			
$\theta = 90°$, if Roof Angle ↑,	ΔCp ↑,	Cp Ridge similar	
$\theta = 0°$, if Roof Angle ↑,	Cp ↑,	Cp Ridge ↑	

APPENDIX C

Preliminary tests in wind tunnel, recording period

Objective:

Study the effect of recording period of 1 second, 3 seconds and 5 seconds on the pressure coefficients.

Procedures:

1 - Calculate the differences between the tests 3 s - 1 s, 5 s - 1 s and 5 s - 3 s on absolute Cp values to obtain
  1.1 average $|\Delta Cp|$
  1.2 STD of $|\Delta Cp|$
  1.3 max ΔCp
  1.4 min ΔCp
2 - Calculate the difference between 3 s - 1 s, 5 s - 1 s, 5 s - 3 s on global Cp values, and calculate
  2.1 average ΔCp
  2.1 STD of ΔCp
  2.3 max ΔCp
  2.4 min ΔCp

Table C.1 Absolute Cp differences.

h = 10 m Location Number	Time 1 s Cp	Time 3 s Cp	Time 5 s Cp	Absolute Differences |3s-1s|	|3s-5s|	|5s-1s|
1	-0.7423	-0.78627	-0.75016	0.0439	0.0361	0.0078
2	-0.7691	-0.73176	-0.72063	0.0373	0.0111	0.0485
3	-0.5215	-0.53974	-0.57099	0.0183	0.0312	0.0495
4	-0.7350	-0.71757	-0.72199	0.0174	0.0044	0.0130
5	-0.1691	-0.17373	-0.17533	0.0046	0.0016	0.0062
6	-0.1940	-0.19968	-0.20667	0.0056	0.0070	0.0126
7	-0.1955	-0.18478	-0.17932	0.0107	0.0055	0.0162
8	-0.1635	-0.15809	-0.16146	0.0054	0.0034	0.0020
9	0.3920	0.387463	0.399086	0.0045	0.0116	0.0071
10	0.5218	0.498579	0.514216	0.0233	0.0156	0.0076
11	0.4908	0.534365	0.517063	0.0436	0.0173	0.0263
13	-0.3274	-0.31192	-0.30348	0.0154	0.0084	0.0239
14	-0.3275	-0.29754	-0.28995	0.0300	0.0076	0.0376
15	0.4[illegible]3	0.461911	0.467677	0.0236	0.0058	0.0294
16	0.5[illegible]08	0.5[illegible]2395	0.578539	0.0284	0.0161	0.0123
17	-0.3434	-0.32183	-0.31927	0.0215	0.0026	0.0241
21	-0.3153	-0.33285	-0.30788	0.0176	0.0250	0.0074
22	-0.3453	-0.31333	-0.32180	0.0320	0.0085	0.0235
23	0.5263	0.520612	0.574713	0.0057	0.0541	0.0484
24	0.4812	0.485081	0.512090	0.0039	0.0270	0.0309
25	0.5306	0.513134	0.535574	0.0174	0.0224	0.0050
26	0.5248	0.584614	0.573904	0.0598	0.0107	0.0491
27	0.5122	0.493569	0.496010	0.0186	0.0024	0.0161
28	-0.6433	-0.60733	-0.64835	0.0360	0.0410	0.0050
29	-0.2689	-0.33488	-0.33139	0.0660	0.0035	0.0625
30	-0.2823	-0.33184	-0.31696	0.0495	0.0149	0.0347
31	-0.2547	-0.30193	-0.31312	0.0472	0.0112	0.0584
32	-0.3328	-0.33857	-0.35495	0.0058	0.0164	0.0221
33	0.4714	0.451578	0.491204	0.0198	0.0396	0.0198
34	0.5134	0.534215	0.545612	0.0208	0.0114	0.0322
35	-0.2403	-0.30539	-0.28028	0.0651	0.0251	0.0400
36	-0.5696	-0.57453	-0.55162	0.0049	0.0229	0.0180
37	-0.3405	-0.30111	-0.31409	0.0394	0.0130	0.0264
38	-0.3102	-0.30213	-0.32741	0.0081	0.0253	0.0172
41	0.4640	0.555207	0.540515	0.0912	0.0147	0.0765
42	0.4785	0.513936	0.491103	0.0355	0.0228	0.0126
43	0.5028	0.518126	0.583182	0.0153	0.0651	0.0804
44	0.5750	0.560652	0.570944	0.0143	0.0103	0.0040
46	-0.2482	-0.21408	-0.24162	0.0341	0.0275	0.0066
47	-0.2816	-0.25618	-0.23508	0.0254	0.0211	0.0465
49	-0.2766	-0.22840	-0.25961	0.0482	0.0312	0.0170
50	-0.2168	-0.22683	-0.23337	0.0100	0.0065	0.0165
51	0.4504	0.518251	0.519140	0.0678	0.0009	0.0687
52	0.5174	0.573612	0.601738	0.0562	0.0281	0.0843
53	0.5140	0.542413	0.551546	0.0284	0.0091	0.0375
54	-0.5763	-0.56352	-0.58723	0.0127	0.0237	0.0110
55	-0.2488	-0.21192	-0.22766	0.0369	0.0157	0.0211
56	-0.2412	-0.24314	-0.25013	0.0020	0.0070	0.0090
57	0.5022	0.498991	0.529021	0.0032	0.0300	0.0269
58	0.5521	0.585151	0.590048	0.0331	0.0049	0.0379
61	-0.2541	-0.26442	-0.26956	0.0103	0.0051	0.0154
63	-0.2761	-0.30120	-0.30480	0.0251	0.0036	0.0287
64	-0.2977	-0.30679	-0.34328	0.0091	0.0365	0.0455
65	0.5370	0.544359	0.562918	0.0074	0.0186	0.0259
66	0.4966	0.478146	0.486836	0.0185	0.0087	0.0098
67	0.5324	0.527773	0.529896	0.0046	0.0021	0.0025

Table C.1 (cont'd.) Absolute Cp differences.

h = 10 m Location Number	Time 1 s Cp	Time 3 s Cp	Time 5 s Cp	Absolute Differences |3s-1s|	|3s-5s|	|5s-1s|
68	0.5879	0.584143	0.593604	0.0038	0.0095	0.0057
71	-0.3478	-0.30584	-0.32877	0.0420	0.0229	0.0190
72	-0.3298	-0.31091	-0.33285	0.0189	0.0219	0.0030
73	-0.2993	-0.29499	-0.32297	0.0043	0.0280	0.0237
74	-0.3209	-0.33538	-0.35177	0.0145	0.0164	0.0308
75	0.4403	0.421712	0.442236	0.0186	0.0205	0.0020
76	0.5470	0.551474	0.565276	0.0045	0.0138	0.0183
77	0.5155	0.474833	0.480542	0.0407	0.0057	0.0350
78	-0.5900	-0.61781	-0.56693	0.0278	0.0509	0.0230
81	-0.29017	-0.31815	-0.31591	0.0280	0.0022	0.0257
82	-0.32102	-0.33738	-0.32989	0.0164	0.0075	0.0089
83	0.364783	0.350087	0.392073	0.0147	0.0420	0.0273
84	0.540893	0.508794	0.52394	0.0321	0.0151	0.0170
85	-0.28379	-0.28878	-0.30678	0.0050	0.0180	0.0230
87	-0.26720	-0.28720	-0.30243	0.0200	0.0152	0.0352
88	-0.31827	-0.28694	-0.30988	0.0313	0.0229	0.0084
89	-0.17856	-0.17172	-0.18006	0.0068	0.0083	0.0015
90	-0.18960	-0.19027	-0.18589	0.0007	0.0044	0.0037
91	-0.29719	-0.28718	-0.29404	0.0100	0.0069	0.0031
92	-0.15442	-0.16000	-0.17173	0.0056	0.0117	0.0173
93	-0.53709	-0.57374	-0.57760	0.0366	0.0039	0.0405
94	-0.73642	-0.76961	-0.78711	0.0332	0.0175	0.0507
95	-0.81680	-0.75511	-0.78297	0.0617	0.0279	0.0338
96	-0.74801	-0.75730	-0.76771	0.0093	0.0104	0.0197
			Average	0.024084	0.016959	0.025022
			Std. Dev.	0.018671	0.012898	0.018930
			Maximum	0.091168	0.065056	0.084290
			Minimum	0.000671	0.000888	0.001494

Table C.2 Cp differences.

h = 10 m Differences with signs

Location Number	3s-1s	3s-5s	5s-1s
1	-0.0439	-0.0361	-0.0078
2	0.0373	-0.0111	0.0485
3	-0.0183	0.0312	-0.0495
4	0.0174	0.0044	0.0130
5	-0.0046	0.0016	-0.0062
6	-0.0056	0.0070	-0.0126
7	0.0107	-0.0055	0.0162
8	0.0054	0.0034	0.0020
9	-0.0045	-0.0116	0.0071
10	-0.0233	-0.0156	-0.0076
11	0.0436	0.0173	0.0263
13	0.0154	-0.0084	0.0239
14	0.0300	-0.0076	0.0376
15	0.0236	-0.0058	0.0294
16	-0.0284	-0.0161	-0.0123
17	0.0215	-0.0026	0.0241
21	-0.0176	-0.0250	0.0074
22	0.0320	0.0085	0.0235
23	-0.0057	-0.0541	0.0484
24	0.0039	-0.0270	0.0309
25	-0.0174	-0.0224	0.0050
26	0.0598	0.0107	0.0491
27	-0.0186	-0.0024	-0.0161
28	0.0360	0.0410	-0.0050
29	-0.0660	-0.0035	-0.0625
30	-0.0495	-0.0149	-0.0347
31	-0.0472	0.0112	-0.0584
32	-0.0058	0.0164	-0.0221
33	-0.0198	-0.0396	0.0198
34	0.0208	-0.0114	0.0322
35	-0.0651	-0.0251	-0.0400
36	-0.0049	-0.0229	0.0180
37	0.0394	0.0130	0.0264
38	0.0081	0.0253	-0.0172
41	0.0912	0.0147	0.0765
42	0.0355	0.0228	0.0126
43	0.0153	-0.0651	0.0804
44	-0.0143	-0.0103	-0.0040
46	0.0341	0.0275	0.0066
47	0.0254	-0.0211	0.0465
49	0.0482	0.0312	0.0170
50	-0.0100	0.0065	-0.0165
51	0.0678	-0.0009	0.0687
52	0.0562	-0.0281	0.0843
53	0.0284	-0.0091	0.0375
54	0.0127	0.0237	-0.0110
55	0.0369	0.0157	0.0211
56	-0.0020	0.0070	-0.0090
57	-0.0032	-0.0300	0.0269
58	0.0331	-0.0049	0.0379
61	-0.0103	0.0051	-0.0154
63	-0.0251	0.0036	-0.0287
64	-0.0091	0.0365	-0.0455
65	0.0074	-0.0186	0.0259
66	-0.0185	-0.0087	-0.0098
67	-0.0046	-0.0021	-0.0025

Table C.2 (cont'd) Cp differences.

h = 10 m Differences with signs

Location Number	3s-1s	3s-5s	5s-1s
68	-0.0038	-0.0095	0.0057
71	0.0420	0.0229	0.0190
72	0.0189	0.0219	-0.0030
73	0.0043	0.0280	-0.0237
74	-0.0145	0.0164	-0.0308
75	-0.0186	-0.0205	0.0020
76	0.0045	-0.0138	0.0183
77	-0.0407	-0.0057	-0.0350
78	-0.0278	-0.0509	0.0230
81	-0.0280	-0.0022	-0.0257
82	-0.0164	-0.0075	-0.0089
83	-0.0147	-0.0420	0.0273
84	-0.0321	-0.0151	-0.0170
85	-0.0050	0.0180	-0.0230
87	-0.0200	0.0152	-0.0352
88	0.0313	0.0229	0.0084
89	0.0068	0.0083	-0.0015
90	-0.0007	-0.0044	0.0037
91	0.0100	0.0069	0.0031
92	-0.0056	0.0117	-0.0173
93	-0.0366	0.0039	-0.0405
94	-0.0332	0.0175	-0.0507
95	0.0617	0.0279	0.0338
96	-0.0093	0.0104	-0.0197
	0.002833	-0.00152	0.004357
	0.030342	0.021252	0.031072
	0.091168	0.041013	0.084290
	-0.06600	-0.06505	-0.06251

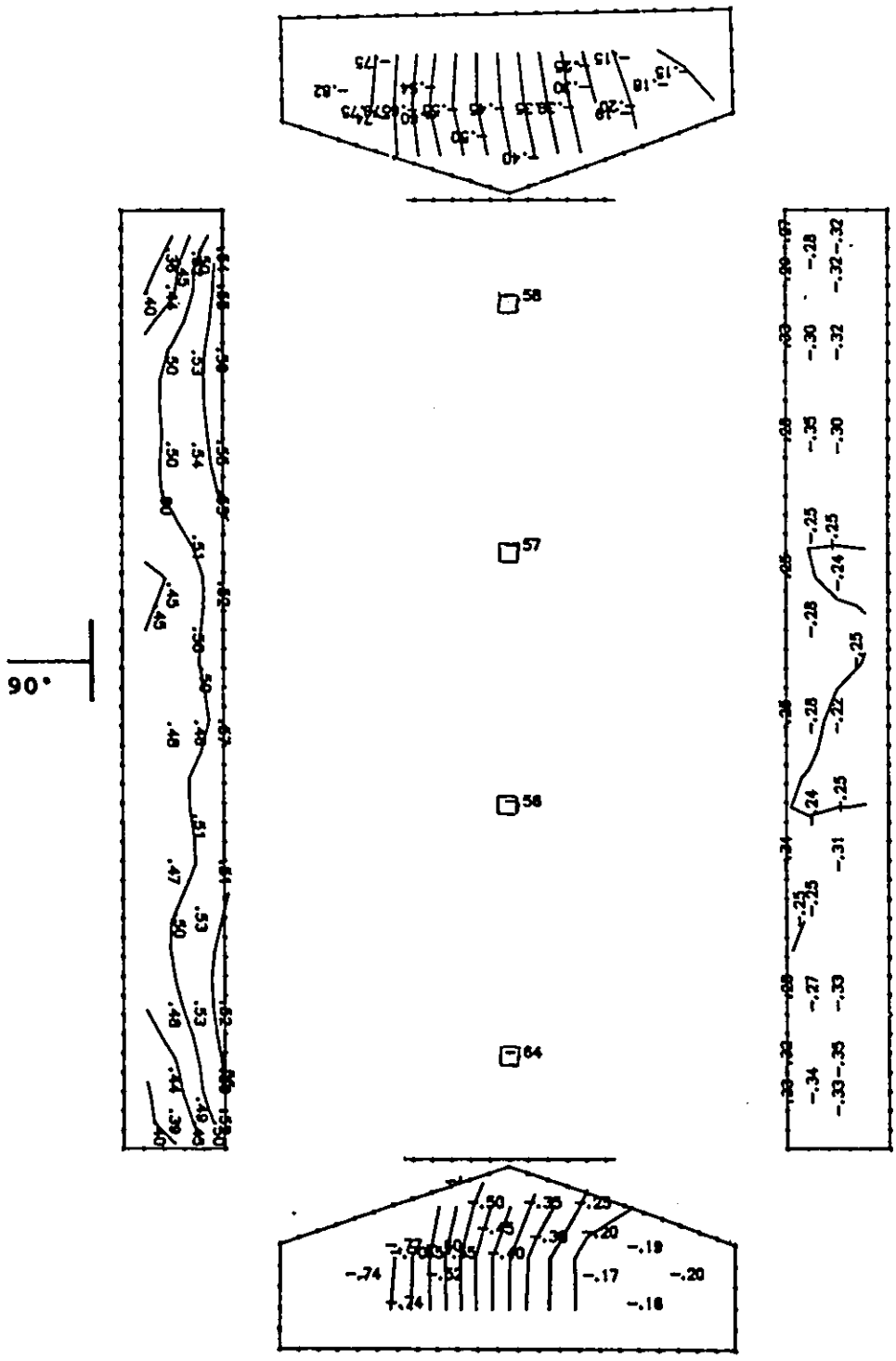

Figure C.1 Cps contour lines: sealed model with chimney, 1 second, wind angle of 90°.

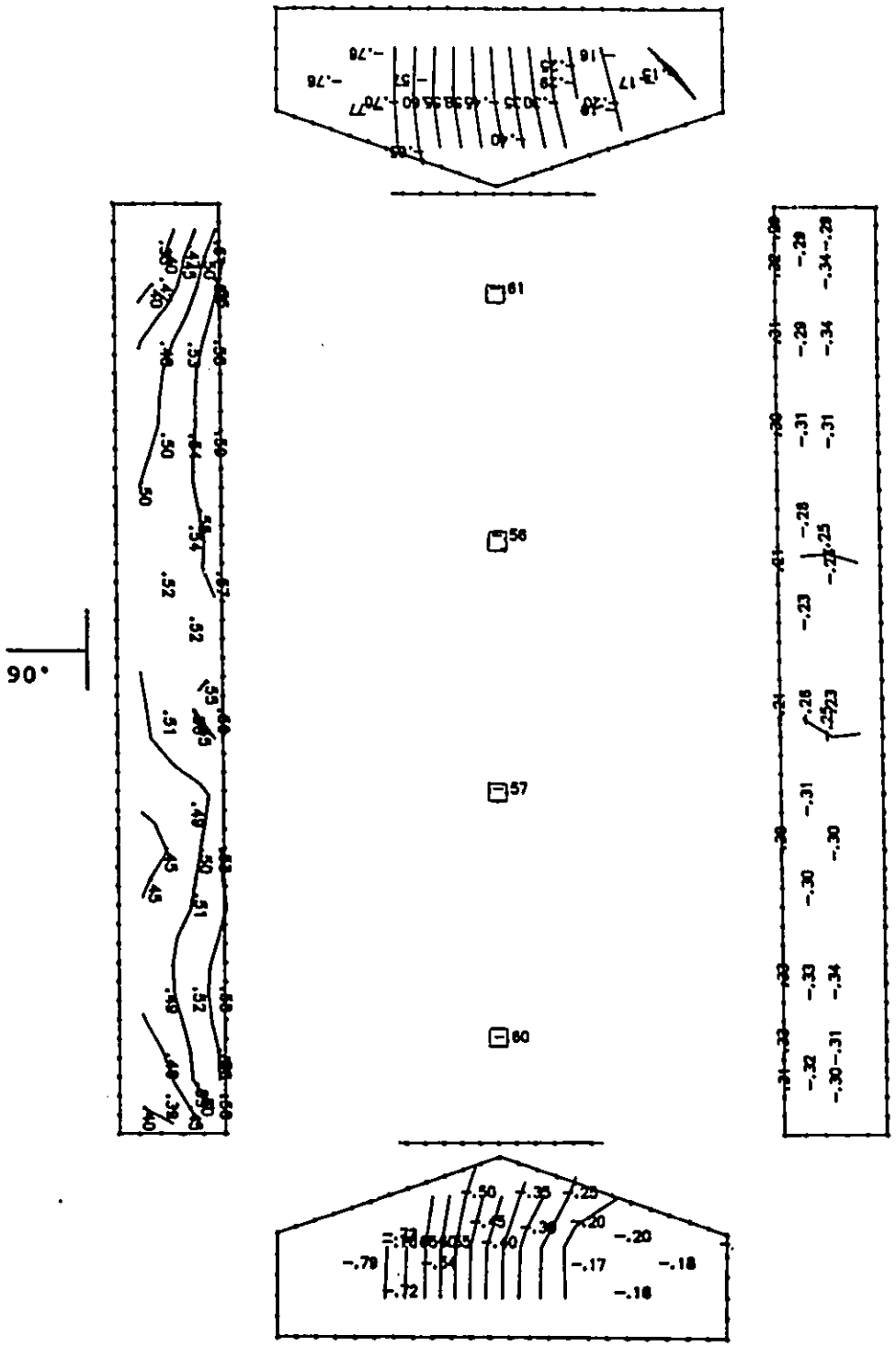

Figure C.2 Cps contour lines: sealed model with chimney, 3 seconds, wind angle of 90°.

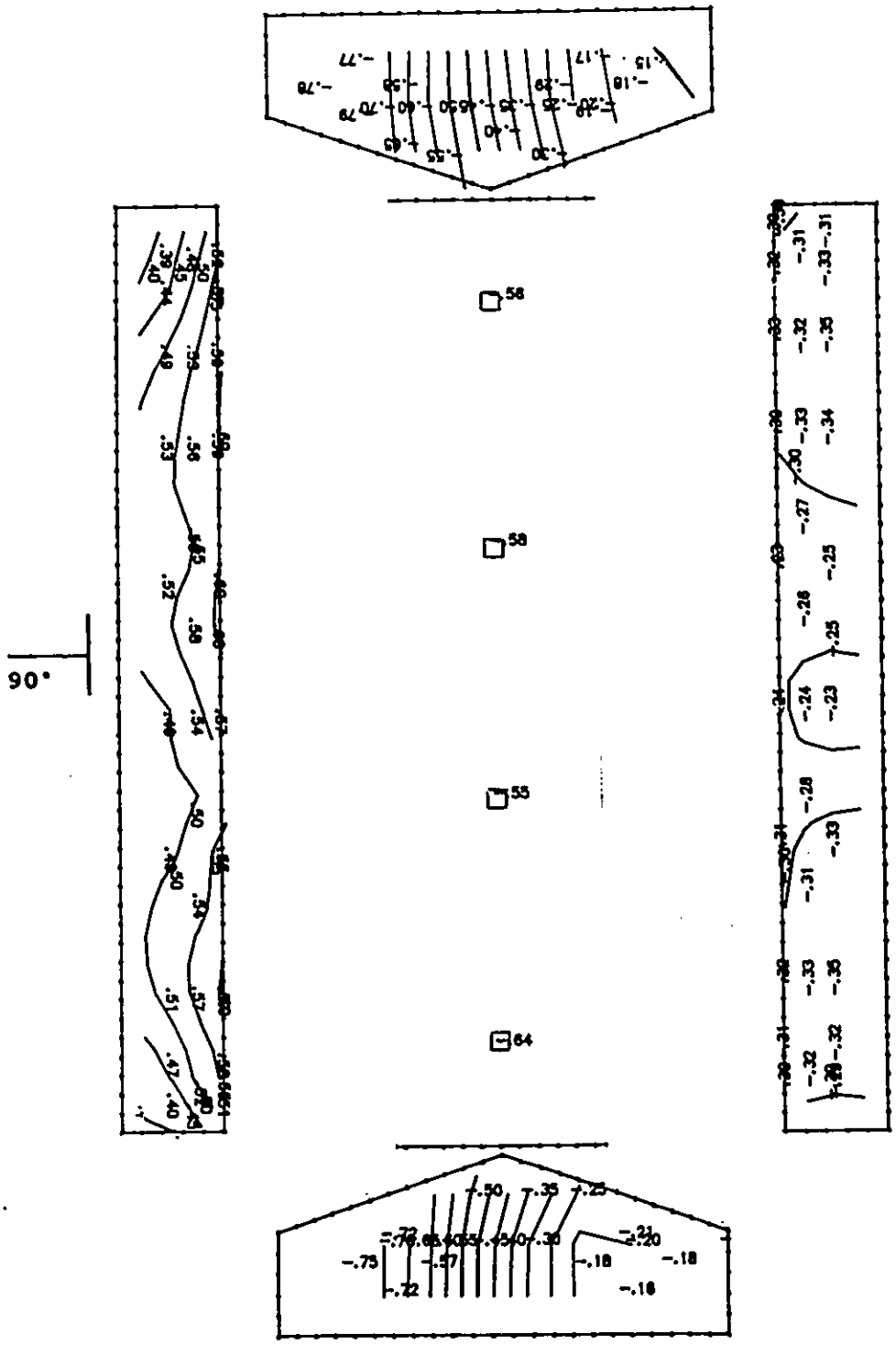

Figure C.3 Cps contour lines: sealed model with chimney, 5 seconds, wind angle of 90°.

APPENDIX D

Concentration decay method with optical density data processing

The following four figures present the methodology to calculate the effective ventilation rate coefficient, C_{KQ10}, from the voltage output of the silicone diode photodetector and laser. Figure D.1 shows a typical voltage output versus time. The useful part of the rate of decay curve was fairly short. The data presented in Figs. D.1, D.2 and D.3 shows that this useful data were collected during a period of 0.5 s to 2 s. Therefore, the sampling rate was established at 200 Hz and about 200 data points were available for data processing.

Some spikes are visible in Figs. D.1 and D.2. Also, other tests, not presented here, show large bumps during the decay period. These can be attributed to the recirculation of smoke in front of the laser beam. This is mainly attributable to the infiltration of residual smoke from the tubes and manifold below the scale model. As an effect, these spikes and bumps elongated the rate of decay process, causing an underestimation of C_{KQ10}. In future work, the smoke injection system should have sealed shut-off valves.

The initial voltage varied between 170 to 205 mV. Fig. D.2 shows that the optical density value (OD) was about 3 at those voltages. This indicates that the visibility inside the model was about 0.33 m. This also indicated that the laser's light beam was scattered and did not reach the photodetector. As soon as the laser beam was able to pass through the smoke, the voltage output increased (Fig. D.1). Accordingly, the optical density dropped until it reached a value of 0.0, indicating that the scale model was totally clear of smoke.

In Fig. D.3, the final value of the optical density was about 1.0. This final value may indicate:

1 - A high concentration of smoke in the wind tunnel and in the air intake.
2 - Contamination of the laser enclosure.

Since the NRCC wind tunnel is a closed loop, the concentration of the smoke was increasing during the day. The maximum levels of smoke contamination were reached by the end of the week. Large final OD values were recorded when smoke was able to infiltrate the protective enclosure of the laser. To solve this problem, the tests were halted, the laser lenses cleaned, and the enclosure carefully resealed. The effect of smoke contamination was not considered critical because the effect of refeeding and the final optical density values were substracted, as in Eq. 4.9.

Figure D.4 shows the basic methodology for the calculation of the effective ventilation rate. At the beginning of the test, the first part of the curve is fairly flat. The actual rate of decay started when the difference from 0.0 was about 0.2 for this test and ended when a vertical difference of 0.4 was recorded at the end of the process. For the example in Fig. D., the value of KQ was -0.363 with a linear correlation of -0.9866. This indicates that the effective ventilation rates for this particular test was

$$KQ = -0.363\, m^3/s$$

The dimensionless C_{KQ10} could be evaluated knowing that

$$C_{KQ10} = \frac{-KQ}{V_{10} As} = 0.612$$

where

V_{10} = 9.8 m/s (for most tests)
As = 0.0605 m^2

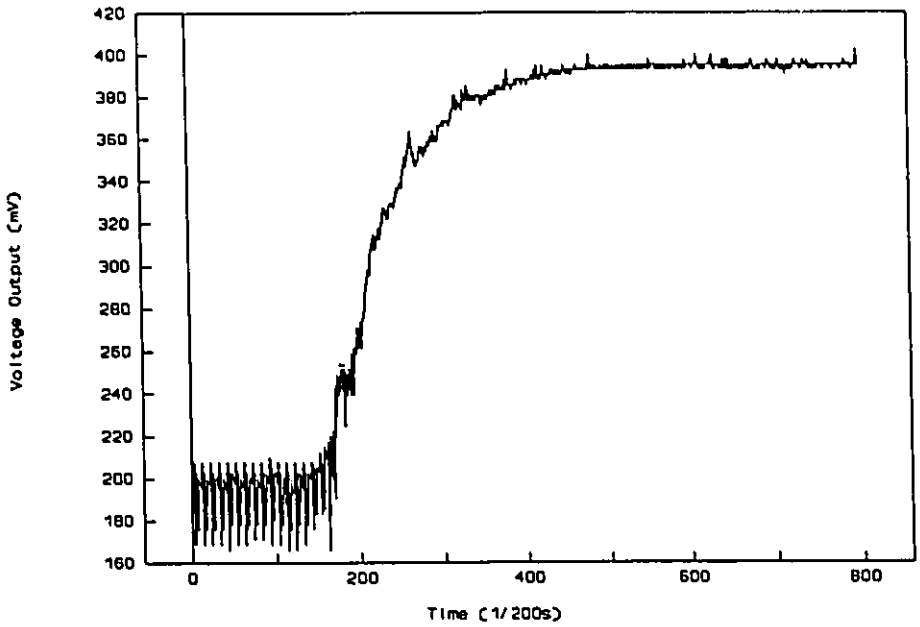

Figure D.1 Typical voltage output for optical density measurements.

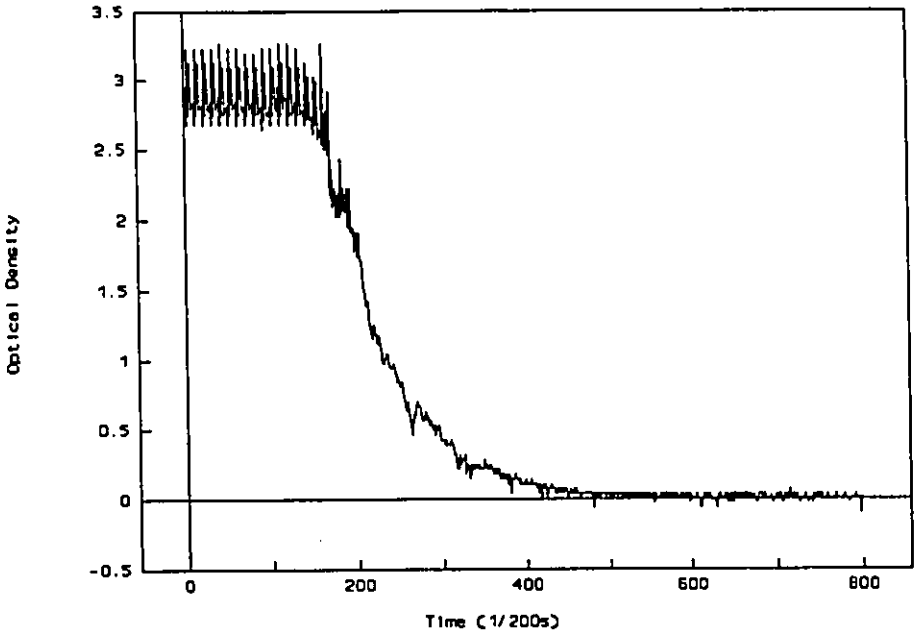

Figure D.2 Typical optical density measurement for smoke's concentration decay.

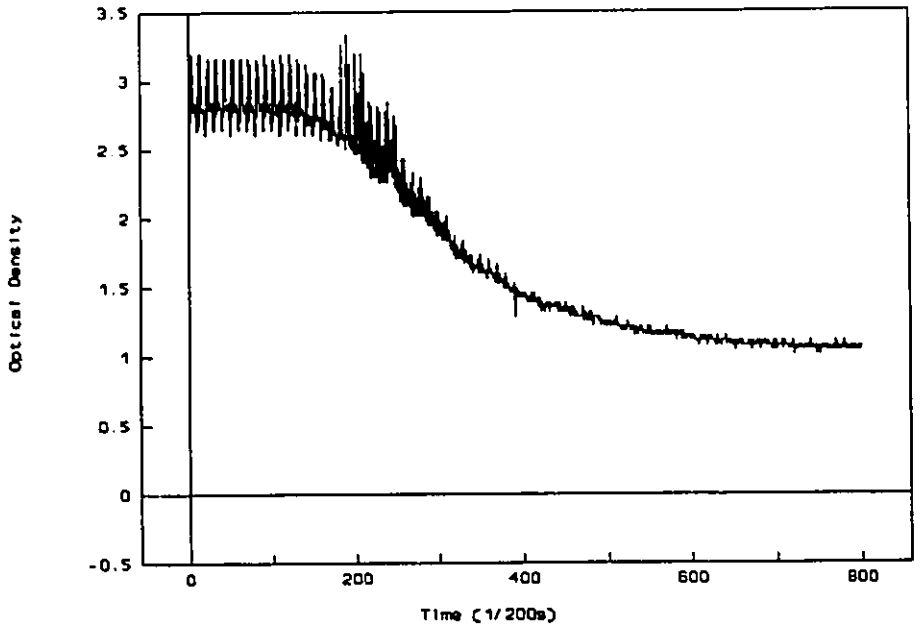

Figure D.3 Example of wind tunnel contamination, the final OD value did not equal 0.0 because of the smoke in the air intake.

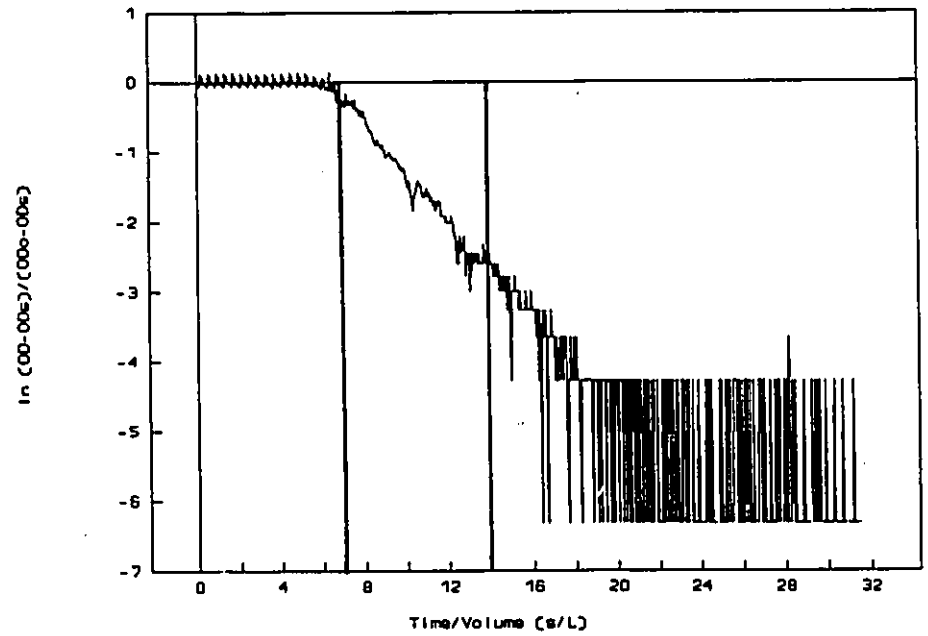

Figure D.4 Calculation of KQ from the concentration decay method, correlation = -0.9866, slope = -0.363.

APPENDIX E

Contour lines of the external pressure coefficients, complete data

Appendix E contains the contour lines for the external pressure coefficients for the 84 open model tests and the 21 sealed model tests.

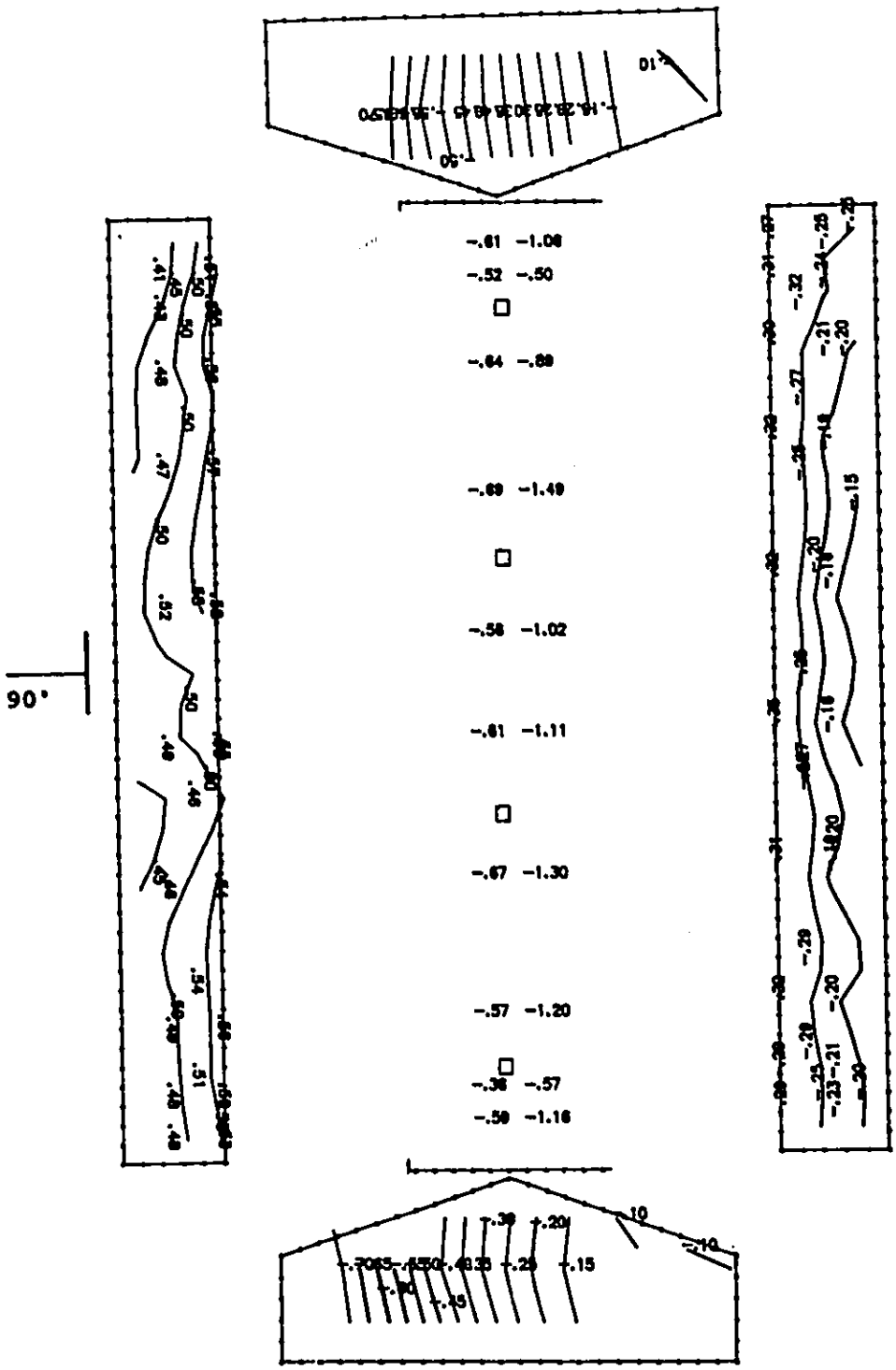

Figure E.1a Cps contour lines: open model, chimney, simulated 800 mm sidewall openings, closed end walls, wind angle of 90°.

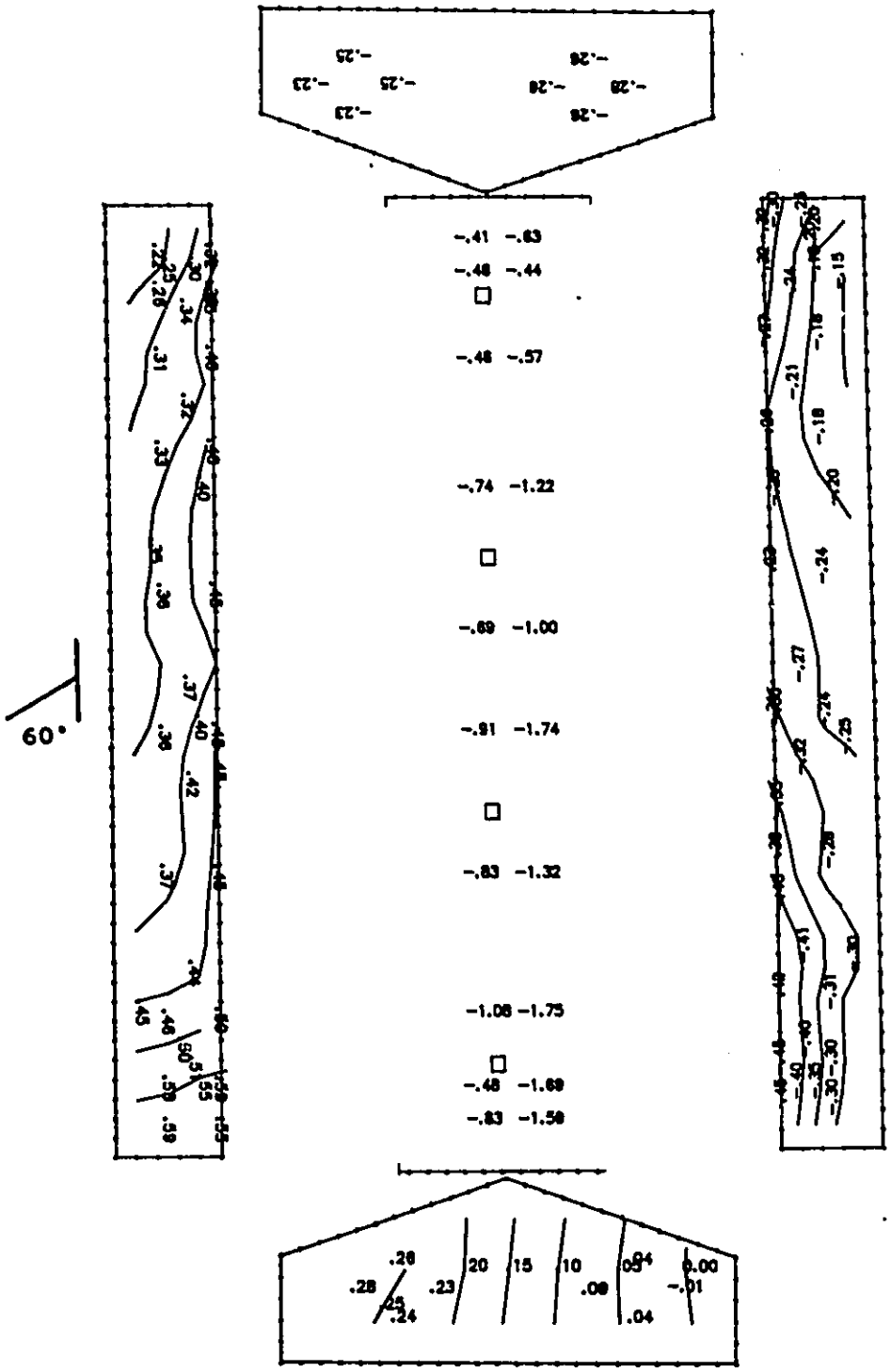

Figure E.1b Cps contour lines: open model, chimney, simulated 800 mm sidewall openings, closed end walls, wind angle of 60°.

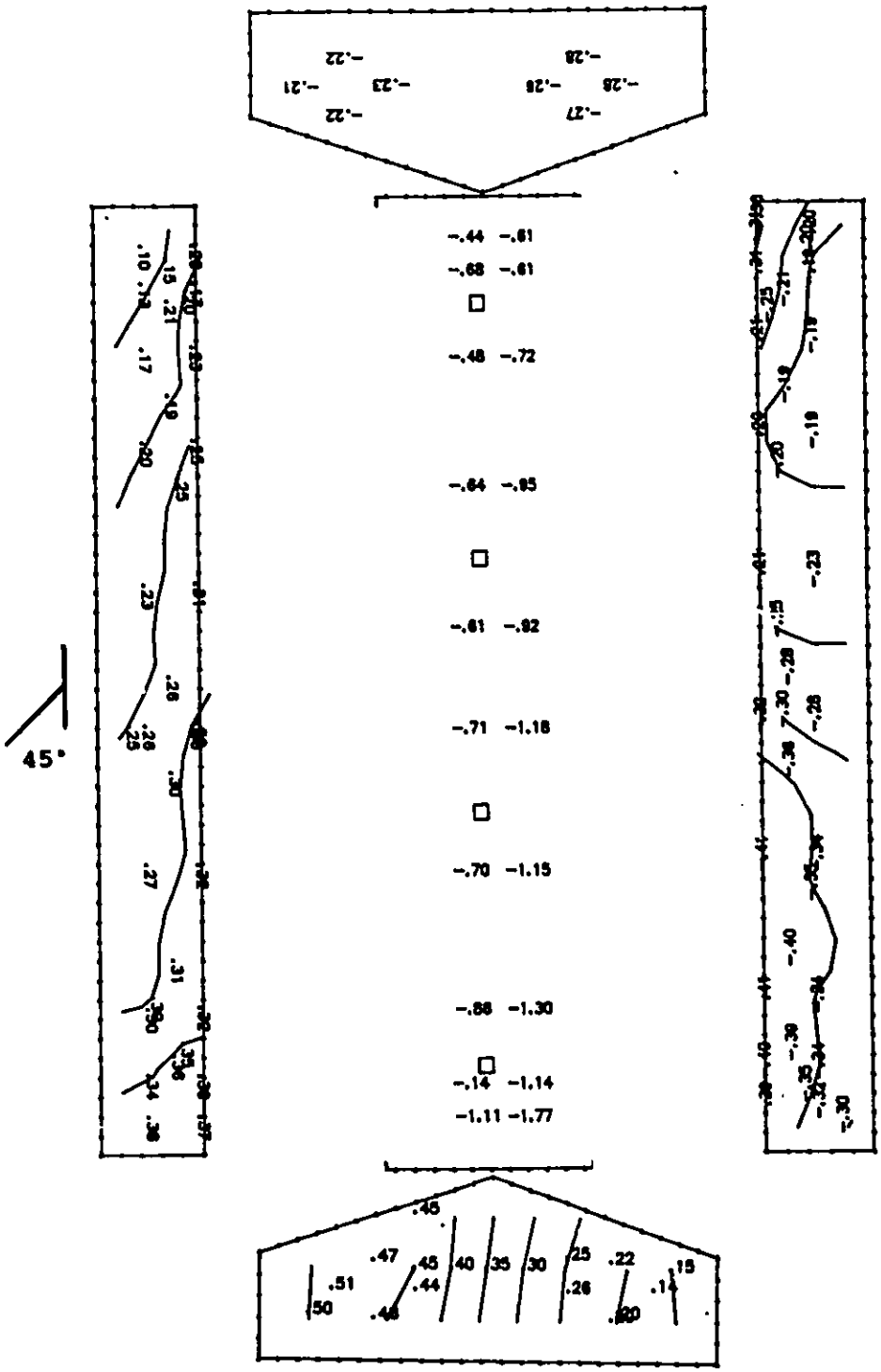

Figure E.1c Cps contour lines: open model, chimney, simulated 800 mm sidewall openings, closed end walls, wind angle of 45°.

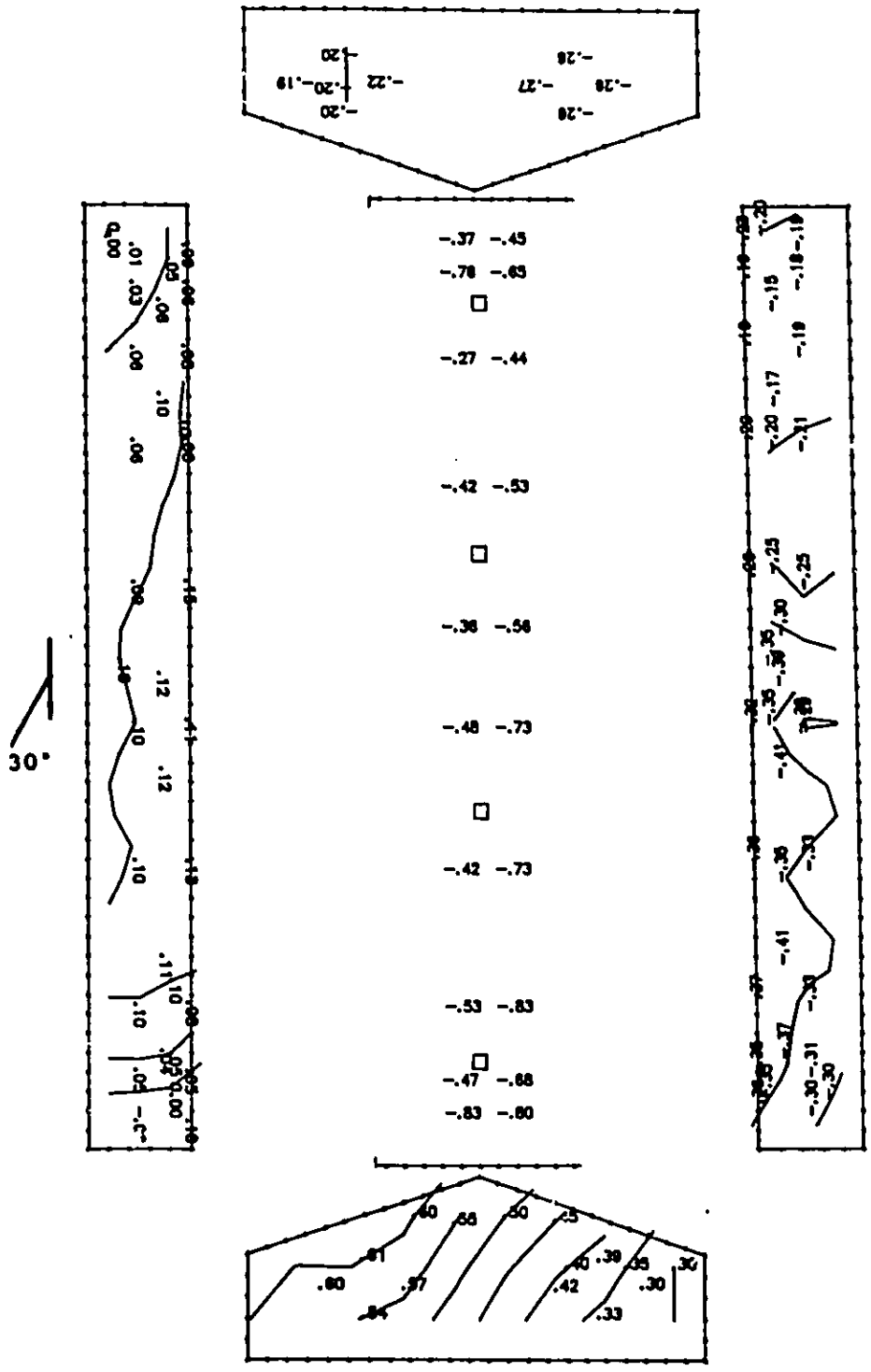

Figure E.1d Cps contour lines: open model, chimney, simulated 800 mm sidewall openings, closed end walls, wind angle of 30°.

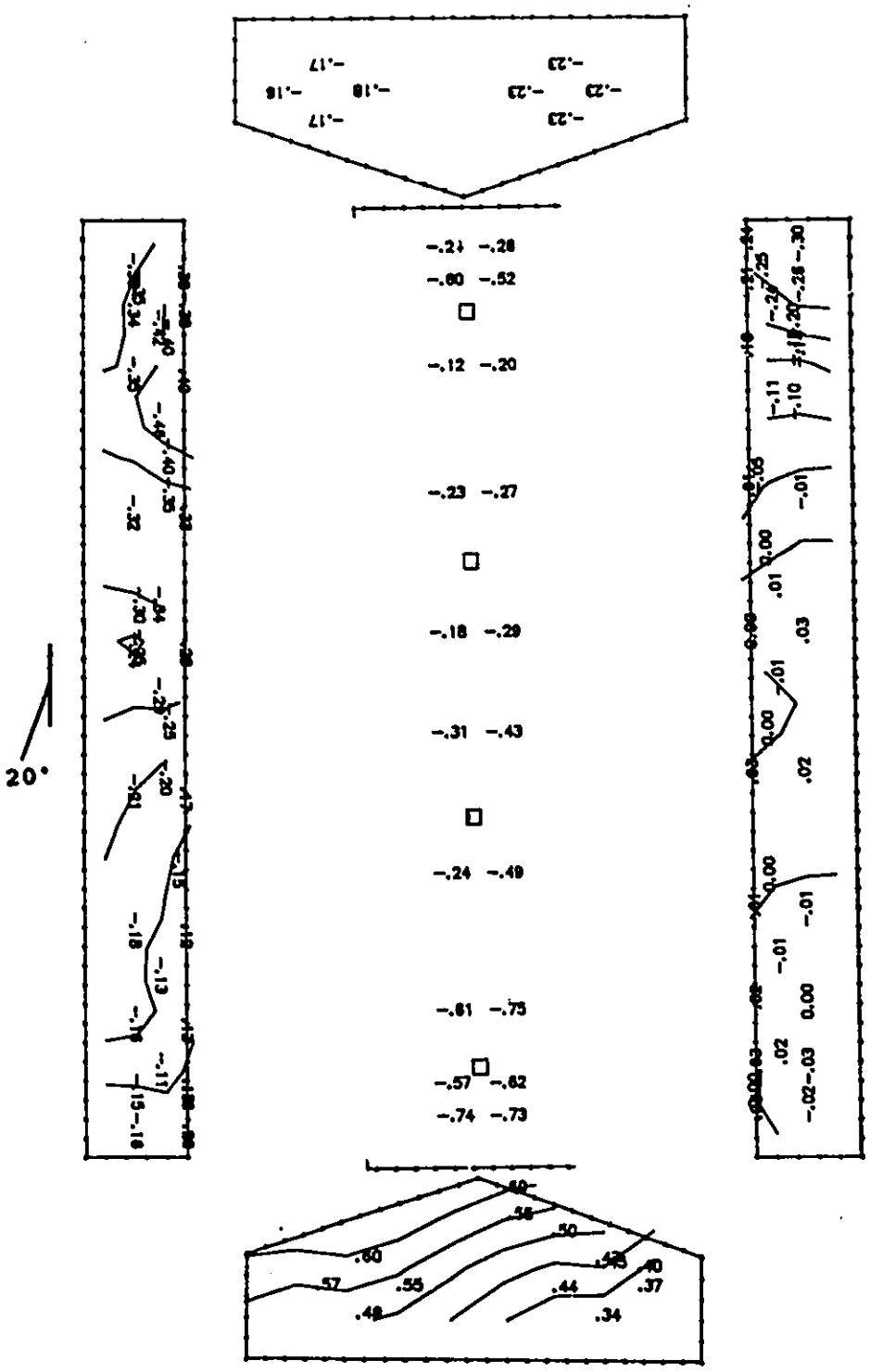

Figure E.1e Cps contour lines: open model, chimney, simulated 800 mm sidewall openings, closed end walls, wind angle of 20°.

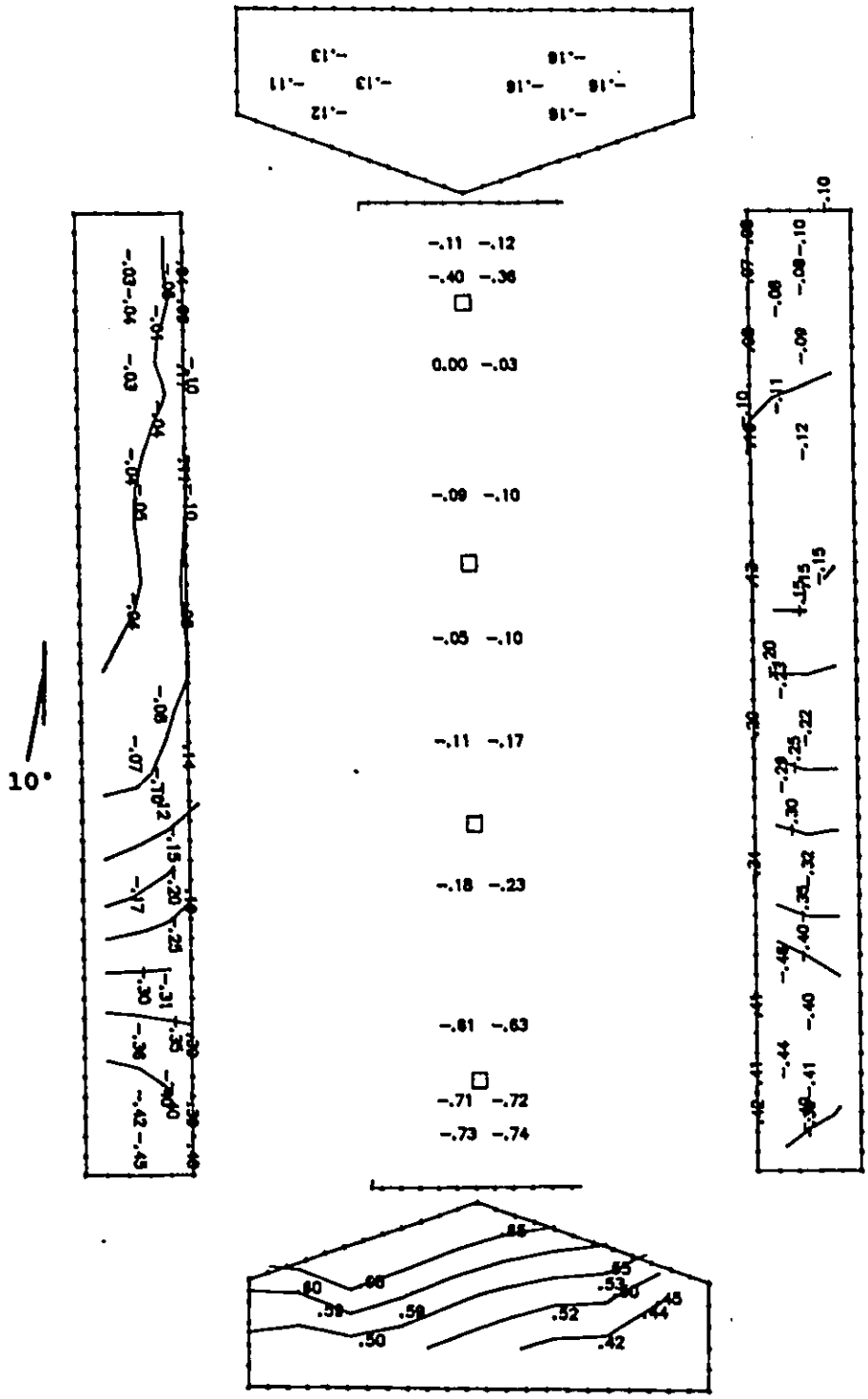

Figure E.1f Cps contour lines: open model, chimney, simulated 800 mm sidewall openings, closed end walls, wind angle of 10°.

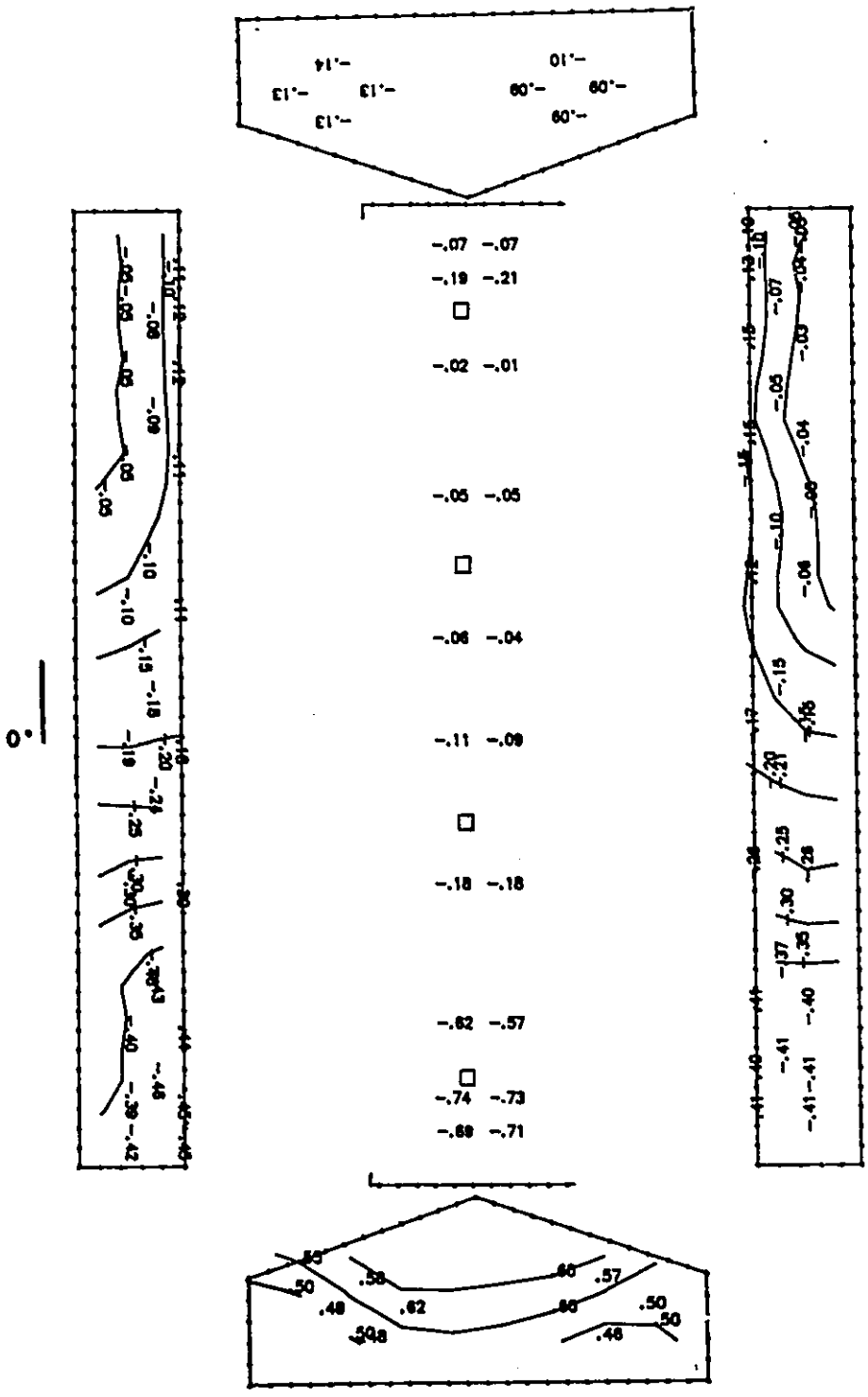

Figure E.1g Cps contour lines: open model, chimney, simulated 800 mm sidewall openings, closed end walls, wind angle of 0°.

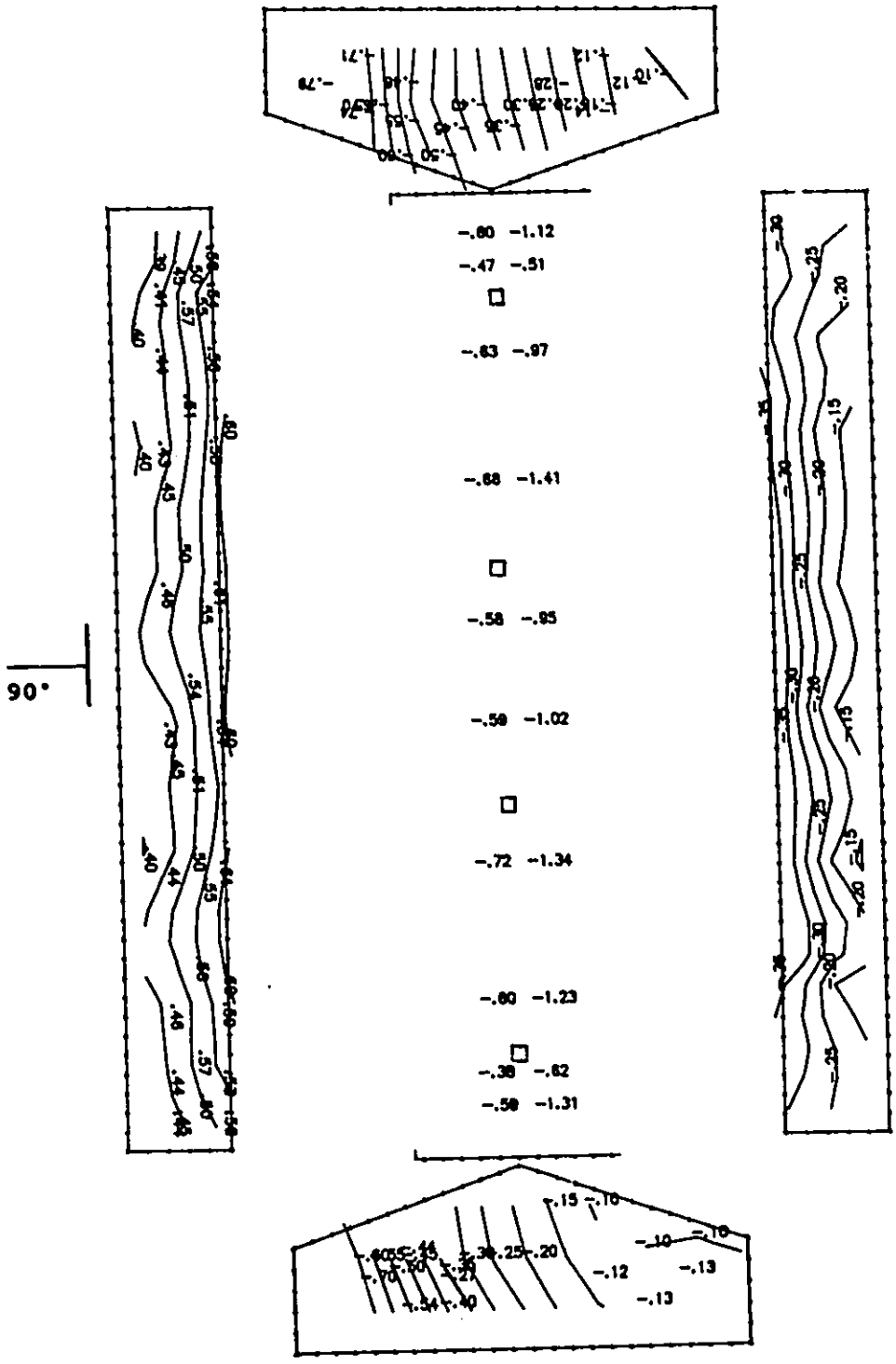

Figure E.2a Cps contour lines: open model, chimney, simulated 1100 mm sidewall openings, closed end walls, wind angle of 90°.

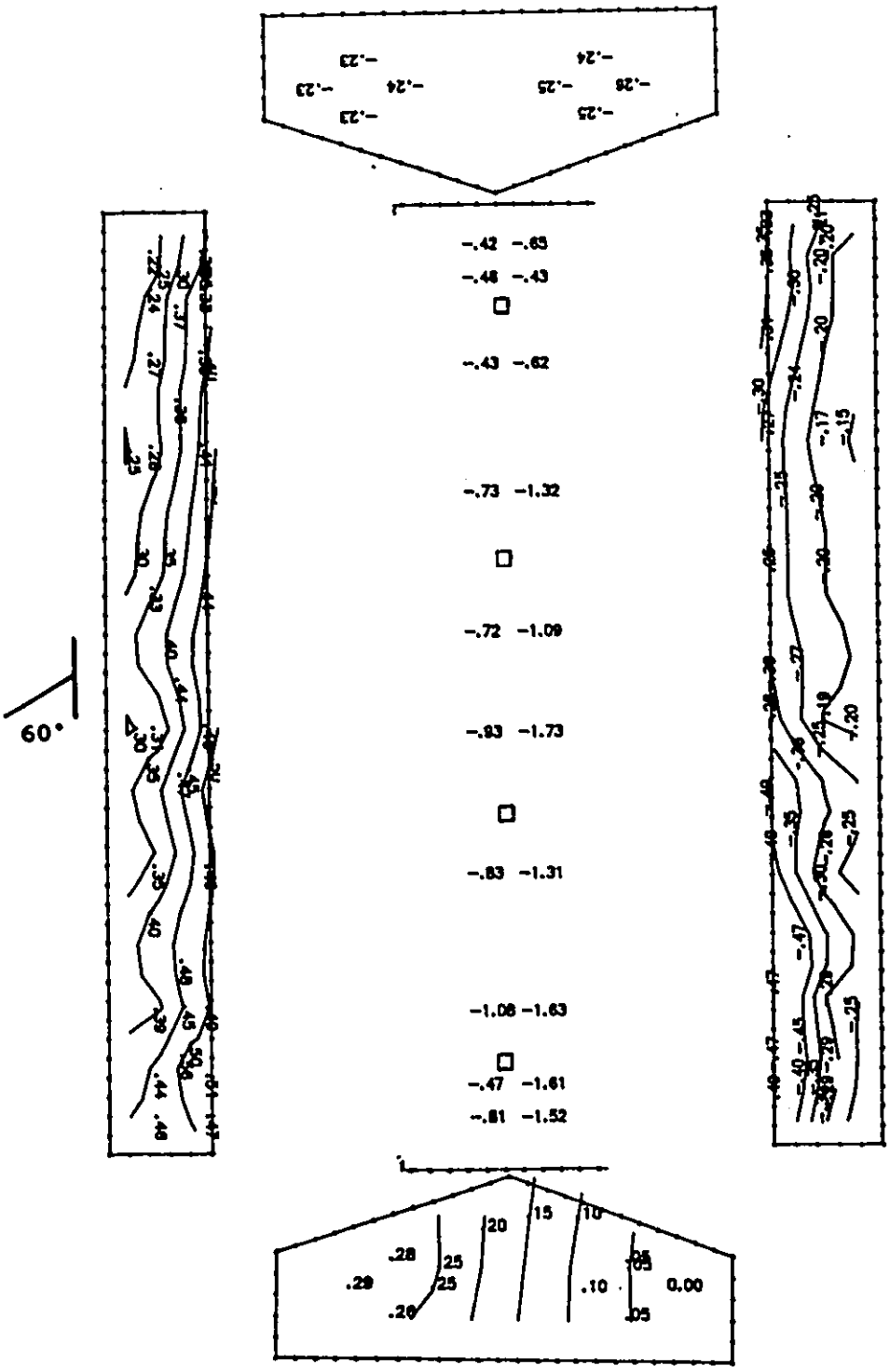

Figure E.2b Cps contour lines: open model, chimney, simulated 1100 mm sidewall openings, closed end walls, wind angle of 60°.

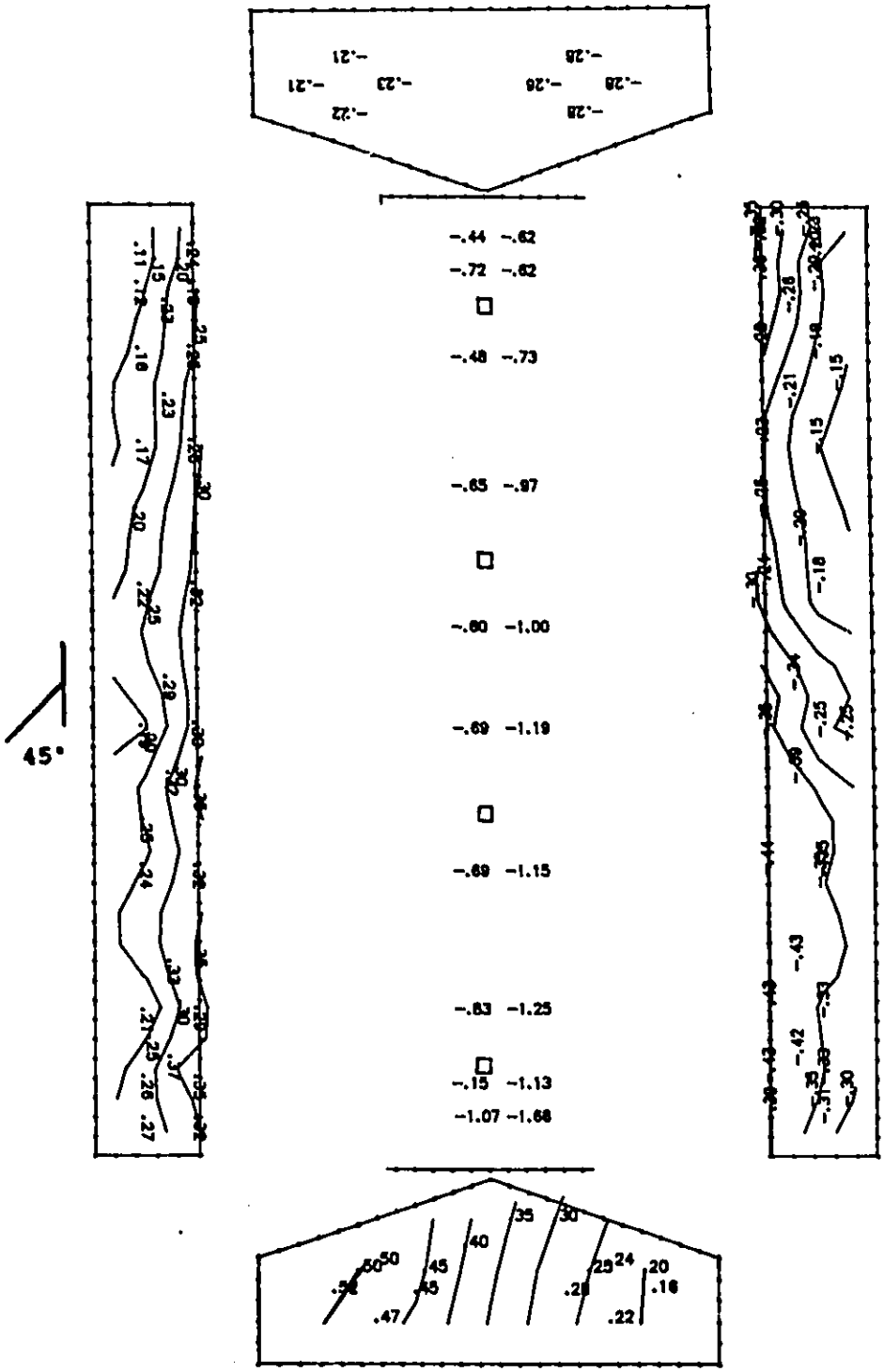

Figure E.2c Cps contour lines: open model, chimney, simulated 1100 mm sidewall openings, closed end walls, wind angle of 45°.

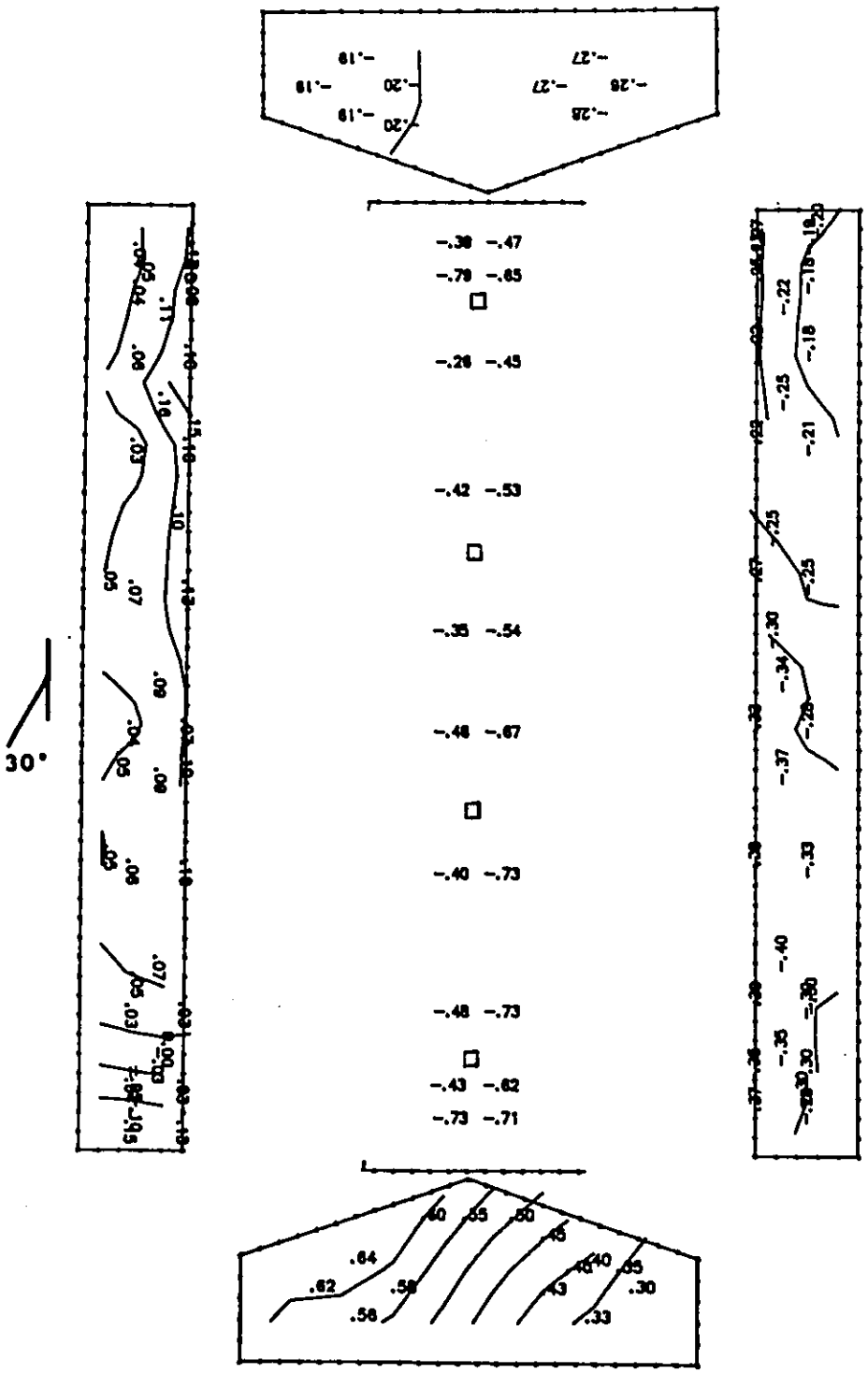

Figure E.2d Cps contour lines: open model, chimney, simulated 1100 mm sidewall openings, closed end walls, wind angle of 30°.

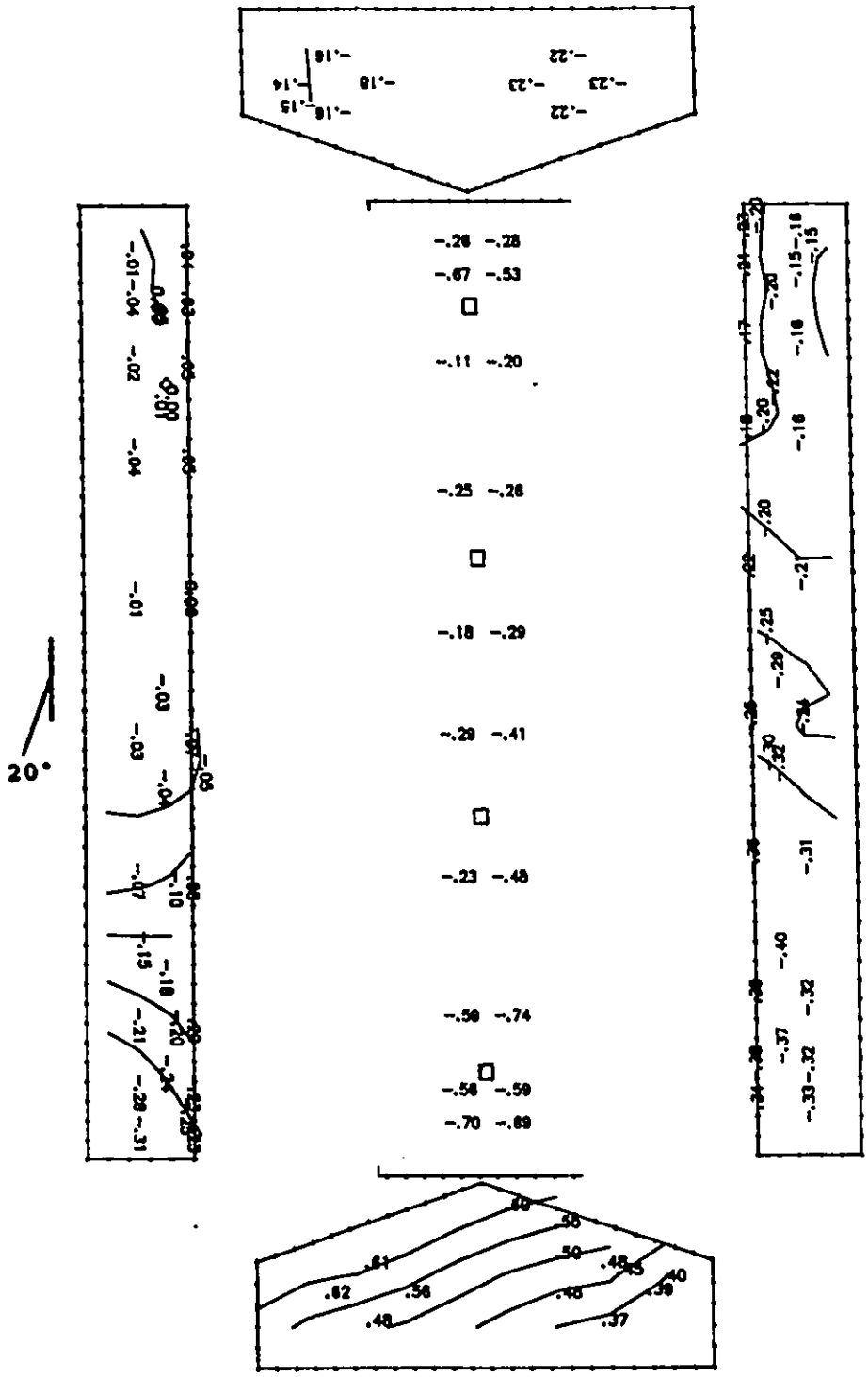

Figure E.2e Cps contour lines: open model, chimney, simulated 1100 mm sidewall openings, closed end walls, wind angle of 20°.

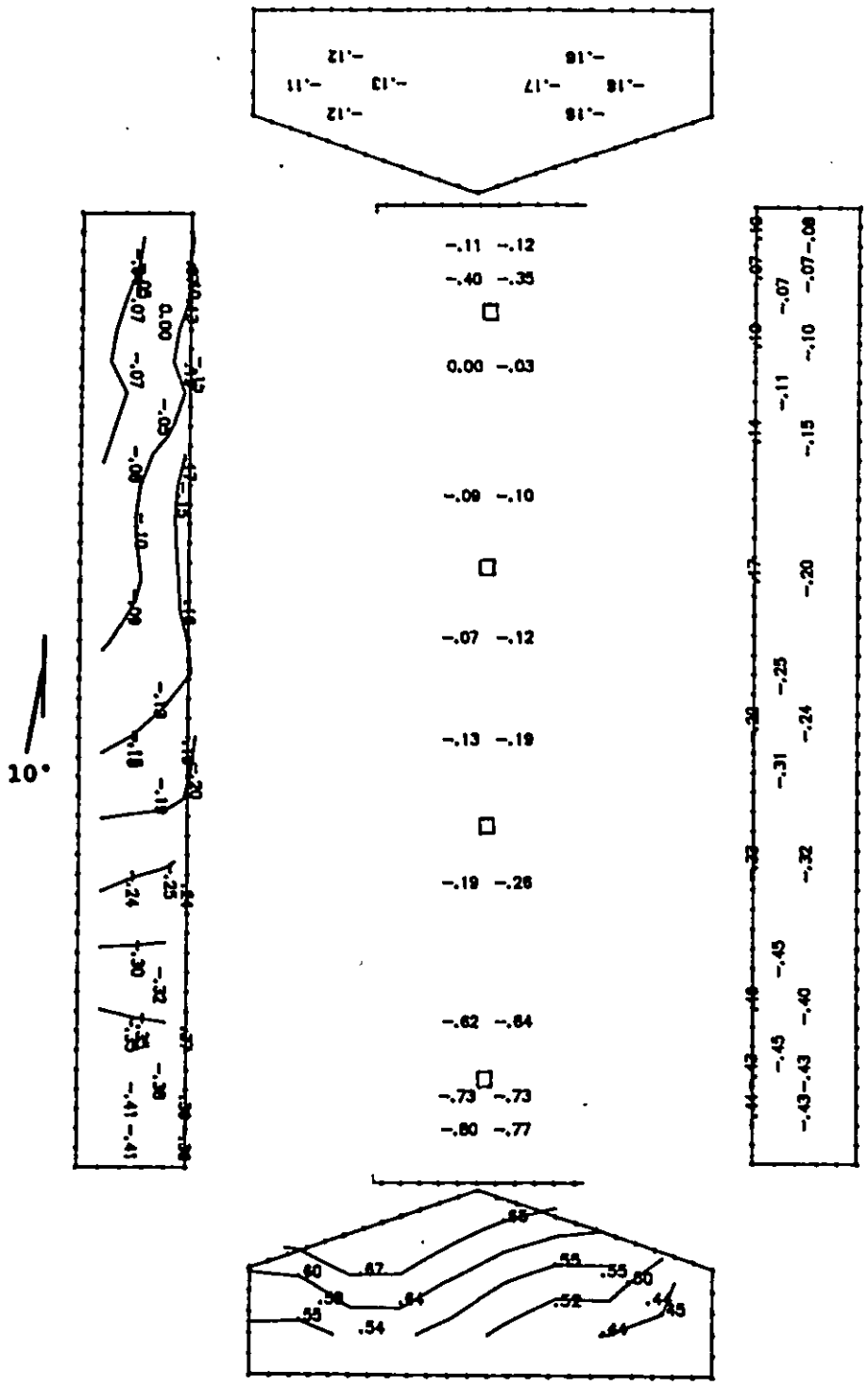

Figure E.2f Cps contour lines: open model, chimney, simulated 1100 mm sidewall openings, closed end walls, wind angle of 10°.

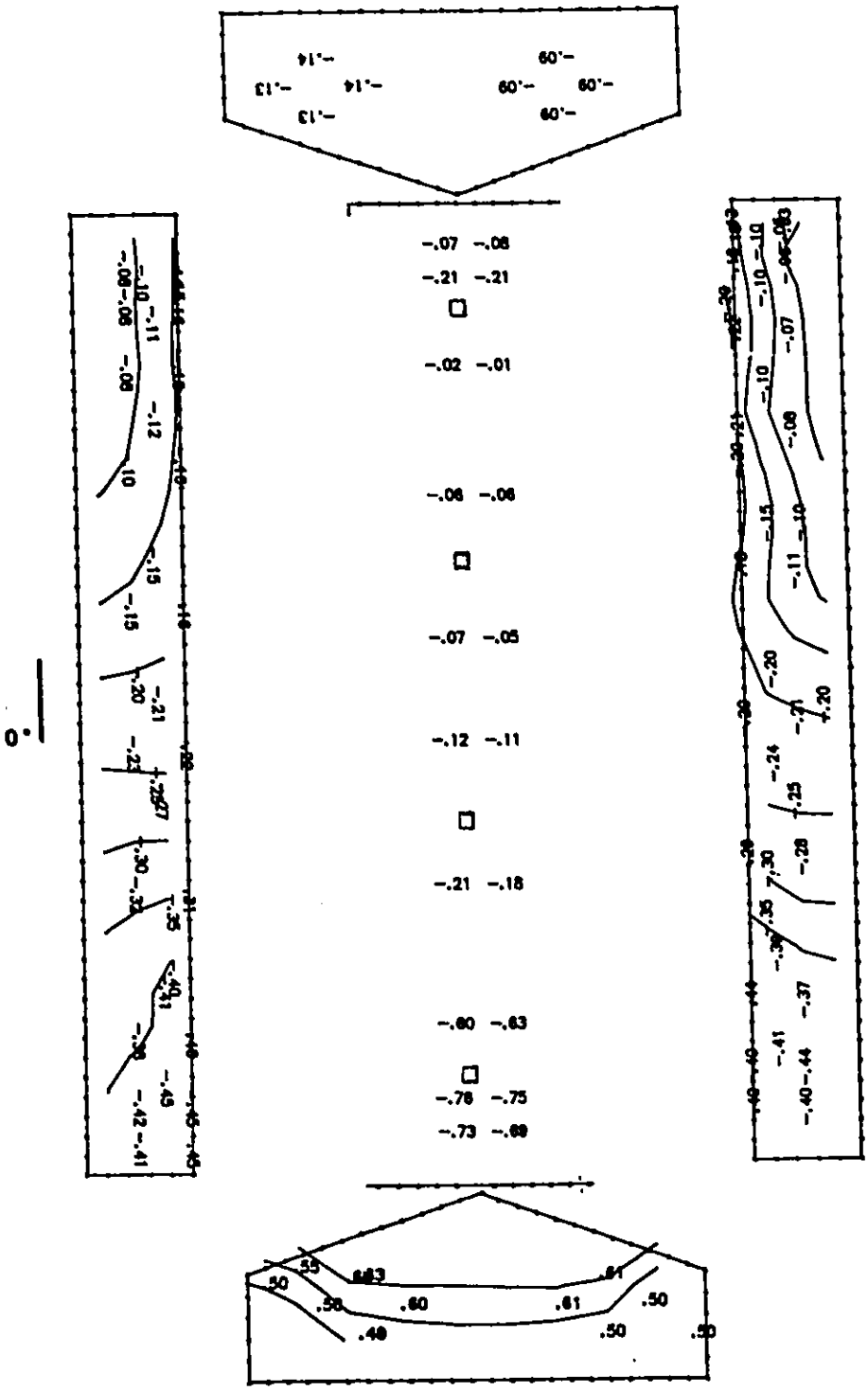

Figure E.2g Cps contour lines: open model, chimney, simulated 1100 mm sidewall openings, closed end walls, wind angle of 0°.

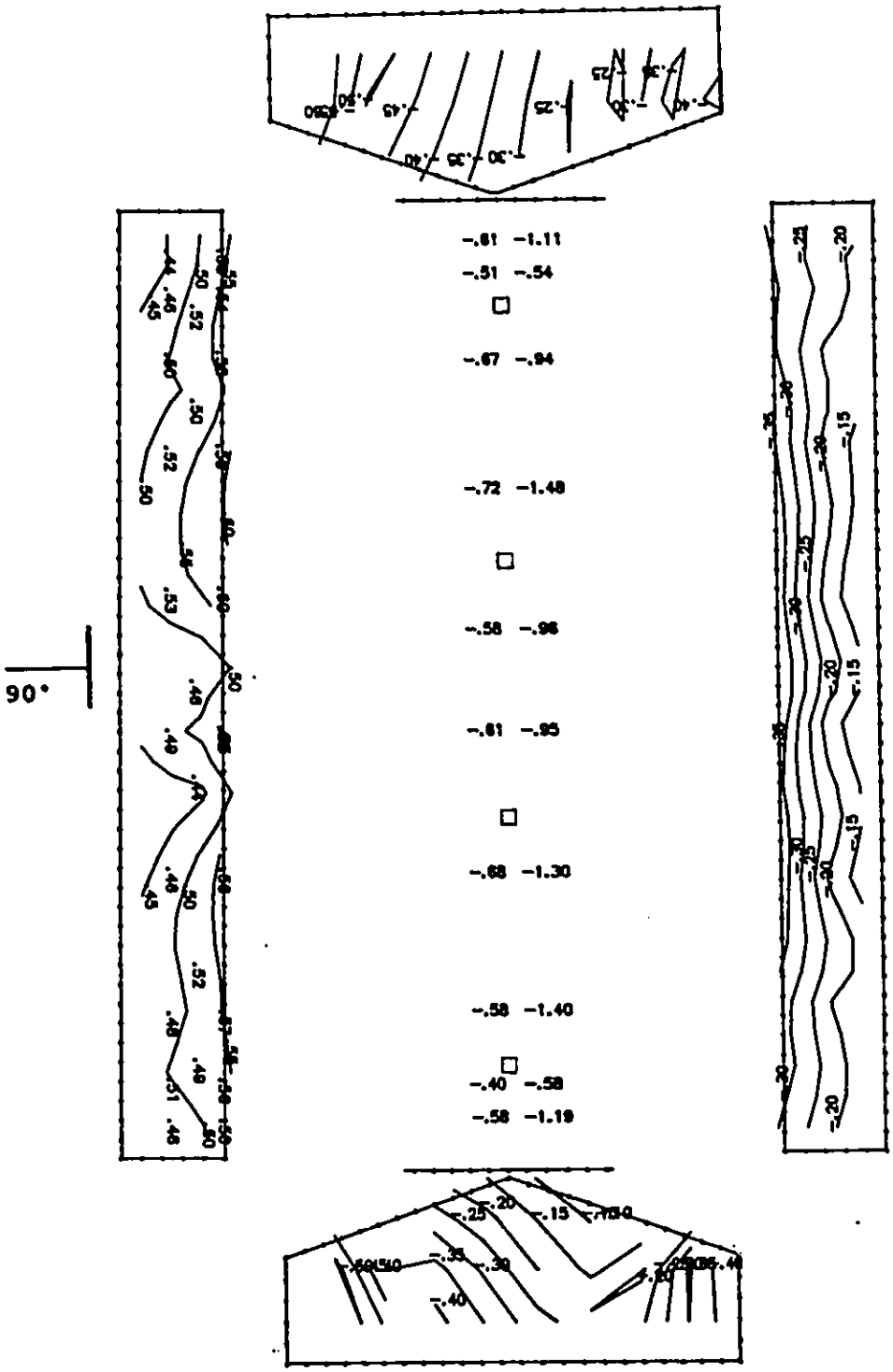

Figure E.3a Cps contour lines: open model, chimney, simulated 800 mm sidewall openings, open end walls, wind angle of 90°.

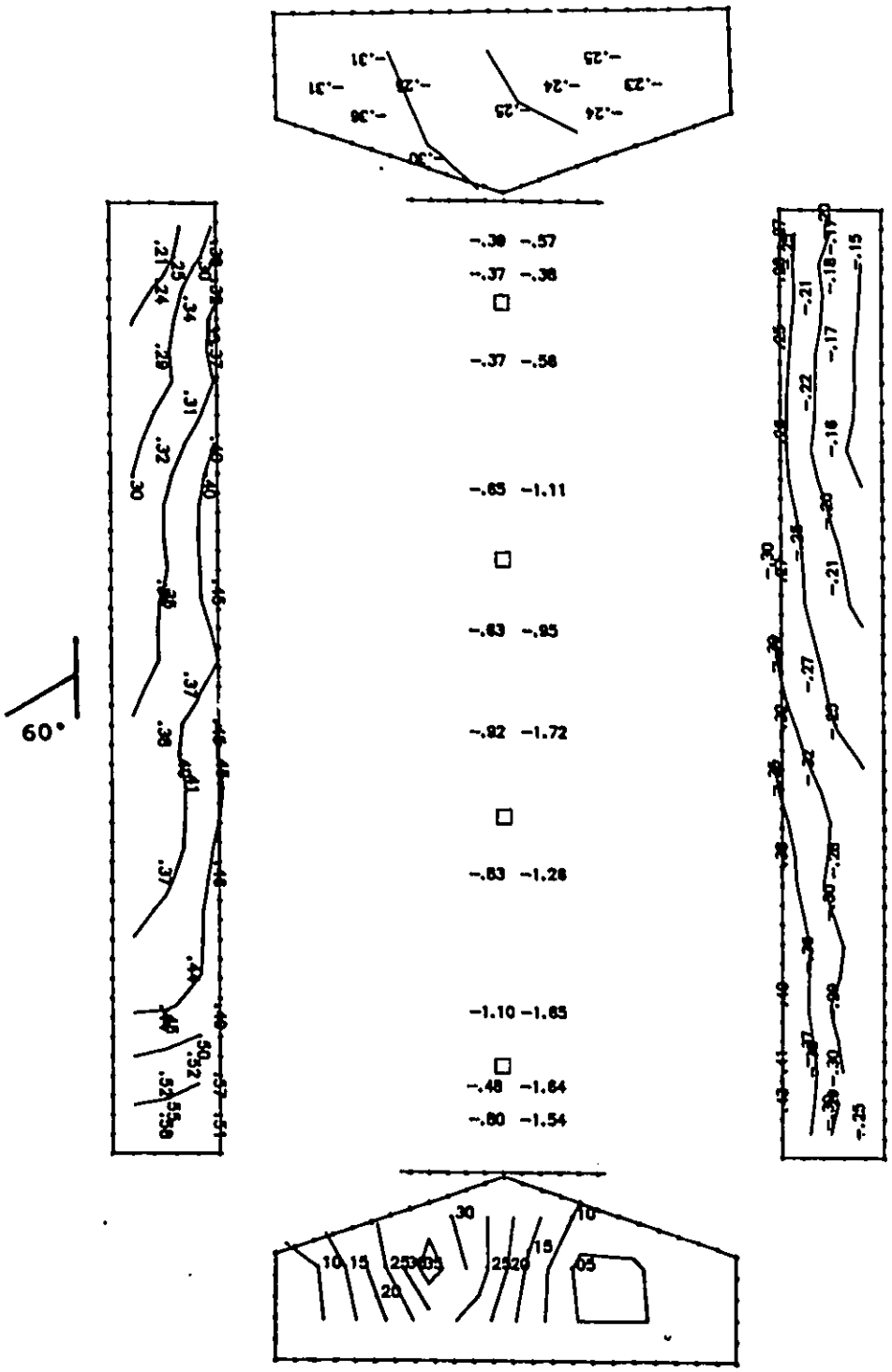

Figure E.3b Cps contour lines: open model, chimney, simulated 800 mm sidewall openings, open end walls, wind angle of 60°.

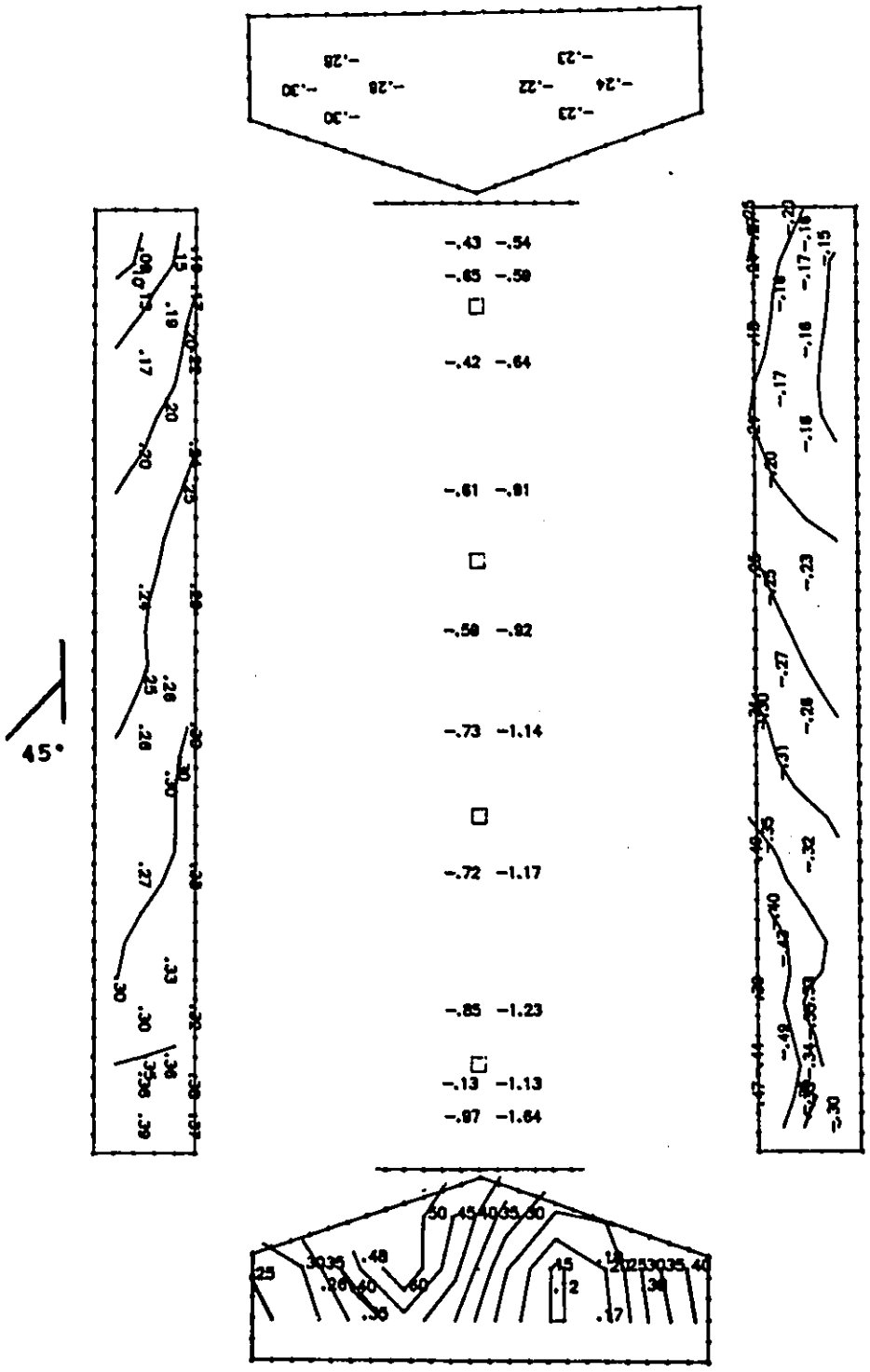

Figure E.3c Cps contour lines: open model, chimney, simulated 800 mm sidewall openings, open end walls, wind angle of 45°.

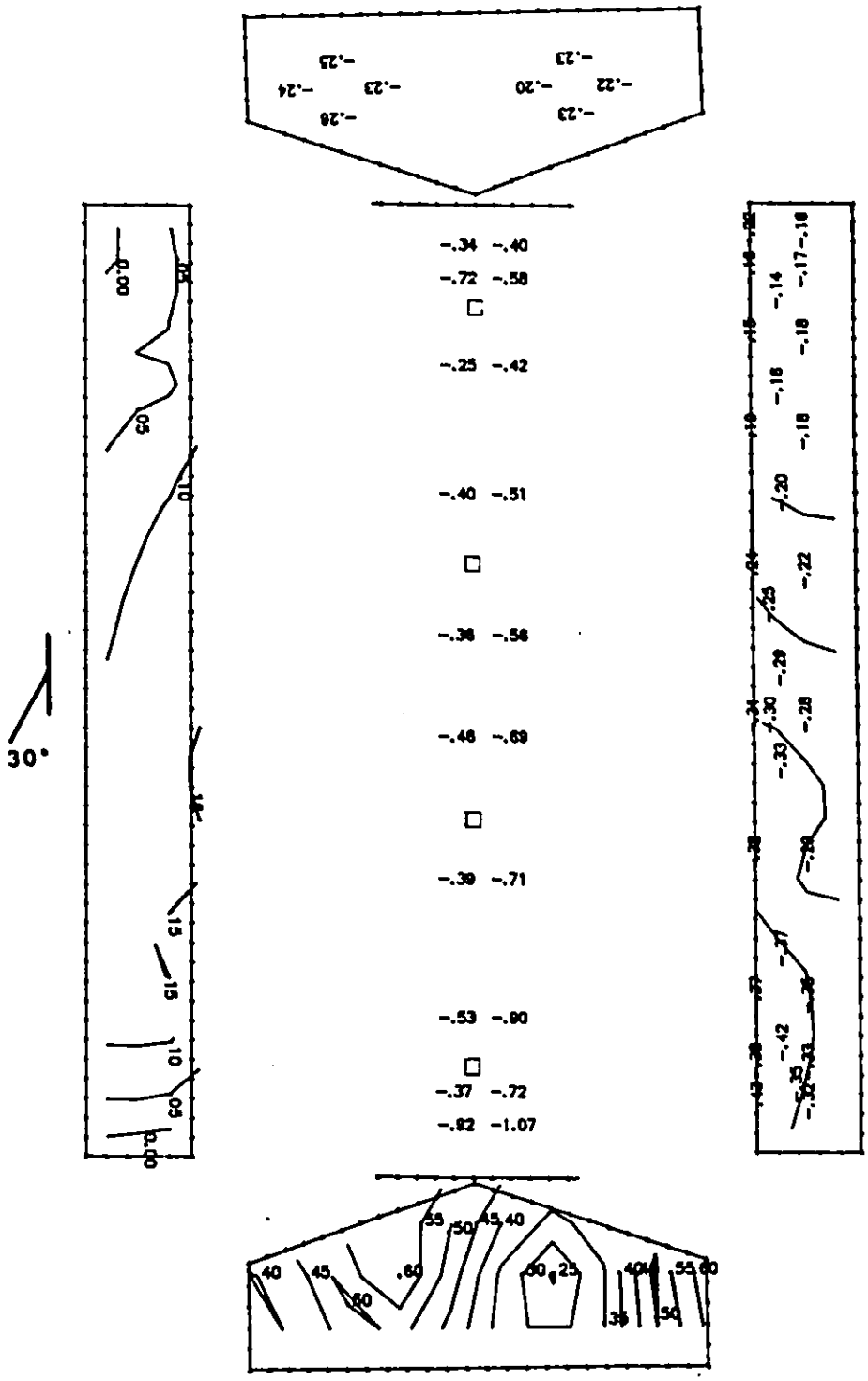

Figure E.3d Cps contour lines: open model, chimney, simulated 800 mm sidewall openings, open end walls, wind angle of 30°.

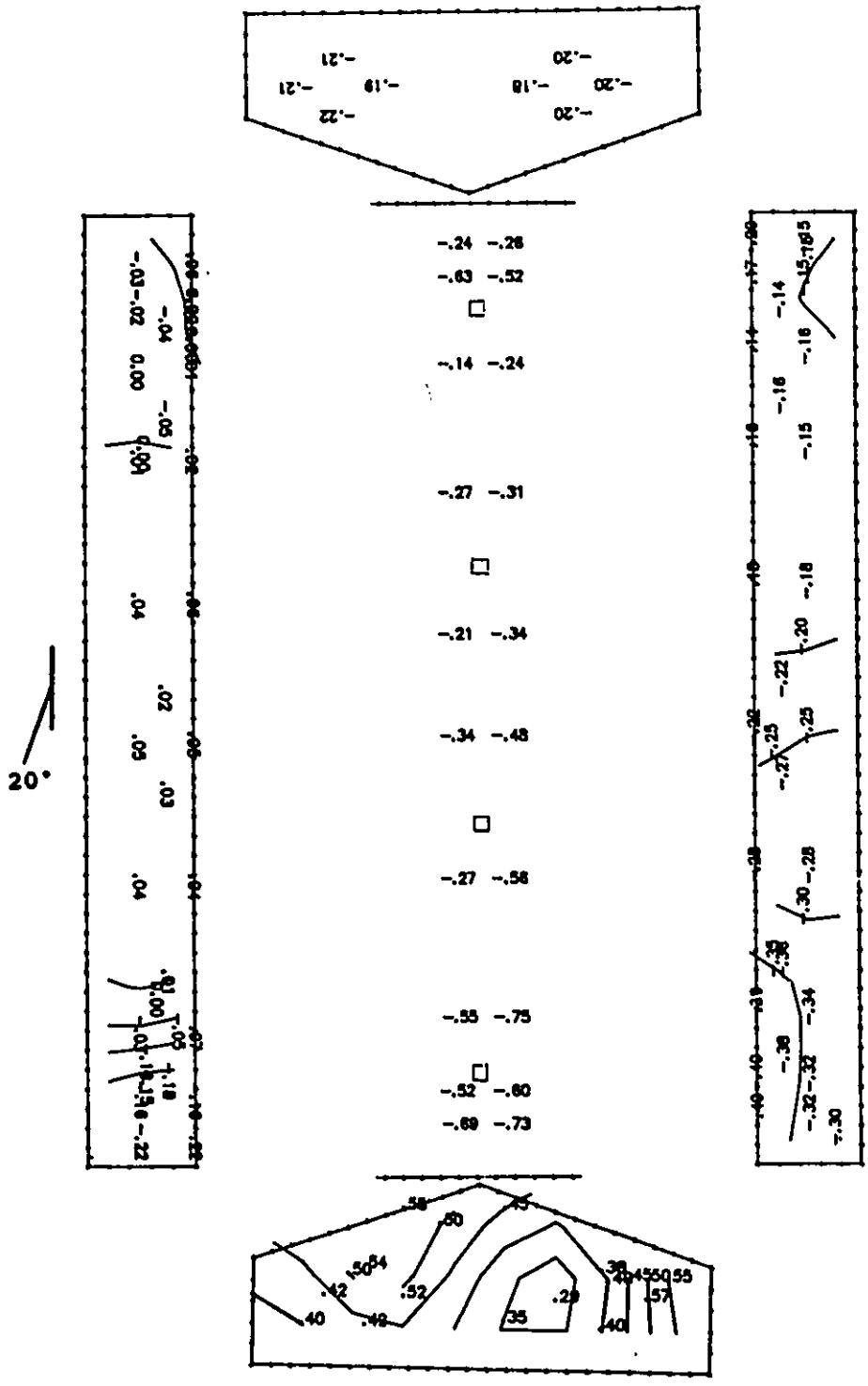

Figure E.3e Cps contour lines: open model, chimney, simulated 800 mm sidewall openings, open end walls, wind angle of 20°.

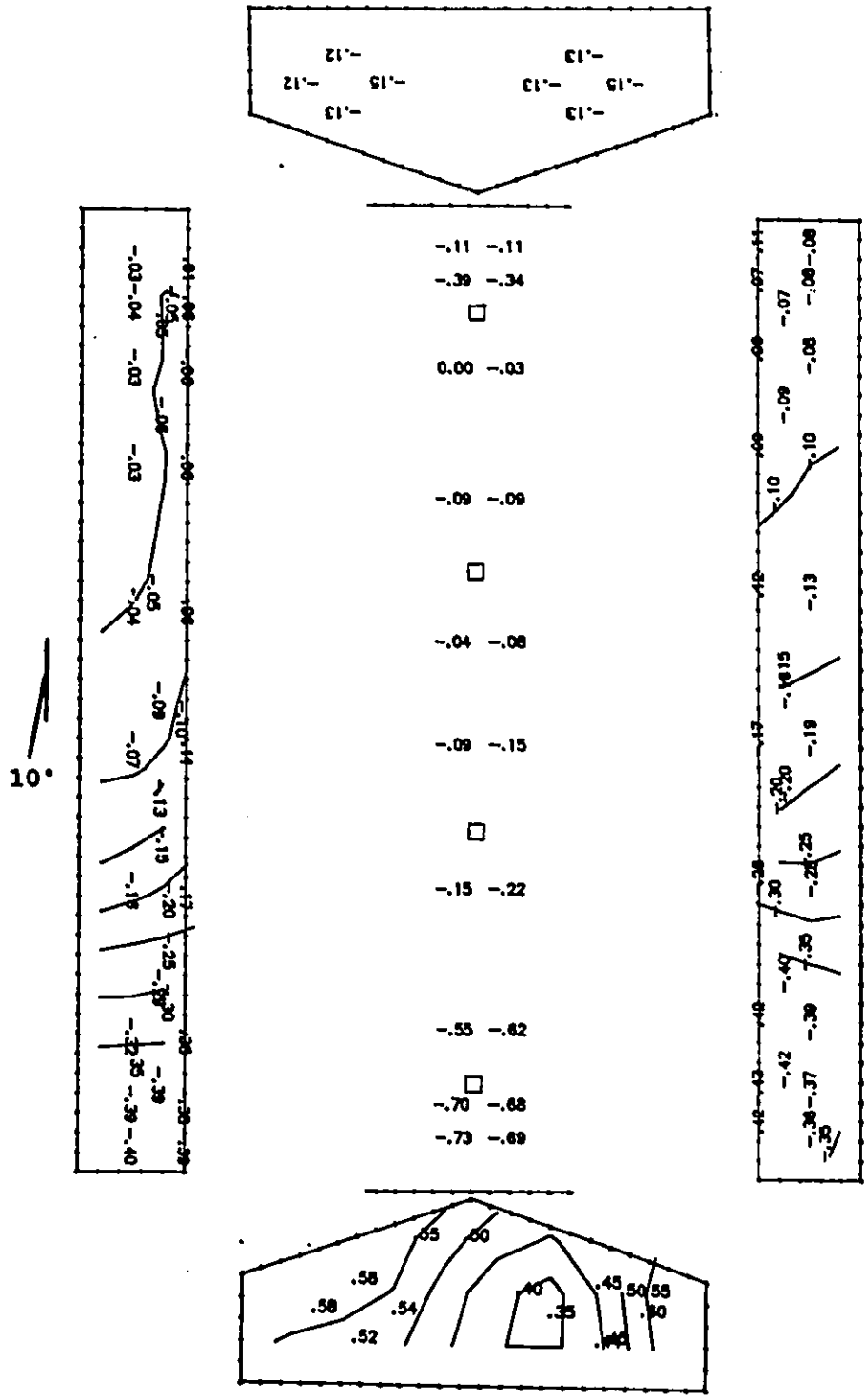

Figure E.3f Cps contour lines: open model, chimney, simulated 800 mm sidewall openings, open end walls, wind angle of 10°.

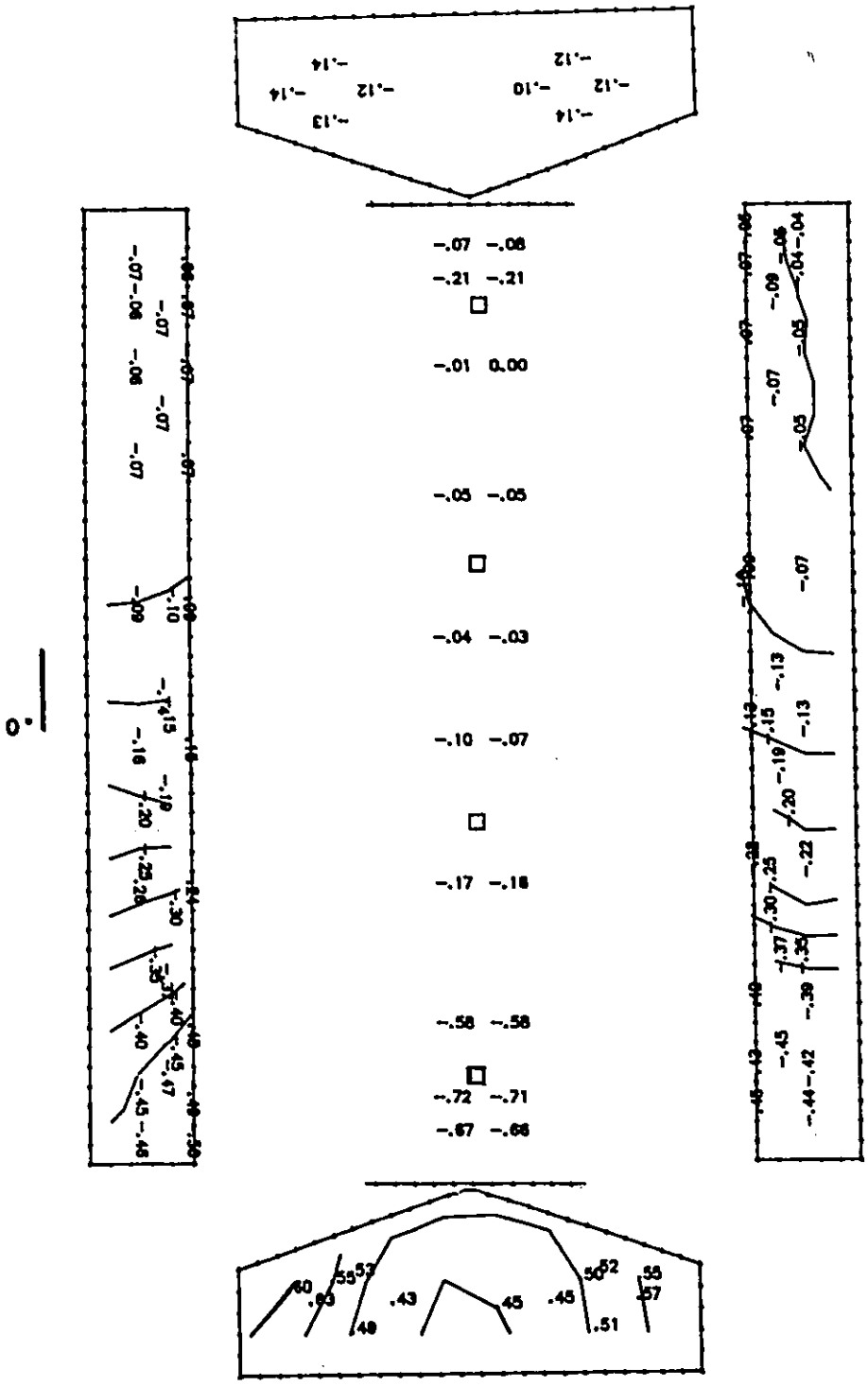

Figure E.3g Cps contour lines: open model, chimney, simulated 800 mm sidewall openings, open end walls, wind angle of 0°.

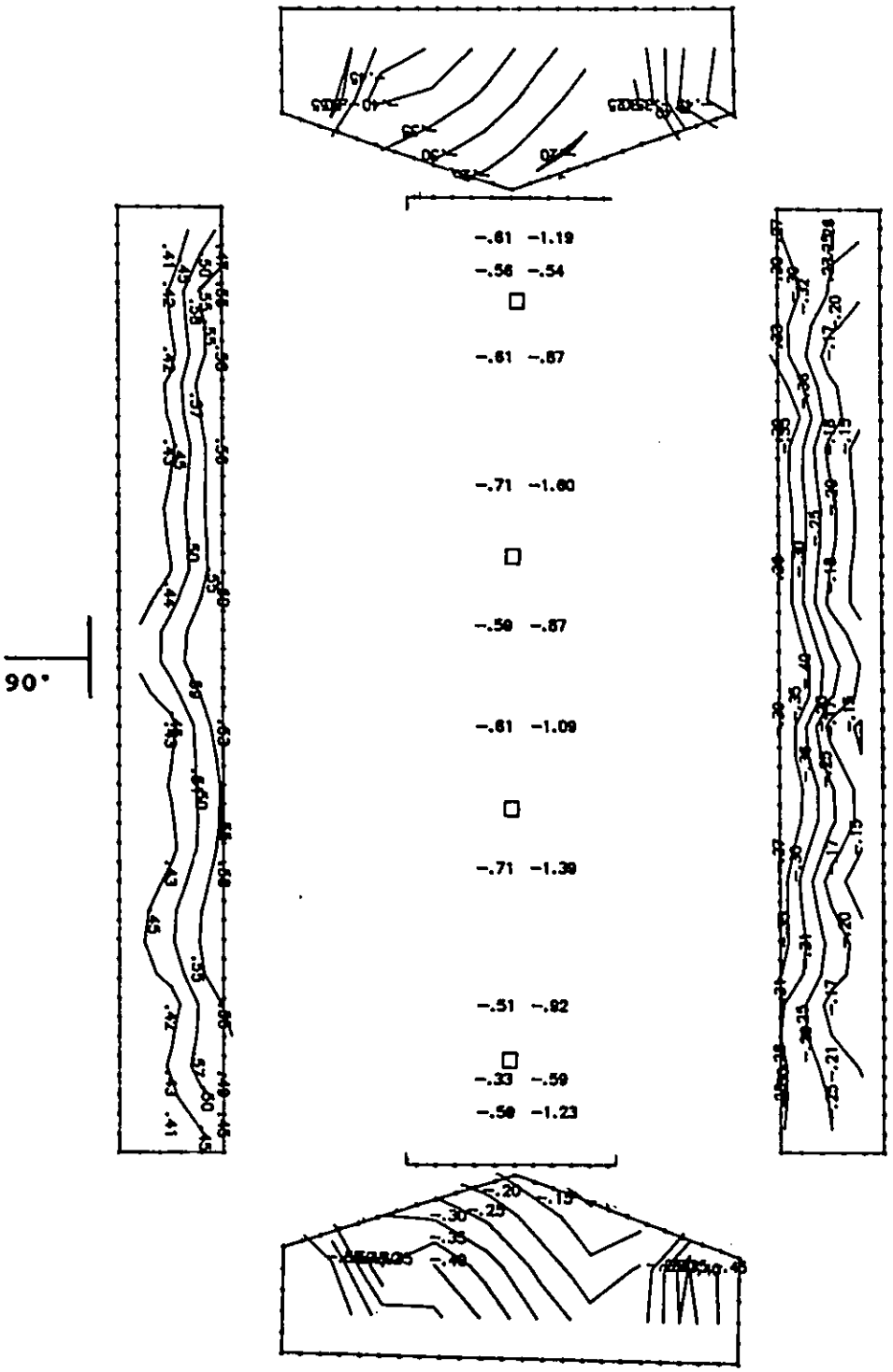

Figure E.4a Cps contour lines: open model, chimney, simulated 1100 mm sidewall openings, open end walls, wind angle of 90°.

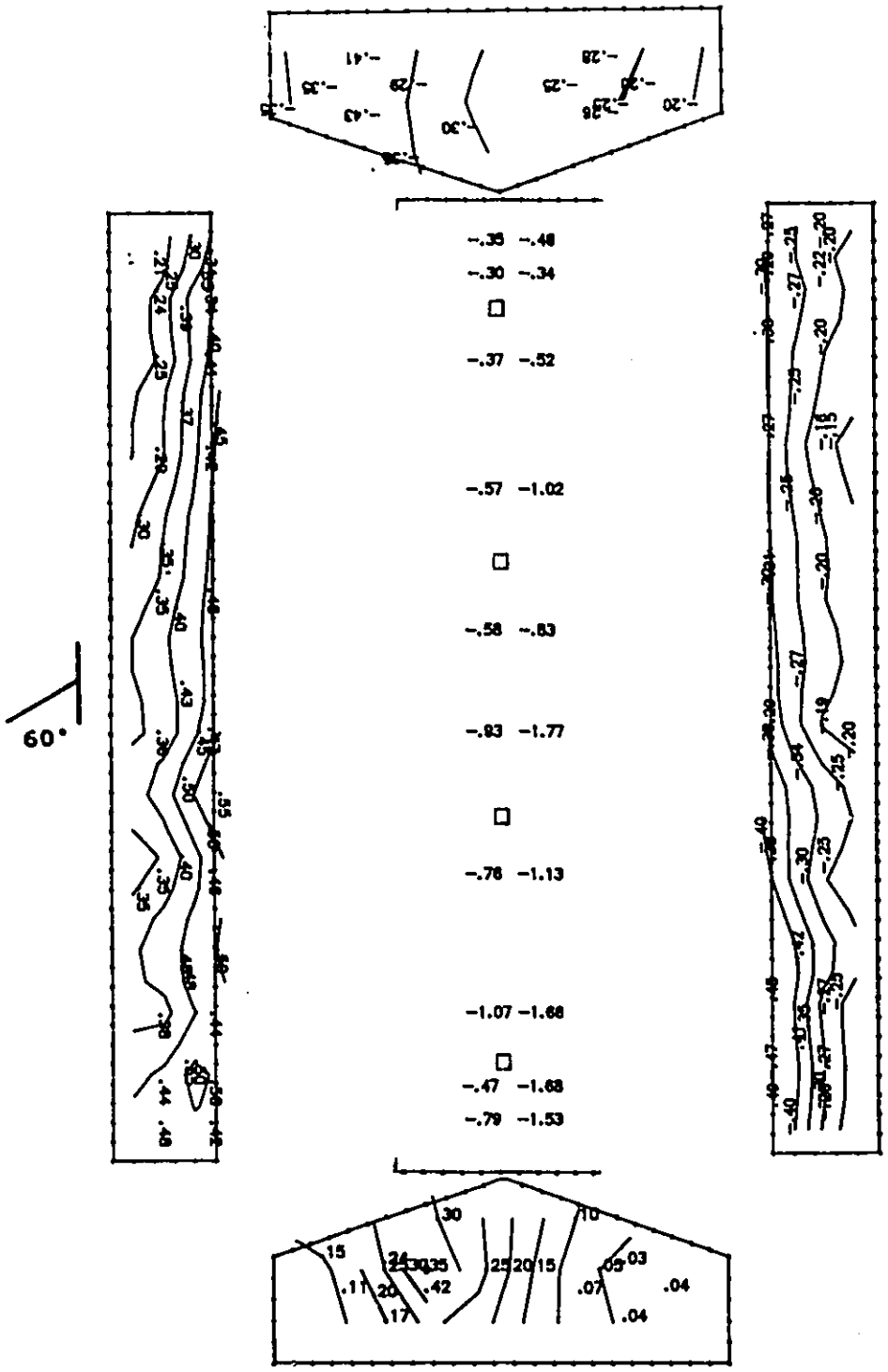

Figure E.4b Cps contour lines: open model, chimney, simulated 1100 mm sidewall openings, open end walls, wind angle of 60°.

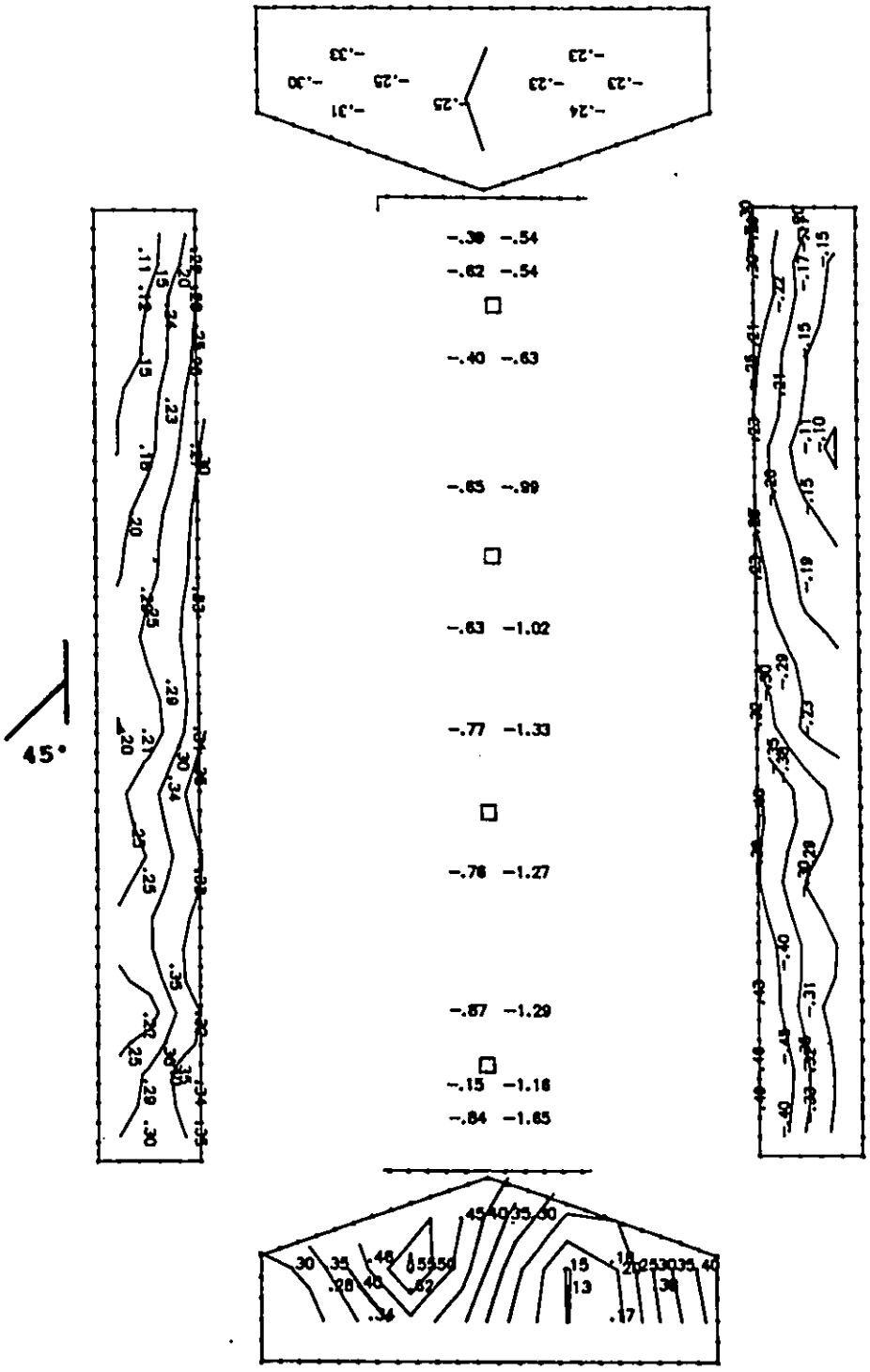

Figure E.4c Cps contour lines: open model, chimney, simulated 1100 mm sidewall openings, open end walls, wind angle of 45°.

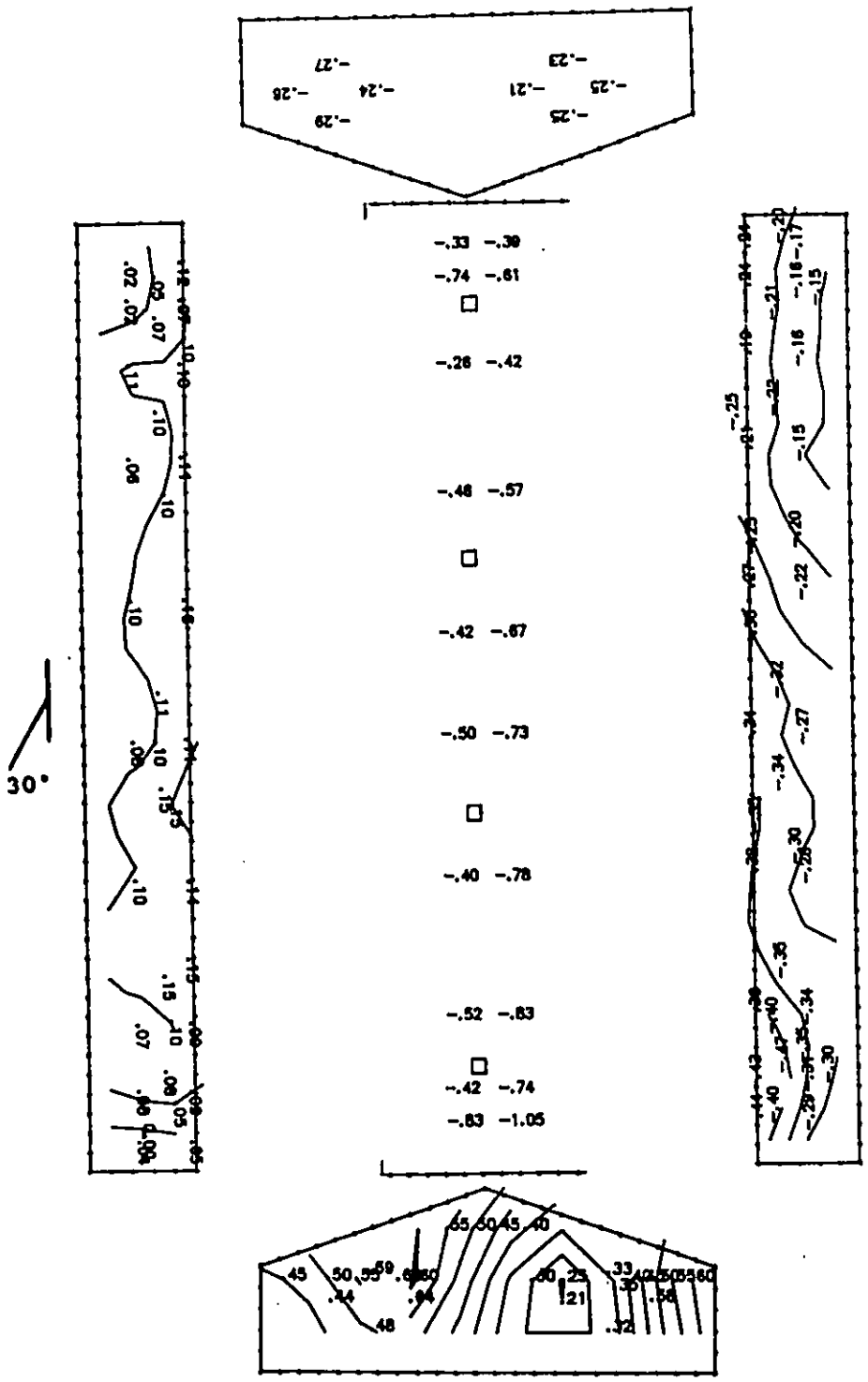

Figure E.4d Cps contour lines: open model, chimney, simulated 1100 mm sidewall openings, open end walls, wind angle of 30°.

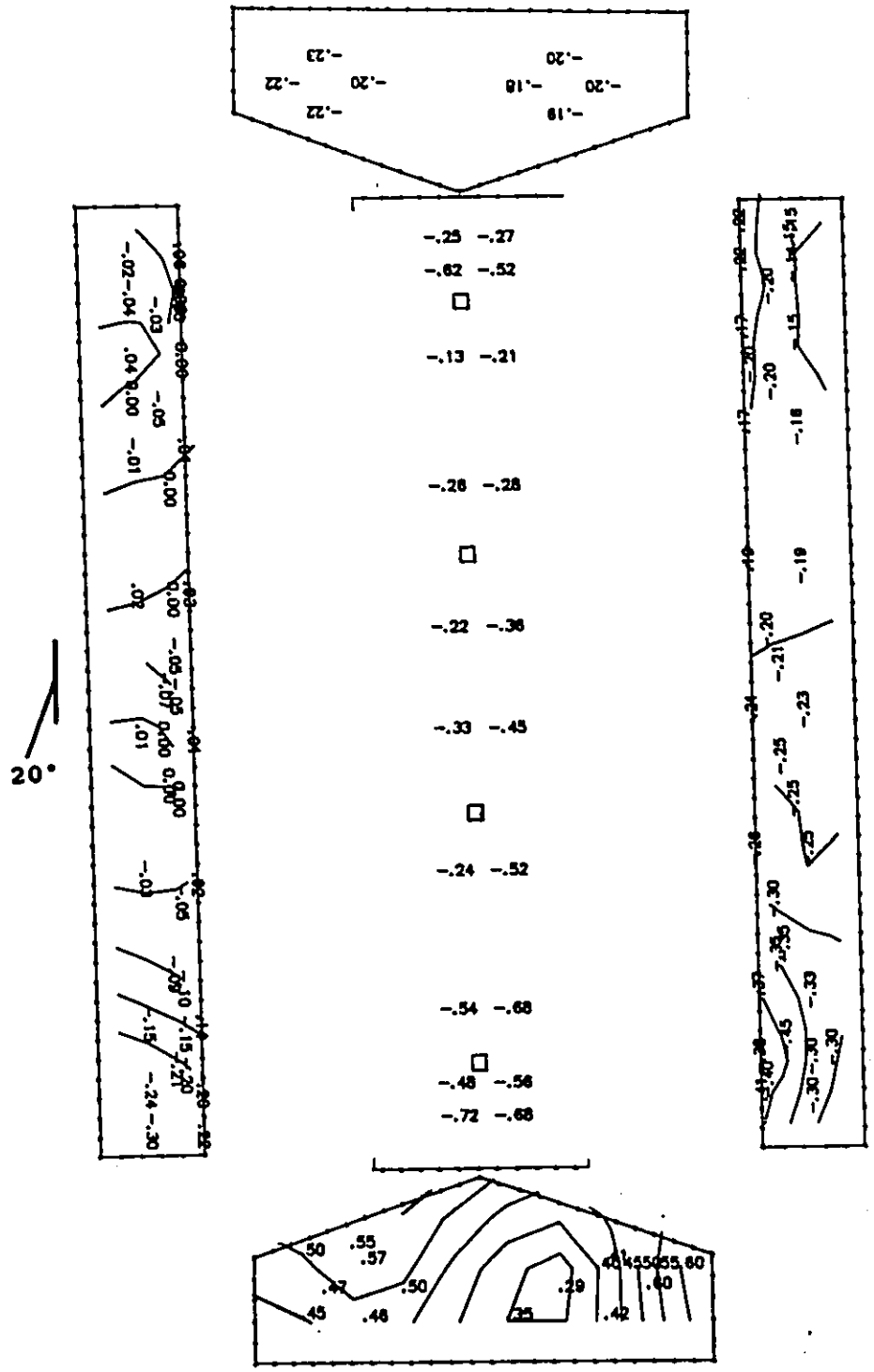

Figure E.4e Cps contour lines: open model, chimney, simulated 1100 mm sidewall openings, open end walls, wind angle of 20°.

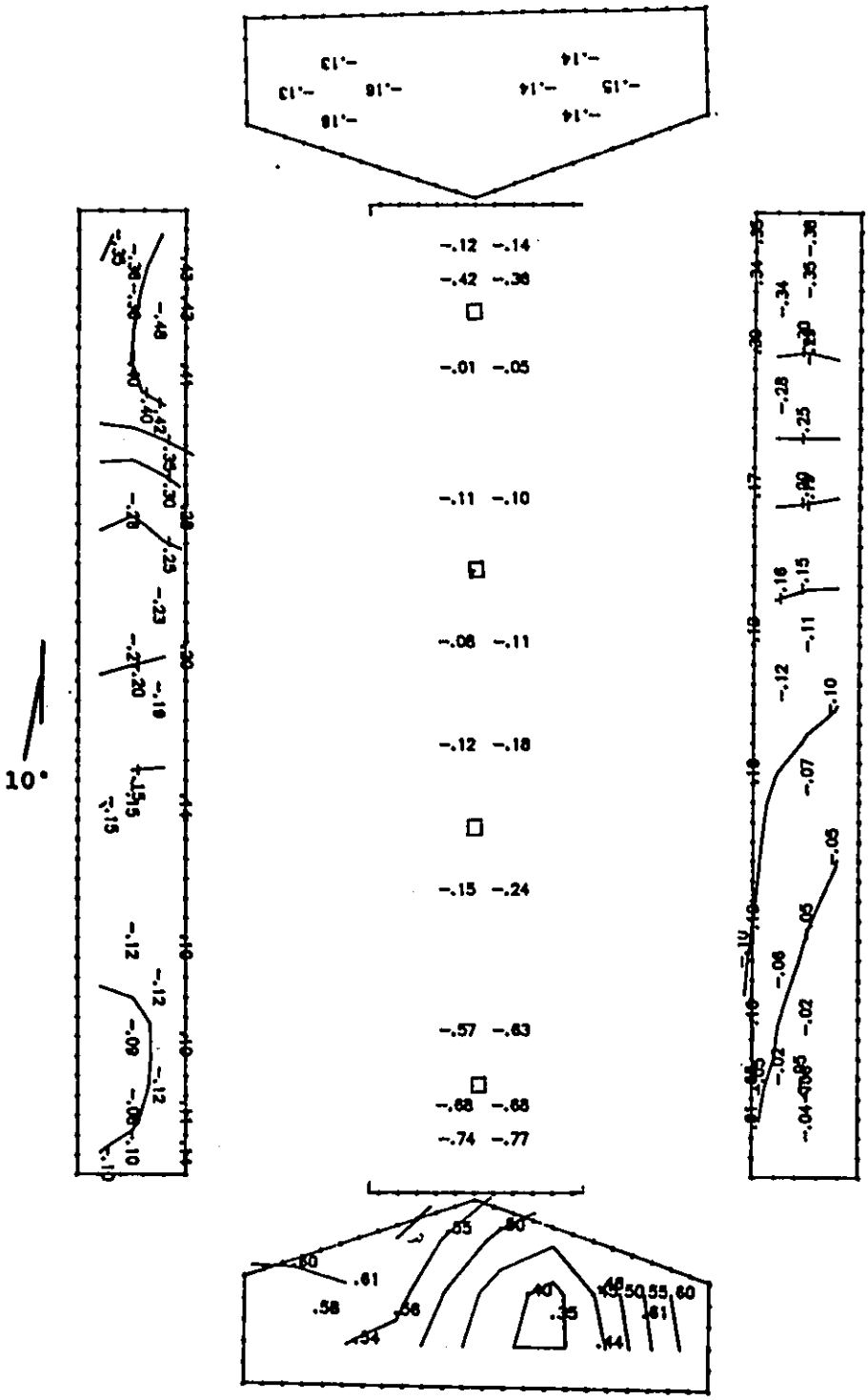

Figure E.4f Cps contour lines: open model, chimney, simulated 1100 mm sidewall openings, open end walls, wind angle of 10°.

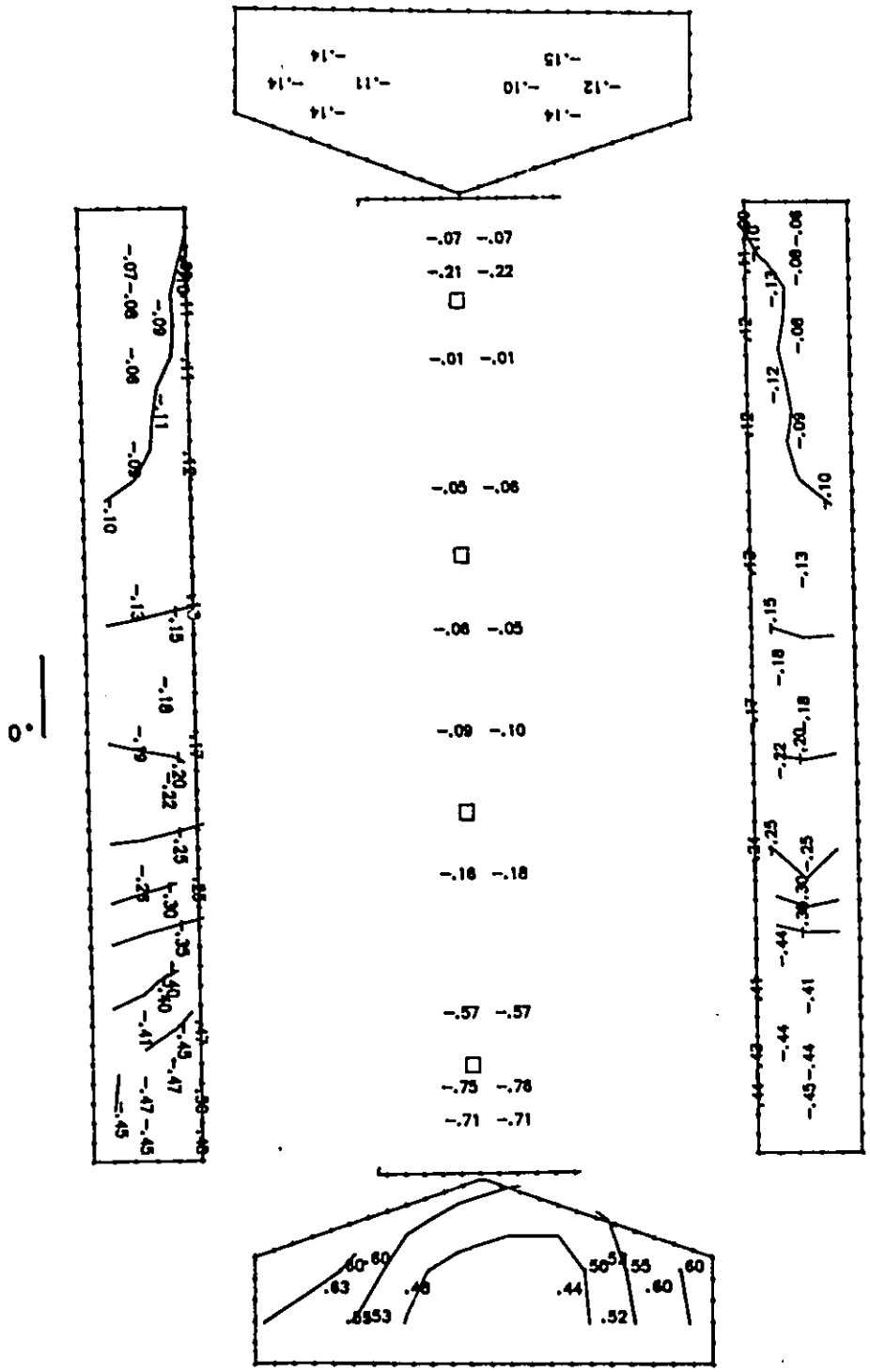

Figure E.4g Cps contour lines: open model, chimney, simulated 1100 mm sidewall openings, open end walls, wind angle of 0°.

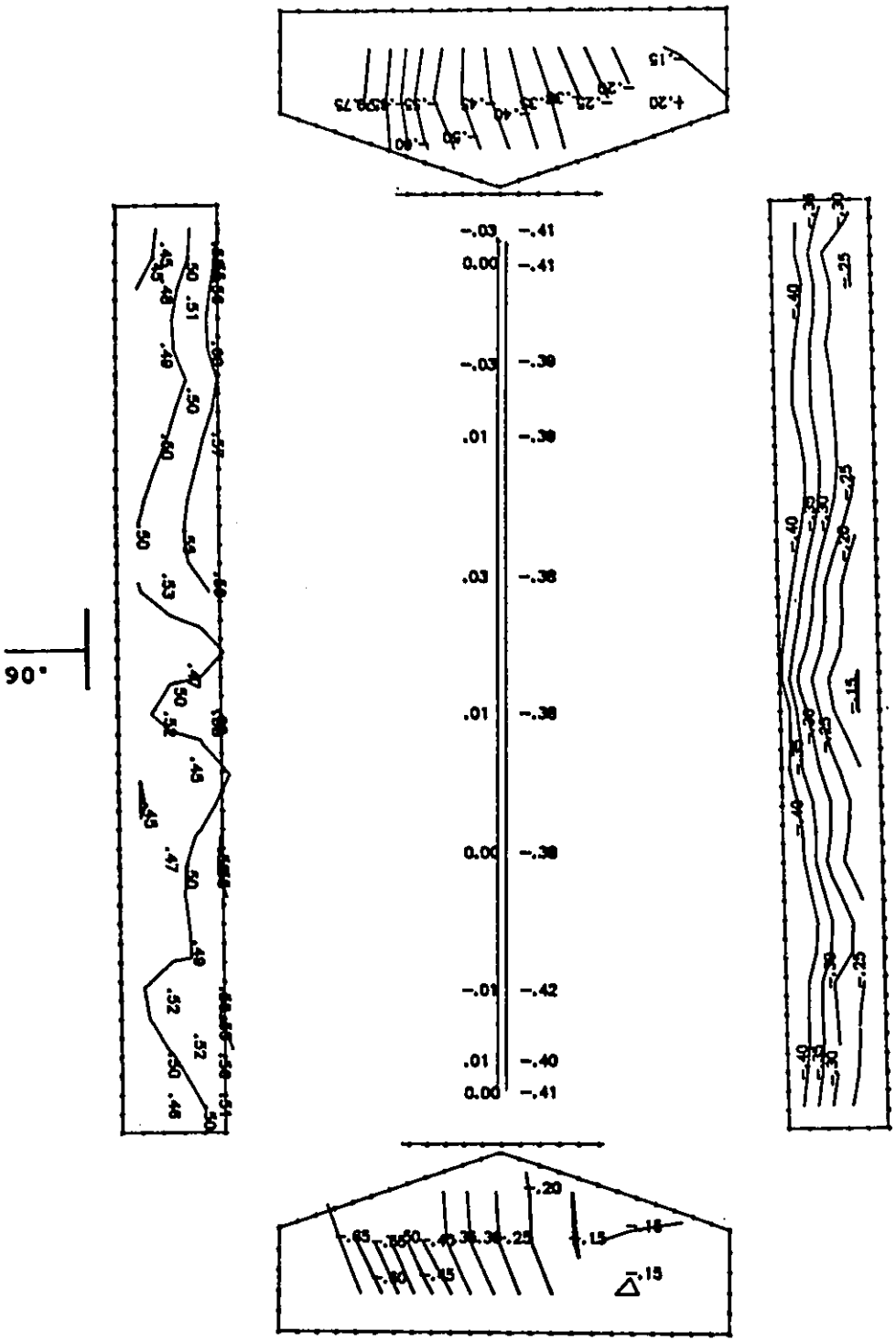

Figure E.5a Cps contour lines: open model, simulated 150 mm ridge and 800 mm sidewall openings, closed end walls, wind angle of 90°.

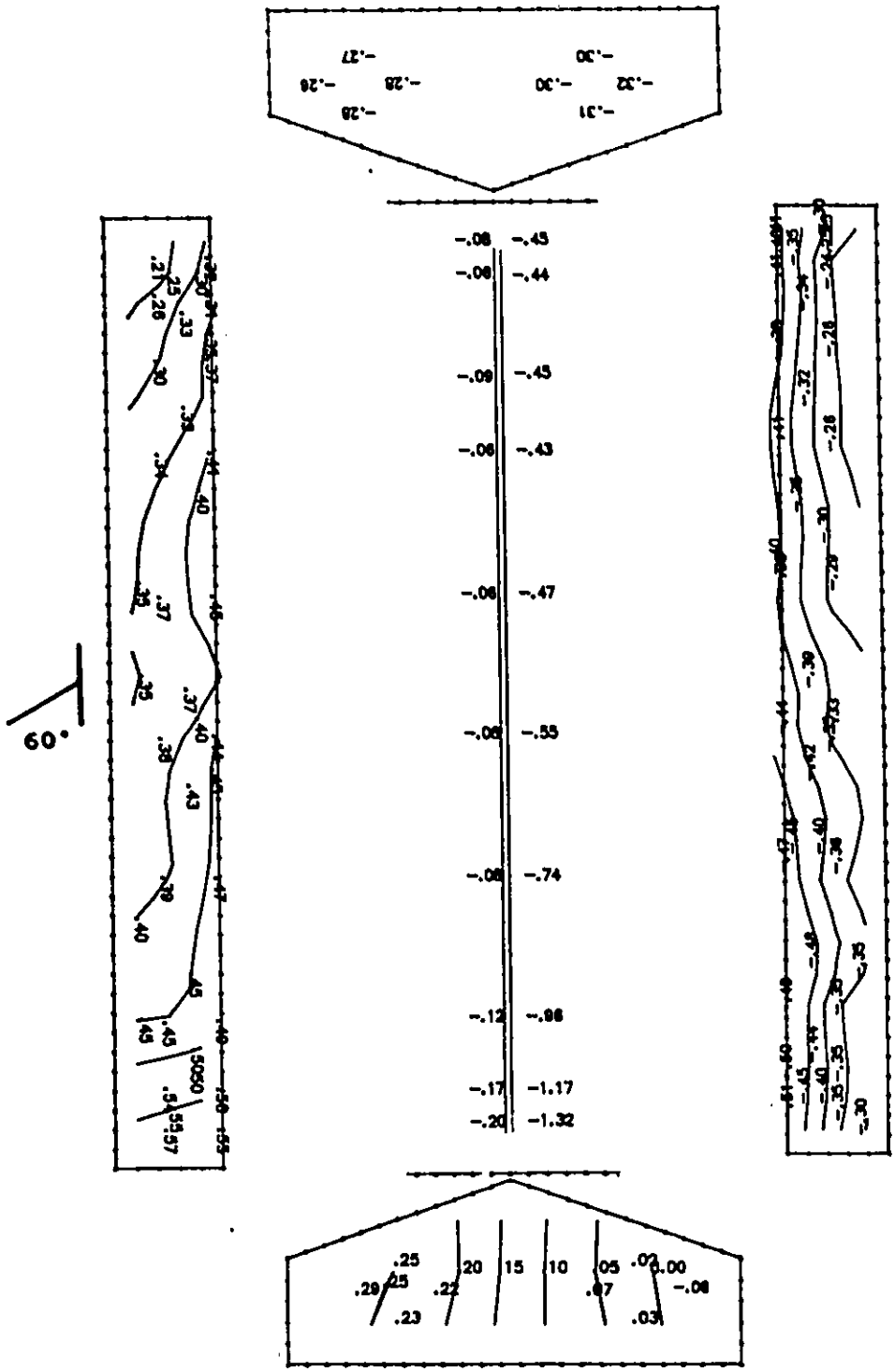

Figure E.5b Cps contour lines: open model, simulated 150 mm ridge and 800 mm sidewall openings, closed end walls, wind angle of 60°.

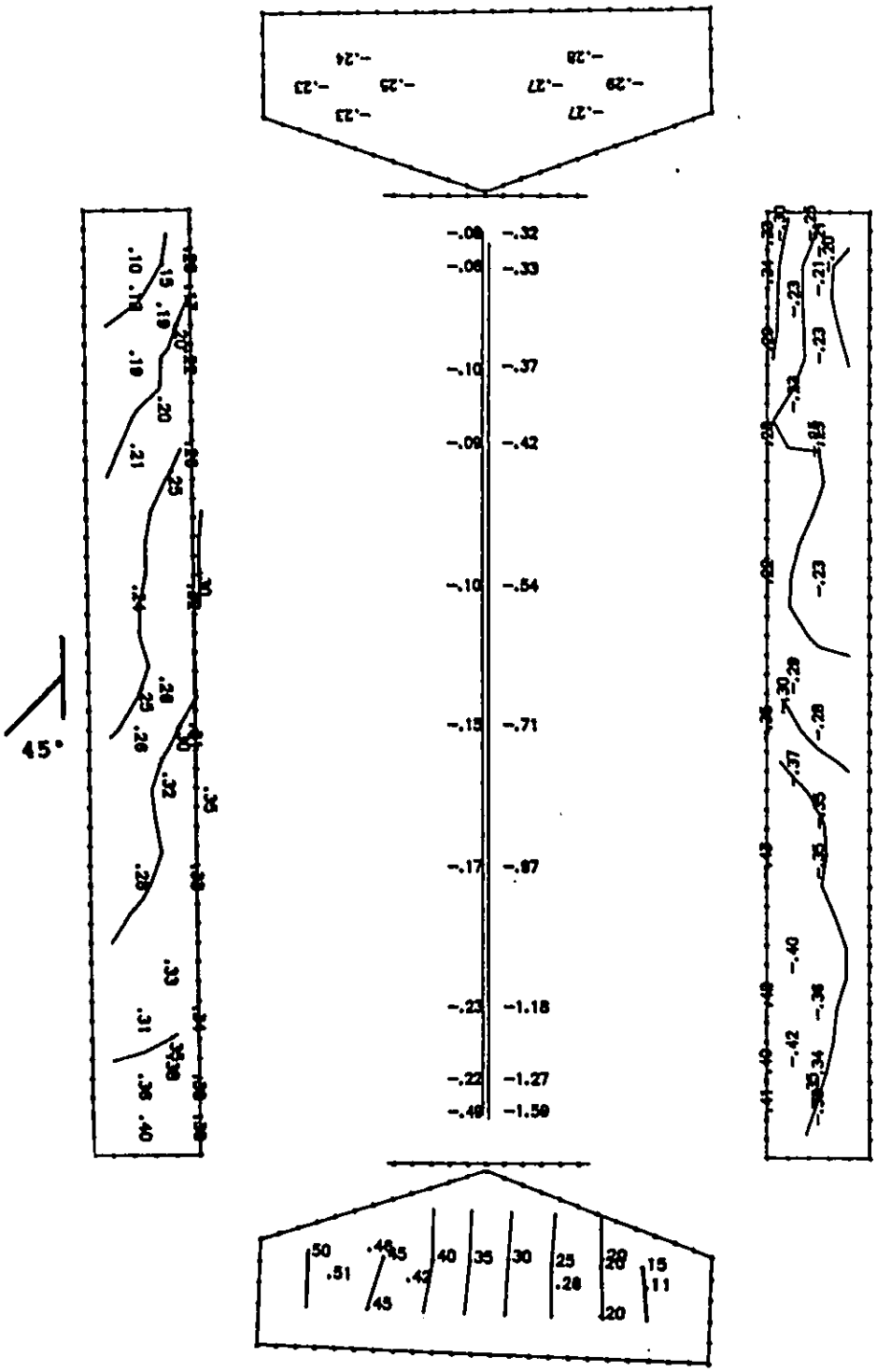

Figure E.5c Cps contour lines: open model, simulated 150 mm ridge and 800 mm sidewall openings, closed end walls, wind angle of 45°.

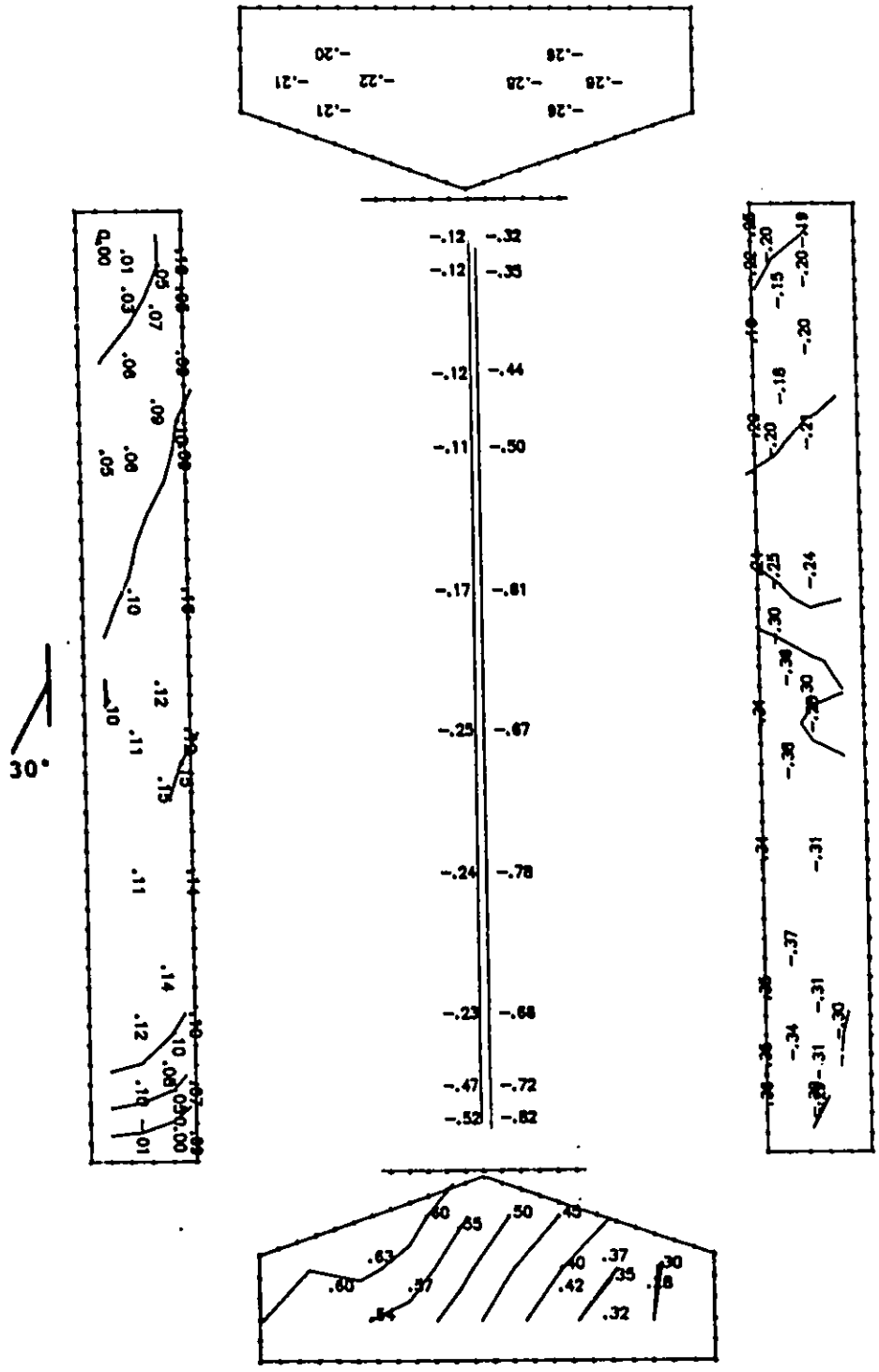

Figure E.5d Cps contour lines: open model, simulated 150 mm ridge and 800 mm sidewall openings, closed end walls, wind angle of 30°.

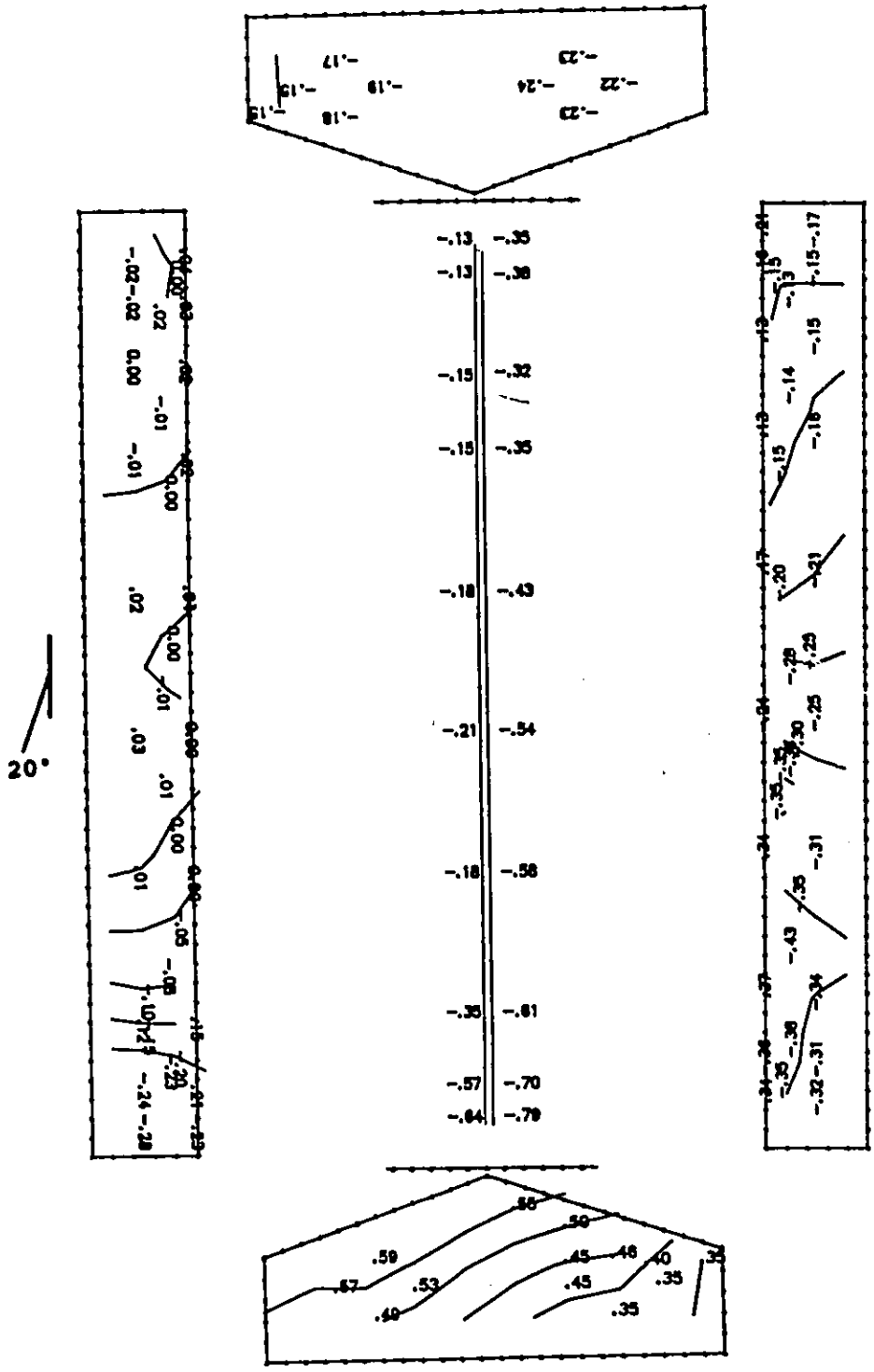

Figure E.5e Cps contour lines: open model, simulated 150 mm ridge and 800 mm sidewall openings, closed end walls, wind angle of 20°.

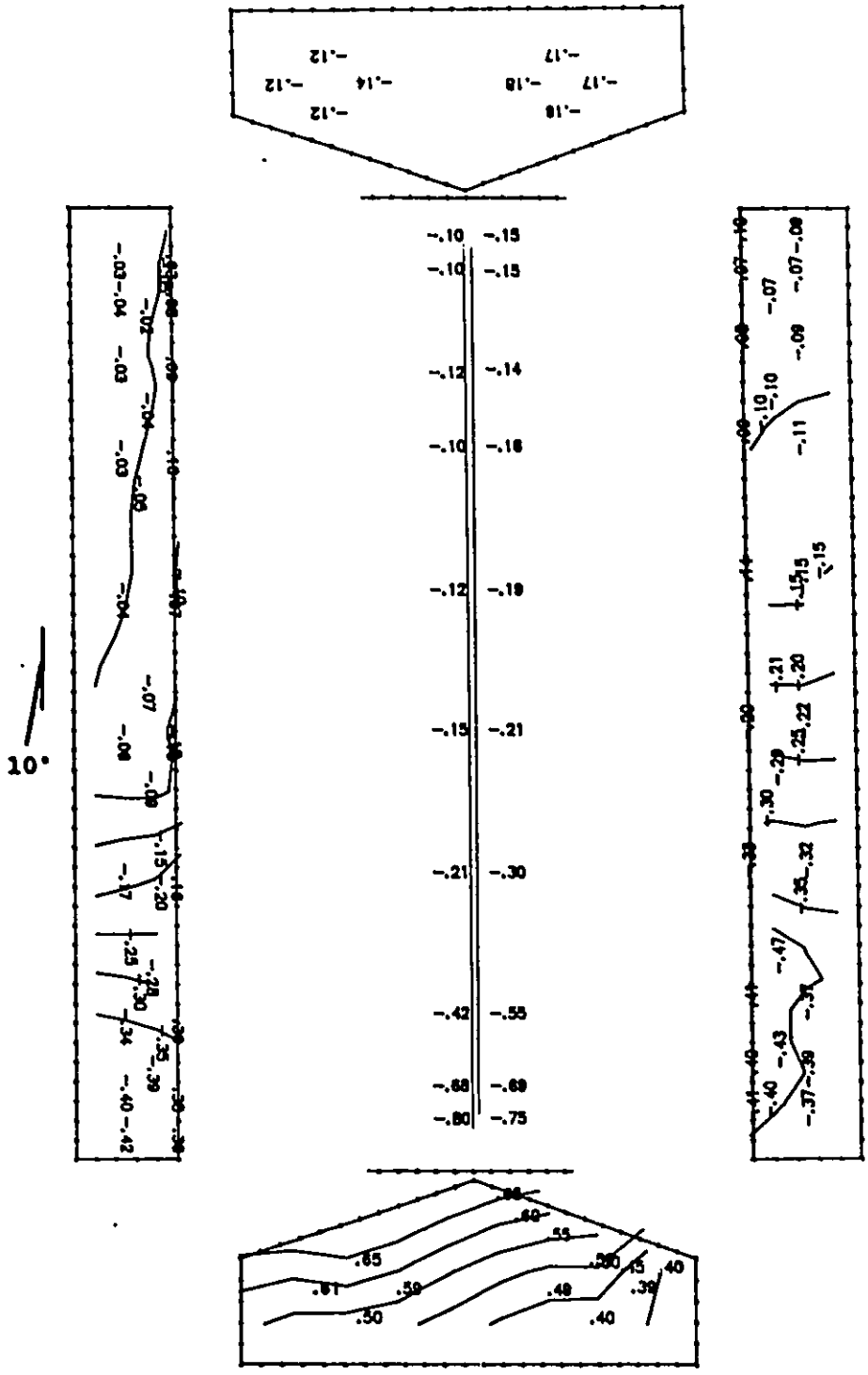

Figure E.5f Cps contour lines: open model, simulated 150 mm ridge and 800 mm sidewall openings, closed end walls, wind angle of 10°.

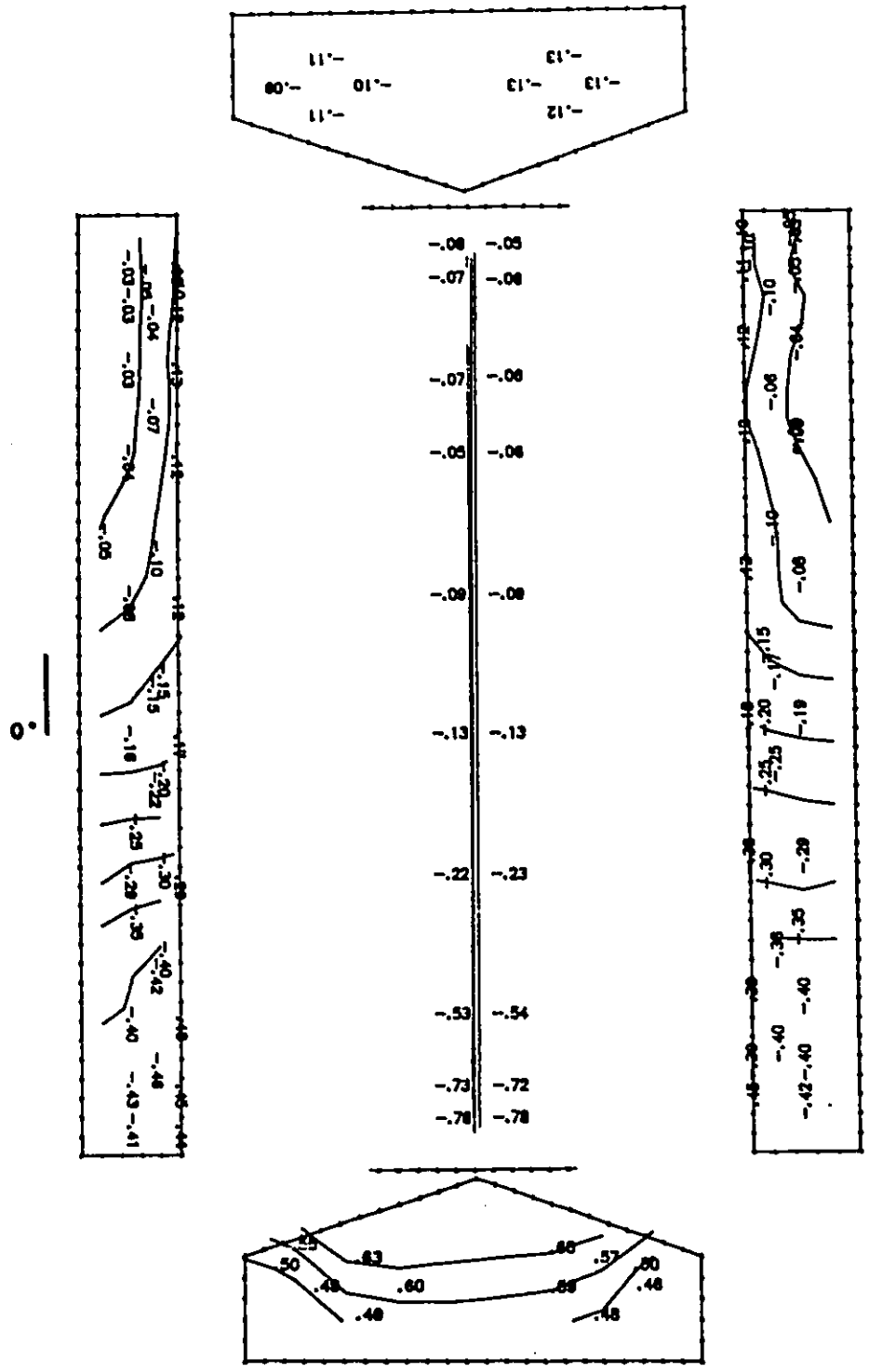

Figure E.5g Cps contour lines: open model, simulated 150 mm ridge and 800 mm sidewall openings, closed end walls, wind angle of 0°.

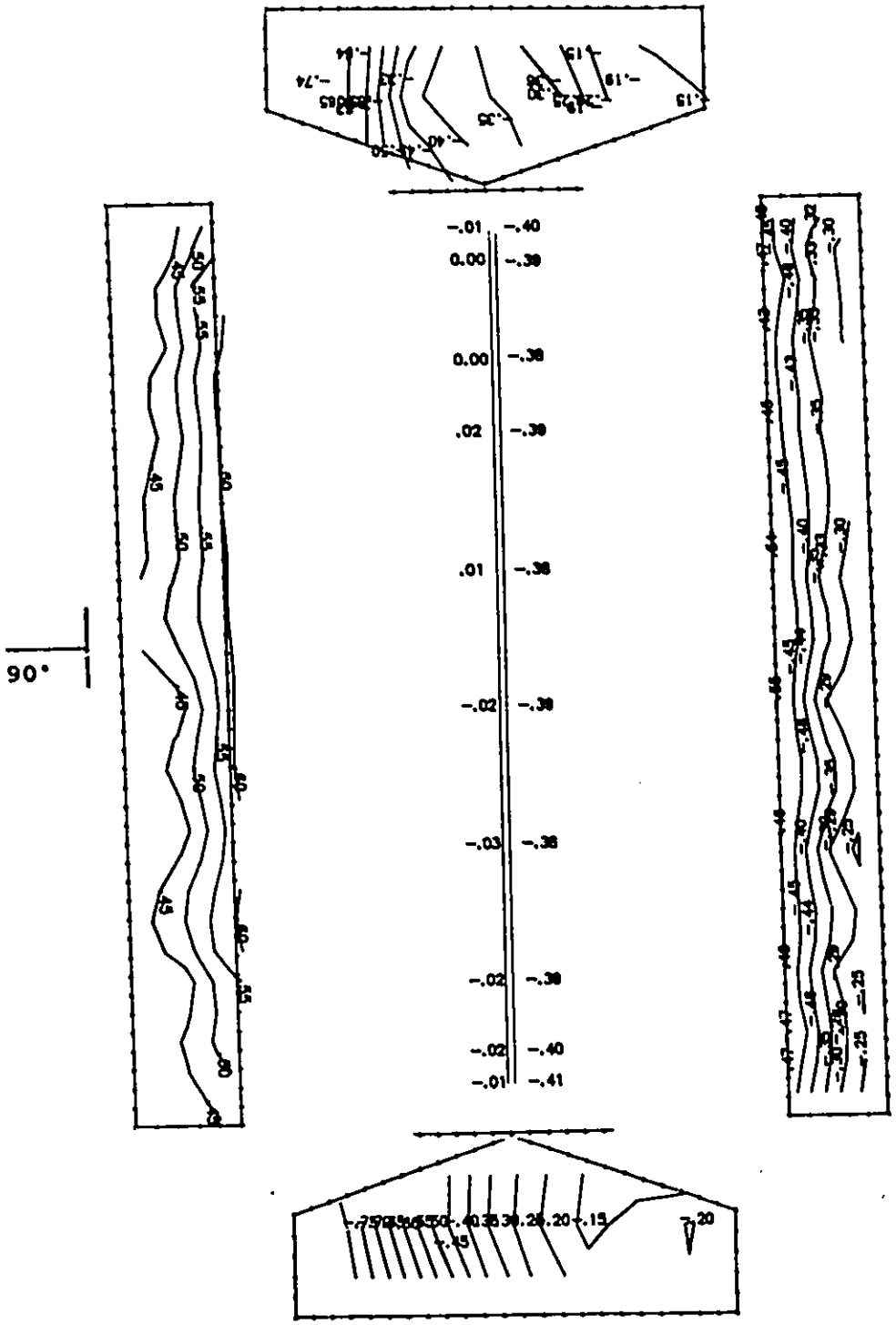

Figure E.6a Cps contour lines: open model, simulated 150 mm ridge and 1100 mm sidewall openings, closed end walls, wind angle of 90°.

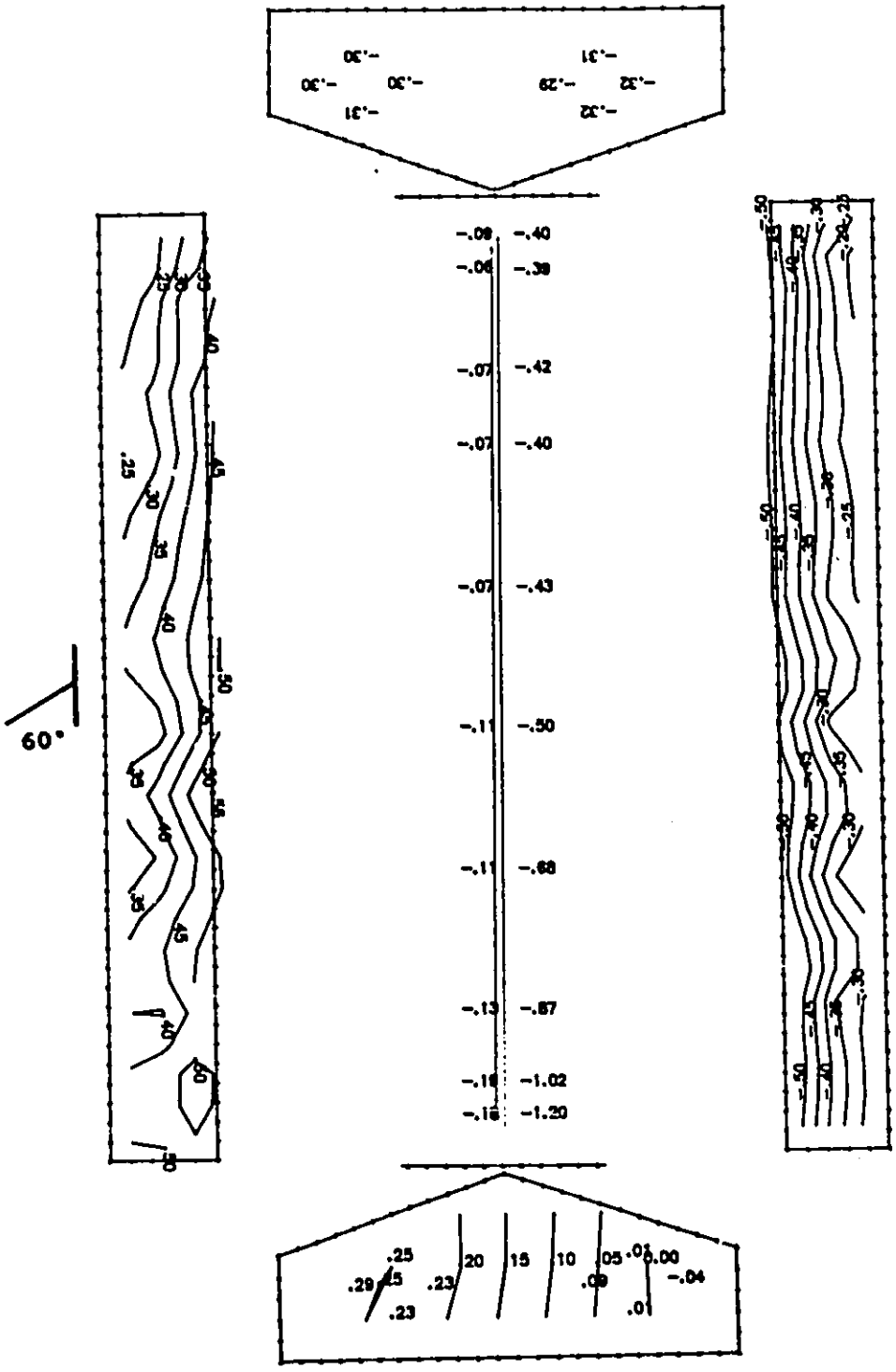

Figure E.6b Cps contour lines: open model, simulated 150 mm ridge and 1100 mm sidewall openings, closed end walls, wind angle of 60°.

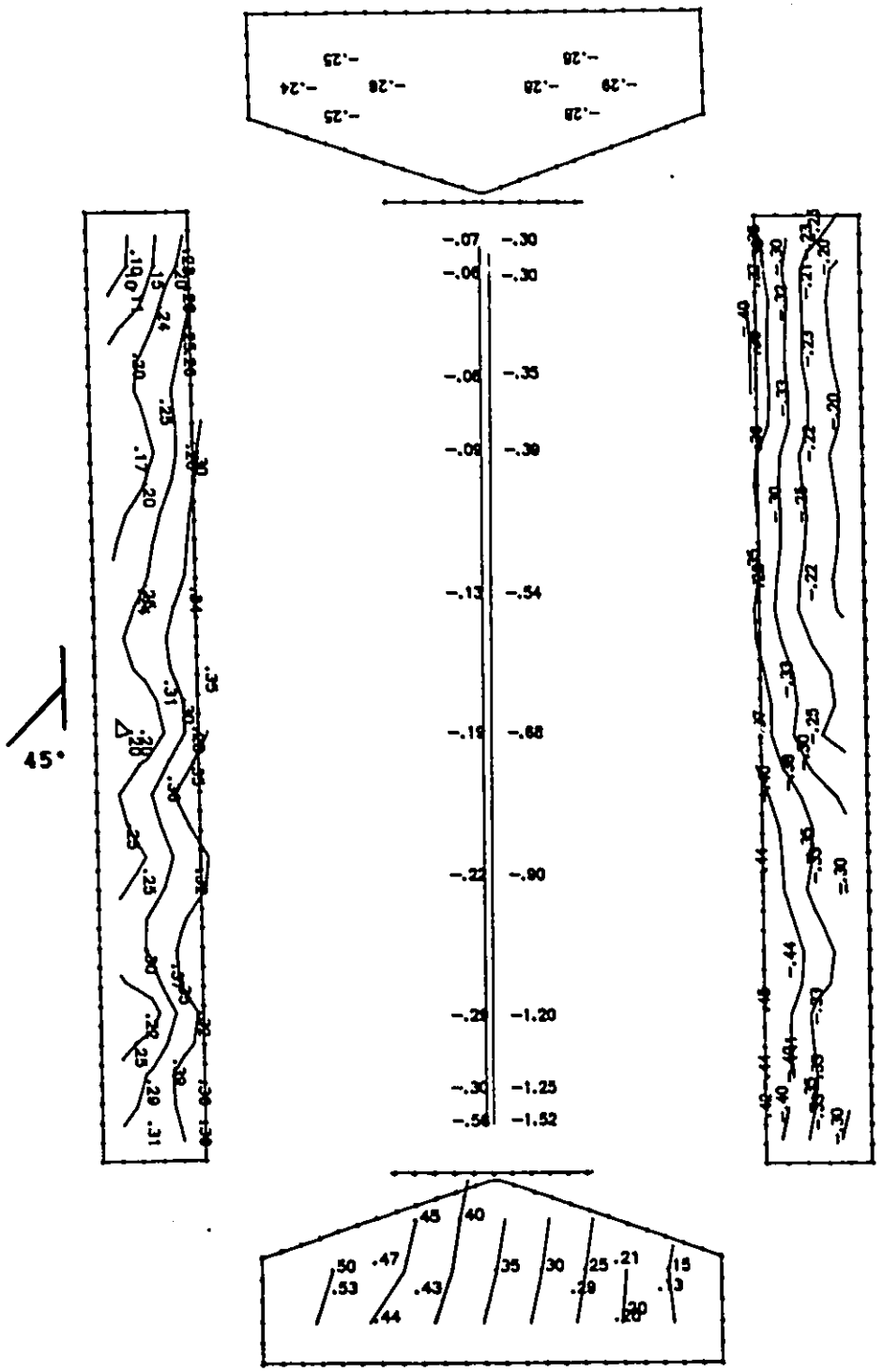

Figure E.6c Cps contour lines: open model, simulated 150 mm ridge and 1100 mm sidewall openings, closed end walls, wind angle of 45°.

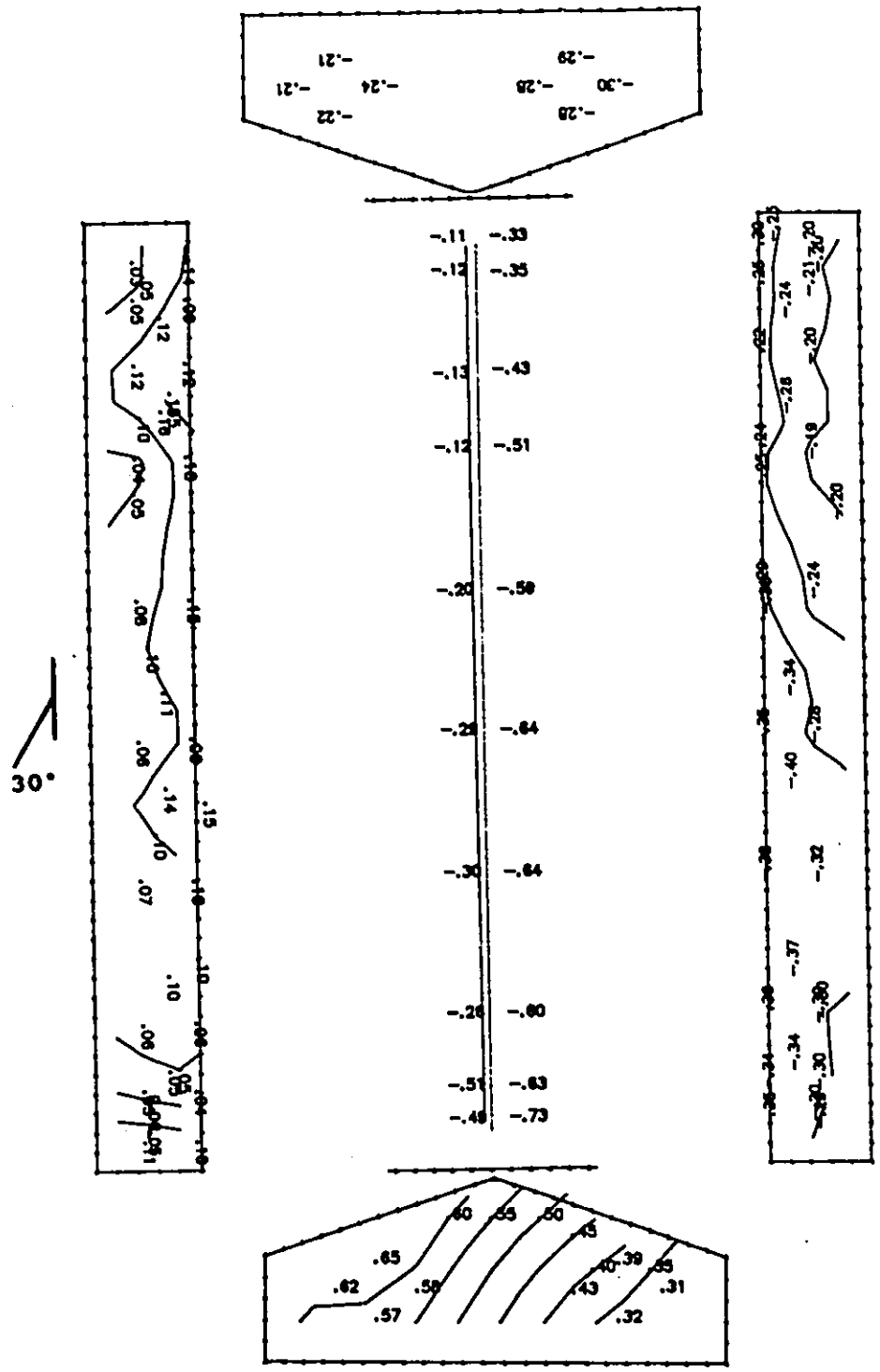

Figure E.6d Cps contour lines: open model, simulated 150 mm ridge and 1100 mm sidewall openings, closed end walls, wind angle of 30°.

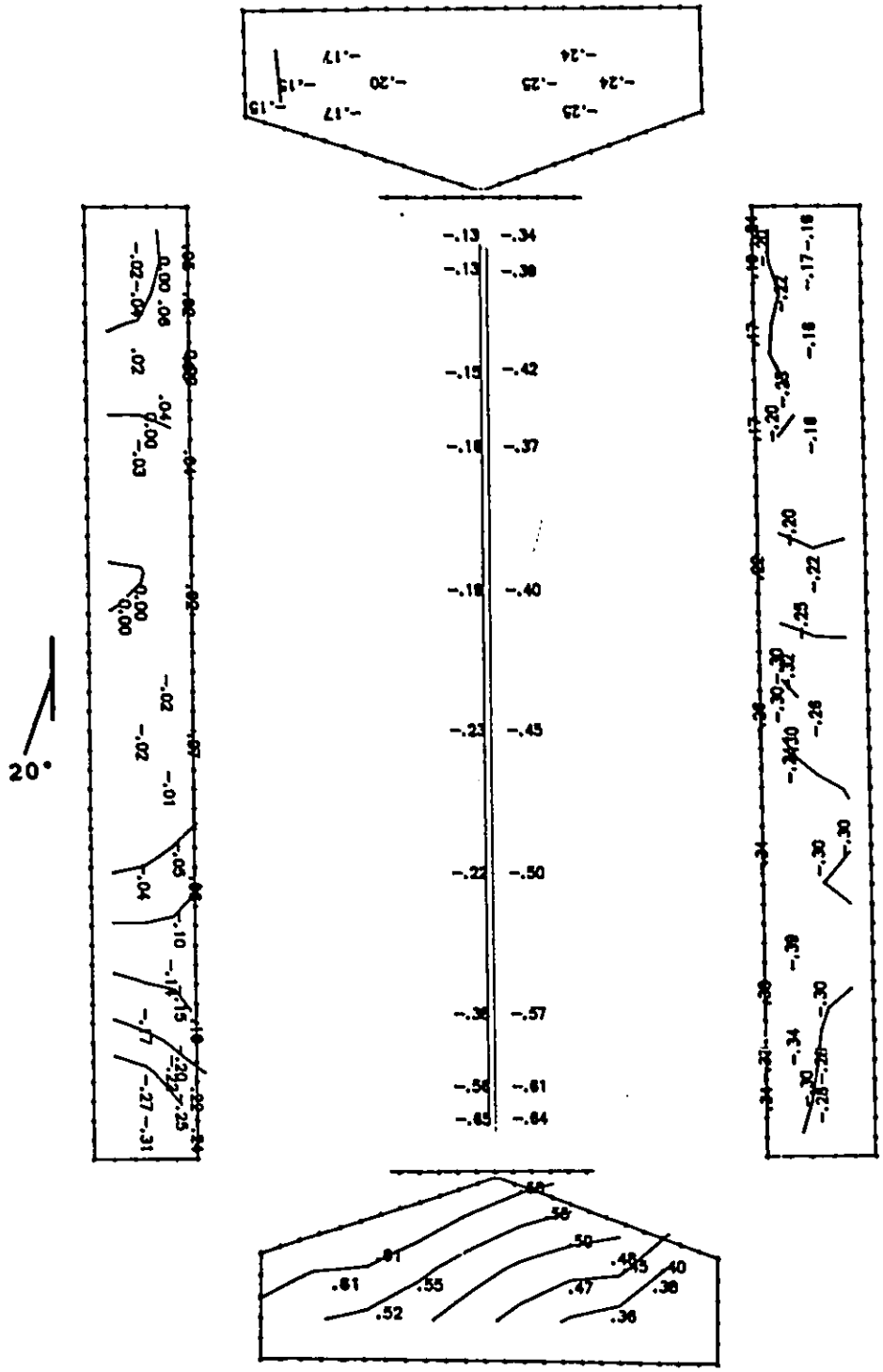

Figure E.6e Cps contour lines: open model, simulated 150 mm ridge and 1100 mm sidewall openings, closed end walls, wind angle of 20°.

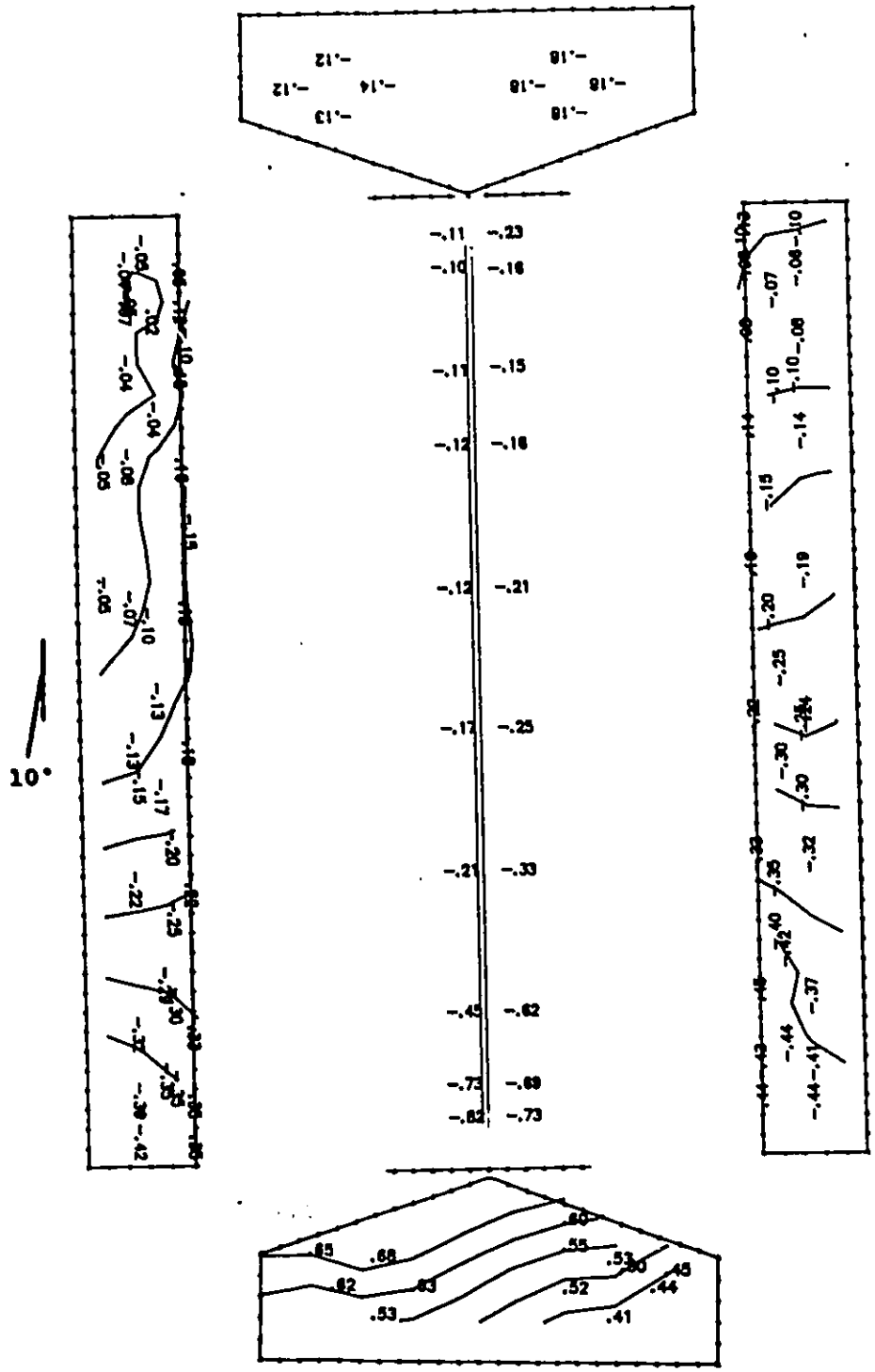

Figure E.6f Cps contour lines: open model, simulated 150 mm ridge and 1100 mm sidewall openings, closed end walls, wind angle of 10°.

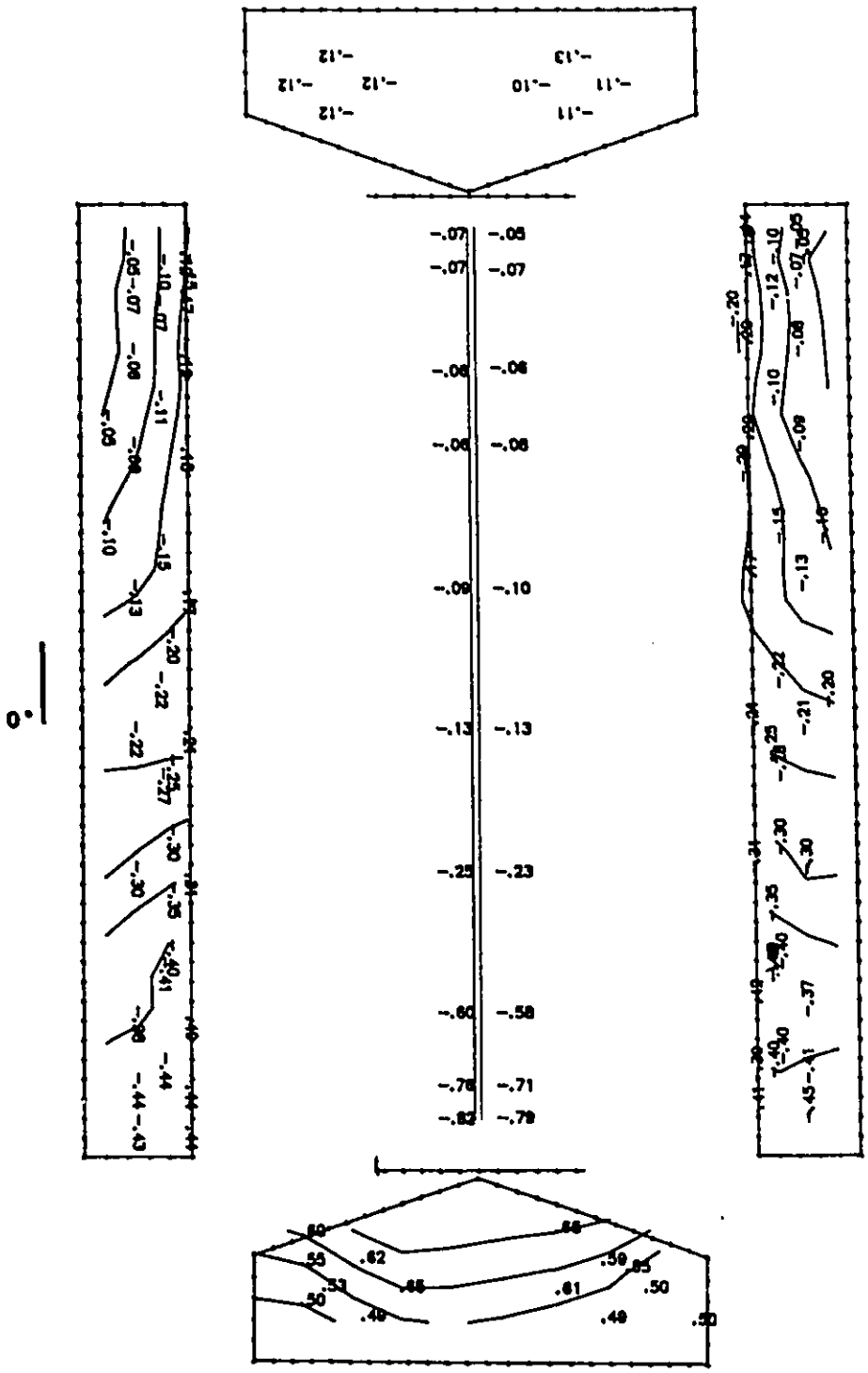

Figure E.6g Cps contour lines: open model, simulated 150 mm ridge and 1100 mm sidewall openings, closed end walls, wind angle of 0°.

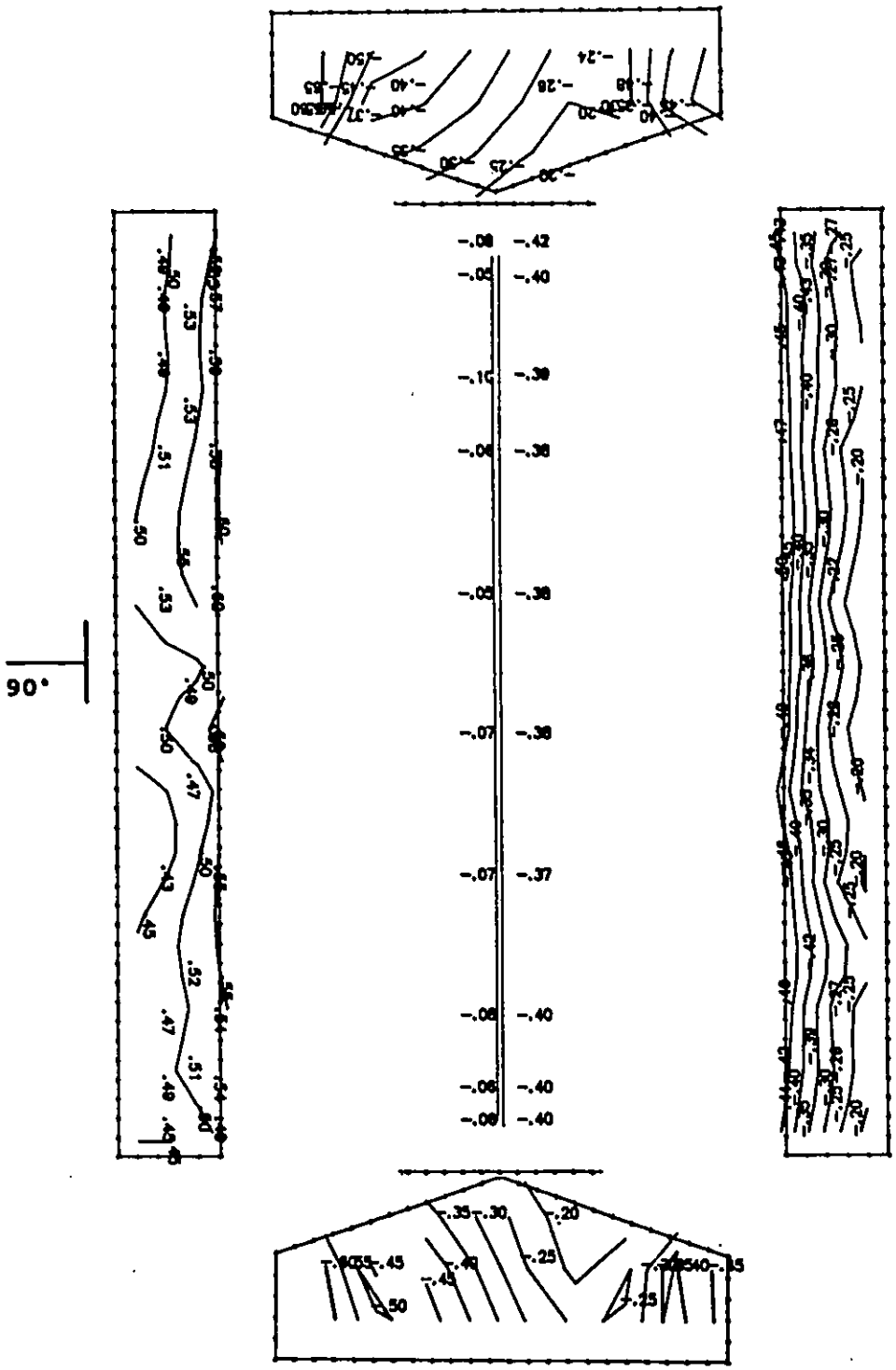

Figure E.7a Cps contour lines: open model, simulated 150 mm ridge and 800 mm sidewall openings, open end walls, wind angle of 90°.

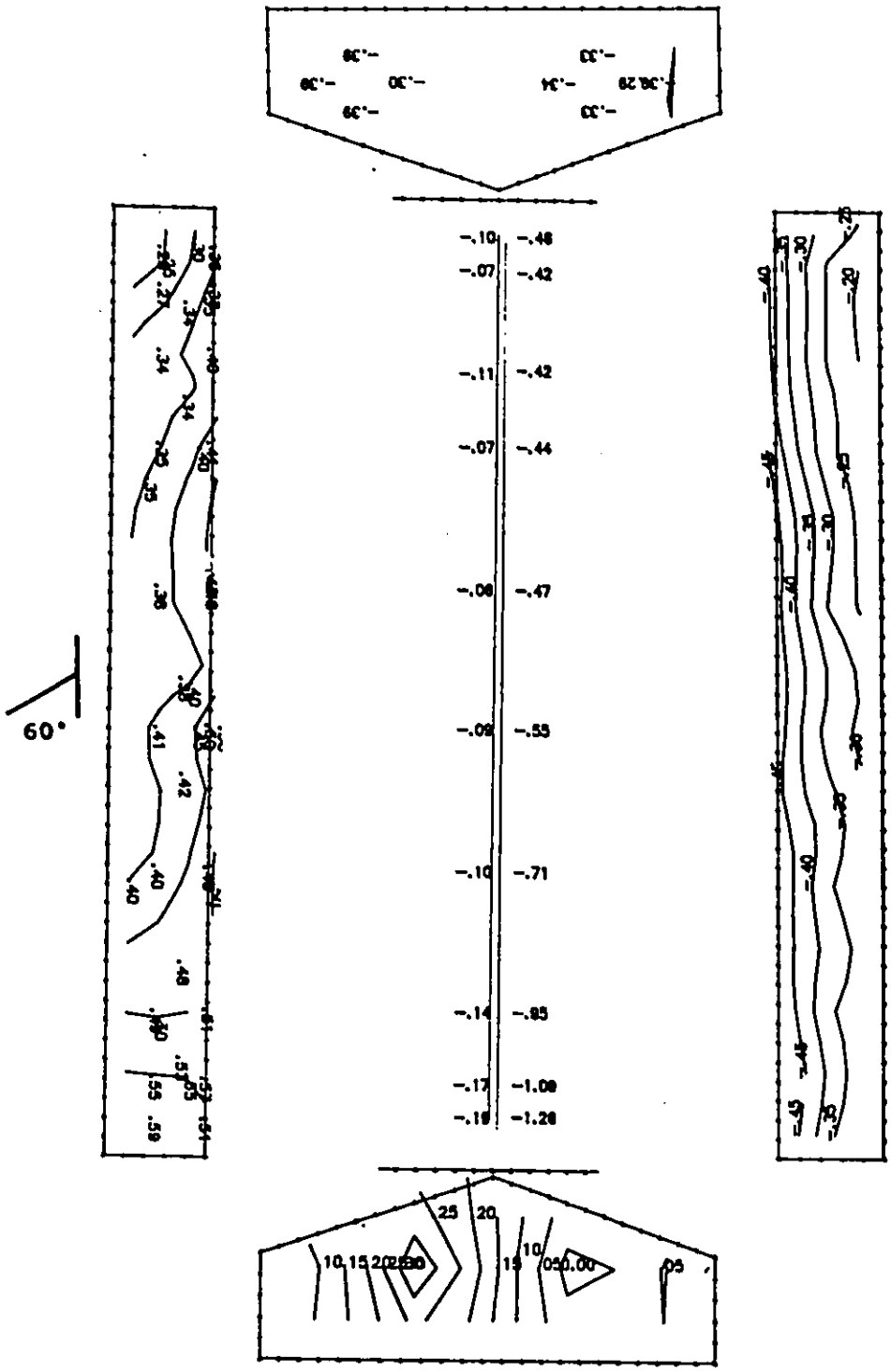

Figure E.7b Cps contour lines: open model, simulated 150 mm ridge and 800 mm sidewall openings, open end walls, wind angle of 60°.

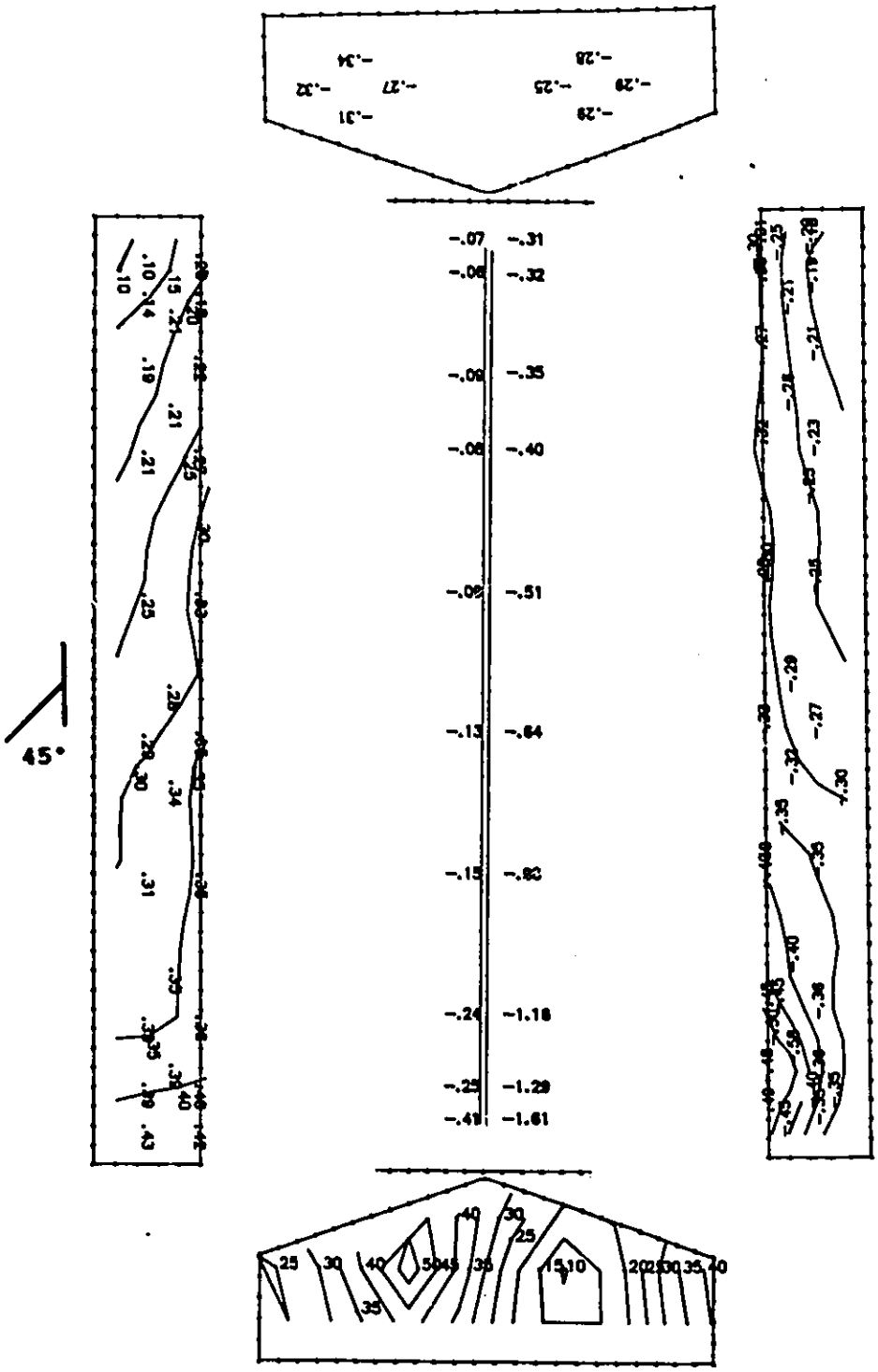

Figure E.7c Cps contour lines: open model, simulated 150 mm ridge and 800 mm sidewall openings, open end walls, wind angle of 45°.

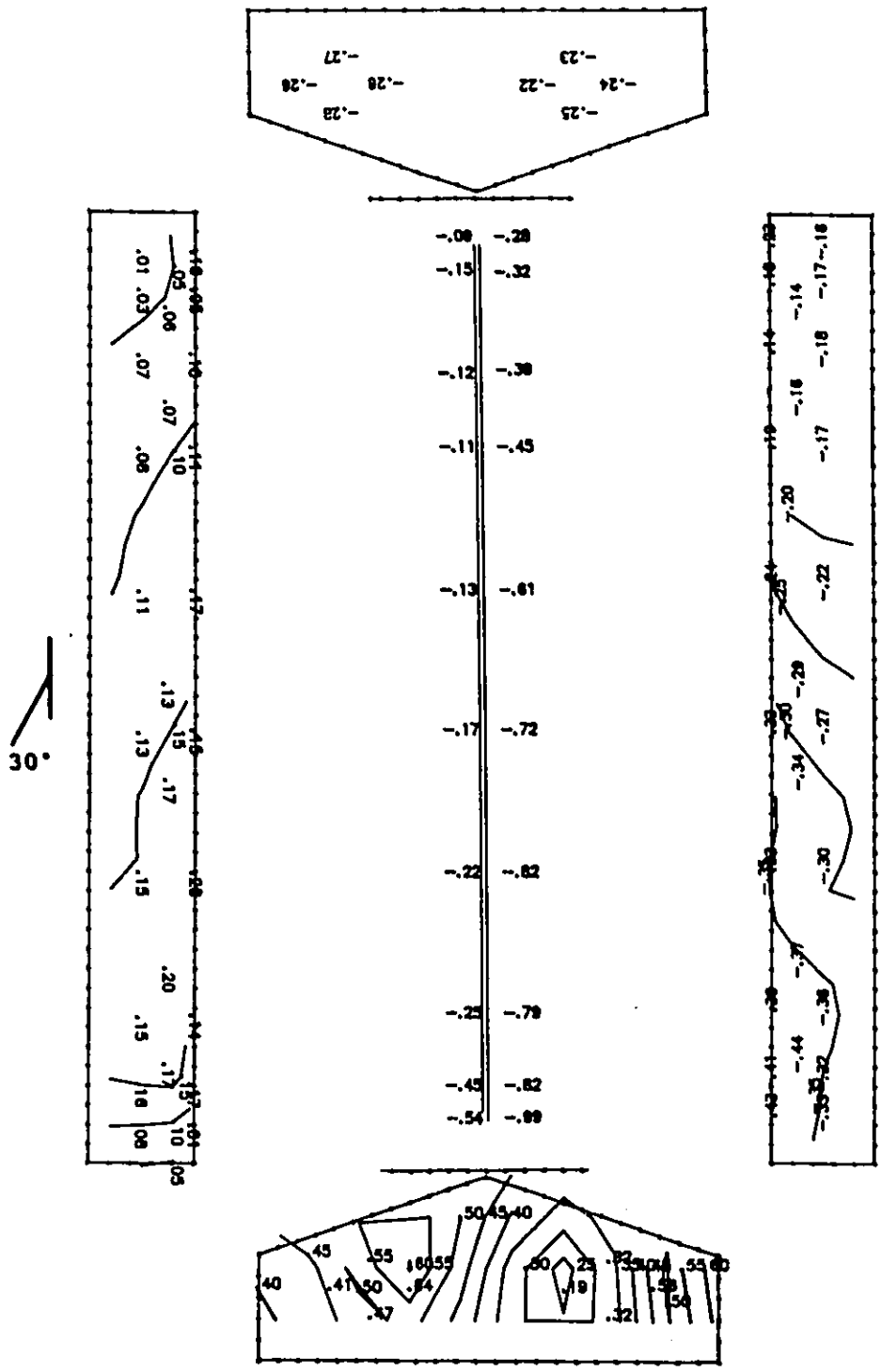

Figure E.7d Cps contour lines: open model, simulated 150 mm ridge and 800 mm sidewall openings, open end walls, wind angle of 30°.

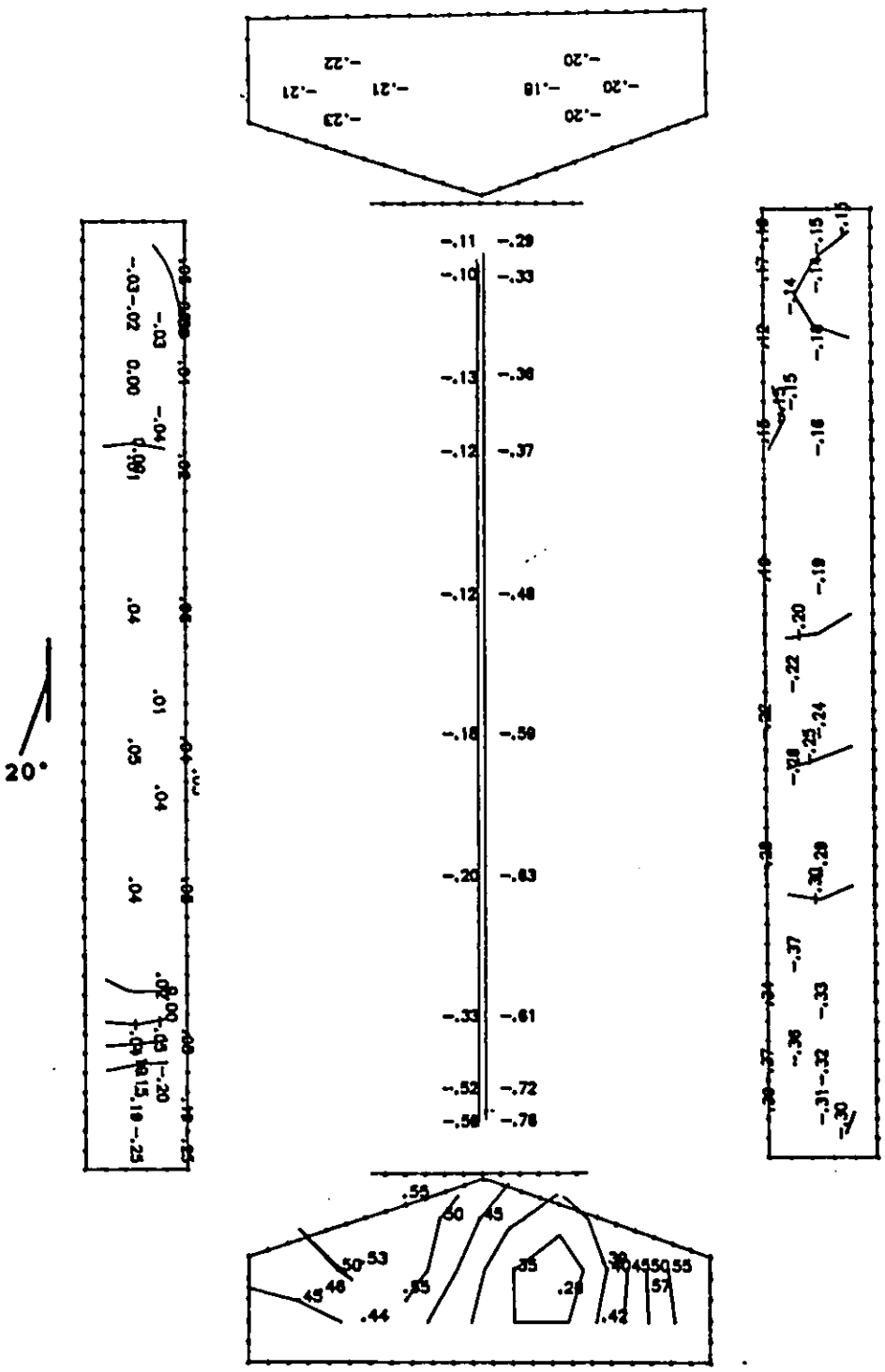

Figure E.7e Cps contour lines: open model, simulated 150 mm ridge and 800 mm sidewall openings, open end walls, wind angle of 20°.

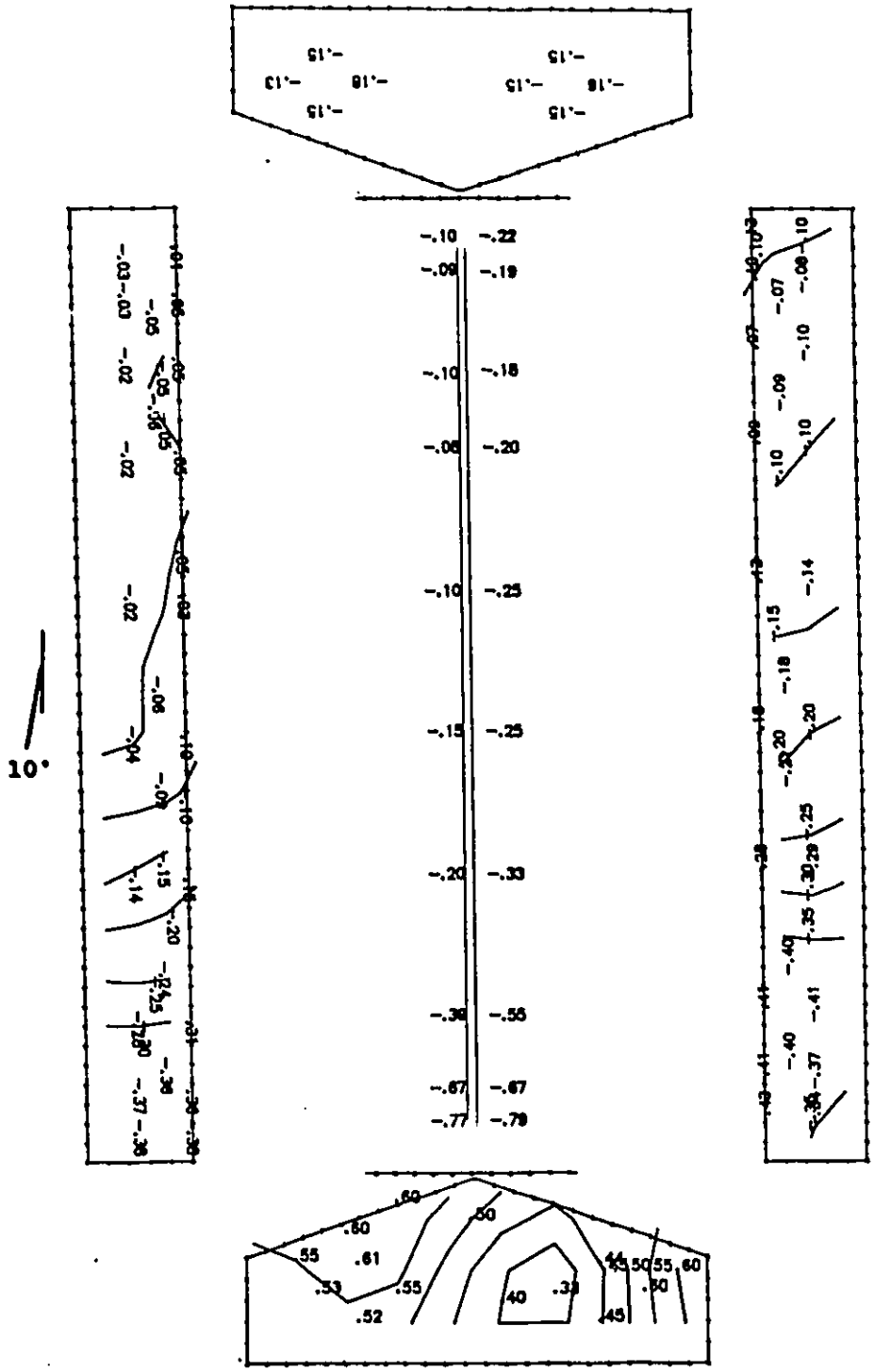

Figure E.7f Cps contour lines: open model, simulated 150 mm ridge and 800 mm sidewall openings, open end walls, wind angle of 10°.

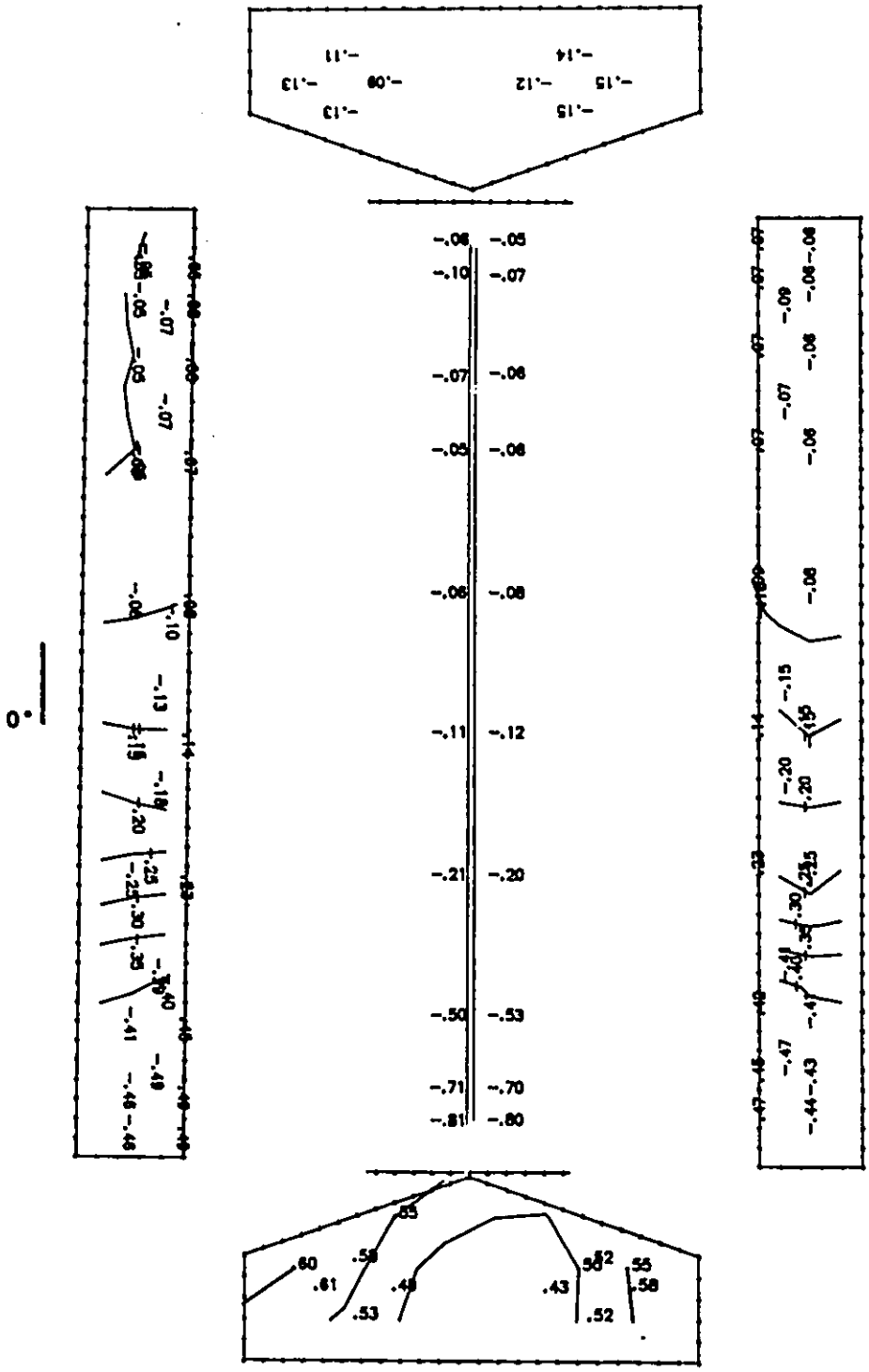

Figure E.7g Cps contour lines: open model, simulated 150 mm ridge and 800 mm sidewall openings, open end walls, wind angle of 0°.

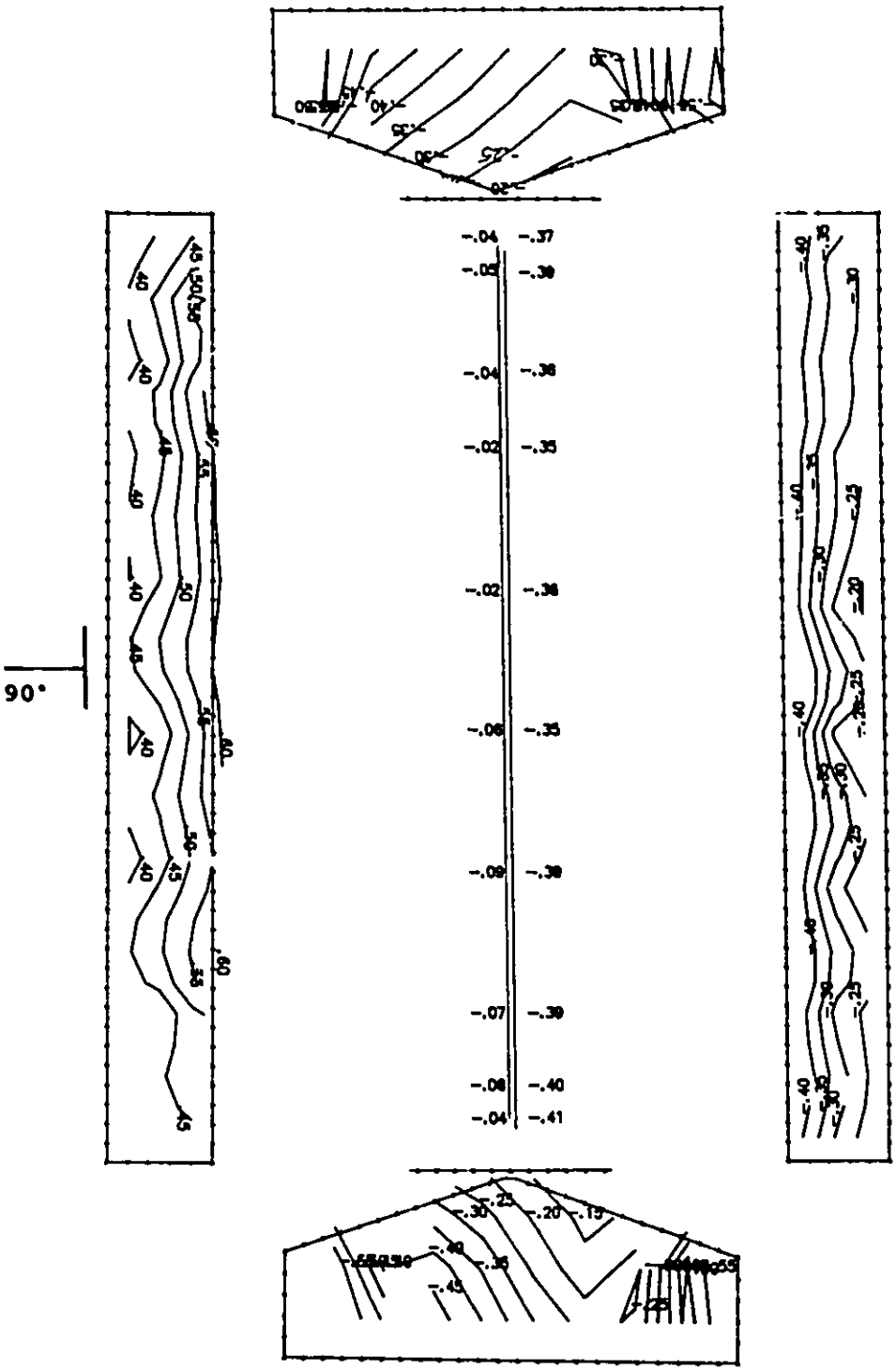

Figure E.8a Cps contour lines: open model, simulated 150 mm ridge and 1100 mm sidewall openings, open end walls, wind angle of 90°.

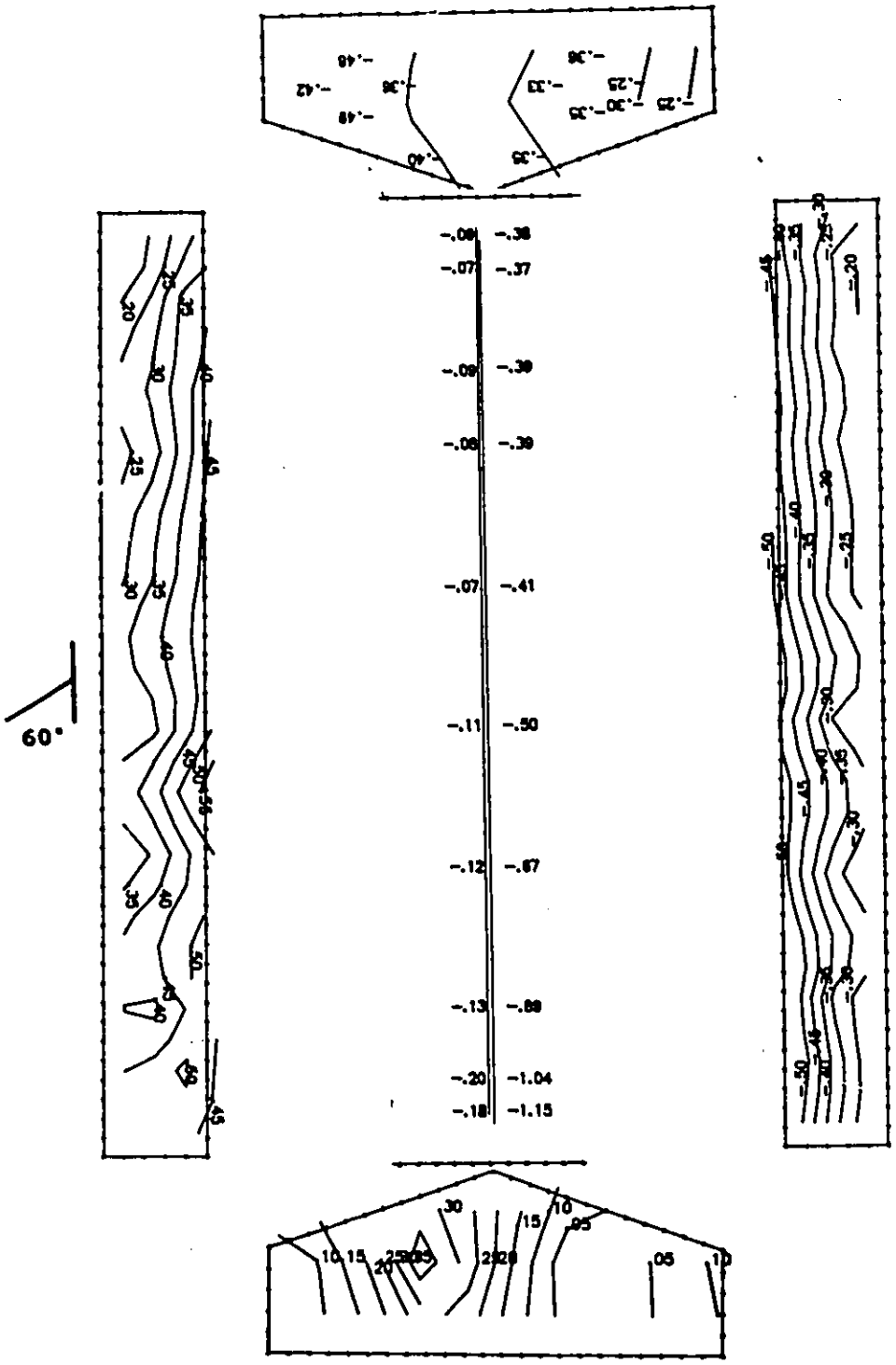

Figure E.8b Cps contour lines: open model, simulated 150 mm ridge and 1100 mm sidewall openings, open end walls, wind angle of 60°.

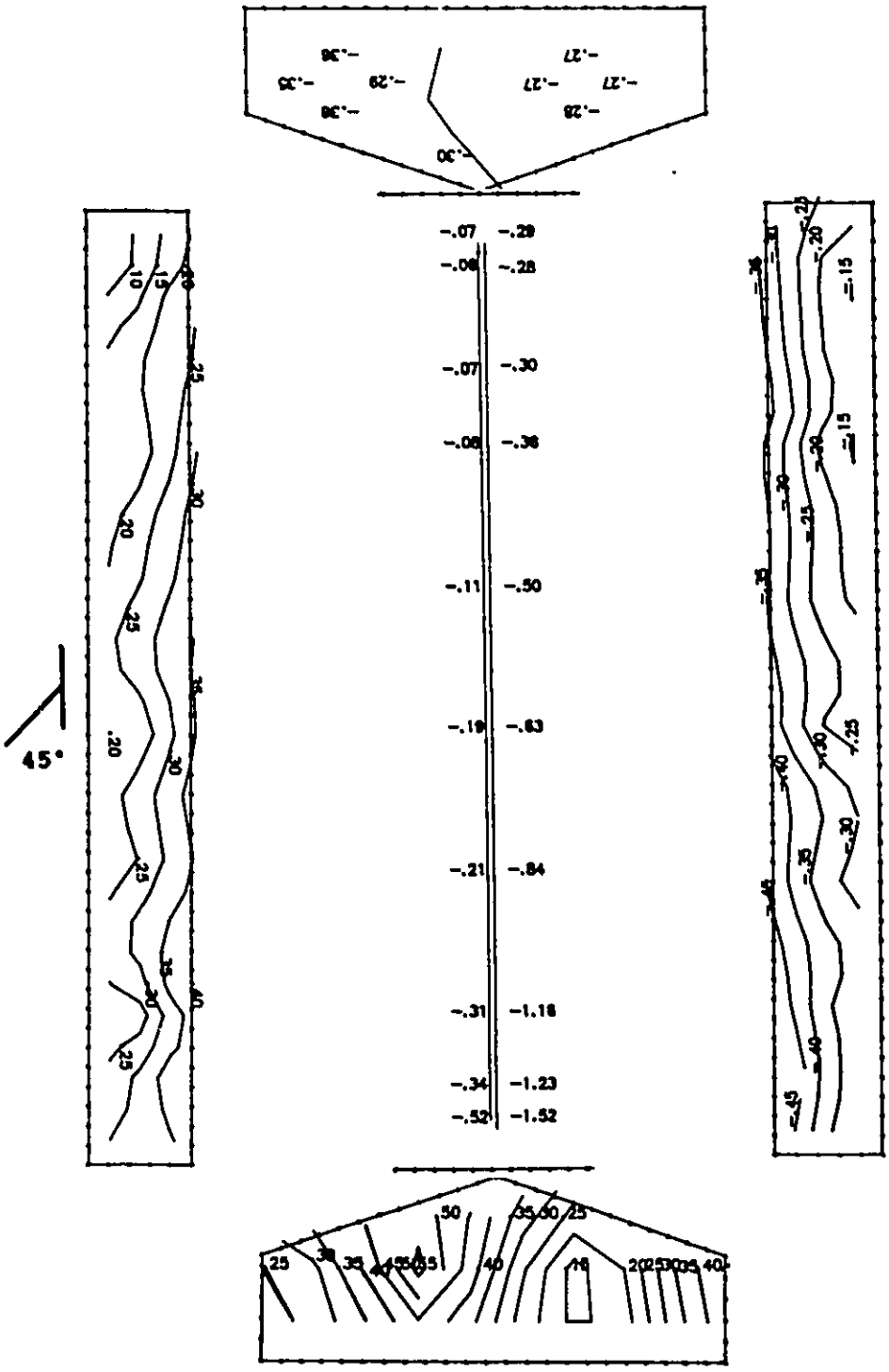

Figure E.8c Cps contour lines: open model, simulated 150 mm ridge and 1100 mm sidewall openings, open end walls, wind angle of 45°.

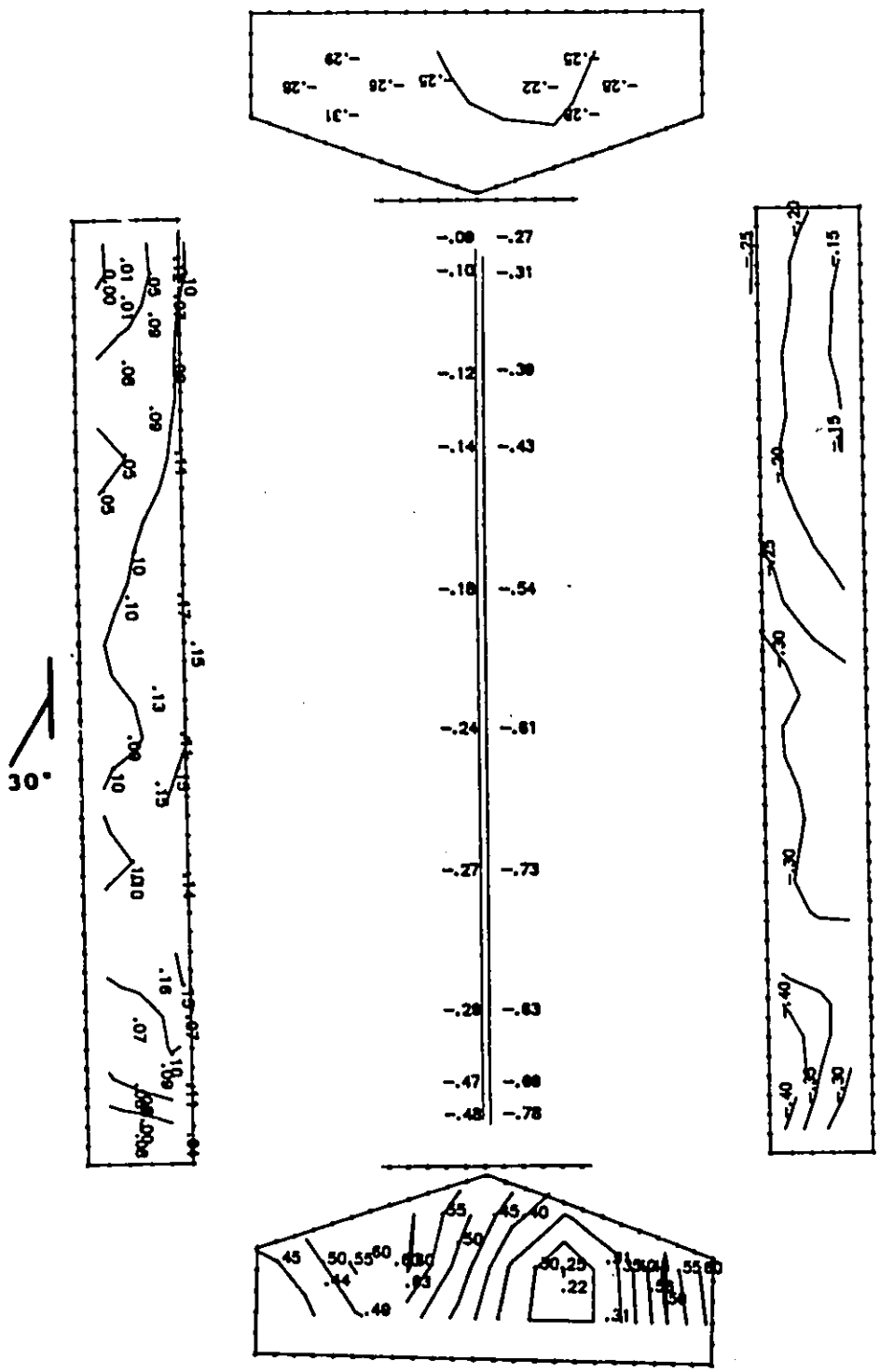

Figure E.8d Cps contour lines: open model, simulated 150 mm ridge and 1100 mm sidewall openings, open end walls, wind angle of 30°.

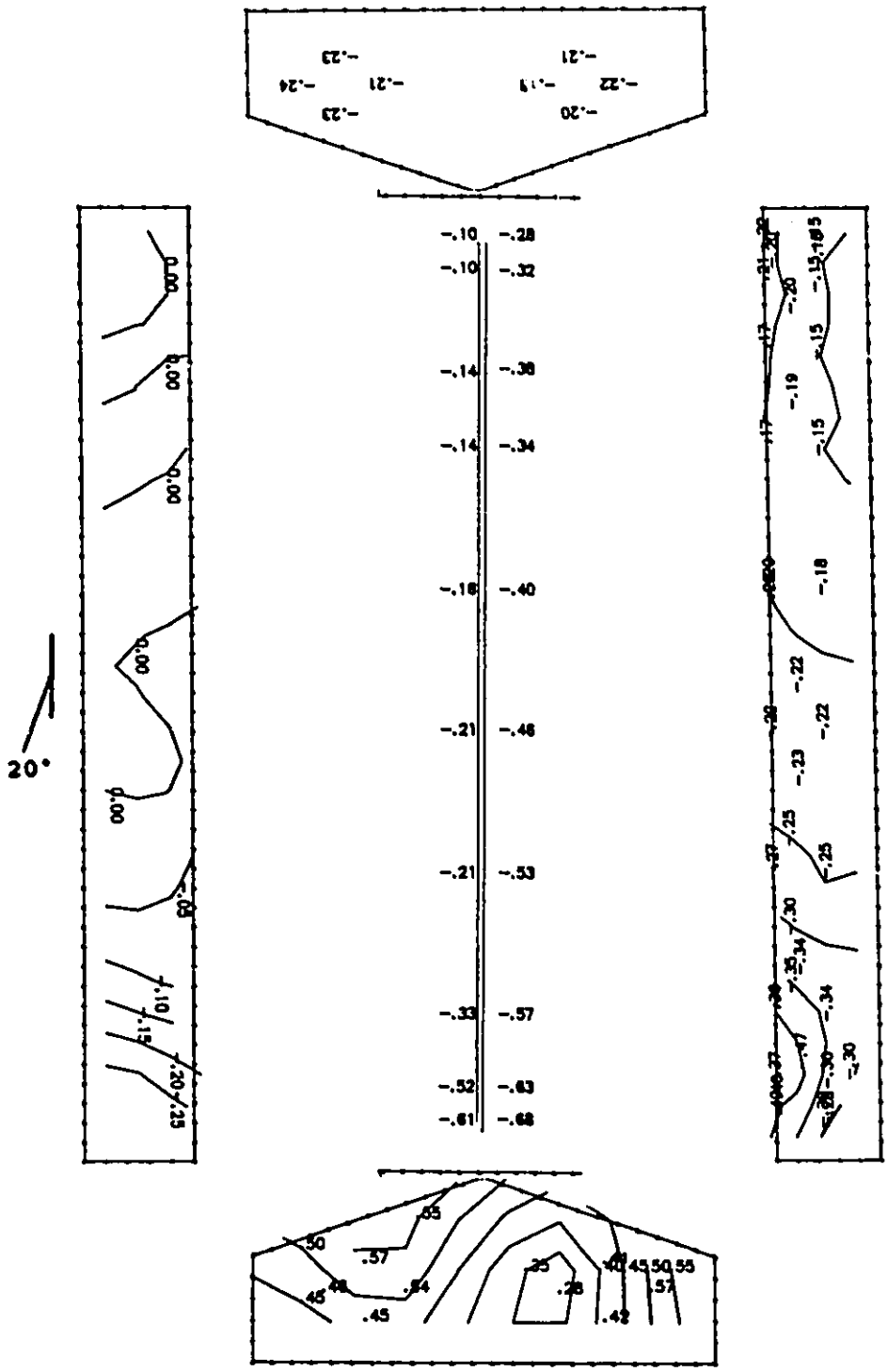

Figure E.8e Cps contour lines: open model, simulated 150 mm ridge and 1100 mm sidewall openings, open end walls, wind angle of 20°.

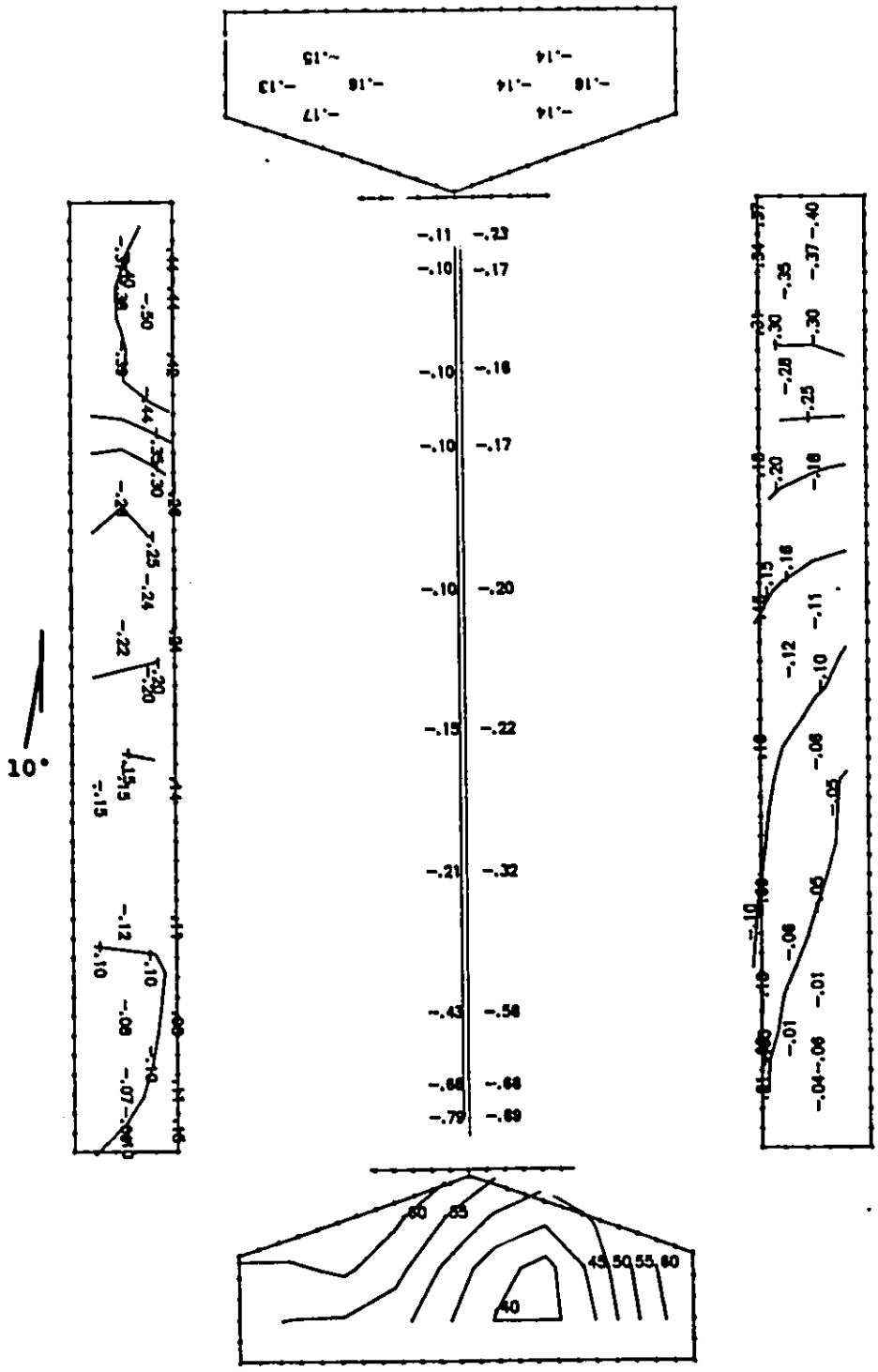

Figure E.8f Cps contour lines: open model, simulated 150 mm ridge and 1100 mm sidewall openings, open end walls, wind angle of 10°.

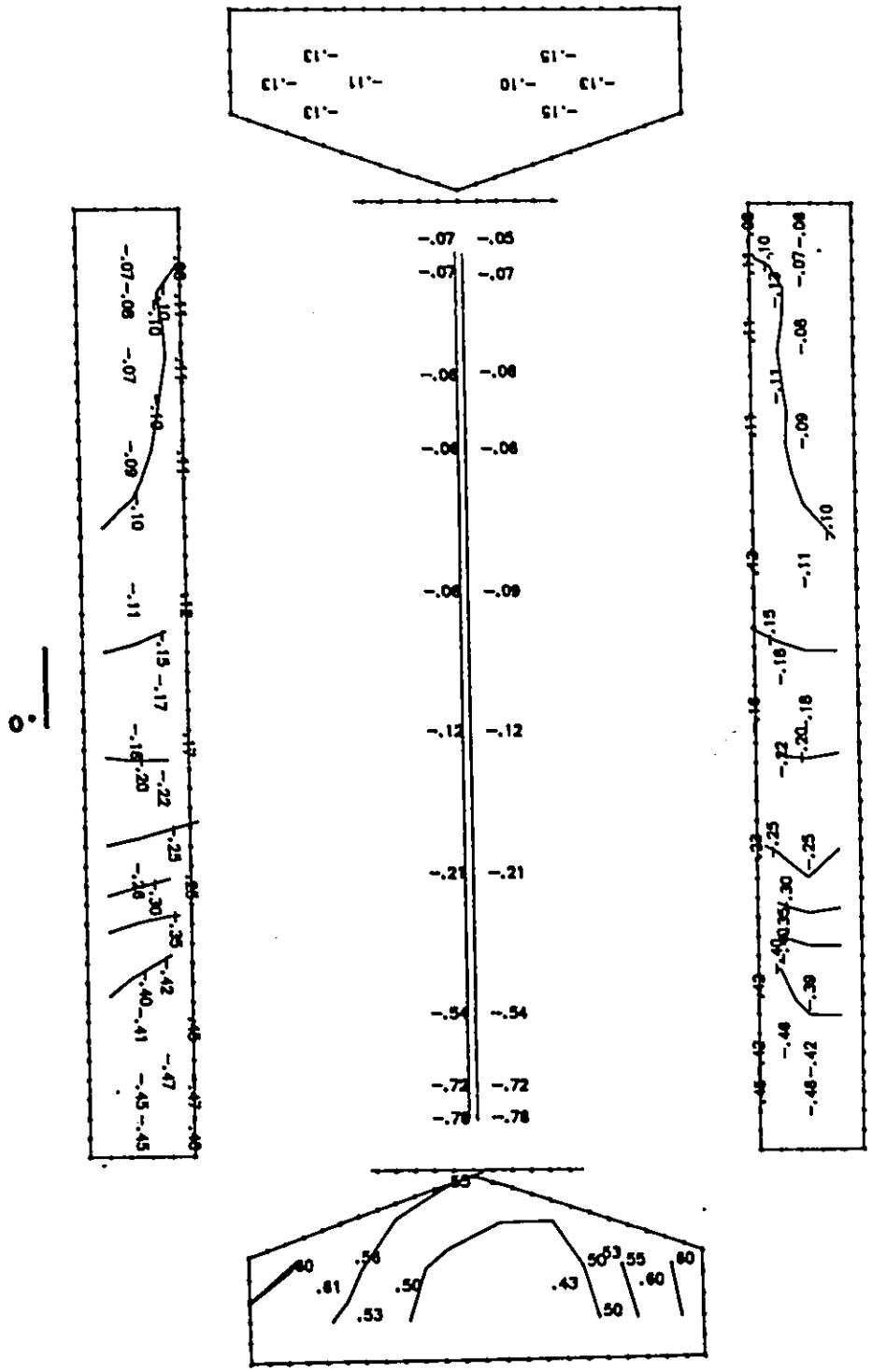

Figure E.8g Cps contour lines: open model, simulated 150 mm ridge and 1100 mm sidewall openings, open end walls, wind angle of 0°.

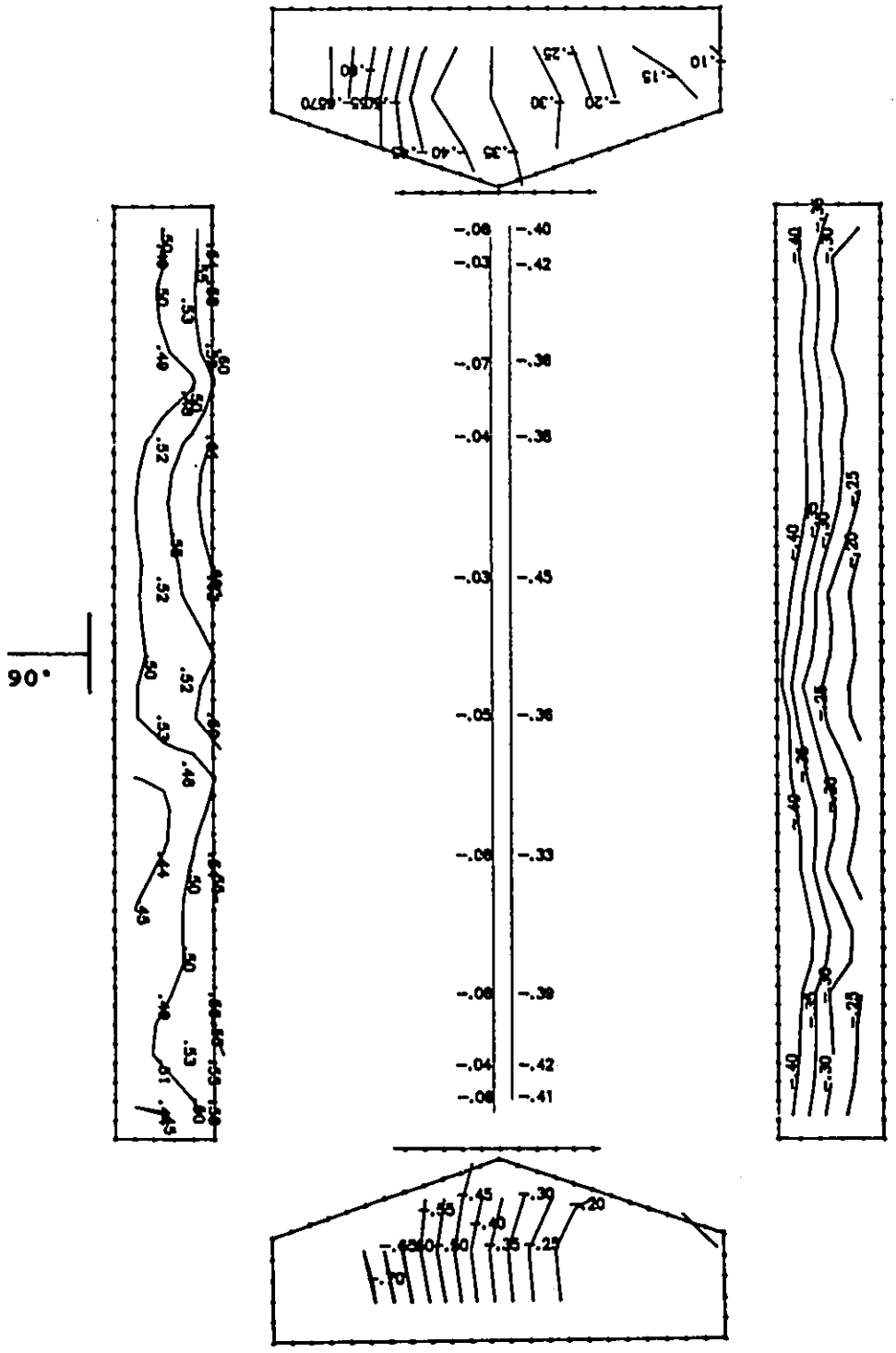

Figure E.9a Cps contour lines: open model, simulated 400 mm ridge and 800 mm sidewall openings, closed end walls, wind angle of 90°.

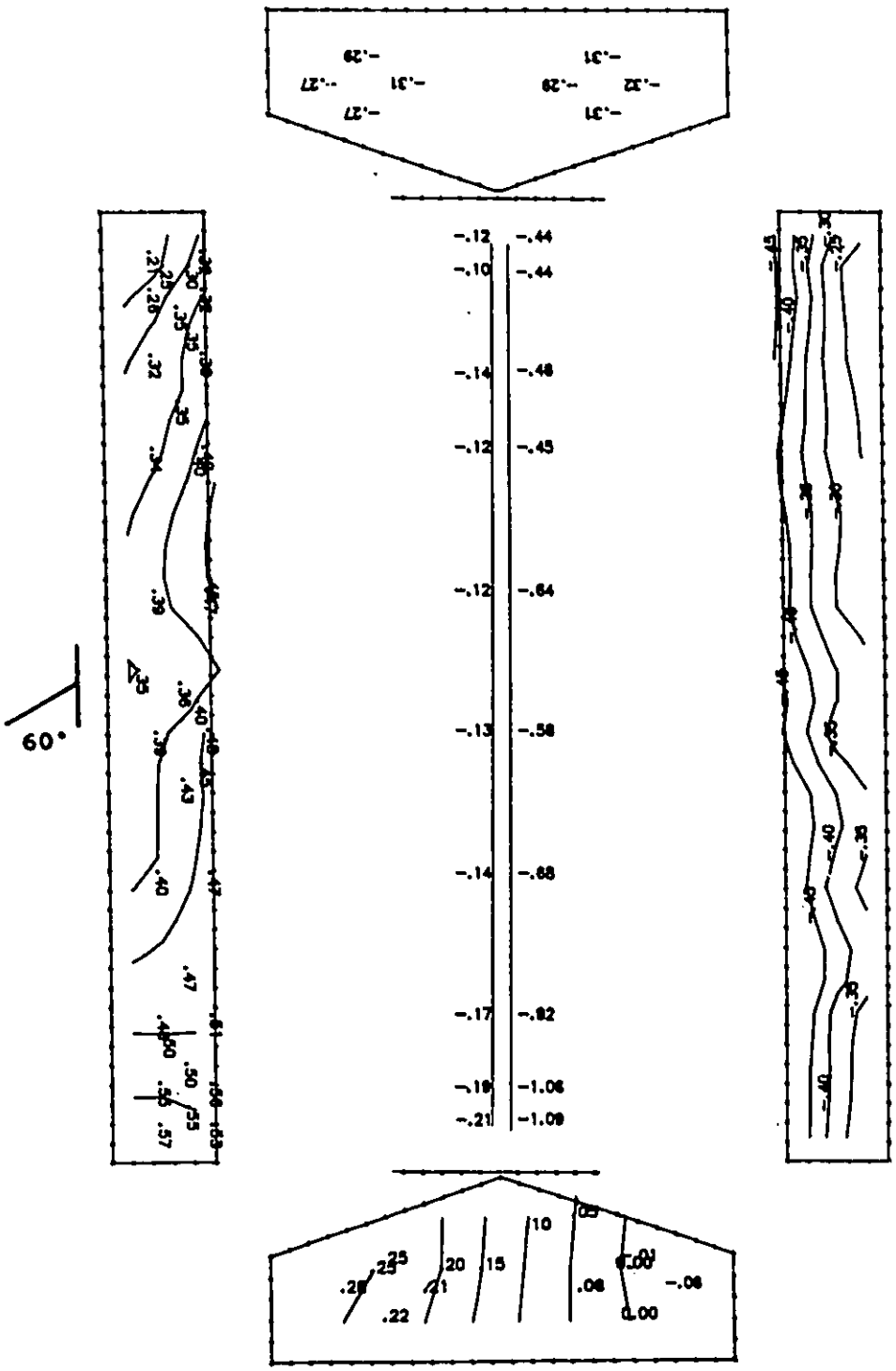

Figure E.9b Cps contour lines: open model, simulated 400 mm ridge and 800 mm sidewall openings, closed end walls, wind angle of 60°.

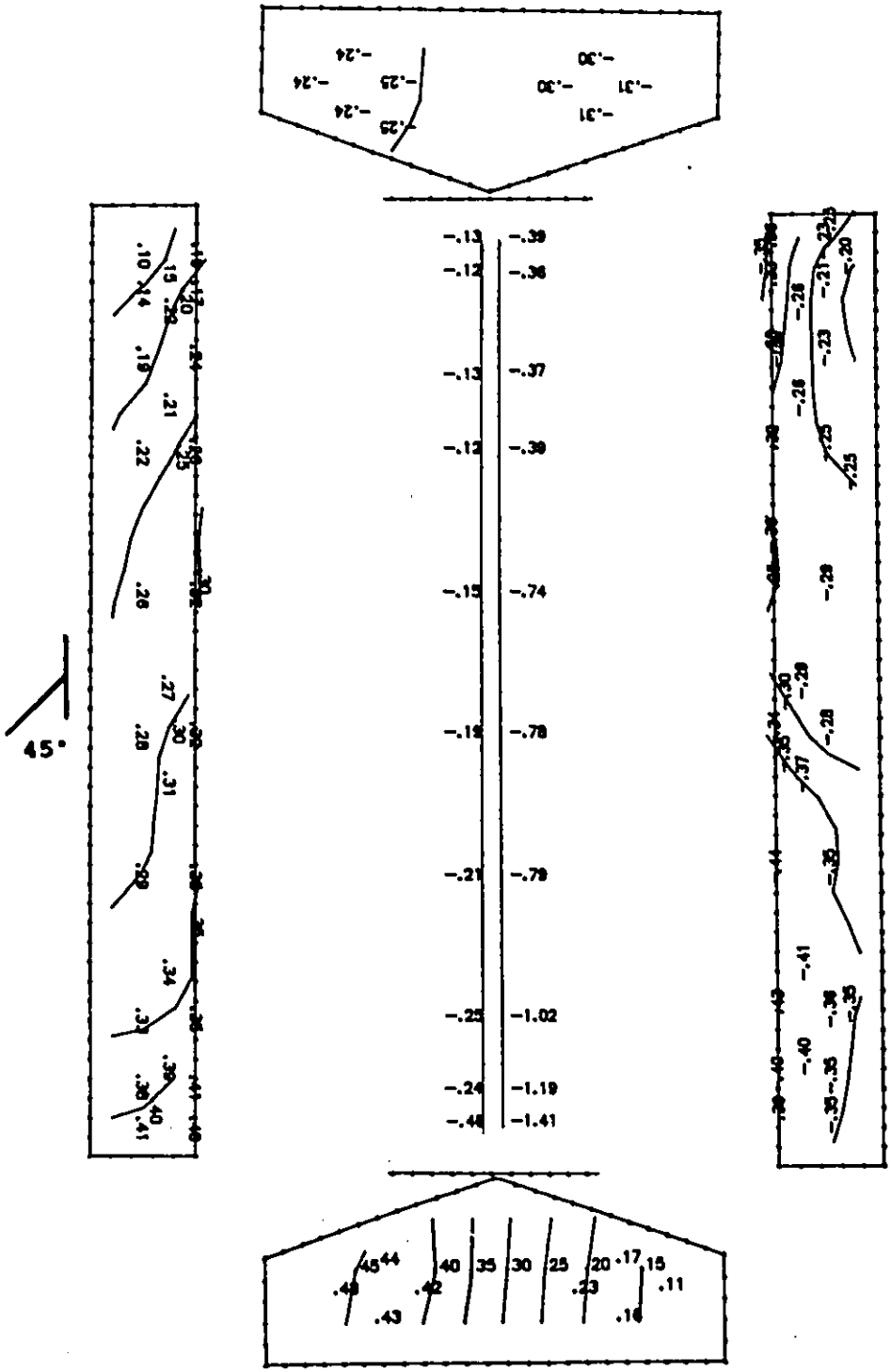

Figure E.9c Cps contour lines: open model, simulated 400 mm ridge and 800 mm sidewall openings, closed end walls, wind angle of 45°.

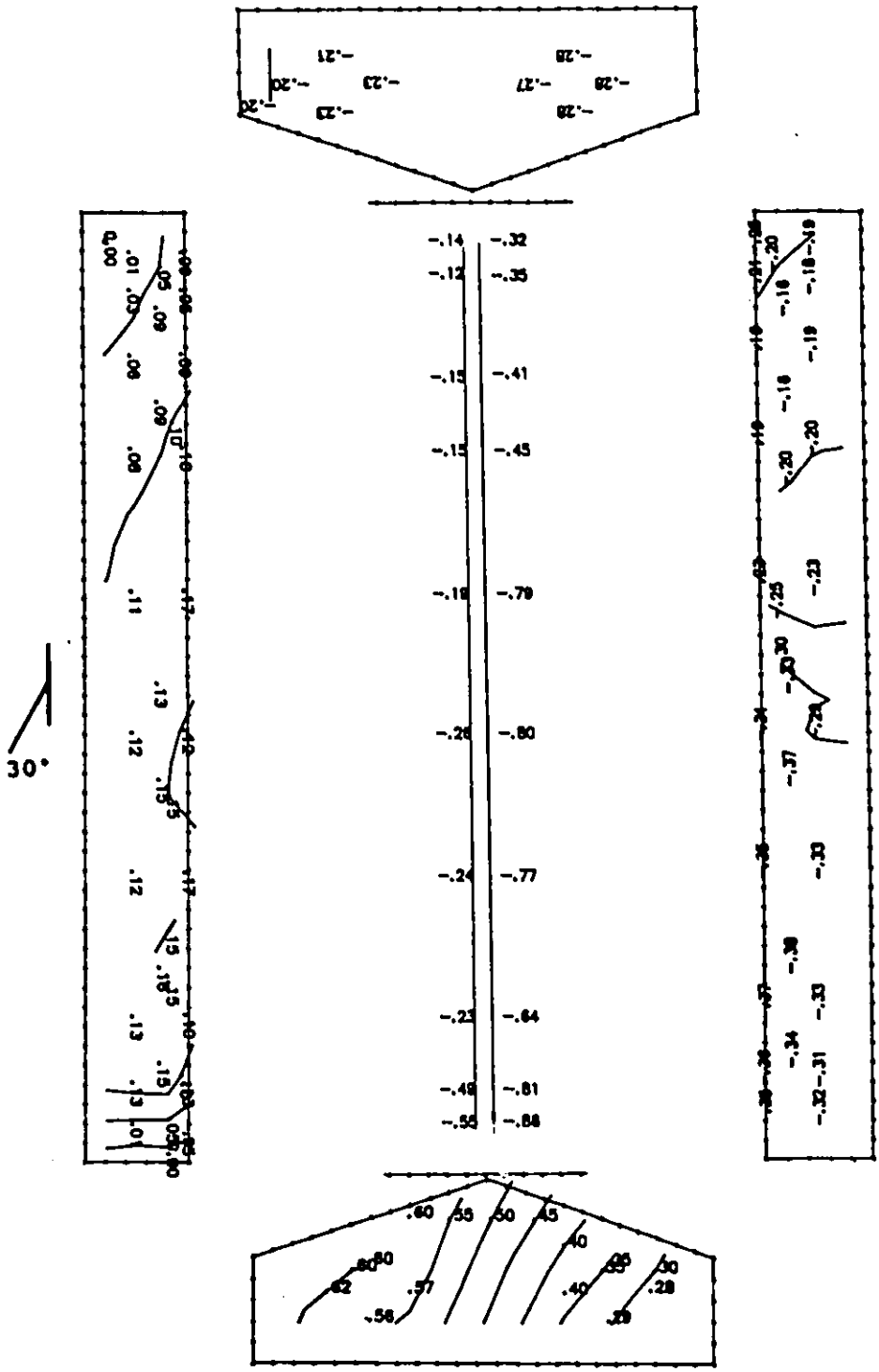

Figure E.9d Cps contour lines: open model, simulated 400 mm ridge and 800 mm sidewall openings, closed end walls, wind angle of 30°.

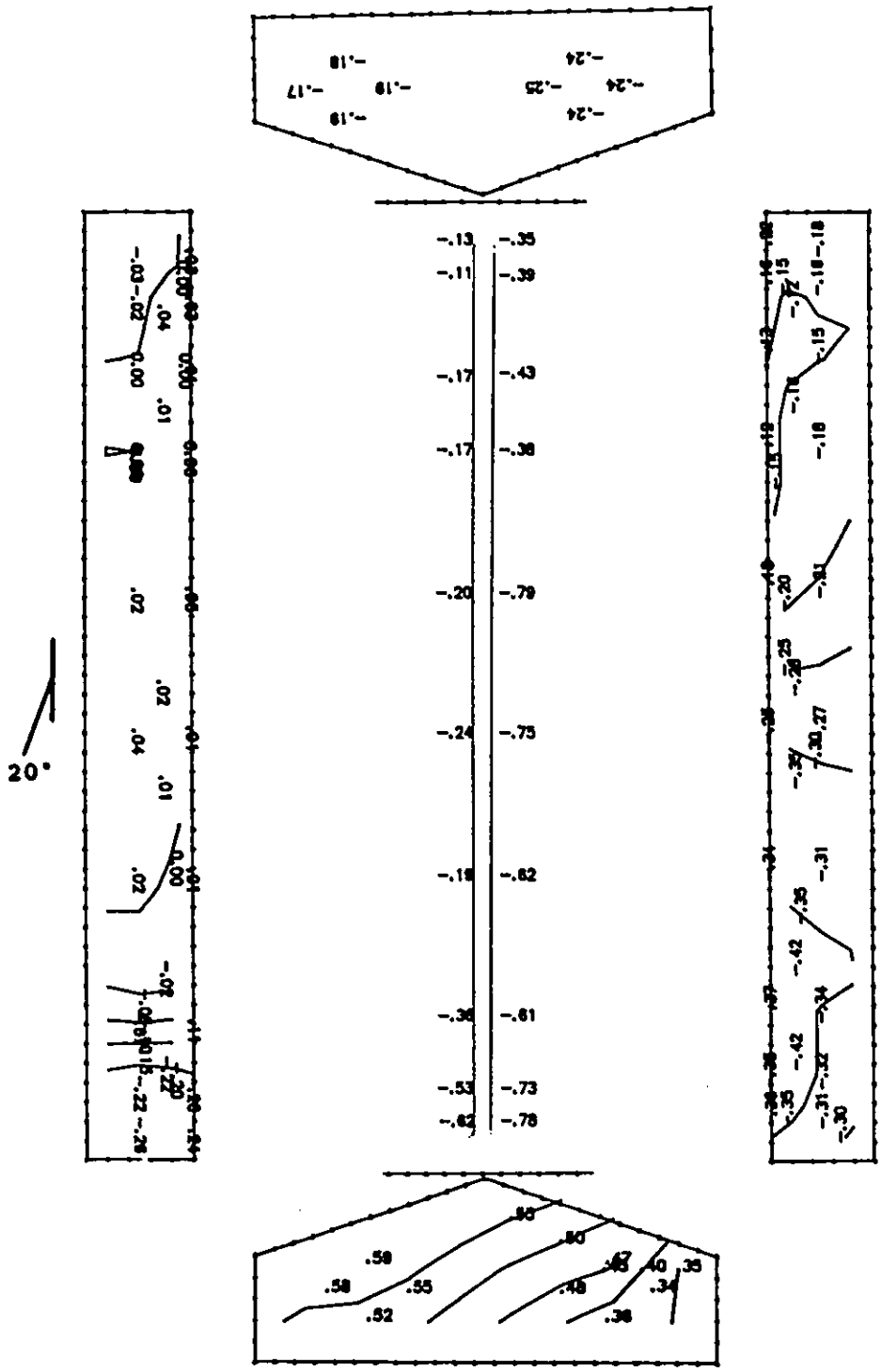

Figure E.9e Cps contour lines: open model, simulated 400 mm ridge and 800 mm sidewall openings, closed end walls, wind angle of 20°.

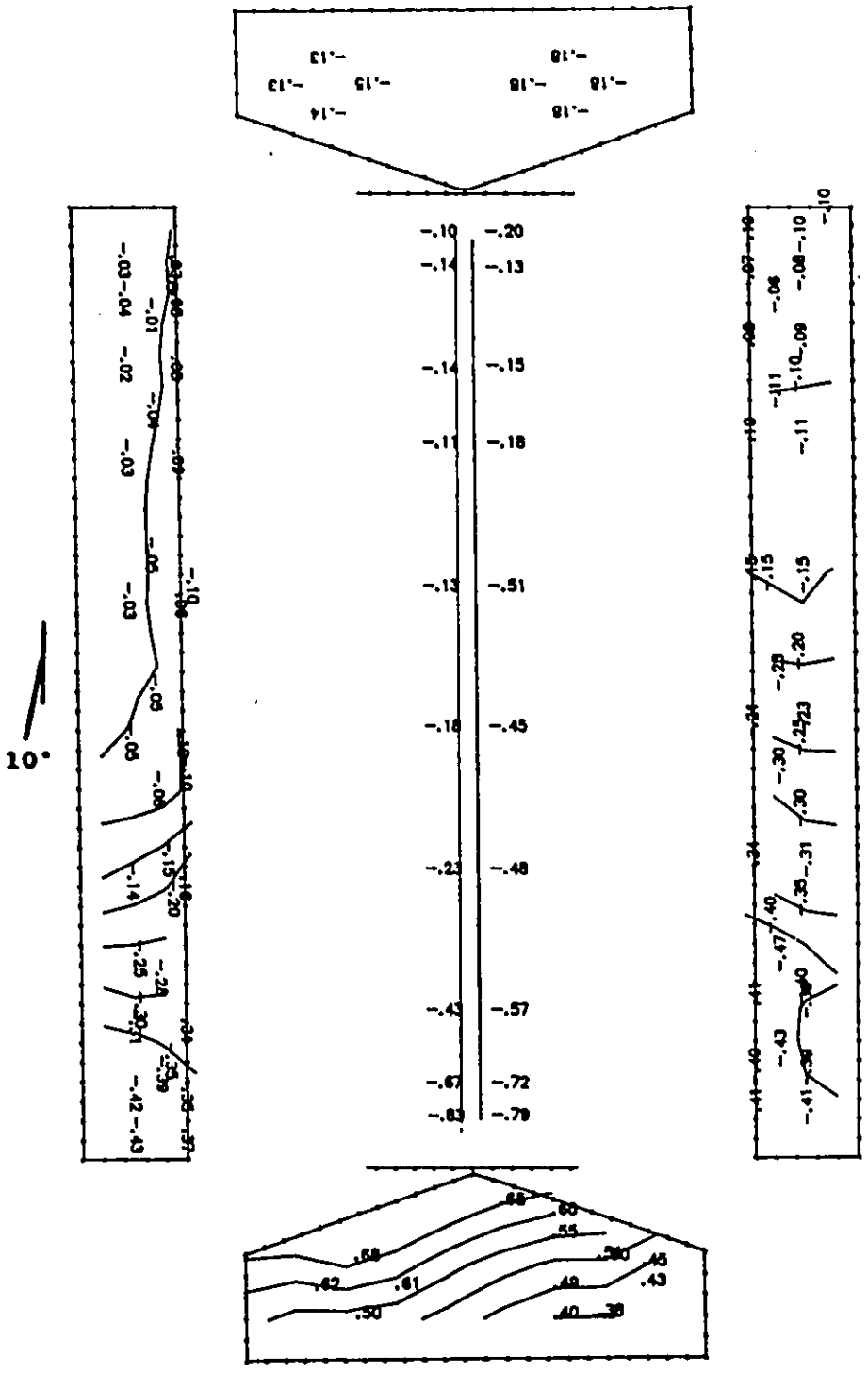

Figure E.9f Cps contour lines: open model, simulated 400 mm ridge and 800 mm sidewall openings, closed end walls, wind angle of 10°.

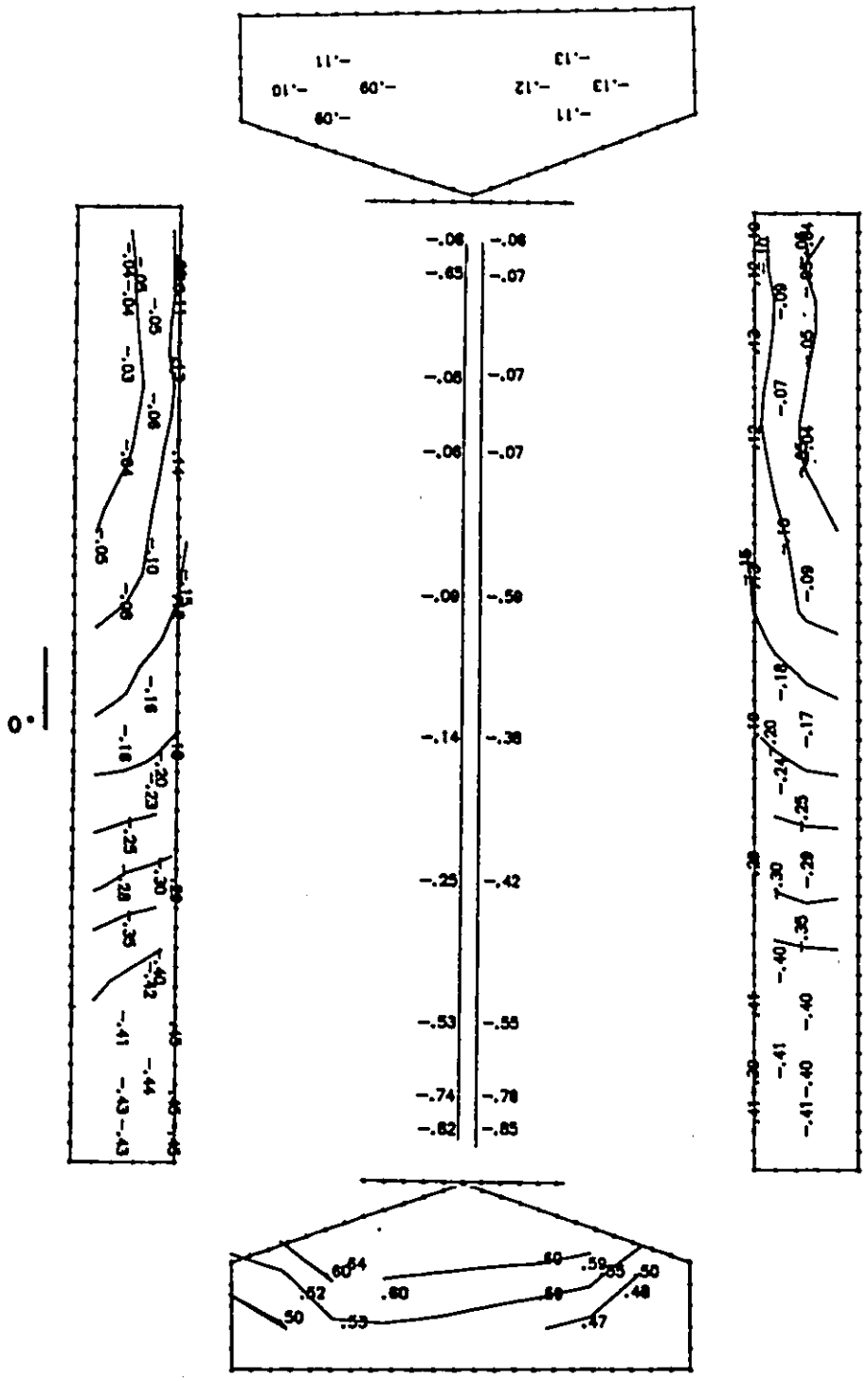

Figure E.9g Cps contour lines: open model, simulated 400 mm ridge and 800 mm sidewall openings, closed end walls, wind angle of 0°.

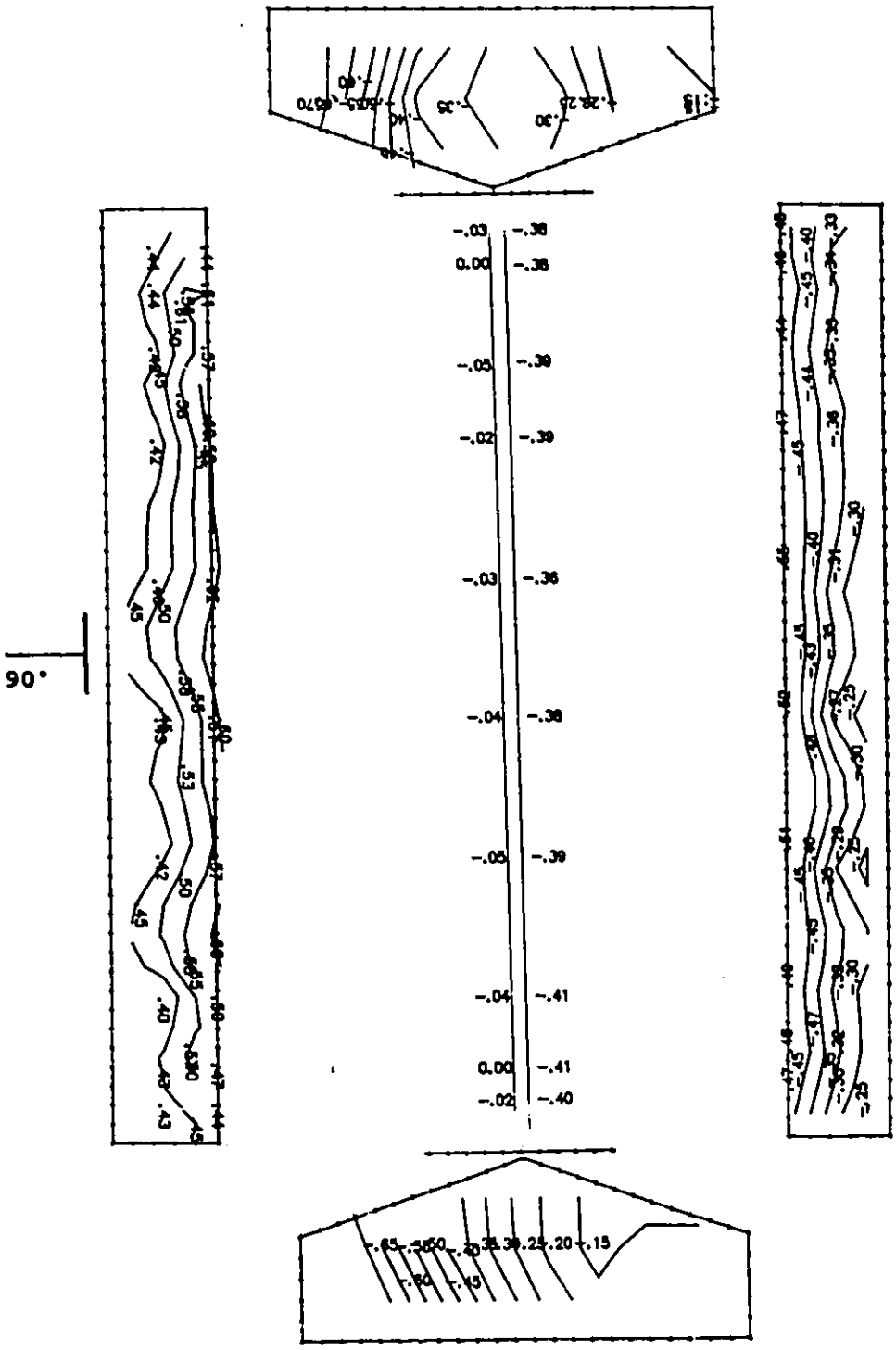

Figure E.10a Cps contour lines: open model, simulated 400 mm ridge and 1100 mm sidewall openings, closed end walls, wind angle of 90°.

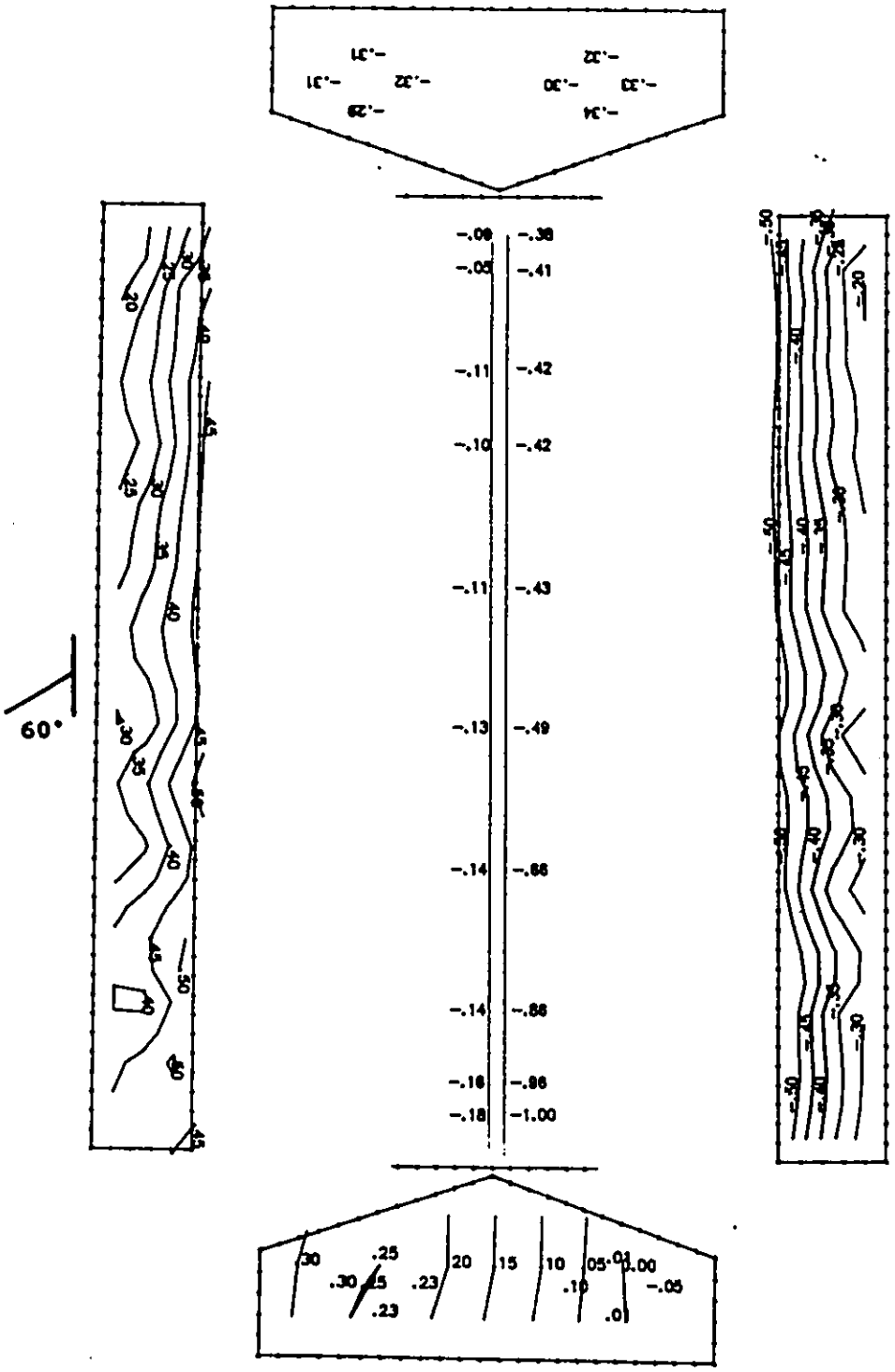

Figure E.10b Cps contour lines: open model, simulated 400 mm ridge and 1100 mm sidewall openings, closed end walls, wind angle of 60°.

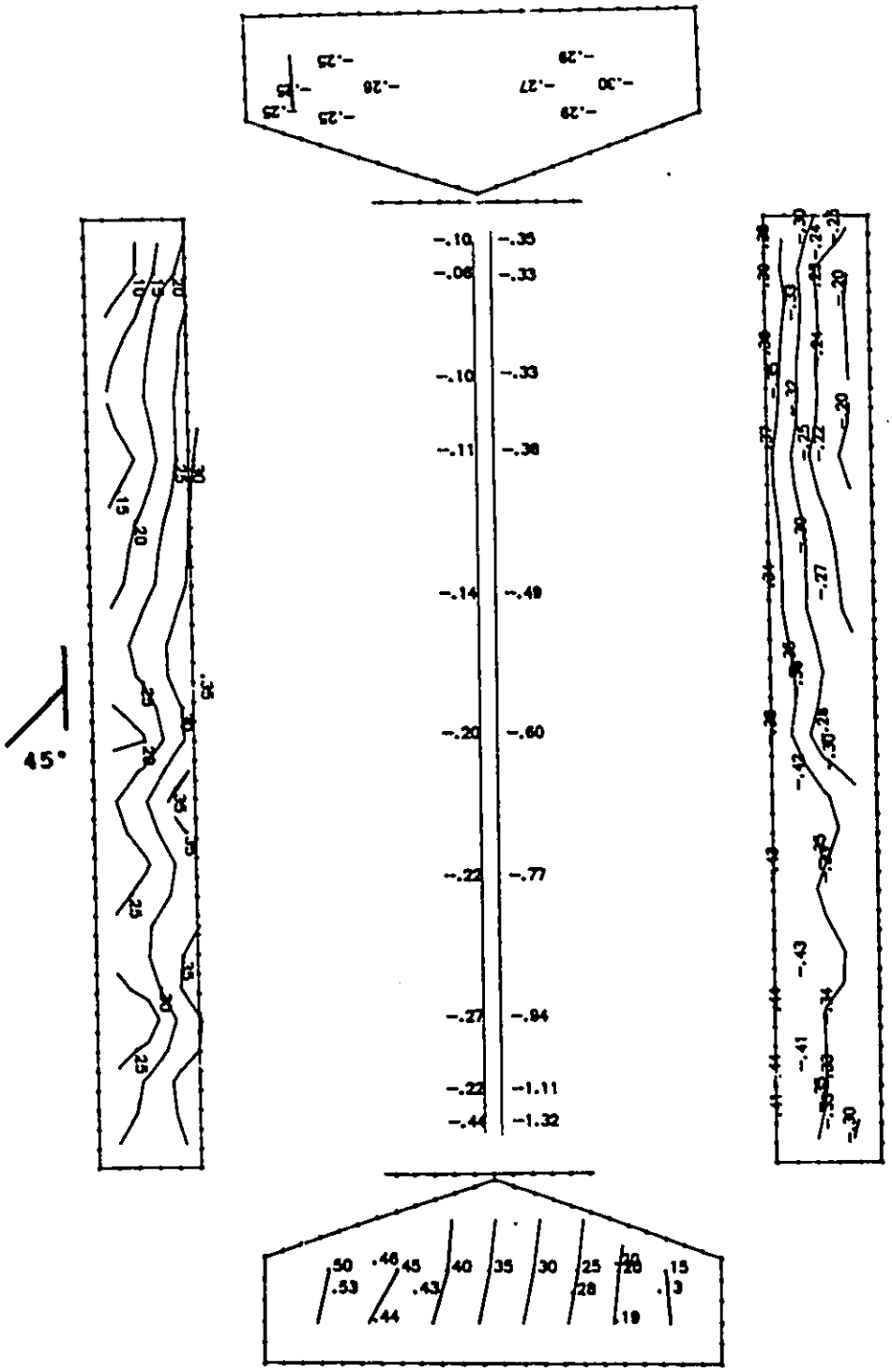

Figure E.10c Cps contour lines: open model, simulated 400 mm ridge and 1100 mm sidewall openings, closed end walls, wind angle of 45°.

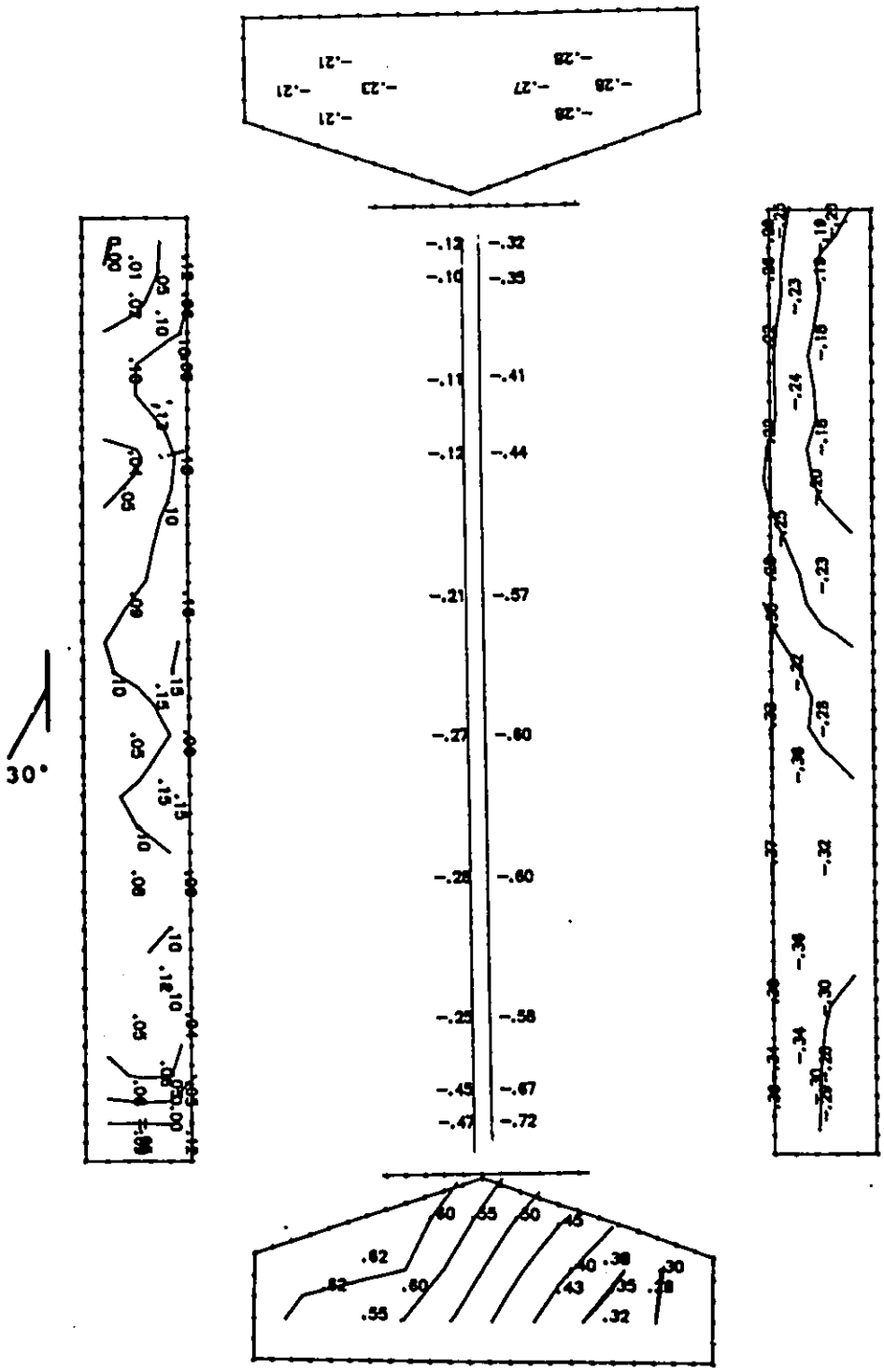

Figure E.10d Cps contour lines: open model, simulated 400 mm ridge and 1100 mm sidewall openings, closed end walls, wind angle of 30°.

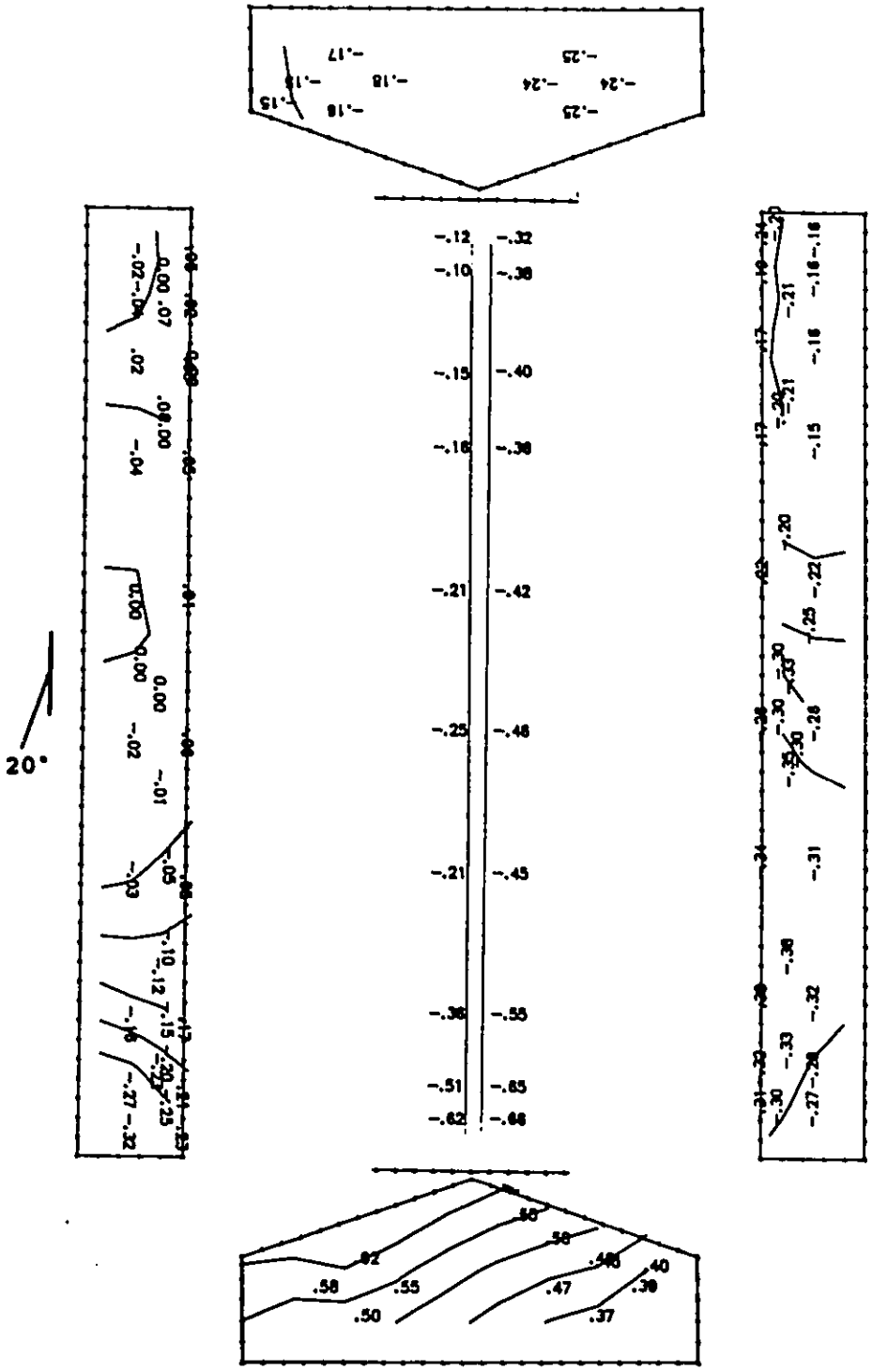

Figure E.10e Cps contour lines: open model, simulated 400 mm ridge and 1100 mm sidewall openings, closed end walls, wind angle of 20°.

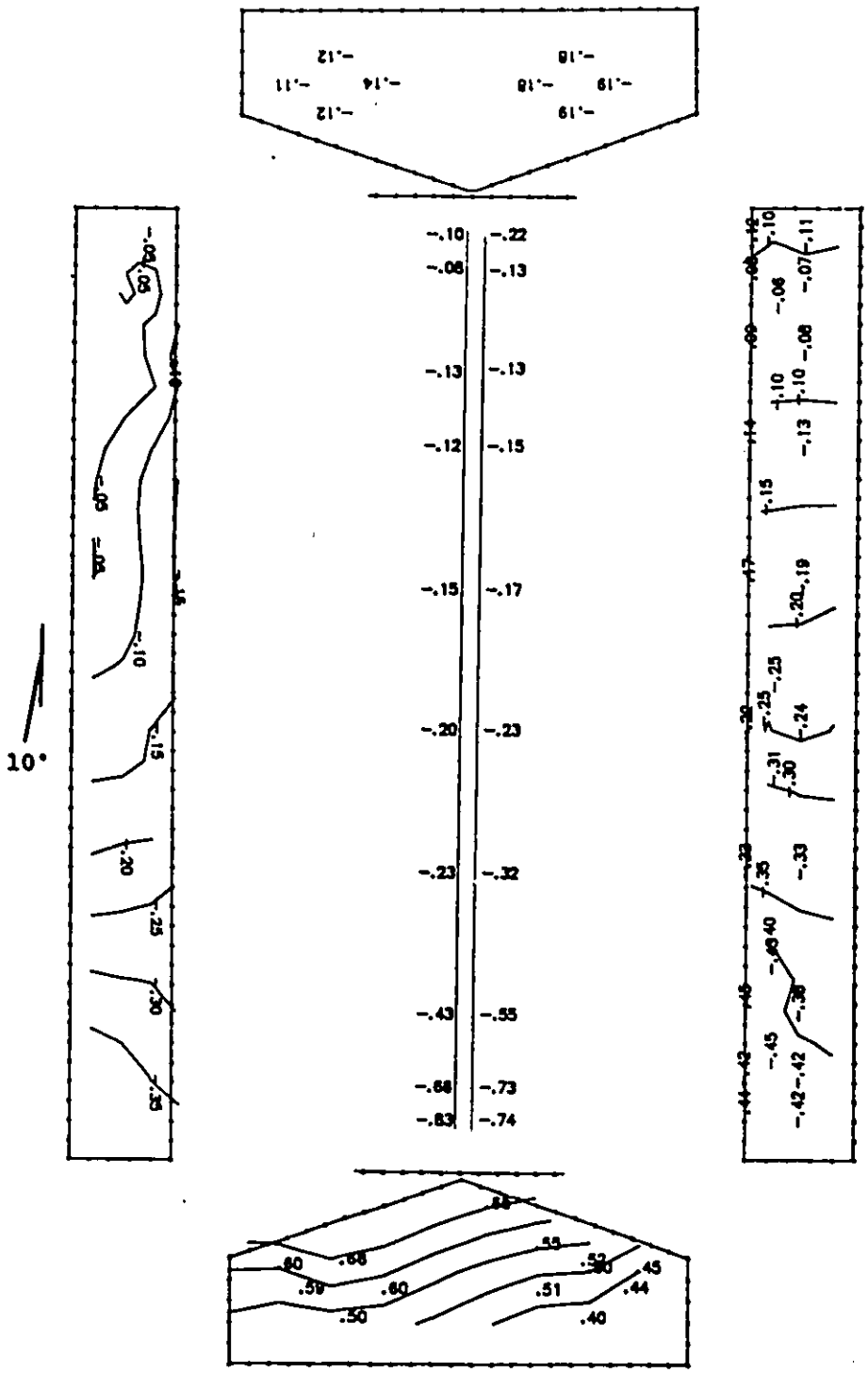

Figure E.10f Cps contour lines: open model, simulated 400 mm ridge and 1100 mm sidewall openings, closed end walls, wind angle of 10°.

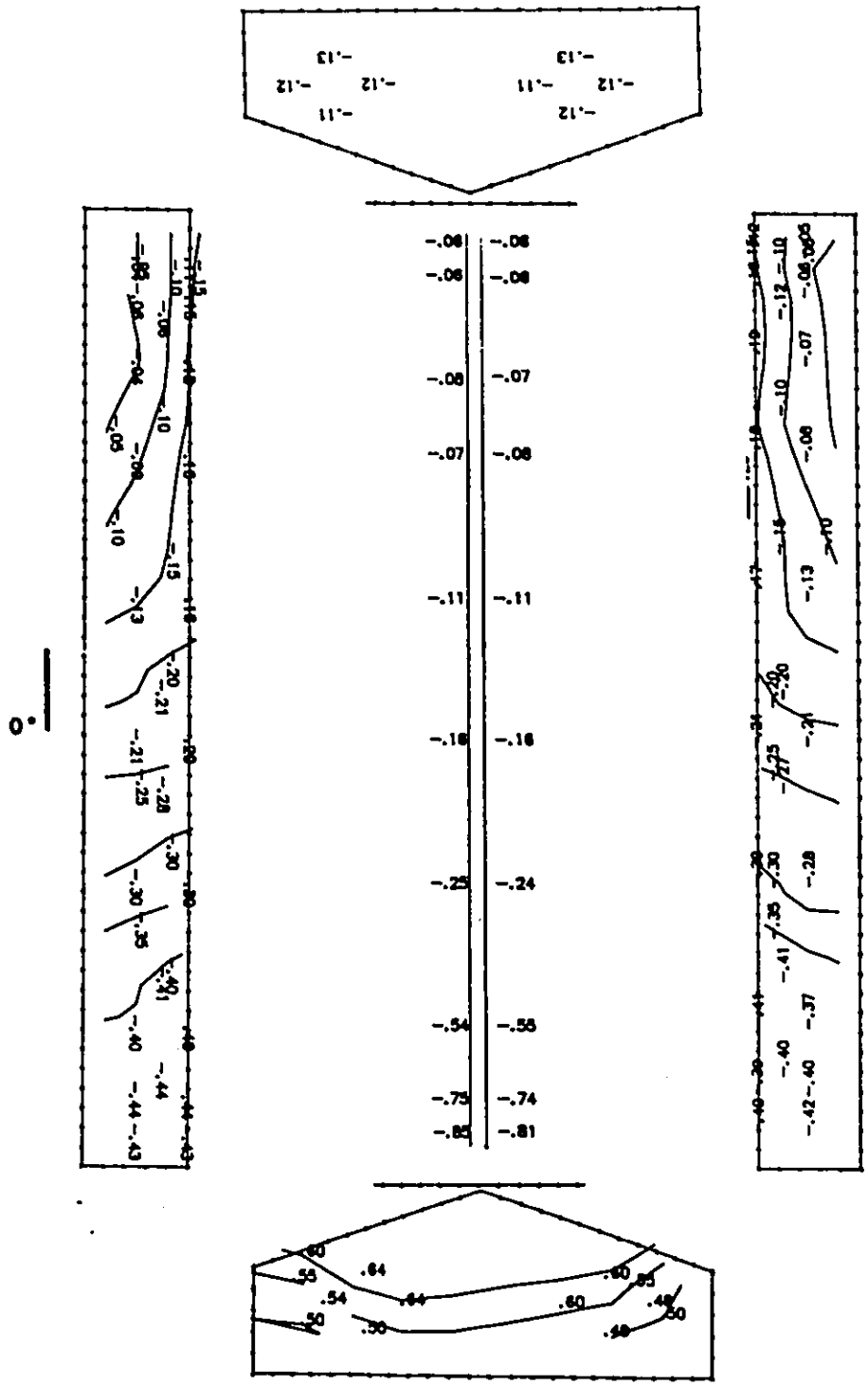

Figure E.10g Cps contour lines: open model, simulated 400 mm ridge and 1100 mm sidewall openings, closed end walls, wind angle of 0°.

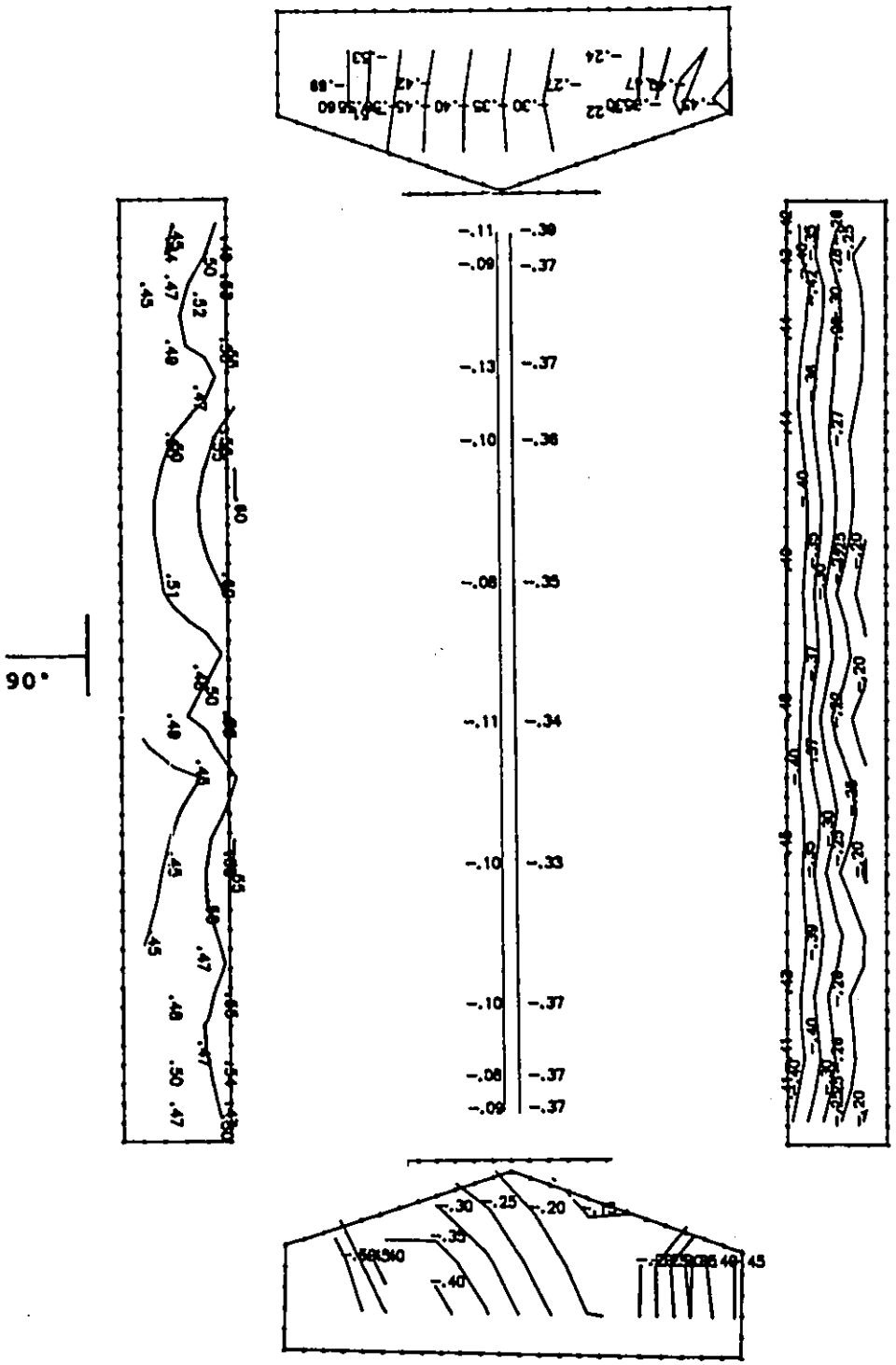

Figure E.11a Cps contour lines: open model, simulated 400 mm ridge and 800 mm sidewall openings, open end walls, wind angle of 90°.

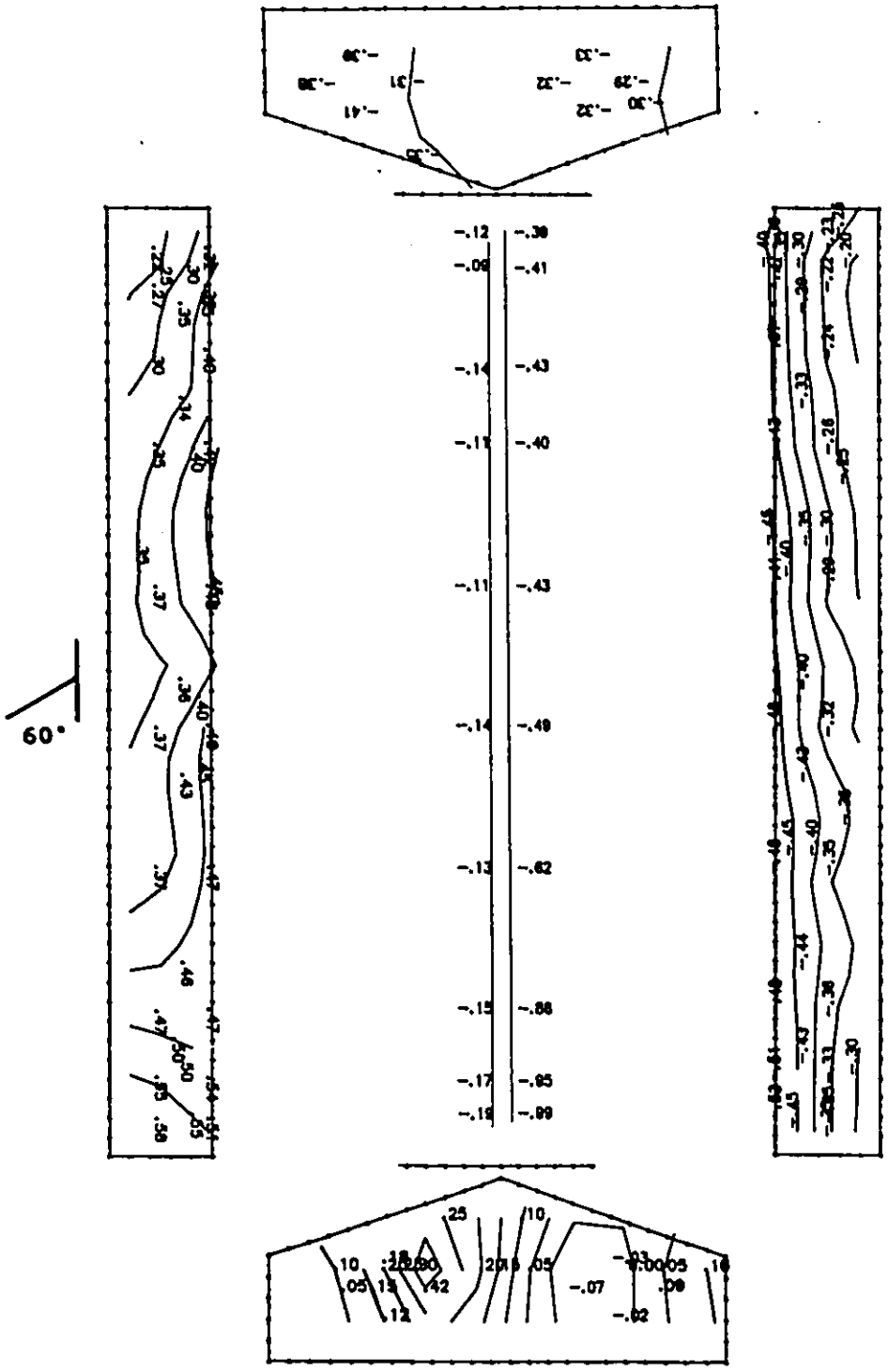

Figure E.11b Cps contour lines: open model, simulated 400 mm ridge and 800 mm sidewall openings, open end walls, wind angle of 60°.

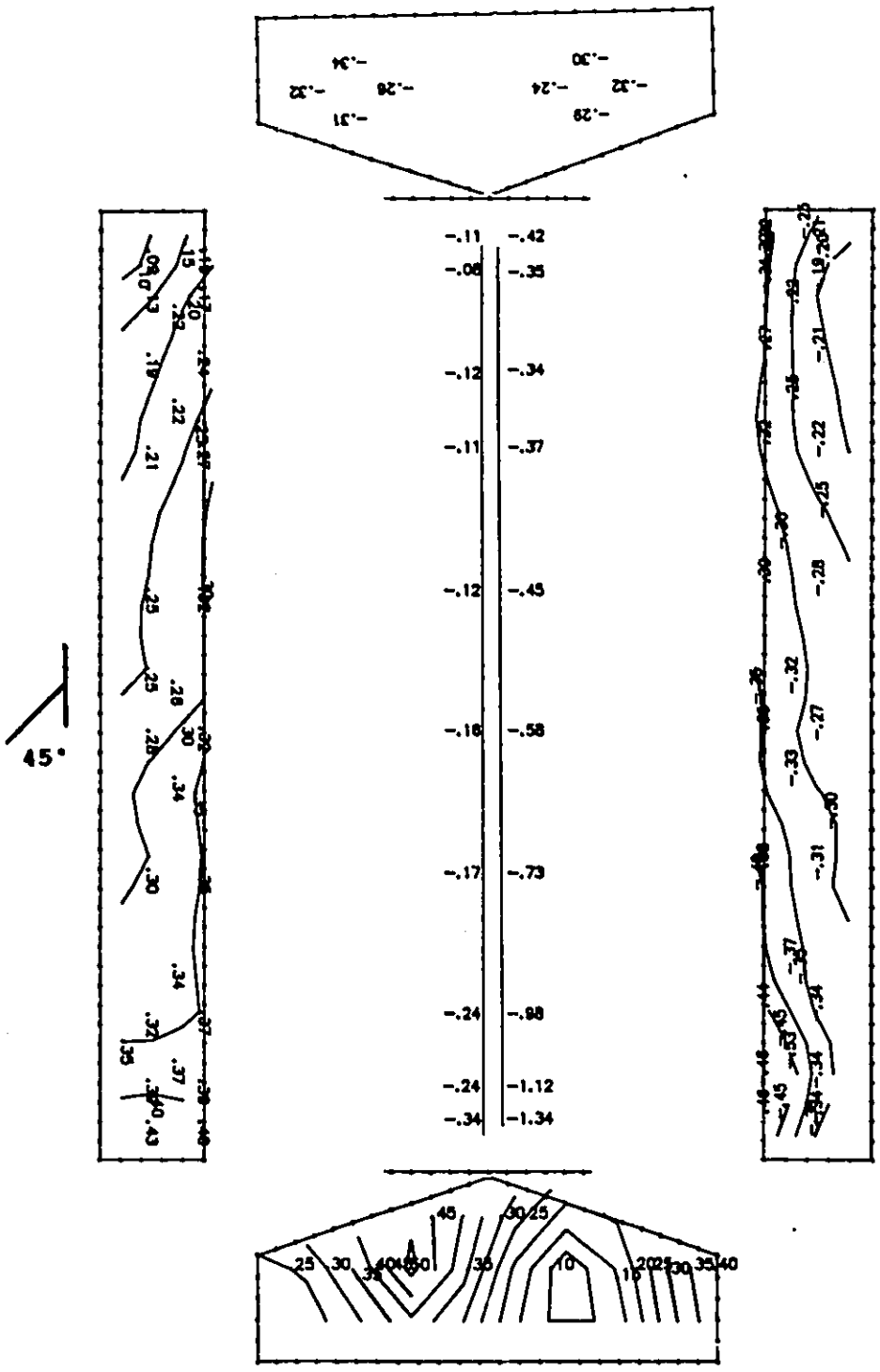

Figure E.11c Cps contour lines: open model, simulated 400 mm ridge and 800 mm sidewall openings, open end walls, wind angle of 45°.

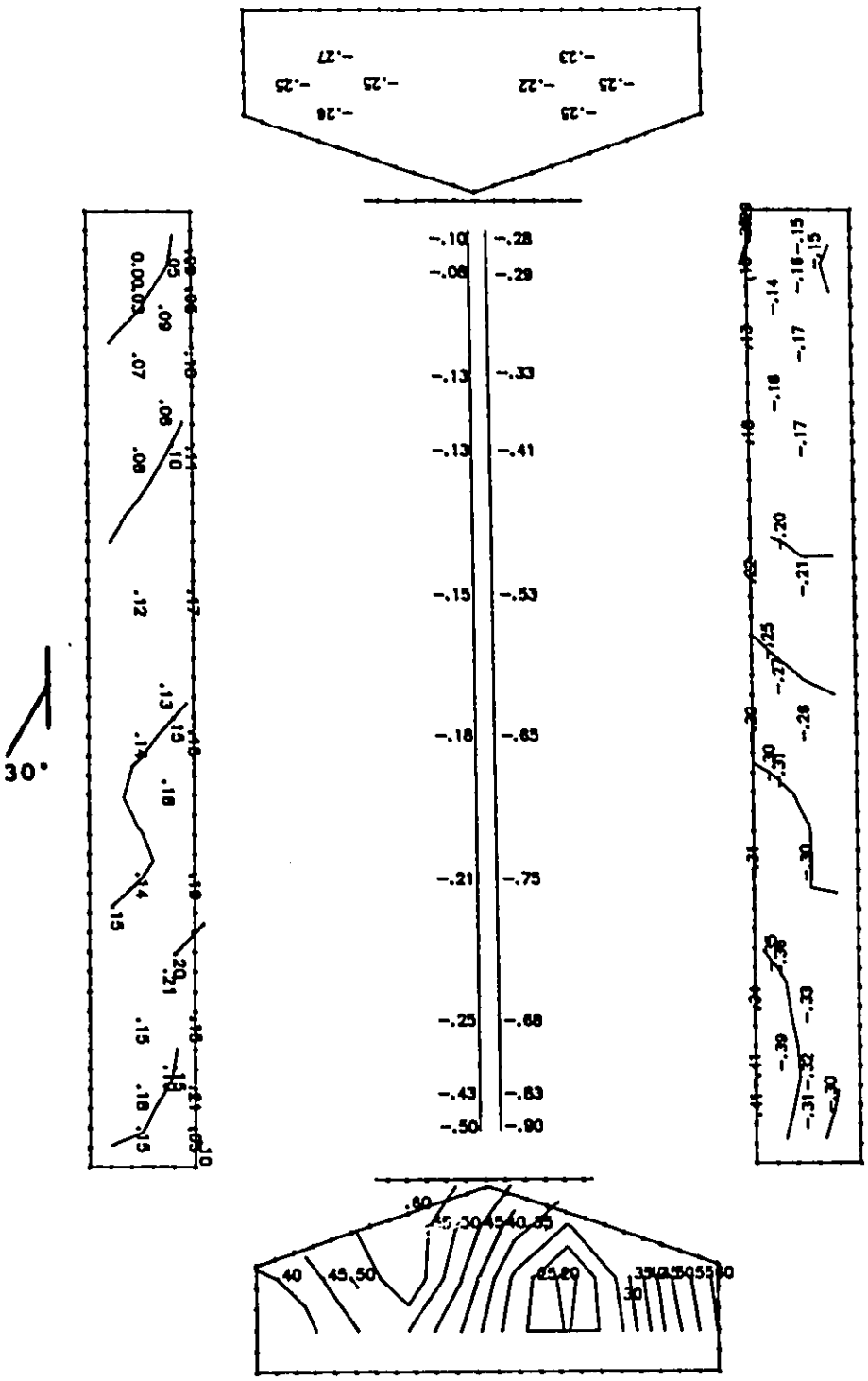

Figure E.11d Cps contour lines: open model, simulated 400 mm ridge and 800 mm sidewall openings, open end walls, wind angle of 30°.

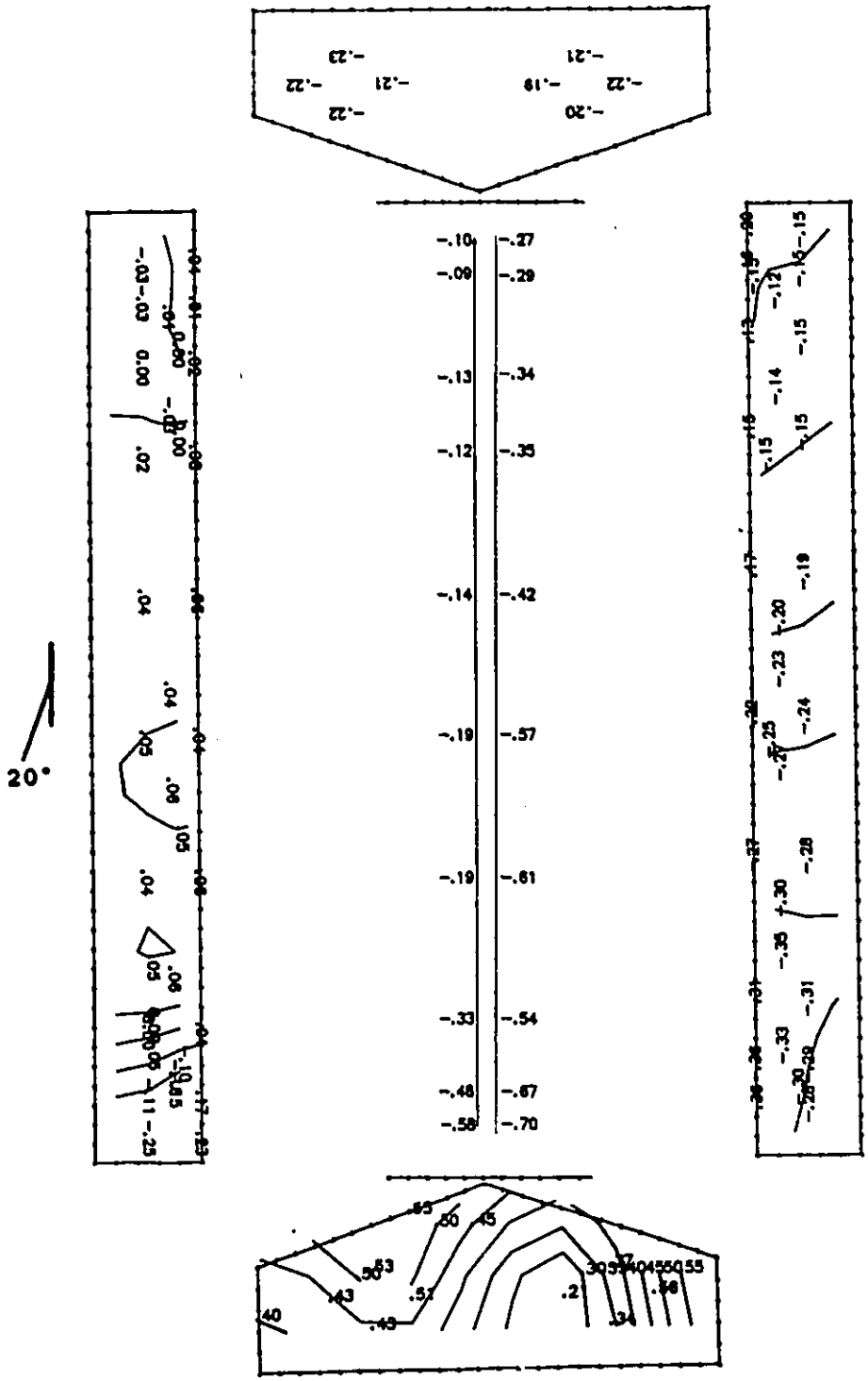

Figure E.11e Cps contour lines: open model, simulated 400 mm ridge and 800 mm sidewall openings, open end walls, wind angle of 20°.

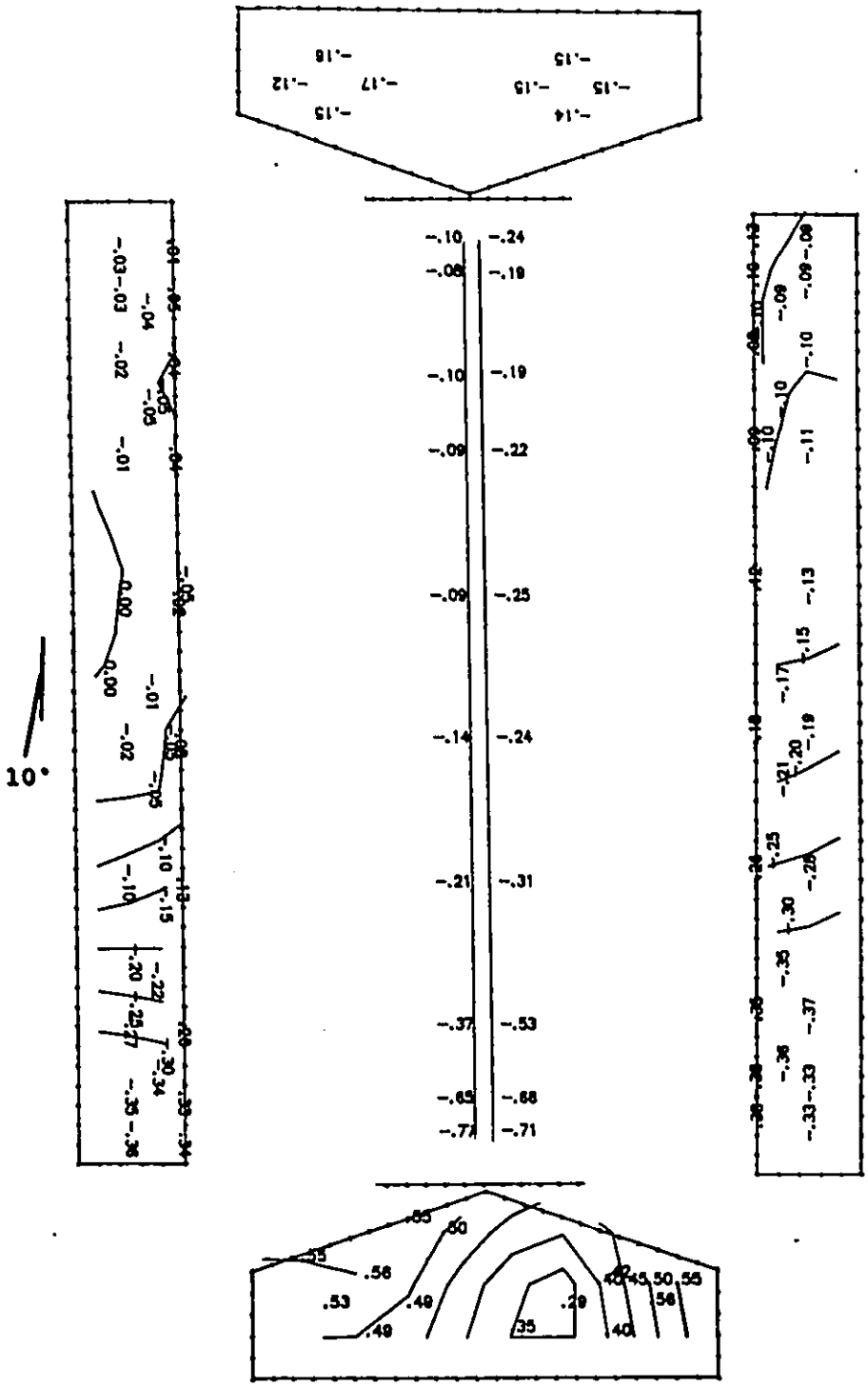

Figure E.11f Cps contour lines: open model, simulated 400 mm ridge and 800 mm sidewall openings, open end walls, wind angle of 10°.

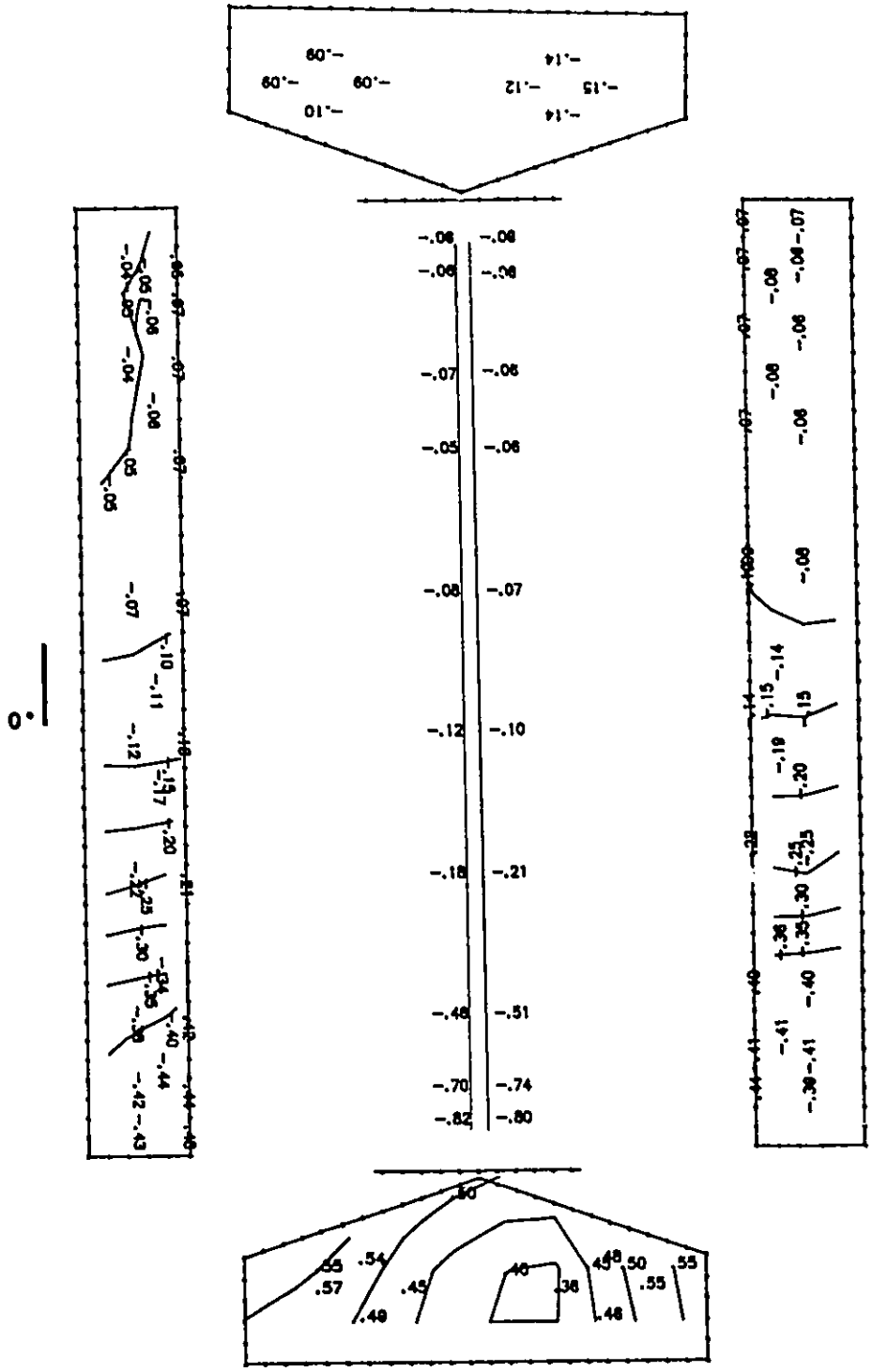

Figure E.11g Cps contour lines: open model, simulated 400 mm ridge and 800 mm sidewall openings, open end walls, wind angle of 0°.

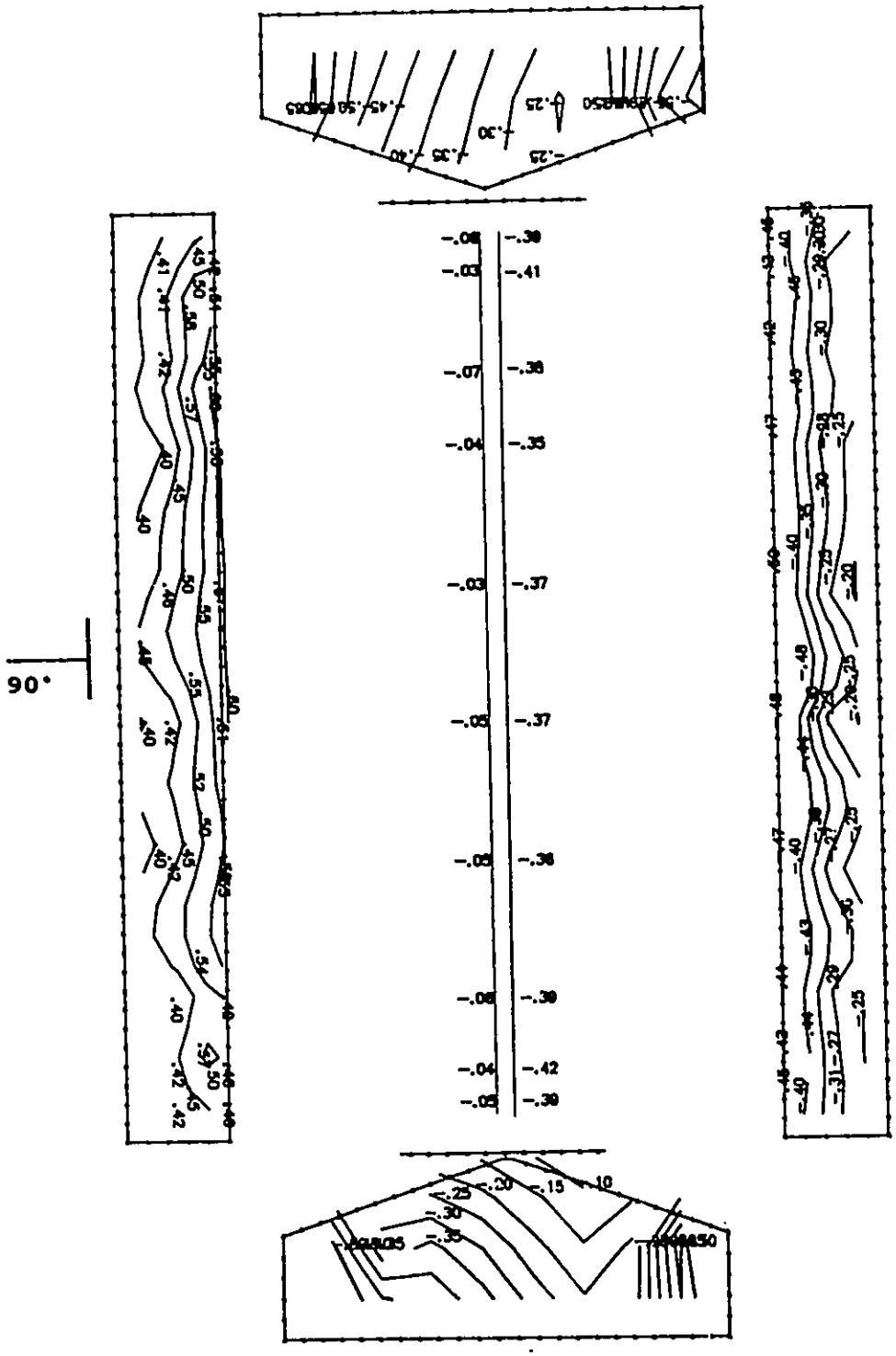

Figure E.12a Cps contour lines: open model, simulated 400 mm ridge and 1100 mm sidewall openings, open end walls, wind angle of 90°.

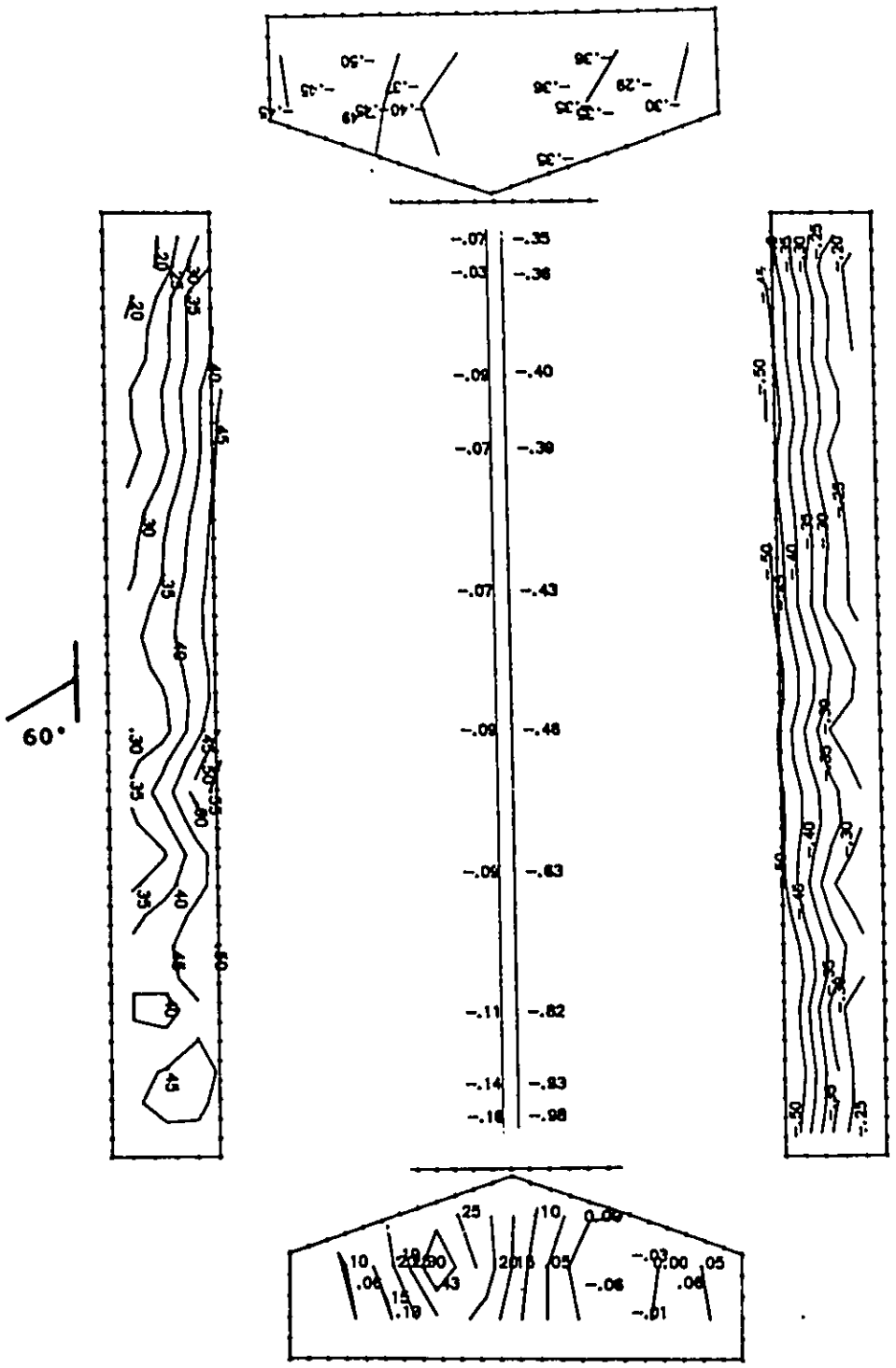

Figure E.12b Cps contour lines: open model, simulated 400 mm ridge and 1100 mm sidewall openings, open end walls, wind angle of 60°.

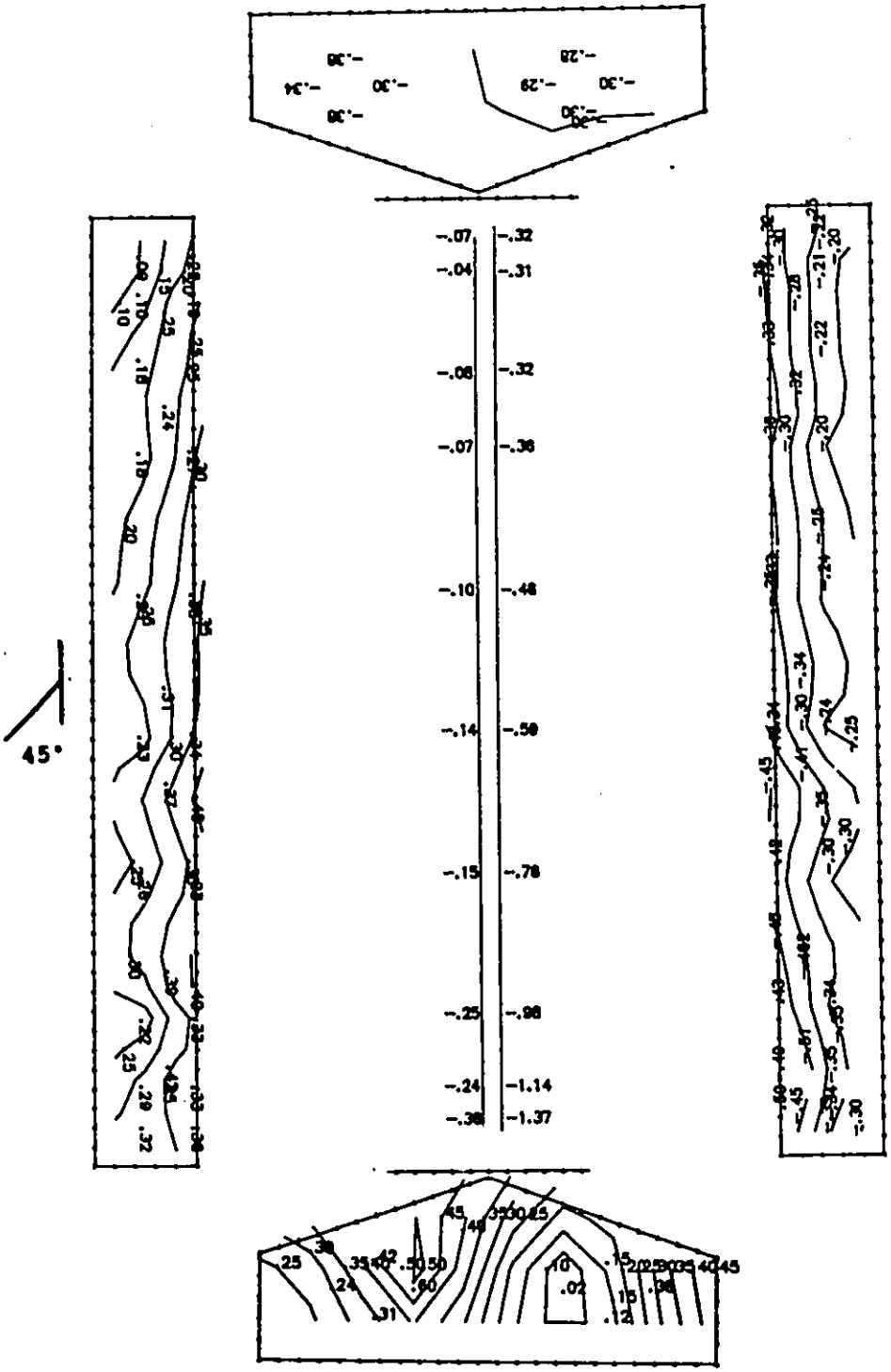

Figure E.12c Cps contour lines: open model, simulated 400 mm ridge and 1100 mm sidewall openings, open end walls, wind angle of 45°.

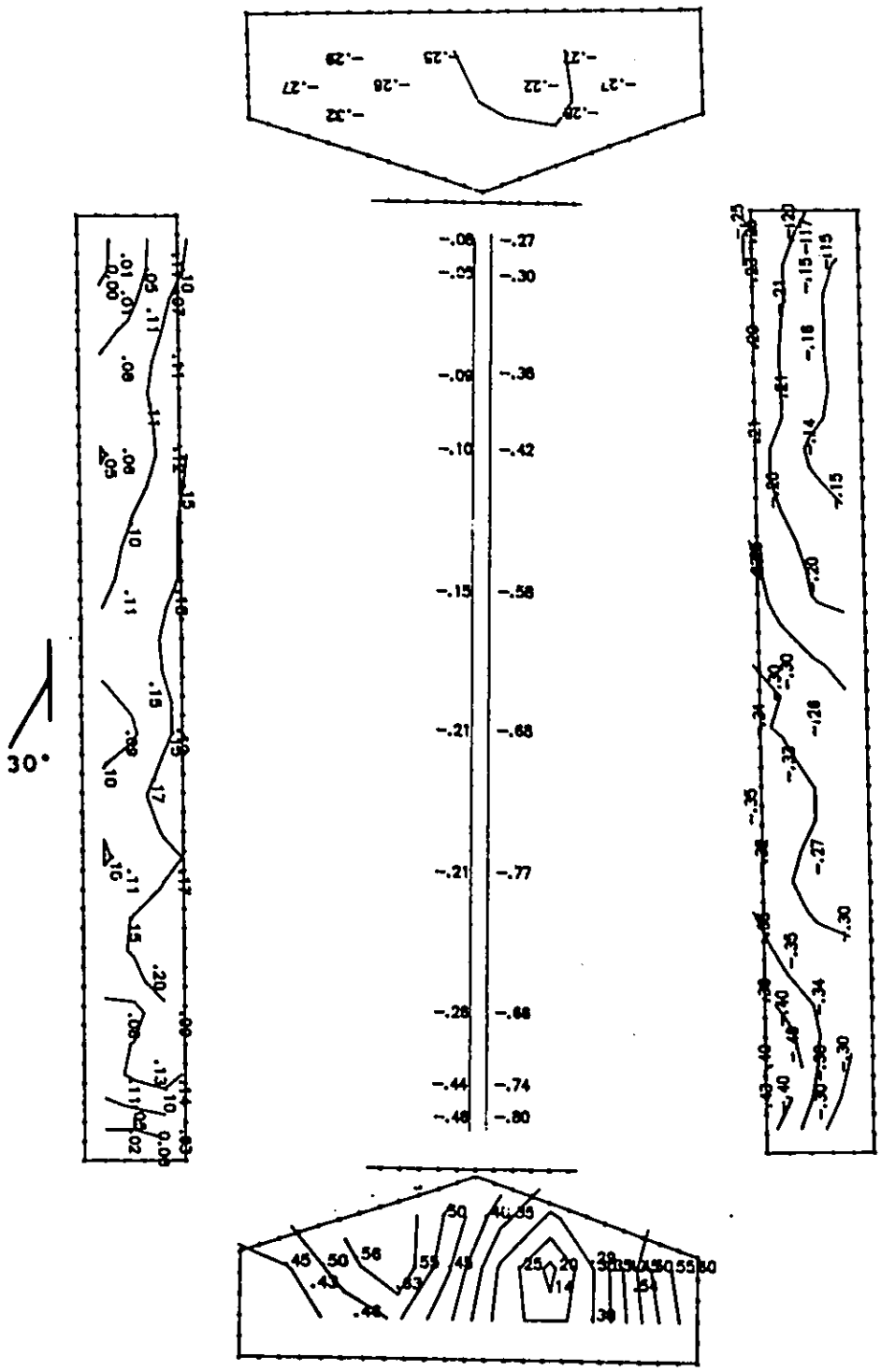

Figure E.12d Cps contour lines: open model, simulated 400 mm ridge and 1100 mm sidewall openings, open end walls, wind angle of 30°.

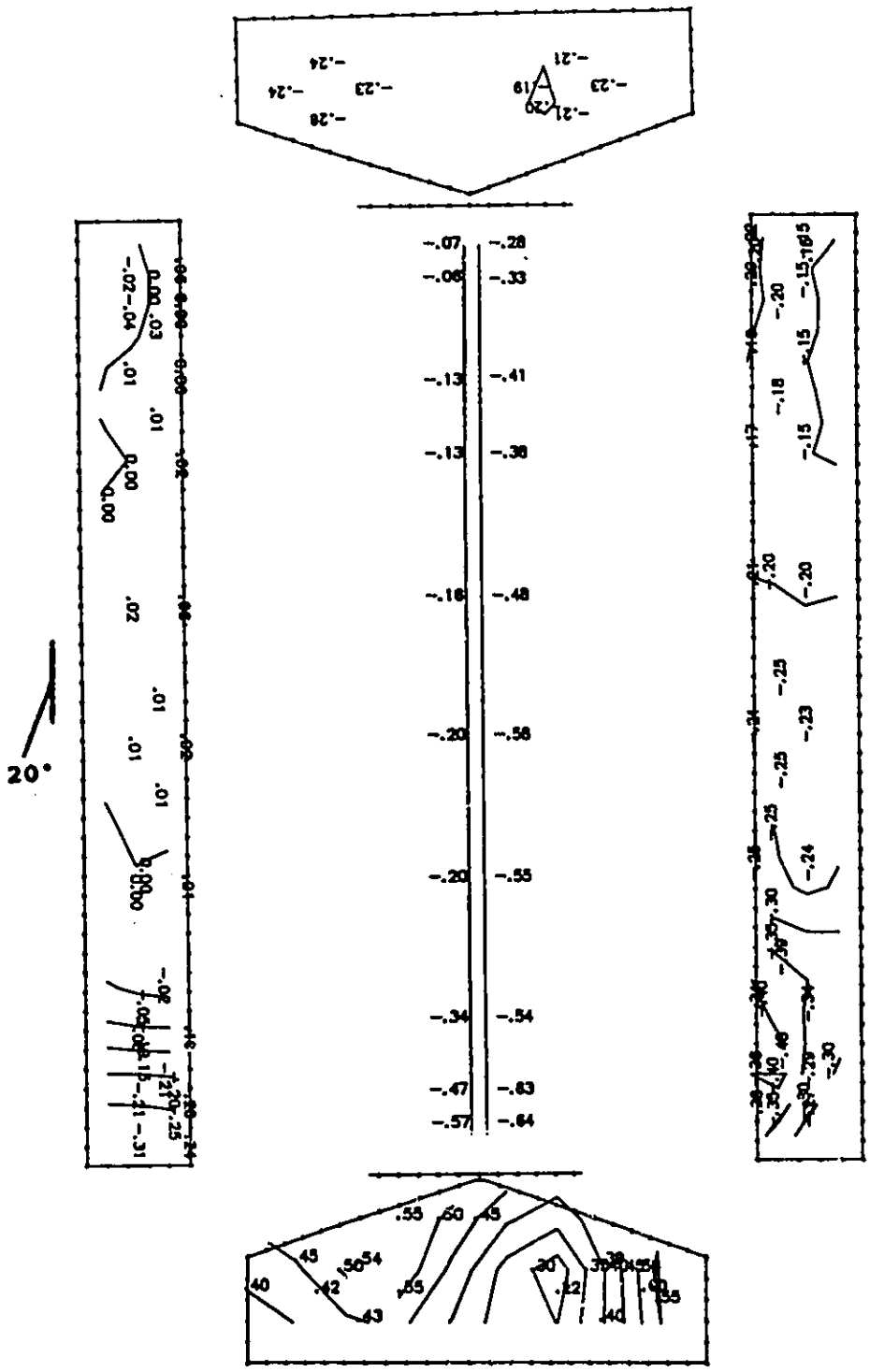

Figure E.12e Cps contour lines: open model, simulated 400 mm ridge and 1100 mm sidewall openings, open end walls, wind angle of 20°.

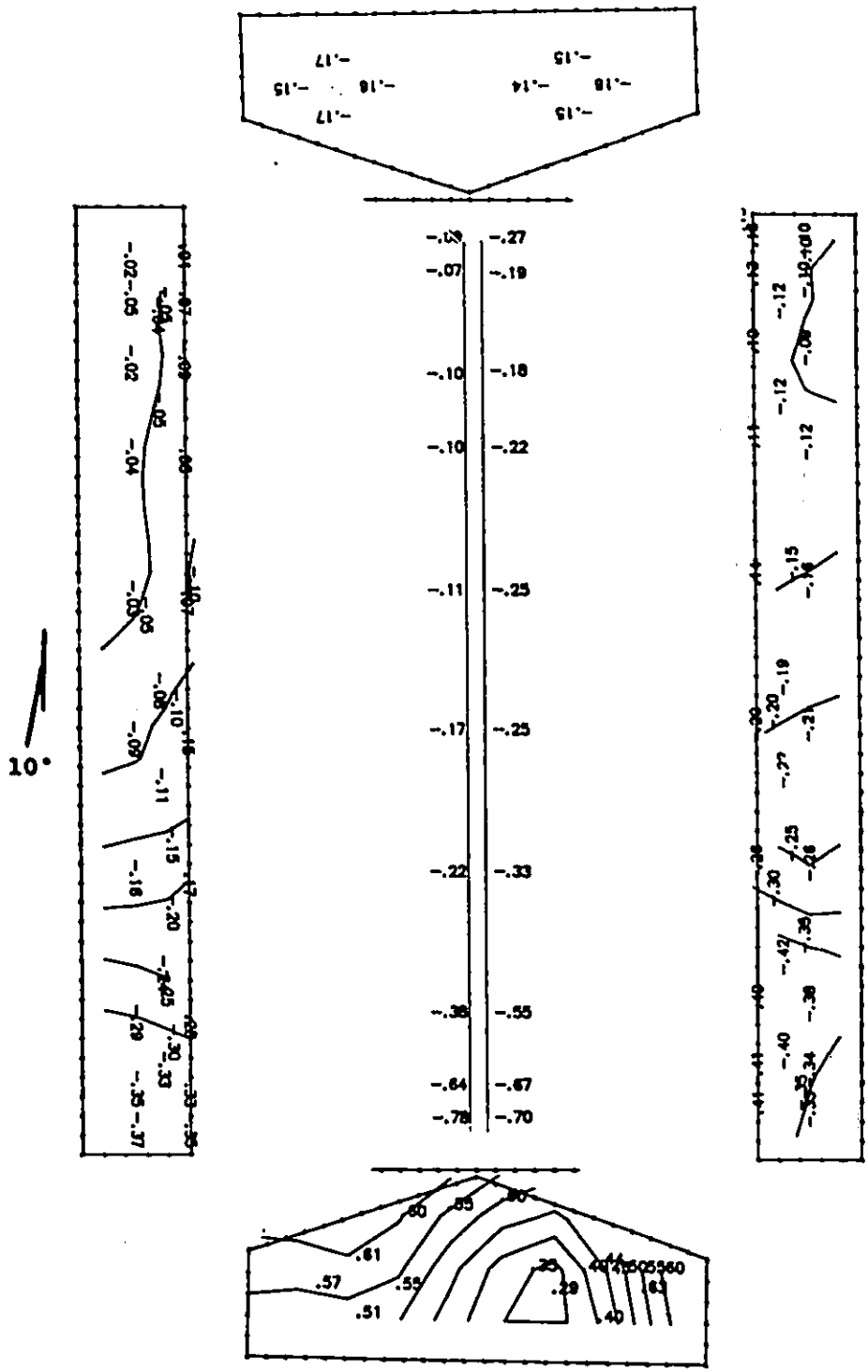

Figure E.12f Cps contour lines: open model, simulated 400 mm ridge and 1100 mm sidewall openings, open end walls, wind angle of 10°.

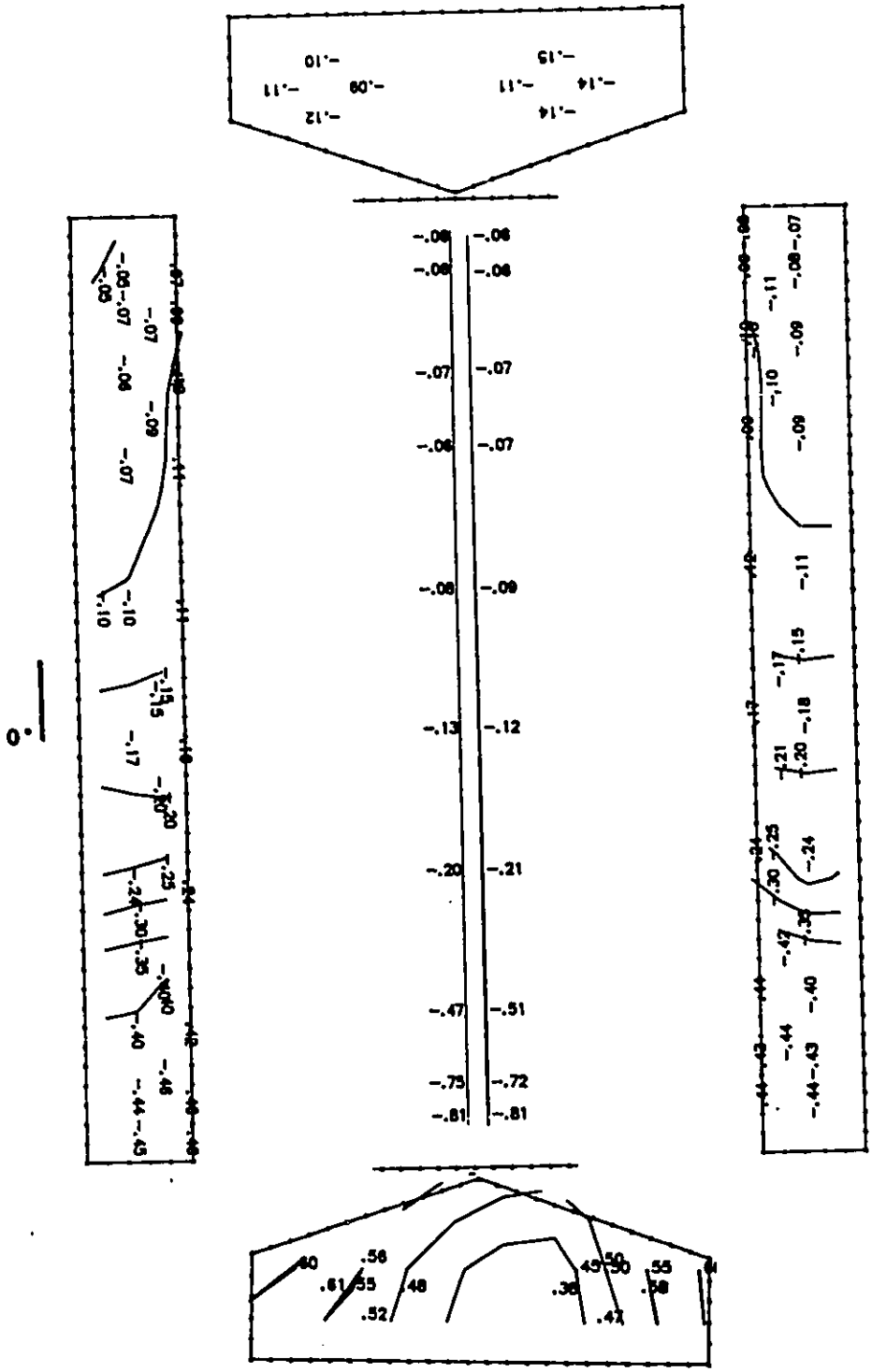

Figure E.12g Cps contour lines: open model, simulated 400 mm ridge and 1100 mm sidewall openings, open end walls, wind angle of 0°.

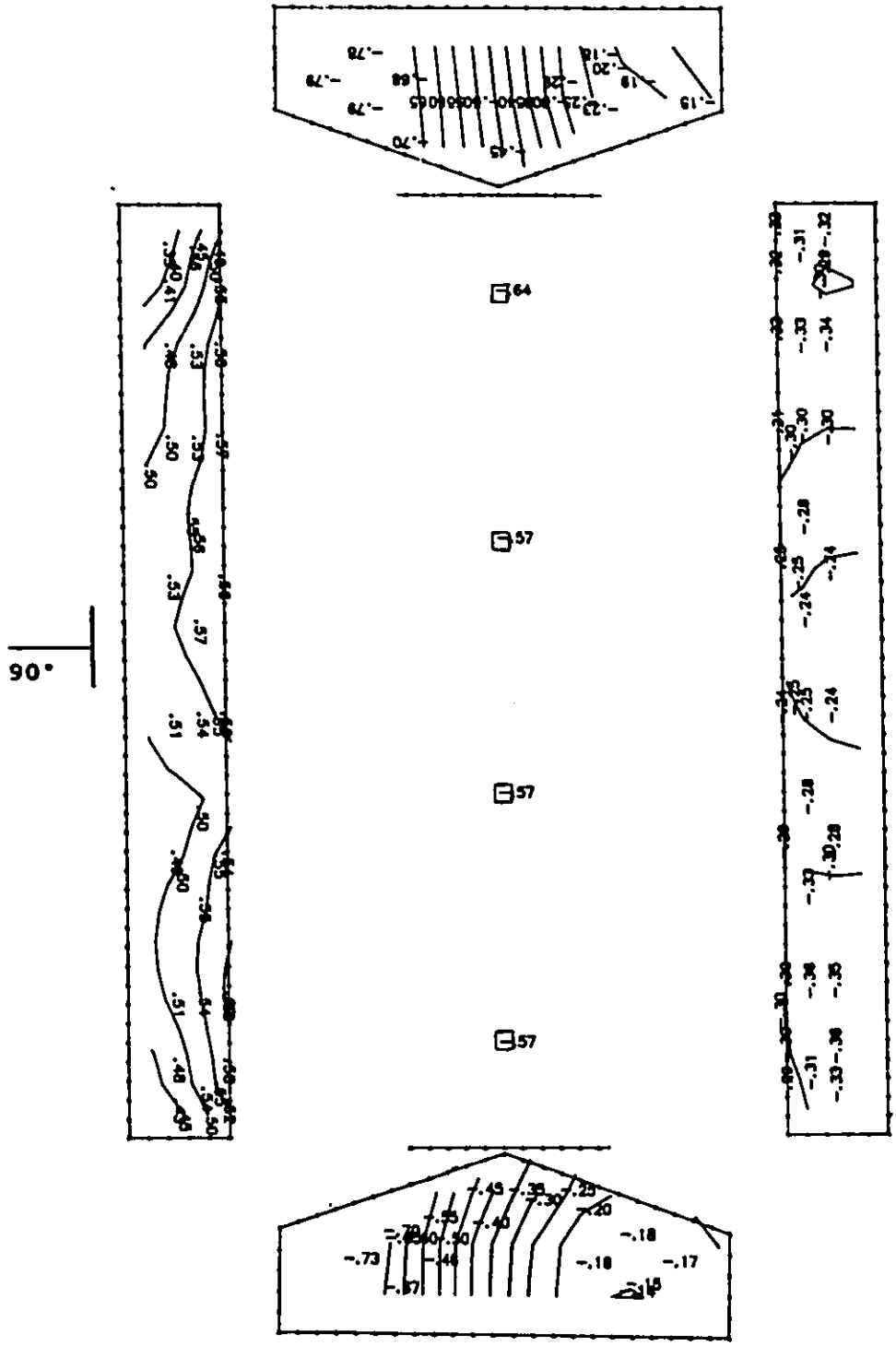

Figure E.13a Cps contour lines: sealed model with chimney, wind angle of 90°.

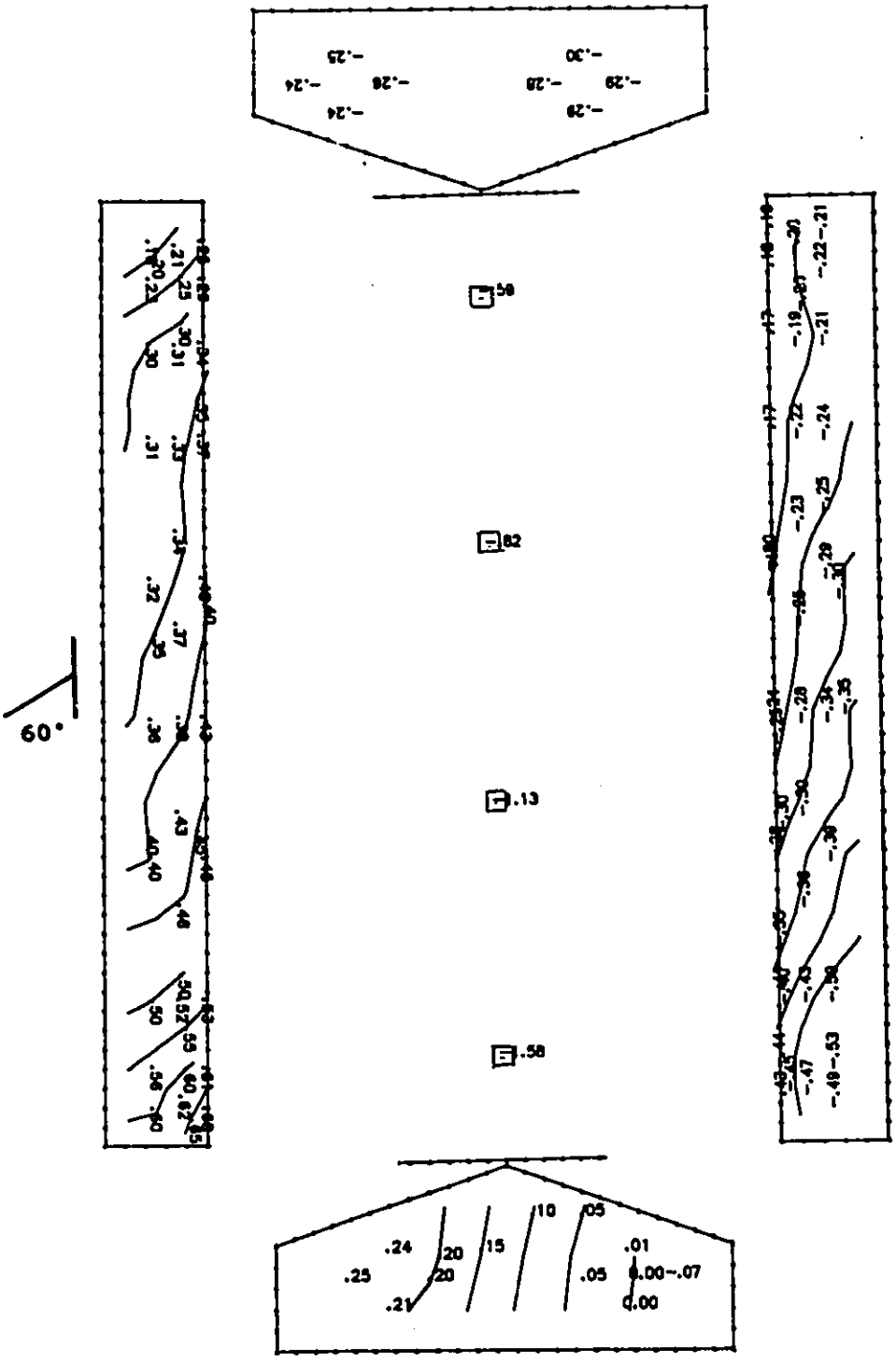

Figure E.13b Cps contour lines: sealed model with chimney, wind angle of 60°.

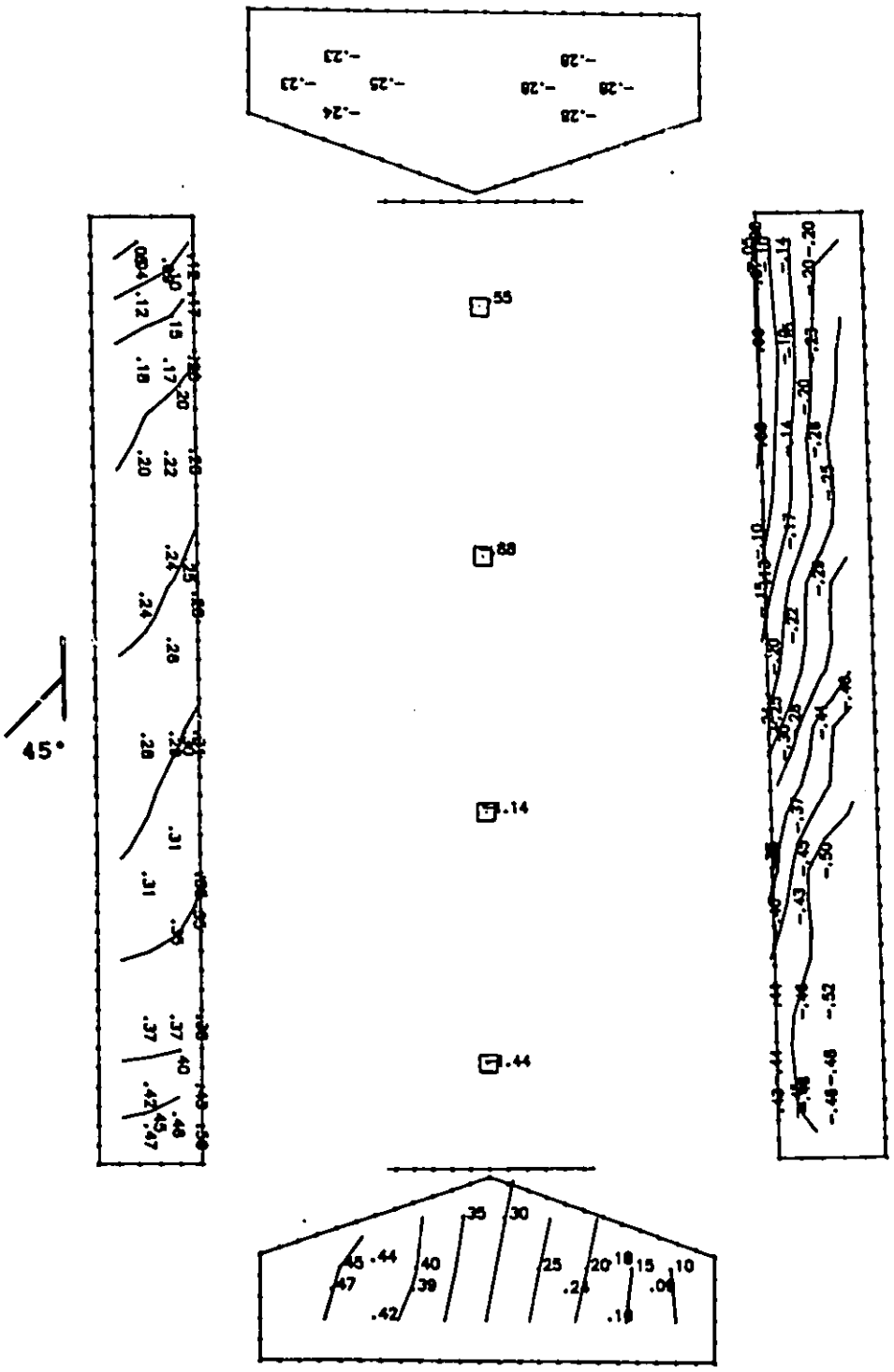

Figure E.13c Cps contour lines: sealed model with chimney, wind angle of 45°.

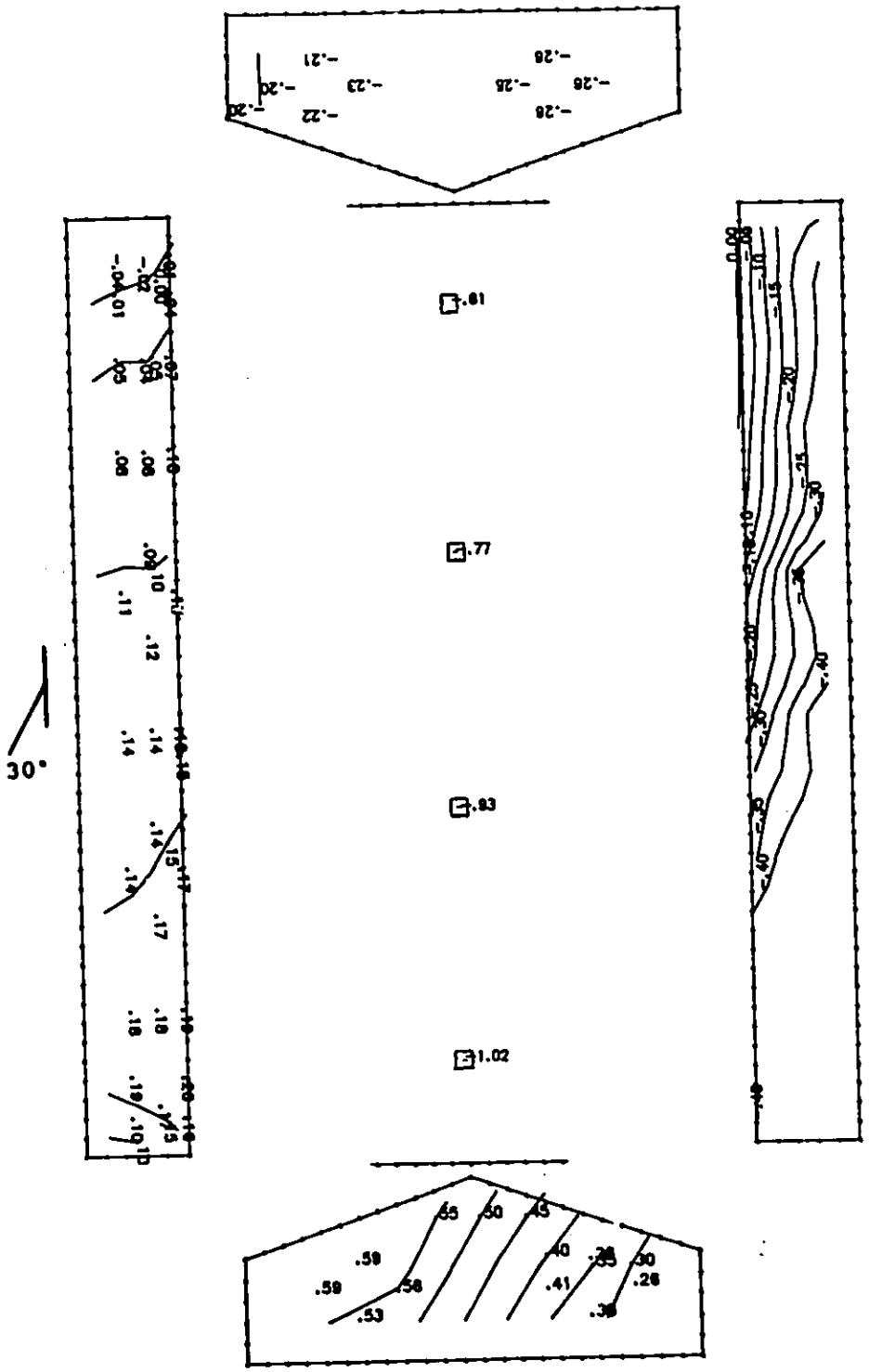

Figure E.13d Cps contour lines: sealed model with chimney, wind angle of 30°.

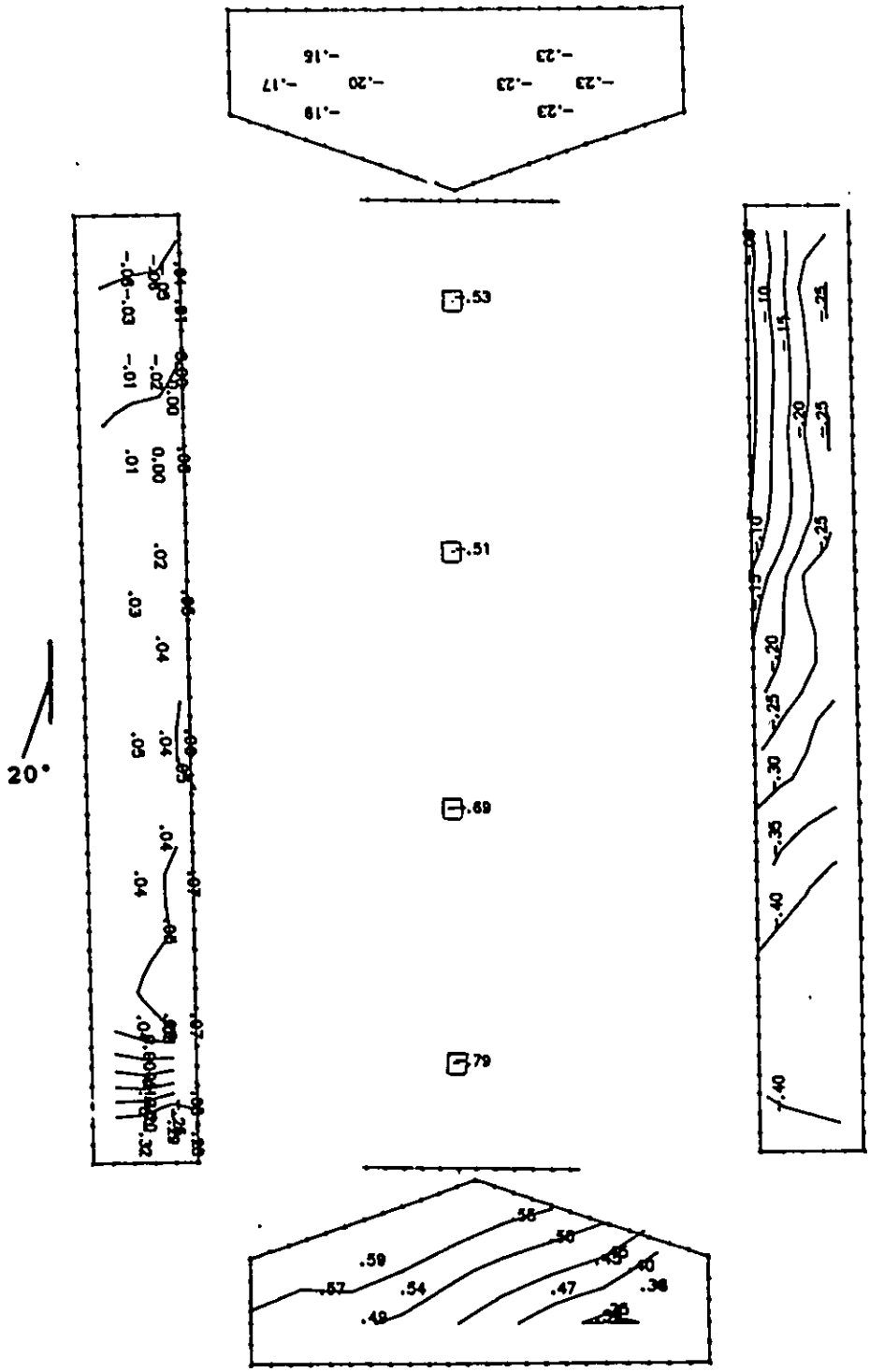

Figure E.13e Cps contour lines: sealed model with chimney, wind angle of 20°.

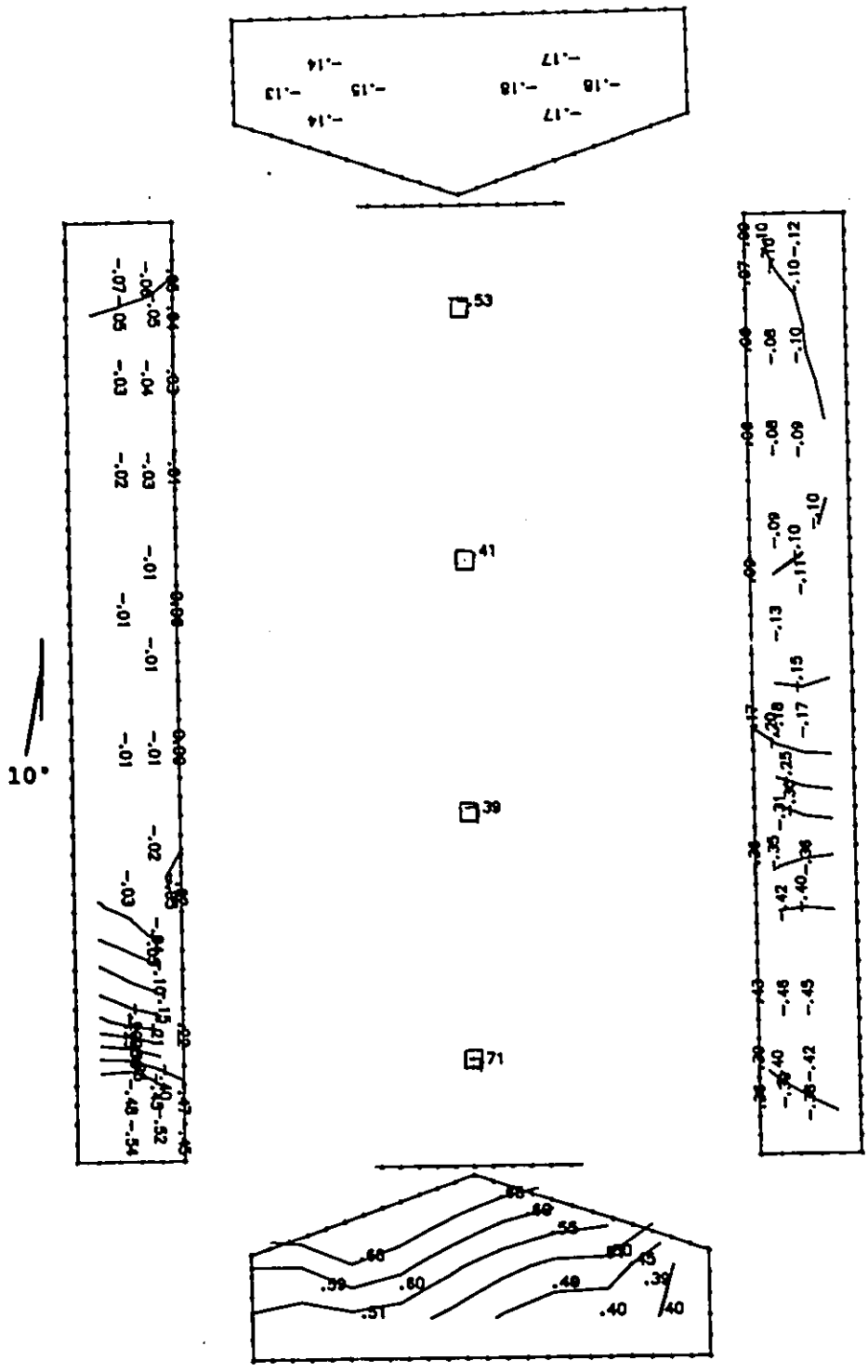

Figure E.13f Cps contour lines: sealed model with chimney, wind angle of 10°.

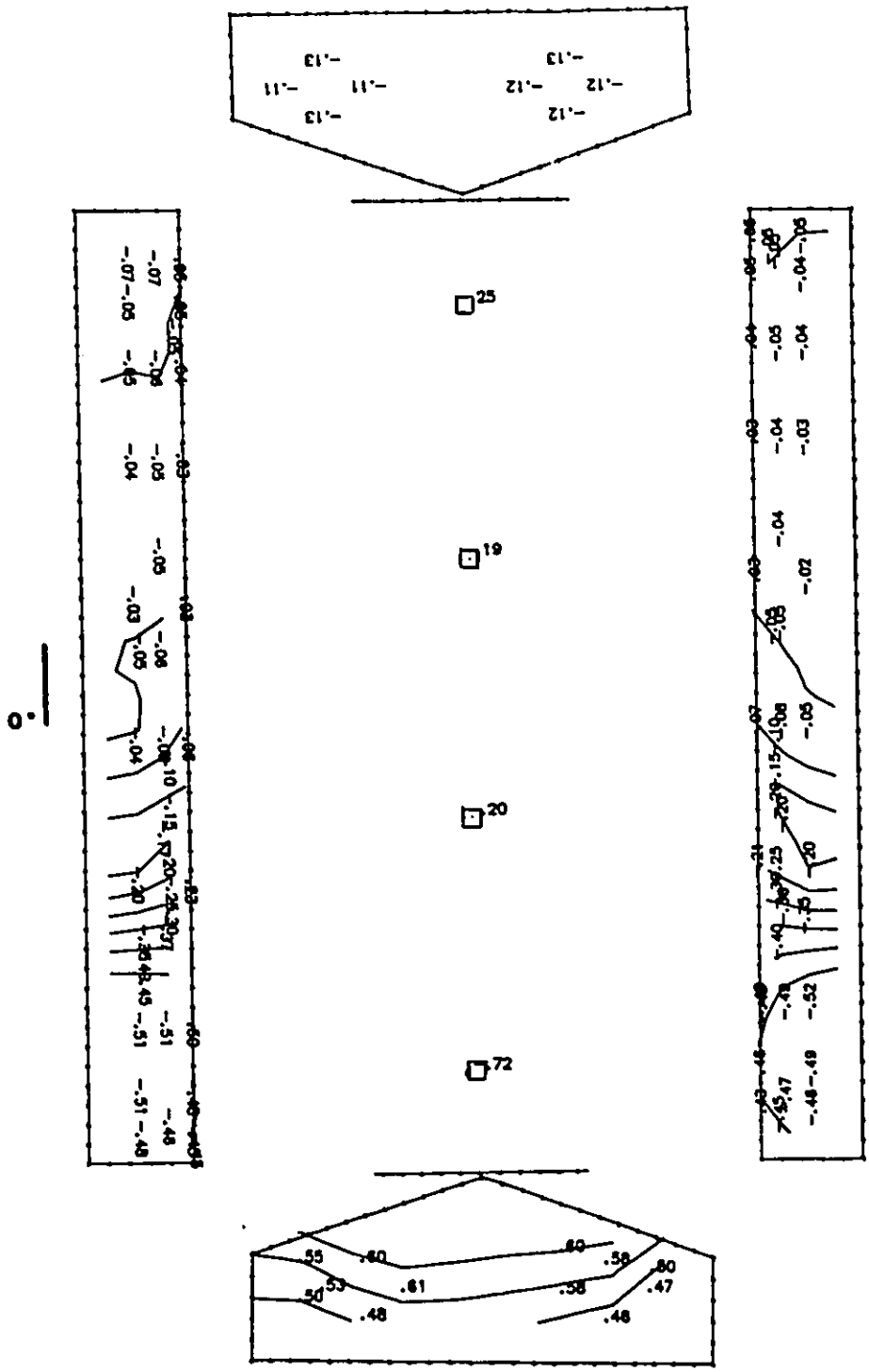

Figure E.13g Cps contour lines: sealed model with chimney, wind angle of 0°.

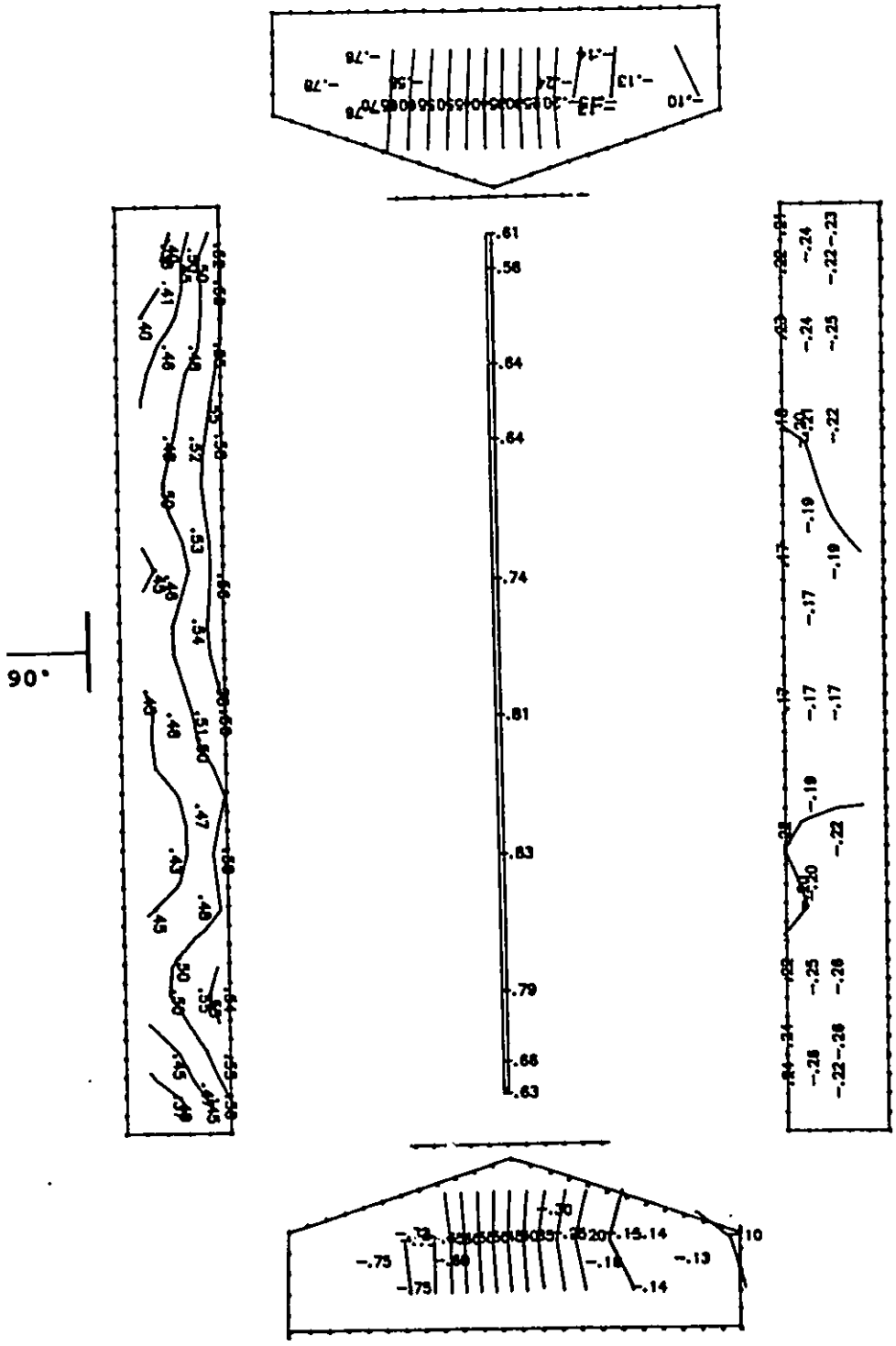

Figure E.14a Cps contour lines: sealed model with simulated 150 mm ridge, wind angle of 90°.

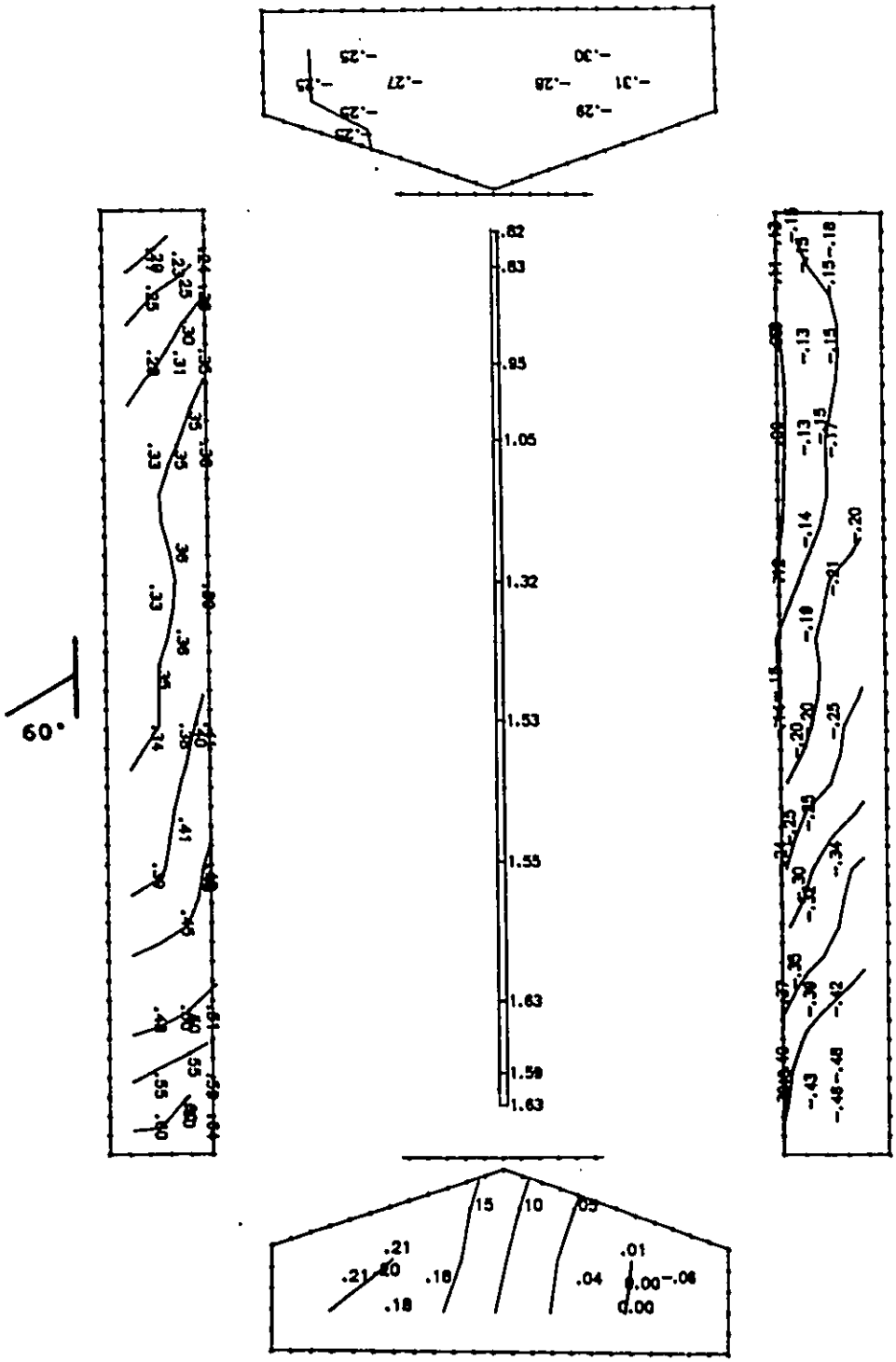

Figure E.14b Cps contour lines: sealed model with simulated 150 mm ridge, wind angle of 60°.

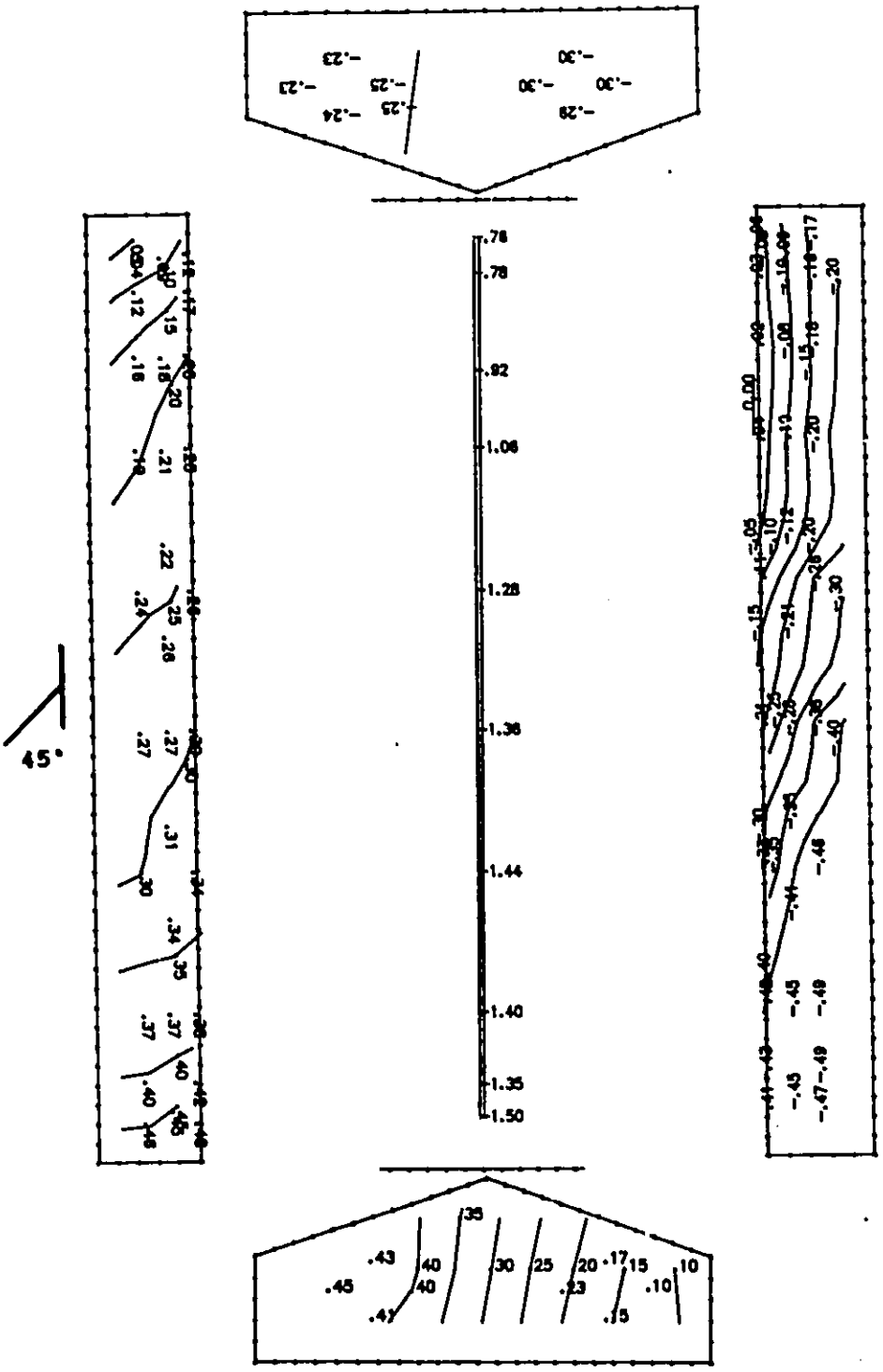

Figure E.14c Cps contour lines: sealed model with simulated 150 mm ridge, wind angle of 45°.

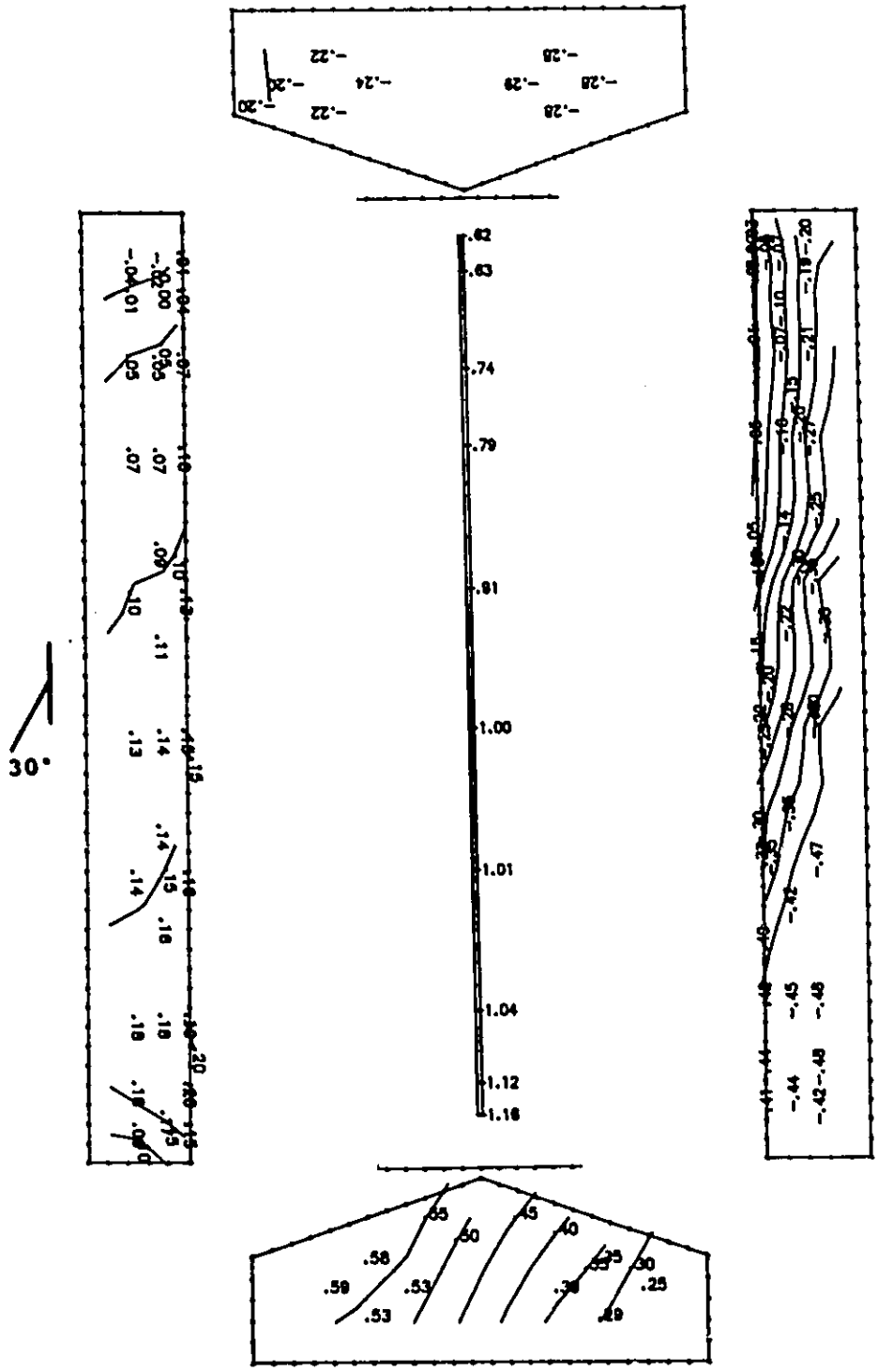

Figure E.14d Cps contour lines: sealed model with simulated 150 mm ridge, wind angle of 30°.

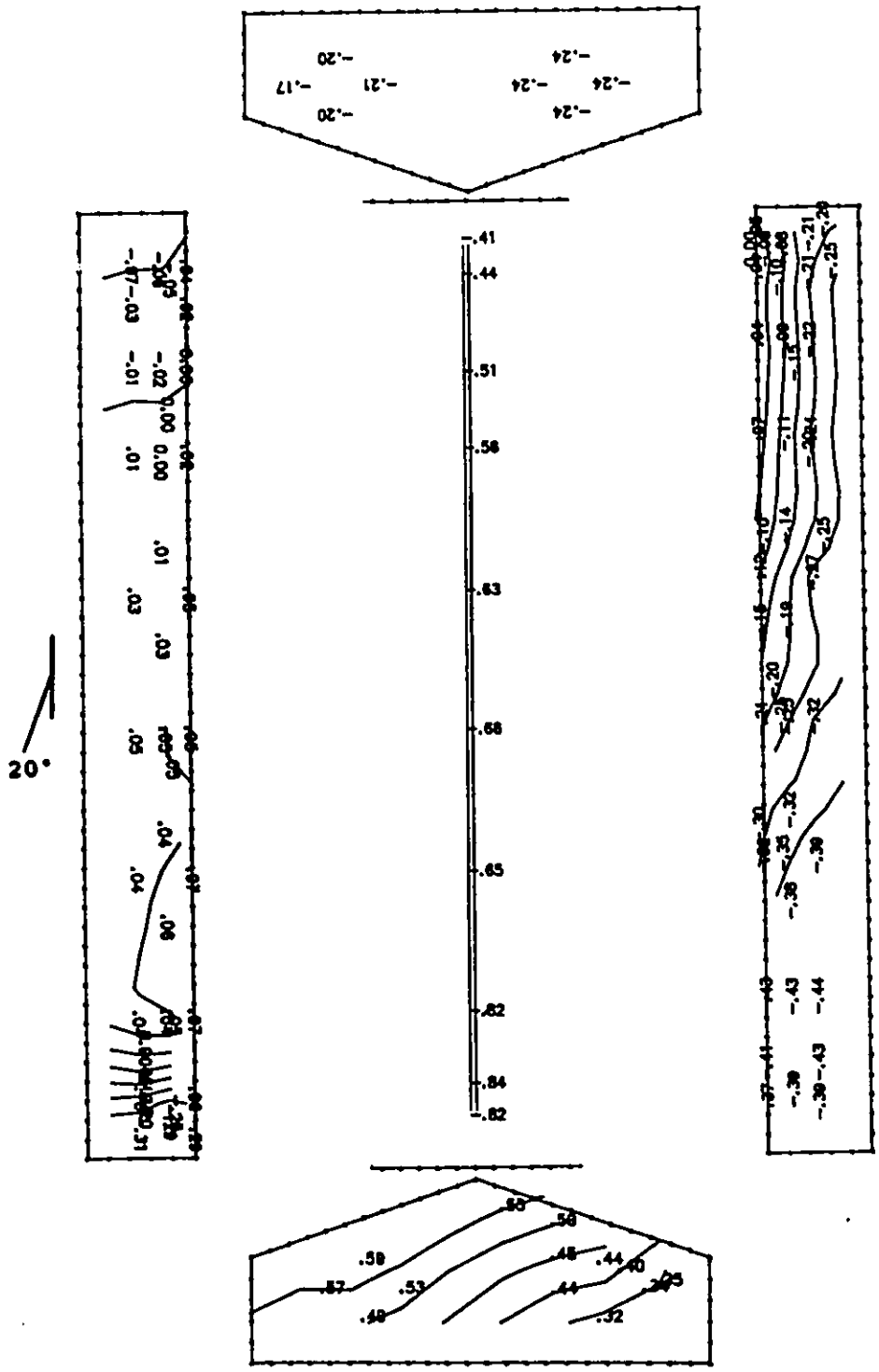

Figure E.14e Cps contour lines: sealed model with simulated 150 mm ridge, wind angle of 20°.

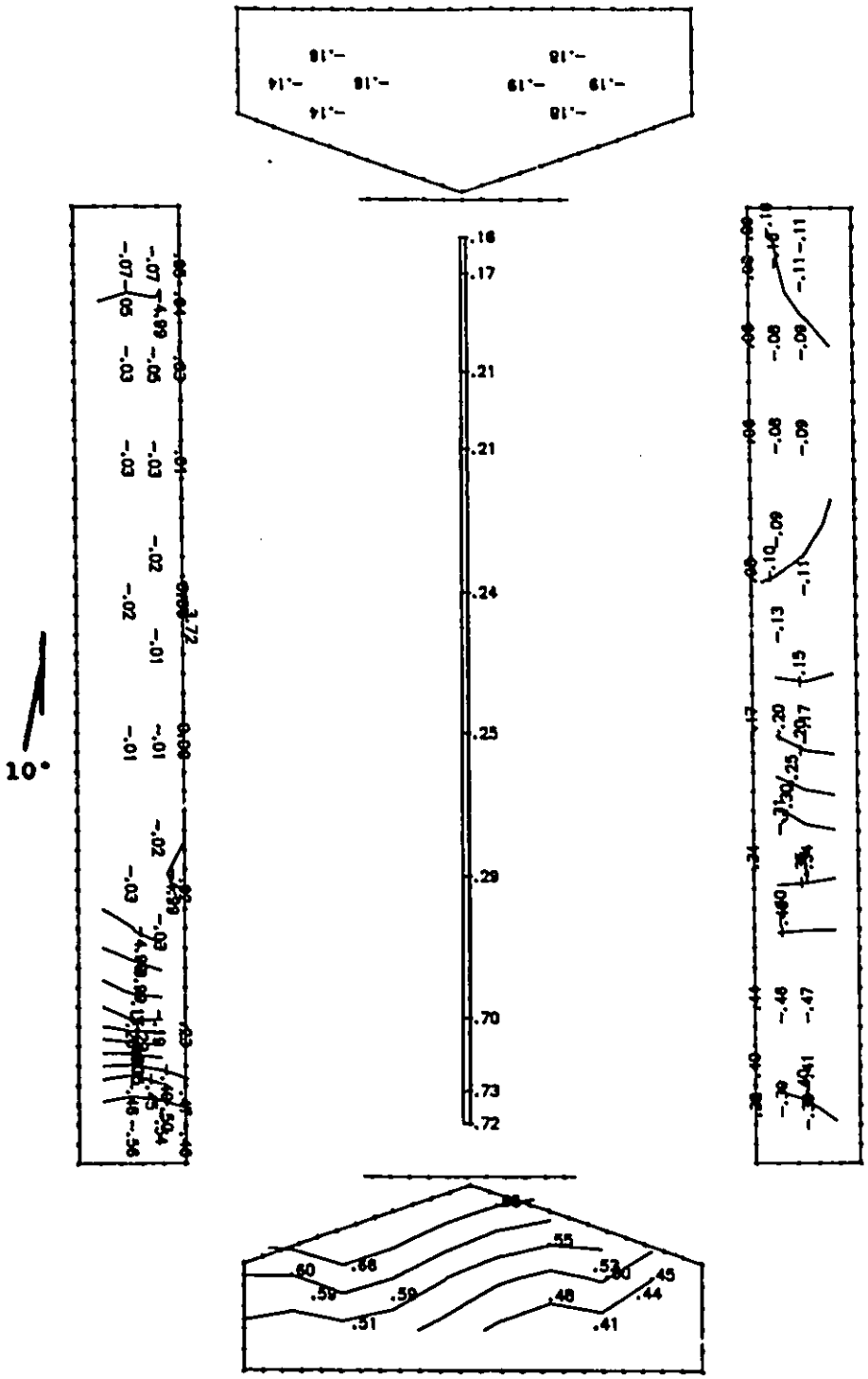

Figure E.14f Cps contour lines: sealed model with simulated 150 mm ridge, wind angle of 10°.

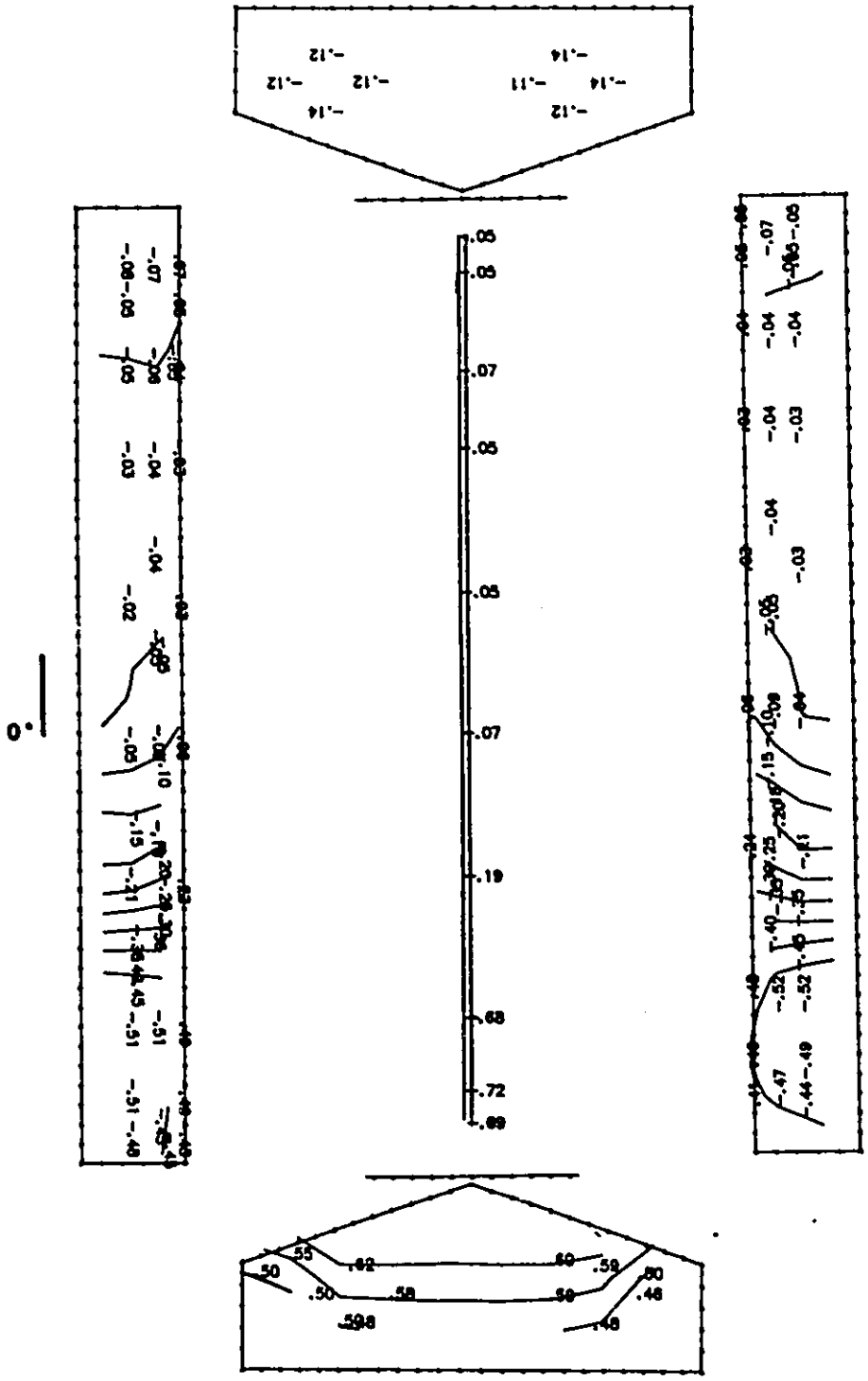

Figure E.14g Cps contour lines: sealed model with simulated 150 mm ridge, wind angle of 0°.

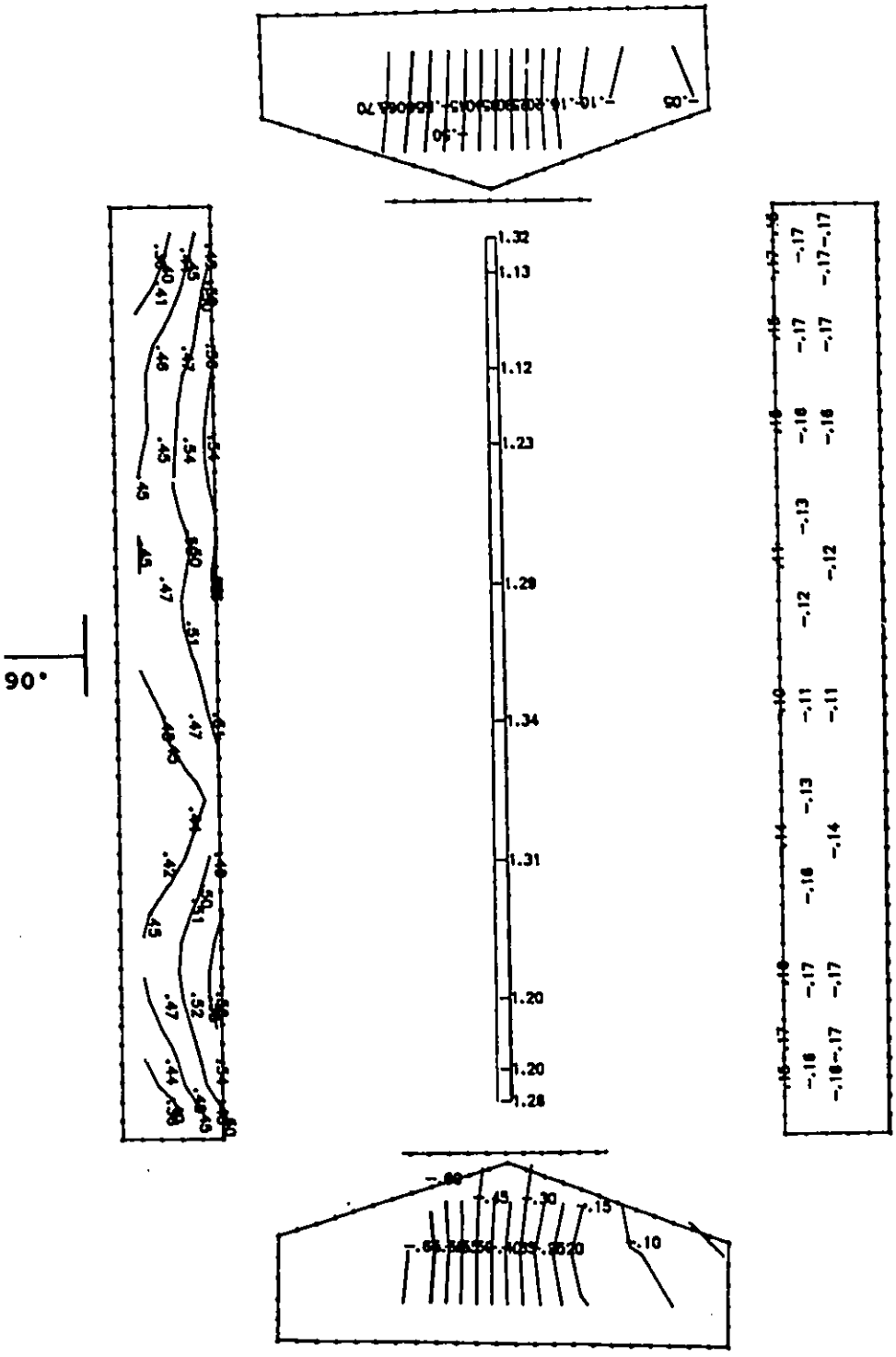

Figure E.15a Cps contour lines: sealed model with simulated 400 mm ridge, wind angle of 90°.

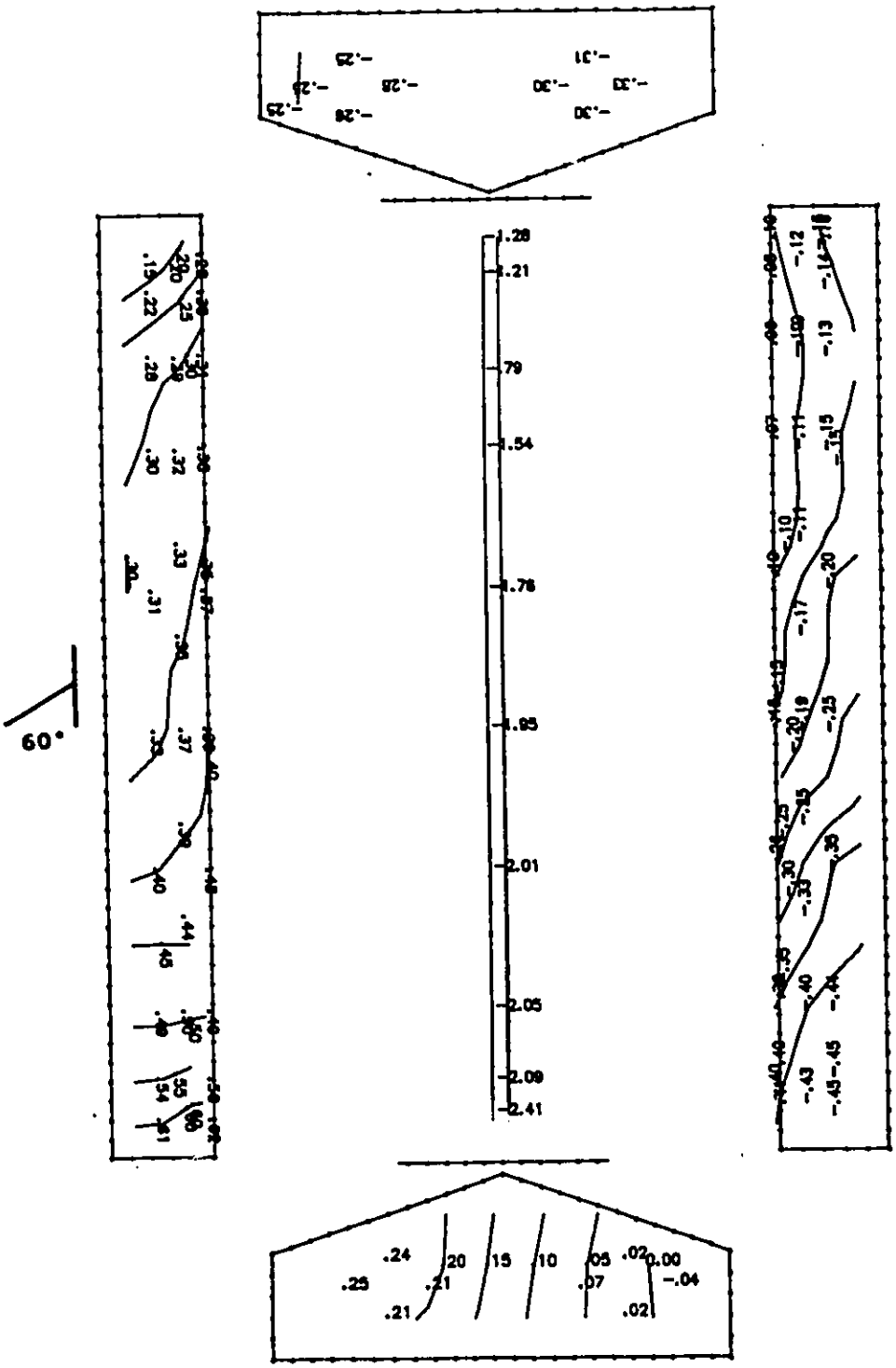

Figure E.15b Cps contour lines: sealed model with simulated 400 mm ridge, wind angle of 60°.

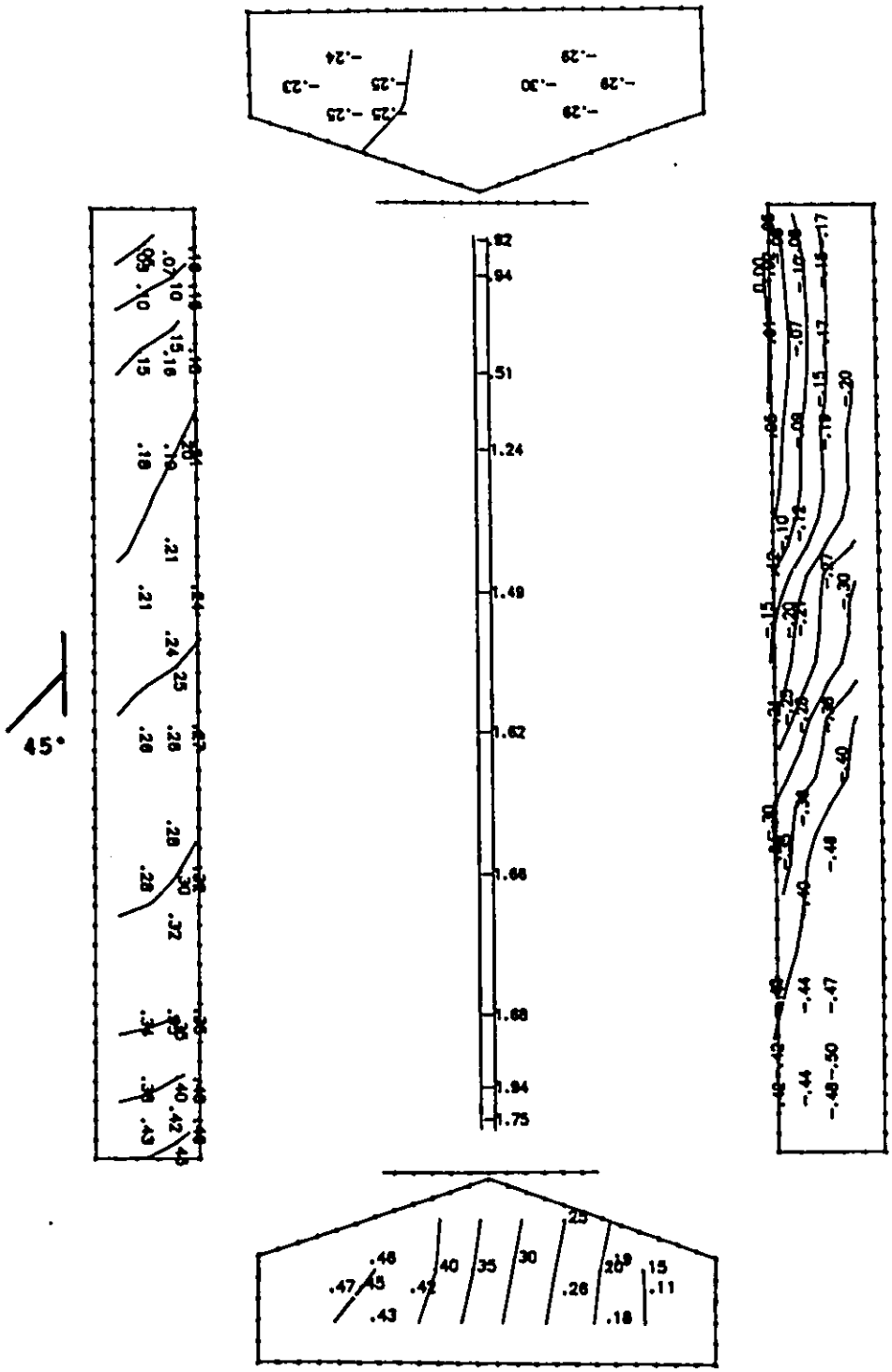

Figure E.15c Cps contour lines: sealed model with simulated 400 mm ridge, wind angle of 45°.

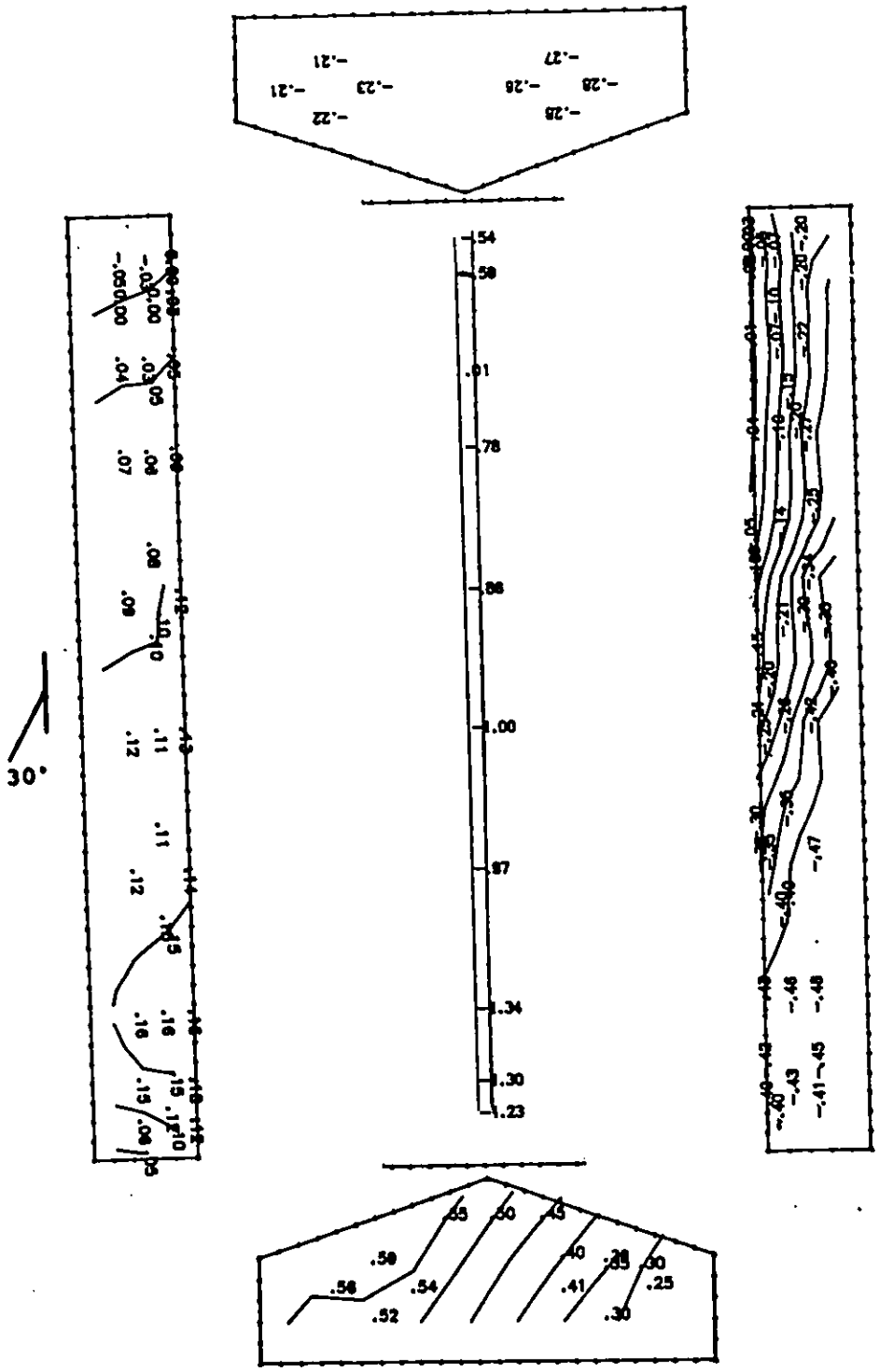

Figure E.15d Cps contour lines: sealed model with simulated 400 mm ridge, wind angle of 30°.

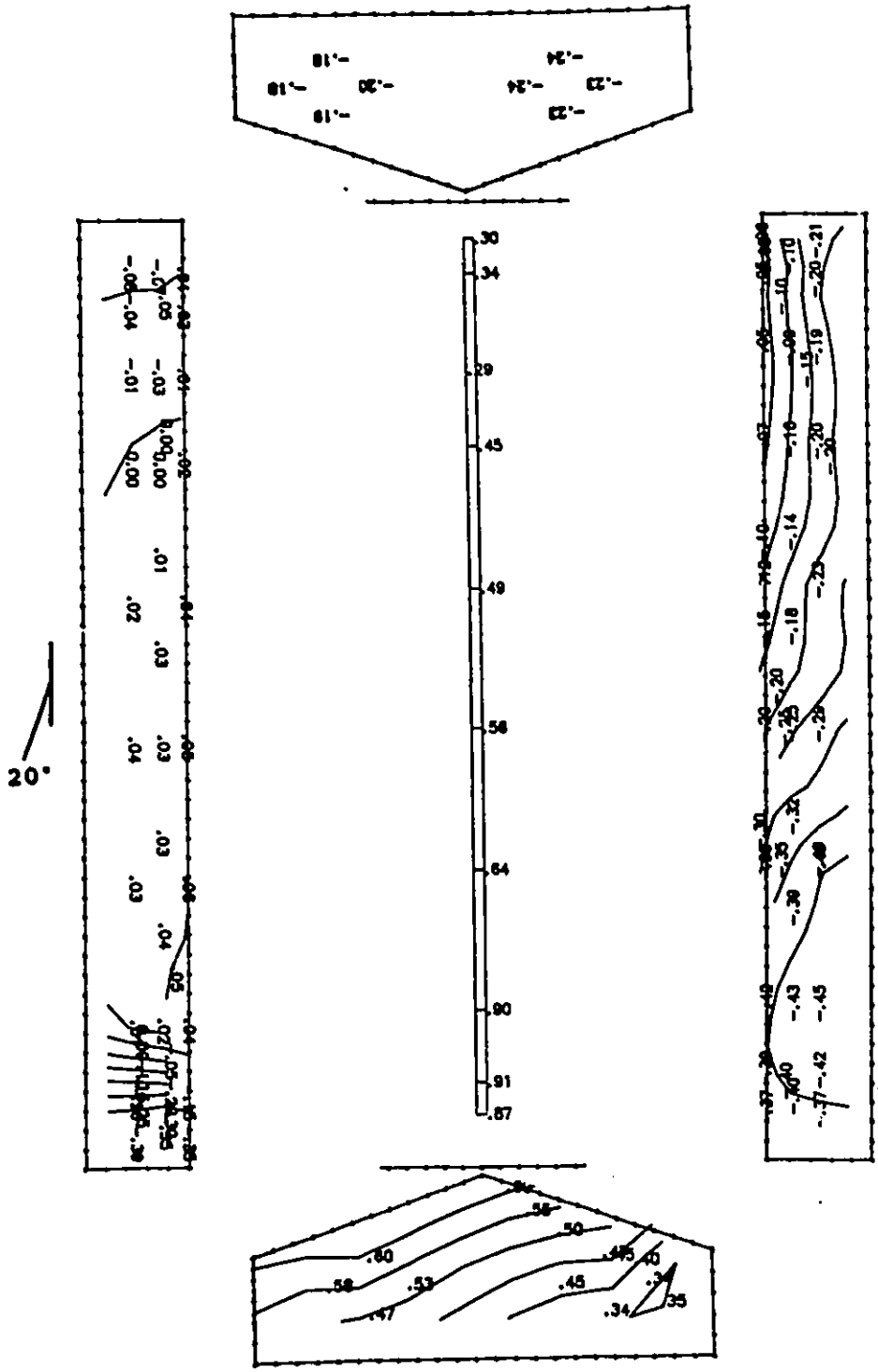

Figure E.15e Cps contour lines: sealed model with simulated 400 mm ridge, wind angle of 20°.

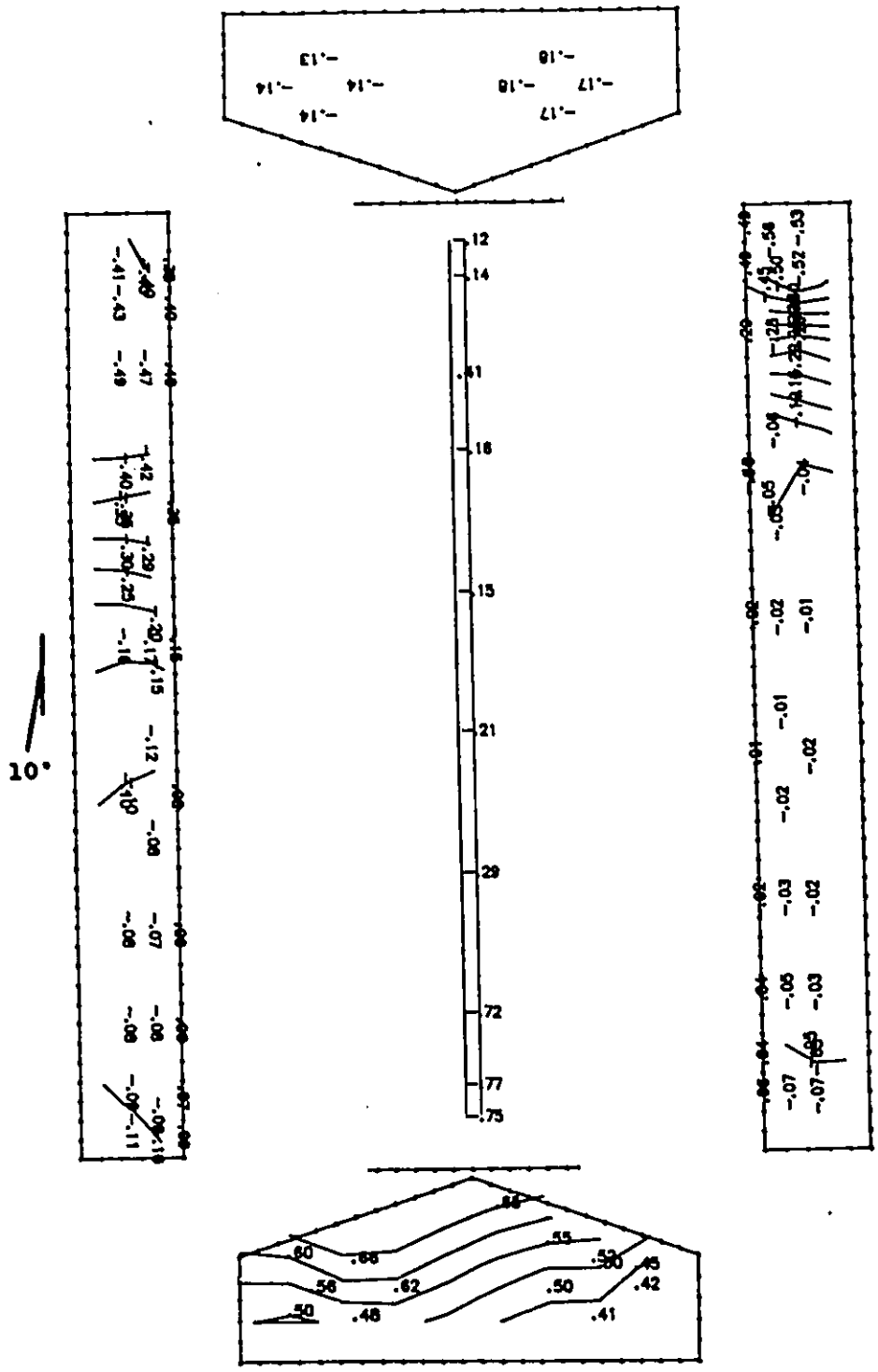

Figure E.15f Cps contour lines: sealed model with simulated 400 mm ridge, wind angle of 10°.

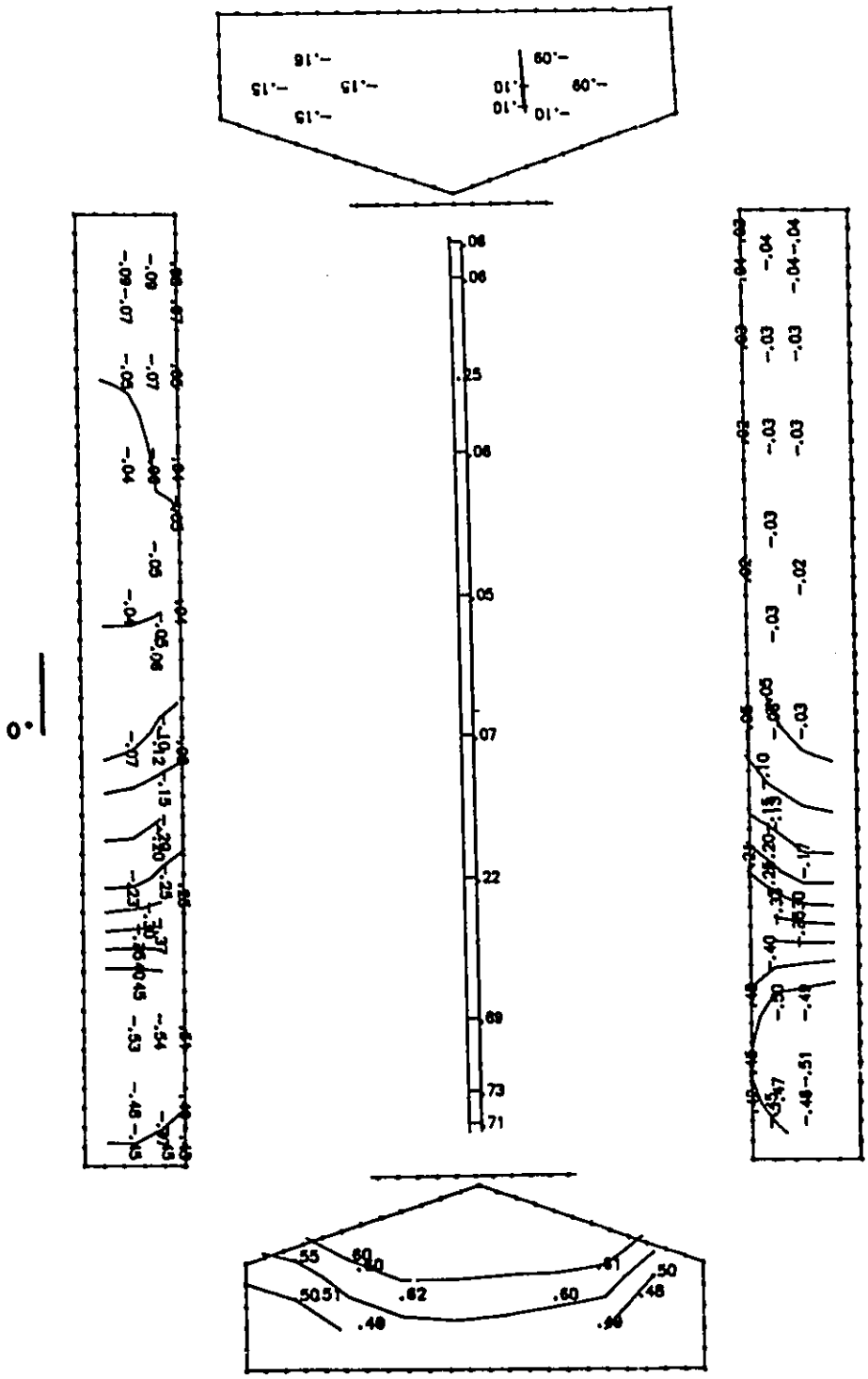

Figure E.15g Cps contour lines: sealed model with simulated 400 mm ridge, wind angle of 0°.

APPENDIX F

Internal pressure coefficients

1 - Measured Cp_{in}.
2 - Internal airflow patterns.
3 - Calculated Cp_{in}.

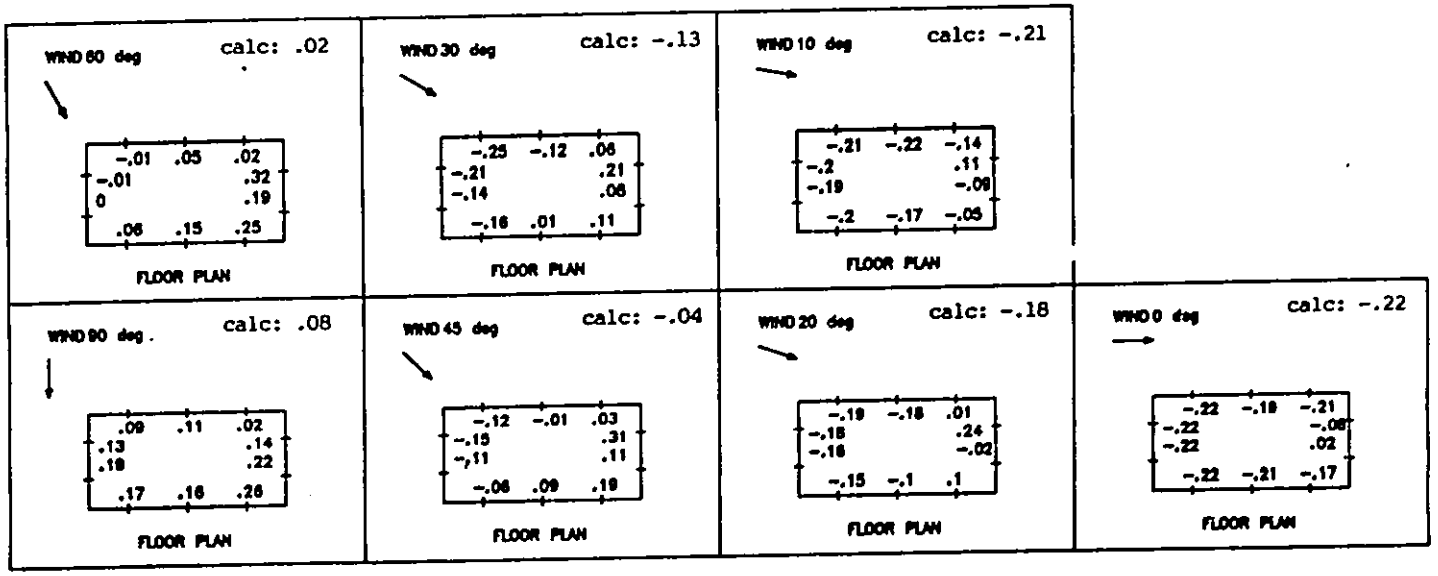

Figure F.1 Measured Cp_{in}: open model, chimney, simulated 1100 mm sidewall openings, closed end walls, 7 wind angles of incidence, configuration #1.

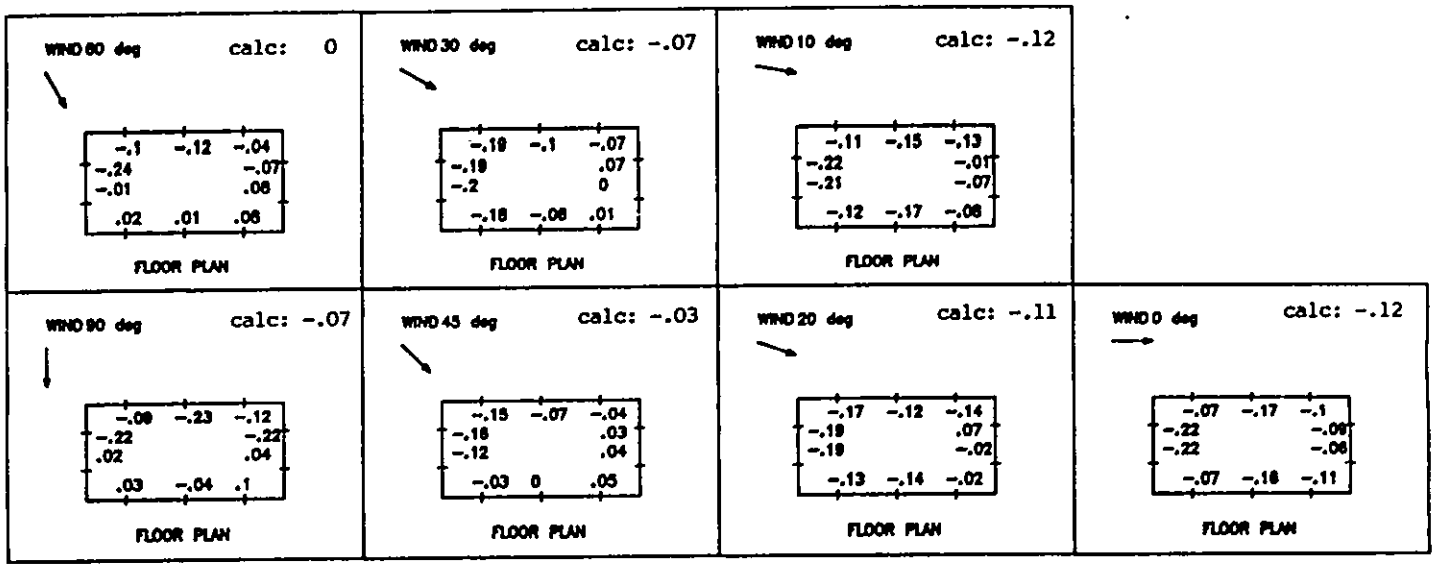

Figure F.2 Measured Cp_{in}: open model, chimney, simulated 800 mm sidewall openings, closed end walls, 7 wind angles of incidence, configuration #2.

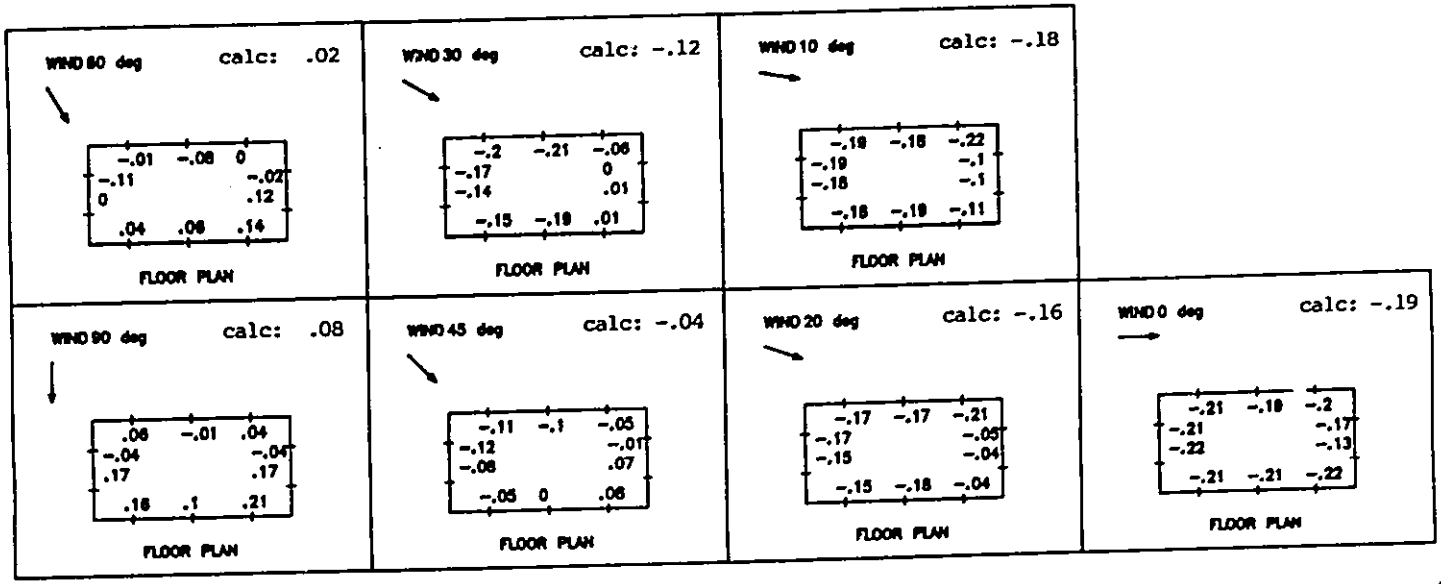

Figure F.3 Measured Cp_{in}: open model, chimney, simulated 800 mm sidewall openings, open end walls, 7 wind angles of incidence, configuration #2.

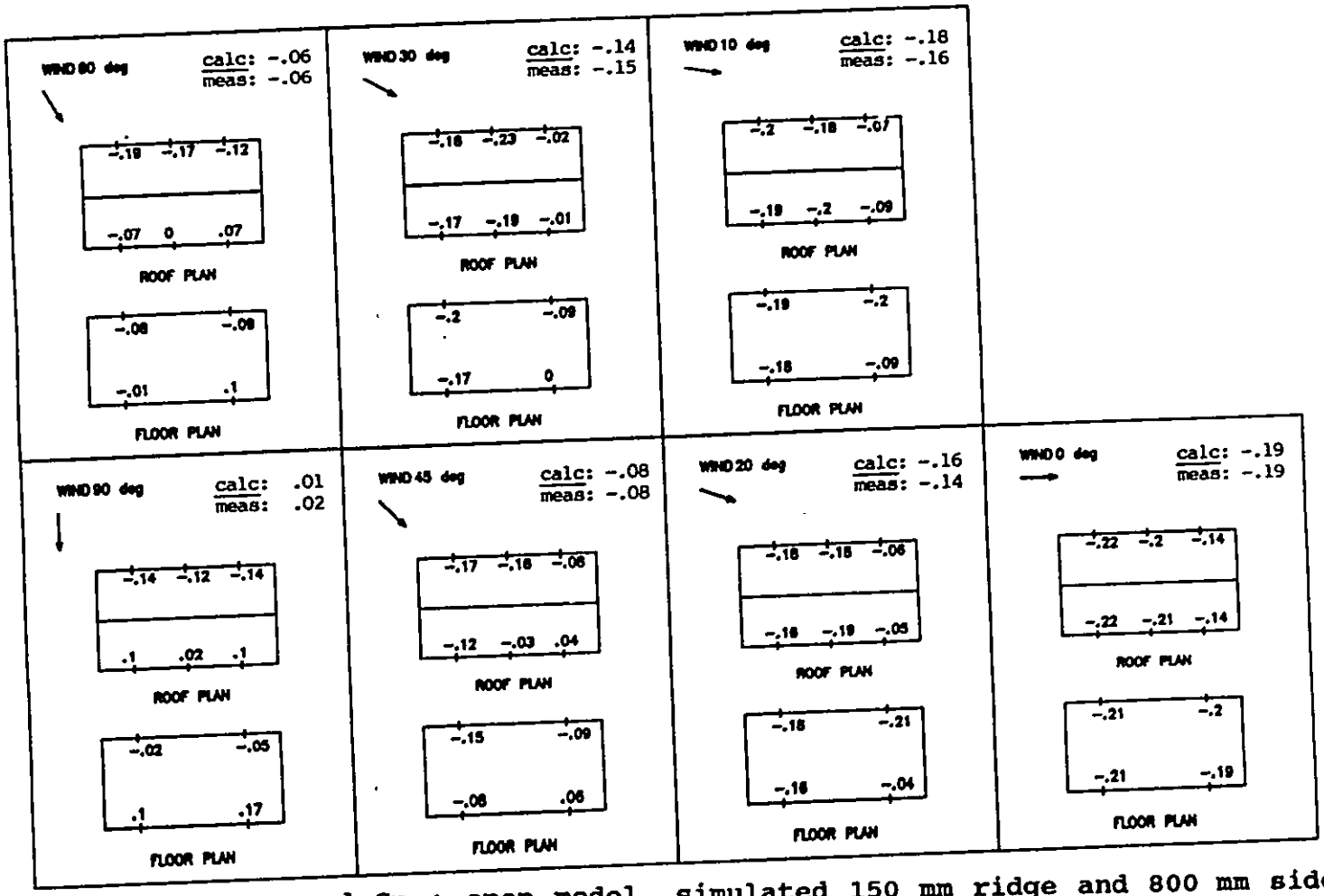

Figure F.4 Measured Cp_{in}: open model, simulated 150 mm ridge and 800 mm sidewall openings, closed end walls, 7 wind angles of incidence, configuration #3.

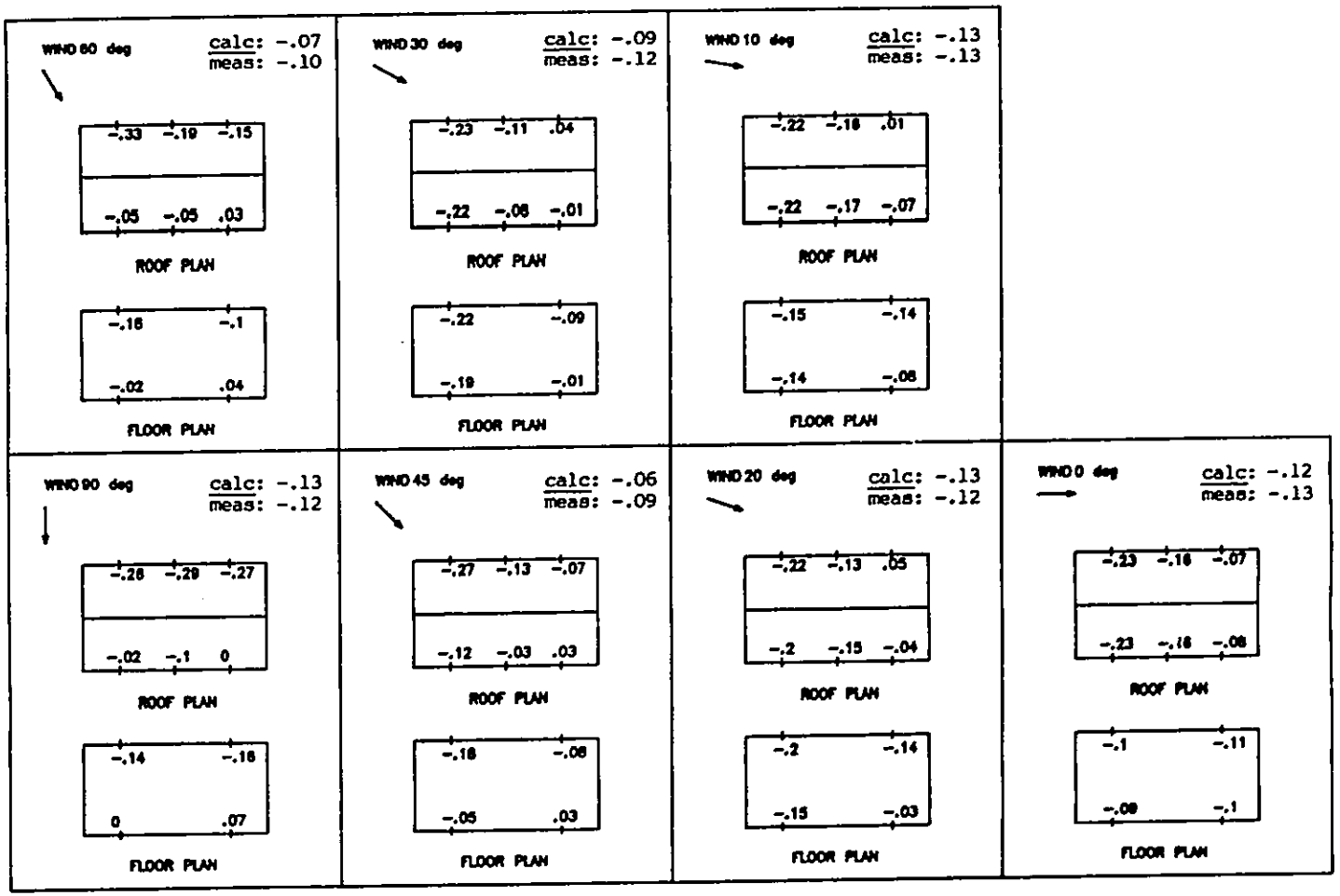

Figure F.5 Measured Cp_{in}: open model, simulated 150 mm ridge and 800 mm sidewall openings, open end walls, 7 wind angles of incidence, configuration #3.

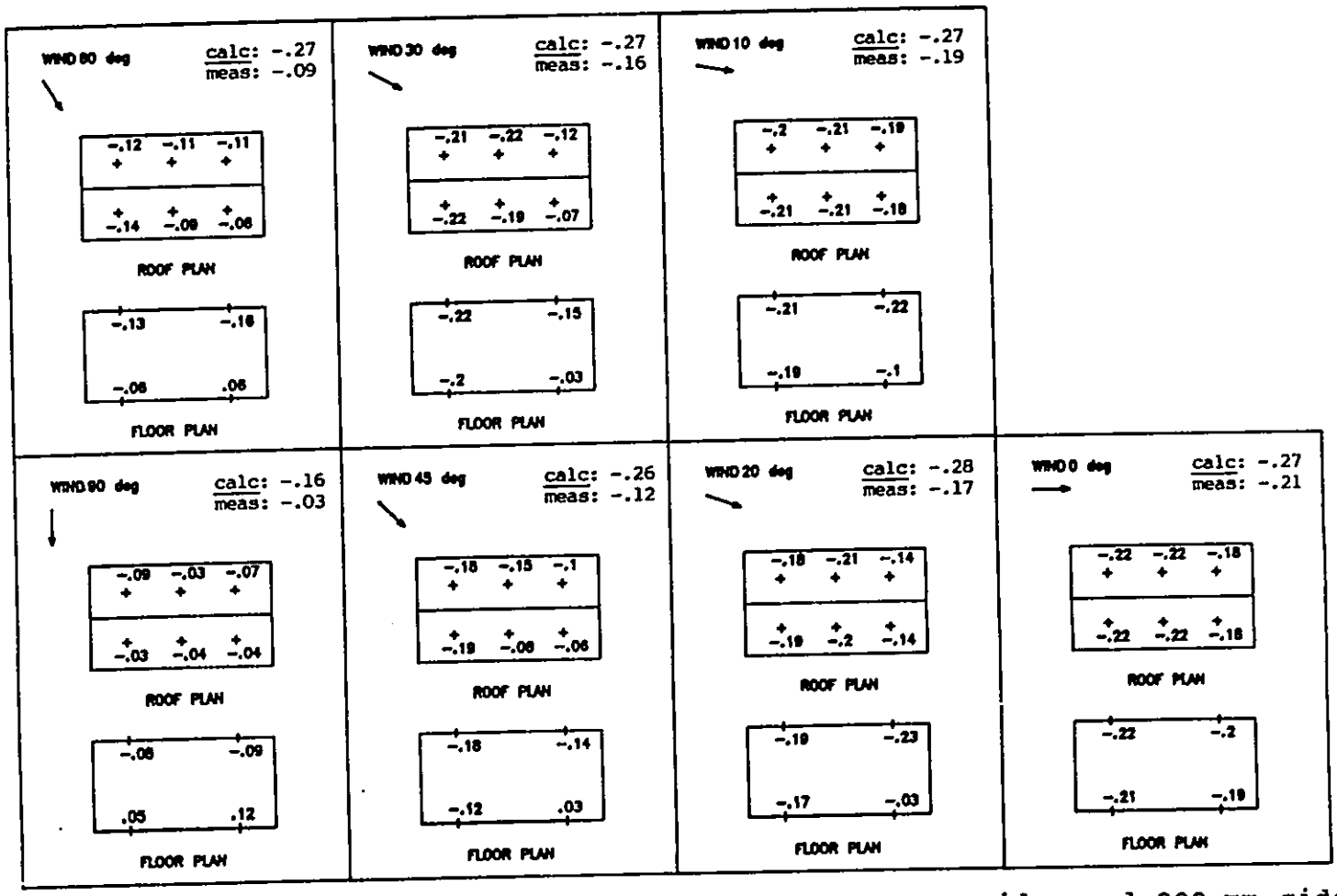

Figure F.6 Measured Cp_{in}: open model, simulated 400 mm ridge and 800 mm sidewall openings, closed end walls, 7 wind angles of incidence, configuration #4.

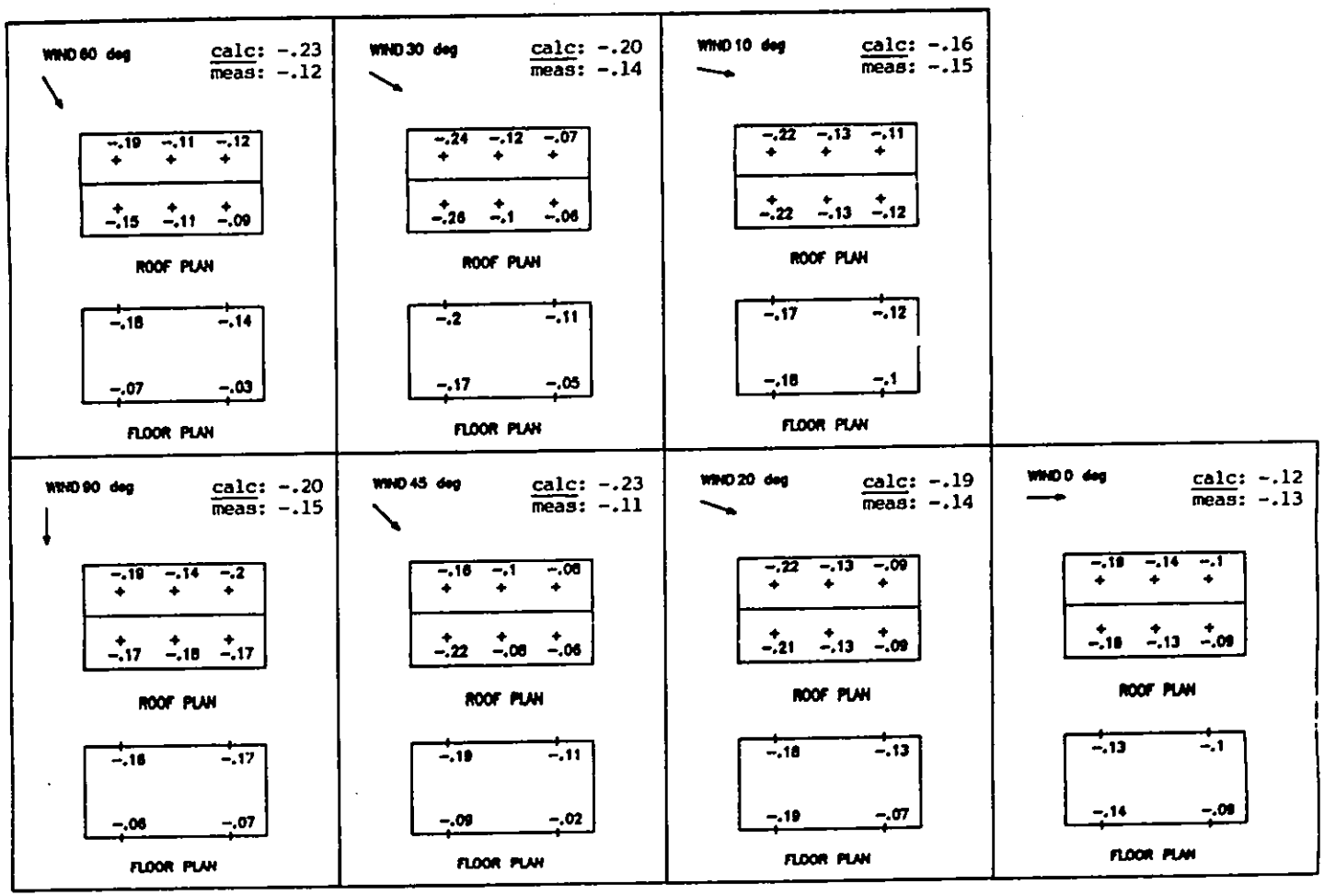

Figure F.7 Measured Cp_{in}: open model, simulated 400 mm ridge and 800 mm sidewall openings, open end walls, 7 wind angles of incidence, configuration #5.

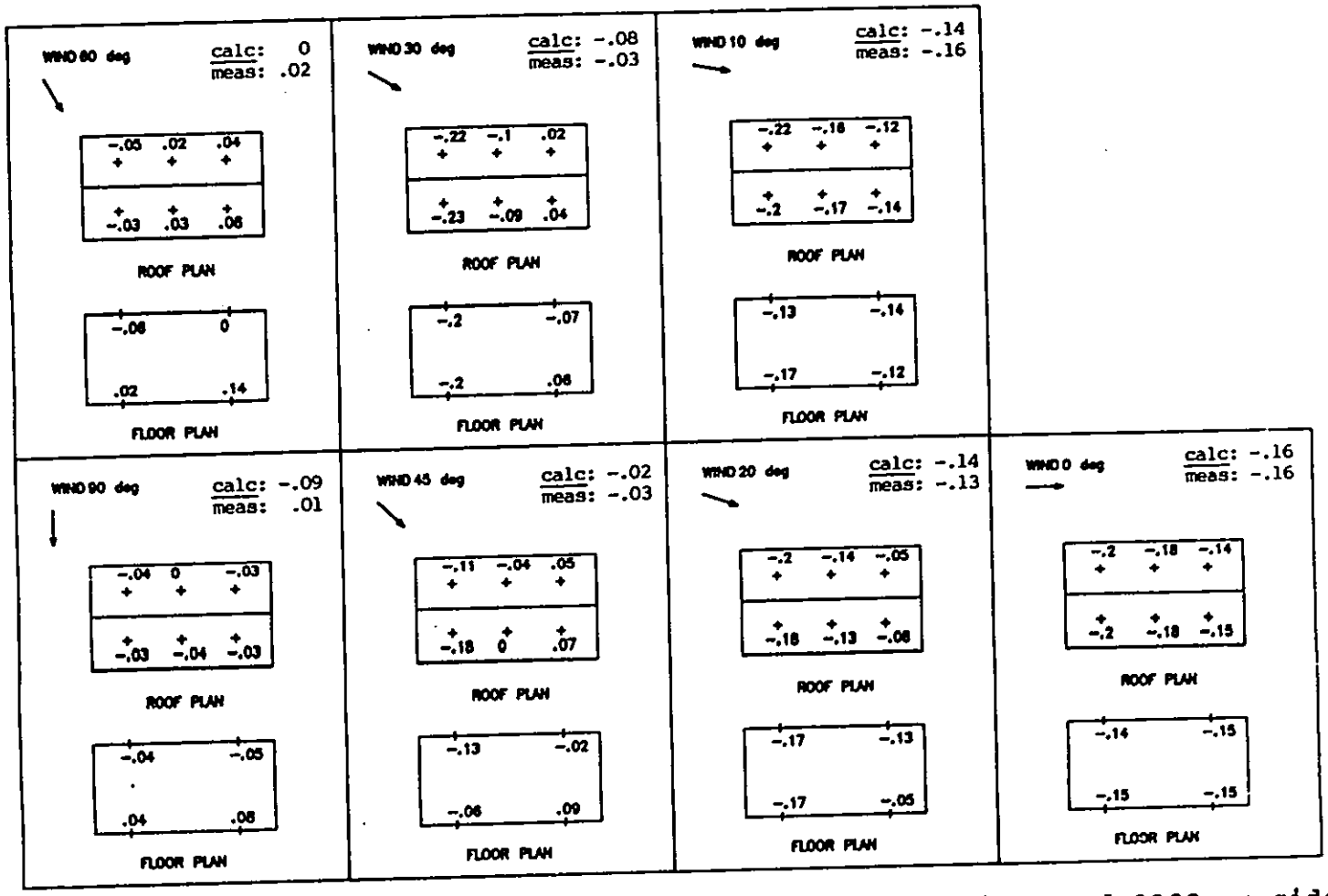

Figure F.8 Measured Cp_{in}: open model, simulated 400 mm ridge and 1100 mm sidewall openings, open end walls, 7 wind angles of incidence, configuration #5.

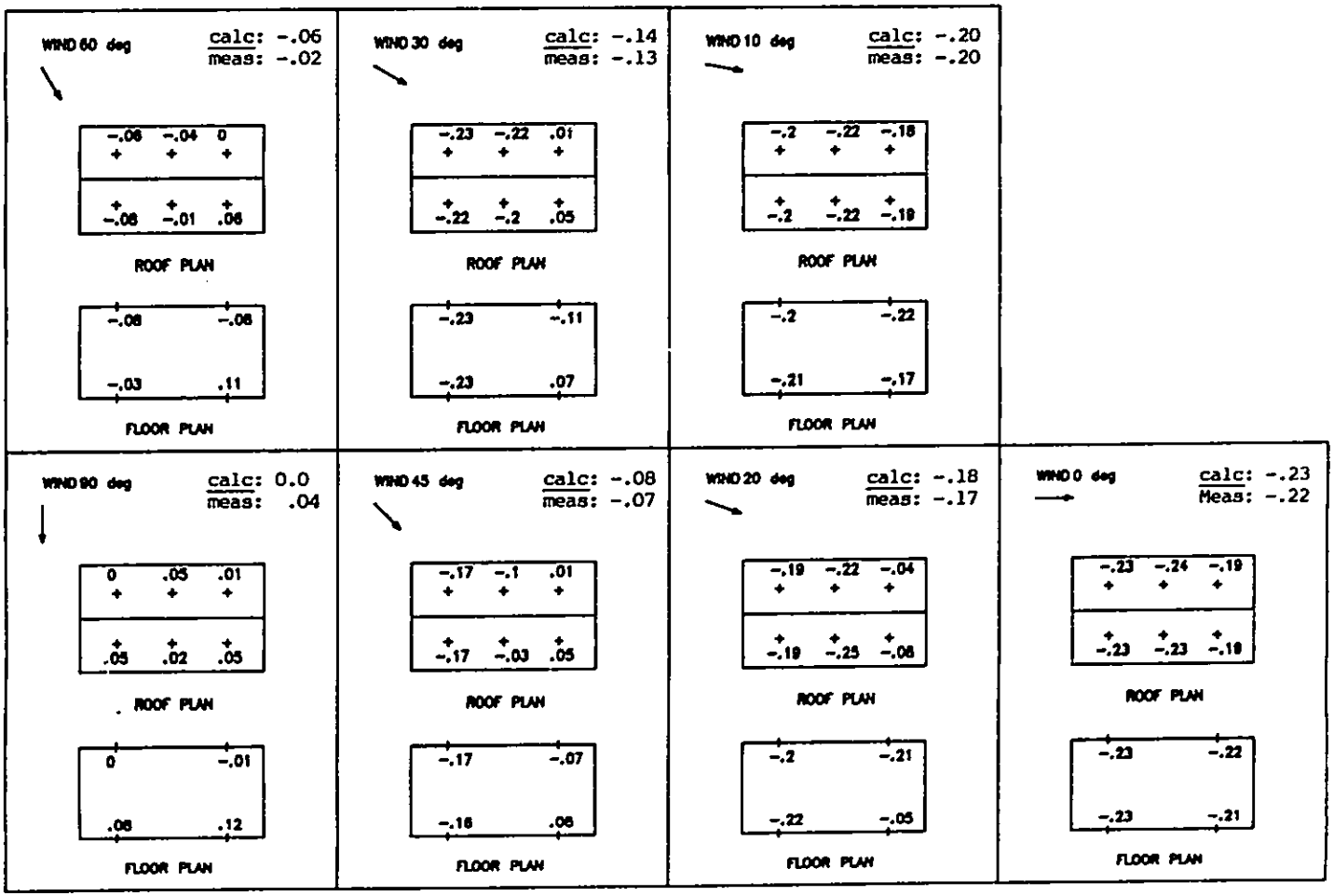

Figure F.9 Measured Cp_{in}: open model, simulated 150 mm ridge and 1100 mm sidewall openings, closed end walls, 7 wind angles of incidence, configuration #5.

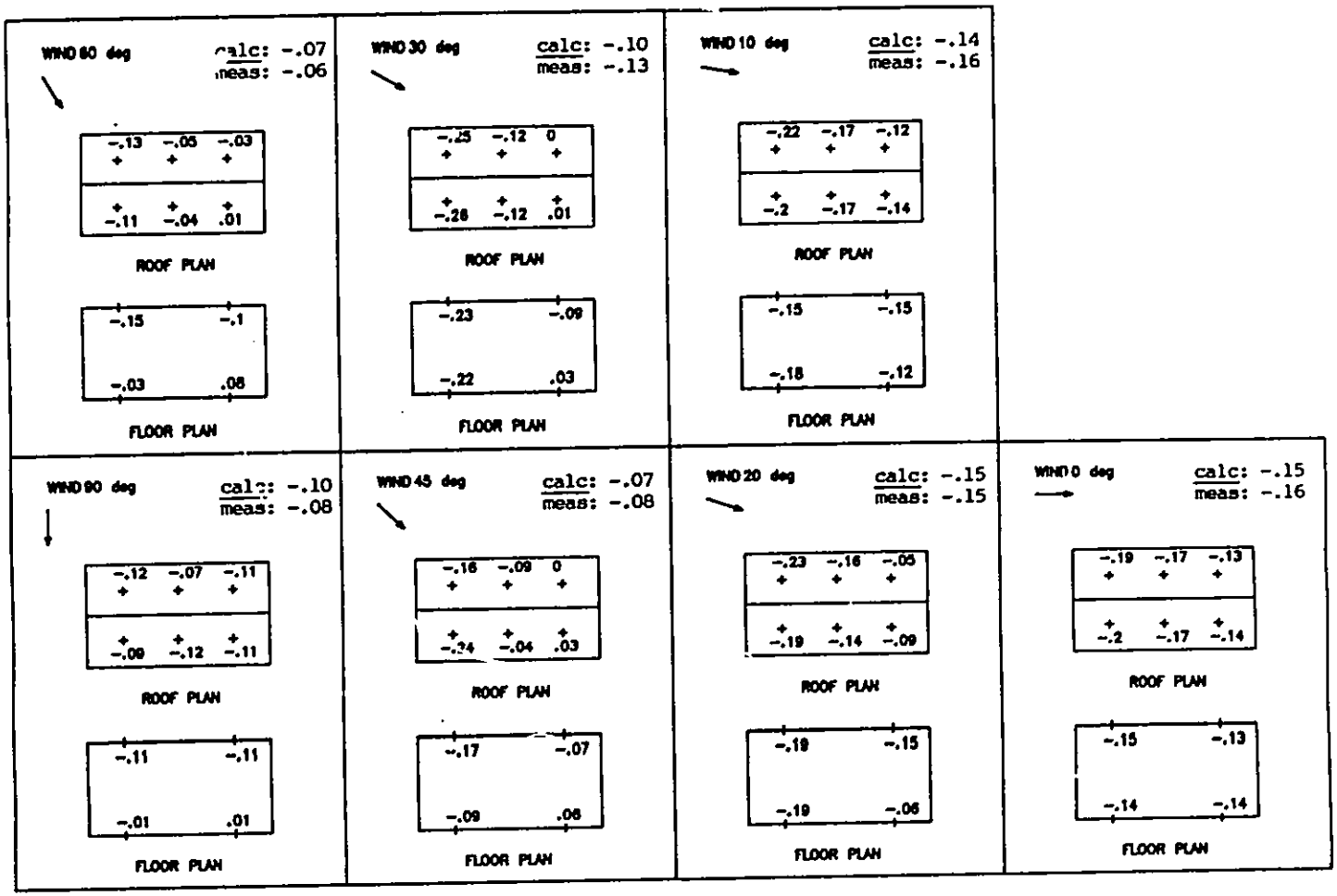

Figure F.10 Measured Cp_{in}: open model, simulated 150 mm ridge and 1100 mm sidewall openings, open end walls, 7 wind angles of incidence, configuration #5.

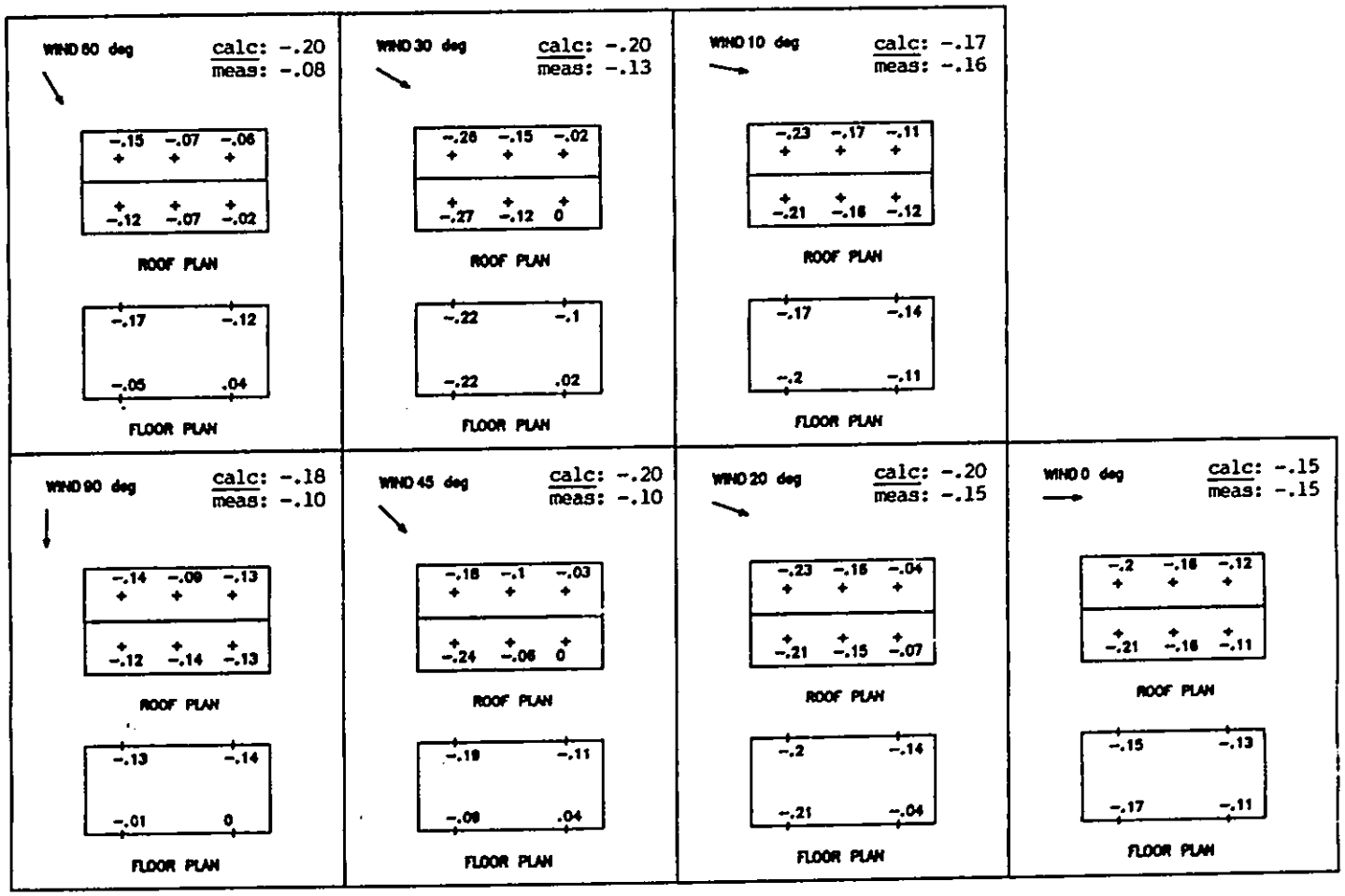

Figure F.11 Measured Cp_{in}: open model, chimney, simulated 1100 mm sidewall openings, open end walls, 7 wind angles of incidence, configuration #5.

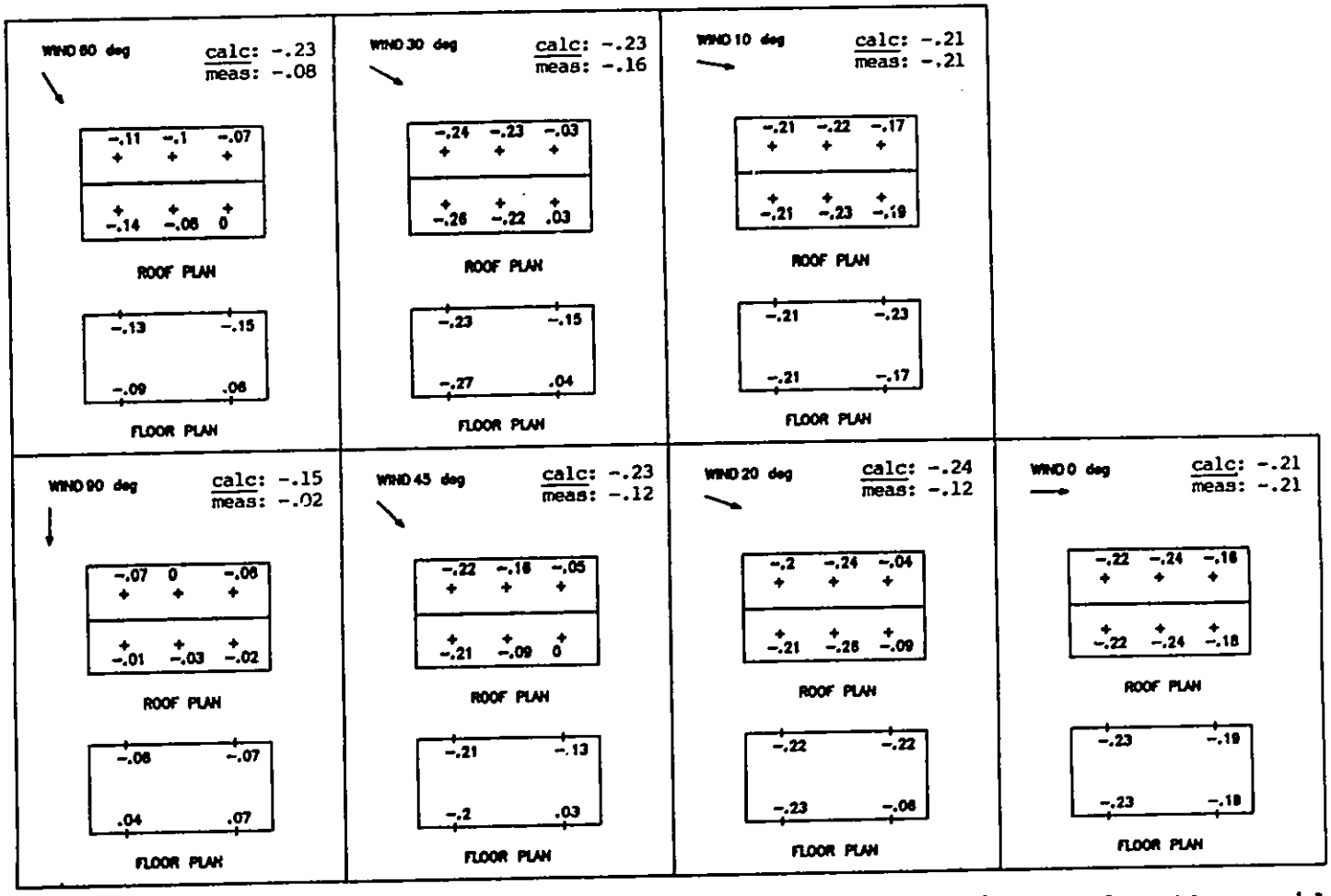

Figure F.12 Measured Cp_{in}: open model, simulated 400 mm ridge and 1100 mm sidewall openings, closed end walls, 7 wind angles of incidence, configuration #5.

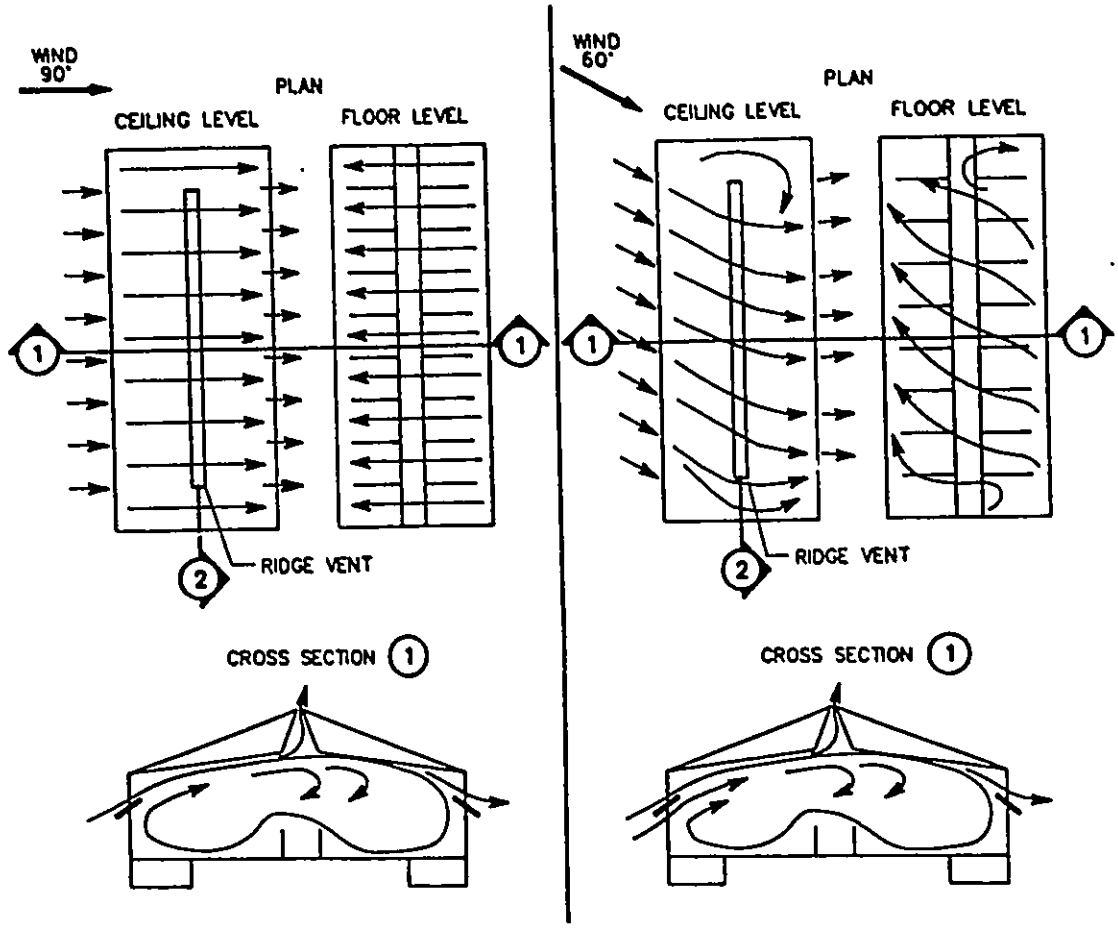

Figure F.13 Airflow patterns with standard ridge opening (150 mm full scale), doors open (30°) both sides, wind at 90° and 60° (Choinière et al., 1988c).

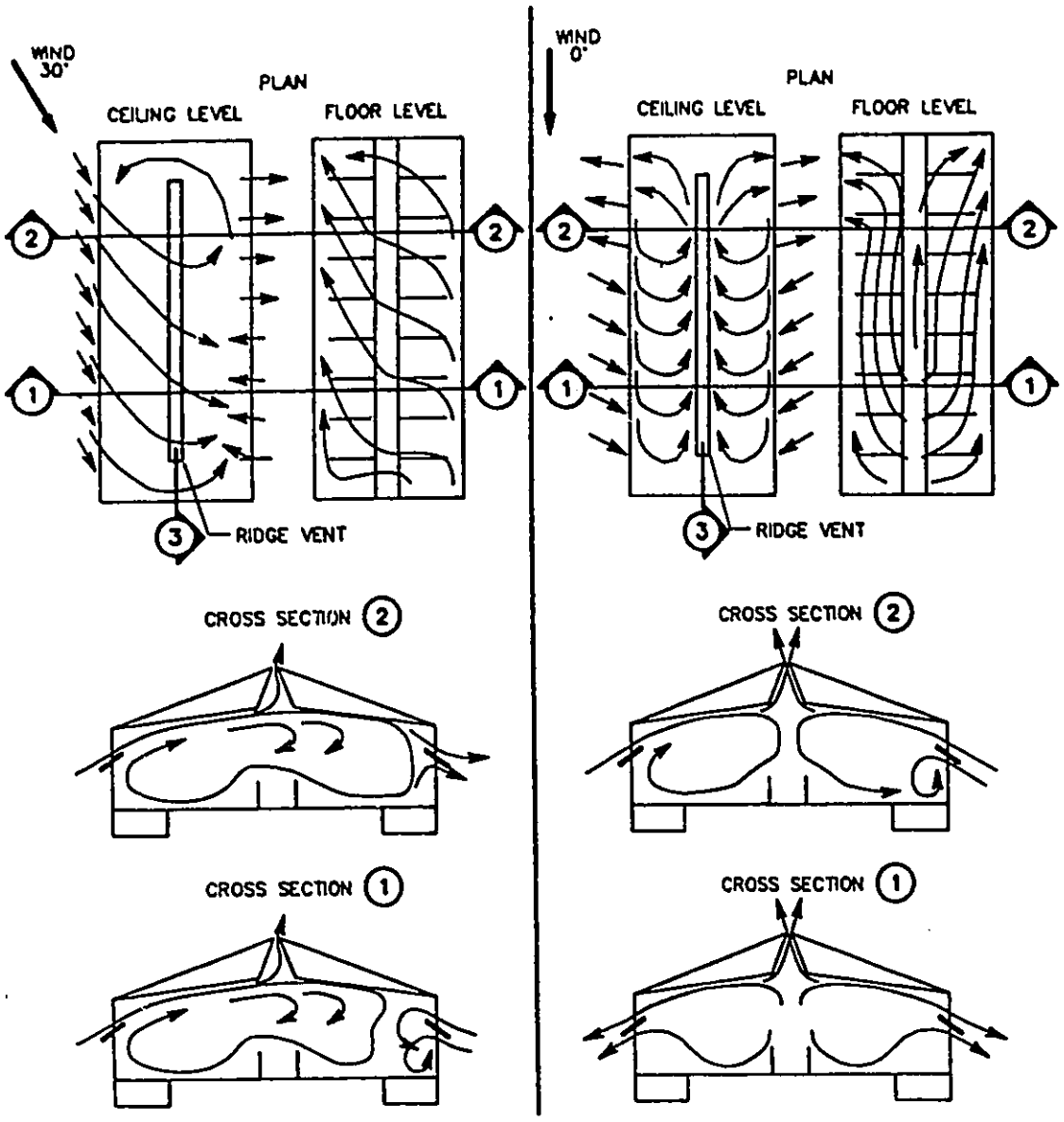

Figure F.14 Airflow patterns with standard ridge opening (150 mm full scale), doors open (30°) both sides, wind at 30° and 0° (Choinière et al., 1988c).

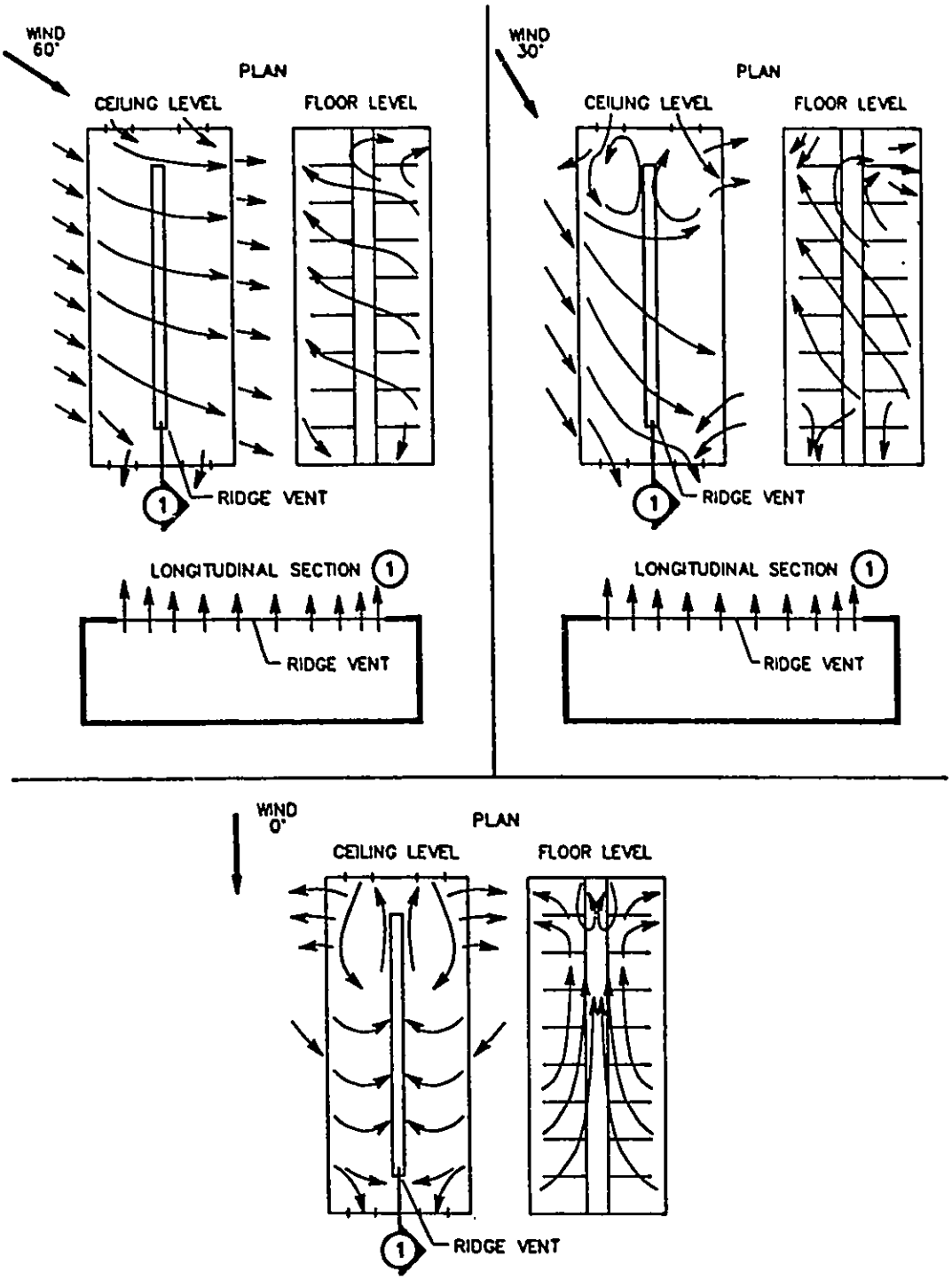

Figure F.15 Effect of openings in end walls, wind at 60°, 30° and 0° (Choinière et al., 1988c).

Table F.1 Calculated Cp_{in} for the sealed models.

Sidewall: / End Wall:	1100 mm open	1100 mm closed	800 mm open	800 mm closed
Wind Angles		150 mm Ridge		
90	-0.0138	0.0641	-0.0558	0.0341
60	-0.0087	-0.0147	-0.0327	-0.0447
45	-0.0372	-0.0612	-0.0492	-0.0792
30	-0.0676	-0.0916	-0.0736	-0.1096
20	-0.1074	-0.1314	-0.1074	-0.1434
10	-0.1080	-0.1439	-0.1080	-0.1499
0	-0.1040	-0.1459	-0.0980	-0.1459
		400 mm Ridge		
90	-0.0908	-0.0549	-0.1208	-0.1088
60	-0.1098	-0.1218	-0.1578	-0.1817
45	-0.1217	-0.1517	-0.1636	-0.2116
30	-0.1314	-0.1614	-0.1554	-0.2033
20	-0.1454	-0.1813	-0.1573	-0.2053
10	-0.1289	-0.1529	-0.1289	-0.1589
0	-0.1098	-0.1397	-0.0978	-0.1457
		Chimney		
90	-0.0061	0.0887	-0.0420	0.0768
60	-0.0022	0.0218	-0.0022	0.0098
45	0.0028	-0.0212	0.0028	-0.0332
30	-0.0505	-0.0804	-0.0445	-0.0864
20	-0.0918	-0.1158	-0.0918	-0.1218
10	-0.1021	-0.1321	-0.0961	-0.1321
0	-0.1077	-0.1496	-0.1017	-0.1556

Table F.2 Calculated Cp_{in} for the open models.

Sidewall: End Wall:	1100 mm open	1100 mm closed	800 mm open	800 mm closed
Wind Angles		150 mm Ridge		
90	-0.1048	0.0004	-0.1268	0.0089
60	-0.0657	-0.0572	-0.0682	-0.0605
45	-0.0678	-0.0791	-0.0616	-0.0813
30	-0.0992	-0.1392	-0.0896	-0.1363
20	-0.1463	-0.1839	-0.1253	-0.1630
10	-0.1439	-0.1974	-0.1308	-0.1764
0	-0.1536	-0.2256	-0.1220	-0.1908
		400 mm Ridge		
90	-0.1770	-0.1466	-0.2004	-0.1639
60	-0.1977	-0.2269	-0.2346	-0.2726
45	-0.1960	-0.2267	-0.2250*	-0.2624
30	-0.1984	-0.2303	-0.2048*	-0.2717
20	-0.1985	-0.2384	-0.1940*	-0.2848
10	-0.1713	-0.2050	-0.1593*	-0.2692
0	-0.1471	-0.2116	-0.1203*	-0.2668
		Chimney		
90	-0.0868	0.0821	-0.0735	0.0844
60	-0.0002	0.0208	-0.0060	0.0195
45	-0.0205	-0.0428	-0.0272	-0.0434
30	-0.0778	-0.1282	-0.0726	-0.1156
20	-0.1363	-0.1826	-0.1082	-0.1592
10	-0.1443	-0.2101	-0.1238	-0.1765
0	-0.1591	-0.2228	-0.1237	-0.1876

* Recording problems at ridge level during wind tunnel tests.

APPENDIX G

Air inlet and outlet zones based on pressure differences, complete data

The local ΔCps for the open and sealed models are presented in Figs. G.1 to G.24.

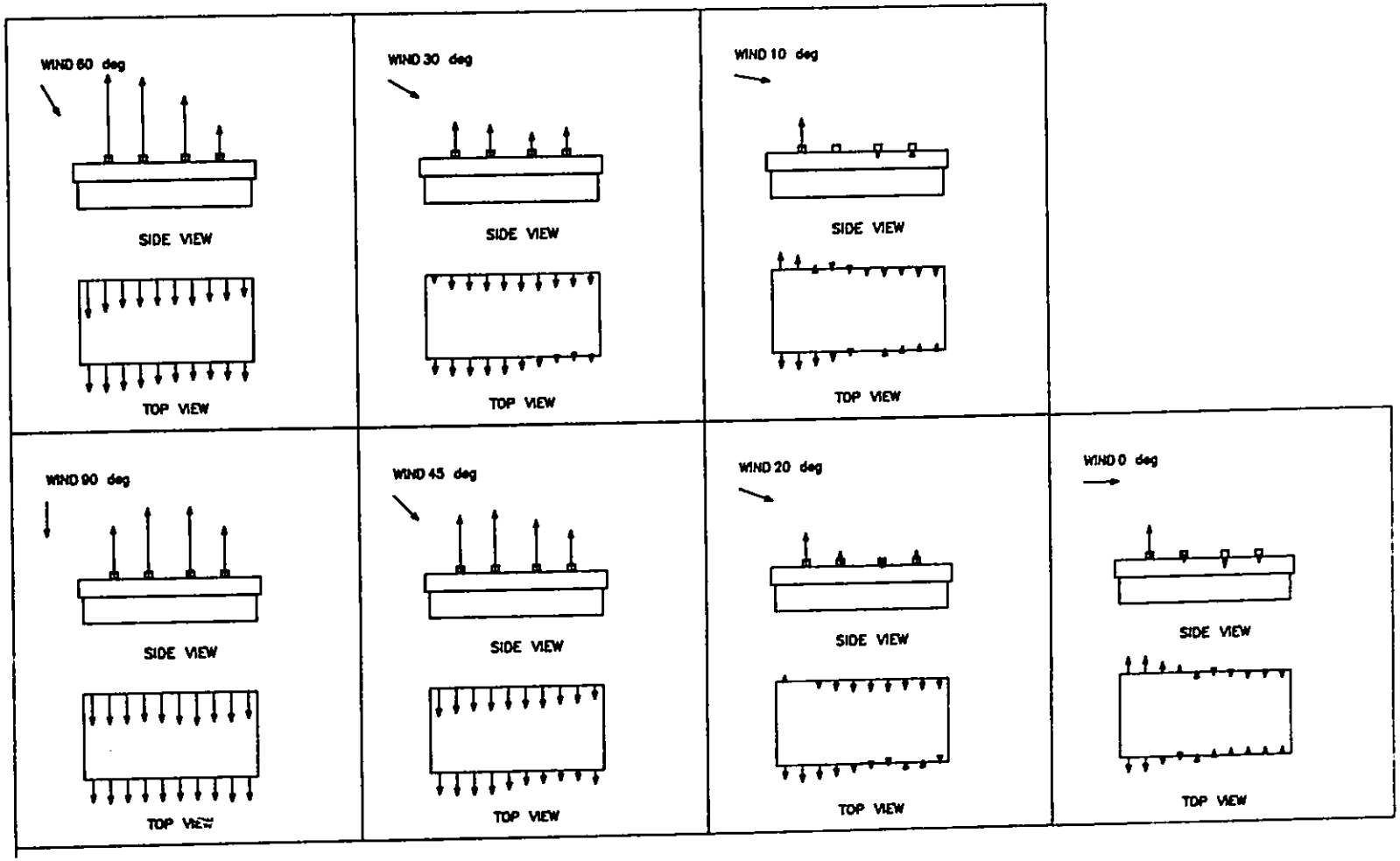

Figure G.1 ΔCps (in-out): open model, chimney, simulated 800 mm sidewall openings, closed end walls, 7 wind angles of incidence.

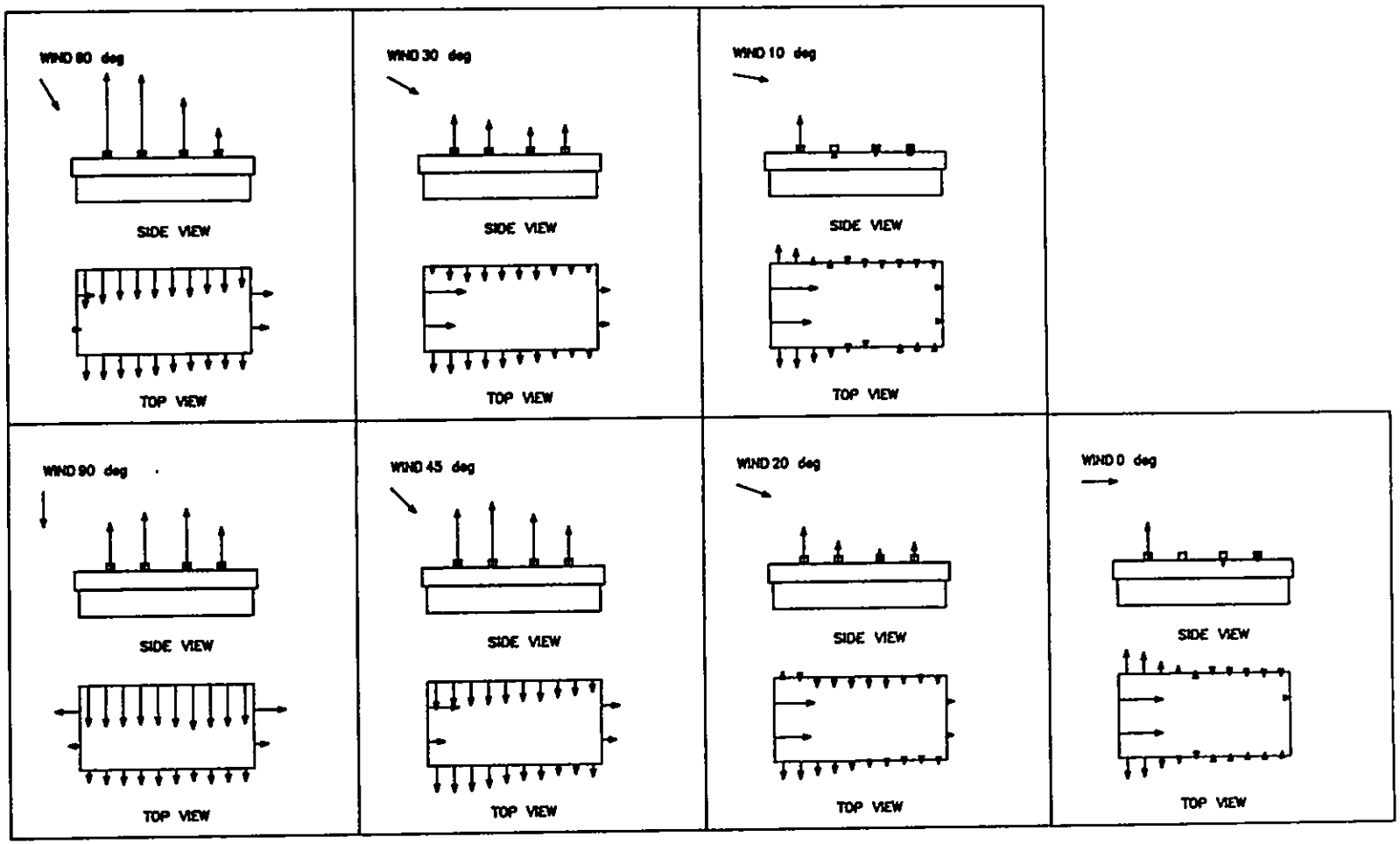

Figure G.2 ΔCps (in-out): open model, chimney, simulated 800 mm sidewall openings, open end walls, 7 wind angles of incidence.

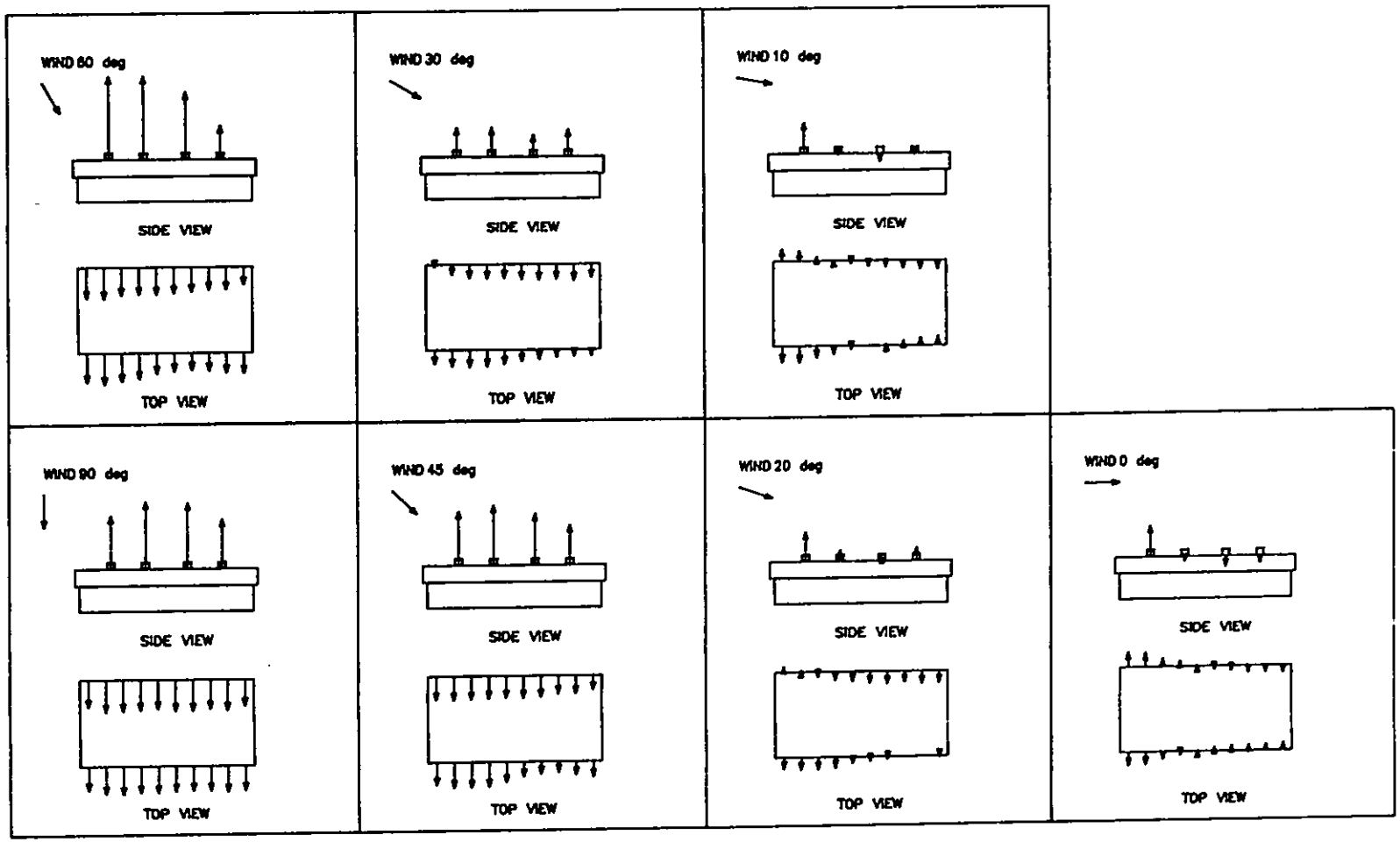

Figure G.3 ΔCps (in-out): open model, chimney, simulated 1100 mm sidewall openings, closed end walls, 7 wind angles of incidence.

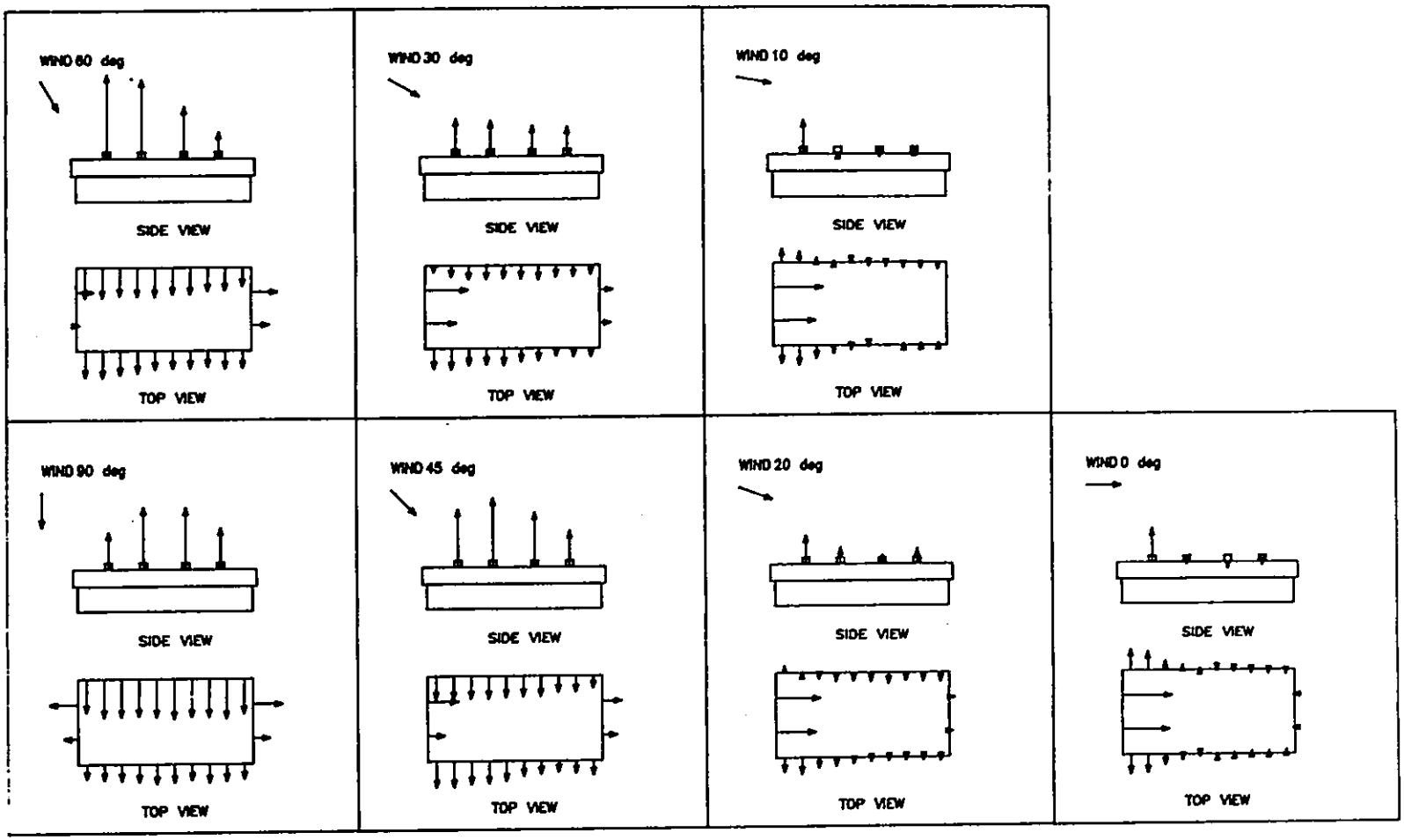

Figure G.4 ΔCps (in-out): open model, chimney, simulated 1100 mm sidewall openings, open end walls, 7 wind angles of incidence.

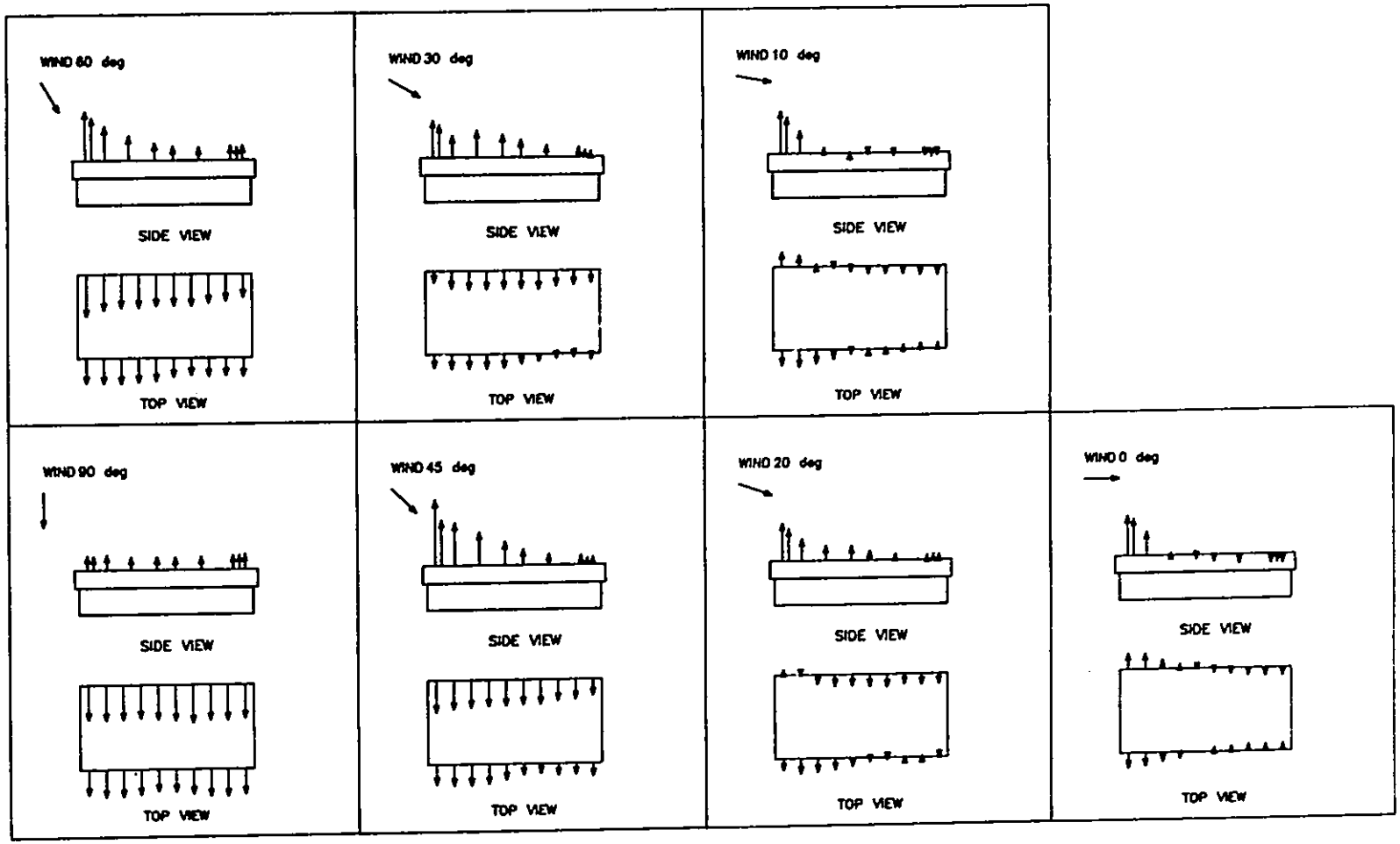

Figure G.5 ΔCps (in-out): open model, simulated 150 mm ridge and 800 mm sidewall openings, closed end walls, 7 wind angles of incidence.

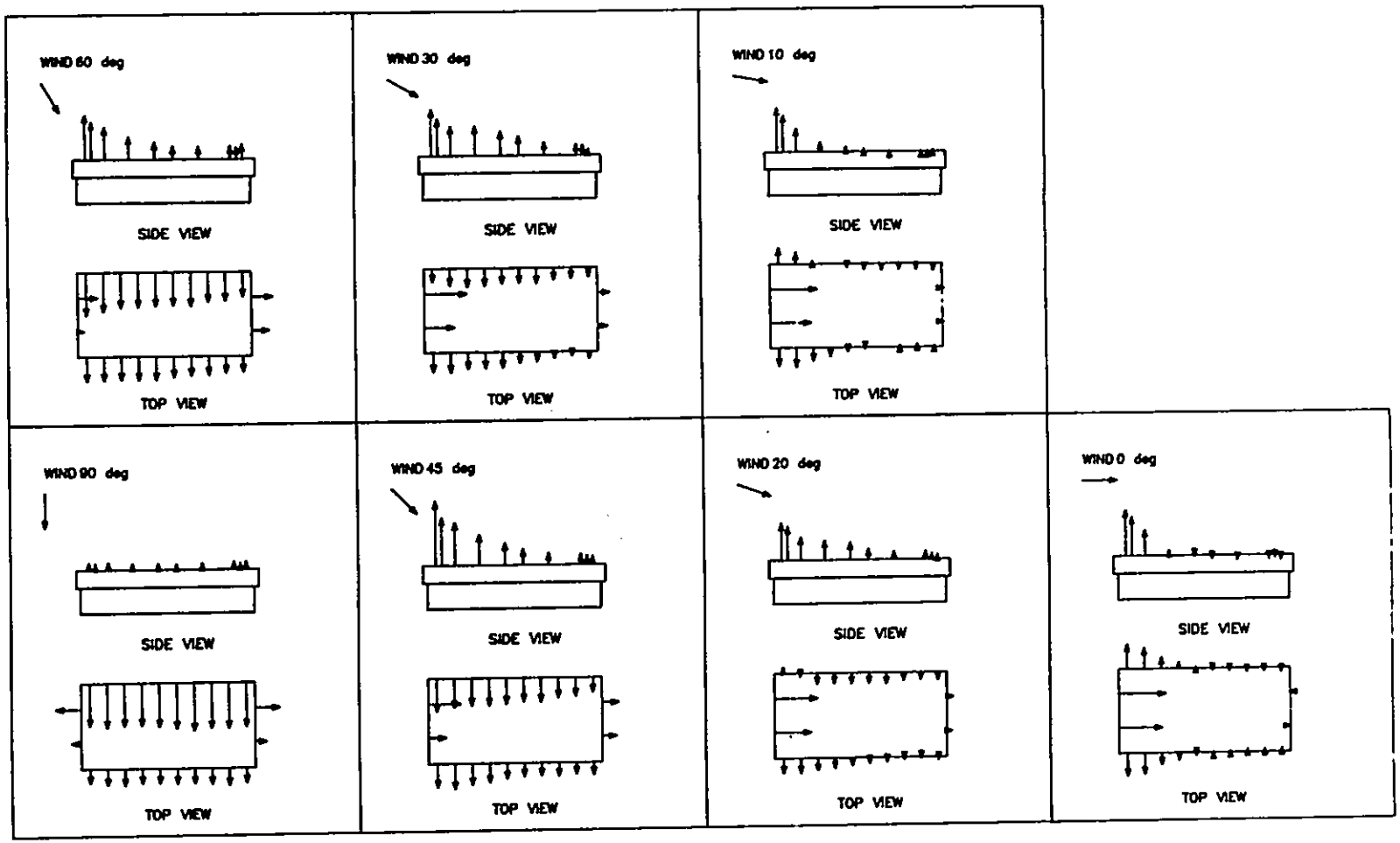

Figure G.6 ΔCps (in-out): open model, simulated 150 mm ridge and 800 mm sidewall openings, open end walls, 7 wind angles of incidence.

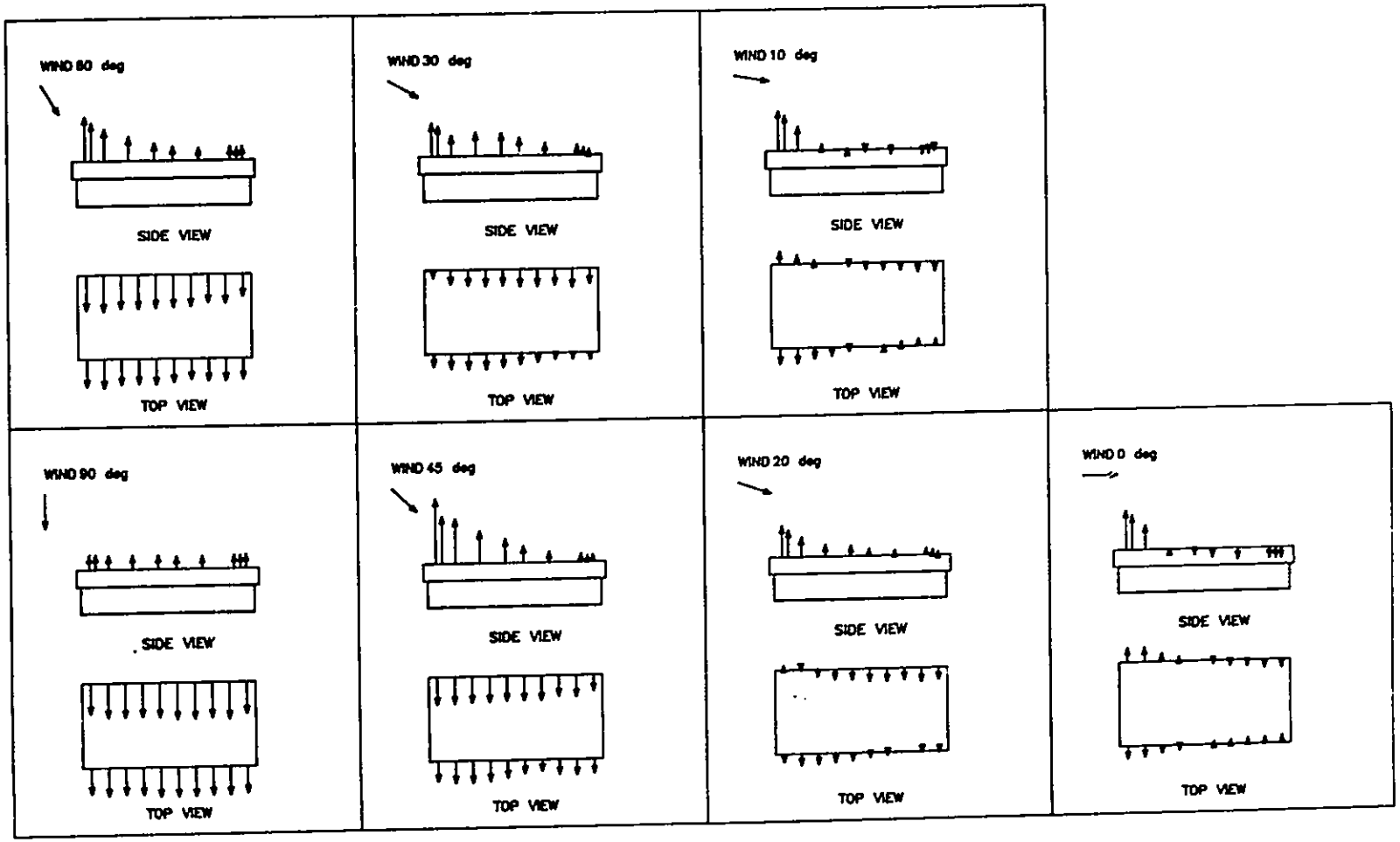

Figure G.7 ΔCps (in-out): open model, simulated 150 mm ridge and 1100 mm sidewall openings, closed end walls, 7 wind angles of incidence.

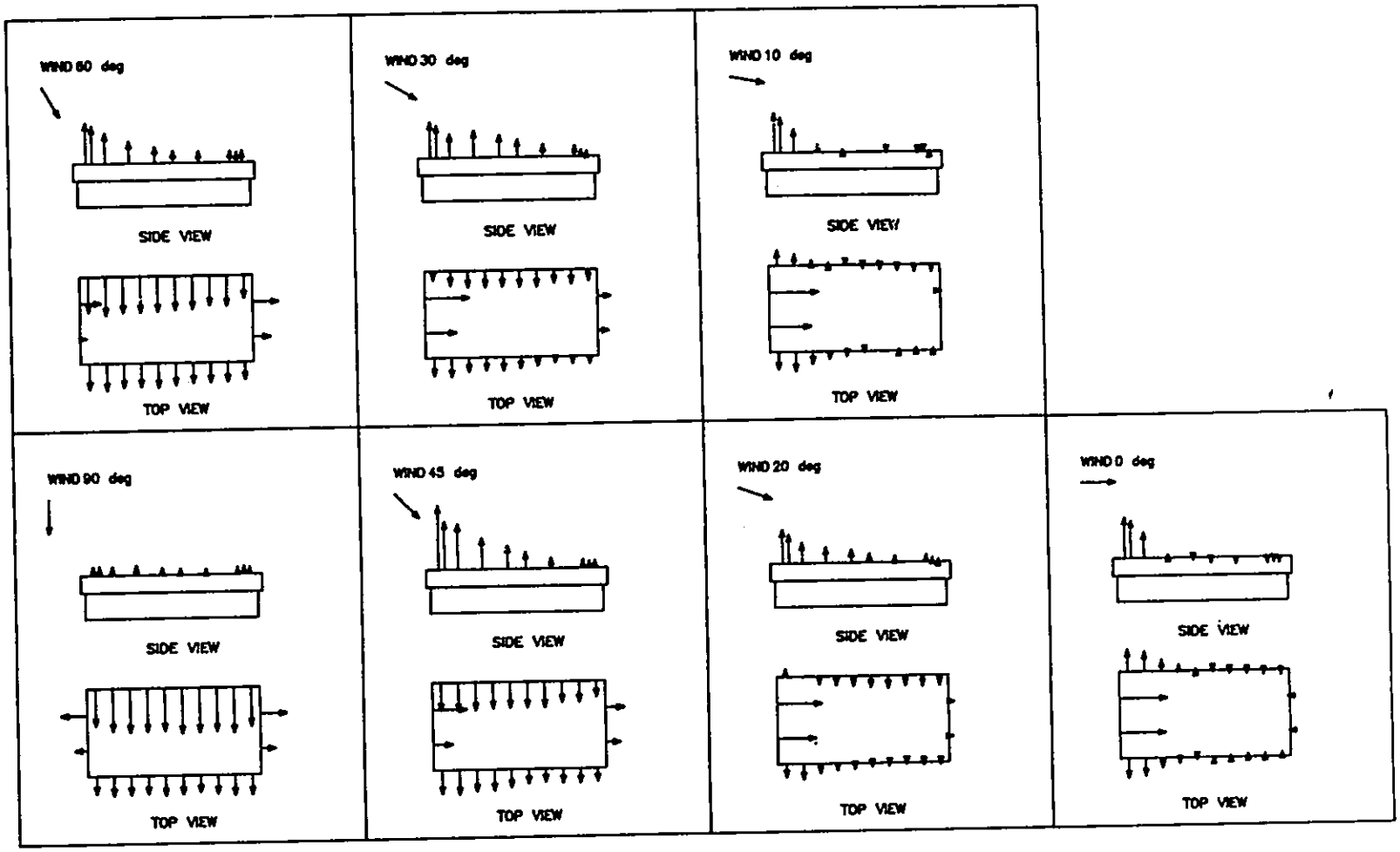

Figure G.8 ΔCps (in-out): open model, simulated 150 mm ridge and 1100 mm sidewall openings, open end walls, 7 wind angles of incidence.

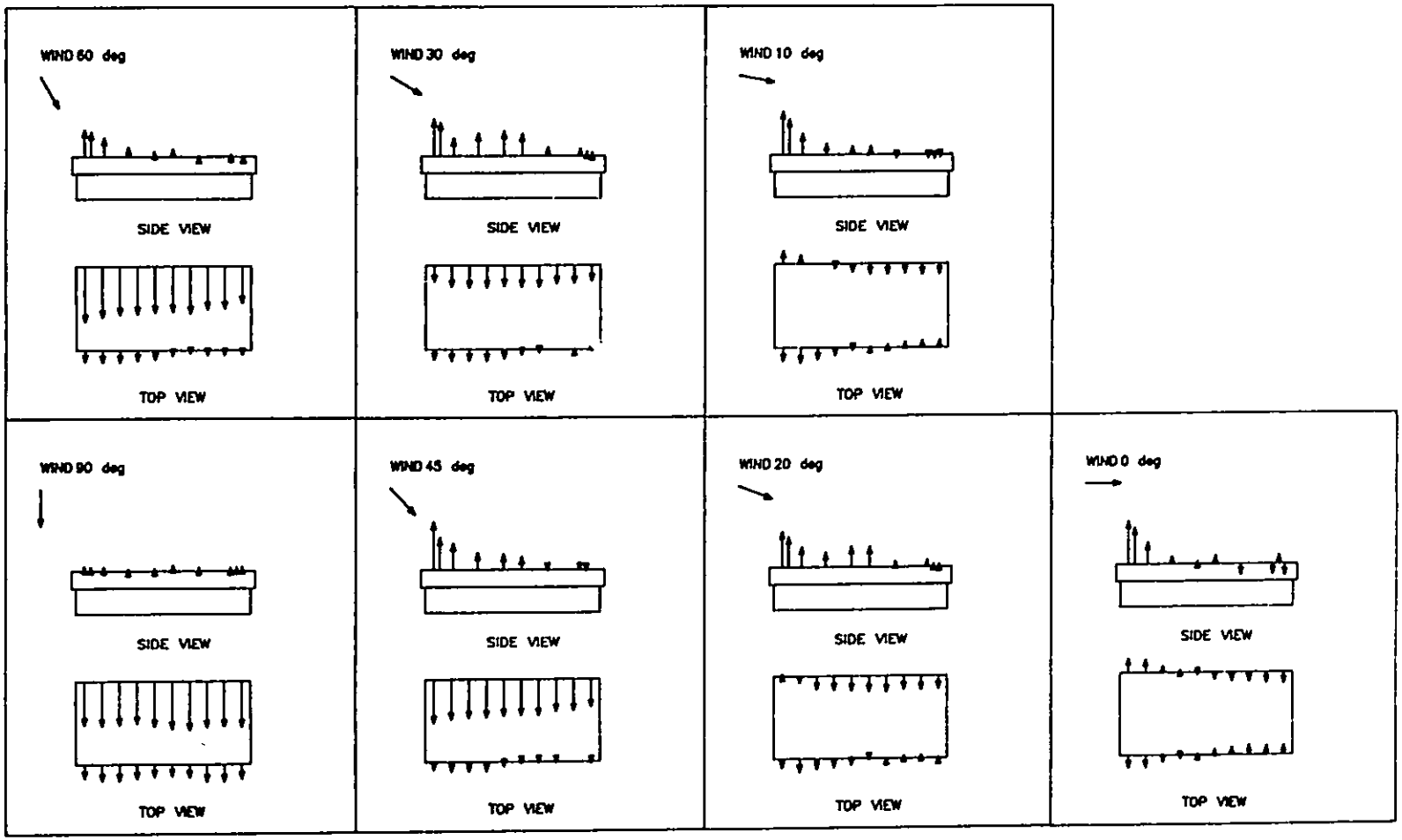

Figure G.9 ΔCps (in-out): open model, simulated 400 mm ridge and 800 mm sidewall openings, closed end walls, 7 wind angles of incidence.

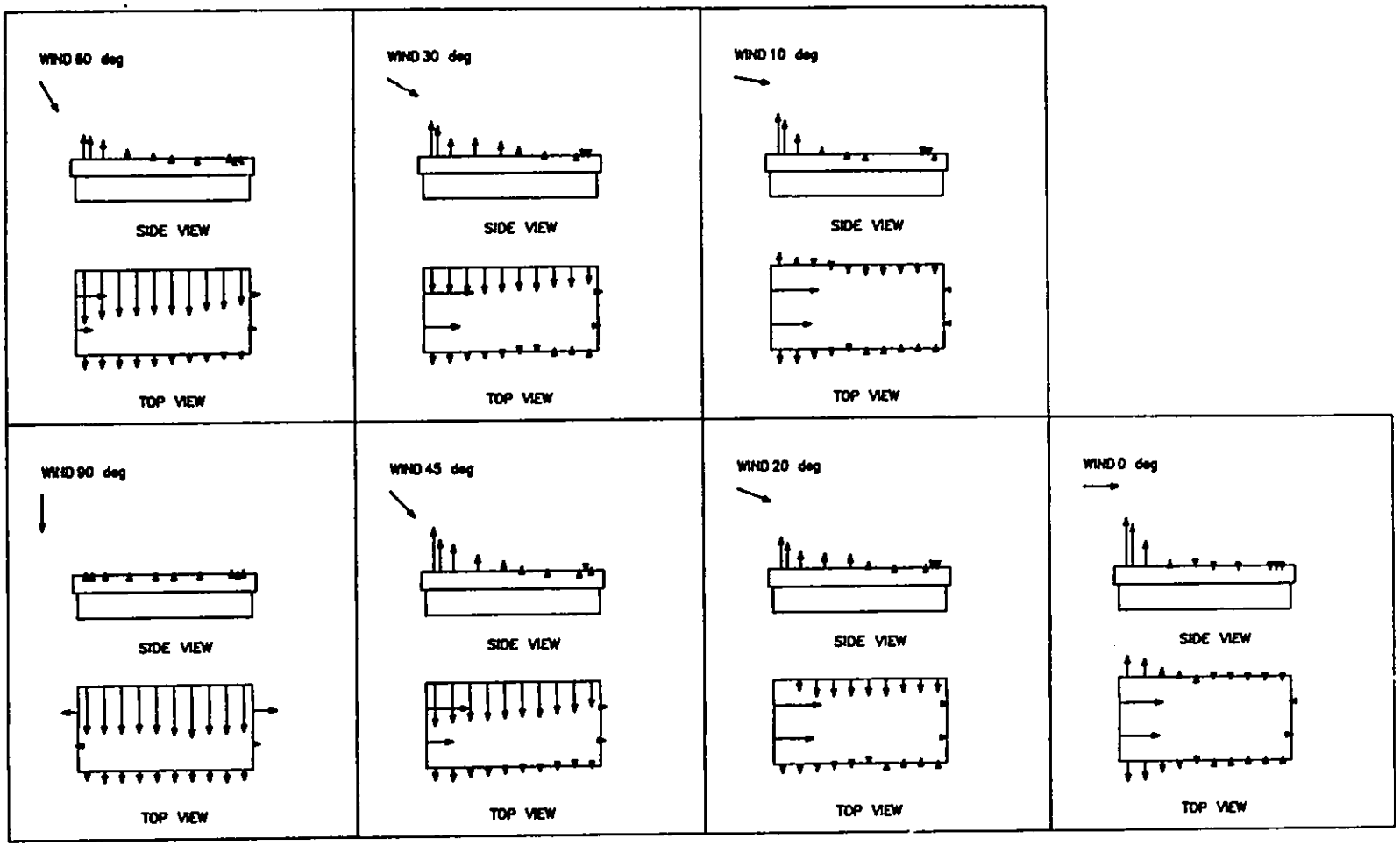

Figure G.10 ΔCps (in-out): open model, simulated 400 mm ridge and 800 mm sidewall openings, open end walls, 7 wind angles of incidence.

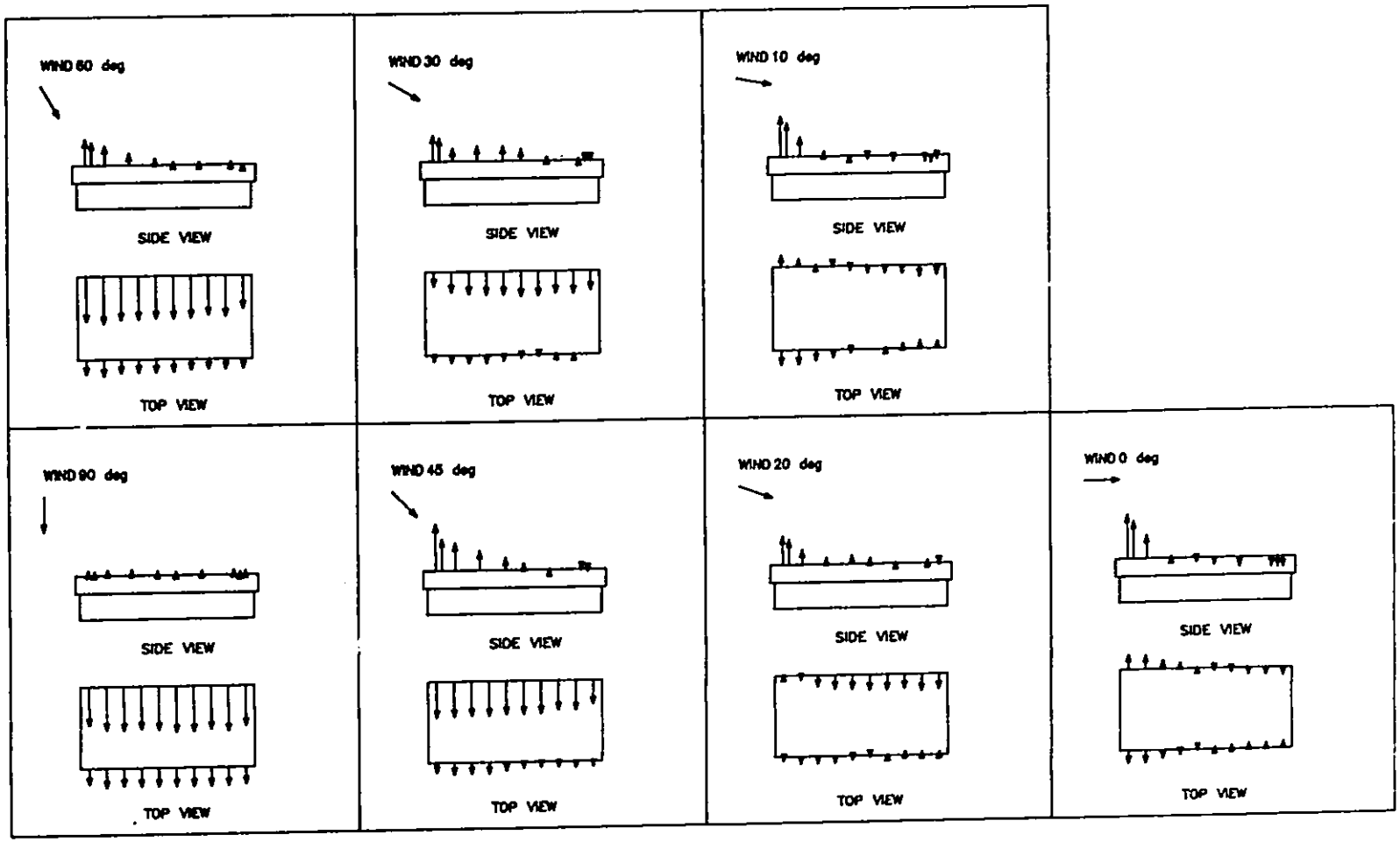

Figure G.11 ΔCps (in-out): open model, simulated 400 mm ridge and 1100 mm sidewall openings, closed end walls, 7 wind angles of incidence.

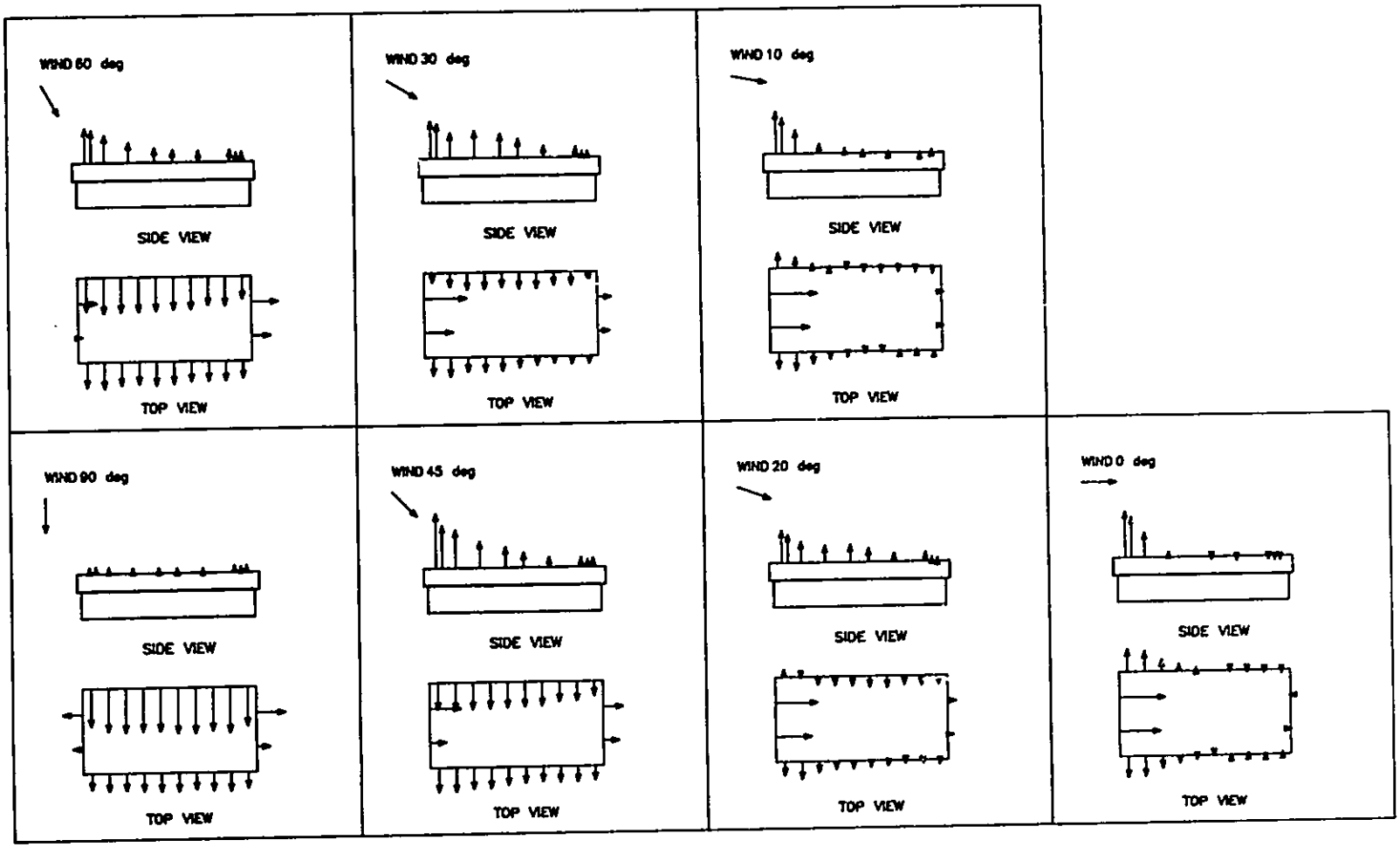

Figure G.12 ΔCps (in-out): open model, simulated 400 mm ridge and 1100 mm sidewall openings, open end walls, 7 wind angles of incidence.

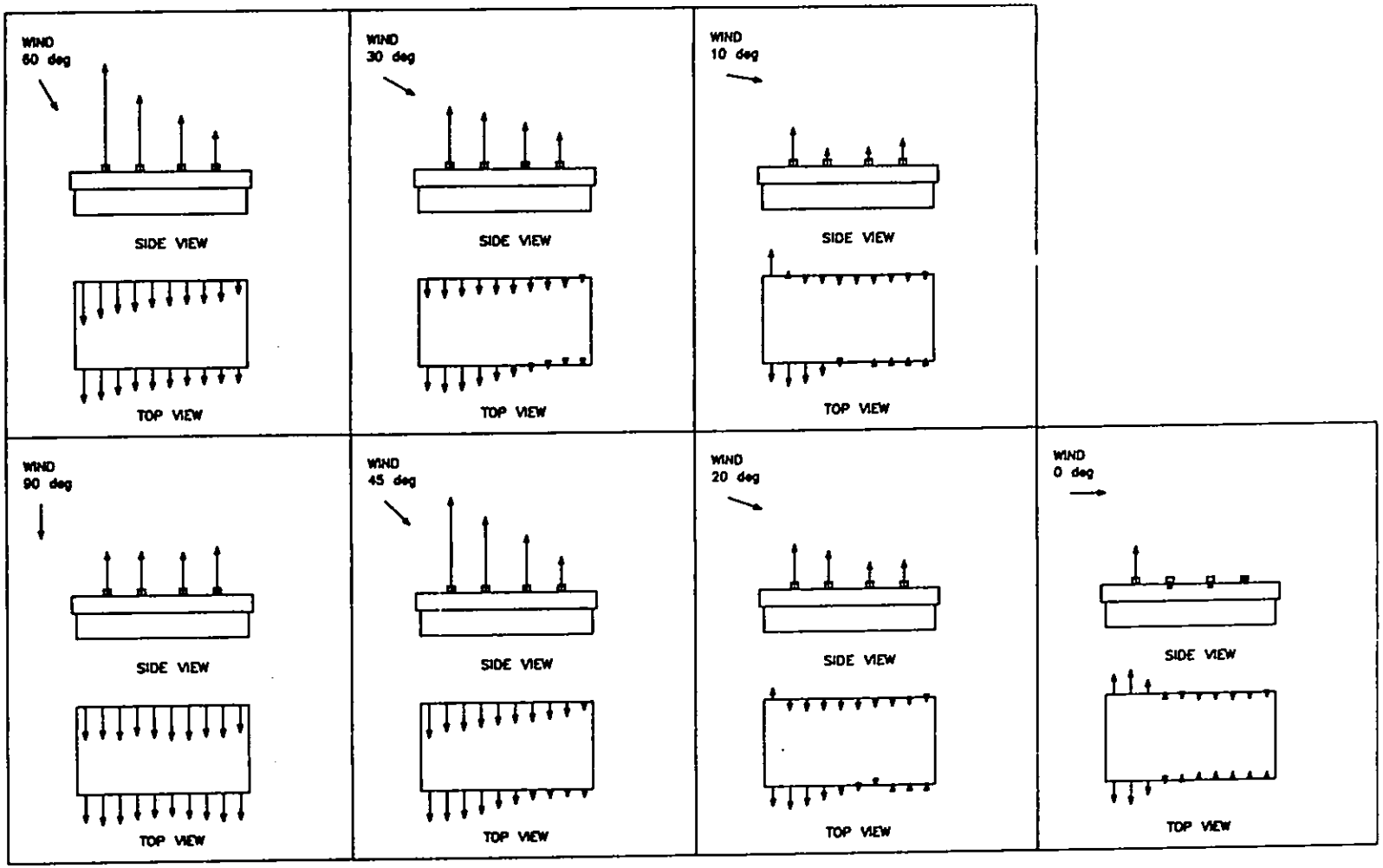

Figure G.13 ΔCps (in-out): sealed model, chimney, simulated 800 mm sidewall openings, closed end walls, 7 wind angles of incidence.

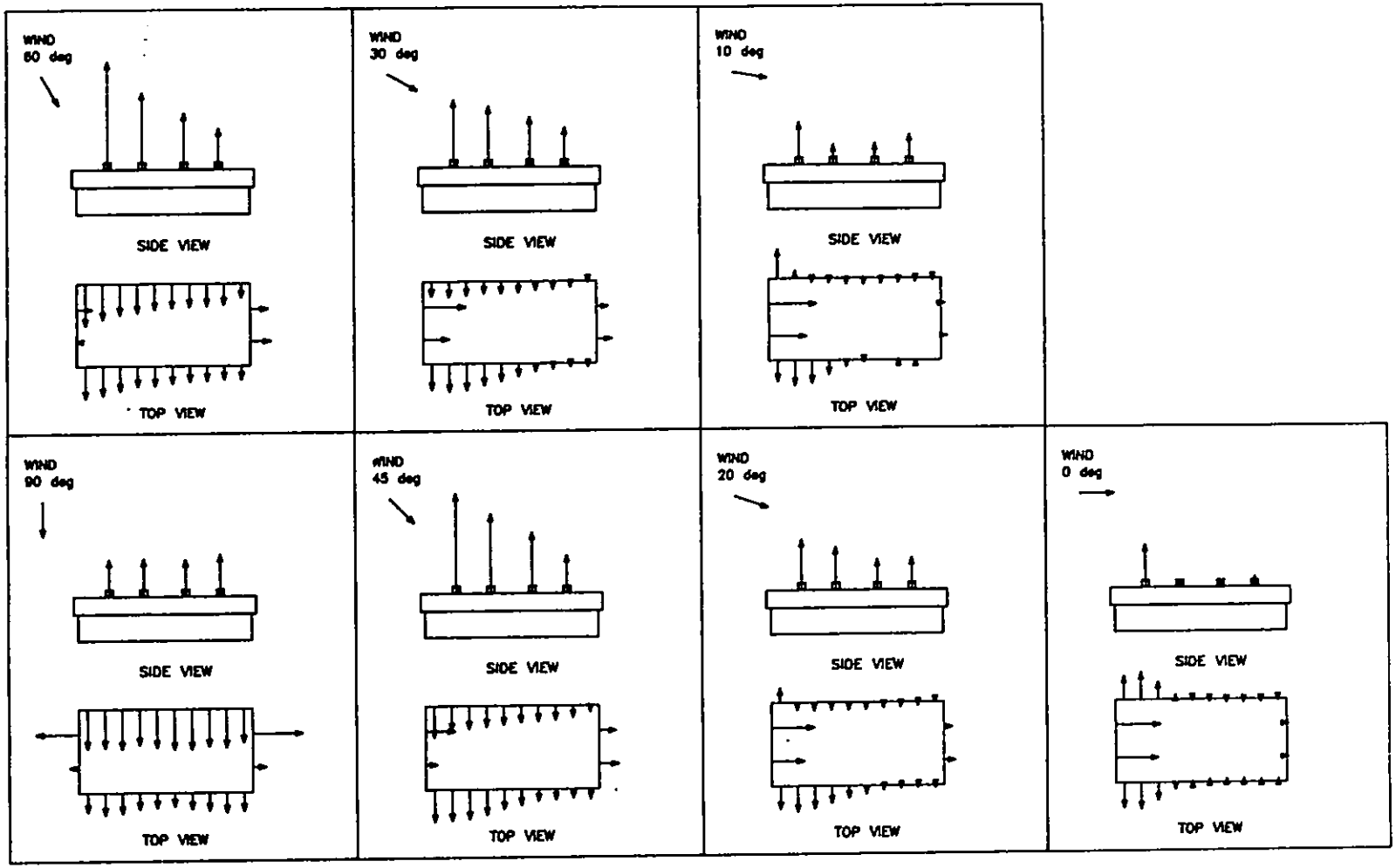

Figure G.14 ΔCps (in-out): sealed model, chimney, simulated 800 mm sidewall openings, open end walls, 7 wind angles of incidence.

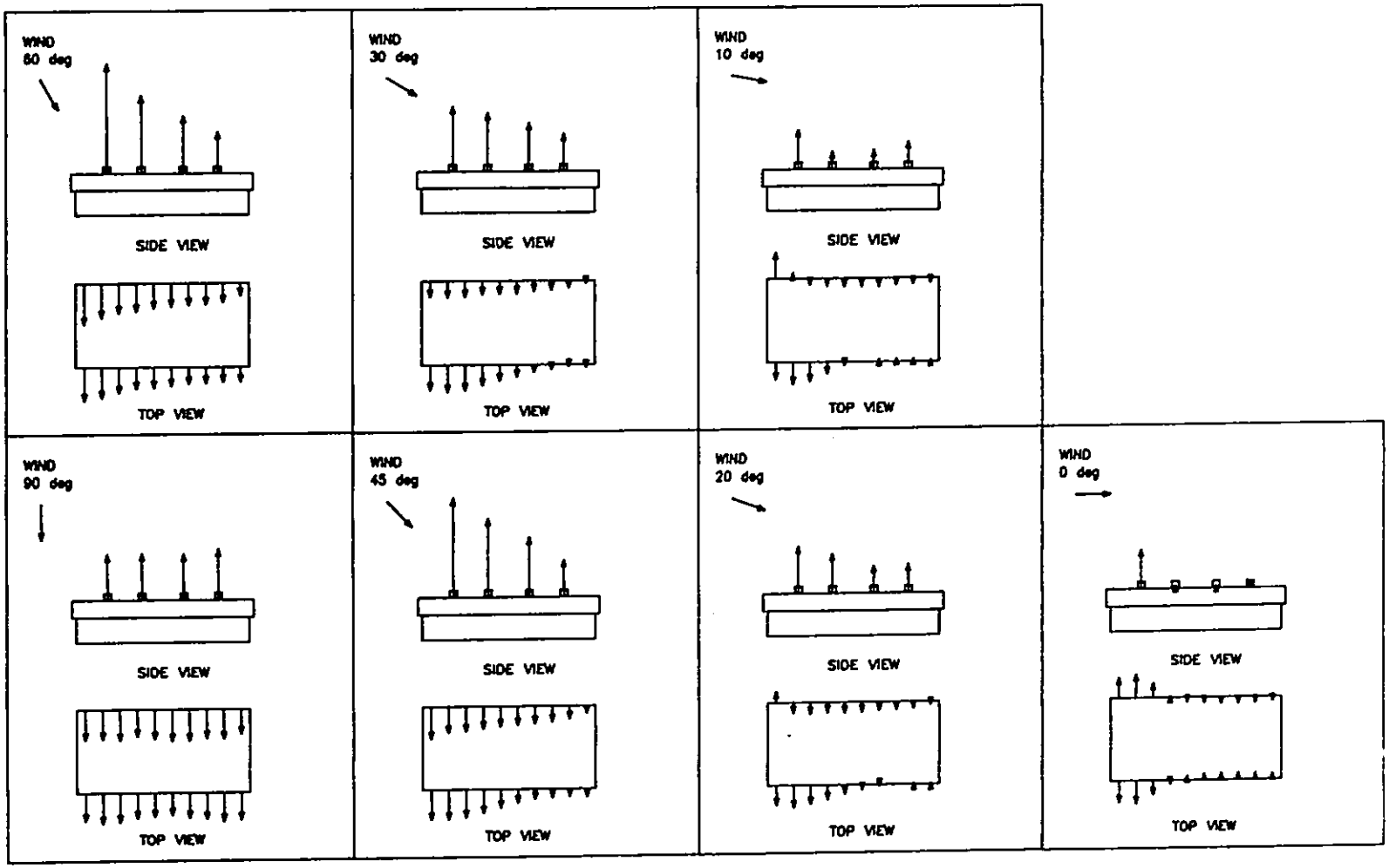

Figure G.15 ΔCps (in-out): sealed model, chimney, simulated 1100 mm sidewall openings, closed end walls, 7 wind angles of incidence.

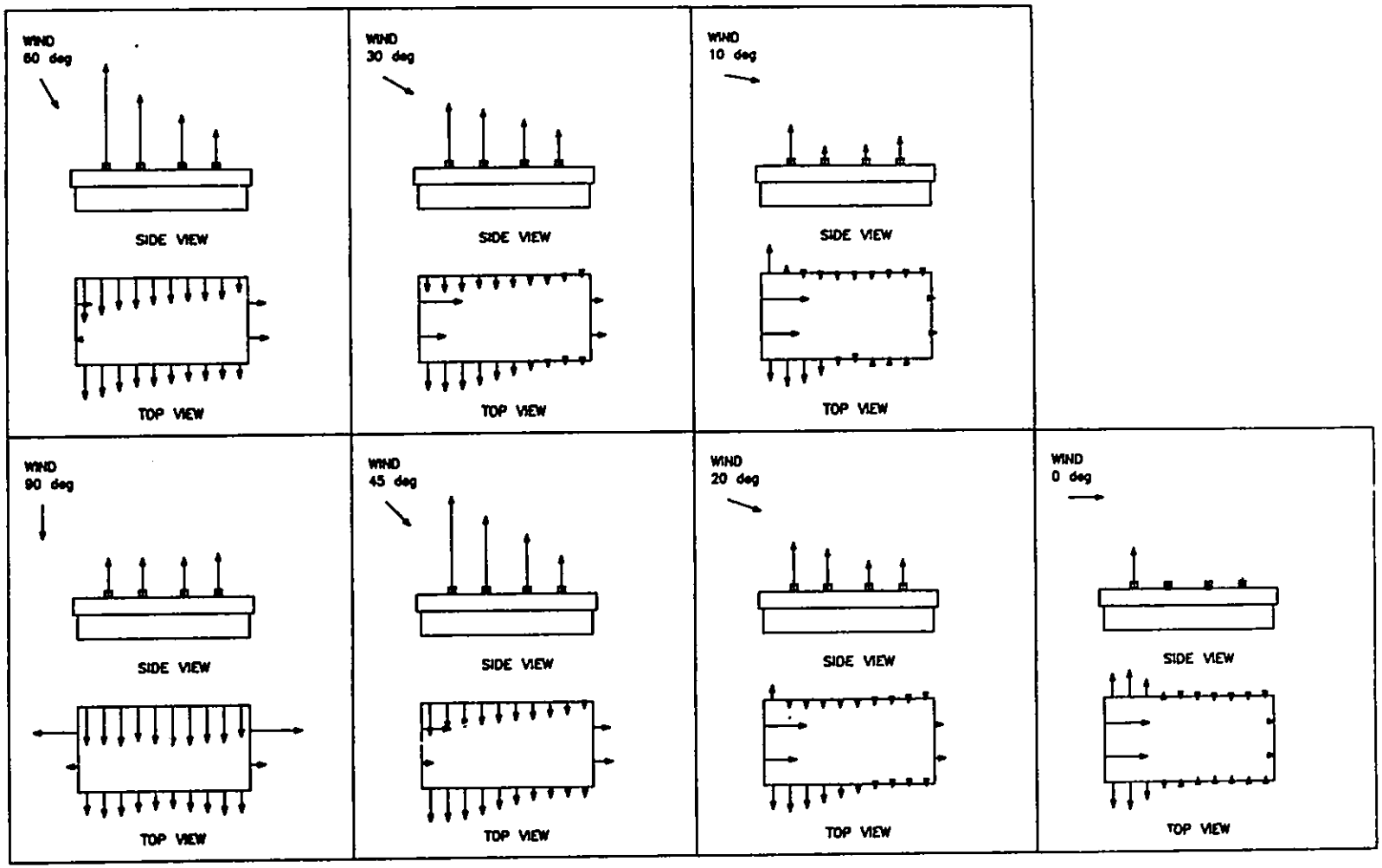

Figure G.16 ΔCps (in-out): sealed model, chimney, simulated 1100 mm sidewall openings, open end walls, 7 wind angles of incidence.

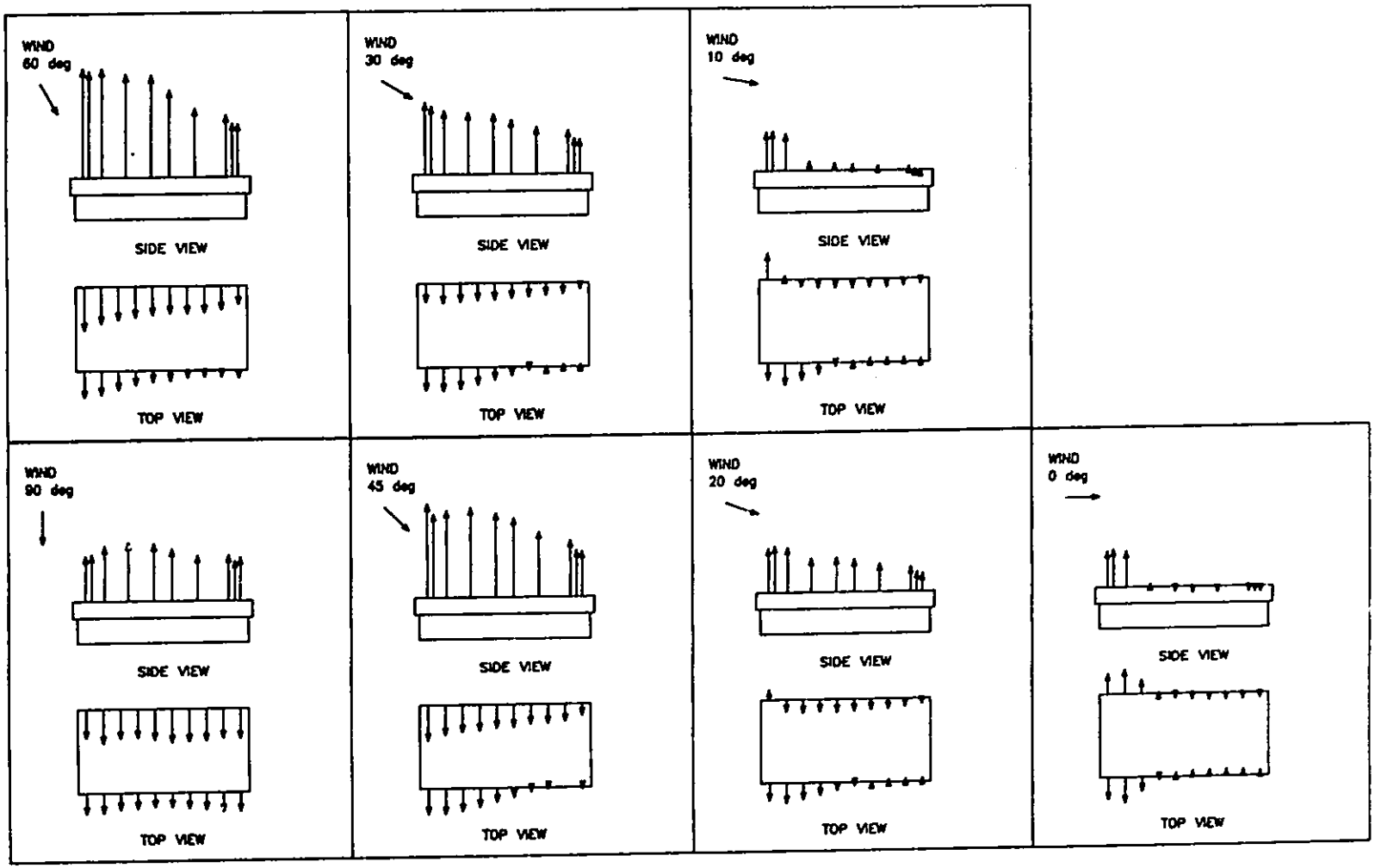

Figure G.17 ΔCps (in-out): sealed model, simulated 150 mm ridge and 800 mm sidewall openings, closed end walls, 7 wind angles of incidence.

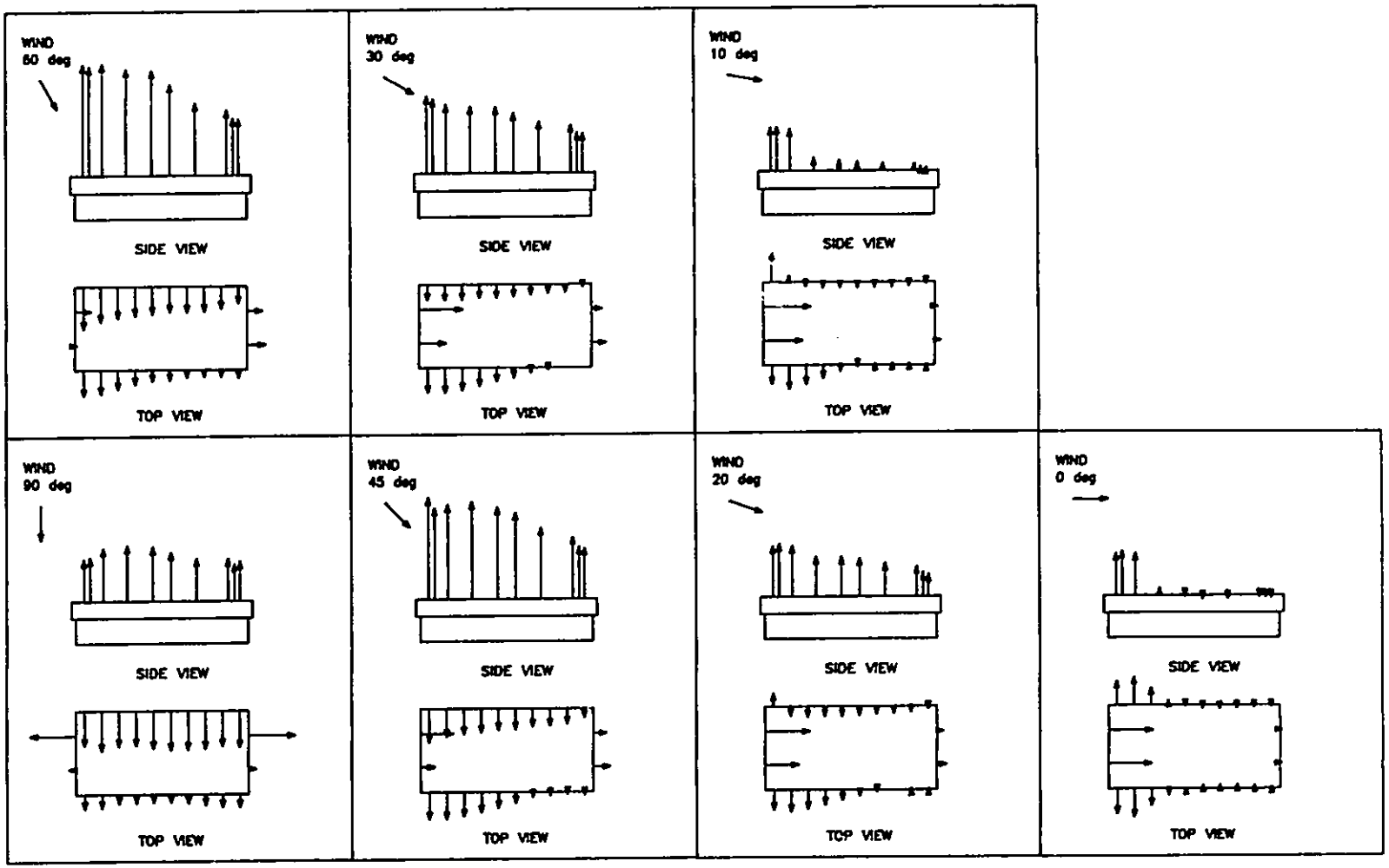

Figure G.18 ΔCps (in-out): sealed model, simulated 150 mm ridge and 800 mm sidewall openings, open end walls, 7 wind angles of incidence.

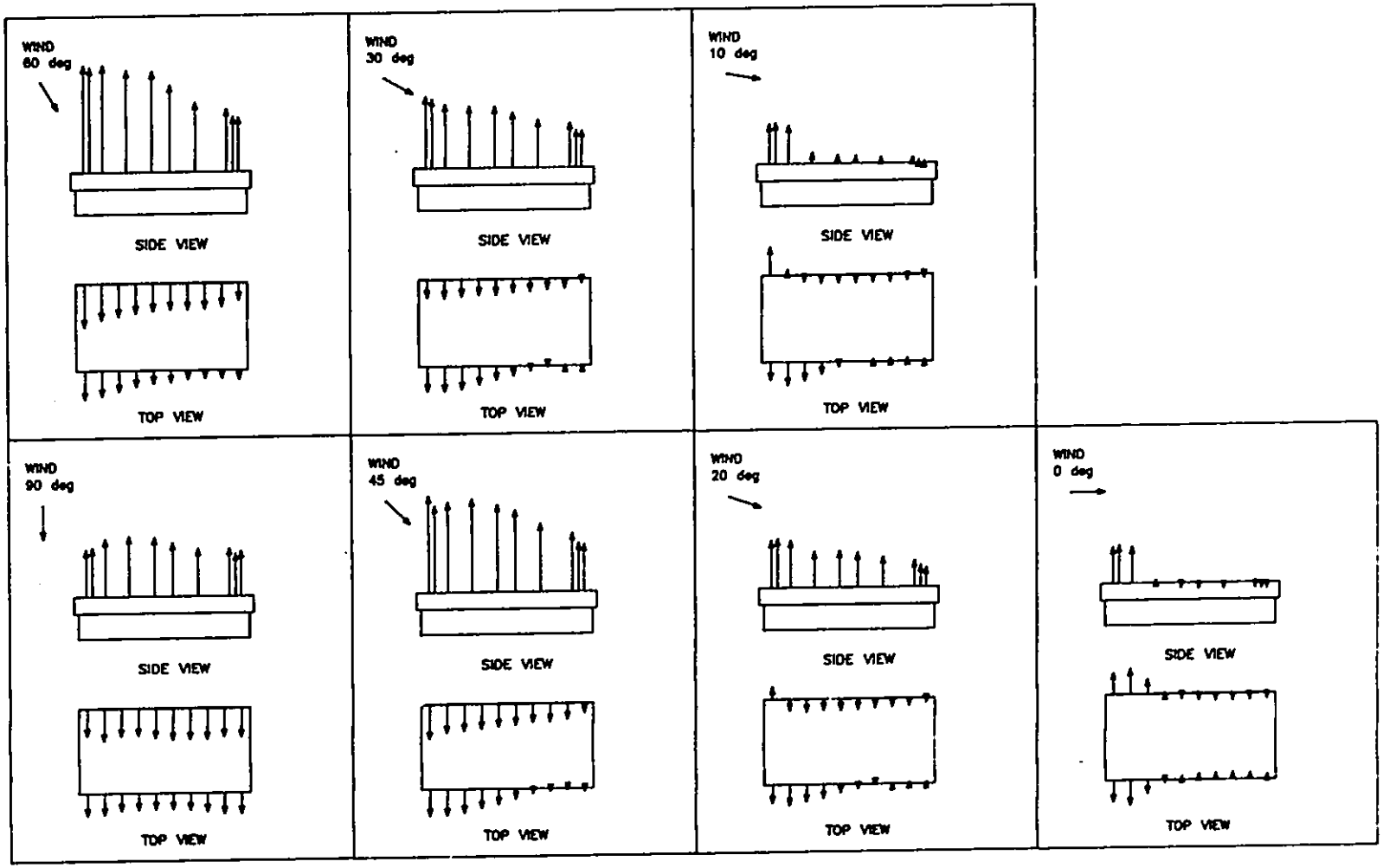

Figure G.19 ΔCps (in-out): sealed model, simulated 150 mm ridge and 1100 mm sidewall openings, closed end walls, 7 wind angles of incidence.

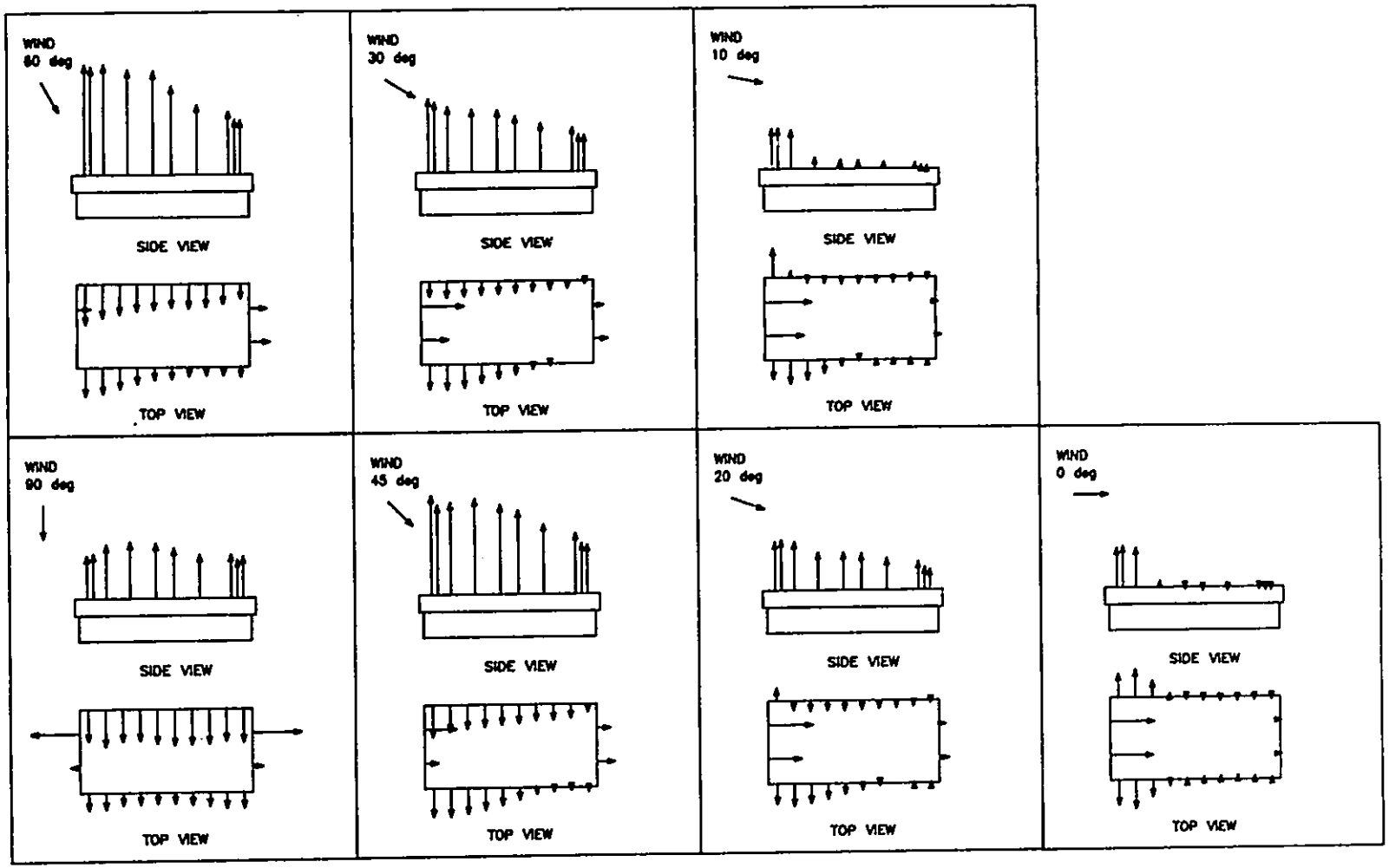

Figure G.20 ΔCps (in-out): sealed model, simulated 150 mm ridge and 1100 mm sidewall openings, open end walls, 7 wind angles of incidence.

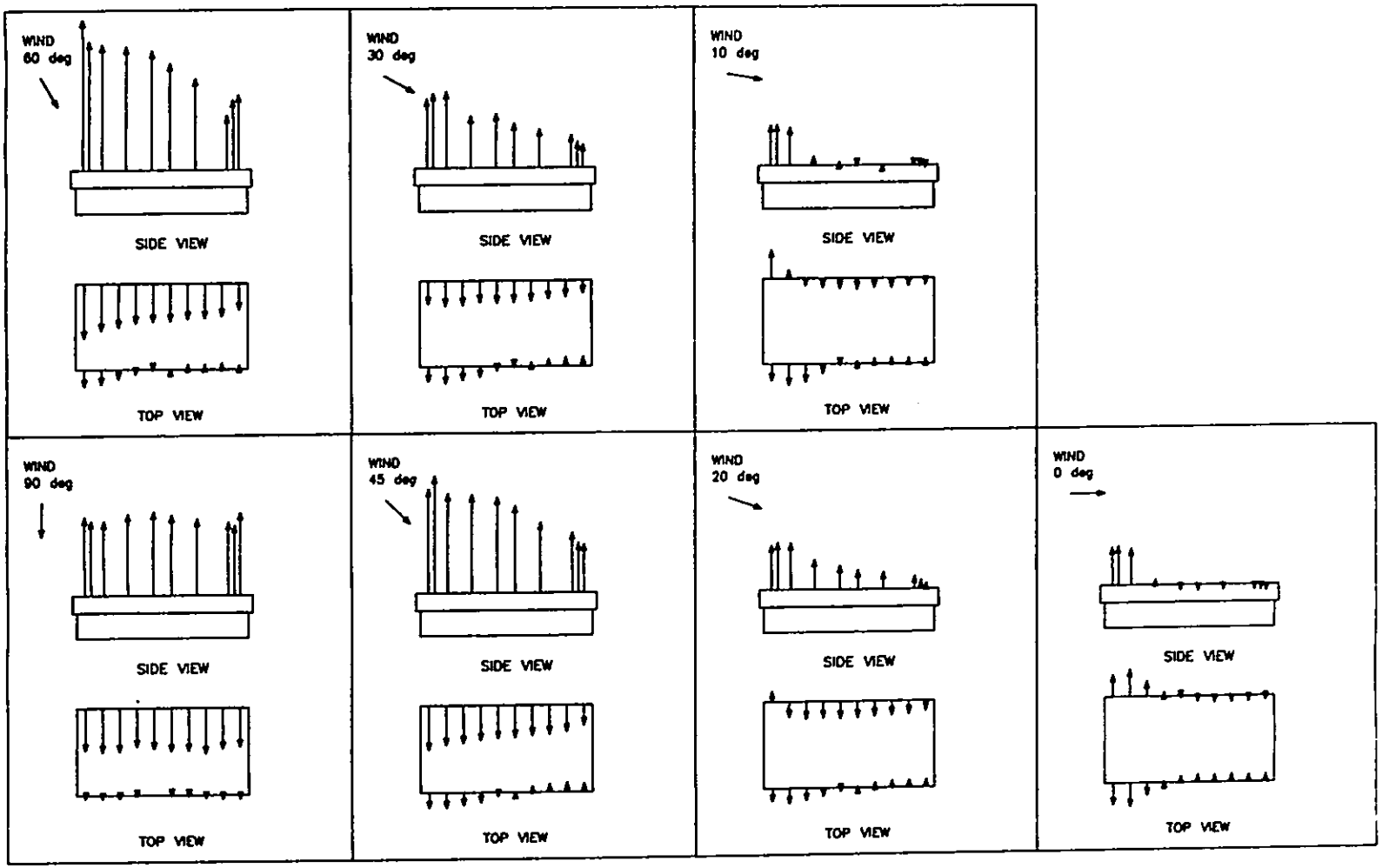

Figure G.21 ΔCps (in-out): sealed model, simulated 400 mm ridge and 800 mm sidewall openings, closed end walls, 7 wind angles of incidence.

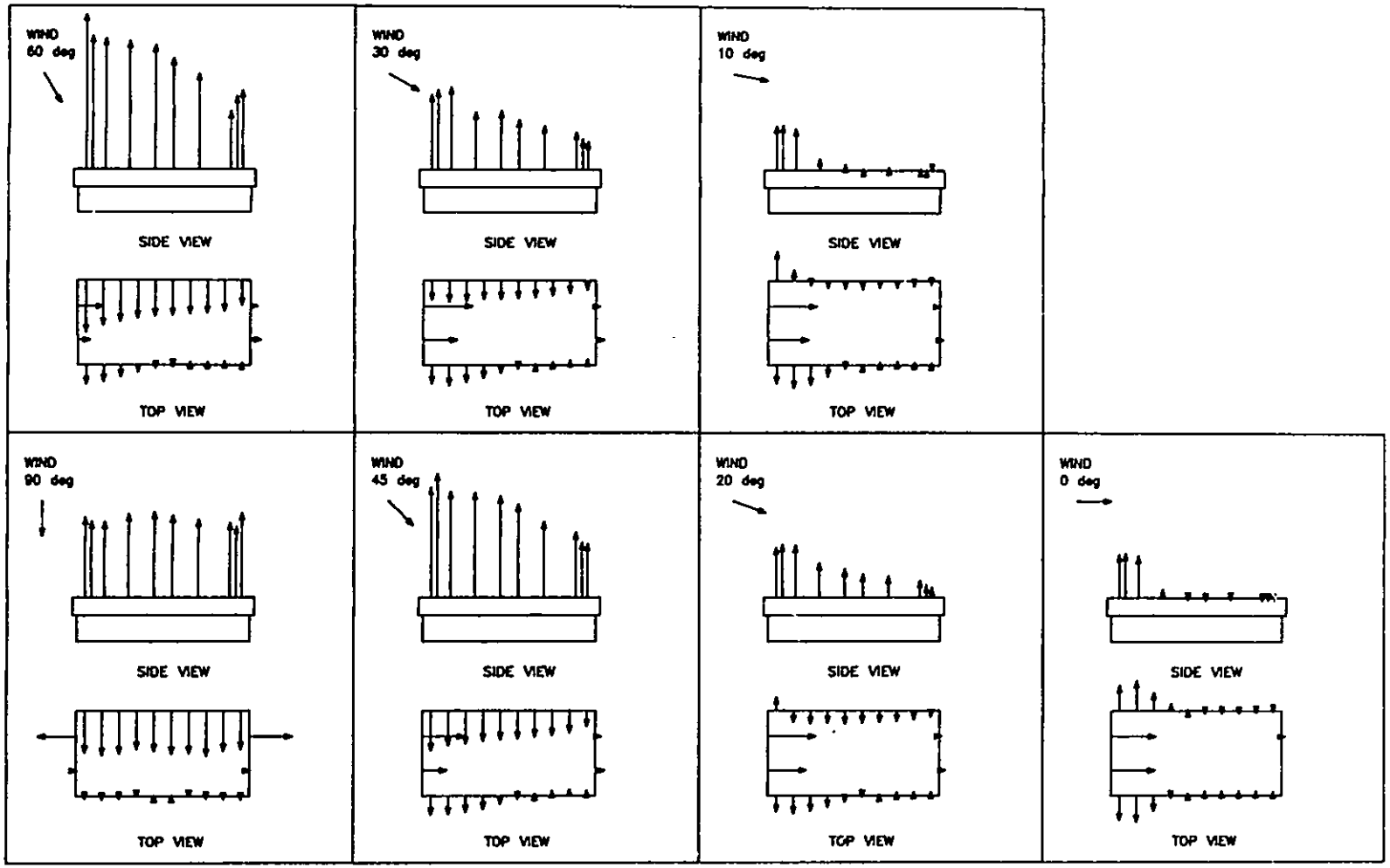

Figure G.22 ΔCps (in-out): sealed model, simulated 400 mm ridge and 800 mm sidewall openings, open end walls, 7 wind angles of incidence.

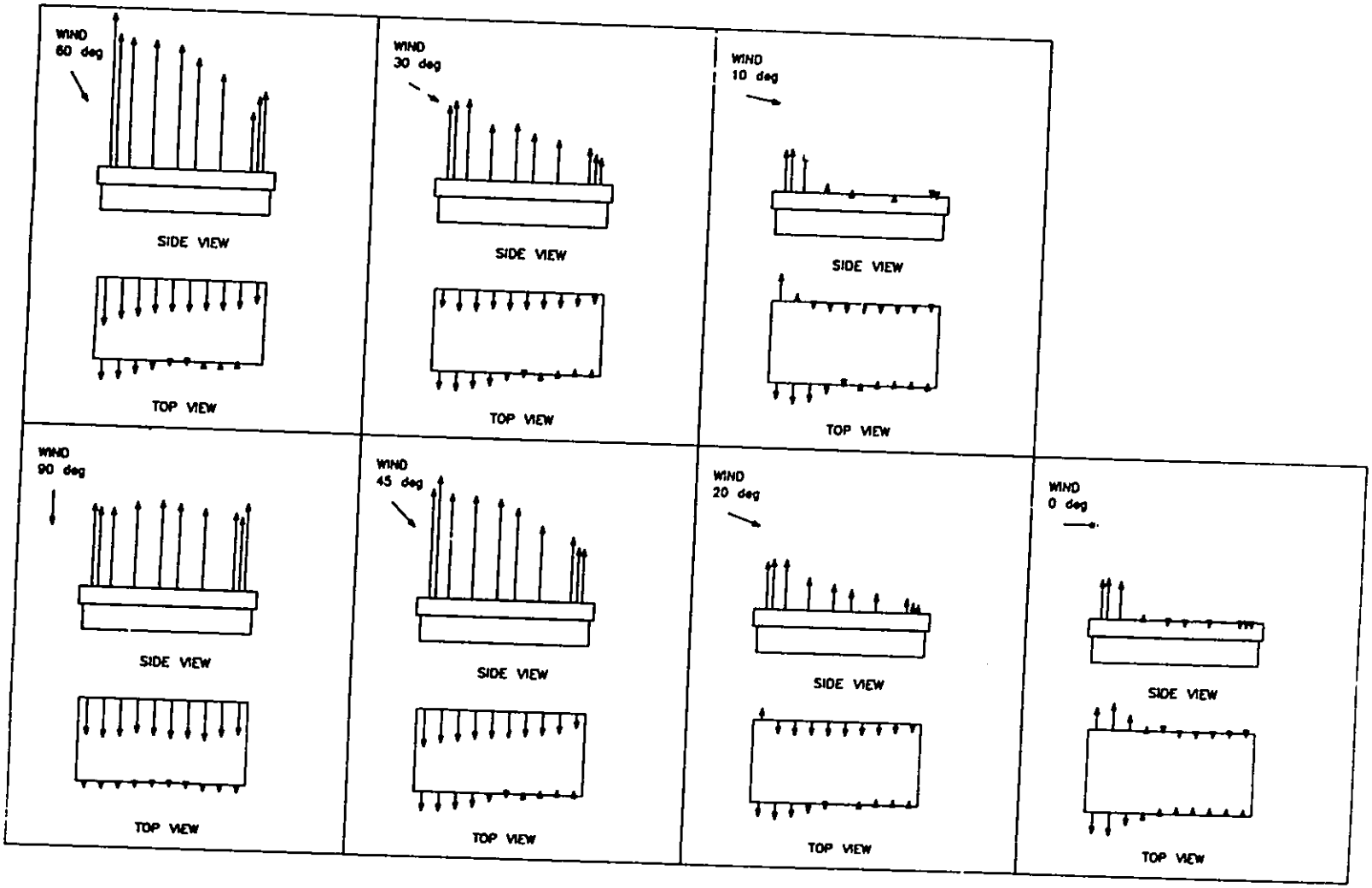

Figure G.23 ΔCps (in-out): sealed model, simulated 400 mm ridge and 1100 mm sidewall openings, closed end walls, 7 wind angles of incidence.

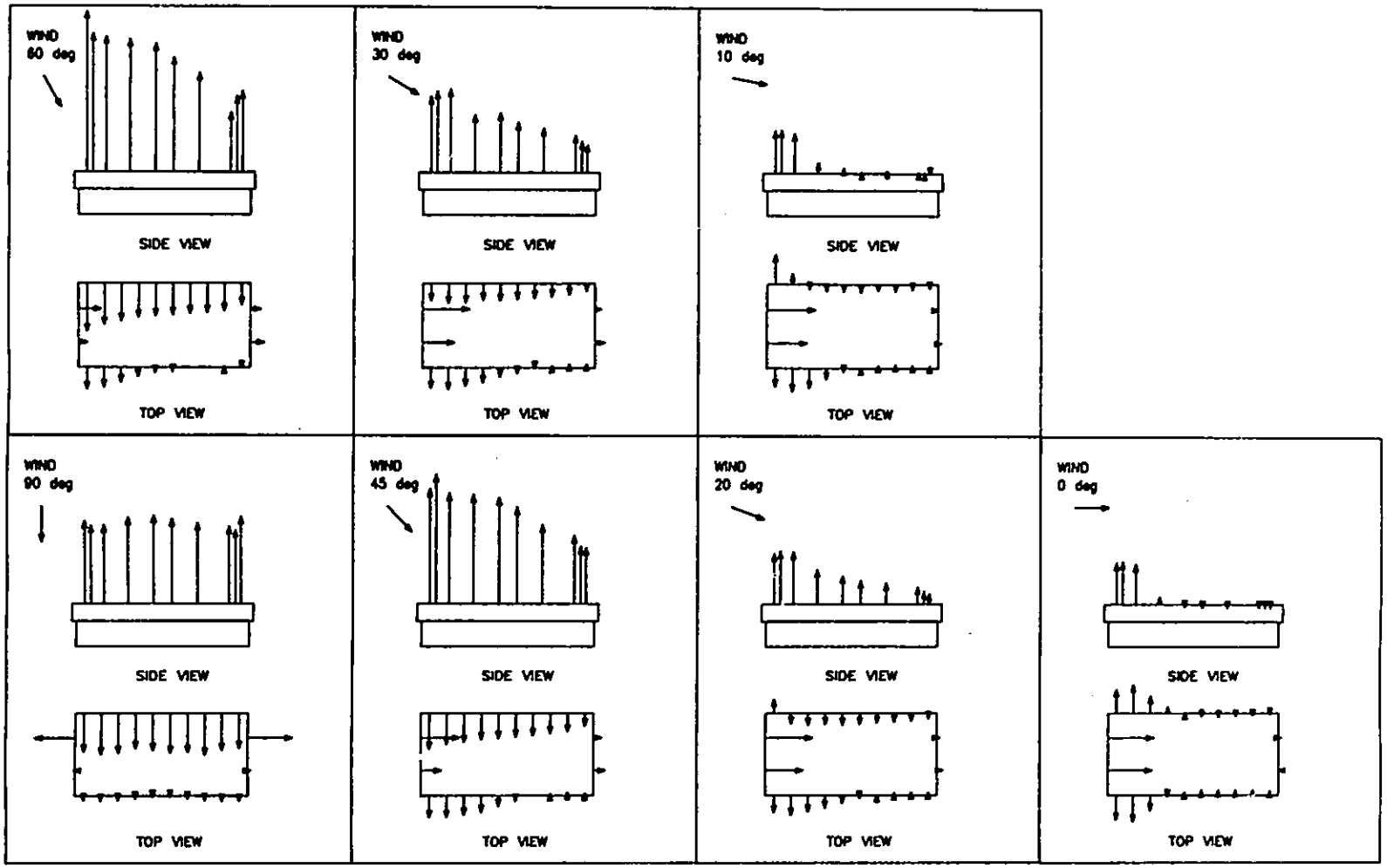

Figure G.24 ΔCps (in-out): sealed model, simulated 400 mm ridge and 1100 mm sidewall openings, open end walls, 7 wind angles of incidence.

APPENDIX H

Airflow diagrams, complete data

Appendix H contains the airflow diagrams which represent the local inflows and outflows over each roof, sidewall and end wall opening. There are 12 figures for the open model and 12 for the sealed model.

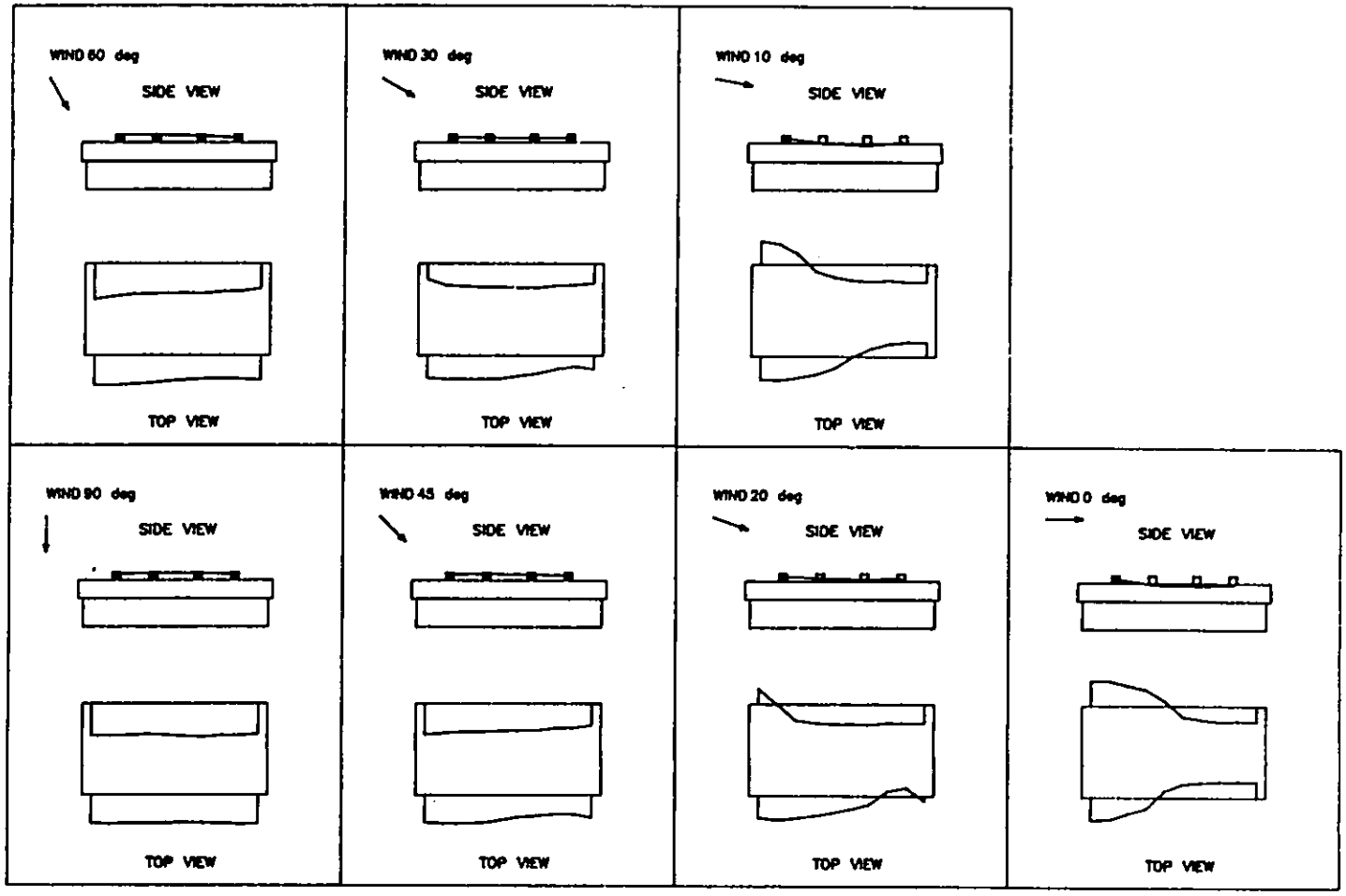

Figure H.1 Airflow diagrams: open model, chimney, simulated 800 mm sidewall openings, closed end walls, 7 wind angles of incidence.

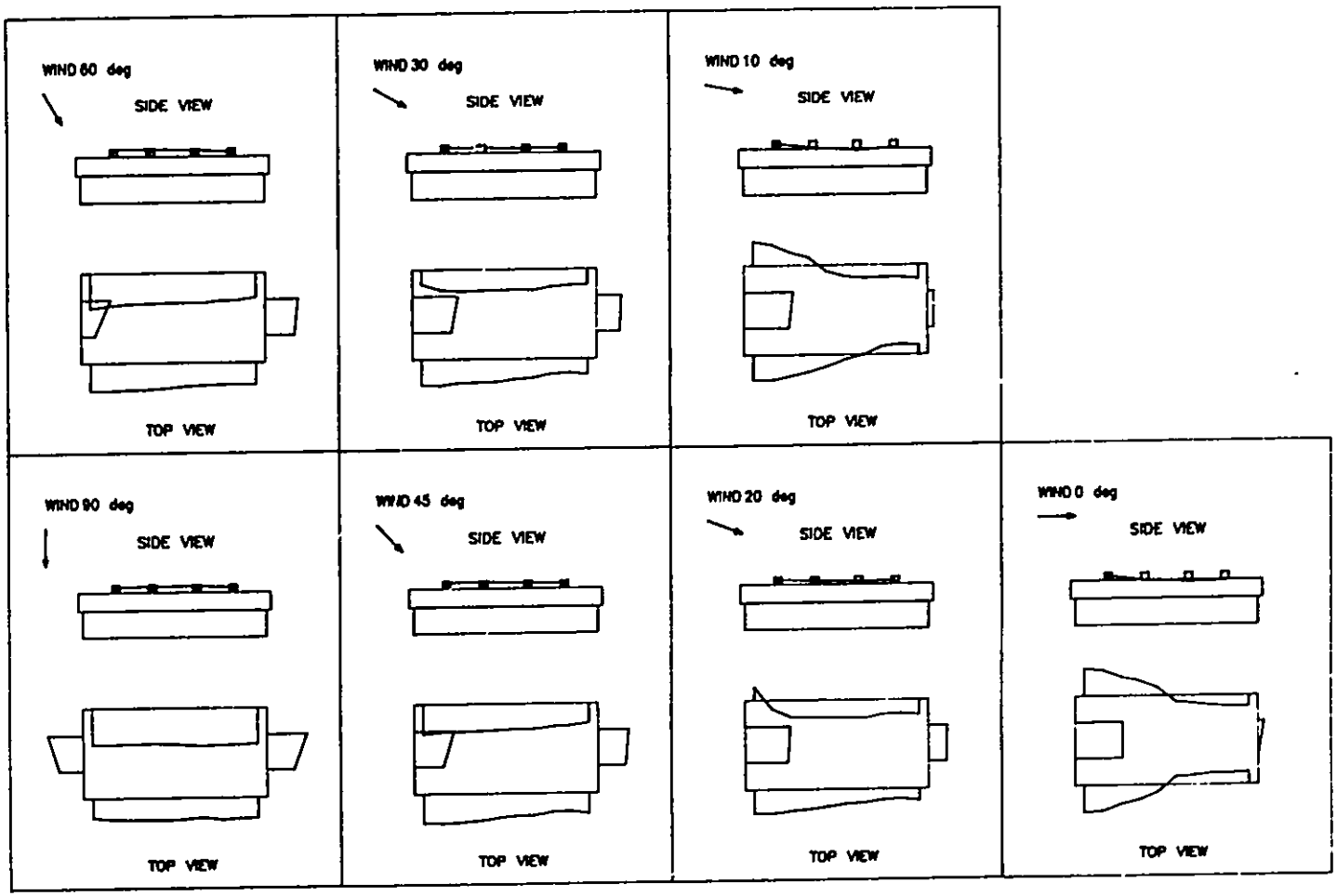

Figure H.2 Airflow diagrams: open model, chimney, simulated 800 mm sidewall openings, open end walls, 7 wind angles of incidence.

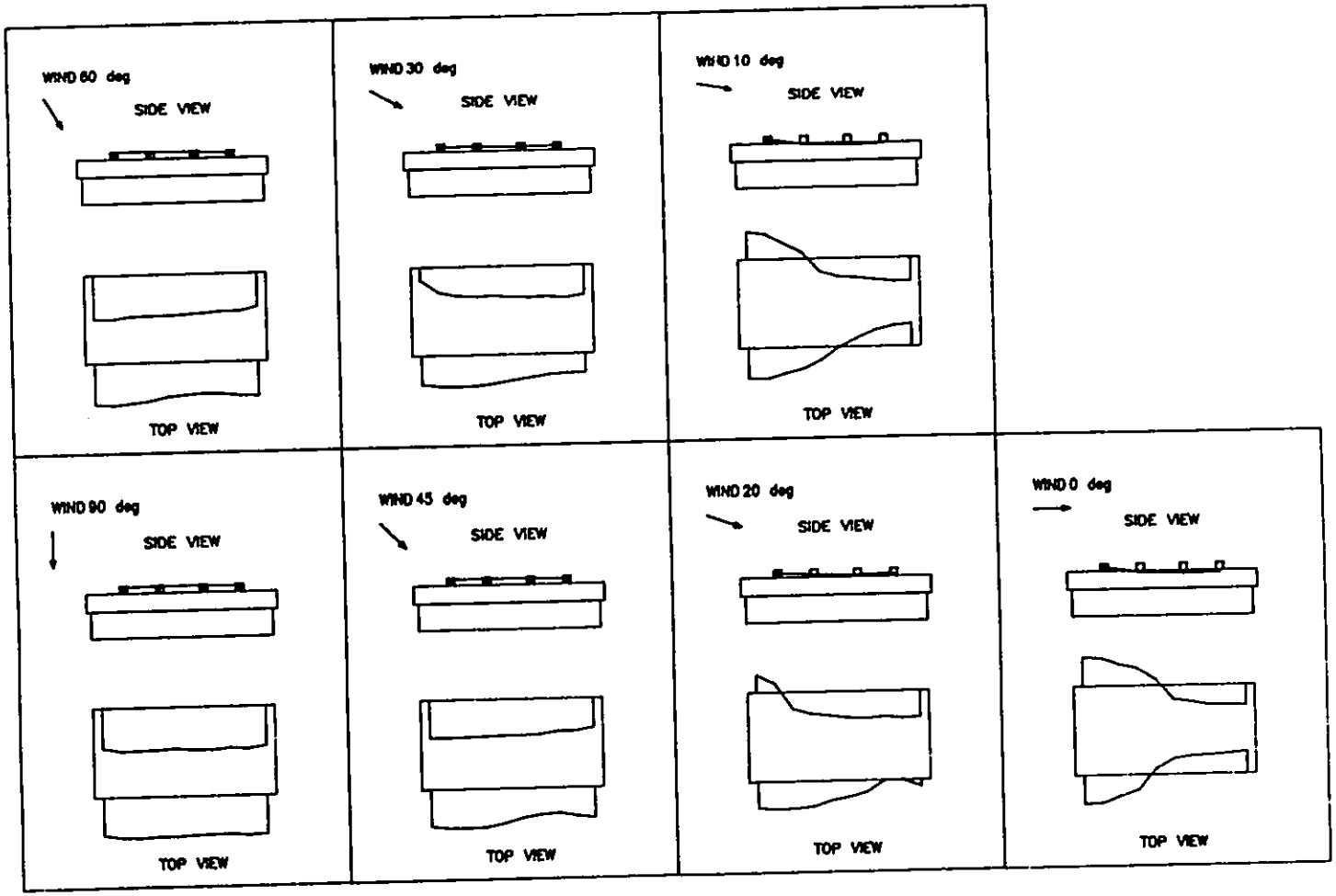

Figure H.3 Airflow diagrams: open model, chimney, simulated 1100 mm sidewall openings, closed end walls, 7 wind angles of incidence.

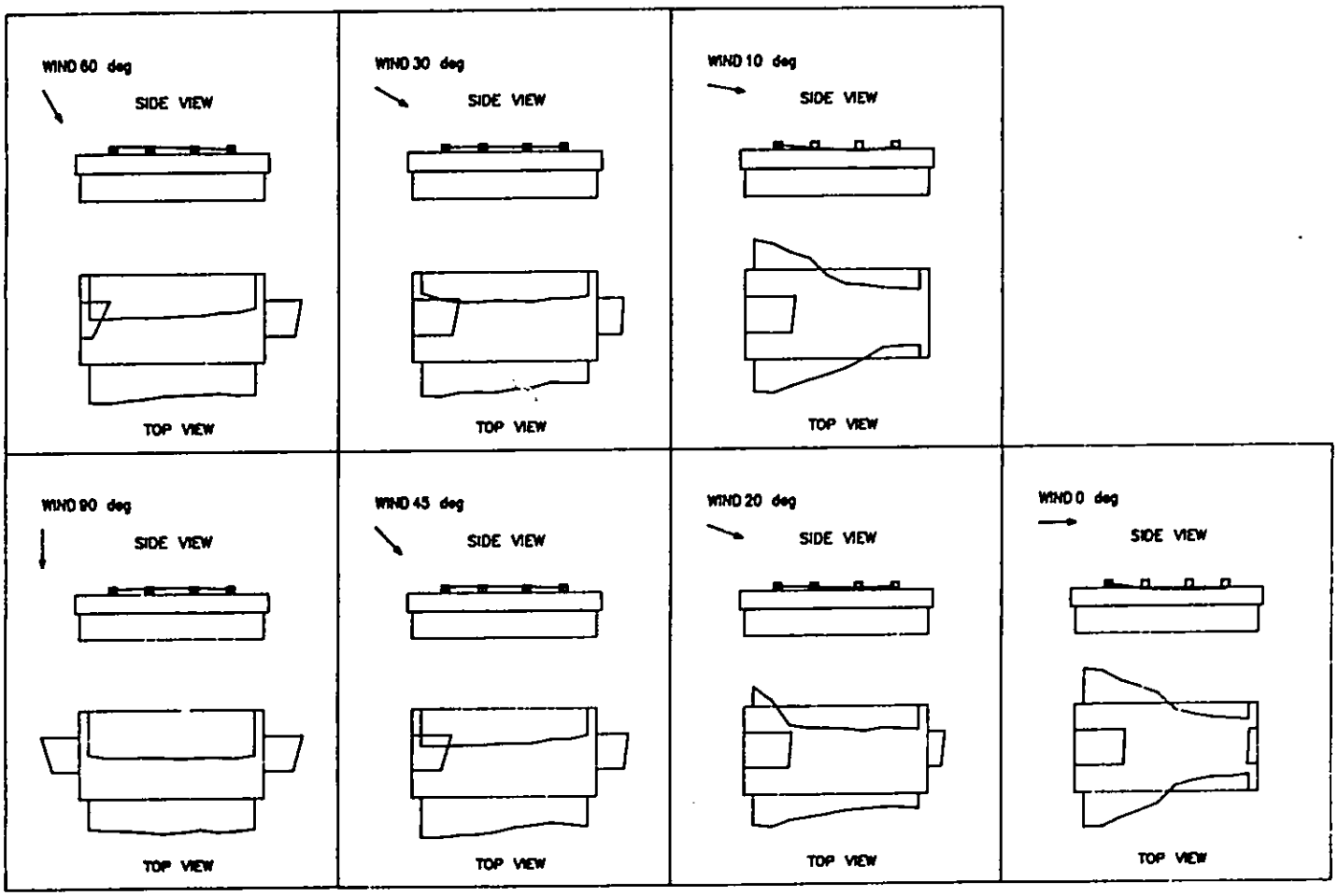

Figure H.4 Airflow diagrams: open model, chimney, simulated 1100 mm sidewall openings, open end walls, 7 wind angles of incidence.

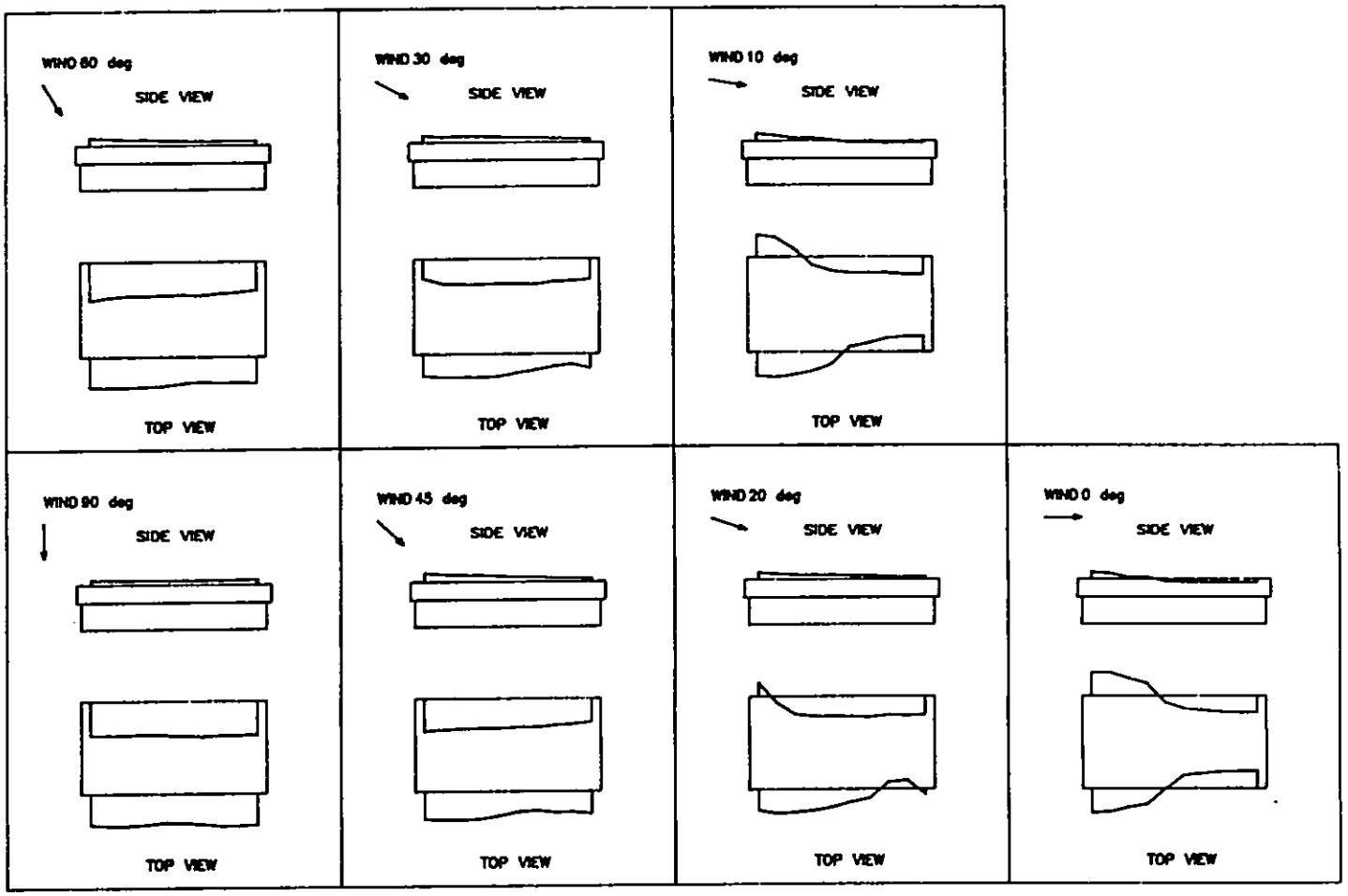

Figure H.5 Airflow diagrams: open model, simulated 150 mm ridge and 800 mm sidewall openings, closed end walls, 7 wind angles of incidence.

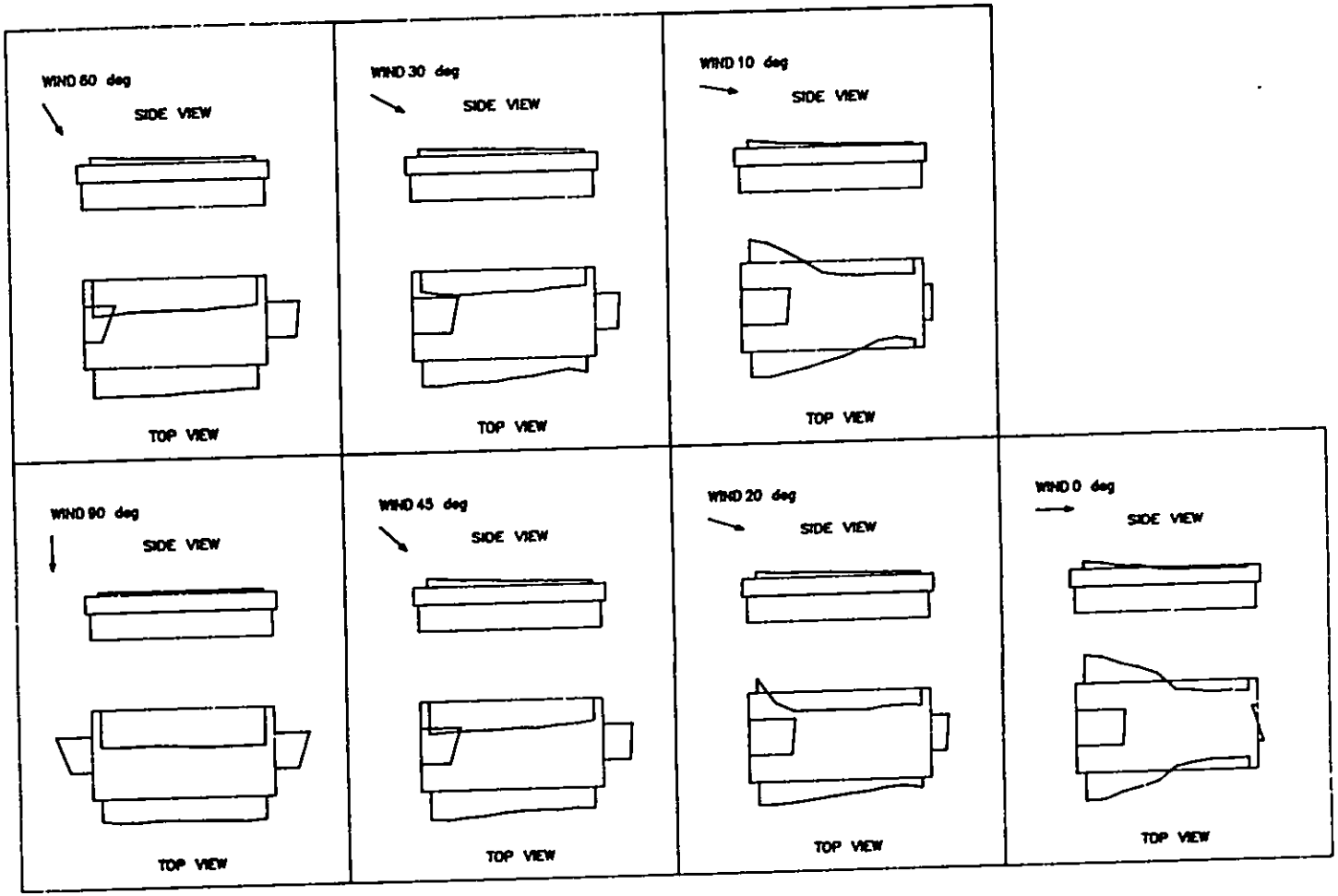

Figure H.6 Airflow diagrams: open model, simulated 150 mm ridge and 800 mm sidewall openings, open end walls, 7 wind angles of incidence.

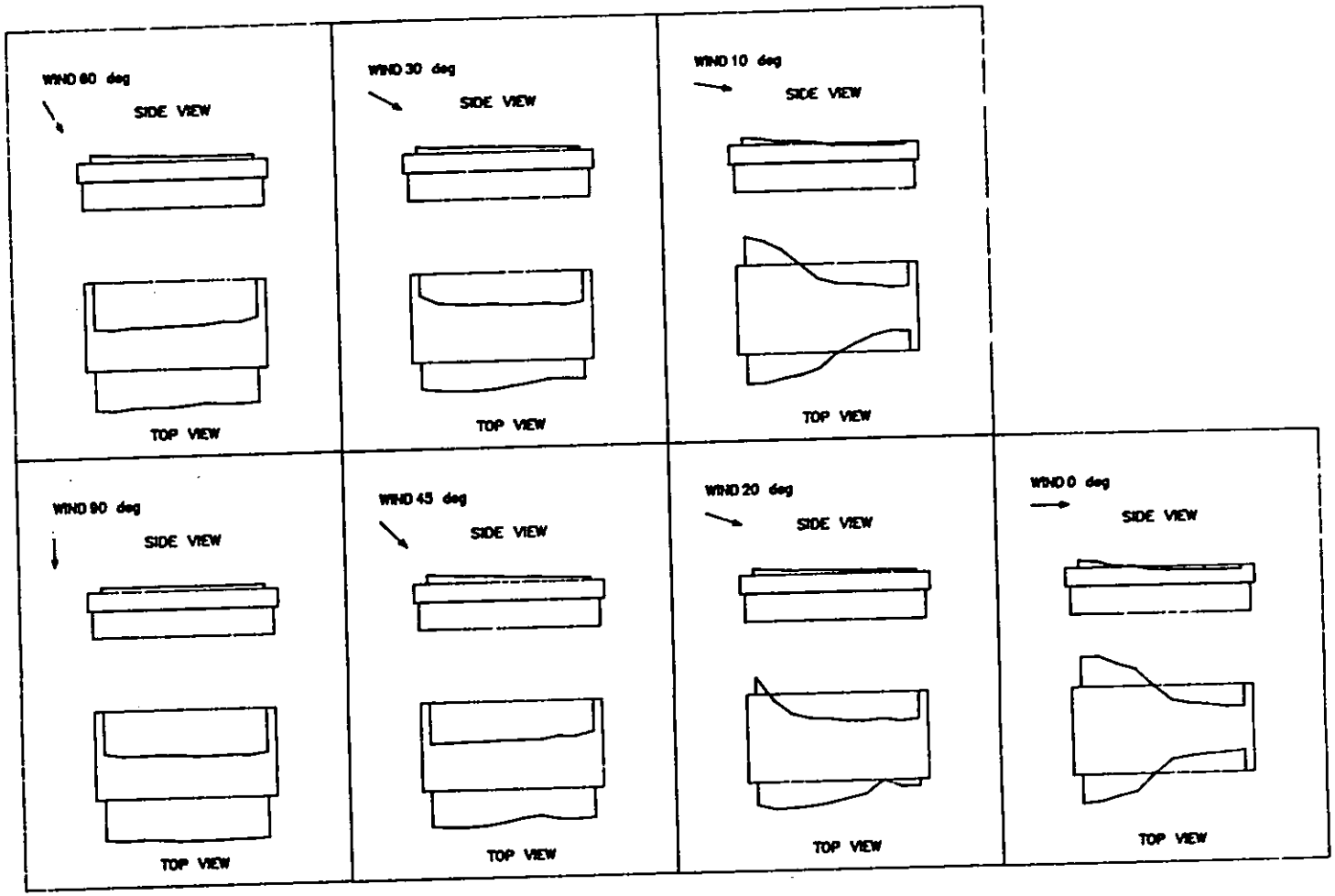

Figure H.7 Airflow diagrams: open model, simulated 150 mm ridge and 1100 mm sidewall openings, closed end walls, 7 wind angles of incidence.

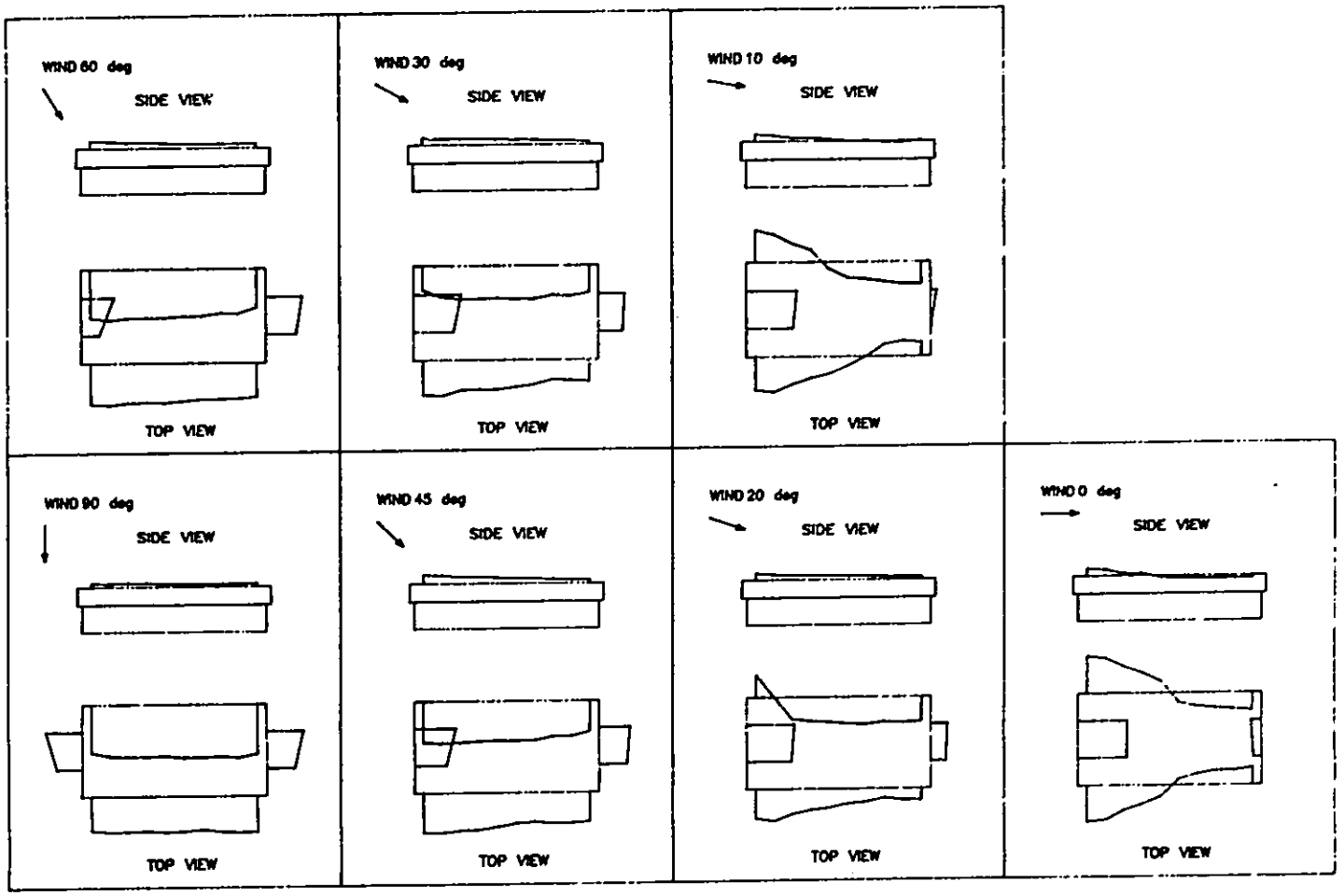

Figure H.8 Airflow diagrams: open model, simulated 150 mm ridge and 1100 mm sidewall openings, open end walls, 7 wind angles of incidence.

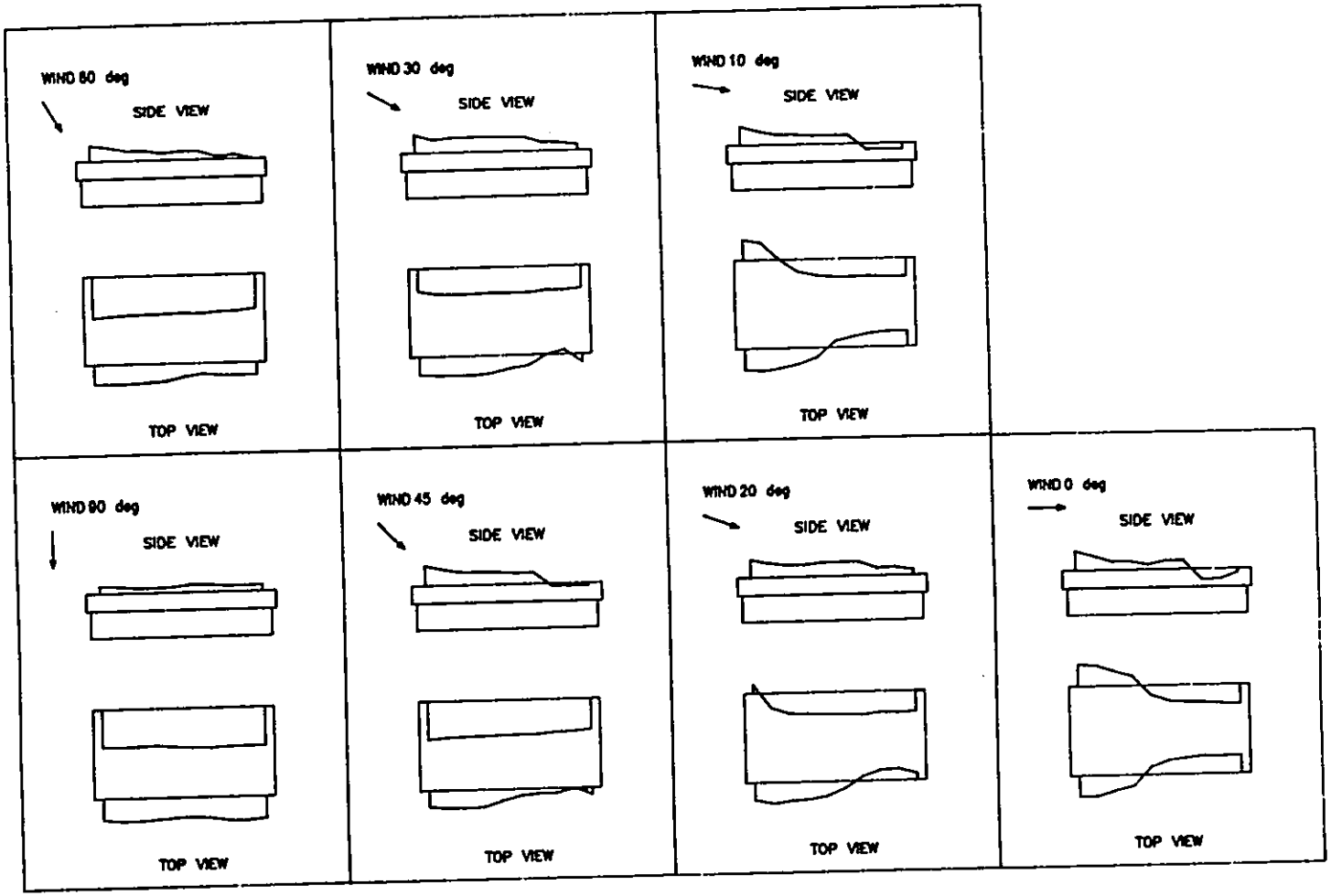

Figure H.9 Airflow diagrams: open model, simulated 400 mm ridge and 800 mm sidewall openings, closed end walls, 7 wind angles of incidence.

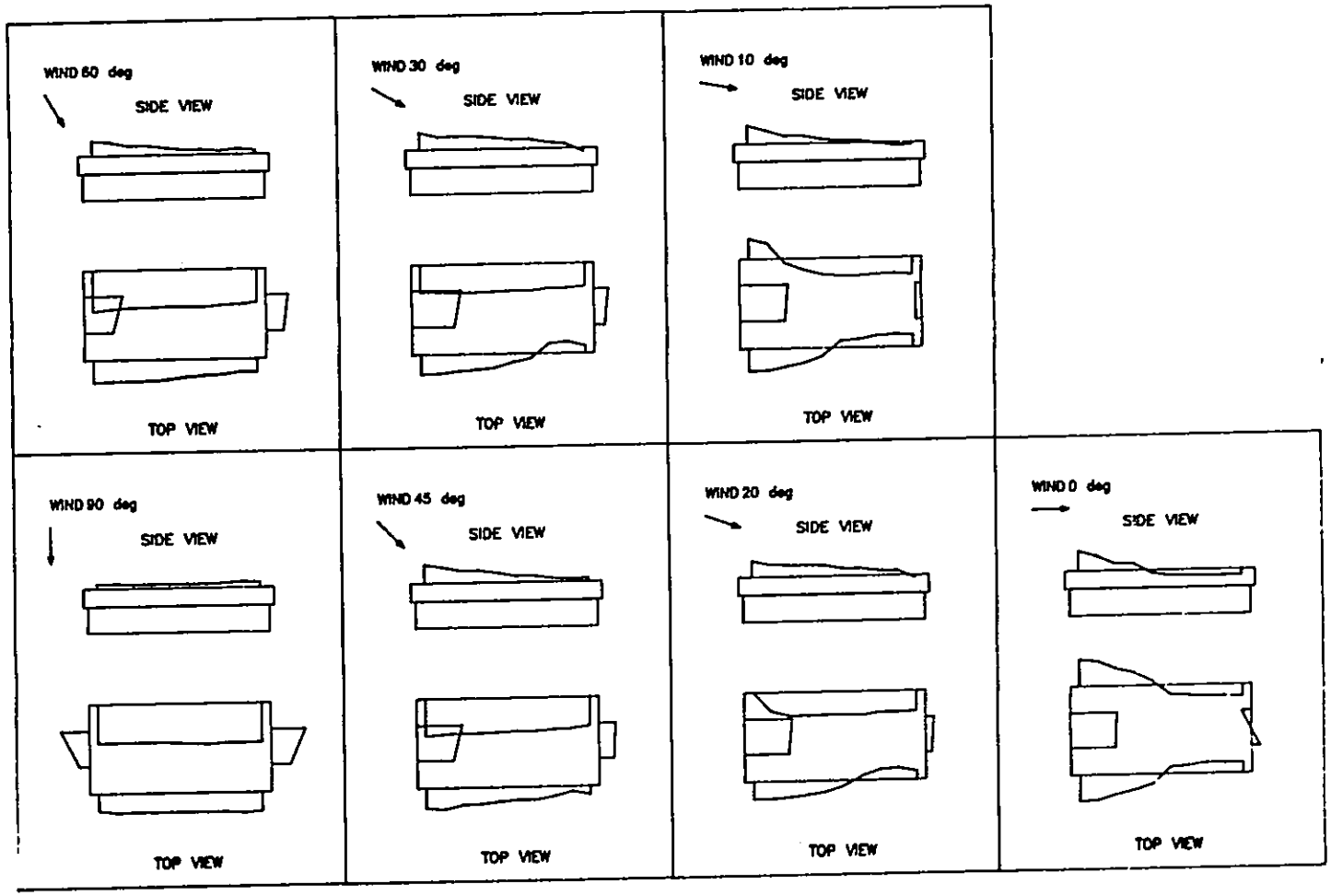

Figure H.10 Airflow diagrams: open model, simulated 400 mm ridge and 800 mm sidewall openings, open end walls, 7 wind angles of incidence.

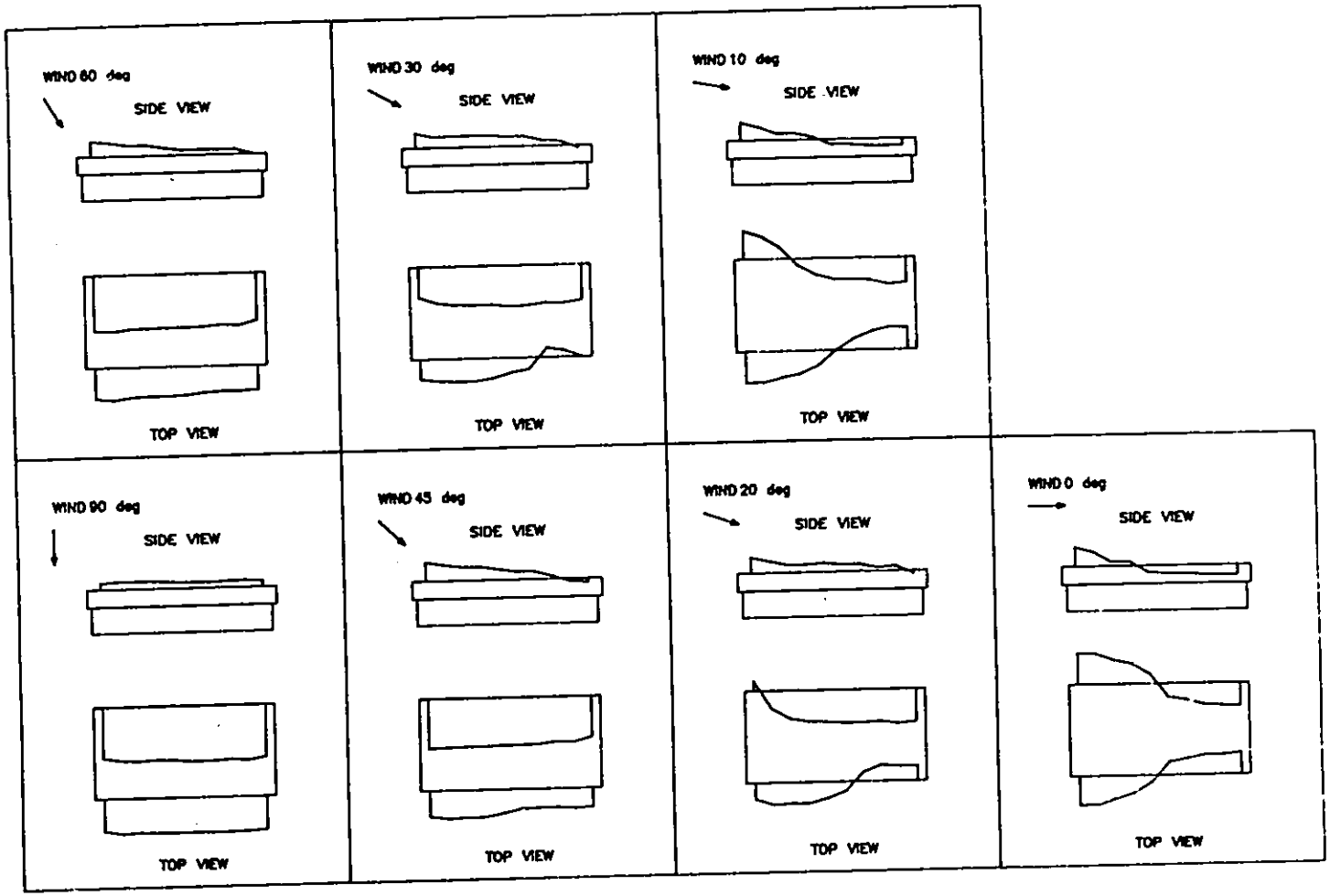

Figure H.11 Airflow diagrams: open model, simulated 400 mm ridge and 1100 mm sidewall openings, closed end walls, 7 wind angles of incidence.

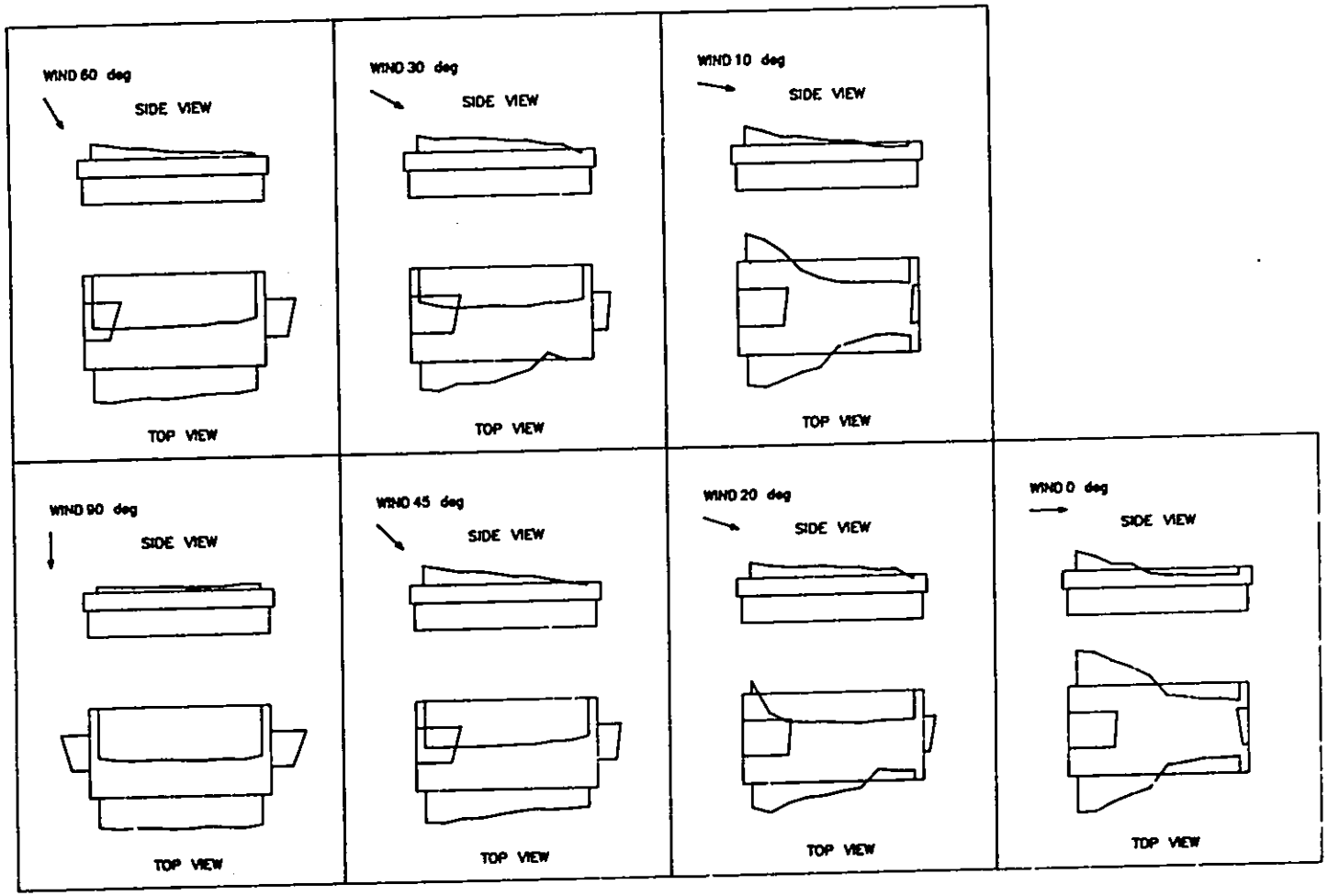

Figure H.12 Airflow diagrams: open model, simulated 400 mm ridge and 1100 mm sidewall openings, open end walls, 7 wind angles of incidence.

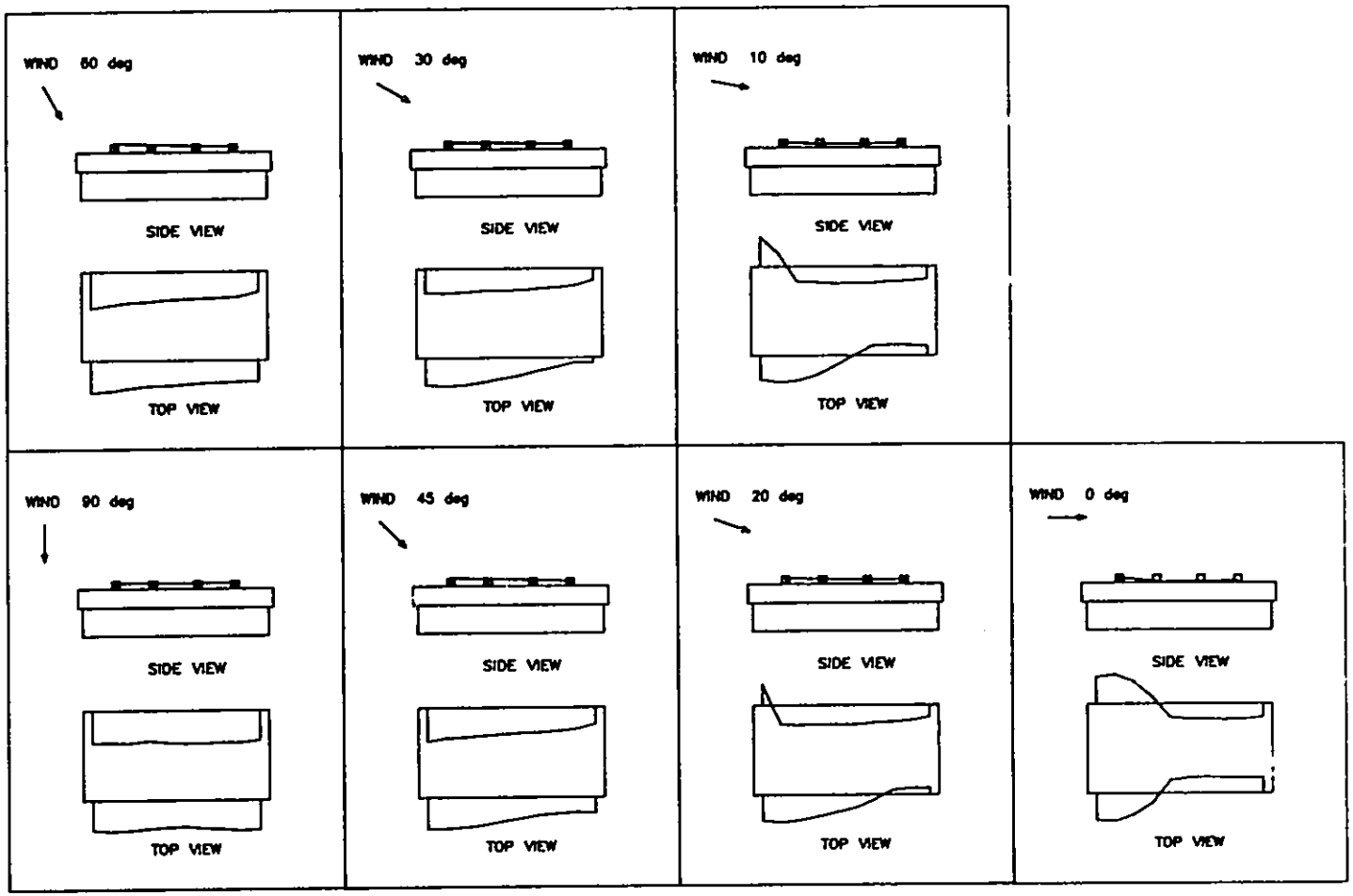

Figure H.13 Airflow diagrams: sealed model, chimney, simulated 800 mm sidewall openings, closed end walls, 7 wind angles of incidence.

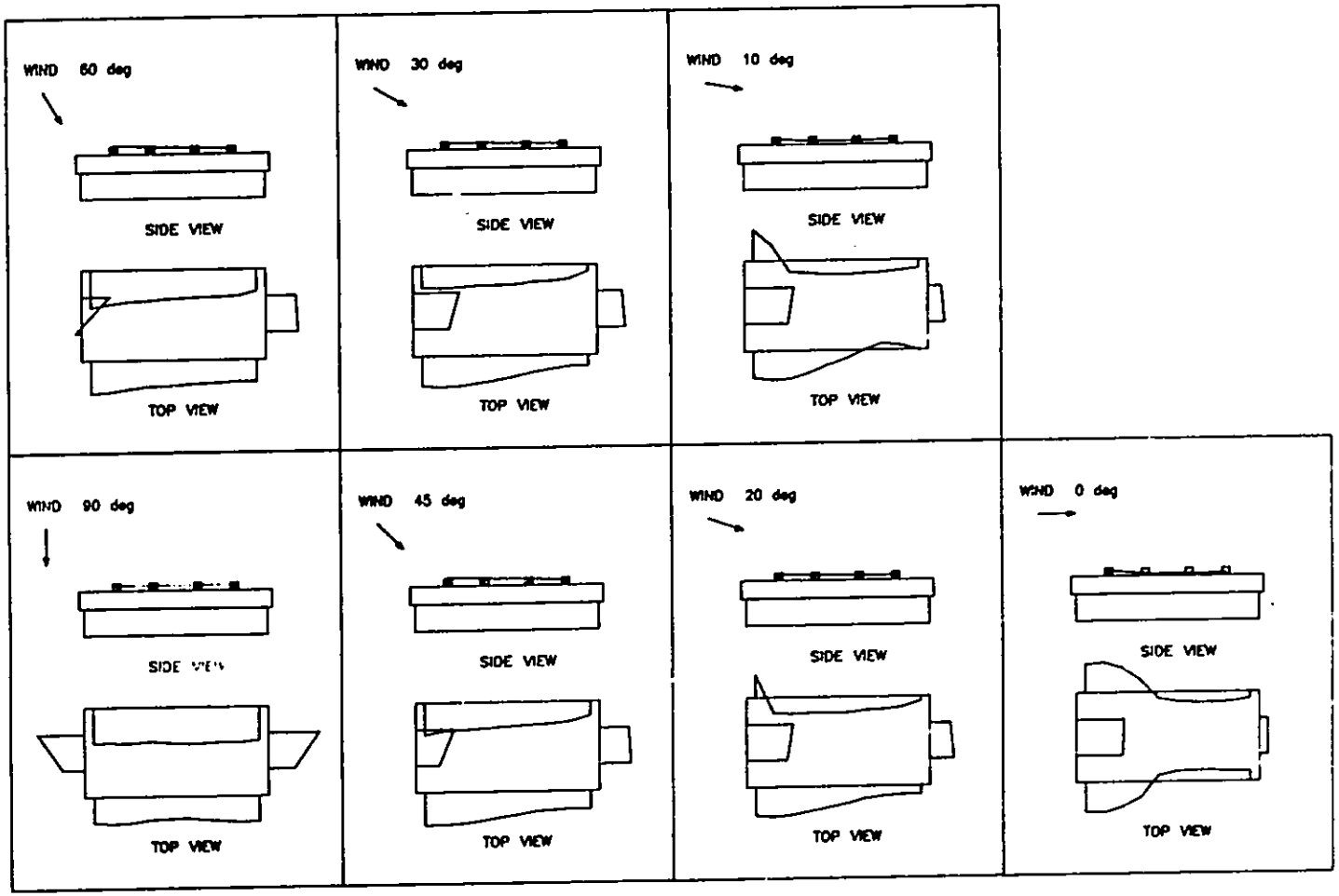

Figure H.14 Airflow diagrams: sealed model, chimney, simulated 800 mm sidewall openings, open end walls, 7 wind angles of incidence.

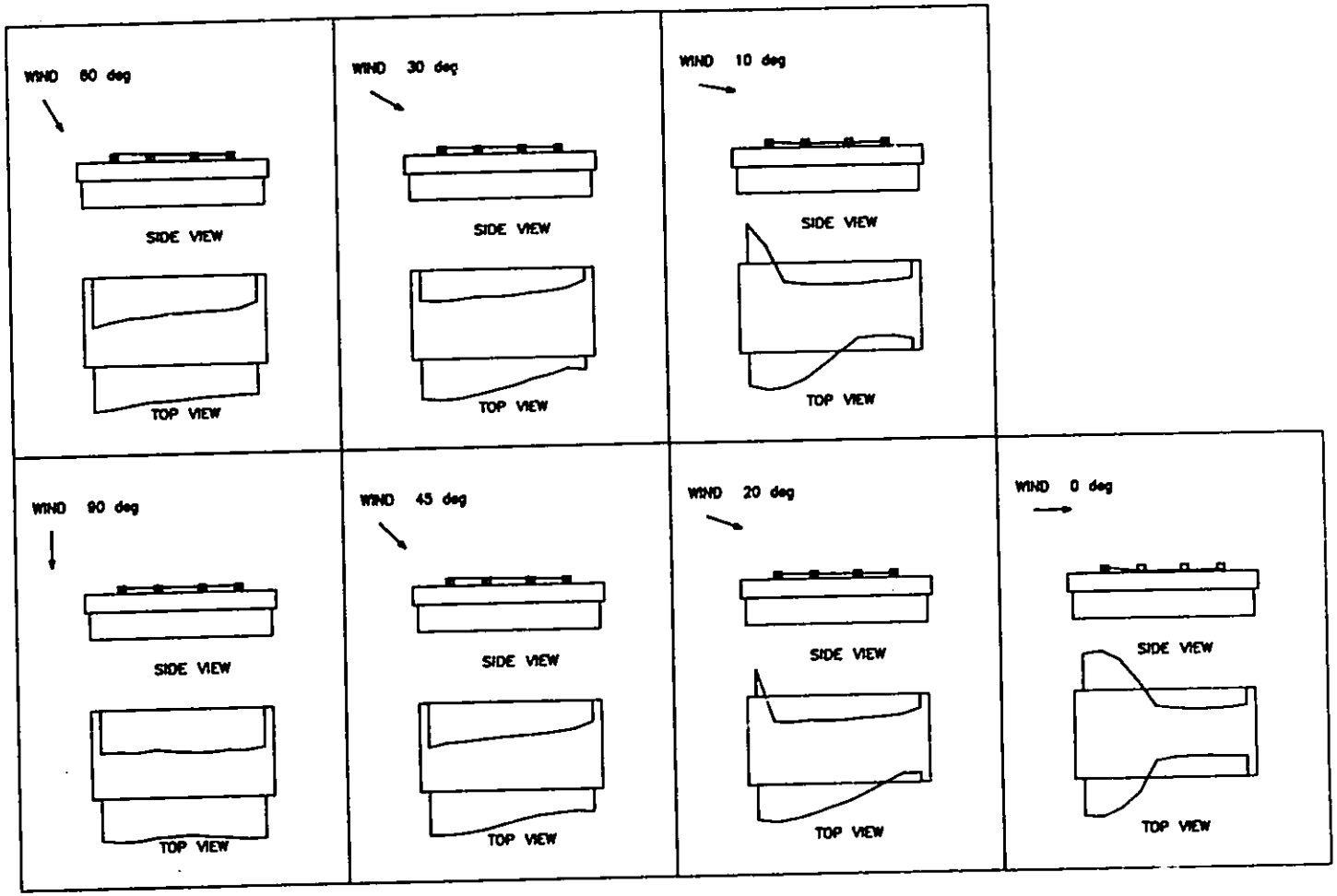

Figure H.15 Airflow diagrams: sealed model, chimney, simulated 1100 mm sidewall openings, closed end walls, 7 wind angles of incidence.

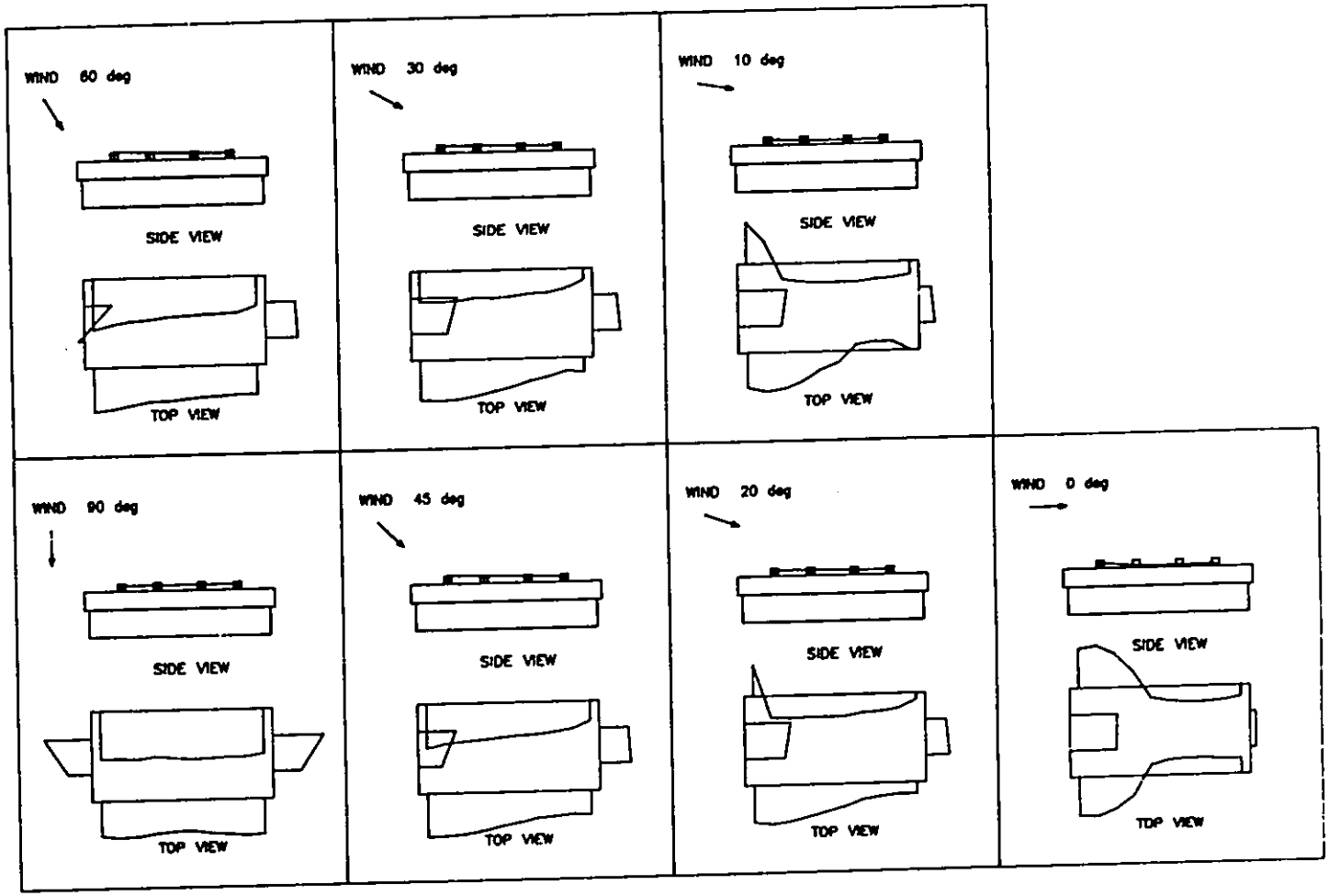

Figure H.16 Airflow diagrams: sealed model, chimney, simulated 1100 mm sidewall openings, open end walls, 7 wind angles of incidence.

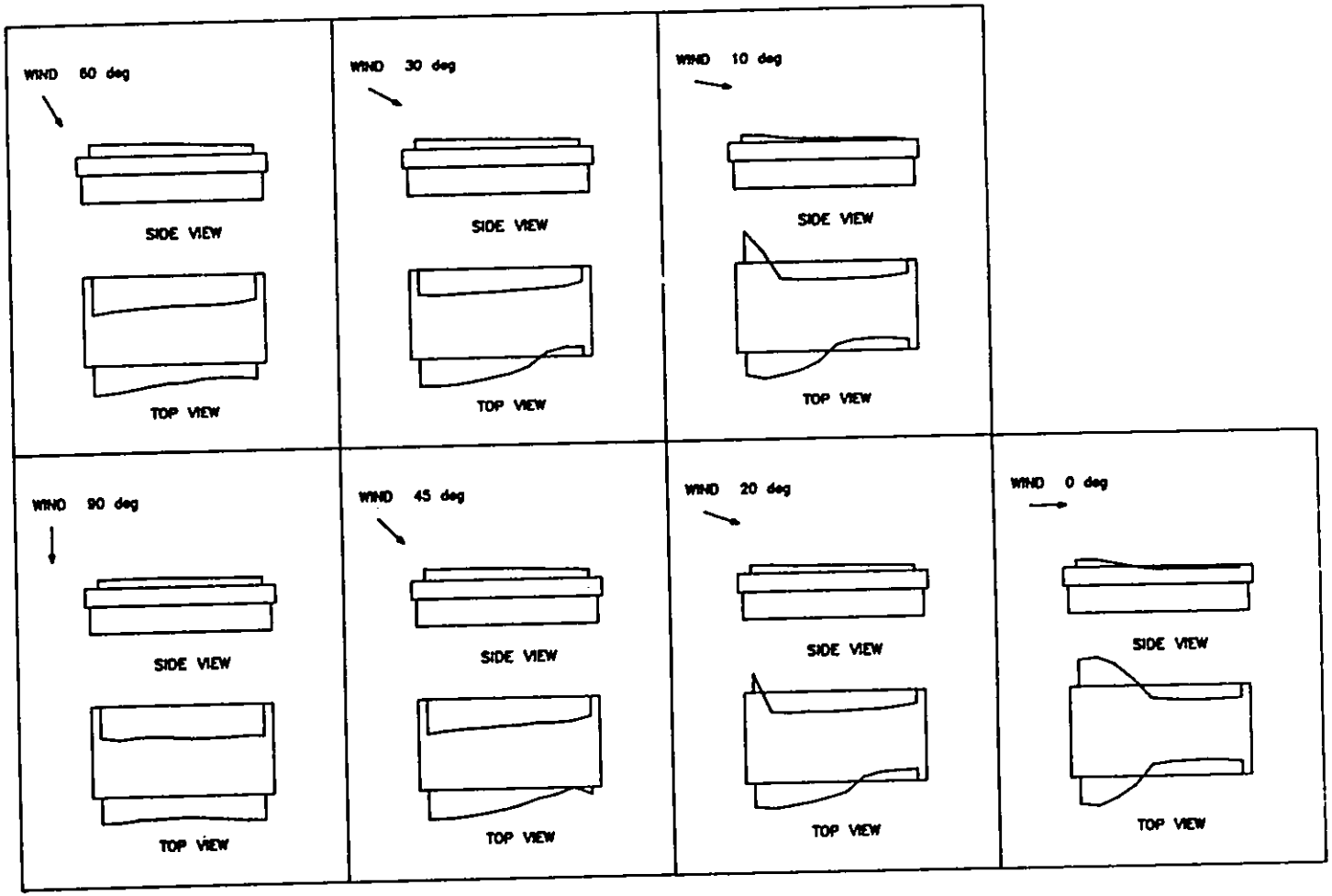

Figure H.17 Airflow diagrams: sealed model, simulated 150 mm ridge and 800 mm sidewall openings, closed end walls, 7 wind angles of incidence.

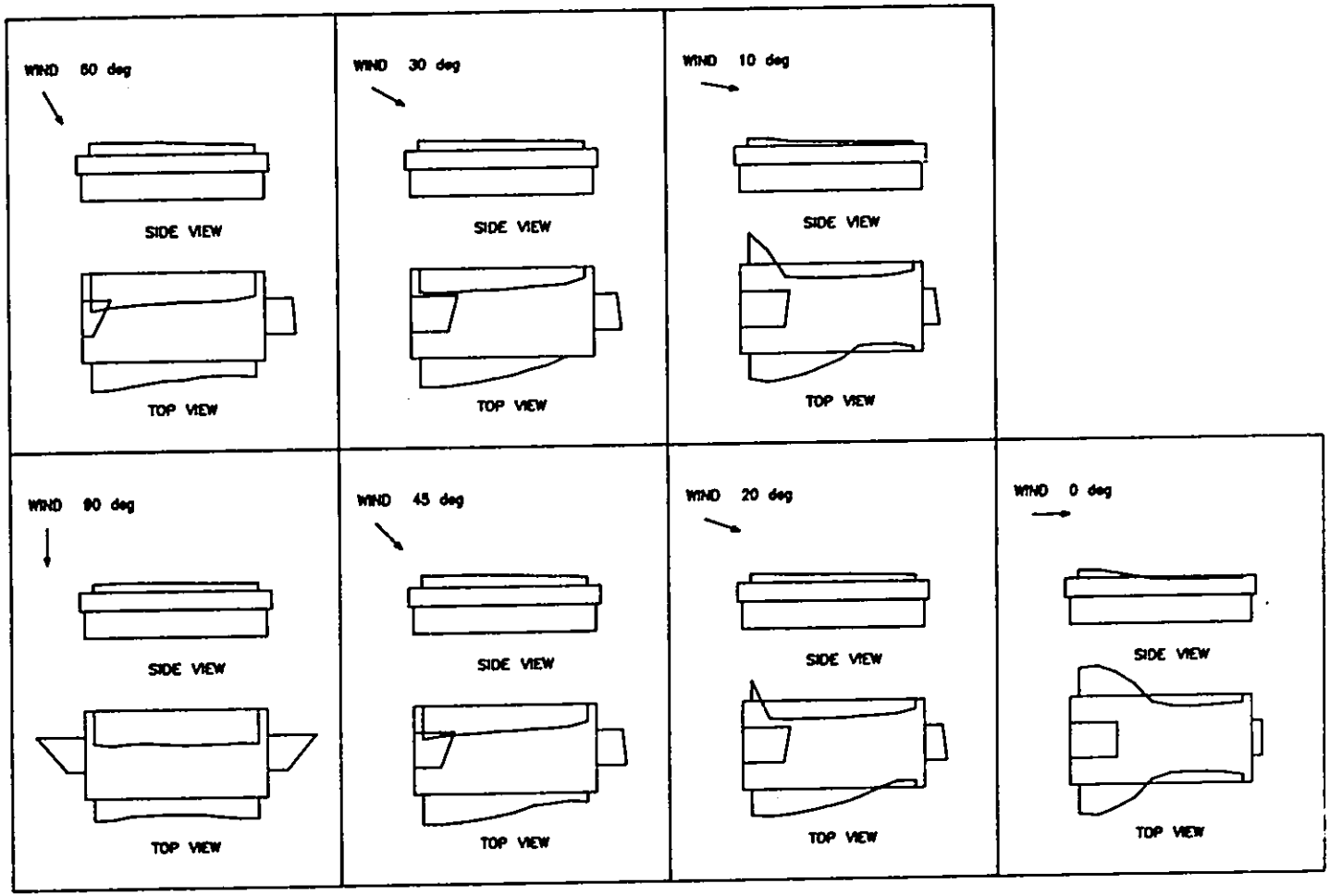

Figure H.18 Airflow diagrams: sealed model, simulated 150 mm ridge and 800 mm sidewall openings, open end walls, 7 wind angles of incidence.

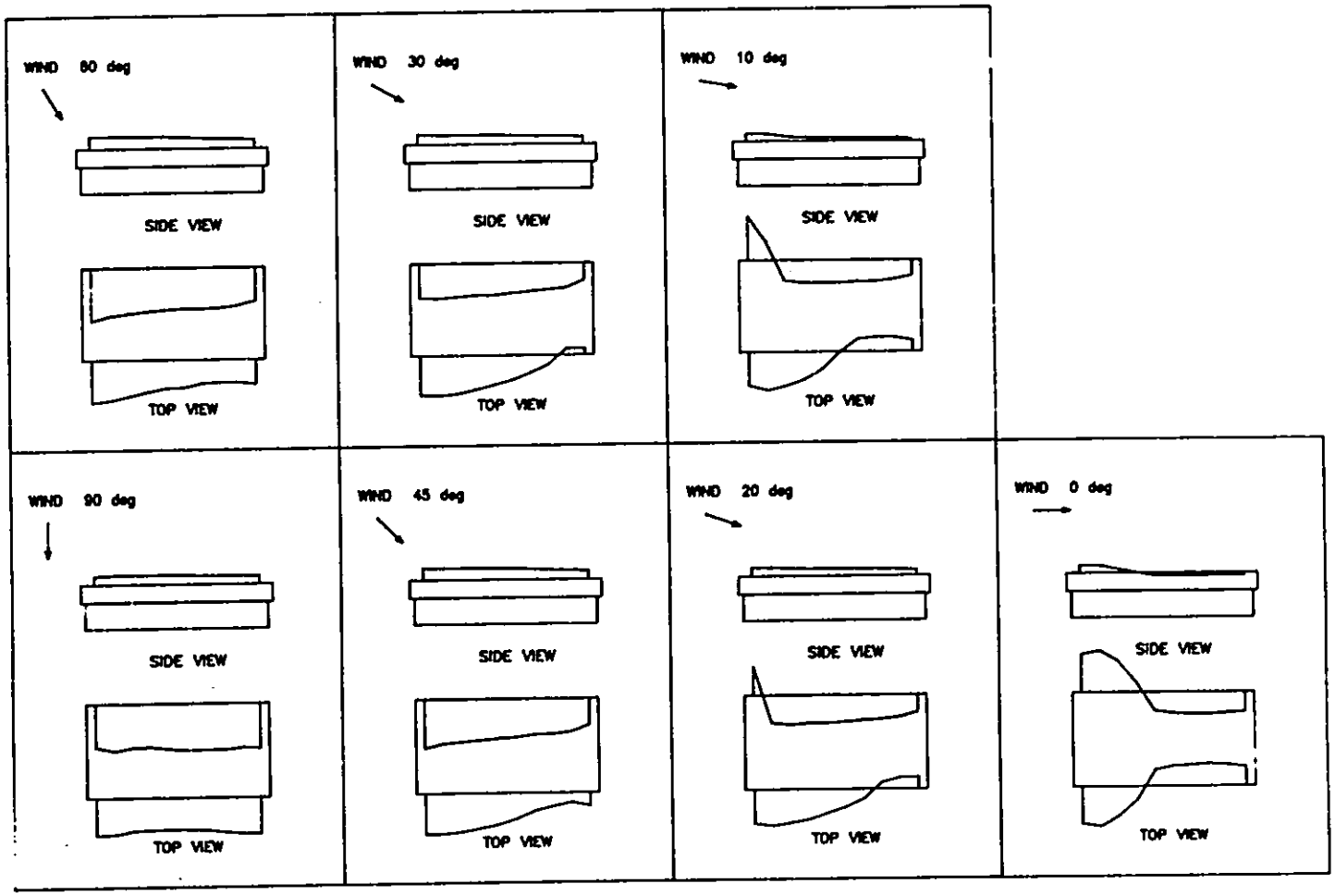

Figure H.19 Airflow diagrams: sealed model, simulated 150 mm ridge and 1100 mm sidewall openings, closed end walls, 7 wind angles of incidence.

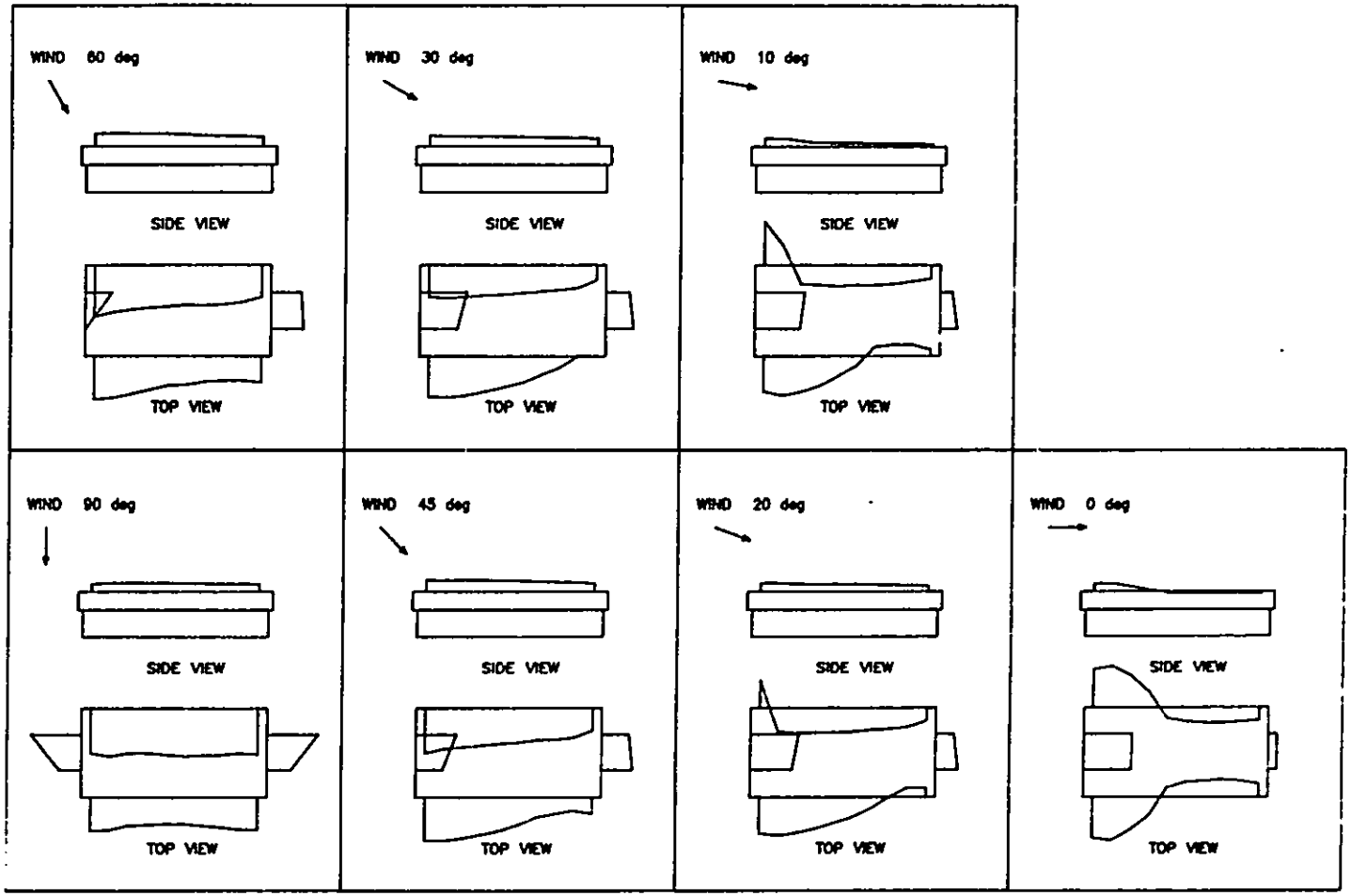

Figure H.20 Airflow diagrams: sealed model, simulated 150 mm ridge and 1100 mm sidewall openings, open end walls, 7 wind angles of incidence.

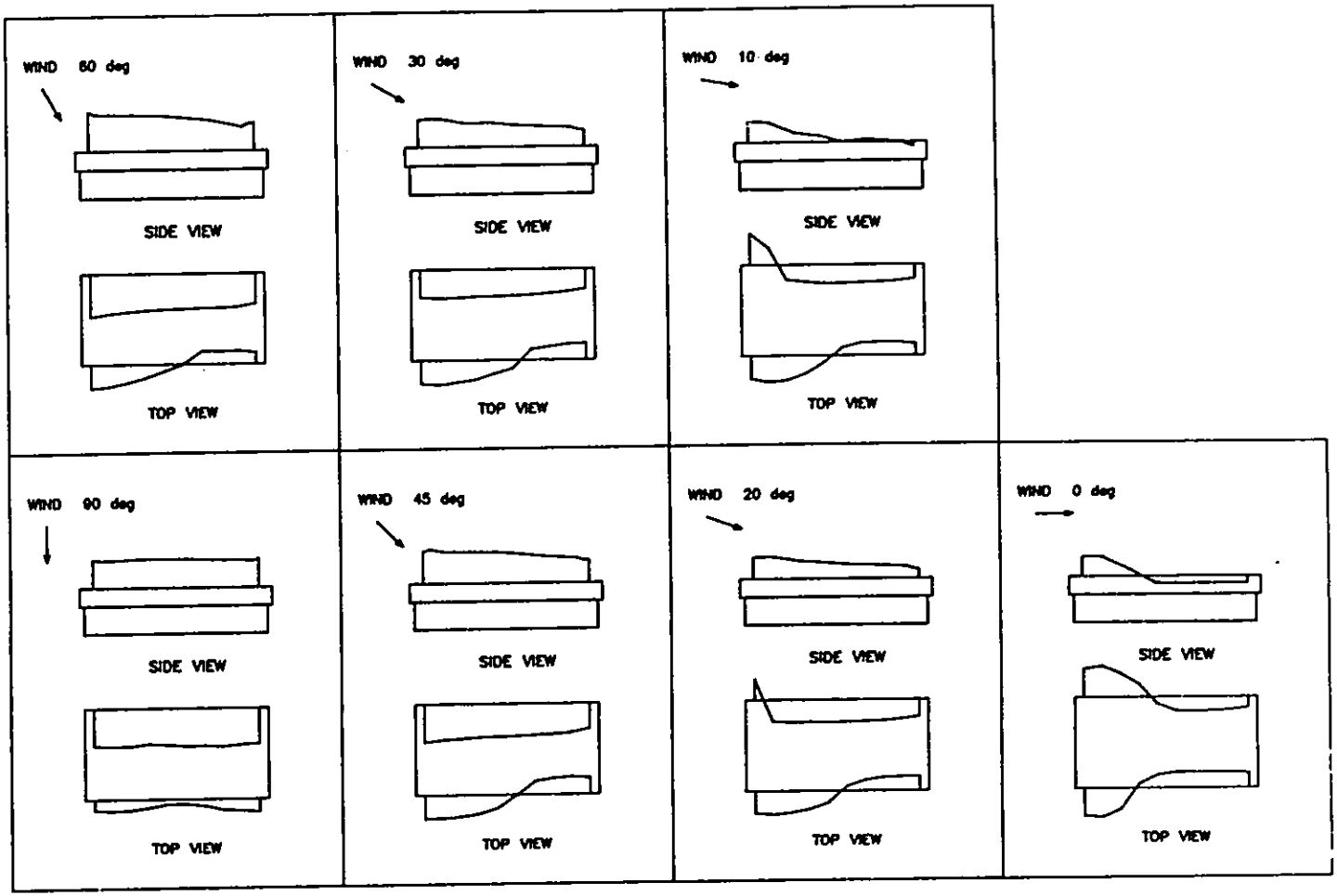

Figure H.21 Airflow diagrams: sealed model, simulated 400 mm ridge and 800 mm sidewall openings, closed end walls, 7 wind angles of incidence.

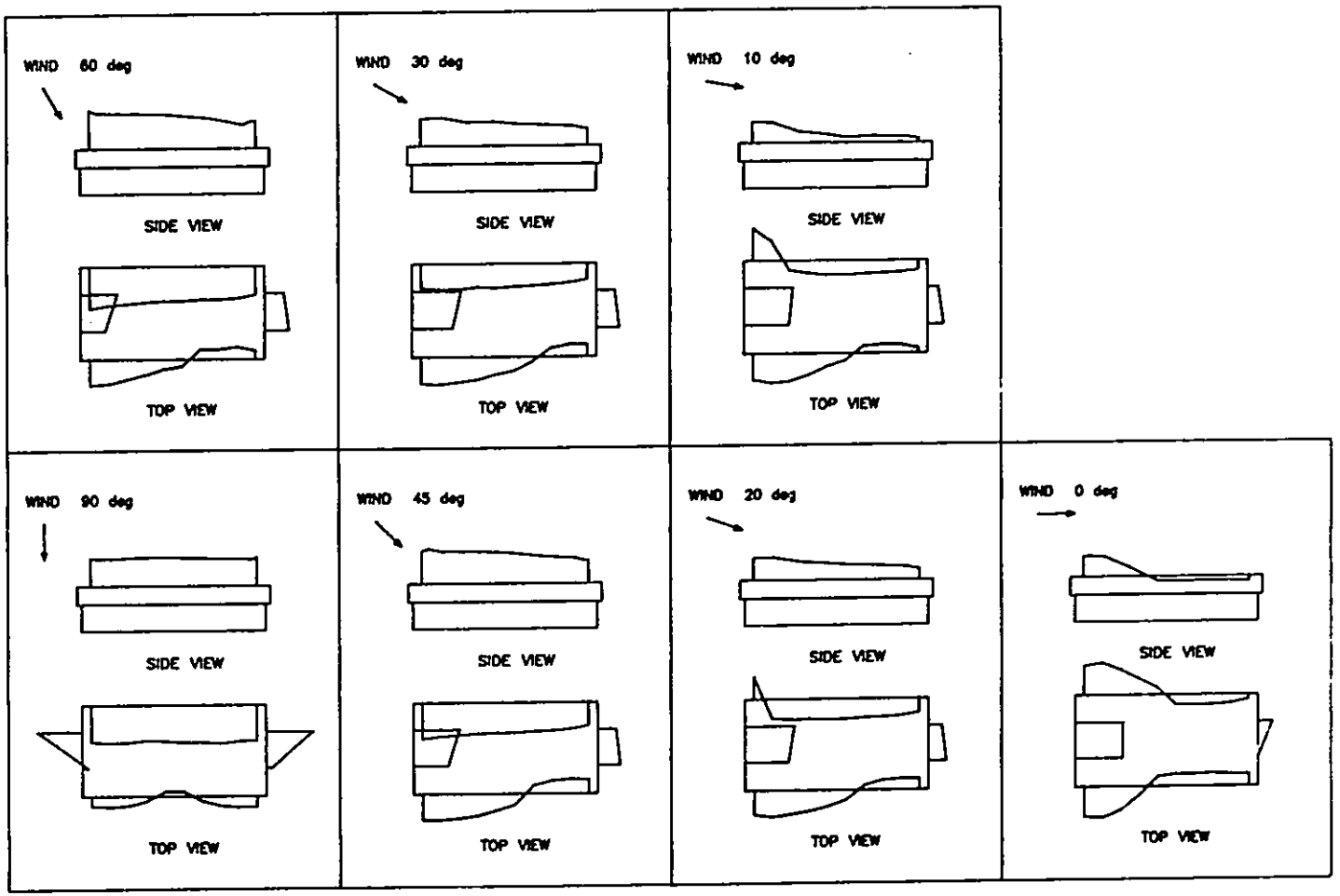

Figure H.22 Airflow diagrams: sealed model, simulated 400 mm ridge and 800 mm sidewall openings, open end walls, 7 wind angles of incidence.

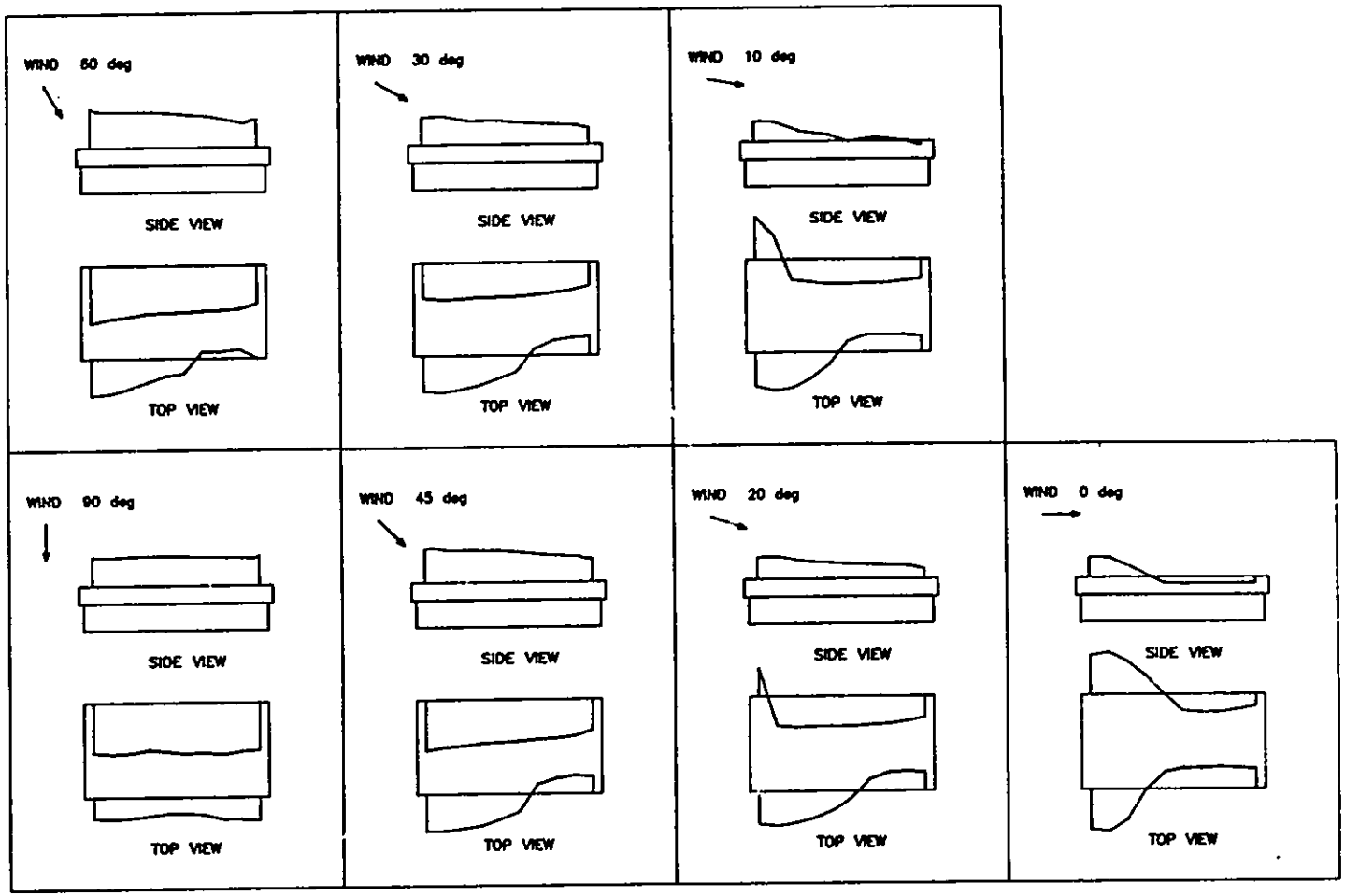

Figure H.23 Airflow diagrams: sealed model, simulated 400 mm ridge and 1100 mm sidewall openings, closed end walls, 7 wind angles of incidence.

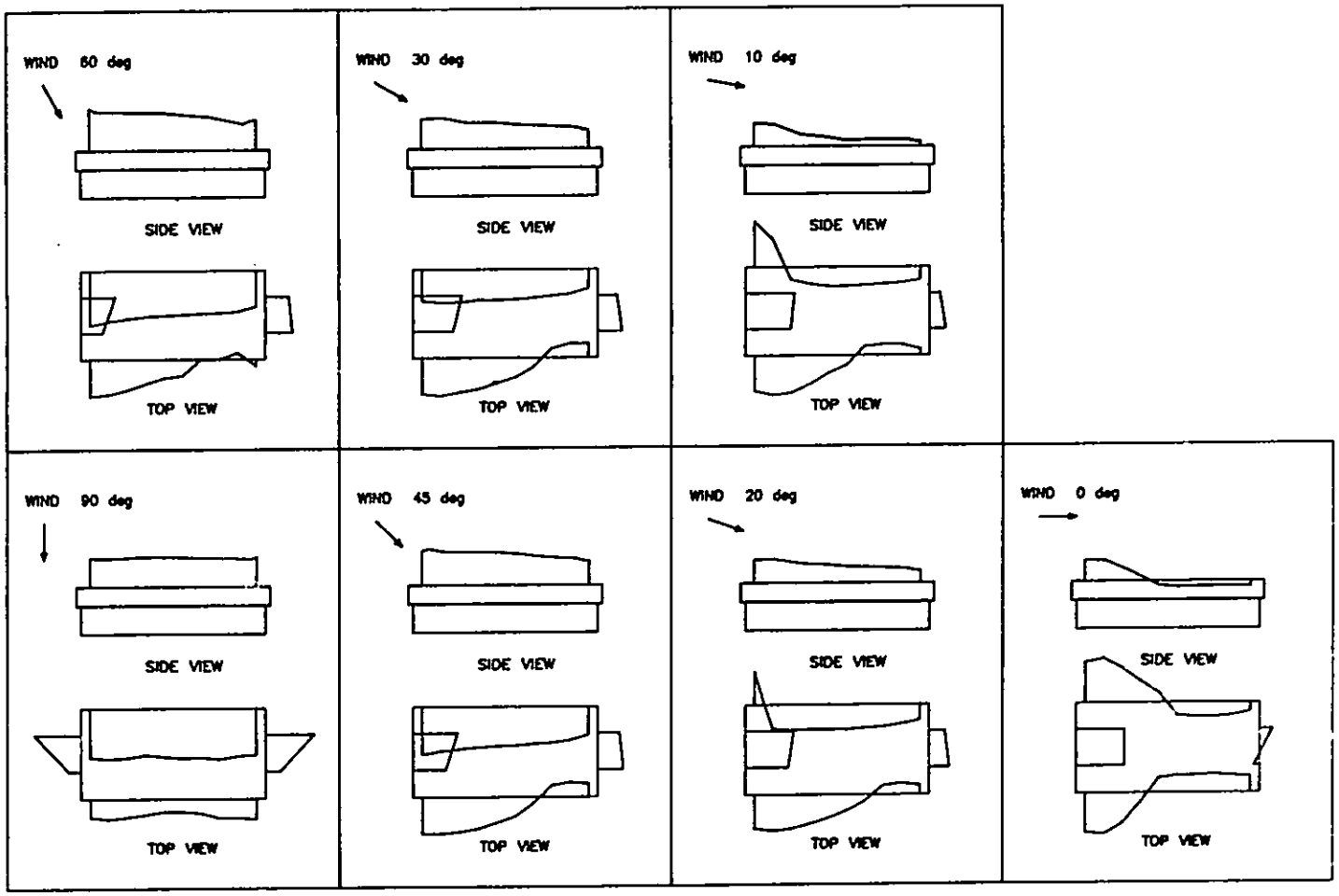

Figure H.24 Airflow diagrams: sealed model, simulated 400 mm ridge and 1100 mm sidewall openings, open end walls, 7 wind angles of incidence.

APPENDIX I

Ventilation rate coefficients

Appendix I contains the calculated ventilation rate coefficients, C_{Q10}, for open and sealed models. The differences between these two model types are presented.

Table I.1 C_{q10} for open and sealed models.

Code	Angle	Cq open	Cq sealed	Cq(open-sealed)
150-1100-op	90	0.462789	0.431609	0.031180
	60	0.456046	0.406677	0.049370
	45	0.413956	0.386648	0.027309
	30	0.344391	0.328066	0.016326
	20	0.264446	0.289499	-0.025053
	10	0.229532	0.259394	-0.029862
	0	0.249713	0.262543	-0.012830
150-1100-cl	90	0.429472	0.397913	0.031559
	60	0.405475	0.377373	0.028102
	45	0.355589	0.336627	0.018963
	30	0.281691	0.283720	-0.002028
	20	0.204257	0.244031	-0.039774
	10	0.194083	0.221057	-0.026974
	0	0.199838	0.231714	-0.031876
150-800-op	90	0.482880	0.447723	0.035158
	60	0.481826	0.437076	0.044751
	45	0.444932	0.420071	0.024862
	30	0.383376	0.366196	0.017181
	20	0.311612	0.321185	-0.009572
	10	0.264277	0.286194	-0.021916
	0	0.273708	0.282904	-0.009195
150-800-cl	90	0.426760	0.409353	0.017408
	60	0.406734	0.391649	0.015085
	45	0.355059	0.347594	0.007465
	30	0.285925	0.302637	-0.016711
	20	0.221491	0.259684	-0.038192
	10	0.210089	0.229294	-0.019205
	0	0.220708	0.238133	-0.017425
400-1100-op	90	0.498525	0.457689	0.040837
	60	0.527410	0.480308	0.047103
	45	0.505996	0.469876	0.036121
	30	0.441833	0.402340	0.039494
	20	0.375173	0.343565	0.031608
	10	0.323609	0.292122	0.031487
	0	0.357209	0.290688	0.066521
400-1100-cl	90	0.488685	0.443265	0.045421
	60	0.473319	0.445653	0.027667
	45	0.443088	0.430815	0.012274
	30	0.365448	0.358251	0.007197
	20	0.304357	0.296461	0.007897
	10	0.292992	0.246830	0.046162
	0	0.319450	0.257921	0.061530
400-800-op	90	0.511935	0.492378	0.019558
	60	0.566803	0.564900	0.001903
	45	0.544713	0.549538	-0.004824
	30	0.520364	0.467046	0.053318
	20	0.441844	0.394272	0.047572
	10	0.376223	0.326299	0.049925
	0	0.406061	0.315160	0.090901

Table I.1 (cont.) C_{q10} for open and sealed models.

Code	Angle	Cq open	Cq sealed	Cq(open-sealed)
400-800-cl	90	0.499794	0.463349	0.036445
	60	0.497537	0.513131	-0.015593
	45	0.475947	0.487980	-0.012032
	30	0.327157	0.402278	-0.075121
	20	0.279843	0.330749	-0.050906
	10	0.262119	0.262656	-0.000536
	0	0.272856	0.278638	-0.005781
ch-1100-op	90	0.445240	0.437056	0.008185
	60	0.417043	0.388590	0.028454
	45	0.385891	0.365191	0.020700
	30	0.330528	0.311006	0.019522
	20	0.253414	0.262416	-0.009001
	10	0.217316	0.246709	-0.029392
	0	0.236947	0.256236	-0.019289
ch-1100-cl	90	0.389682	0.396381	-0.006698
	60	0.366405	0.361222	0.005183
	45	0.328062	0.321020	0.007042
	30	0.258720	0.256693	0.002027
	20	0.187933	0.214523	-0.026589
	10	0.187063	0.207551	-0.020488
	0	0.187961	0.222846	-0.034885
ch-800-op	90	0.460240	0.449922	0.010319
	60	0.431802	0.403888	0.027915
	45	0.408865	0.385973	0.022892
	30	0.350424	0.334395	0.016030
	20	0.295373	0.285436	0.009938
	10	0.248908	0.264570	-0.015662
	0	0.256760	0.273751	-0.016990
ch-800-cl	90	0.388548	0.399880	-0.011332
	60	0.367823	0.365476	0.002348
	45	0.328143	0.324899	0.003244
	30	0.266647	0.259047	0.007600
	20	0.203429	0.219912	-0.016483
	10	0.198378	0.210390	-0.012011
	0	0.201735	0.225670	-0.023935

APPENDIX J

Effective ventilation coefficients, C_{KQ10}, measured by the decay rate method

Table J.1 Results from measurements of the concentration decay metod to calculate the dimentionless effective ventilation rate coefficient.

Description	Angle	Flow Rate, kQ (m^3/s)	Curve Correlation Factor	Wind Speed at 10 m (m/s)	Sidewall Opening Area m^2	CkQ 10	Averaged CkQ 10	Standard Deviation for CkQ 10
OP-150-1100-0	90	0.2668	0.9938	10.12	0.0605	0.4359	0.4351	0.0162
		0.2534	0.9947	10.10	0.0605	0.4145		
		0.2616	0.9933	10.05	0.0605	0.4301		
		0.2717	0.9936	9.77	0.0605	0.4597		
	60	0.2797	0.9932	9.88	0.0605	0.4677	0.4860	0.0098
		0.2927	0.9945	9.90	0.0605	0.4888		
		0.2927	0.9918	9.78	0.0605	0.4946		
		0.2949	0.9930	10.05	0.0605	0.4849		
		0.2981	0.9930	9.98	0.0605	0.4940		
	45	0.2905	0.9941	9.76	0.0605	0.4922	0.5202	0.0182
		0.3162	0.9928	9.56	0.0605	0.5466		
		0.2992	0.9933	9.68	0.0605	0.5110		
		0.3006	0.9905	9.52	0.0605	0.5217		
		0.3064	0.9928	9.56	0.0605	0.5296		
	30	0.2393	0.9932	9.76	0.0605	0.4054	0.4072	0.0153
		0.2520	0.9925	9.54	0.0605	0.4368		
		0.2367	0.9910	9.95	0.0605	0.3932		
		0.2385	0.9916	9.86	0.0605	0.3999		
		0.2323	0.9925	9.59	0.0605	0.4005		
	20	0.1749	0.9930	9.86	0.0605	0.2932	0.2962	0.0087
		0.1690	0.9912	9.95	0.0605	0.2808		
		0.1770	0.9937	9.63	0.0605	0.3039		
		0.1813	0.9926	9.87	0.0605	0.3041		
		0.1713	0.9915	9.47	0.0605	0.2989		
	10	0.1392	0.9930	10.04	0.0605	0.2292	0.2301	0.0059
		0.1436	0.9914	9.99	0.0605	0.2376		
		0.1419	0.9899	10.01	0.0605	0.2342		
		0.1357	0.9935	9.78	0.0605	0.2293		
		0.1303	0.9938	9.78	0.0605	0.2202		
	0	0.1397	0.9938	9.88	0.0605	0.2336	0.2212	0.0087
		0.1365	0.9933	10.30	0.0605	0.2191		
		0.1316	0.9923	10.50	0.0605	0.2071		
		0.1357	0.9880	9.95	0.0605	0.2254		
		0.1357	0.9908	10.16	0.0605	0.2209		
OP-150-1100-C	90	0.2642	0.9886	10.17	0.0605	0.4294	0.4175	0.0104
		0.2461	0.9951	9.83	0.0605	0.4137		
		0.2524	0.9945	9.94	0.0605	0.4199		
		0.2361	0.9958	9.77	0.0605	0.3995		
		0.2549	0.9899	9.91	0.0605	0.4251		
	60	0.3248	0.9803	9.59	0.0605	0.5599	0.5859	0.0653
		0.3361	0.9761	9.79	0.0605	0.5672		
		0.3110	0.9904	9.82	0.0605	0.5235		
		0.3391	0.9803	9.90	0.0605	0.5663		
		0.4166	0.9816	9.67	0.0605	0.7124		

Table J.1 (cont'd.) Results from measurements of the concentration decay metod to calculate the dimentionless effective ventilation rate coefficient.

Description	Angle	Flow Rate, kQ (m^3/s)	Curve Correl-ation Factor	Wind Speed at 10 m (m/s)	Sidewall Opening Area m^2	CkQ 10	Averaged CkQ 10	Standard Deviation for CkQ 10
	45	0.3762	0.9657	9.52	0.0605	0.6529	0.6223	0.0356
		0.3850	0.9588	9.82	0.0605	0.6480		
		0.3379	0.9860	9.92	0.0605	0.5628		
		0.3729	0.9806	9.51	0.0605	0.6481		
		0.3468	0.9638	9.56	0.0605	0.5995		
	30	0.2003	0.9563	9.85	0.0605	0.3362	0.4002	0.1694
		0.2339	0.9743	9.91	0.0605	0.3901		
		0.1185	0.9719	9.94	0.0605	0.1971		
		0.2156	0.9794	9.73	0.0605	0.3663		
		0.4321	0.9383	10.04	0.0605	0.7114		
	20	0.1566	0.9834	9.95	0.0605	0.2602	0.2517	0.0097
		0.1468	0.9835	9.65	0.0605	0.2514		
		0.1437	0.9755	9.79	0.0605	0.2425		
		0.1459	0.9844	10.05	0.0605	0.2399		
		0.1565	0.9900	9.77	0.0605	0.2648		
	10	0.1350	0.9944	9.77	0.0605	0.2284	0.2308	0.0107
		0.1463	0.9916	9.86	0.0605	0.2453		
		0.1365	0.9952	9.63	0.0605	0.2344		
		0.1285	0.9908	10.00	0.0605	0.2124		
		0.1368	0.9933	9.68	0.0605	0.2336		
	0	0.1628	0.9958	9.68	0.0605	0.2780	0.2721	0.0094
		0.1557	0.9964	9.29	0.0605	0.2770		
		0.1647	0.9947	9.77	0.0605	0.2787		
		0.1504	0.9960	9.79	0.0605	0.2538		
		0.1632	0.9932	9.88	0.0605	0.2729		
OP-150-800-0	90	0.2062	0.9924	10.36	0.044	0.4523	0.4779	0.0206
		0.2201	0.9887	10.25	0.044	0.4882		
		0.2046	0.9934	10.25	0.044	0.4538		
		0.2245	0.9776	10.23	0.044	0.4986		
		0.2185	0.9887	10.00	0.044	0.4965		
	60	0.2029	0.9907	10.09	0.044	0.4570	0.4695	0.0222
		0.2182	0.9868	10.07	0.044	0.4927		
		0.2184	0.9942	10.31	0.044	0.4814		
		0.1977	0.9953	10.40	0.044	0.4320		
		0.2168	0.9943	10.17	0.044	0.4846		
	45	0.1931	0.9083	10.36	0.044	0.4235	0.4314	0.0777
		0.1678	0.9462	10.50	0.044	0.3631		
		0.1830	0.9484	10.25	0.044	0.4059		
		0.1760	0.9545	10.44	0.044	0.3832		
		0.2571	0.9762	10.05	0.044	0.5813		
	30	0.1507	0.8856	10.34	0.044	0.3314	0.3768	0.0589
		0.1749	0.9167	9.86	0.044	0.4032		
		0.1301	0.8714	10.26	0.044	0.2882		
		0.1889	0.8734	10.49	0.044	0.4092		
		0.2057	0.8590	10.34	0.044	0.4523		

Table J.1 (cont'd.) Results from measurements of the concentration decay metod to calculate the dimentionless effective ventilation rate coefficient.

Description	Angle	Flow Rate, kQ (m^3/s)	Curve Correl-ation Factor	Wind Speed at 10 m (m/s)	Sidewall Opening Area m^2	CkQ 10	Averaged CkQ 10	Standard Deviation for CkQ 10
	20	0.1336	0.9440	10.28	0.044	0.2952	0.3317	0.0498
		0.1481	0.9788	10.00	0.044	0.3366		
		0.1333	0.9706	10.17	0.044	0.2979		
		0.1431	0.9832	10.76	0.044	0.3022		
		0.1897	0.9831	10.10	0.044	0.4267		
	10	0.1111	0.9921	10.36	0.044	0.2437	0.2736	0.0402
		0.1299	0.9931	10.45	0.044	0.2824		
		0.1050	0.9937	10.32	0.044	0.2312		
		0.1241	0.9904	10.65	0.044	0.2649		
		0.1550	0.9853	10.18	0.044	0.3460		
	0	0.1044	0.9903	10.21	0.044	0.2325	0.2553	0.0229
		0.1116	0.9922	10.38	0.044	0.2445		
		0.1279	0.9906	10.52	0.044	0.2764		
		0.1065	0.9907	10.31	0.044	0.2348		
		0.1327	0.9918	10.45	0.044	0.2885		
OP-150-800-C	90	0.2046	0.9928	10.59	0.044	0.4389	0.4294	0.0131
		0.1903	0.9961	10.09	0.044	0.4286		
		0.2031	0.9950	10.30	0.044	0.4482		
		0.1857	0.9960	10.26	0.044	0.4114		
		0.1884	0.9955	10.19	0.044	0.4200		
	60	0.2299	0.9936	10.39	0.044	0.5030	0.5408	0.0357
		0.2601	0.9925	10.40	0.044	0.5683		
		0.2693	0.9880	10.76	0.044	0.5687		
		0.2629	0.9924	10.44	0.044	0.5723		
		0.2367	0.9873	10.94	0.044	0.4916		
	45	0.2393	0.9850	10.39	0.044	0.5235	0.5379	0.0857
		0.2730	0.9845	10.72	0.044	0.5786		
		0.2389	0.9888	10.74	0.044	0.5057		
		0.1927	0.9684	10.66	0.044	0.4109		
		0.3192	0.9918	10.81	0.044	0.6709		
	30	0.1814	0.9874	10.58	0.044	0.3896	0.3877	0.0199
		0.1925	0.9809	10.87	0.044	0.4026		
		0.1807	0.9900	10.78	0.044	0.3811		
		0.1703	0.9873	10.94	0.044	0.3537		
		0.1936	0.9829	10.70	0.044	0.4113		
	20	0.1583	0.9870	10.57	0.044	0.3404	0.3273	0.0283
		0.1712	0.9687	10.70	0.044	0.3637		
		0.1547	0.9903	10.72	0.044	0.3279		
		0.1519	0.9826	10.56	0.044	0.3270		
		0.1332	0.9784	10.92	0.044	0.2773		
	10	0.1141	0.9850	10.62	0.044	0.2442	0.2520	0.0219
		0.1355	0.9734	10.98	0.044	0.2804		
		0.1098	0.9908	10.72	0.044	0.2327		
		0.1069	0.9911	10.68	0.044	0.2274		
		0.1323	0.9881	10.92	0.044	0.2754		

Table J.1 (cont'd.) Results from measurements of the concentration decay metod to calculate the dimentionless effective ventilation rate coefficient.

Description	Angle	Flow Rate, kQ (m^3/s)	Curve Correl-ation Factor	Wind Speed at 10 m (m/s)	Sidewall Opening Area m^2	CkQ 10	Averaged CkQ 10	Standard Deviation for CkQ 10
	0	0.1482	0.9806	10.79	0.044	0.3122	0.2957	0.0419
		0.1301	0.9888	10.63	0.044	0.2781		
		0.1116	0.9792	10.75	0.044	0.2360		
		0.1371	0.9835	10.78	0.044	0.2892		
		0.1706	0.9665	10.67	0.044	0.3633		
OP-400-1100-O	90	0.2504	0.9945	10.30	0.0605	0.4019	0.4132	0.0104
		0.2529	0.9944	10.28	0.0605	0.4064		
		0.2516	0.9955	10.09	0.0605	0.4121		
		0.2683	0.9951	10.26	0.0605	0.4323		
		0.2643	0.9954	10.57	0.0605	0.4133		
	60	0.2998	0.8715	10.13	0.0605	0.4892	0.4676	0.0449
		0.3324	0.7810	10.05	0.0605	0.5465		
		0.2723	0.8780	10.32	0.0605	0.4360		
		0.2635	0.8974	10.14	0.0605	0.4294		
		0.2689	0.9218	10.17	0.0605	0.4371		
	45	0.2644	0.9811	10.04	0.0605	0.4353	0.4818	0.0722
		0.2484	0.9756	10.28	0.0605	0.3992		
		0.3776	0.9868	10.61	0.0605	0.5884		
		0.3083	0.9748	10.10	0.0605	0.5043		
	30	0.2812	0.9563	10.23	0.0605	0.4542	0.3965	0.0670
		0.2557	0.9124	10.54	0.0605	0.4009		
		0.1918	0.9558	10.34	0.0605	0.3067		
		0.3012	0.9254	10.30	0.0605	0.4835		
		0.2078	0.9464	10.18	0.0605	0.3373		
	20	0.1854	0.9939	10.26	0.0605	0.2987	0.3075	0.0089
		0.1972	0.9901	10.14	0.0605	0.3214		
		0.1935	0.9950	10.23	0.0605	0.3125		
		0.1813	0.9954	10.08	0.0605	0.2973		
		0.1917	0.9934	10.31	0.0605	0.3073		
	10	0.1469	0.9947	10.23	0.0605	0.2373	0.2337	0.0110
		0.1506	0.9931	10.26	0.0605	0.2426		
		0.1344	0.9947	10.41	0.0605	0.2133		
		0.1502	0.9955	10.19	0.0605	0.2435		
		0.1436	0.9953	10.25	0.0605	0.2317		
	0	0.1429	0.9966	10.21	0.0605	0.2314	0.2288	0.0022
		0.1464	0.9967	10.49	0.0605	0.2307		
		0.1462	0.9962	10.56	0.0605	0.2289		
		0.1447	0.9944	10.49	0.0605	0.2280		
		0.1435	0.9962	10.53	0.0605	0.2253		
OP-400-1100-C	90	0.2461	0.9956	9.83	0.0605	0.4137	0.4018	0.0094
		0.2429	0.9959	10.16	0.0605	0.3953		
		0.2422	0.9949	9.82	0.0605	0.4077		
		0.2422	0.9961	10.34	0.0605	0.3873		
		0.2407	0.9956	9.82	0.0605	0.4051		

Table J.1 (cont'd.) Results from measurements of the concentration decay metod to calculate the dimentionless effective ventilation rate coefficient.

Description	Angle	Flow Rate, kQ (m^3/s)	Curve Correl-ation Factor	Wind Speed at 10 m (m/s)	Sidewall Opening Area m^2	CkQ 10	Averaged CkQ 10	Standard Deviation for CkQ 10
	60	0.5120	0.9916	10.07	0.0605	0.8408	0.6347	0.1127
		0.3080	0.9459	10.14	0.0605	0.5019		
		0.3745	0.9903	10.07	0.0605	0.6150		
		0.3904	0.9932	10.14	0.0605	0.6362		
		0.3561	0.9844	10.16	0.0605	0.5796		
	45	0.4735	0.9635	10.18	0.0605	0.7687	0.6343	0.0862
		0.3090	0.9836	10.10	0.0605	0.5055		
		0.4046	0.9917	10.38	0.0605	0.6446		
		0.4169	0.9910	10.44	0.0605	0.6601		
		0.3739	0.9803	10.43	0.0605	0.5927		
	30	0.2091	0.9595	9.81	0.0605	0.3524	0.4542	0.2382
		0.2311	0.9747	10.10	0.0605	0.3780		
		0.1824	0.9662	10.26	0.0605	0.2939		
		0.5791	0.9550	10.32	0.0605	0.9272		
		0.1987	0.9446	10.28	0.0605	0.3193		
	20	0.1499	0.9913	10.18	0.0605	0.2433	0.2560	0.0173
		0.1489	0.9900	10.07	0.0605	0.2445		
		0.1731	0.9871	9.91	0.0605	0.2887		
		0.1505	0.9867	10.17	0.0605	0.2446		
		0.1554	0.9917	9.92	0.0605	0.2588		
	10	0.1369	0.9939	9.99	0.0605	0.2266	0.2365	0.0055
		0.1462	0.9960	10.14	0.0605	0.2382		
		0.1488	0.9951	10.16	0.0605	0.2422		
		0.1462	0.9939	10.27	0.0605	0.2353		
		0.1491	0.9958	10.26	0.0605	0.2402		
	0	0.1848	0.9920	9.99	0.0605	0.3058	0.2941	0.0124
		0.1905	0.9952	10.39	0.0605	0.3031		
		0.1881	0.9951	10.23	0.0605	0.3038		
		0.1725	0.9954	10.22	0.0605	0.2790		
		0.1735	0.9947	10.28	0.0605	0.2788		
OP-400-800-0	90	0.2195	0.9946	10.53	0.044	0.4738	0.4523	0.0122
		0.2154	0.9958	10.71	0.044	0.4571		
		0.2067	0.9940	10.52	0.044	0.4467		
		0.2132	0.9940	11.02	0.044	0.4397		
		0.2076	0.9949	10.62	0.044	0.4443		
	60	0.2283	0.9955	10.81	0.044	0.4798	0.4656	0.0077
		0.2188	0.9964	10.79	0.044	0.4609		
		0.2195	0.9946	10.78	0.044	0.4630		
		0.2202	0.9967	10.94	0.044	0.4573		
		0.2181	0.9972	10.62	0.044	0.4667		
	45	0.2243	0.9909	10.84	0.044	0.4703	0.4768	0.0499
		0.2224	0.9915	10.94	0.044	0.4619		
		0.2611	0.9740	10.88	0.044	0.5455		
		0.1937	0.9885	11.10	0.044	0.3967		
		0.2465	0.9949	10.99	0.044	0.5095		

Table J.1 (cont'd.) Results from measurements of the concentration decay metod to calculate the dimentionless effective ventilation rate coefficient.

Description	Angle	Flow Rate, kQ (m^3/s)	Curve Correl-ation Factor	Wind Speed at 10 m (m/s)	Sidewall Opening Area m^2	CkQ 10	Averaged CkQ 10	Standard Deviation for CkQ 10
	30	0.1907	0.9636	11.20	0.044	0.3869	0.3793	0.0934
		0.2545	0.9066	10.93	0.044	0.5292		
		0.1459	0.9566	11.08	0.044	0.2991		
		0.1461	0.9596	10.99	0.044	0.3020		
	20	0.1503	0.9934	10.98	0.044	0.3111	0.3134	0.0372
		0.1649	0.9909	10.89	0.044	0.3441		
		0.1779	0.9870	11.06	0.044	0.3656		
		0.1351	0.9933	11.14	0.044	0.2757		
		0.1317	0.9945	11.06	0.044	0.2707		
	10	0.1089	0.9852	10.99	0.044	0.2251	0.2511	0.0334
		0.1152	0.9951	10.97	0.044	0.2387		
		0.1553	0.9948	11.24	0.044	0.3140		
		0.1082	0.9919	11.02	0.044	0.2231		
		0.1247	0.9900	11.14	0.044	0.2545		
	0	0.1419	0.9932	11.20	0.044	0.2879	0.2654	0.0184
		0.1316	0.9962	11.01	0.044	0.2717		
		0.1183	0.9964	11.36	0.044	0.2368		
		0.1375	0.9921	11.23	0.044	0.2783		
		0.1230	0.9944	11.07	0.044	0.2525		
OP-400-800-C	90	0.1826	0.9968	10.31	0.044	0.4025	0.4193	0.0162
		0.1874	0.9963	10.26	0.044	0.4152		
		0.1994	0.9966	10.16	0.044	0.4462		
		0.1939	0.9960	10.30	0.044	0.4279		
		0.1869	0.9950	10.49	0.044	0.4049		
	60	0.2664	0.9912	10.26	0.044	0.5902	0.5566	0.0423
		0.2512	0.9875	10.36	0.044	0.5509		
		0.2810	0.9866	10.48	0.044	0.6095		
		0.2434	0.9881	10.14	0.044	0.5454		
		0.2289	0.9838	10.68	0.044	0.4869		
	45	0.2750	0.9901	10.54	0.044	0.5928	0.6365	0.0872
		0.2899	0.9819	10.52	0.044	0.6265		
		0.2654	0.9906	10.65	0.044	0.5666		
		0.2653	0.9676	10.22	0.044	0.5900		
		0.3737	0.9024	10.53	0.044	0.8066		
	30	0.1973	0.9782	10.48	0.044	0.4279	0.4377	0.0614
		0.2146	0.9590	10.58	0.044	0.4609		
		0.1965	0.9908	10.40	0.044	0.4294		
		0.1556	0.8812	10.40	0.044	0.3400		
		0.2418	0.9640	10.36	0.044	0.5303		
	20	0.1142	0.9866	10.30	0.044	0.2520	0.2634	0.0308
		0.0994	0.9853	10.40	0.044	0.2172		
		0.1117	0.9870	10.04	0.044	0.2529		
		0.1355	0.9891	10.19	0.044	0.3021		
		0.1323	0.9885	10.27	0.044	0.2927		

Table J.1 (cont'd.) Results from measurements of the concentration decay metod to calculate the dimentionless effective ventilation rate coefficient.

Description	Angle	Flow Rate, kQ (m^3/s)	Curve Correl-ation Factor	Wind Speed at 10 m (m/s)	Sidewall Opening Area m^2	CkQ 10	Averaged CkQ 10	Standard Deviation for CkQ 10
	10	0.1318	0.9943	10.28	0.044	0.2912	0.2931	0.0088
		0.1298	0.9947	10.44	0.044	0.2826		
		0.1318	0.9923	10.35	0.044	0.2894		
		0.1345	0.9915	10.44	0.044	0.2928		
		0.1401	0.9924	10.30	0.044	0.3092		
	0	0.1615	0.9895	10.09	0.044	0.3637	0.3497	0.0144
		0.1590	0.9916	10.13	0.044	0.3567		
		0.1639	0.9935	10.44	0.044	0.3568		
		0.1624	0.9895	10.58	0.044	0.3488		
		0.1437	0.9915	10.13	0.044	0.3224		
OP-CH-1100-0	90	0.2434	0.9958	9.88	0.0605	0.4070	0.4077	0.0091
		0.2493	0.9966	10.05	0.0605	0.4099		
		0.2462	0.9964	10.32	0.0605	0.3942		
		0.2542	0.9956	10.01	0.0605	0.4196		
	60	0.2697	0.9942	9.64	0.0605	0.4624	0.4661	0.0196
		0.2973	0.9952	10.05	0.0605	0.4888		
		0.2947	0.9950	9.98	0.0605	0.4883		
		0.2708	0.9961	10.16	0.0605	0.4407		
		0.2794	0.9960	10.26	0.0605	0.4502		
	45	0.2893	0.9934	10.26	0.0605	0.4661	0.4628	0.0159
		0.2684	0.9952	10.23	0.0605	0.4335		
		0.2893	0.9954	10.25	0.0605	0.4667		
		0.2950	0.9941	10.12	0.0605	0.4820		
		0.2789	0.9945	9.90	0.0605	0.4658		
	30	0.2121	0.9909	9.50	0.0605	0.3691	0.3565	0.0142
		0.2079	0.9938	9.99	0.0605	0.3440		
		0.2207	0.9956	10.35	0.0605	0.3525		
		0.2265	0.9946	9.94	0.0605	0.3768		
		0.2059	0.9948	10.00	0.0605	0.3403		
	20	0.1587	0.9943	9.95	0.0605	0.2436	0.2638	0.0092
		0.1572	0.9939	10.28	0.0605	0.2526		
		0.1619	0.9943	10.23	0.0605	0.2615		
		0.1573	0.9942	9.98	0.0605	0.2606		
		0.1701	0.9937	10.01	0.0605	0.2808		
	10	0.1223	0.9940	9.86	0.0605	0.2050	0.2110	0.0052
		0.1262	0.9951	9.83	0.0605	0.2121		
		0.1249	0.9958	10.04	0.0605	0.2056		
		0.1234	0.9938	9.59	0.0605	0.2127		
		0.1306	0.9942	9.85	0.0605	0.2192		
	0	0.1322	0.9943	9.58	0.0605	0.2282	0.2113	0.0124
		0.1243	0.9962	9.85	0.0605	0.2087		
		0.1282	0.9963	9.54	0.0605	0.2222		
		0.1193	0.9963	10.16	0.0605	0.1942		
		0.1218	0.9962	9.91	0.0605	0.2031		

Table J.1 (cont'd.) Results from measurements of the concentration decay metod to calculate the dimentionless effective ventilation rate coefficient.

Description	Angle	Flow Rate, kQ (m^3/s)	Curve Correl-ation Factor	Wind Speed at 10 m (m/s)	Sidewall Opening Area m^2	CkQ 10	Averaged CkQ 10	Standard Deviation for CkQ 10
OP-CH-1100-C	90	0.2528	0.9949	10.36	0.0605	0.4032	0.4065	0.0110
		0.2667	0.9966	10.34	0.0605	0.4265		
		0.2517	0.9951	10.19	0.0605	0.4081		
		0.2455	0.9960	10.30	0.0605	0.3941		
		0.2476	0.9966	10.22	0.0605	0.4004		
	60	0.5399	0.9864	10.09	0.0605	0.8843	0.7613	0.1560
		0.4082	0.9853	10.07	0.0605	0.6703		
		0.6086	0.9780	10.01	0.0605	1.0046		
		0.3621	0.9846	9.99	0.0605	0.5992		
		0.3877	0.9919	9.88	0.0605	0.6483		
	45	0.2725	0.9823	10.12	0.0605	0.4452	0.4611	0.0385
		0.3063	0.9528	10.19	0.0605	0.4966		
		0.3106	0.9771	10.32	0.0605	0.4973		
		0.2420	0.9819	10.14	0.0605	0.3944		
		0.2881	0.9736	10.09	0.0605	0.4719		
	30	0.2728	0.9630	10.25	0.0605	0.4401	0.3266	0.0576
		0.1932	0.9886	10.28	0.0605	0.3105		
		0.1749	0.9857	10.30	0.0605	0.2807		
		0.1815	0.9918	10.07	0.0605	0.2980		
		0.1886	0.9791	10.26	0.0605	0.3039		
	20	0.1117	0.9950	9.77	0.0605	0.1890	0.1771	0.0078
		0.1065	0.9892	10.05	0.0605	0.1751		
		0.1020	0.9929	9.99	0.0605	0.1688		
		0.1056	0.9932	9.54	0.0605	0.1830		
		0.1038	0.9924	10.12	0.0605	0.1696		
	10	0.1255	0.9938	10.18	0.0605	0.2037	0.2044	0.0113
		0.1209	0.9955	10.40	0.0605	0.1921		
		0.1194	0.9942	9.90	0.0605	0.1994		
		0.1236	0.9944	10.17	0.0605	0.2009		
		0.1379	0.9922	10.10	0.0605	0.2256		
	0	0.1762	0.9943	9.63	0.0605	0.3025	0.2621	0.0220
		0.1547	0.9954	9.86	0.0605	0.2594		
		0.1437	0.9905	9.98	0.0605	0.2381		
		0.1589	0.9918	10.00	0.0605	0.2626		
		0.1529	0.9941	10.19	0.0605	0.2479		
OP-CH-800-O	90	0.1995	0.9866	10.44	0.044	0.4343	0.4464	0.0108
		0.2007	0.9866	10.36	0.044	0.4402		
		0.2083	0.9693	10.34	0.044	0.4580		
		0.1978	0.9859	10.25	0.044	0.4387		
		0.2117	0.9841	10.44	0.044	0.4609		
	60	0.1968	0.9617	10.45	0.044	0.4279	0.4318	0.0250
		0.1867	0.9649	10.57	0.044	0.4015		
		0.2201	0.9632	10.48	0.044	0.4774		
		0.1917	0.9679	10.34	0.044	0.4215		
		0.1983	0.9786	10.47	0.044	0.4306		

Table J.1 (cont'd.) Results from measurements of the concentration decay metod to calculate the dimentionless effective ventilation rate coefficient.

Description	Angle	Flow Rate, kQ (m^3/s)	Curve Correl-ation Factor	Wind Speed at 10 m (m/s)	Sidewall Opening Area m^2	CkQ 10	Averaged CkQ 10	Standard Deviation for CkQ 10
	45	0.2647	0.9647	10.58	0.044	0.5685	0.5200	0.0676
		0.2910	0.9350	10.63	0.044	0.6220		
		0.2362	0.9239	10.61	0.044	0.5061		
		0.1989	0.9679	10.40	0.044	0.4346		
		0.2129	0.9715	10.32	0.044	0.4687		
	30	0.1638	0.9195	10.80	0.044	0.3447	0.3637	0.1002
		0.2506	0.9109	10.52	0.044	0.5415		
		0.1624	0.9223	10.80	0.044	0.3417		
		0.1067	0.9124	10.52	0.044	0.2306		
		0.1714	0.8990	10.81	0.044	0.3602		
	20	0.1386	0.9964	10.59	0.044	0.2973	0.3028	0.0118
		0.1541	0.9939	11.10	0.044	0.3156		
		0.1464	0.9962	10.56	0.044	0.3152		
		0.1356	0.9941	10.84	0.044	0.2843		
		0.1417	0.9965	10.67	0.044	0.3018		
	10	0.1226	0.9955	10.67	0.044	0.2611	0.2503	0.0123
		0.1175	0.9966	10.96	0.044	0.2437		
		0.1216	0.9962	10.50	0.044	0.2631		
		0.1129	0.9941	10.99	0.044	0.2334		
	0	0.1309	0.9925	10.76	0.044	0.2764	0.2293	0.0284
		0.1072	0.9955	10.75	0.044	0.2267		
		0.1010	0.9967	11.07	0.044	0.2073		
		0.1009	0.9963	11.10	0.044	0.2066		
OP-CH-800-C	90	0.1844	0.9962	10.22	0.044	0.4101	0.4059	0.0088
		0.1859	0.9952	10.39	0.044	0.4067		
		0.1918	0.9959	10.54	0.044	0.4135		
		0.1879	0.9964	10.40	0.044	0.4106		
		0.1760	0.9962	10.28	0.044	0.3889		
	60	0.2422	0.9899	10.13	0.044	0.5434	0.5670	0.0267
		0.2736	0.9881	10.52	0.044	0.5912		
		0.2655	0.9925	10.13	0.044	0.5957		
		0.2390	0.9956	10.28	0.044	0.5281		
		0.2639	0.9906	10.40	0.044	0.5766		
	45	0.2218	0.9932	10.44	0.044	0.4829	0.4923	0.0470
		0.2232	0.9873	10.54	0.044	0.4811		
		0.2190	0.9886	10.45	0.044	0.4762		
		0.2110	0.9817	10.89	0.044	0.4403		
		0.2652	0.9847	10.38	0.044	0.5809		
	30	0.1709	0.9829	10.65	0.044	0.3648	0.3445	0.0243
		0.1622	0.9924	10.18	0.044	0.3621		
		0.1598	0.9851	10.16	0.044	0.3576		
		0.1579	0.9921	10.59	0.044	0.3387		
		0.1391	0.9797	10.56	0.044	0.2995		

Table J.1 (cont'd.) Results from measurements of the concentration decay metod to calculate the dimentionless effective ventilation rate coefficient.

Description	Angle	Flow Rate, kQ (m^3/s)	Curve Correl-ation Factor	Wind Speed at 10 m (m/s)	Sidewall Opening Area m^2	CkQ 10	Averaged CkQ 10	Standard Deviation for CkQ 10
	20	0.0969	0.9953	10.45	0.044	0.2107	0.2075	0.0115
		0.0963	0.9908	10.08	0.044	0.2172		
		0.0880	0.9923	10.63	0.044	0.1881		
		0.1023	0.9947	10.85	0.044	0.2142		
	10	0.1042	0.9943	10.45	0.044	0.2266	0.2239	0.0086
		0.0977	0.9935	10.74	0.044	0.2068		
		0.1052	0.9950	10.54	0.044	0.2268		
		0.1079	0.9960	10.67	0.044	0.2298		
		0.1071	0.9945	10.61	0.044	0.2295		
	0	0.1312	0.9950	10.70	0.044	0.2787	0.2878	0.0158
		0.1494	0.9941	10.65	0.044	0.3189		
		0.1361	0.9968	10.97	0.044	0.2820		
		0.1337	0.9952	11.02	0.044	0.2757		
		0.1338	0.9963	10.72	0.044	0.2836		

Table J.2 Differences between the measured C_{kq10} (by concentration decay) and the calculated C_{q10} (by pressure difference method).

Description	Angle	Averaged CkQ 10	CQ 10 Open Model	CQ 10 Sealed Model	CkQ10-CQ10 Open	CkQ10-CQ10 Sealed
OP-150-1100-O	90	0.4351	0.4628	0.4316	-0.0277	0.0035
	60	0.4860	0.4560	0.4067	0.0299	0.0793
	45	0.5202	0.4140	0.3866	0.1063	0.1336
	30	0.4072	0.3444	0.3281	0.0628	0.0791
	20	0.2962	0.2644	0.2895	0.0317	0.0067
	10	0.2301	0.2295	0.2594	0.0006	-0.0293
	0	0.2212	0.2497	0.2625	-0.0285	-0.0413
OP-150-1100-C	90	0.4175	0.4295	0.3979	-0.0120	0.0196
	60	0.5859	0.4055	0.3774	0.1804	0.2085
	45	0.6223	0.3556	0.3366	0.2667	0.2856
	30	0.4002	0.2817	0.2837	0.1185	0.1165
	20	0.2517	0.2043	0.2440	0.0475	0.0077
	10	0.2308	0.1941	0.2211	0.0367	0.0098
	0	0.2721	0.1998	0.2317	0.0722	0.0404
OP-150-800-O	90	0.4779	0.4829	0.4477	-0.0050	0.0302
	60	0.4695	0.4818	0.4371	-0.0123	0.0324
	45	0.4314	0.4449	0.4201	-0.0136	0.0113
	30	0.3768	0.3834	0.3662	-0.0065	0.0107
	20	0.3317	0.3116	0.3212	0.0201	0.0105
	10	0.2736	0.2643	0.2862	0.0094	-0.0126
	0	0.2553	0.2737	0.2829	-0.0184	-0.0276
OP-150-800-C	90	0.4294	0.4268	0.4094	0.0027	0.0201
	60	0.5408	0.4067	0.3916	0.1341	0.1491
	45	0.5379	0.3551	0.3476	0.1829	0.1903
	30	0.3877	0.2859	0.3026	0.1018	0.0850
	20	0.3273	0.2215	0.2597	0.1058	0.0676
	10	0.2520	0.2101	0.2293	0.0419	0.0227
	0	0.2957	0.2207	0.2381	0.0750	0.0576
OP-400-1100-O	90	0.4132	0.4985	0.4577	-0.0853	-0.0445
	60	0.4676	0.5274	0.4803	-0.0598	-0.0127
	45	0.4818	0.5060	0.4699	-0.0242	0.0119
	30	0.3965	0.4418	0.4023	-0.0453	-0.0058
	20	0.3075	0.3752	0.3436	-0.0677	-0.0361
	10	0.2337	0.3236	0.2921	-0.0899	-0.0584
	0	0.2288	0.3572	0.2907	-0.1284	-0.0618
OP-400-1100-C	90	0.4018	0.4887	0.4433	-0.0869	-0.0414
	60	0.6347	0.4733	0.4457	0.1614	0.1890
	45	0.6343	0.4431	0.4308	0.1912	0.2035
	30	0.4542	0.3654	0.3583	0.0887	0.0959
	20	0.2560	0.3044	0.2965	-0.0484	-0.0405
	10	0.2365	0.2930	0.2468	-0.0565	-0.0103
	0	0.2941	0.3195	0.2579	-0.0253	0.0362

Table J.2 (cont'd.) Differences between the measured C_{kQ10} (by concentration decay) and the calculated C_{Q10} (by pressure difference method).

Description	Angle	Averaged CkQ 10	CQ 10 Open Model	CQ 10 Sealed Model	CkQ10-CQ10 Open	CkQ10-CQ10 Sealed
OP-400-800-O	90	0.4523	0.5119	0.4924	-0.0597	-0.0401
	60	0.4656	0.5668	0.5649	-0.1012	-0.0993
	45	0.4768	0.5447	0.5495	-0.0679	-0.0728
	30	0.3793	0.5204	0.4670	-0.1410	-0.0877
	20	0.3134	0.4418	0.3943	-0.1284	-0.0808
	10	0.2511	0.3762	0.3263	-0.1251	-0.0752
	0	0.2654	0.4061	0.3152	-0.1406	-0.0497
OP-400-800-C	90	0.4193	0.4998	0.4633	-0.0805	-0.0440
	60	0.5566	0.4975	0.5131	0.0590	0.0434
	45	0.6365	0.4759	0.4880	0.1605	0.1485
	30	0.4377	0.3272	0.4023	0.1106	0.0354
	20	0.2634	0.2798	0.3307	-0.0165	-0.0674
	10	0.2931	0.2621	0.2627	0.0309	0.0304
	0	0.3497	0.2729	0.2786	0.0768	0.0711
OP-CH-1100-O	90	0.4077	0.4452	0.4371	-0.0376	-0.0294
	60	0.4661	0.4170	0.3886	0.0491	0.0775
	45	0.4628	0.3859	0.3652	0.0769	0.0976
	30	0.3565	0.3305	0.3110	0.0260	0.0455
	20	0.2638	0.2534	0.2624	0.0104	0.0014
	10	0.2110	0.2173	0.2467	-0.0064	-0.0358
	0	0.2113	0.2369	0.2562	-0.0257	-0.0450
OP-CH-1100-C	90	0.4065	0.3897	0.3964	0.0168	0.0101
	60	0.7613	0.3664	0.3612	0.3949	0.4001
	45	0.4611	0.3281	0.3210	0.1330	0.1401
	30	0.3266	0.2587	0.2567	0.0679	0.0699
	20	0.1771	0.1879	0.2145	-0.0108	-0.0374
	10	0.2044	0.1871	0.2076	0.0173	-0.0032
	0	0.2621	0.1880	0.2228	0.0741	0.0393
OP-CH-800-O	90	0.4464	0.4602	0.4499	-0.0138	-0.0035
	60	0.4318	0.4318	0.4039	-0.0000	0.0279
	45	0.5200	0.4089	0.3860	0.1111	0.1340
	30	0.3637	0.3504	0.3344	0.0133	0.0293
	20	0.3028	0.2954	0.2854	0.0075	0.0174
	10	0.2503	0.2489	0.2646	0.0014	-0.0142
	0	0.2293	0.2568	0.2738	-0.0275	-0.0445
OP-CH-800-C	90	0.4059	0.3885	0.3999	0.0174	0.0061
	60	0.5670	0.3678	0.3655	0.1992	0.2015
	45	0.4923	0.3281	0.3249	0.1641	0.1674
	30	0.3445	0.2666	0.2590	0.0779	0.0855
	20	0.2075	0.2034	0.2199	0.0041	-0.0124
	10	0.2239	0.1984	0.2104	0.0255	0.0135
	0	0.2878	0.2017	0.2257	0.0861	0.0621

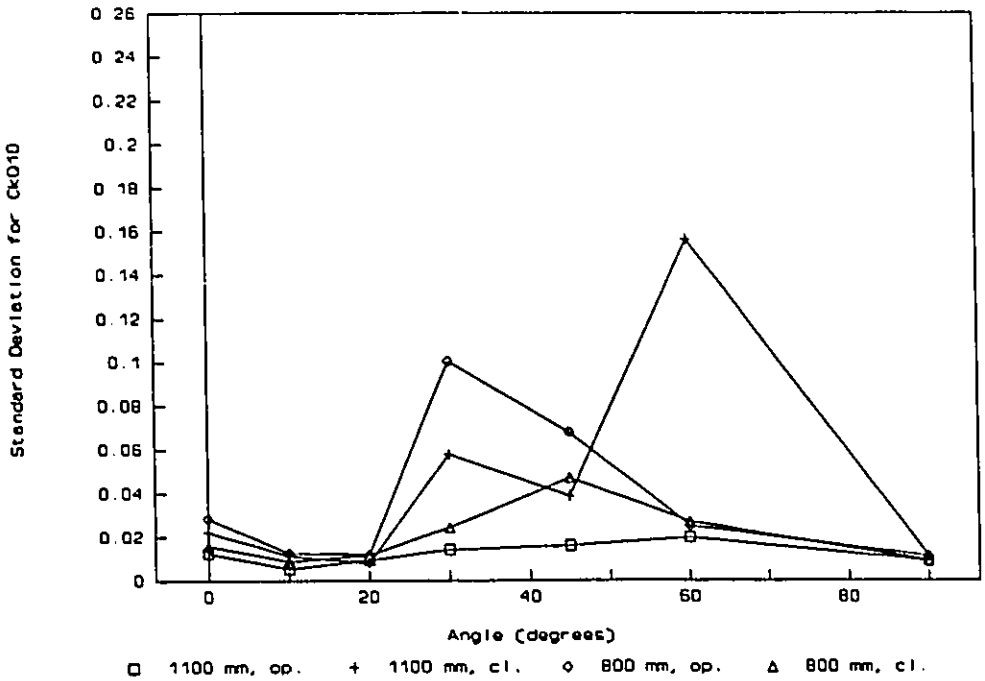

Figure J.1 Standard deviation for C_{kq10} versus wind angles, chimney.

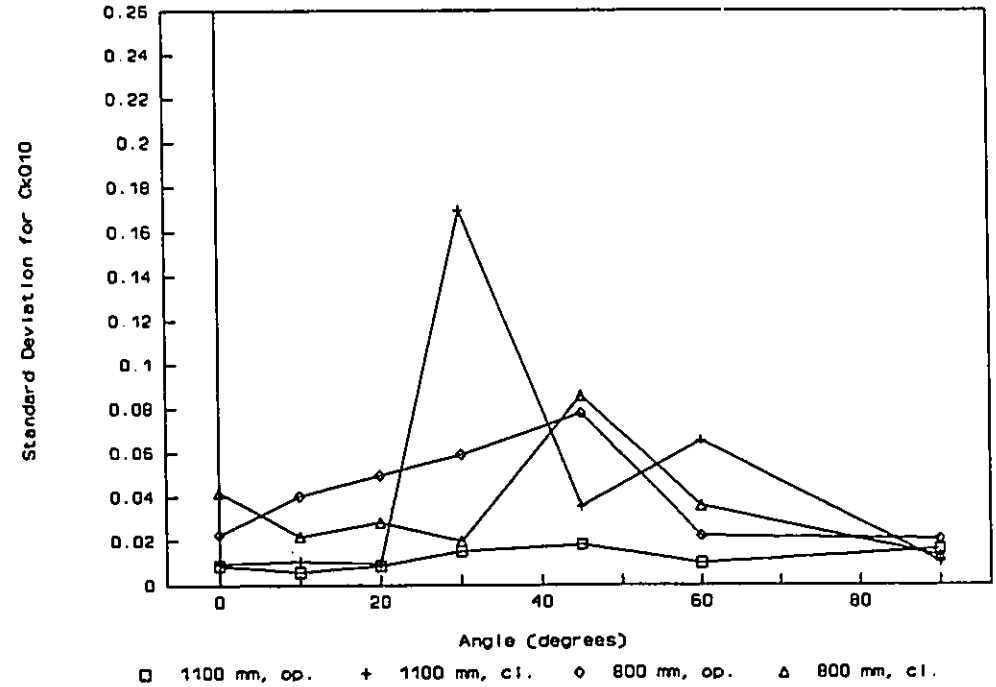

Figure J.2 Standard deviation for C_{kq10} versus wind angles, simulated 150 mm ridge.

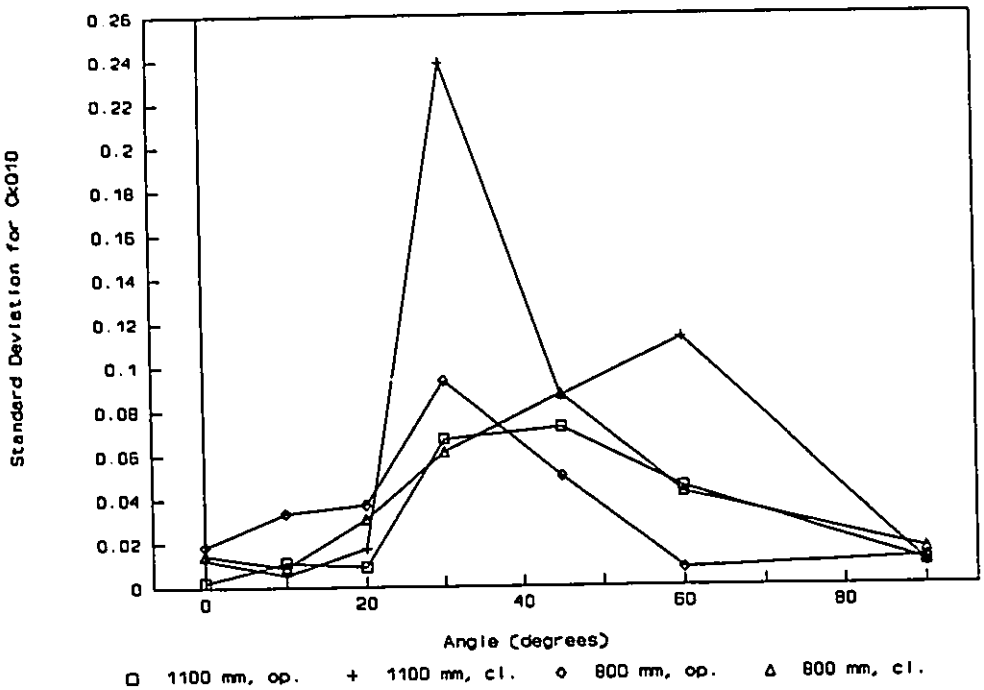

Figure J.3 Standard deviation for C_{kq10} versus wind angles, simulated 400 mm ridge.

APPENDIX K

Adjusted data for OP-400-800-C, complete set

Appendix K contains the contour lines, internal pressure coefficients (Cp_{in}), air inlet and outlet zones, airflow diagrams, calculated ventilation rate coefficients (C_{q10}) with the differences between open and closed model types, and the differences between the effective ventilation coefficients (C_{Kq10}) and calculated ventilation coefficients (C_{q10}) for all wind angles of incidence, especially those adjusted for: 45°, 30°, 20°, 10° and 0°.

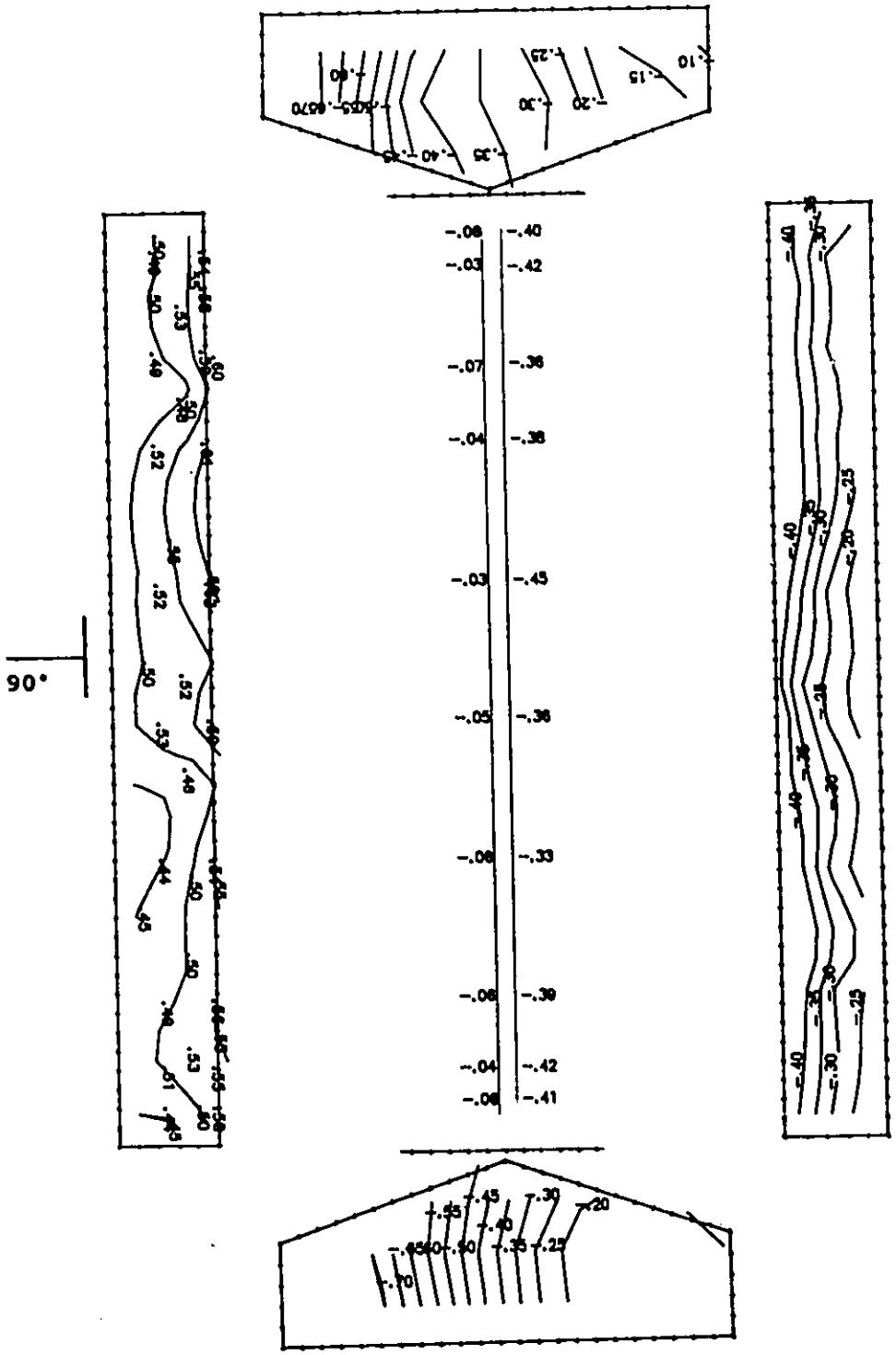

Figure K.1a Cps contour lines: open model, simulated 400 mm ridge and 800 mm sidewall openings, closed end walls, wind angle of 90°.

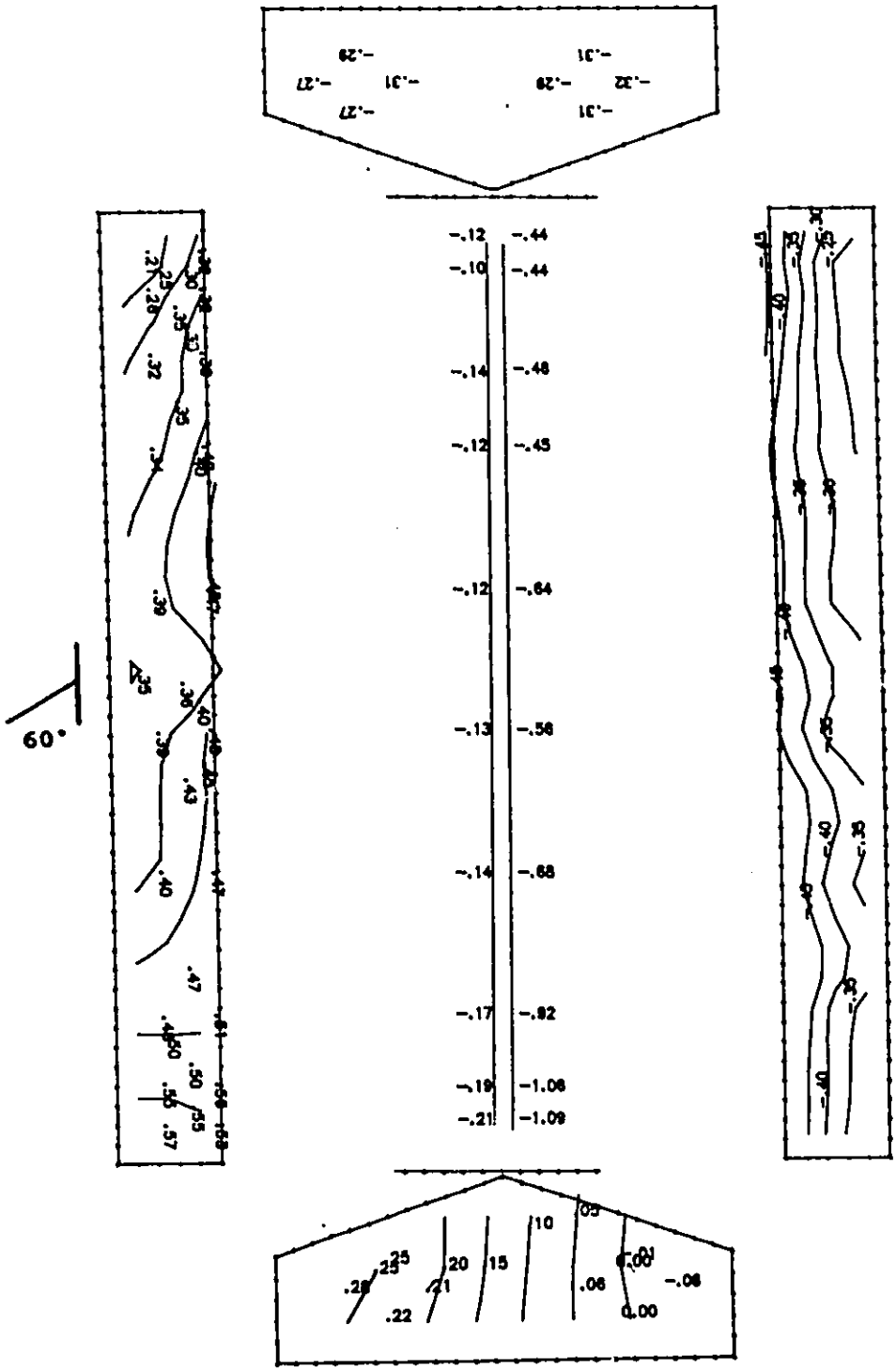

Figure K.1b Cps contour lines: open model, simulated 400 mm ridge and 800 mm sidewall openings, closed end walls, wind angle of 60°.

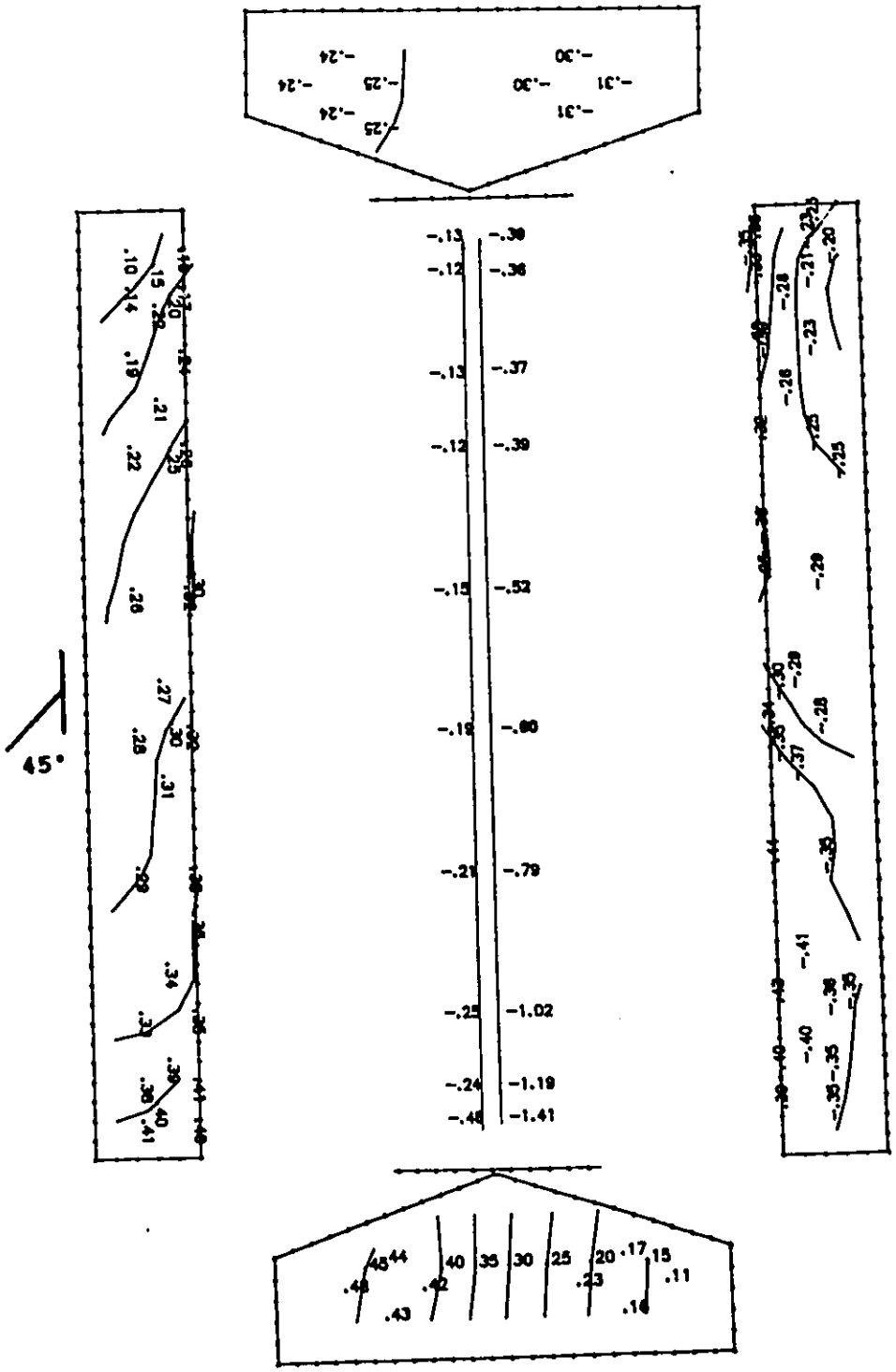

Figure K.1c Cps contour lines: open model, simulated 400 mm ridge and 800 mm sidewall openings, closed end walls, wind angle of 45°.

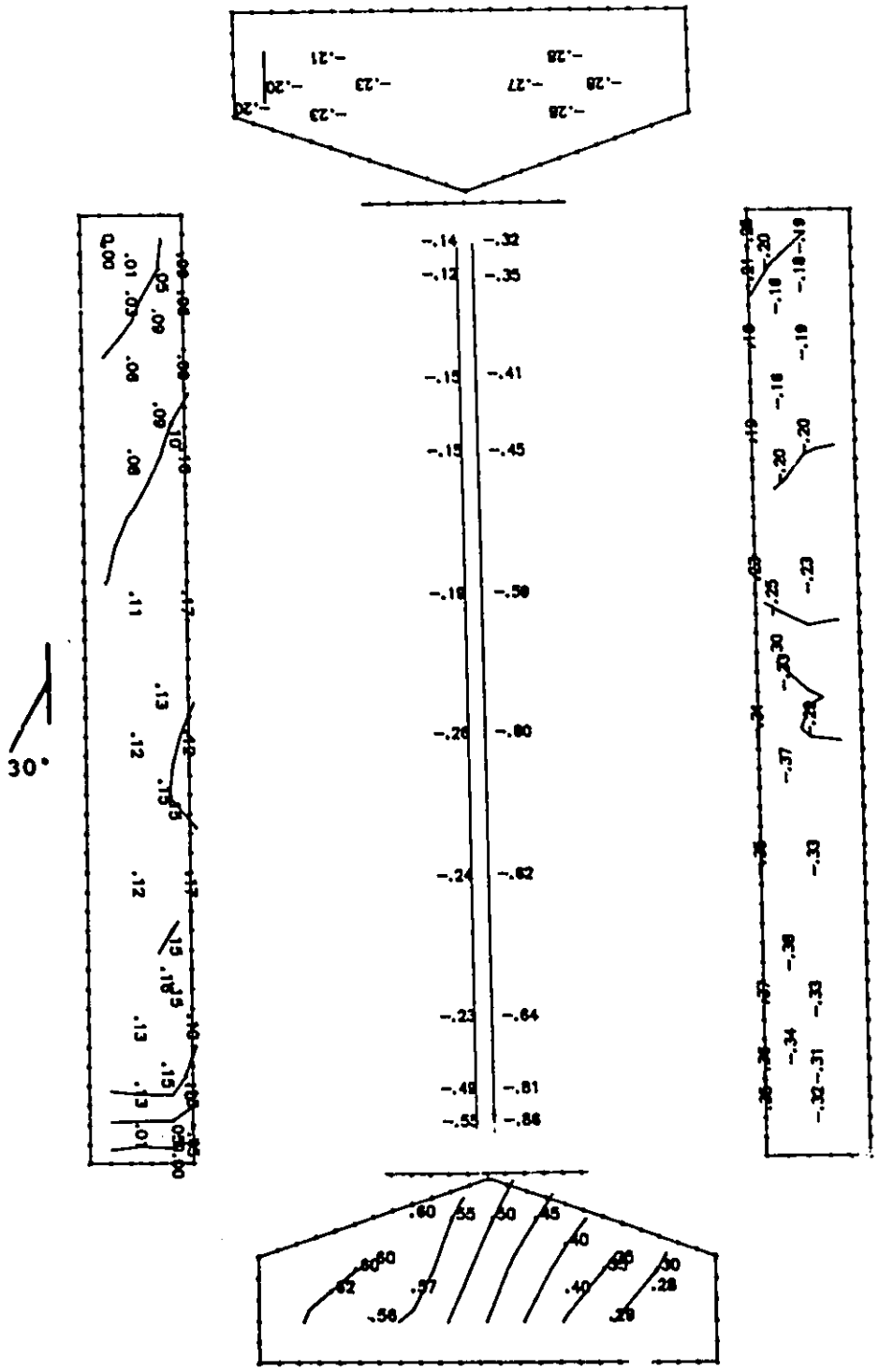

Figure K.1d Cps contour lines: open model, simulated 400 mm ridge and 800 mm sidewall openings, closed end walls, wind angle of 30°.

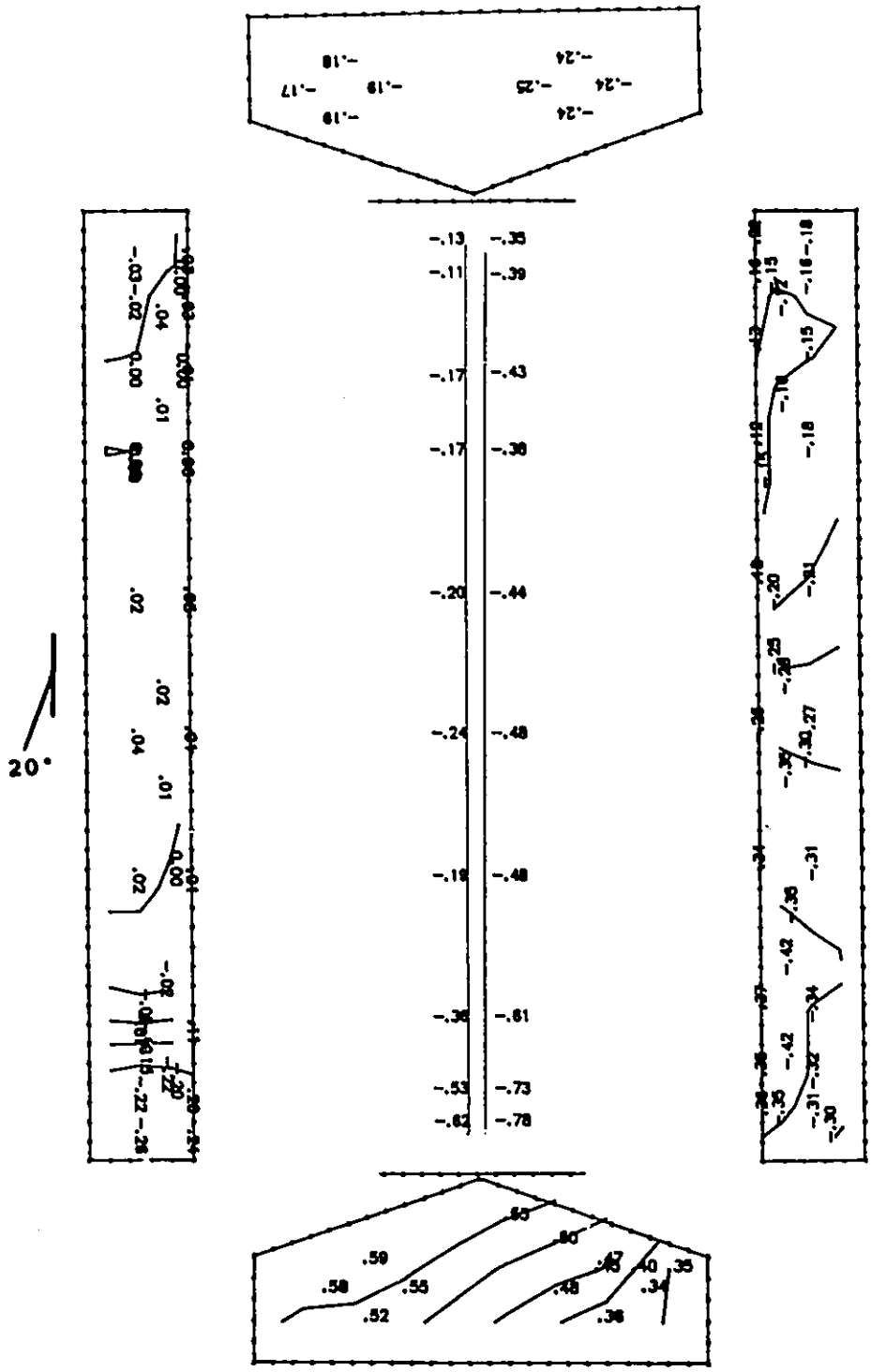

Figure K.1e Cps contour lines: open model, simulated 400 mm ridge and 800 mm sidewall openings, closed end walls, wind angle of 20°.

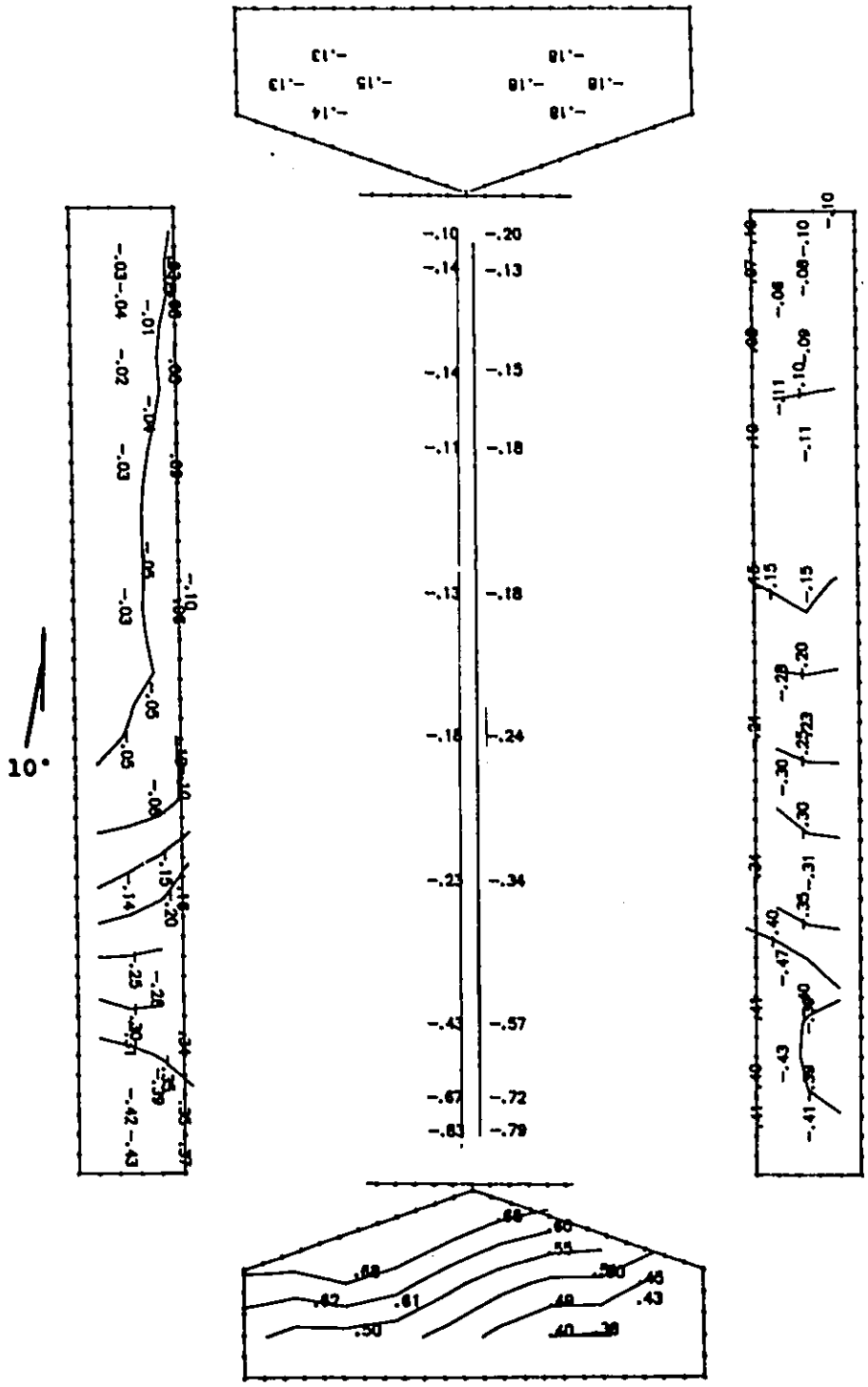

Figure K.1f Cps contour lines: open model, simulated 400 mm ridge and 800 mm sidewall openings, closed end walls, wind angle of 10°.

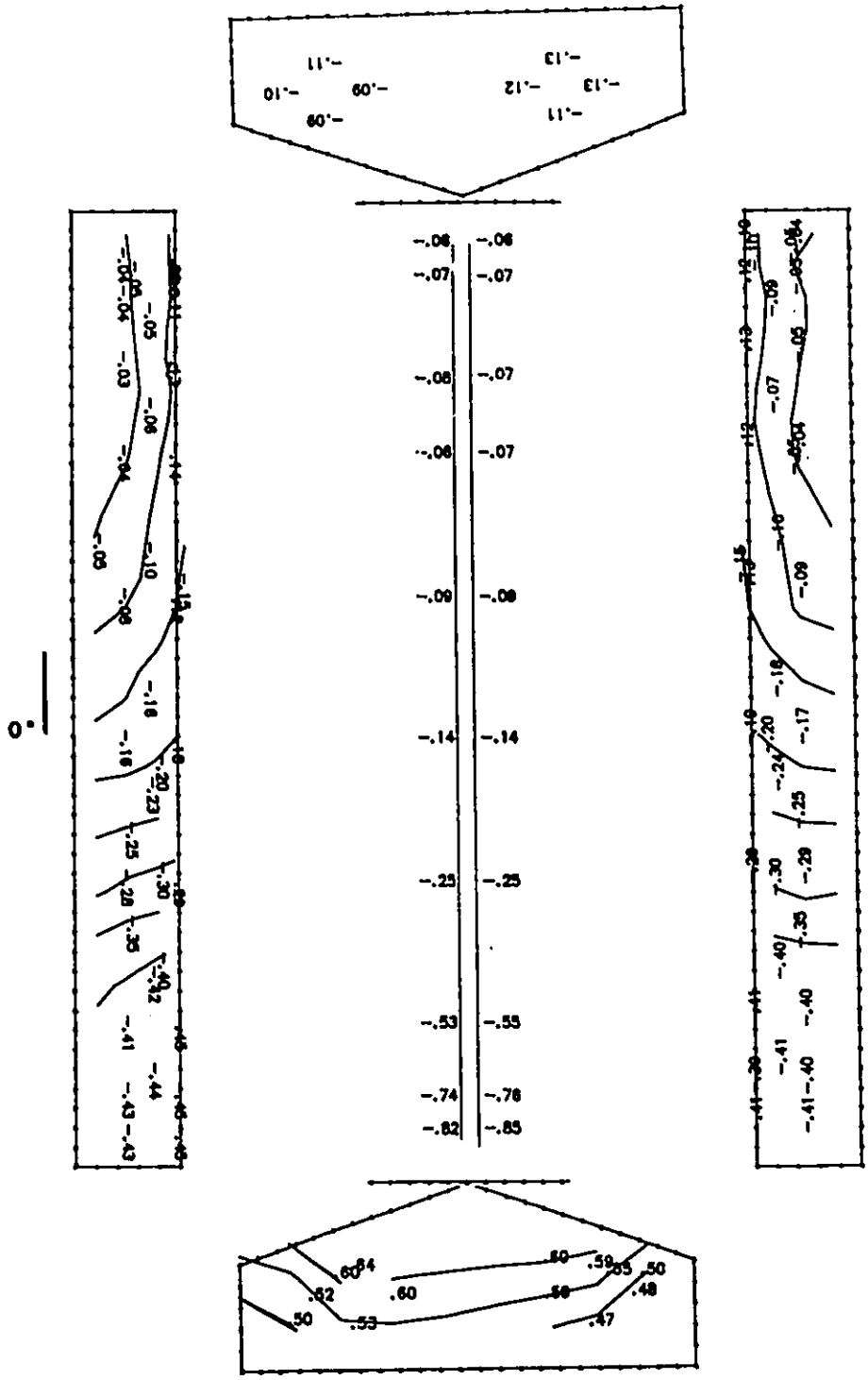

Figure K.1g Cps contour lines: open model, simulated 400 mm ridge and 800 mm sidewall openings, closed end walls, wind angle of 0°.

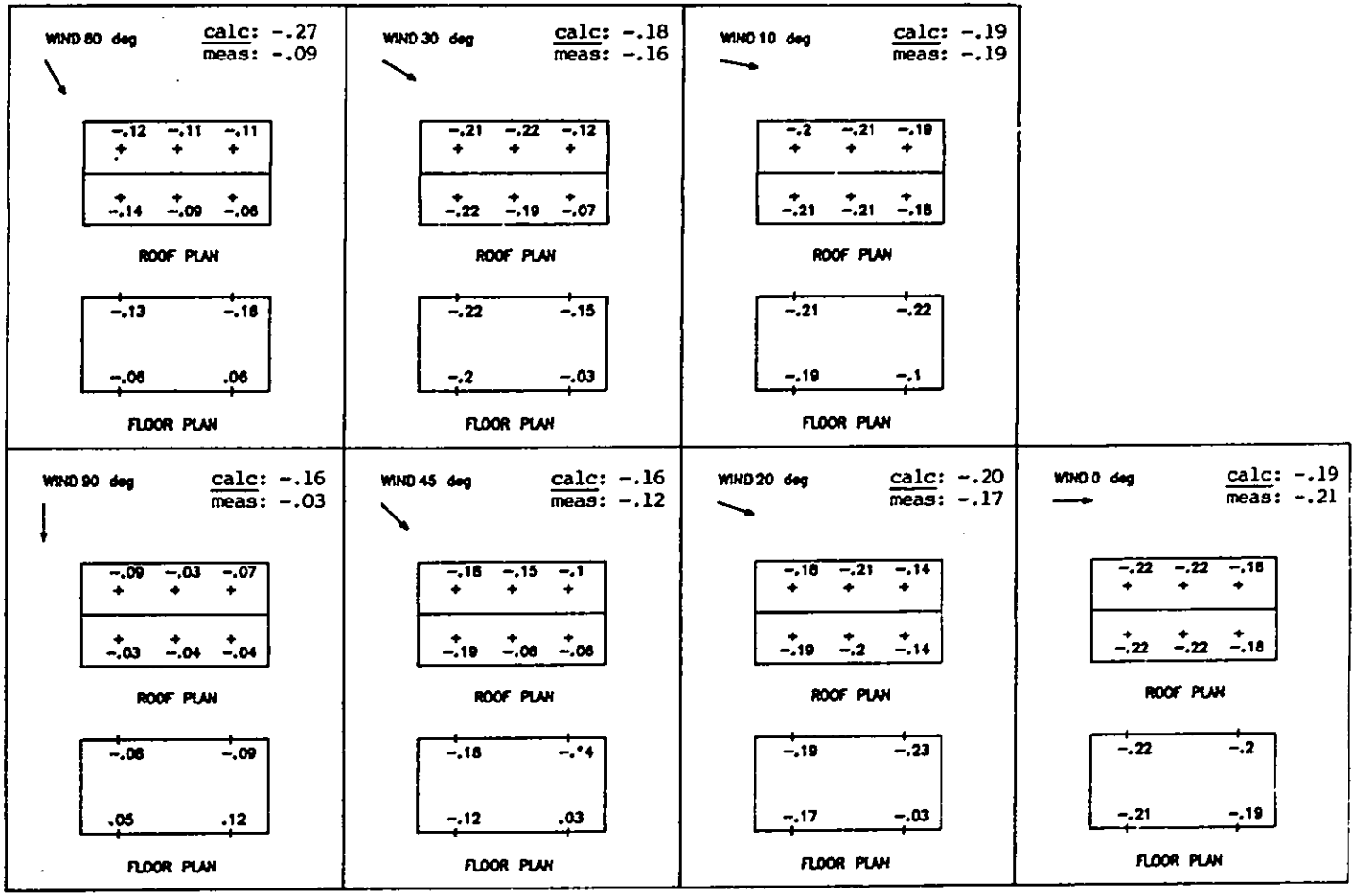

Figure K.2 Measured Cp_{in}: open model, simulated 400 mm ridge and 1100 mm sidewall openings, closed end walls, 7 wind angles of incidence, configuration #4.

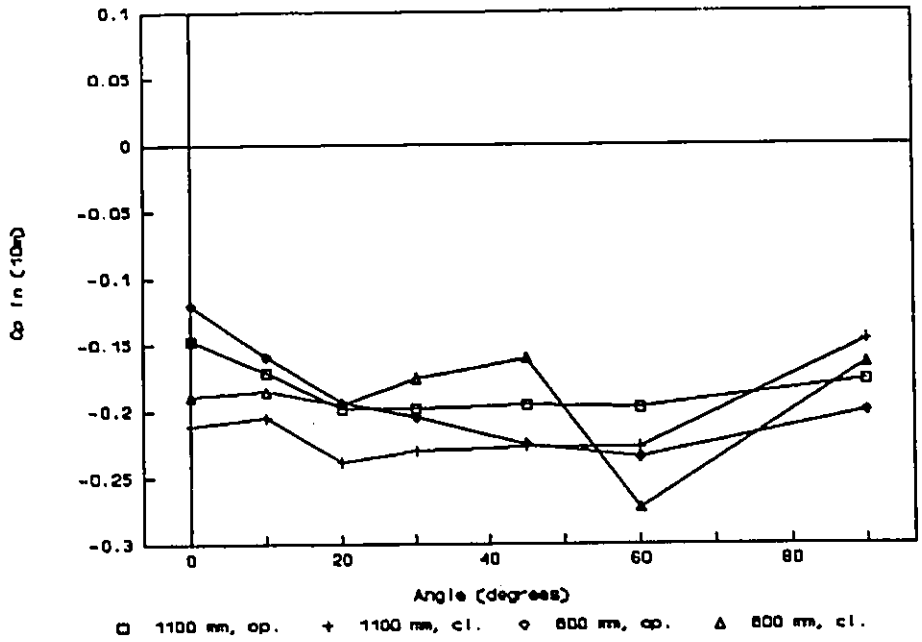

Figure K.3 Open model, simulated 400 mm ridge, internal pressure coefficients, open and closed end walls.

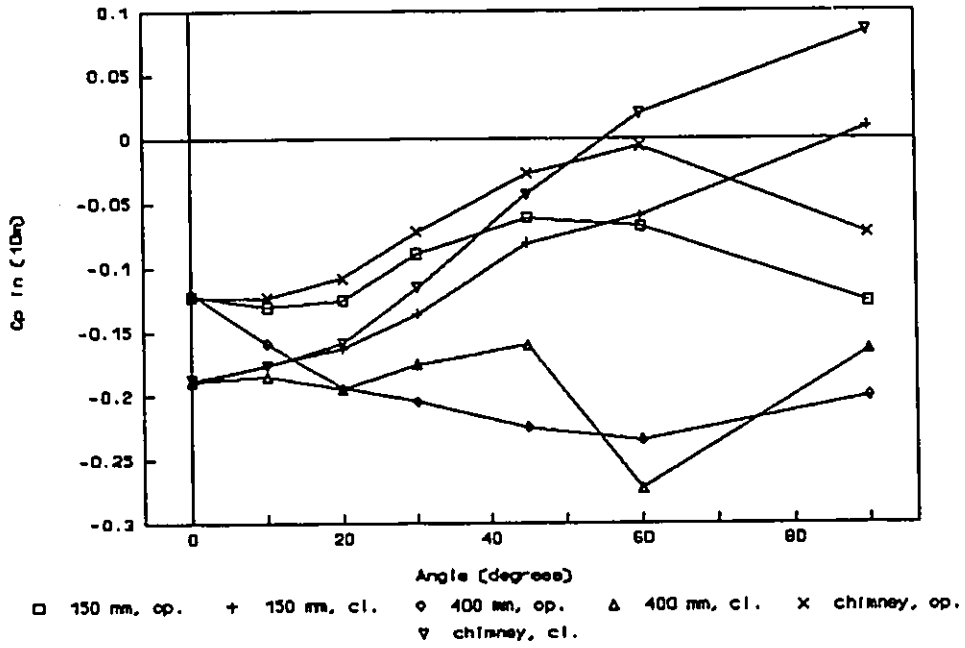

Figure K.4 Open model, simulated 800 mm sidewall, internal pressure coefficients, open and closed end walls.

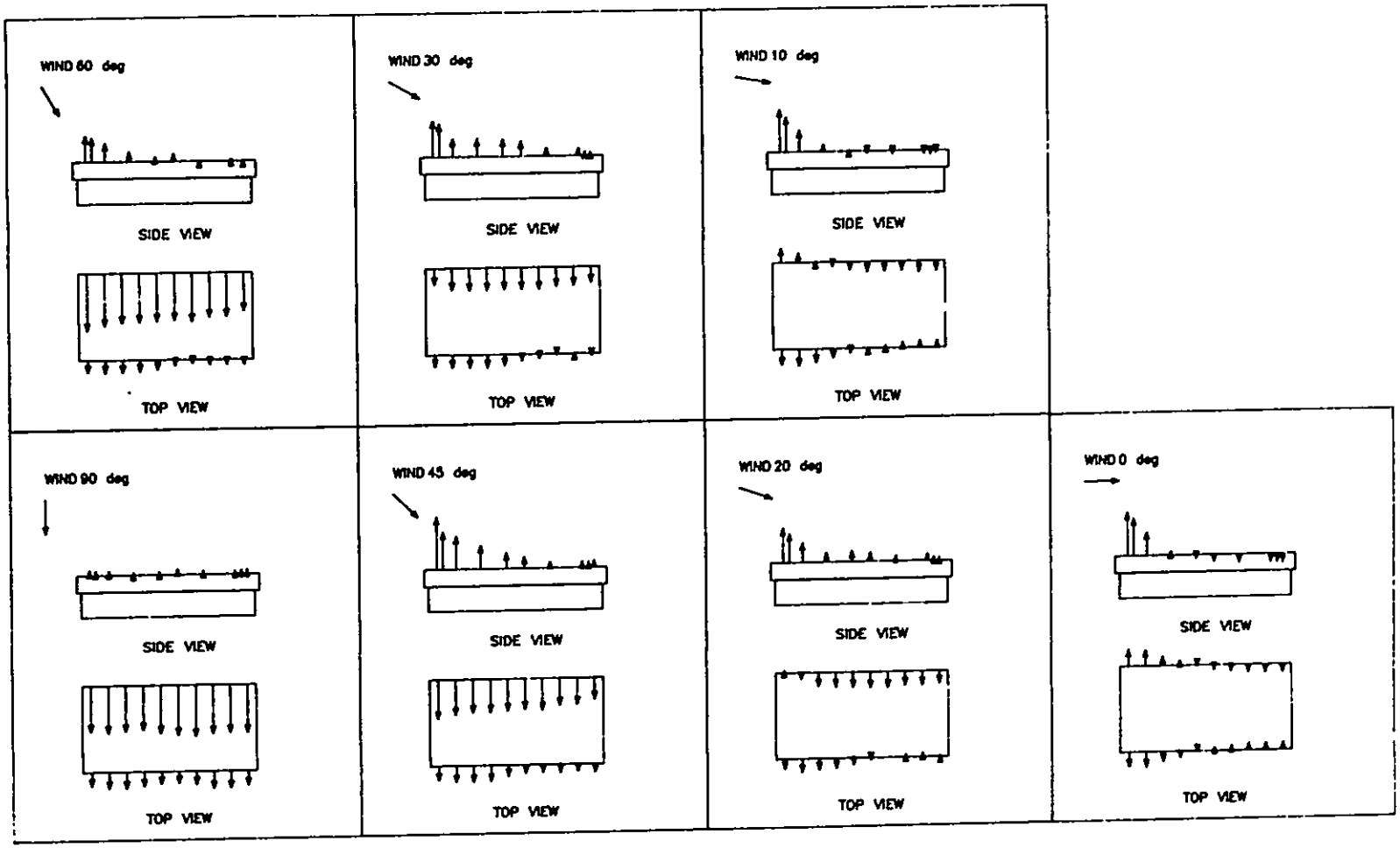

Figure K.5 ΔCps (in-out): open model, simulated 400 mm ridge and 800 mm sidewall openings, closed end walls, 7 wind angles of incidence.

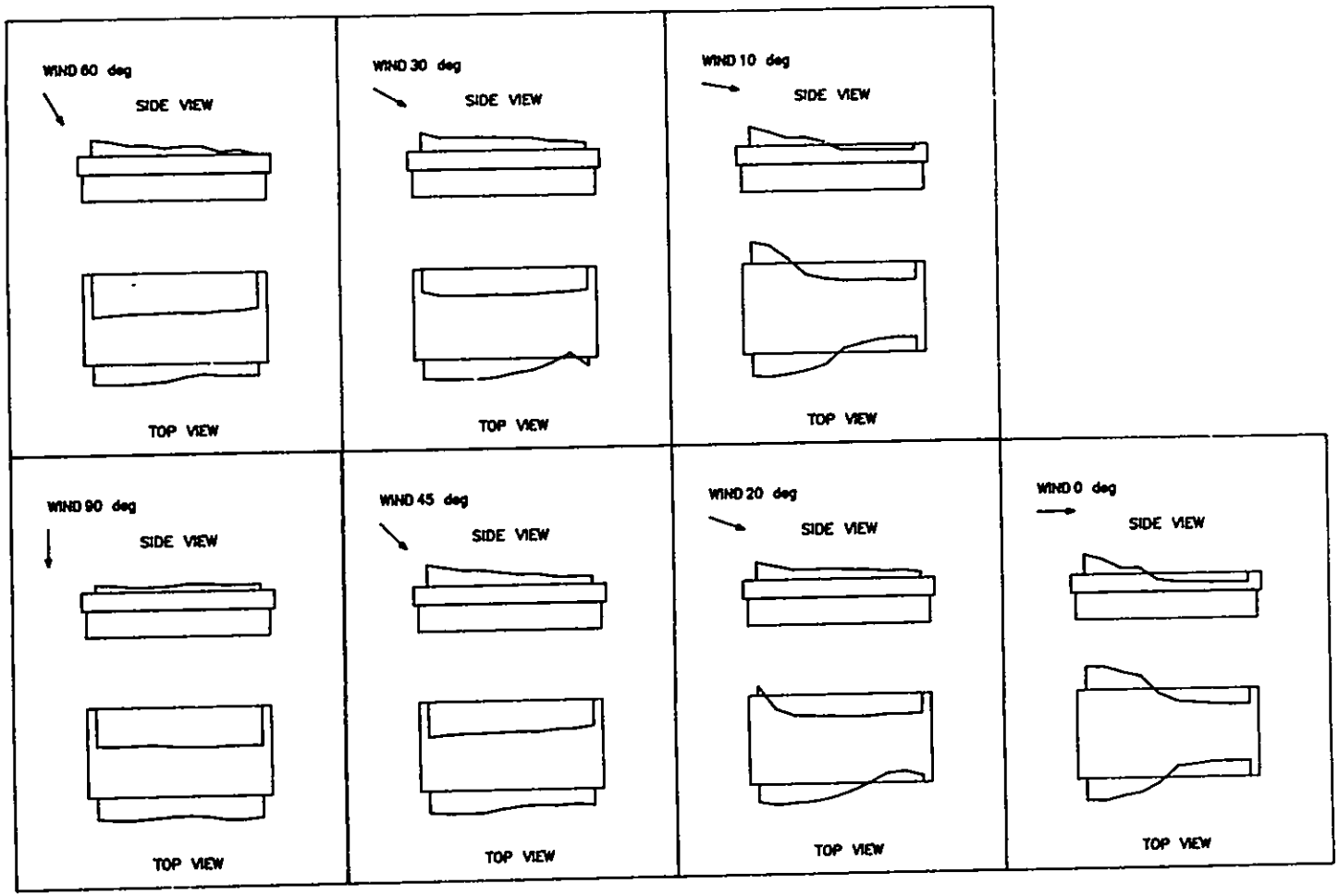

Figure K.6 Airflow diagrams: open model, simulated 400 mm ridge and 800 mm sidewall openings, closed end walls, 7 wind angles of incidence.

Table K.1 C_{q10} for open and sealed models.

Code	Angle	Cq open	Cq sealed	Cq(open-sealed)
150-1100-op	90	0.462789	0.431609	0.031180
	60	0.456046	0.406677	0.049370
	45	0.413956	0.386648	0.027309
	30	0.344391	0.328066	0.016326
	20	0.264446	0.289499	-0.025053
	10	0.229532	0.259394	-0.029862
	0	0.249713	0.262543	-0.012830
150-1100-cl	90	0.429472	0.397913	0.031559
	60	0.405475	0.377373	0.028102
	45	0.355589	0.336627	0.018963
	30	0.281691	0.283720	-0.002028
	20	0.204257	0.244031	-0.039774
	10	0.194083	0.221057	-0.026974
	0	0.199838	0.231714	-0.031876
150-800-op	90	0.482880	0.447723	0.035158
	60	0.481826	0.437076	0.044751
	45	0.444932	0.420071	0.024862
	30	0.383376	0.366196	0.017181
	20	0.311612	0.321185	-0.009572
	10	0.264277	0.286194	-0.021916
	0	0.273708	0.282904	-0.009195
150-800-cl	90	0.426760	0.409353	0.017408
	60	0.406734	0.391649	0.015085
	45	0.355059	0.347594	0.007465
	30	0.285925	0.302637	-0.016711
	20	0.221491	0.259684	-0.038192
	10	0.210089	0.229294	-0.019205
	0	0.220708	0.238133	-0.017425
400-1100-op	90	0.498525	0.457689	0.040837
	60	0.527410	0.480308	0.047103
	45	0.505996	0.469876	0.036121
	30	0.441833	0.402340	0.039494
	20	0.375173	0.343565	0.031608
	10	0.323609	0.292122	0.031487
	0	0.357209	0.290688	0.066521
400-1100-cl	90	0.488685	0.443265	0.045421
	60	0.473319	0.445653	0.027667
	45	0.443088	0.430815	0.012274
	30	0.365448	0.358251	0.007197
	20	0.304357	0.296461	0.007897
	10	0.292992	0.246830	0.046162
	0	0.319450	0.257921	0.061530
400-800-op	90	0.511935	0.492378	0.019558
	60	0.566803	0.564900	0.001903
	45	0.544713	0.549538	-0.004824
	30	0.520364	0.467046	0.053318
	20	0.441844	0.394272	0.047572
	10	0.376223	0.326299	0.049925
	0	0.406061	0.315160	0.090901

Table K.1 (cont.) C_{q10} for open and sealed models.

Code	Angle	Cq open	Cq sealed	Cq(open-sealed)
400-800-cl	90	0.499794	0.463349	0.036445
	60	0.497537	0.513131	-0.015593
	45	0.398504	0.487980	-0.089476
	30	0.322867	0.402278	-0.079411
	20	0.268254	0.330749	-0.062495
	10	0.245871	0.262656	-0.016785
	0	0.258406	0.278638	-0.020232
ch-1100-op	90	0.445240	0.437056	0.008185
	60	0.417043	0.388590	0.028454
	45	0.385891	0.365191	0.020700
	30	0.330528	0.311006	0.019522
	20	0.253414	0.262416	-0.009001
	10	0.217316	0.246709	-0.029392
	0	0.236947	0.256236	-0.019289
ch-1100-cl	90	0.389682	0.396381	-0.006698
	60	0.366405	0.361222	0.005183
	45	0.328062	0.321020	0.007042
	30	0.258720	0.256693	0.002027
	20	0.187933	0.214523	-0.026589
	10	0.187063	0.207551	-0.020488
	0	0.187961	0.222846	-0.034885
ch-800-op	90	0.460240	0.449922	0.010319
	60	0.431802	0.403888	0.027915
	45	0.408865	0.385973	0.022892
	30	0.350424	0.334395	0.016030
	20	0.295373	0.285436	0.009938
	10	0.248908	0.264570	-0.015662
	0	0.256760	0.273751	-0.016990
ch-800-cl	90	0.388548	0.399880	-0.011332
	60	0.367823	0.365476	0.002348
	45	0.328143	0.324899	0.003244
	30	0.266647	0.259047	0.007600
	20	0.203429	0.219912	-0.016483
	10	0.198378	0.210390	-0.012011
	0	0.201735	0.225670	-0.023935

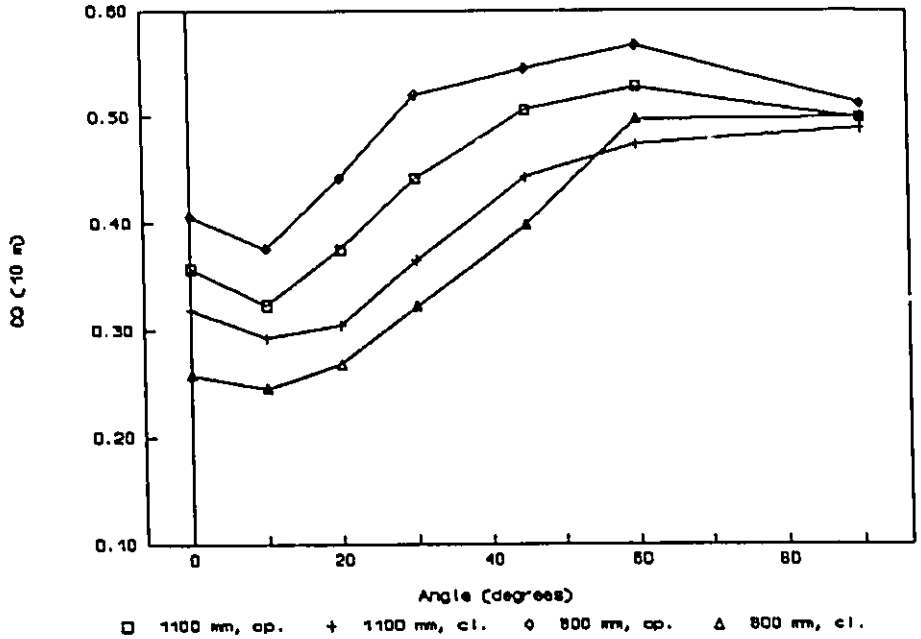

Figure K.7 Open model ventilation rate coefficients, C_{Q10}, simulated 400 mm ridge.

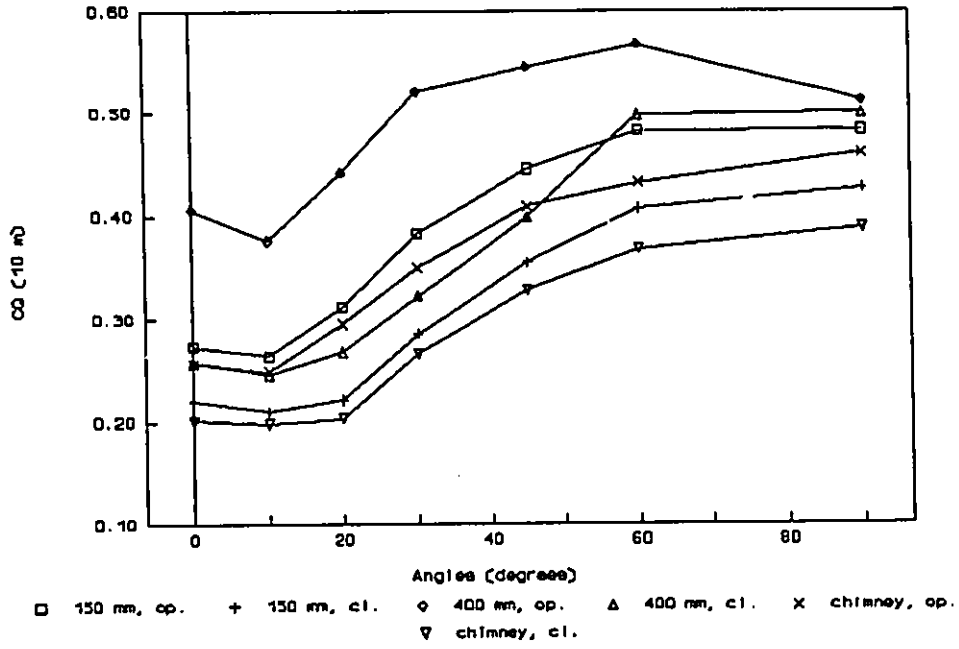

Figure K.8 Open model, comparison among chimney, simulated 150 mm and 400 mm ridges with simulated 800 mm sidewall.

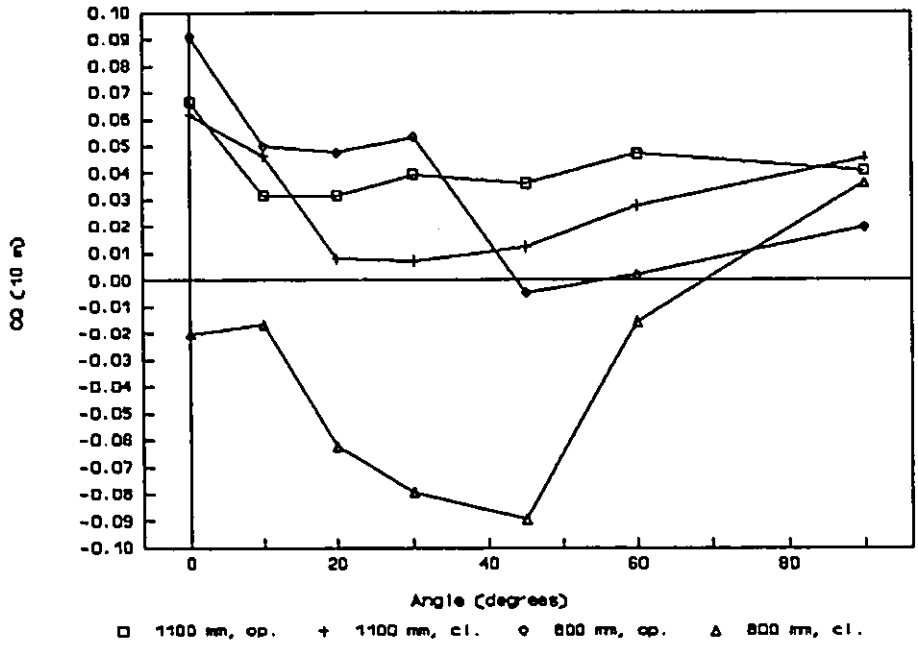

Figure K.9 C_{010} differences (open - sealed), simulated 400 mm ridge.

Table K.2 Differences between the measured C_{q10} (by concentration decay method) and the calculated C_{Q10} (by pressure difference method).

Description	Angle	Averaged CkQ 10	CQ 10 Open Model	CQ 10 Sealed Model	CkQ10-CQ10 Open	CkQ10-CQ10 Sealed
OP-150-1100-O	90	0.4351	0.4628	0.4316	-0.0277	0.0035
	60	0.4860	0.4560	0.4067	0.0299	0.0793
	45	0.5202	0.4140	0.3866	0.1063	0.1336
	30	0.4072	0.3444	0.3281	0.0628	0.0791
	20	0.2962	0.2644	0.2895	0.0317	0.0067
	10	0.2301	0.2295	0.2594	0.0006	-0.0293
	0	0.2212	0.2497	0.2625	-0.0285	-0.0413
OP-150-1100-C	90	0.4175	0.4295	0.3979	-0.0120	0.0196
	60	0.5859	0.4055	0.3774	0.1804	0.2085
	45	0.6223	0.3556	0.3366	0.2667	0.2856
	30	0.4002	0.2817	0.2837	0.1185	0.1165
	20	0.2517	0.2043	0.2440	0.0475	0.0077
	10	0.2308	0.1941	0.2211	0.0367	0.0098
	0	0.2721	0.1998	0.2317	0.0722	0.0404
OP-150-800-O	90	0.4779	0.4829	0.4477	-0.0050	0.0302
	60	0.4695	0.4818	0.4371	-0.0123	0.0324
	45	0.4314	0.4449	0.4201	-0.0136	0.0113
	30	0.3768	0.3834	0.3662	-0.0065	0.0107
	20	0.3317	0.3116	0.3212	0.0201	0.0105
	10	0.2736	0.2643	0.2862	0.0094	-0.0126
	0	0.2553	0.2737	0.2829	-0.0184	-0.0276
OP-150-800-C	90	0.4294	0.4268	0.4094	0.0027	0.0201
	60	0.5408	0.4067	0.3916	0.1341	0.1491
	45	0.5379	0.3551	0.3476	0.1829	0.1903
	30	0.3877	0.2859	0.3026	0.1018	0.0850
	20	0.3273	0.2215	0.2597	0.1058	0.0676
	10	0.2520	0.2101	0.2293	0.0419	0.0227
	0	0.2957	0.2207	0.2381	0.0750	0.0576
OP-400-1100-O	90	0.4132	0.4985	0.4577	-0.0853	-0.0445
	60	0.4676	0.5274	0.4803	-0.0598	-0.0127
	45	0.4818	0.5060	0.4699	-0.0242	0.0119
	30	0.3965	0.4418	0.4023	-0.0453	-0.0058
	20	0.3075	0.3752	0.3436	-0.0677	-0.0361
	10	0.2337	0.3236	0.2921	-0.0899	-0.0584
	0	0.2288	0.3572	0.2907	-0.1284	-0.0618
OP-400-1100-C	90	0.4018	0.4887	0.4433	-0.0869	-0.0414
	60	0.6347	0.4733	0.4457	0.1614	0.1890
	45	0.6343	0.4431	0.4308	0.1912	0.2035
	30	0.4542	0.3654	0.3583	0.0887	0.0959
	20	0.2560	0.3044	0.2965	-0.0484	-0.0405
	10	0.2365	0.2930	0.2468	-0.0565	-0.0103
	0	0.2941	0.3195	0.2579	-0.0253	0.0362

Table K.2 (cont.) Differences between the measured C_{KQ10} (by concentration decay method) and the calculated C_{Q10} (by pressure difference method).

Description	Angle	Averaged CkQ 10	CQ 10 Open Model	CQ 10 Sealed Model	CkQ10-CQ10 Open	CkQ10-CQ10 Sealed
OP-400-800-O	90	0.4523	0.5119	0.4924	-0.0597	-0.0401
	60	0.4656	0.5668	0.5649	-0.1012	-0.0993
	45	0.4768	0.5447	0.5495	-0.0679	-0.0728
	30	0.3793	0.5204	0.4670	-0.1410	-0.0877
	20	0.3134	0.4418	0.3943	-0.1284	-0.0808
	10	0.2511	0.3762	0.3263	-0.1251	-0.0752
	0	0.2654	0.4061	0.3152	-0.1406	-0.0497
OP-400-800-C	90	0.4193	0.4998	0.4633	-0.0805	-0.0440
	60	0.5566	0.4975	0.5131	0.0590	0.0434
	45	0.6365	0.3985	0.4880	0.1605	0.1485
	30	0.4377	0.3229	0.4023	0.1106	0.0354
	20	0.2634	0.2683	0.3307	-0.0165	-0.0674
	10	0.2931	0.2459	0.2627	0.0309	0.0304
	0	0.3497	0.2584	0.2786	0.0768	0.0711
OP-CH-1100-O	90	0.4077	0.4452	0.4371	-0.0376	-0.0294
	60	0.4661	0.4170	0.3886	0.0491	0.0775
	45	0.4628	0.3859	0.3652	0.0769	0.0976
	30	0.3565	0.3305	0.3110	0.0260	0.0455
	20	0.2638	0.2534	0.2624	0.0104	0.0014
	10	0.2110	0.2173	0.2467	-0.0064	-0.0358
	0	0.2113	0.2369	0.2562	-0.0257	-0.0450
OP-CH-1100-C	90	0.4065	0.3897	0.3964	0.0168	0.0101
	60	0.7613	0.3664	0.3612	0.3949	0.4001
	45	0.4611	0.3281	0.3210	0.1330	0.1401
	30	0.3266	0.2587	0.2567	0.0679	0.0699
	20	0.1771	0.1879	0.2145	-0.0108	-0.0374
	10	0.2044	0.1871	0.2076	0.0173	-0.0032
	0	0.2621	0.1880	0.2228	0.0741	0.0393
OP-CH-800-O	90	0.4464	0.4602	0.4499	-0.0138	-0.0035
	60	0.4318	0.4318	0.4039	-0.0000	0.0279
	45	0.5200	0.4089	0.3860	0.1111	0.1340
	30	0.3637	0.3504	0.3344	0.0133	0.0293
	20	0.3028	0.2954	0.2854	0.0075	0.0174
	10	0.2503	0.2489	0.2646	0.0014	-0.0142
	0	0.2293	0.2568	0.2738	-0.0275	-0.0445
OP-CH-800-C	90	0.4059	0.3885	0.3999	0.0174	0.0061
	60	0.5670	0.3678	0.3655	0.1992	0.2015
	45	0.4923	0.3281	0.3249	0.1641	0.1674
	30	0.3445	0.2666	0.2590	0.0779	0.0855
	20	0.2075	0.2034	0.2199	0.0041	-0.0124
	10	0.2239	0.1984	0.2104	0.0255	0.0135
	0	0.2878	0.2017	0.2257	0.0861	0.0621

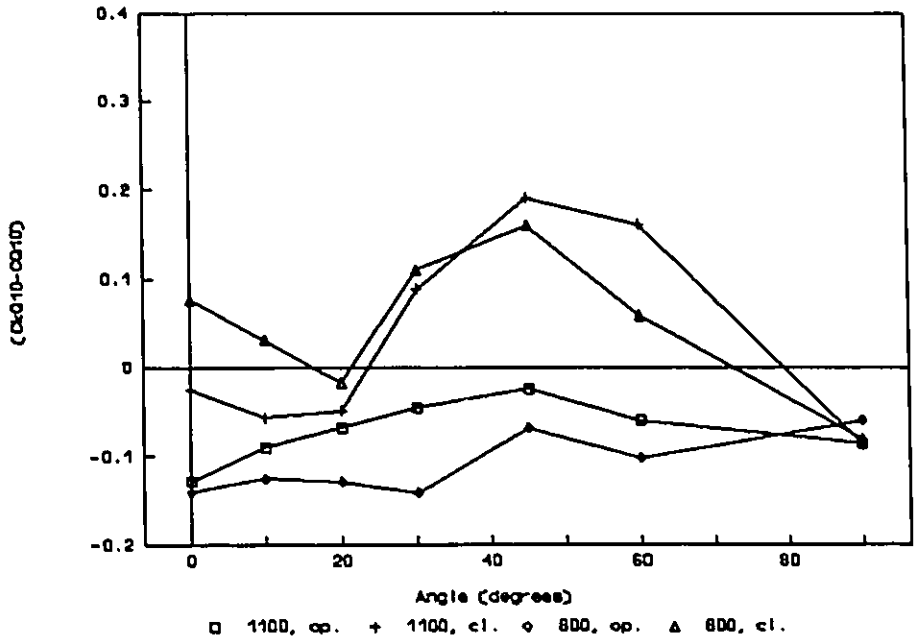

Figure K.10 400 mm ridge, differences between measured C_{KQ10} and calculated C_{Q10}.

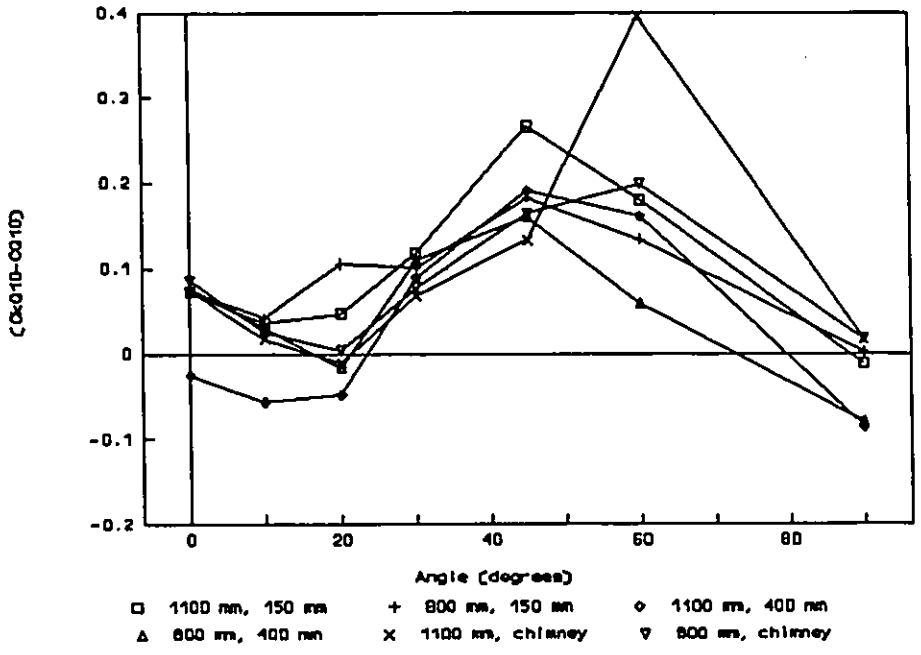

Figure K.11 Closed end walls, differences between measured C_{KQ10} and calculated C_{Q10} for 800 mm and 1100 mm sidewalls used with chimney, 150 mm and 400 mm ridges.